(ISSN 1411-9420 (print); 2460-1578 (online))

Indonesian Journal of Chemistry

Vol. 20, No. 2, April 2020

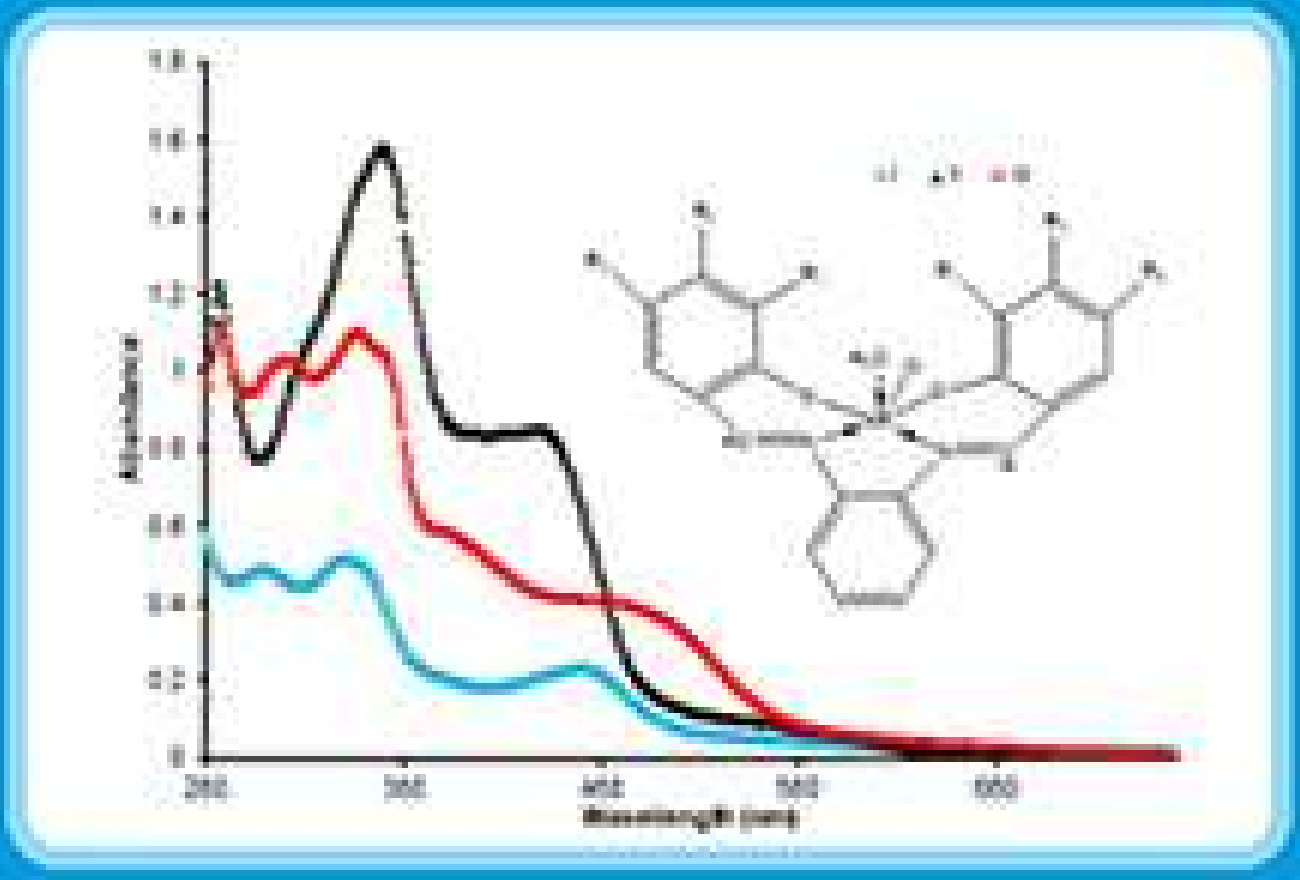

Accredited by RISTEKDIKTI
No. 21/E/KPT/2018

Indones. J. Chem | Vol. 20 | No. 2 | PP 257-492 | Yogyakarta April 2020 | (ISSN 1411-9420 (print) 2460-1578 (online))

Methyl-3-(2-hydroxy-5-nitrophenyl amino)-3-phenylpropanoate Based Colorimetric Sensor for Oxyanions

Venty Suryanti*, Fajar Rakhman Wibowo, and Sekar Handayani

Department of Chemistry, Faculty of Mathematics and Natural Sciences, Universitas Sebelas Maret, Jl. Ir. Sutami 36A, Surakarta 57126, Indonesia

** Corresponding author:*

email: venty@mipa.uns.ac.id

Received: October 10, 2018
Accepted: November 1, 2018

DOI: 10.22146/ijc.39559

Abstract: *A colorimetric anion sensor of methyl-3-(2-hydroxy-5-nitrophenyl amino)-3-phenylpropanoate bearing –OH and –NH groups as binding sites and nitrophenyl as a signaling unit, has been successfully accomplished. The compound functioned as a colorimetric chemosensor for $H_2PO_4^-$ and AcO^-, in particular, the sensor showed significant naked-eye detectable color change from colorless to light yellow. In contrast, no color change was detected upon addition of other anions such as SO_4^{2-}, NO_3^-, and ClO_4^-. The anion sensing ability of the sensor was further investigated by UV-Vis absorption spectroscopy in acetone. Characteristic UV-Vis spectra changes were revealed upon addition of $H_2PO_4^-$ and AcO^-.*

Keywords: *anion sensor; cinnamaldehyde; chemosensor; oxyanions*

■ INTRODUCTION

The development of colorimetric chemosensors capable of recognizing biologically important anions has received great attention. Molecules containing NH fragments, such as amines, amides, sulfonamides, ureas/thioureas, pyrroles/calixpyrrole, and imidazoliums groups have been widely used as binding sites for the detection of anions or toxic metal ions *via* hydrogen bonding interactions [1-4]. Likewise, compounds containing –OH group have been reported for colorimetric sensing of anions with successive color changes utilizing hydrogen-bonding ability of alcohol and phenolic -OH groups with different anions [5]. Chromogenic signaling units, such as a nitrophenyl group is frequently linked covalently to the sensor moiety. The presence of an electron-withdrawing nitro (NO_2) group enhances the acidity of the anion recognition moiety to the sensors, which enables the deprotonation of the hydrogen bond donor followed by the donation of the proton to the anions [6-9]. Suryanti et al. [10] have reported fluoride and cyanide anion sensors based on *N*-acetyl glyoxylic amides, which have two NH groups as anion binding sites and a nitrophenyl moiety as a signaling unit. These compounds also have been reported as a receptor for anions HSO_4^-, Cl^-, Br^- and NO_3^- [11].

Application of organic compounds as colorimetric chemosensors in biomedical and environmental sciences has been reported. A Schiff base derivative of cinnamaldehyde, 4-chloro-2-[(3-(4-(dimethylamino) phenyl)allyl-dene)amino]phenol, has been established as a colorimetric Ni^{2+} sensor in aqueous solution [12]. A cinnamaldehyde derivative, methyl-3-(2-hydroxy-5-nitrophenyl amino)-3-phenylpropanoate 4 has been prepared by a three-step synthetic reaction from cinnamaldehyde (Scheme 1) [13]. Cinnamaldehyde **1** was oxidized into cinnamic acid **2**, followed by esterification reaction with methanol to give methyl cinnamate **3**. The addition reaction of methyl cinnamate with 2-amino-4-nitrophenol produced compound **4**, which comprises amine and hydroxyl groups as anion binding sites and nitrophenyl moiety as a signaling unit. This compound was expected to bind to anions *via* strong hydrogen bond functionalities on amine and/or hydroxyl moiety. In this work, we report the colorimetric sensing of compound 4 towards a variety of oxyanions, such as $H_2PO_4^-$, AcO^-, SO_4^{2-}, NO_3^-, and ClO_4^-.

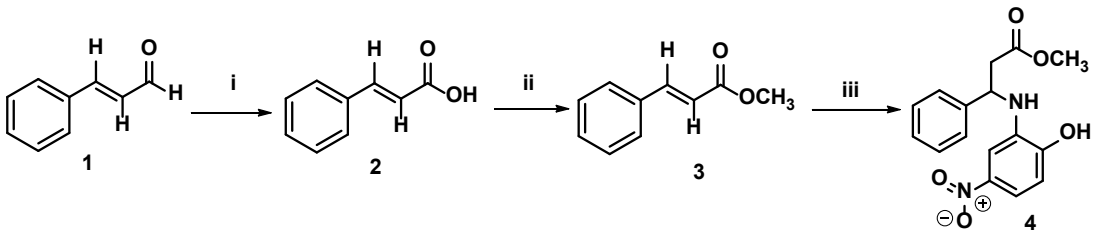

Scheme 1. Reagents and reactions: (i) $(C_2H_5)_2O$, H_2O, Polysorbate 20, CrO_3, 6 h, r.t. (ii) CH_3OH, *sat*. HCl, reflux, 6 h. (iii) CH_2Cl_2, reflux, 48 h

■ EXPERIMENTAL SECTION

Materials

All anions in the form of tetrabutylammonium salts were purchased from Sigma–Aldrich Chemical Company and used without further purification. All reagents and solvents employed were of analytical grade and also used without further purification.

Instrumentation

The UV-Vis spectra were recorded on a UV-Vis Shimadzu Lambda 25 spectrophotometer at room temperature. The ^{1}H NMR spectra were measured with an Agilent VNMR 400 MHz instrument at 25 °C. The ESI mass spectrum was recorded on a Waters LCT XE ESI-TOF.

Procedure

Synthesis of Methyl-3-(2-hydroxy-5-nitrophenylamino) -3-phenylpropanoate (4)

The synthesis of compound **4** was accomplished based on previously published procedures using cinnamaldehyde as a starting material [13]. The first step was the oxidation reaction of cinnamaldehyde **1** with chromium trioxide (CrO_3) in diethyl ether and water in the presence of polysorbate 20 as phase transfer catalyst to give cinnamic acid **2**. The reaction was then followed by esterification of the acid with methanol under reflux for 6 h in the presence of concentrated HCl. The last step was the reaction between 2-amino-4-nitrophenol with the ester **3** in dichloromethane under reflux for 48 h to give the compound **4**. This procedure gave compound **4** in 65% yields and m.p. 80 °C. ^{1}H NMR (400 MHz, CD_3OD): δ 3.62 (s, OCH_3, 3H), 6.51 (d, Ar-CHCH, *J*=16 Hz, 2H), 6.75 (m, Ar-CHCH, *J*=8.7 Hz, 1H), 7.37 (dd, 3 x Ar-H, *J*=10.9, 8.1 Hz, 3H), 7.50 (dd, *J*=10.9, 8.1 Hz, 1H), 7.56 (m, 3 x Ar-H, 3H), 7.67(m, Ar-H, 1H). MS (ESI-TOF) m/z calculated for $C_{16}H_{16}N_2O_5$ $(M-H)^-$ 315.3007. Found 315.3002.

Anion binding studies

A solution of compound **4** in acetone with a concentration of 10^{-5} M was added with 10^{-3} M oxyanion (as tetrabutylammonium salts) solution with variations amount of moles equivalent to compound **4** (0-10 moles equivalent). The resulting product was then analyzed by naked eye and characterization using UV-Vis spectroscopy.

Computational studies

The molecular structure of compound **4** which has the most stable conformation was reacted with AcO^- or $H_2PO_4^-$ ions. The interaction that occurs was calculated using ONIOM with the method HF/basis set 6-311G (d, p) as a low layer and the DFT/cc-PVDZ method as a high layer. The result was a log archive which was used for UV-Vis characterization.

Statistical Analysis

Experimental results were performed in triplicate, and the data were presented as mean ± SD. The results were compared by one-way ANOVA. The difference was considered as statistically significant if $p \leq 0.05$.

■ RESULTS AND DISCUSSION

Since protic solvents will compete with anions in forming hydrogen-bonding interaction with the sensor, the colorimetric sensing ability of compound **4** was performed in aprotic solvents, such as acetone. The anions were added as their tetrabutylammonium salts to compound 4 solutions (1×10^{-5} M). The visible color

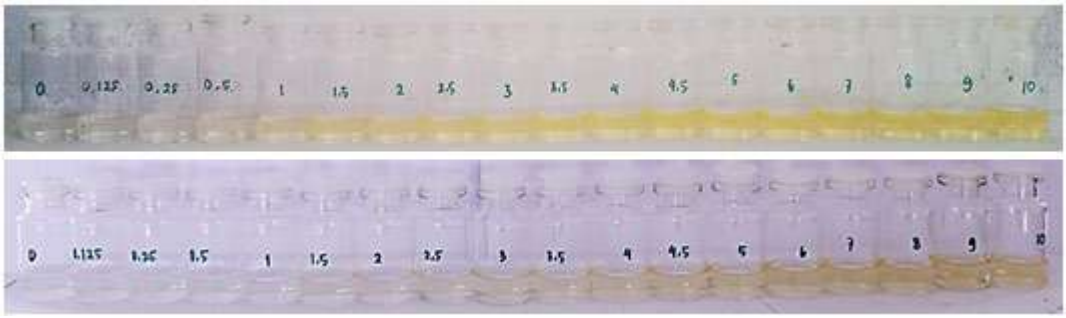

Fig 1. Color changes observed for compound **4** in acetone upon addition of the anions as TBA salts: $H_2PO_4^-$ (upper) and AcO^- (lower)

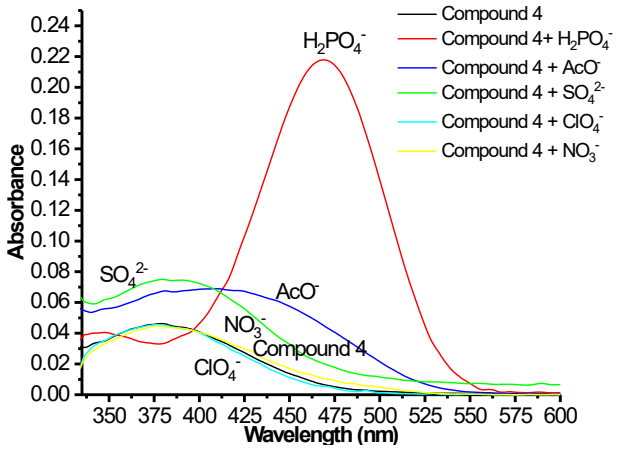

Fig 2. The absorption spectra of compound **4** (1×10^{-5} M) in acetone solution upon addition of 4 eq. of anions as TBA salts, such as $H_2PO_4^-$, AcO^-, SO_4^{2-}, NO_3^-, and ClO_4^-

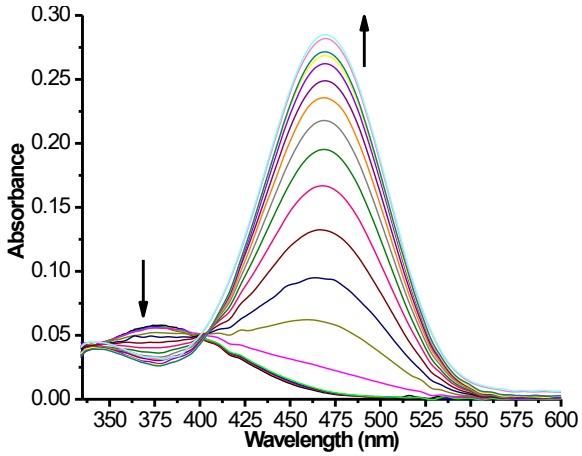

Fig 3. The absorption spectra of compound **4** (1×10^{-5} M) in acetone solution upon the addition 0-10 eq. of tetrabutylammonium dihydrogen phosphate

and the UV-Vis spectral changes towards anions were studied. Since peaks of protons from –OH and –NH groups did not appear in ^{1}H NMR spectra, the colorimetric sensing ability of sensor **4** was not monitored by ^{1}H NMR Spectroscopy.

Visual Color Change Observation

A solution of compound **4** changed from colorless to faint yellow upon the addition of 1 eq. of $H_2PO_4^-$ or 2.0 eq. of AcO^-. The coloration of the solution was intensified with increasing anions concentration. The color changes of compound **4** upon the addition of $H_2PO_4^-$ or AcO^- ions were detected by the naked eye. The representative photographs showing the color change of solutions of compound **4** by $H_2PO_4^-$ or AcO^- ions are shown in Fig. 1. Under similar experimental conditions, the addition of SO_4^{2-}, NO_3^- or ClO_4^- to the solution of compound **4** did not exhibit any naked-eye detectable color change.

Anion Recognition Studies by UV-Vis Spectroscopy and Computational Methods

As preliminary studies, the spectroscopic behaviors of compound **4** in acetone were investigated upon addition 4 eq. of various anions, such as $H_2PO_4^-$, AcO^-, SO_4^{2-}, NO_3^-, and ClO_4^-. One characteristic absorption peak for UV–Vis spectra of compound **4** was observed at 379 nm in the absence of anions. As shown in Fig. 2, compound **4** reveals insignificant perturbation upon addition of 4 eq. of NO_3^- and ClO_4^-. In contrast, significant UV-Vis absorption spectra changes were noticed in the presence of $H_2PO_4^-$ where the absorption band at 379 nm disappeared, and a new absorption band

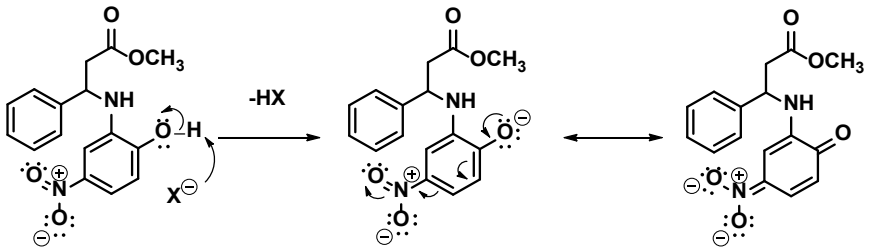

Scheme 2. Resonance structure of the deprotonated form of compound **4**

appeared at 475 nm. In the presence of AcO^-, the absorption peak at 379 nm moved to 456 nm. Meanwhile, the UV-Vis absorption spectra increased upon addition of 4 eq. of SO_4^{2-}. The sensing abilities of the sensor towards $H_2PO_4^-$, AcO^- and SO_4^{2-} were then studied by UV-Vis titration experiments.

The UV-Vis absorption spectra changes were obtained upon addition of increasing amount of $H_2PO_4^-$ ions to the acetone solution of sensor **4** (Fig. 3). The absorption peak at 379 nm gradually decreases its intensity, and a strong absorption peak gradually appeared at 469 nm. These new absorption peaks existed upon addition of 1 eq. of $H_2PO_4^-$. Furthermore, the color change from colorless to faint yellow could be detected by naked eye for the solution of compound 4 along with the addition of $H_2PO_4^-$ ions. A clear isosbestic point at 401 and 402 nm was observed during the titration process between the compound **4** and $H_2PO_4^-$ ion, respectively. The development of new bands and the presence of a clear isosbestic point can be explained by initial hydrogen bond formation between $H_2PO_4^-$ and NH and OH groups followed by deprotonation which subsequent intramolecular charge-transfer (ICT) transitions within the whole structure of the sensor **4** (Fig. 4 and Scheme 2) [14-15].

A similar phenomenon of UV–Vis absorption was also observed upon addition of AcO^- to a solution of compound 4 (Fig. 5). As the concentration of AcO^- was increased, the absorption peak at 379 nm disappeared while a new absorption peak at 456 nm developed. This new absorption peak appeared upon addition of 2 eq. of AcO^-. These spectral characteristics were also accompanied by a visual color change of the solution from colorless to faint yellow upon addition of AcO^-. These

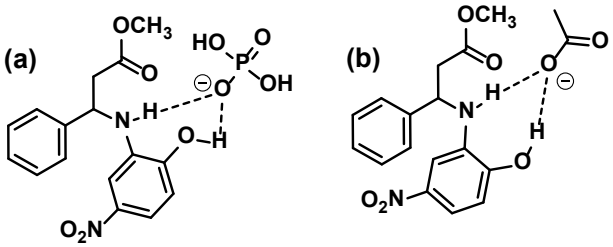

Fig 4. Proposed initial hydrogen bonding interactions between compound **4** and $H_2PO_4^-$ (a) or AcO^- (b)

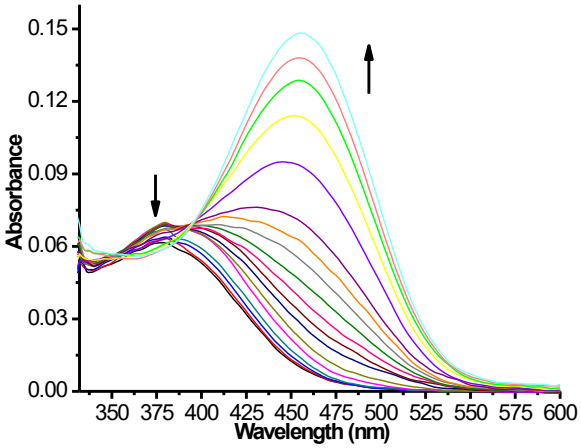

Fig 5. The absorption spectra of compound **4** (1×10^{-5} M) in acetone solution upon the addition 0-10 eq. of tetrabutylammonium acetate

results suggest that AcO^- initially formed hydrogen bonding interactions with sensor **4**, followed by deprotonation of compound **4** upon further addition of AcO^- with the subsequent ICT transitions within the entire structure of the compound **4** (Fig. 4 and Scheme 2) [16]. However, an approximate isosbestic point at 392 nm was observed during the titration process, indicating that deprotonation was not complete and the hydrogen-bonded complex and the deprotonated compound **4** were both existed.

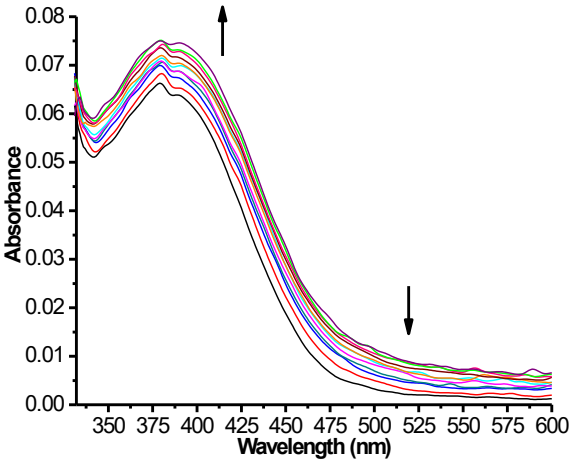

Fig 6. The absorption spectra of compound **4** (1×10^{-5} M) in acetone solution upon the addition 0-10 eq. of tetrabutylammonium sulphate

The possibility of deprotonation occurs in –OH proton because the electronegativity of oxygen atom is greater than that of nitrogen atom so that the partial positive charge of hydrogen atom will be more easily removed from the oxygen atom compared to the nitrogen atom. The –OH proton (the partial positive charge) interacts strongly with oxyanion (a negative charge). In addition, -OH group also facilitates the withdrawal of electrons by NO_2 groups. Consequently, the hydrogen atom is easily separated from the oxygen atom. The loss of the –OH proton causes electron delocalization in the structure of compound **4** to a more stable form (Fig. 4).

Under similar experimental conditions, increasing of UV-Vis absorption spectra were found in the addition of less basic anion such as SO_4^{2-} (Fig. 6). However no changes in absorption peaks of UV-Vis spectra. These findings implied that SO_4^{2-} formed weak hydrogen bonding interactions with compound **4**, which was not able to pursue deprotonation of compound **4**. Hence, no visible color changes were observed. On the contrary, the addition of weakly basic anions such as NO_2^- and ClO_4^- did not show any noticeable spectra or color changes which suggest no interaction or complexation of these anions with compound **4**.

Computational data revealed that the UV-Vis spectrum of compound **4** gave an absorption peak in the wavelength of 306.35 nm. The interaction of compound **4** with anions causes a shift in the wavelength to 544.34 and 560.11 nm for AcO^- and $H_2PO_4^-$, respectively. The UV-Vis spectra resulting from the interaction of compounds **4** with AcO^- and $H_2PO_4^-$ oxyanion caused a longer (bathochromic) wavelength shift. This indicates that an electronic structure of compound **4** changes due to conformational changes due to the addition of AcO^- and $H_2PO_4^-$ to receptor compounds. The UV-Vis spectra shift since the presence of oxyanion is related to the formation of hydrogen bonds and/or deprotonation between the ions with the protons of -NH and -OH groups which causes a decrease in energy for electronic transition through delocalization.

In the experiment data, the interaction of receptor compounds with anions causes a shift in the wavelength to 410 and 475 nm for AcO^- and $H_2PO_4^-$, respectively. The wavelength difference occurred in the experiment with the theory from computational data was related to the difference in oxyanion used. The wavelengths that have been produced experimentally and the theory have the corresponding results where the addition of AcO^- and $H_2PO_4^-$ oxyanions can shift the wavelength towards the visible area.

Compounds **4** were selective for $H_2PO_4^-$ and AcO^- over other oxyanions such as SO_4^{2-}, NO_3^-, and ClO_4^-. This can be explained by basicity and/or the hydrogen bonding ability of the anions. Among the tested oxyanions, the order of basicity of oxyanions was $AcO^- > H_2PO_4^- > SO_4^{2-} > NO_3^- > ClO_4^-$. As the basicity and hydrogen bonding ability of $H_2PO_4^-$ and AcO^- are higher than that of the rest of the tested anions, they provide strong hydrogen bonding interactions and undergo deprotonation reactions with compound **4** [17-18]. Meanwhile, SO_4^{2-} established weak hydrogen bonding interactions with compound **4**, which was not able to undertake deprotonation reactions. Conversely, the weakly basic anions such as NO_3^- and ClO_4^- were unable to establish hydrogen bonding interactions nor deprotonation reactions.

Interestingly, the deprotonation of compound **4** took place at higher concentrations of AcO^- than that of $H_2PO_4^-$. This was an unexpected result as the AcO^- has higher basicity than that of $H_2PO_4^-$ which should have considered greater hydrogen bond donor capacity to the

NH and/or OH groups. The selectivity of the anions toward sensor **4** can be explained on the degree of shape complementarity between the host and anionic guests. Thus, sensor **4** employs better affinities for $H_2PO_4^-$ with tetrahedral geometry than that of AcO^- with planar Y-shaped geometry [19-20].

■ CONCLUSION

We have developed a novel colorimetric sensor **4** based on an organic compound from cinnamaldehyde containing NH and OH groups as binding sites and a nitrophenyl moiety as a signaling unit. Compound **4** was selective for $H_2PO_4^-$ and AcO^- over other examined oxyanions. Both anions exhibited hydrogen bonding interactions with the compound **4** and induced deprotonation of the sensor **4**. The subsequent intramolecular charge-transfer transitions of the compound **4** then occurred resulting in the visible color and the UV–Vis spectra changes. However, the sensor **4** showed better affinities for tetrahedral geometry of $H_2PO_4^-$ than that of Y-shaped geometry of AcO^-. These results showed that the organic compound based cinnamaldehyde derivative could provide a very important application in anion recognition and sensing of chemical, environmental and biological systems.

■ ACKNOWLEDGMENTS

The authors acknowledge their thanks to Universitas Sebelas Maret and Ministry of Research, Technology and Higher Education Indonesia for the financial support of this research.

■ REFERENCES

[1] Esteban-Gómez, D., Fabbrizzi, L., and Licchelli, M., 2005 Why, on interaction of urea-based receptors with fluoride, beautiful colors develop, *J. Org. Chem.*, 70 (14), 5717–5720.

[2] Amendola, V., Esteban-Gomez, D., Fabbrizzi, L., and Licchelli, M., 2006 What anions do to N-H containing receptors, *Acc. Chem. Res.*, 39 (5), 343–353.

[3] Ahmad, I., Sharma, A., and Ghosh, T., 2012, Selective colorimetric sensing of CN^- by dihydropyrazol-3-ol derivative in CH_3CN/H_2O medium, *Supramol. Chem.*, 24 (4), 221–227.

[4] Erdemir, S., Kocyigit, O., Alici, O., and Malkondu, S., 2013, Naked-eye detection of F^- ions by two novel colorimetric receptors, *Tetrahedron Lett.*, 54 (7), 613–617.

[5] Gale, P.A., 2010, Anion receptor chemistry: Highlights from 2008 and 2009, *Chem. Soc. Rev.*, 39 (10), 3746–3771.

[6] Gale, P.A., Navakhun, K., Camiolo, S., Light, M.E., and Hursthouse, M.B., 2002, Anion-anion assembly: A new class of anionic supramolecular polymer containing 3,4-dichloro-2,5-diamido-substituted pyrrole anion dimers, *J. Am. Chem. Soc.*, 124 (38), 11228–11229.

[7] Gunnlaugsson, T., Kruger, P.E., Jensen, P., Pfeffer, F.M., and Hussey, G.M., 2003, Simple naphthalimide based anion sensors: deprotonation induced colour changes and CO_2 fixation, *Tetrahedron Lett.*, 44 (49), 8909–8913.

[8] Boiocchi, M., Del Boca, L., Gómez, D.E., Fabbrizzi, L., Licchelli, M., and Monzani, E., 2004, Nature of urea-fluoride interaction: incipient and definitive proton transfer, *J. Am. Chem. Soc.*, 126 (50), 16507–16514.

[9] Park, J.J., Kim, Y.H., Kim, C., and Kang, J., 2011, Fine tuning of receptor polarity for the development of selective naked eye anion receptor, *Tetrahedron Lett.*, 52 (26), 3361–3366.

[10] Suryanti, V., Bhadbhade, M., Chawla, H.M., Howe, E., Thordarson, P., Black, D.S., and Kumar, N., 2014, Novel colorimetric anion sensors based on *N*-acetylglyoxylic amides containing nitrophenyl signalling units, *Spectrochim. Acta, Part A*, 121, 662–669.

[11] Suryanti, V., Bhadbhade, M., Black, D.S., and Kumar, N., 2017, *N*-acetylglyoxylic amide bearing a nitrophenyl group as anion receptors: NMR and X-ray investigations on anion binding and selectivity, *J. Mol. Struct.*, 1146, 571–576.

[12] Peralta-Domínguez, D., Rodríguez, M., Ramos-Ortíz, G., Maldonado, J.L., Meneses-Nava, M.A., Barbosa-García, O., Santillan, R., and Farfán, N.,

2015, A Schiff base derivative from cinnamaldehyde for colorimetric detection of Ni^{2+} in water, *Sens. Actuators, B*, 207, 511–517.

[13] Suryanti, V., Wibowo, F.R., Pranoto, Isnaeni, S.R., Sari, M.R.K., and Handayani, S., 2016, Addition reaction of methyl cinnamate with 2-amino-4-nitrophenol, *IOP Conf. Ser. Mater. Sci. Eng.*, 107, 012062.

[14] Lin, T.P., Chen, C.Y., Wen, Y.S., and Sun, S.S., 2007, Synthesis, photophysical, and anion-sensing properties of quinoxalinebis(sulfonamide) functionalized receptors and their metal complexes, *Inorg. Chem.*, 46 (22), 9201–9212.

[15] Lv, Y., Wei, W., and Xie, Y., 2015, A BODIPY-phenol-based sensor for selectively recognizing three basic anions, *J. Chil. Chem. Soc.*, 60 (1), 2843–2846.

[16] Yen, Y.P., and Ho, K.W., 2006, Synthesis of colorimetric receptor for dicarboxylate anions: A unique color change for malonate, *Tetrahedron Lett.*, 47 (7), 1193–1196.

[17] Amendola, V., Boiocchi, M., Fabbrizzi, L., and Palchetti, A., 2005, Anion receptors containing -NH binding sites: Hydrogen-bond formation or neat proton transfer?, *Chem. Eur. J.*, 11 (1), 120–127.

[18] Amendola, V., Bergamaschi, G., Boiocchi, M., Fabbrizzi, L., and Milani, M., 2010, The squaramide versus urea contest for anion recognition, *Chem. Eur. J.*, 16 (14), 4368–4380.

[19] Jia, C., Wu, B., Li, S., Yang, Z., Zhao, Q., Liang, J., Li, Q.S., and Yang, X.J., 2010, A fully complementary, high-affinity receptor for phosphate and sulfate based on an acyclic tris(urea) scaffold, *Chem. Commun.*, 46 (29), 5376–5378.

[20] Makuc, D., Hiscock, J.R., Light, M.E., Gale, P.A., and Plavec, J., 2011, NMR studies of anion-induced conformational changes in diindolylureas and diindolylthioureas, *Beilstein J. Org. Chem.*, 7, 1205–1214.

Conformational and Topology Analysis of Diphenylthiourea and Diarylhalidethiourea Compounds Using DFT

Nur Najwa-Alyani Mohd Nabil[1] and Lee Sin Ang[2,*]

[1]*Fakulti Sains Gunaan, Universiti Teknologi MARA, 40450 Shah Alam, Selangor Darul Ehsan, Malaysia*

[2]*Fakulti Sains Gunaan, Universiti Teknologi MARA, Cawangan Perlis, Kampus Arau, 02600 Arau, Perlis Indera Kayangan, Malaysia*

Corresponding author:

email: anglee631@perlis.uitm.edu.my

Received: November 9, 2018
Accepted: January 11, 2019

DOI: 10.22146/ijc.40663

Abstract: *The disubstituted thiourea compounds have shown its reliability on their usages in various industries compared to the thiourea compounds. However, they also show capability to exist in different configurations, which would render them to possess different properties and hence affect their usability by unsuspected users. In this study, investigation was carried out on the polymorphism of five disubstituted thiourea compounds in which the phenyl rings and arylhalide acted as substituents. Using the B3LYP/DEF2–TZVP model chemistry with D3–BJ and gCP correctional schemes, the energetic analysis on the possible structural arrangements of the compounds was performed. The topology analysis of non-covalent interaction and electrostatic potential surfaces was used for understanding the interaction and reactivity of the constitute molecules of the compounds. Energetic results show that for all interested compounds, CT and TT configurations may coexist. Between the two types of substituents, phenyl substituted molecules are more flexible with better capability to be nucleophilic compounds. On the other hand, the arylhalide substituted molecules form better electrophilic compounds. The reactive sites of the molecules rotated to the stable new configurations are similar to the molecules in their original configurations observed from experiments.*

Keywords: *conformational analysis; topology analysis; thiourea substituent compounds; density functional theory*

■ INTRODUCTION

Thiourea molecules have three potential coordination sites: the sulphur of thiourea moiety (S_T) and the two nitrogen atoms of the NH group. One of the thiourea derivatives, the symmetrically disubstituted thioureas, which have the form RHN–(C=S)–NHR' where R=R', have received much interest due to their diverse applications in medicine, agriculture, and chemical industries [1-5]. In addition, disubstituted thioureas are known to form stable, neutral coordination compounds with various transition metal ions [6].

This study focusses on five disubstituted thiourea compounds, as listed in Table 1. Two types of substituents were considered, namely phenyl rings and arylhalides. The phenyl substituted (Ph) compounds are labelled as Ph-1, 2, 3 and 4 to indicate compounds from different works. For arylhalide substituted (Ah) compounds, Ph-F, Ph-Cl and Ph-Br were considered, indicating attachment of fluorine, chlorine and bromine atoms to the phenyl ring. The attachment of the halogens at the ortho- and the para- site to the phenyl ring (as shown in Fig. 1) is appended with o- and p-, respectively. Experimentally, for these compounds, the structural arrangements of the molecules are shown to have preference towards the trans-trans (TT) and cis-trans (CT) configurations. As shown in Table 1, there is no connection between the crystal system and occurrence of TT or CT configurations. Thus, all these compounds show unrelated relationship of the configuration, crystal system and type of substituent. It has to be mentioned that

Table 1. List of the phenyl and arylhalide substituted compounds considered in this study

No.	Compound	Original configuration of the molecules	Crystal system	Substituent
1	1,3-diphenylthiourea ($C_{13}H_{12}N_2S_1$) [7-8] (*)	TT	orthorhombic	Ph–1
		CT	monoclinic	Ph–2
		TT	orthorhombic	Ph–3
		TT	orthorhombic	Ph–4
2	1,3-bis(4-fluorophenyl)thiourea ($C_{13}H_{10}F_2N_2S_1$) [9]	TT	orthorhombic	Ph–F–p
3	1,3-bis(4-chlorophenyl)thiourea ($C_{13}H_{10}N_2S_1$) [10-11]	TT	orthorhombic	Ph–Cl–p–1
		TT	monoclinic	Ph–Cl–p–2
4	1,3-bis(4-bromophenyl)thiourea ($C_{13}H_{10}Br_2N_2S_1$) [12]	TT	monoclinic	Ph–Br–p
5	1,3-bis(2-chlorophenyl)thiourea ($C_{13}H_{10}Cl_2N_2S_1$) [13-14]	CT	orthorhombic	Ph–Cl–o–1
		TT	monoclinic	Ph–Cl–o–2

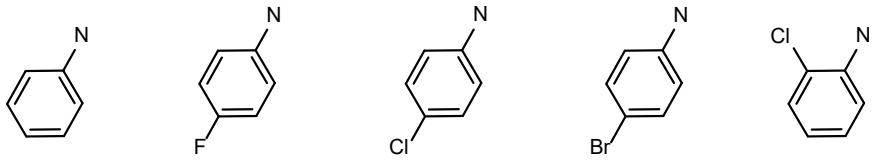

Ph Ph–F–p Ph–Cl–p Ph–Br–p Ph–Cl–o

Fig 1. The molecular structure of the arylhalide substituent compounds

cis-cis (CC) configuration is conspicuously missing in Table 1 as it is not found to be favorable for these thiourea derivatives.

The existence of the same compounds with different stable configurations (CT and TT, shown in Table 1) as found from the experiments rendered the compounds conformationally polymorphic. In general, polymorphic compounds with different structural arrangements, would lead to different properties of the compounds due to the different intra– and intermolecular interaction. For the compounds considered in this study, those in TT configuration always have the molecules stack in head-to-tail to form zigzag tapes. It involves twin NH···S_T contacts of 2.50 to 2.70 Bohr [7-12,14]. The NH···S_T contact can be interpreted as hydrogen-bonding interactions to a bifurcated sulphur acceptor. It is similar in the TT configuration of the arylhalide compounds as the NH··· S_T hydrogen bonds are known as a characteristic part of the solid-state assembly of thiourea molecules [15]. The head-to-tail orientation is common for TT configuration as dimer aromatic rings are favored to be in T-shaped (90° angle between dimer) or slipped parallel [16]. However, for CT configuration compounds, centrosymmetric orientation is shown with one NH···S_T interaction with opposite substituents away from the thiourea moiety.

This work is carried out to study the polymorphic phenomenon of the Ph- and Ah-substituted thiourea compounds. It is aimed to find the effect of different configurations to the properties of the molecules without changing the intermolecular hydrogen bonding and geometry of the molecules. Changing the entire geometry of the molecule to the minimum forces would exchange the real crystal structure of the molecules and lose the effect of the configuration changes. The addition of the halogens to the phenyl ring at different sites may alter the intra- and intermolecular interactions significantly, resulting in configurations that are stable but yet-to-be-found from experiments. Furthermore, the electronic properties of the compounds in the gaseous state of monomer and dimer systems would also be investigated, as to provide insights to alterations in the properties between the original and predicted configurations.

■ COMPUTATIONAL METHODS

The geometries of interested compounds, taken from Cambridge Structural Database (CSD), were all fixed with rotation only along the C–N bond between the thiourea moiety and its substituents. Avoiding the geometry changes will preserve the interaction for the parts not affected by the rotation (as obtained from experimental studies). The cis- (C) and trans- (T) orientations referred in the following sections are based on the relative orientation of the hydrogen to the sulphur in each conformer as depicted in Fig. 2. For the calculations of the dimer systems, the same sides of each molecule were rotated simultaneously.

The calculations were carried out using the Gaussian 09 suite of programs [17]. Previous electronic properties study on the other thiourea derivative molecules was proved reliable using B3LYP [18]. Thus, the single point calculations were performed at B3LYP level of theory with the DEF2-TZVP as the basis set. Previous study had suggested that DEF2-TZVP offers a good balance between accuracy and performance for molecules [19-20]. At DFT level, DEF2-TZVP basis is proved to be able to achieve results that are almost similar to the DEF2-QZVP [21]. It is also performed well when combined with DFT method [22-23]. However, due to the lack in describing the dispersion, D3-BJ [24] correctional scheme is included in this study. To verify the stability of the method, calculations were performed on the S66 dataset using Cuby4 [25] interfaced with Gaussian 09 [17]. The RMSE obtained is 0.71 kcal/mol. Comparing to the previous study reported by Jan Rezac [26], other methods, i.e. methods MP2/TZ and CCSD/CBS also have similar RMSE energy. Thus, method used in this study is sufficient to be used for the interested compound. For dimers, gCP scheme is included to reduce the basis set superposition error [27]. The total energy is then given as:

$$E_T = E_{SCF} + E_{D3-BJ} + E_{gCP} \quad (1)$$

where E_T is the total energy of the cluster, which is the sum of self-consistent field energy E_{SCF}, corrective energies of dispersion E_{D3-BJ} and counterpoise correction of gCP, E_{gCP}. The relative energy is then used to compare the stability between two different configurations.

Another energy analysis used to study the stability of compounds is by using the interaction energy of the dimers. Interaction energy is caused by interaction of both monomers to form the compound [28]. The positive energy shows the repulsive interaction while the negative shows the attractive interactions.

Topology analysis were performed to complement the energetic results. The non-covalent interaction (NCI) using the reduced density gradient (RDG) was performed using the Multiwfn software [29]. The results are shown through the visual molecular dynamics program (VMD) [30]. The 3D NCI isosurface of a compound is colored according to the corresponding values of sign(λ_2)ρ (shown in Fig. 3). It is an indicator of the types of interactions. For this study, the Blue-Green-Red (BGR) scheme was used where blue indicates bonding interaction, green is of vdW and red indicates non-bonding interactions. 0.3 au isosurface cutoff and color scale of $-0.04 < \rho < 0.02$ were used for this study. These quantities were proved to encapsulate the noncovalent interaction region of interest [31].

The further studies on the reactivity of the compounds were performed using the electrostatic potential (ESP) surfaces. For this study, the color range of red-green-blue (RGB) was used. Red and blue indicate

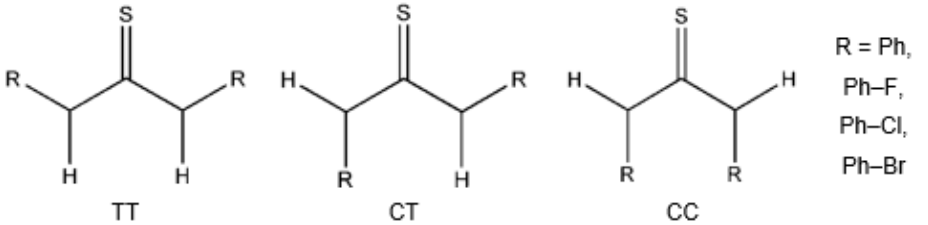

Fig 2. The conformers of the diphenylthiourea and arylhalide thiourea compounds

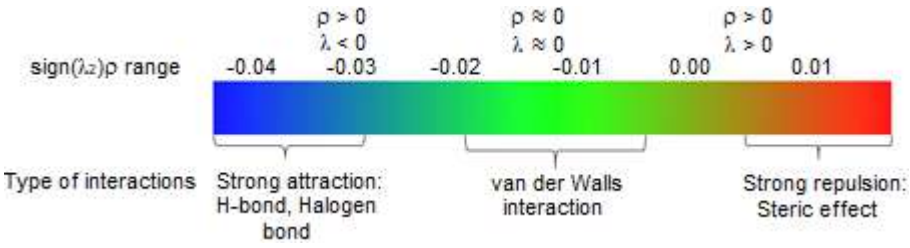

Fig 3. The range of color for the NCI isosurfaces

electron abundance (most negative sites) and depletion (most positive sites) respectively while green color indicates uniform electron distribution. Preferable isosurface of 0.001 au is used in this study as it shows the surface lies beyond the van der Waals radii [32]. The ESP surfaces was post-processed using the Gauss View program [33].

■ RESULTS AND DISCUSSION

Stability Analysis

For the energetic analysis, as tabulated in Table 2, it can be seen that CT configuration is the most preferable configuration, followed by TT configuration. Both of these configurations are the low-energy conformation with relative energy range from 0.1 to 0.2 eV. The CC configuration is the least preferable configuration with high relative energy (between 3.4 to 7.2 eV). This observation can be related to the results from the experiments where only polymorphs in TT and CT configurations were obtained. CT configuration is preferable as it had delocalization between the substituent with the thiourea moiety. The TT configuration are less preferable from the steric repulsive of the nitrogen lone pair and CC configuration had steric repulsion of the substituents [2,34]. Results also show that comparing between Ph- and Ah-substituents, Ph-substituent is more flexible to be in CT, TT and CC configuration while CC only exists for Ph-Cl-p-1 of Ah-substituent.

Even though both the CT and TT configurations are shown to be possible in the monomer systems, rotation of the dimer systems shows that the substituents are too close or overlapping (as shown in Fig. 4 for the dimer of Ph-Cl-p). Thus, those dimers are unable to exist with new configuration in a similar crystal system. However, the possibility for them to exist in different configuration of different crystal systems cannot be discarded.

Table 2. Summaries of the possible configuration for monomer of the Ph- and Ah-substituted molecules. For each set, the minimum energy conformation is used as the reference

Substituent	Most Stable Configuration	Other possible configuration with its relative energy (eV)			
Ph–1	CT	TT	0.1377	CC	6.6177
Ph–2	CT	TT	0.2045		
Ph–3	CT	TT	0.1761	CC	6.5187
Ph–4	CT	TT	0.1731	CC	7.2727
Ph–F	CT	TT	0.1569	CC	3.3776
Ph–Cl–p–1	CT	TT	0.1537	CC	6.4029
Ph–Cl–p–2	CT	TT	0.1031		
Ph–Br	CT	TT	0.1464		
Ph–Cl–o–1 (a)	CT	TT	0.1237		
Ph–Cl–o–1 (b)	CT	TT	0.1860		
Ph–Cl–o–2	CT	TT	0.1779		

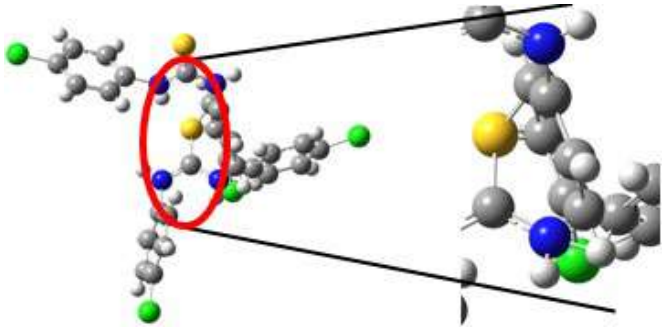

Fig 4. The overlapped structure of the rotated substituent

Interaction Energy

The interaction energy between molecules in the dimeric systems is shown in Table 3. It can be seen that, for all the compounds considered in this study, as the interaction energy is negative, the dimeric molecules are attracting each other. For the magnitude of interaction, molecule with Ph-Br substituent has the highest interaction energy (most negative at –1.0573 eV) while Ph-2 substituent has the lowest (–0.5477 eV).

Between TT and CT configurations, TT has higher interaction than the CT configuration, as evidenced by the molecules with Ph- and Ph-Cl-o substituents. The Ph-2 substituent, as the only polymorph in the CT configuration among the molecules with Ph-substituent, has the smallest value of interaction energy. As for the case of Ph-Cl-o-2 and Ph-Cl-o-1, the CT configuration also has interaction energy that is of lower magnitude compared to the polymorph in TT configuration. However, no significant changes to the interaction energy can be found with or without halogen atom in the systems considered.

As for the effect of the halogens on the phenyl ring, molecules are more cohesive as the halogens in the substituents change from fluorine, chlorine, and bromine in the rank F < Cl < Br. This effect is due to the polarizability of the halogens. Thus, the molecules where the substituents contain fluorine had lower attraction compared to the compound with bromine.

The interaction energies are not affected much by the different attachment sites of the halogen to the phenyl rings. This can be seen from the chlorophenyl substituent Ph-Cl, where the chlorine is either attached to para- or ortho- positions. With this substituent, the interaction

Table 3. Interaction energy of the compounds

Substituent	Interaction Energy (eV)	Configuration
Ph–1	-0.9292	TT
Ph–2	-0.5477	CT
Ph–3	-0.8630	TT
Ph–4	-0.8629	TT
Ph–F	-0.7809	TT
Ph–Cl–p–1	-0.8699	TT
Ph–Cl–p–2	-1.0056	TT
Ph–Br	-1.0573	TT
Ph–Cl–o–1	-0.7306	CT
Ph–Cl–o–2	-0.8806	TT

energies range in between –0.731 to – 1.006 eV, where the higher value is from the attachment to the para-position. In the para-position, the molecules are taking the head-to-tail orientation, with the molecule stack parallel to the thiourea backbone for the case of Ph-Cl-p-2 substituent. However, with higher angle of the zigzag between molecules (Ph-Cl-p-1), the interaction between molecules becomes less. Molecules with Ph-Cl-o-2 substituents have the similar head-to-tail orientation but the molecule is rotated to the substituent of the compound. This orientation has less interaction between the substituent of the molecules. While Ph-Cl-o-2 has dual NH···S_T interaction with close substituents of the molecules, Ph-Cl-o-1 have single NH···S_T interaction with substituents that are away from each other, producing dimer with the weakest interaction energy.

Non-covalent Interaction (NCI)

The noncovalent interaction is shown through the NCI isosurfaces using the RDG plot in Fig. 5. For each monomer, the dual green-red NCI isosurfaces in the region between S_T and the phenyl ring indicate that there are attractive and repulsive interactions. In the TT configuration, the S···π interactions act as the attractive interactions (the green surfaces), while the interaction in the region of S_T-C-N-C_P constitute the repulsive interactions (the red surface). On closer inspection, the wider the divergence between the S_T and carbon of the phenyl ring (C_P) from region of S_T-C-N-C_P, the lesser red isosurface will be shown. These two interactions are typical for the molecules with TT configuration for Ph or

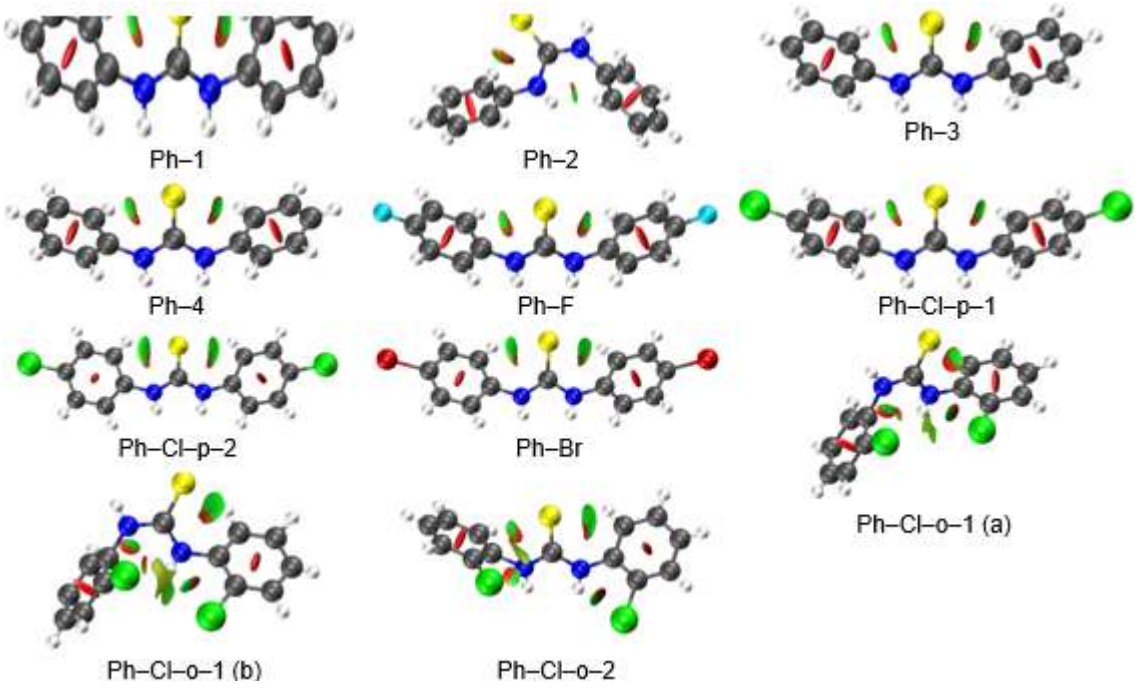

Fig 5. The NCI isosurfaces for the monomers original configuration

Ah-substituents with halogen atom attached at the para-position. The Ph-Cl-o-2 had an extra Cl···N and Cl···S interaction from the ortho-position of the chlorine atoms.

For the molecule with the CT configuration (Ph-2 and Ph-Cl-o-1), the NCI dual green-red isosurfaces in the region between nitrogen of thiourea (N_T) and the phenyl ring for the cis-orientation side comes from the NH···π interaction (for attractive interaction), while the repulsive interaction is from the interaction of N_T-C-N-C_P. However, this dual color region is seen to be smaller than the one from the trans-orientation, and can be attributed from the smaller size of hydrogen as compared to the S_T. The interaction from the trans-orientation side of this CT configuration is the same as in the case of TT orientation. Nevertheless, in the CT configuration, for Ph-Cl-o-1, extra interaction exists in the form of Cl···Cl interaction. This can be seen from the proximity between the chlorine atoms, which is in the ortho-position of the phenyl ring, and the nitrogen of the thiourea moiety. This explains the higher interaction energy of Ph-Cl-o-1 than that of Ph-2 (as discussed in the NCI results for dimer).

For the new configurations of the molecules shown in Fig. 6 (where the substituents are rotated), the NCI isosurfaces are similar as those in the original CT and TT configurations. This indicates that the new configurations are possible as they have similar type of interactions as those that generally appear in the original configurations. CT configuration shows the combination of S···π (for *trans*) and NH···π (for *cis*), while TT configuration show S···π interaction for both sides. The CC configuration shows the large red isosurfaces, indicating large repulsive interaction between substituents. This explains the less preferable CC configuration compared to CT and TT configuration from the energetic aspect. The CC configuration in Fig. 6 is represented using only the molecule with Ph-substituent, as other compounds also have similar patterns.

The non-covalent interactions of the dimer, as can be seen in Fig. 7, show that the intramolecular interaction of the dimer is similar as the monomers (Fig. 5). In between the molecules, the green NCI isosurfaces are found between N-H and S_T, indicating the existence of the N-H···S_T interaction in all the compounds considered in this study. This result agrees with the findings from the experiments in which NH···S_T interaction is important

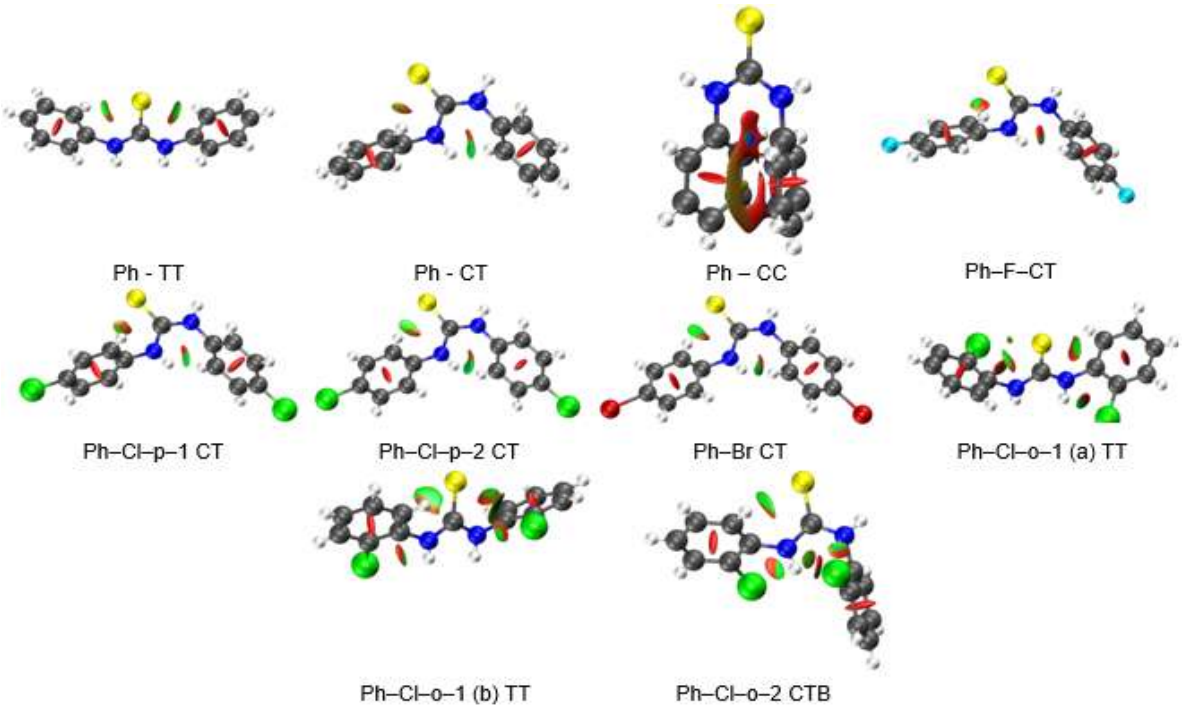

Fig 6. The NCI isosurfaces for the new configuration of the molecules

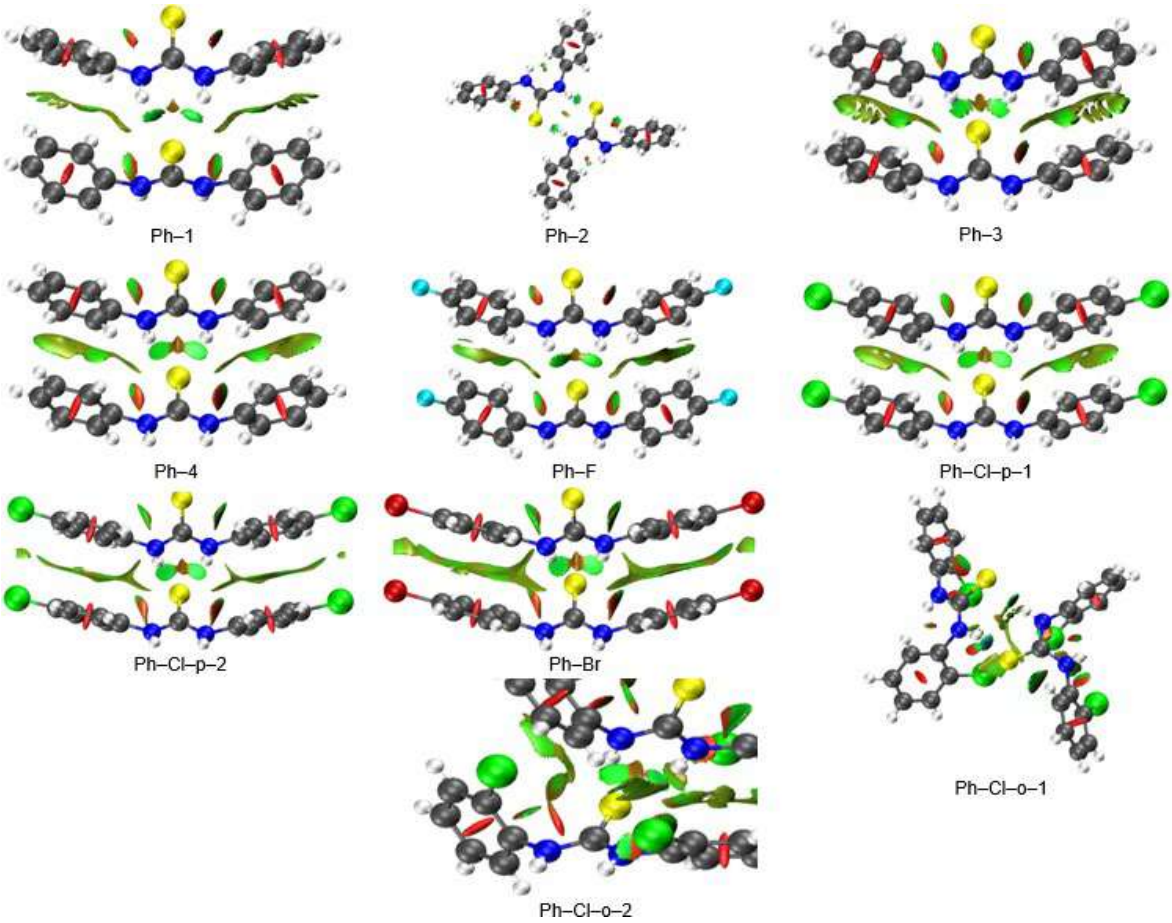

Fig 7. The NCI isosurfaces for the dimer compounds

in holding the molecules in the crystal structure [7-14]. Hence, not only can the NH···S_T hydrogen bonds hold the thiourea molecules in the solid state [15], it is also responsible for the stability of the thiourea derivatives.

The higher interaction energy for dimers in the stacked TT configuration can be related to the NCI isosurfaces which show the dual NH···S_T interaction and wide green region between substituents of the compound. For both Ph- and Ah-substituent, strength of the vdW interaction is shown to depend on the angle and distance between two molecules. Lower angle and distance will have wider vdW interaction resulting to higher interaction energy. For Ah-substituent, Ph-F and Ph-Cl-p-1 show no NCI isosurface exist between halogen atoms, while for Ph-Cl-p-2 and Ph-Br, NCI isosurface appear between halogens. This agrees with the results from interaction energy fi, where Ah-substituent has higher interaction energy range compared to Ph-substituent. The amount of the vdW interaction changes according to Ph-F < Ph-Cl < Ph-Br, which is similar to the interaction energy results. Ph-F had the lowest interaction energy due to the highest angle of 96.82° between molecules.

For the CT configuration in chain arrangement, as exemplified by the Ph-2 and Ph-Cl-o-1 substituents, no enhancements of stability is observed in the dimer as the substituents are diverging from each other. However, as explained in monomer results, since Ph-Cl-o-1 has extra interaction compared to Ph-2, it reflects the higher interaction energy as shown in Table 3. The results from vdW isosurface agree with the observation that the molecules with Ph-Br substituent have the strongest interaction energy, and that the dimers in the CT configuration have the lowest interaction energy compared to the TT configuration.

Electrostatic Potential (ESP)

The reactivity of the monomers and dimers are shown in Fig. 8, 9 and 10. For all the compounds considered, the NH bond of the thiourea moiety always show blue ESP surfaces, indicating positive potentials at the region while the red ESP surfaces at the S_T indicate the negative potentials. However, there are differences in the magnitude of the interactions between the Ph- and Ah-substituted molecules, as tabulated in Table 4. Ph-substituted molecules have lower minimum range of the red and blue surfaces compared to the Ah-substituted molecules due to the inclusion of the halogen atoms. Thus, the Ph-substituted molecules have higher ability to donate its electrons while the Ah-substituted molecules have higher ability to attract electrons.

Quantitative study of different configurations also shows differences to the potentials at the NH bonds of different configurations. In the CT configuration, the potentials of the blue ESPs, with energy that range from 1.50 to 1.60 eV, are smaller than those in the TT configuration which is in between 2.44 and 2.90 eV. Further differences in the electronic properties of the CT and TT configurations occurred in the ESP of the S_T. In the CT configuration (Ph-Cl-o), the ESP of the S_T is in orange-ish color, compared to yellow-ish in the TT configuration. Numerically, the potential at the S_T for Ph-Cl-o is –1.51 and –1.46 eV, while that in TT configurations has values between –1.47 and –1.21 eV. Hence, while the TT configuration has enhancement in the positive potential of the NH sites, it also possesses slightly weaker negative potential for the S_T, compared to those in the CT configuration. The green ESP surfaces at the Ah-substituted molecules indicate that these sites have average potential and that the possibility of involvement in reaction is low. Thus, the change in the structural configuration does affect the electronic properties of the compounds considered.

Fig. 9 shows the ESP surfaces for the rotated molecules. Results show that the reactive sites of all the new configurations are similar to those shown in the original configurations. The electrophilic site (blue surface) of the molecules are at the NH bonds region while nucleophilic site (yellow-red surface) are at the $S_{T'}$. Comparing ESP surfaces between the original and new configurations, energy of new configurations show unclear changes in energy pattern. However, Ph-substituent had lower minimum energy range around –1.68 to –1.69 eV for both TT and CT configurations compared to Ah-substituent, ranging from –1.52 to –1.20 eV. This indicates that Ph-substituent had higher capability to act as a nucleophilic site compared to

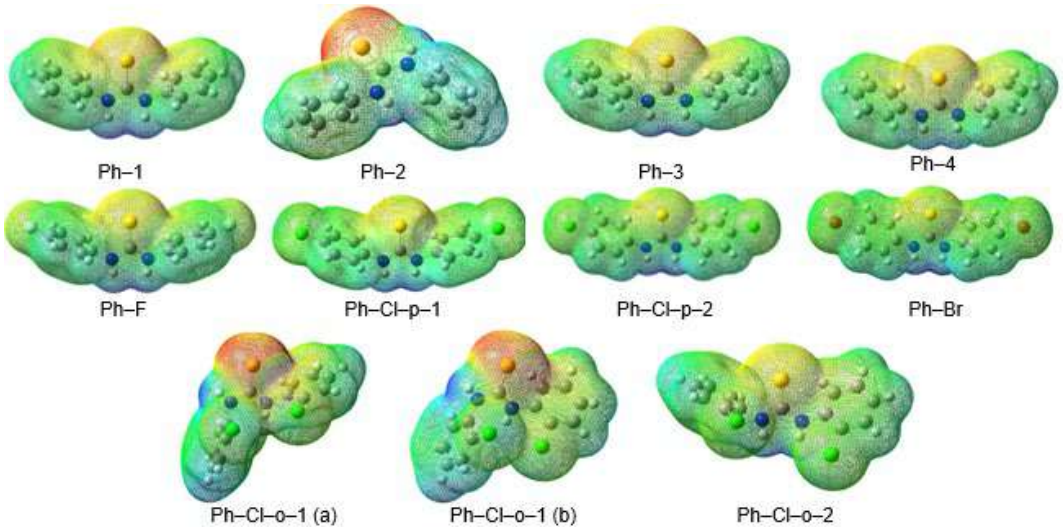

Fig 8. The ESP isosurfaces for the monomers original configuration

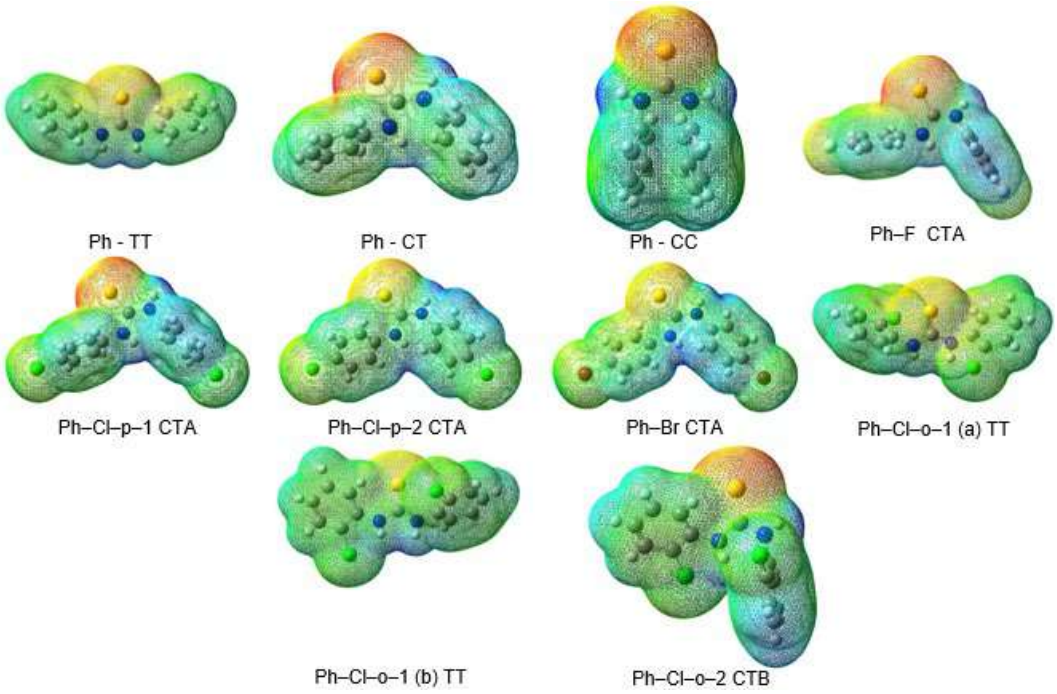

Fig 9. The ESP isosurfaces for the monomers new configuration

Ah-substituent. Hence, the results have similar electronic properties as the original configuration. For potential of blue ESP surfaces, rotation from TT to CT configuration shows a decrease in energy to the range of 1.55 to 1.90 eV, while rotation from CT to TT configuration increase the energy range to 2.31 to 2.41 eV. This shows that the compound of interest had higher capability to act as an electrophilic site in TT configuration. Both Ph- and Ah-substituent had similar energy range indicating that halogen did not have an effect on the potential of NH.

The ESP of the interactions between the components of dimeric systems is shown in Fig. 10. Generally, the electrophilic and nucleophilic sites between the monomers are interacting with each other, where the NH sites attract the electron-rich S_T site. The NCI isosurfaces also exist between the S_T and NH of the two

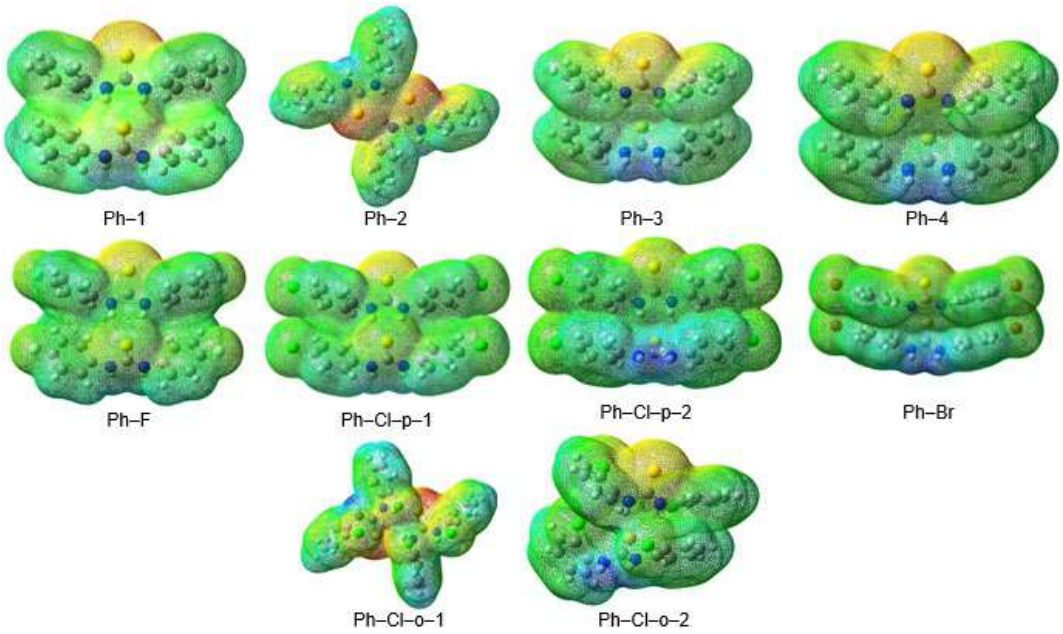

Fig 10. The ESP isosurfaces for the dimer compounds

Table 4. The ESP energy between original and rotated configurations

Substituent	Configuration		Minimum		Maximum	
	Original	Rotated	Original conf.	Rotated conf.	Original conf.	Rotated conf.
Ph–1	TT	CT	-1.6434	-1.6846	2.2682	1.6874
Ph–1	TT	CC	-1.6434	-1.4233	2.2682	1.7218
Ph–2	CT	TT	-1.6740	-1.6899	1.4984	2.3426
Ph–3	TT		-1.6806		2.3903	
Ph–4	TT		-1.6748		2.3878	
Ph–F	TT	CT	-1.4653	-1.4750	2.5707	1.6882
Ph–Cl–p–1	TT	CT	-1.4748	-1.4881	2.6248	1.6798
Ph–Cl–p–2	TT	CT	-1.2288	-1.2206	2.8203	1.8932
Ph–Br	TT	CT	-1.2073	-1.1922	2.8928	1.8705
Ph–Cl–o–1 (a)	CT	TT	-1.5099	-1.5150	1.6005	2.3104
Ph–Cl–o–1 (b)	CT	TT	-1.4594	-1.4288	1.5653	2.4115
Ph–Cl–o–2	TT	CT	-1.4560	-1.4592	2.4424	1.5515

monomers, indicating their importance in the interaction of molecules in crystal systems [7-14]. For the dimers, other than the sites where the monomers interact, the individual monomers also show similar reactive sites as in the case of the monomer, as shown in Fig. 9.

■ CONCLUSION

In this work, we studied the conformational stability of the polymorphic diphenylthiourea and diarylhalidethiourea substituted compounds. Without changing intermolecular hydrogen bonding and geometry of the molecules, energetic study concludes that compounds are more stable in CT configuration as monomers. However, the interaction energy for the molecules in TT configuration is higher. This shows that these compounds are flexible to coexist between CT and TT configurations. From these energetic results, supported by NCI and ESP topology isosurface, molecules rotated to new configurations show similar sites of reactivity as the original configurations.

Ph- and Ah-substituted molecules have similar reactive sites where the sulphur of thiourea moiety acts

as the nucleophilic site, while the NH of thiourea moiety acts as the electrophilic sites. However, quantitative studies of the ESP shows that the Ph-substituted molecules are better electron donors and Ah-substituted molecules are better electron acceptors.

■ REFERENCES

[1] Shashidhar, Thiruvenkatam, V., Shivashankar, S.A., Halli, M.B., and Guru Row, T.N., 2006, 1,3-Bis(4-methoxyphenyl)thiourea, *Acta Crystallogr., Sect. E: Struct. Rep. Online*, 62 (4), o1518–o1519.

[2] Bryantsev, V.S., Firman, T.K., and Hay, B.P., 2005, Conformational analysis and rotational barriers of alkyl- and phenyl-substituted urea derivatives, *J. Phys. Chem. A*, 109 (5), 832–842.

[3] Phetsuksiri, B., Jackson, M., Scherman, H., McNeil, M., Besra, G.S., Baulard, A.R., Slayden, R.A., DeBarber, A.E., Barry, C.E., Baird, M.S., Crick, D.C., and Brennan, P.J., 2003, Unique mechanism of action of the thiourea drug isoxyl on *Mycobacterium tuberculosis*, *J. Biol. Chem.*, 278 (52), 53123–53130.

[4] Li, J., Bourne, S.A., de Villiers, M.M., Crider, A.M., and Caira, M.R., 2011, Polymorphism of the antitubercular isoxyl, *Cryst. Growth Des.*, 11 (11), 4950–4957.

[5] Peña, Ú., Bernès, S., and Gutiérrez, R., 2009, (+)-(S,S)-1,3-Bis[(tetrahydrofuran-2-yl)methyl]thiourea, *Acta Crystallogr., Sect. E: Struct. Rep. Online*, 65 (Pt 1), o96.

[6] Kotke, M., and Schreiner, P.R., 2006, Acid-free, organocatalytic acetalization, *Tetrahedron*, 62 (2-3), 434–439.

[7] Ramnathan, A., Sivakumar, K., Subramanian, K., Janarthanan, N., Ramadas, K., and Fun, H.K., 1995, Symmetrically substituted thiourea derivatives, *Acta Crystallogr., Sect. C: Cryst. Struct. Commun.*, 51 (11), 2446–2450.

[8] Srivastava, P.C., Dwivedi, S., Singh, V., and Butcher, R.J., 2010, Mono- and bis(dialkyl/aryl dithio carbamato) complexes of 1,1,2,3,4,5,6-heptahydro-1,1-dihalido telluranes: Synthesis, spectroscopy, structures and cleavage reaction, *Polyhedron*, 29 (10), 2202–2212.

[9] Štrukil, V., Igrc, M.D., Fábián, L., Eckert-Maksić, M., Childs, S.L., Reid, D.G., Duer, M.J., Halasz, I., Mottillo, C., and Friščić, T., 2012, A model for a solvent-free synthetic organic research laboratory: Click-mechanosynthesis and structural characterization of thioureas without bulk solvents, *Green Chem.*, 14 (9), 2462–2473.

[10] Qin, Y.Q., Jian, F., and Liang, T.L., 2006, 1,3-Bis(4-chlorophenyl)thiourea, *Acta Crystallogr., Sect. E: Struct. Rep. Online*, 62 (11), o5043–o5044.

[11] Sarojini, B.K., Narayana, B., Swamy, M.T., Yathirajan, H.S., and Bolte, M., 2007, Redetermination of *N*,*N*'-bis(4-chlorophenyl) thiourea at 173 K, *Acta Crystallogr., Sect. E: Struct. Rep. Online*, 63 (9), o3879.

[12] Muhammed, N., Zia-ur-Rehman, Ali, S., and Meetsma, A., 2007, 1,3-Bis(4-bromophenyl)thiourea, *Acta Crystallogr., Sect. E: Struct. Rep. Online*, 63 (2), o632–o633.

[13] Ramnathan, A., Sivakumar, K., Subramanian, K., Janarthanan, N., Ramadas, K., and Fun, H.K., 1996, 1,3-Bis(2-chlorophenyl)thiourea, *Acta Crystallogr., Sect. C: Cryst. Struct. Commun.*, 52 (1), 134–136.

[14] Yeo, C.I., and Tiekink, E.R.T., 2011, 1,3-Bis(2-chlorophenyl)thiourea: A monoclinic polymorph, *Acta Crystallogr., Sect. E: Struct. Rep. Online*, 67 (11), o2965.

[15] Lenthall, J.T., Foster, J.A., Anderson, K.M., Probert, M.R., Howard, J.A.K., and Steed, J.W., 2011, Hydrogen bonding interactions with the thiocarbonyl π-system, *CrystEngComm*, 13 (9), 3202–3212.

[16] Tsuzuki, S., Honda, K., Uchimaru, T., Mikami, M., and Tanabe, K., 2002, Origin of attraction and directionality of the π/π interaction: Model chemistry calculations of benzene dimer interaction, *J. Am. Chem. Soc.*, 124 (1), 104–112.

[17] Frisch, M.J., Trucks, G.W., Schlegel, H.B., Scuseria, G.E., Robb, M.A., Cheeseman, J.R., Scalmani, G., Barone, V., Mennucci, B., Petersson, G.A., Nakatsuji, H., Caricato, M., Li, X., Hratchian, H.P., Izmaylov, A.F., Bloino, J., Zheng, G., Sonnenberg,

J.L., Hada, M., Ehara, M., Toyota, K., Fukuda, R., Hasegawa, J., Ishida, M., Nakajima, T., Honda, Y., Kitao, O., Nakai, H., Vreven, T., Montgomery Jr., J.A., Peralta, J.E., Ogliaro, F., Bearpark, M., Heyd, J.J., Brothers, E., Kudin, K.N., Staroverov, V.N., Keith, T., Kobayashi, R., Normand, J., Raghavachari, K., Rendell, A., Burant, J.C., Iyengar, S.S., Tomasi, J., Cossi, M., Rega, N., Millam, J.M., Klene, M., Knox, J.E., Cross, J.B., Bakken, V., Adamo, C., Jaramillo, J., Gomperts, R., Stratmann, R.E., Yazyev, O., Austin, A.J., Cammi, R., Pomelli, C., Ochterski, J.W., Martin, R.L., Morokuma, K., Zakrzewski, V.G., Voth, G.A., Salvador, P., Dannenberg, J.J., Dapprich, S., Daniels, A.D., Farkas, O., Foresman, J.B., Ortiz, J.V., Cioslowski, J., and Fox, D.J., 2013, *Gaussian 09, Revision D.01,* Gaussian Inc., Wallingford CT.

[18] Castro, M., Cruz, J., Otazo-Sánchez, E., and Perez-Marín, L., 2003, Theoretical study of the Hg^{2+} recognition by 1,3-diphenyl-thiourea, *J. Phys. Chem. A,* 107 (42), 9000–9007.

[19] Schäfer, A., Horn, H., and Ahlrichs, R., 1992, Fully optimized contracted Gaussian basis sets for atoms Li to Kr, *J. Chem. Phys.*, 97 (4), 2571–2577.

[20] Peintinger, M.F., Oliveira, D.V., and Bredow, T., 2013, Consistent Gaussian basis sets of triple-zeta valence with polarization quality for solid-state calculations, *J. Comput. Chem.*, 34 (6), 451–459.

[21] Weigend, F. and Ahlrichs, R., 2005, Balanced basis sets of split valence, triple zeta valence and quadruple zeta valence quality for H to Rn: Design and assessment of accuracy, *Phys. Chem. Chem. Phys.*, 7 (18), 3297–3305.

[22] Grimme, S., Brandenburg, J.G., Bannwarth, C., and Hansen, A., 2015, Consistent structures and interactions by density functional theory with small atomic orbital basis sets, *J. Chem. Phys.*, 143 (5), 054107.

[23] Kruse, H., Goerigk, L., and Grimme, S., 2012, Why the standard B3LYP/6-31G* model chemistry should not be used in DFT calculations of molecular thermochemistry: Understanding and correcting the problem, *J. Org. Chem.*, 77 (23), 10824–10834.

[24] Grimme, S., Ehrlich, S., and Goerigk, L., 2011, Effect of the damping function in dispersion corrected density functional theory, *J. Comput. Chem.,* 32 (7), 1456–1465.

[25] Řezáč, J., 2016, Cuby: An integrative framework for computational chemistry, *J. Comput. Chem.*, 37 (13), 1230–1237.

[26] Řezáč, J., Riley, K.E., and Hobza, P., 2011, S66: A well-balanced database of benchmark interaction energies relevant to biomolecular structures, *J. Chem. Theory Comput.*, 7 (8), 2427–2438.

[27] Kruse, H., and Grimme, S., 2012, A geometrical correction for the inter- and intra-molecular basis set superposition error in Hartree-Fock and density functional theory calculations for large systems, *J. Chem. Phys.*, 136 (15), 154101.

[28] Řezáč, J., and Hobza, P., 2016, Benchmark calculations of interaction energies in noncovalent complexes and their applications, *Chem. Rev.*, 116 (9), 5038–5071.

[29] Lu, T., and Chen, F., 2012, Multiwfn: A multifunctional wavefunction analyzer, *J. Comput. Chem.*, 33 (5), 580–592.

[30] Humphrey, W., Dalke, A., and Schulten, K., 1996, Visual Molecular Dynamics, *J. Mol. Graphics*, 14, 33–38.

[31] Johnson, E.R., Keinan, S., Mori-Sánchez, P., Contreras-García, J., Cohen, A.J., and Yang, W., 2010, Revealing noncovalent interactions, *J. Am. Chem. Soc.*, 132 (8), 6498–6506.

[32] Murray, J.S., and Politzer, P., 2009, Molecular surfaces, van der Waals radii and electrostatic potentials in relation to noncovalent interactions, *Croat. Chem. Acta*, 82 (1), 267–275.

[33] Dennington, R., Keith, T., and Millam, J., 2009, *GaussView*, Version 5, Semichem Inc., Shawnee Mission, KS.

[34] Galan, J.F., Germany, E., Pawlowski, A., Strickland, L., and Galinato, M.G., 2014, Theoretical and spectroscopic analysis of *N,N′*-diphenylurea and *N,N′*-dimethyl-*N,N′*-diphenylurea conformations, *J. Phys. Chem. A*, 118 (28), 5304–5315.

Poly(Lactic Acid) (PLA)/Acrylonitrile Butadiene Styrene (ABS) with Graphene Nanoplatelet (GNP) Nanocomposites

Mohd Bijarimi[1,*], Noor Shahadah[1], Azizan Ramli[1], Said Nurdin[1], Waleed Alhadadi[1], Muhammad Zakir Muzakkar[2], and Jamiluddin Jaafar[3]

[1]*Faculty of Chemical and Natural Resources Engineering, Universiti Malaysia Pahang, Lebuhraya Tun Razak 26300, Gambang, Pahang, Malaysia*

[2]*Department of Chemistry, Faculty of Mathematics and Science, Universitas Haluoleo, Kendari 93232, Indonesia*

[3]*Faculty of Mechanical Engineering, Universiti Malaysia Pahang, 26600 Pekan, Pahang, Malaysia*

* ***Corresponding author:***

tel: +609-5492918
email: bijarimi@ump.edu.my

Received: August 3, 2018
Accepted: December 13, 2018

DOI: 10.22146/ijc.40880

Abstract: *A melt blending of poly(lactic acid) (PLA)/acrylonitrile-butadiene-styrene (ABS) with 30:70 PLA:ABS was prepared by a twin screw extruder with a die of 25 mm width and 0.5 mm thickness with various loadings of graphene (0–1.0 wt.%). The PLA/ABS blends were evaluated for mechanical, morphology, thermal properties and interaction of the components in the blend system. Results show the incorporation of graphene nanoplatelet (GNP) improved the tensile and modulus properties. Nevertheless, it was observed that at higher GNP loadings, i.e., 0.6–1.0 wt.%, both tensile and modulus properties showed a decreasing trend. It was also found that the thermal stability for the blend slightly improved when graphene presence in the blend.*

Keywords: *ABS; PLA; melt blending; nanocomposites*

■ INTRODUCTION

Poly(lactic acid) (PLA) is a biodegradable linear aliphatic thermoplastic polyester derived from agricultural products which are renewable resources such as sugarcane, potato, and corn. PLA has huge potential to substitute conventional petroleum-based polymer due to its inherent strength, biocompatibility and low toxicity [1-2]. Unfortunately, the application of PLA in engineering plastic is limited because of low crystallinity, low thermal deformation, and brittleness [3]. Hence, blending PLA with other polymer is the most practical and economical method to improve the elongation and toughness properties of the PLA [3-4].

Acrylonitrile-butadiene-styrene (ABS) used to toughen PLA due to its excellent properties such as high toughness, rigidity, good thermal stability and resistance to chemical and environmental attack. It is also cost-effective, durable and low coefficient of thermal expansion, hence it is easy to mold product with good dimensional stability. These advantages have enabled the ABS to be used in 3D printing material [5-6]. It is known that ABS has been used to toughen the brittleness of PLA, but the modulus and strength properties reduced significantly [7]. In order to overcome these drawbacks, many types of research used nanofillers that act as a reinforcing agent in the binary or ternary blends of polymers [4,8-9]. For example, Desa et al. reported that they had produced a multiwalled carbon nanotubes nanocomposite with improved tensile strength and stiffness as compared to neat PLA [10]. In another study, Weng et al. introduced montmorillonite into ABS matrix and improved mechanical properties and thermal properties of Fused Deposition Modeling (FDM) 3D printed samples [11]. A recent study, Seddik et al. found that immiscibility of PLA and polycaprolactone (PCL) could be overcome by the use of organomontmorillonite (OMMT) nanoclay and graphene in the blend [12].

Graphene is widely used as a filler in polymer blend for applications ranging from electronics, medical and automotive sectors. It has a high Young's modulus, tensile strength, aspect ratio, and thermal conductivity. Polymer

nanocomposites based on graphene is still extensively investigated by both academia and industry due to high levels of stiffness and strength [13-18]. The objectives of this study were to prepare a binary blend of PLA/ABS with the incorporation of graphene nanoplatelet from 0.2–1.0 wt.% and then characterized it for mechanical, thermal, chemical and morphological properties.

■ EXPERIMENTAL SECTION

Materials

Poly(lactic acid) NatureWorks Ingeo™ Biopolymer 3251 thermoplastic resin was used in this study. It has a density of 1.24 g/cm^3 and a melting temperature between 155–170 °C. Acrylonitrile-butadiene-styrene (ABS) was purchased from Toray Plastics (Malaysia) Sdn Bhd. Graphene Nanoplatelets (GNP) grade M with a thickness of 6–8 nm and a surface area of 120–150 m^2/g was purchased from XG Sciences, Inc. The composition of PLA/ABS was fixed at 30:70 by wt.%.

Procedure

PLA, ABS pellets were dried in an oven at 45 °C respectively for 12 h prior to compound mixing. Melt blending of PLA/ABS was carried out via a Haake twin-screw extruder. The temperature profiles used during compounding was between 180–210 °C. The screw rotation speed of the extruder was kept constant 50 rpm. PLA/ABS/GNP extrudates were allowed to cool at ambient temperature. Samples for testing were molded to form a thin film (40 mm wide × 40 mm long x 3 mm thickness). Stress-strain properties characterization was carried out at room temperature according to ASTM D638 using a Universal Testing Machine with a crosshead speed of 50 mm min^{-1}. Microscopy observation was performed on the tensile fractured specimen. The chemical changes after blending were recorded using a Spectrum 400 FT-IR and spectrometer with 4 cm^{-1} resolution and 10 scans at the 4000–600 cm^{-1} region. The glass transition temperature and melting temperatures were determined by using a differential scanning calorimetry (DSC) at a scan rate of 20 °C /min. The thermal decomposition of the nanocomposites was evaluated in a thermogravimetric analyzer from 25 °C to 600 °C at a scanning rate of 20 °C min^{-1} under nitrogen.

■ RESULTS AND DISCUSSION

Stress-strain properties of PLA/ABS nanocomposites are shown in Table 1. The incorporation of graphene nanoplatelet changed the stress-strain properties as compared to pristine PLA/ABS binary blend. It was found that tensile strength for PLA/ABS with 0.2 wt.% of graphene nanoplatelet increased from 7.58 to 9.78 MPa. A similar trend was observed when the GNP content was increased further to 0.6 wt.%. However, further addition of GNP after 0.6 wt.% decreased the tensile strength in the PLA/ABS/GNP nanocomposites. As for Young's modulus, only a small increase was noted when the GNP was increased from 0.2 to 1.0 wt.%. This phenomenon can be explained that the addition of GNP could significantly increase the mechanical properties due to the large aspect ratio of the graphene sheets in the ABS matrix. According to the work of Jiajie Liang et al. the mechanical performance of graphene/PVA nanocomposites was significantly increased when compared with the pristine PVA matrix [19]. Similar observation on the enhancement of tensile strength and modulus due to a small amount of graphene was also reported by Kuilla [20].

Table 1. Summary for tensile strength, Young's modulus and elongation at break for PLA/ABS graphene nanocomposites

Graphene content (%)	Tensile strength (MPa)	Young's modulus (GPa)	Elongation at break (%)
0	7.58	1.20	1.27
0.2	9.78	1.29	1.28
0.4	10.99	1.37	1.66
0.6	10.24	1.30	1.41
0.8	9.67	1.29	1.27
1.0	9.39	1.29	1.24

The SEM images in Fig. 1 shows the magnified of the fractured surface of PLA/ABS blend and PLA/ABS blend with graphene nanocomposite from a tensile test. The morphology observation has shown that the addition of graphene into ABS/PLA blend improved their mechanical properties. It is worth noting that there are two phases visible in Fig. 1(a) which indicates the PLA/ABS blend is immiscible and have low interfacial adhesion between PLA/ABS immiscible phases [21]. On the other hand, Fig. 1(b) and (c) showed less droplet and voids in the continuous matrix when graphene loading increased from 0.2 to 0.4 wt.%. Graphene content in PLA/ABS blend contributed to the homogeneousness of the matrix, as the graphene content increase, PLA/ABS blend become more homogenous, thus increase the tensile modulus. However, the homogeneity reaches its maximum at 0.4 wt.% as the trend of tensile strength and tensile modulus drops. The increment in tensile strength and modulus could be attributed by the much higher modulus of GNP in the matrix that carries more loads of the overall nanocomposite. This can be explained by the transmission electron microscopy (TEM) images as depicted in Fig. 2 where a comparison of PLA/ABS and PLA/ABS/GNP at 0.4 wt.% was made. It is apparent that the presence of graphene nanosheets between the presence of graphene nanosheets in the PLA/ABS nanocomposites that are thought to be responsible for the enhancement of tensile and modulus. Nevertheless, the GNP in the PLA/ABS tends to agglomerate at higher loadings, i.e. above 0.4 wt.% A similar trend was also reported in the previous work, i.e. when graphene loading in PVA matrix reaches its threshold limit, the mechanical properties and the morphology show a significant declination, generally because of the aggregation of graphene [22].

The glass transition temperature (T_g), crystallization temperature (T_c) and melting temperature (T_m) were determined from DSC analysis. Fig. 3 shows the

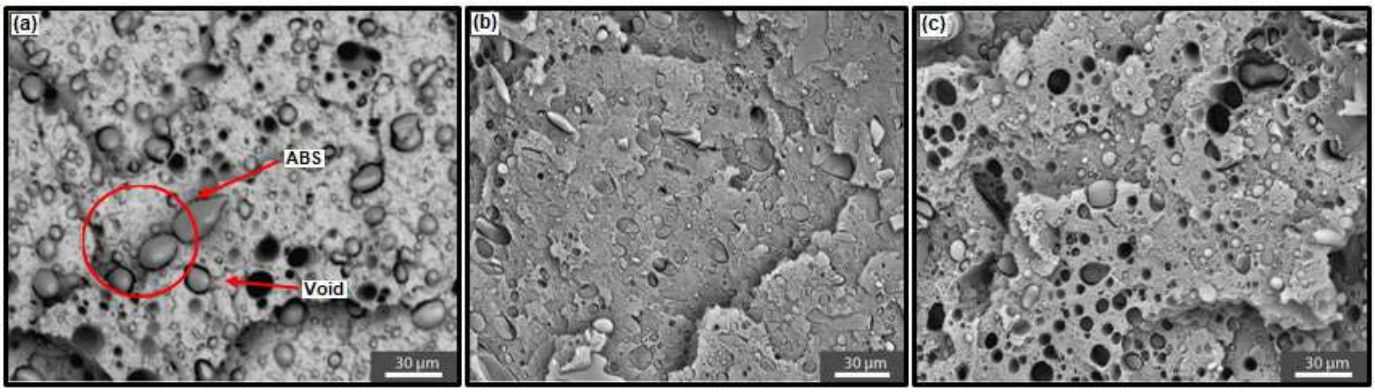

Fig 1. SEM Images of (a) PLA/ABS blend and PLA/ABS with graphene nanocomposite of (b) 0.4 GNP and (c) 0.8 GNP

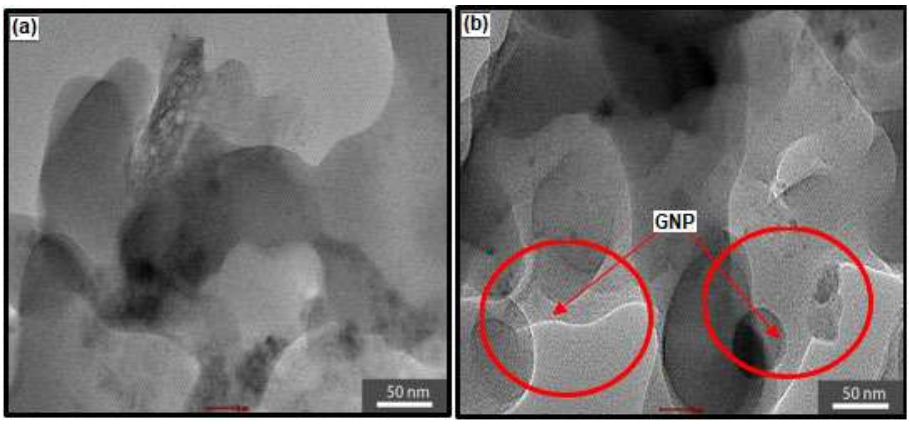

Fig 2. TEM images of (a) PLA/ABS blend and (b) PLA/ABS with graphene nanocomposite of 0.4 GNP

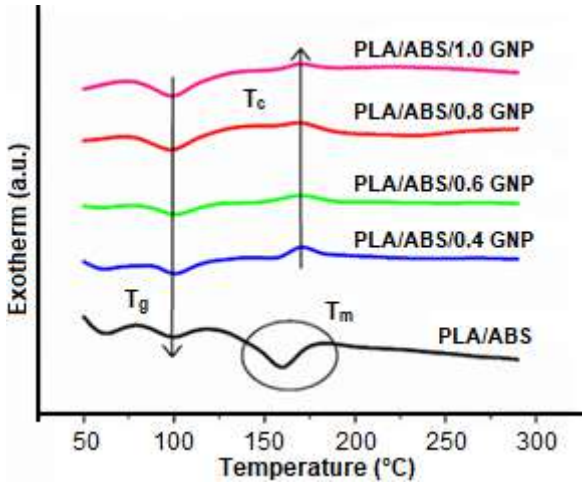

Fig 3. DSC curves of PLA/ABS and PLA/ABS nanocomposite

DSC thermograms for PLA/ABS and nanocomposite with the glass and melting transition regions. From the DSC plot, the glass transition temperatures of PLA/ABS were found to be at 70 °C but gradually shifted to 110 °C when the graphene content increased to 1 wt.%. This can be explained due to the fact that the presence of graphene in the PLA/ABS blend hindered the molecular movement that resulted in an increase in T_g. A similar observation was reported by Liang and co-workers when they found that the T_g of PVA/graphene nanocomposite at 0.7 wt.% of graphene oxide loading was higher at 3.3 °C than the pure PVA matrix [19].

Fig. 4 shows the degradation temperatures for PLA/ABS and nanocomposites. It was observed that the incorporation of graphene in PLA/ABS matrix slightly improved the thermal stability of the blend as evidenced from the TGA plots. Initial decomposition temperature (defined by the temperature at 5% mass loss) for the blend with GNP changed slightly to higher temperature range than blend without GNP as shown in Fig. 4(a). This can be explained due to the fact that the presence of GNP as a superior insulator [11] and thermal barrier [12] for PLA/ABS matrix during decomposition, hence improved the PLA/ABS blend thermal properties. In the derivative thermogravimetric (DTG) curve, maximum degradation temperature for all blends can be seen in Fig. 4(b); where there are two peaks in the DTG curves which indicate the PLA and ABS degraded individually due to the immiscible blend of the two polymers.

Fig. 5 shows FTIR spectra of pure ABS, pure PLA, PLA/ABS blend and PLA/ABS blend with graphene nanocomposite. A strong and sharp peak in the dashed box (a) at wavenumbers 870–660 cm^{-1} can be observed at neat ABS spectrum represent C–H bond for alkyl and aromatic group. There is also a peak at that range wavenumbers on PLA/ABS with and without graphene content, indicates that the ABS component did not have any significant role in this blend [23]. As can be seen in Fig. 5, dashed box (c) shows a peak at 1760–1700 cm^{-1} which indicate the existence of aldehyde/ketone bond (C=O) and dashed box (b) at 1300–1050 cm^{-1} that resemble C–O bond on PLA and PLA/ABS. Based on these observations, the PLA/ABS and PLA/ABS/GNP at

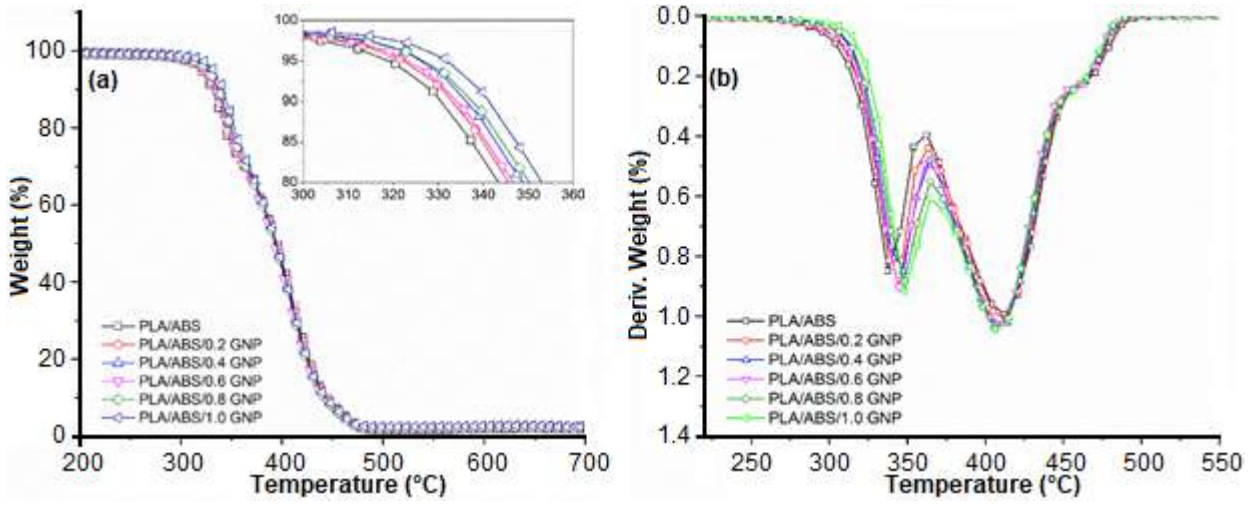

Fig 4. (a) TGA curves and (B) DTG curves of PLA/ABS and PLA/ABS nanocomposite

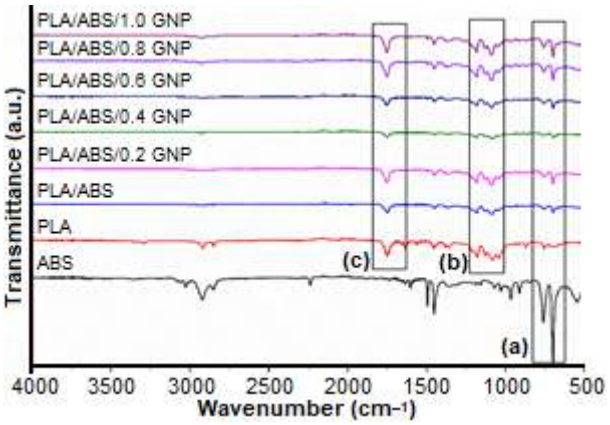

Fig 5. Comparison of FTIR spectra of pure ABS, pure PLA, PLA/ABS and PLA/ABS with nanocomposite

various compositions did not show any significant chemical interaction.

■ CONCLUSION

PLA/ABS graphene nanocomposite was prepared by melt blending and characterized for mechanical, chemical, thermal and morphological properties. The PLA/ABS graphene nanocomposites at 0.4 wt.% GNP loading has shown the highest tensile strength property. The initial degradation temperature and glass transition temperatures shifted to a higher temperature in the presence of graphene as compared to pristine PLA/ABS blend.

■ ACKNOWLEDGMENTS

The authors wish to acknowledge Universiti Malaysia Pahang (UMP) for the financial assistance provided under the internal research grants (RDU160336 and RDU180351).

■ REFERENCES

[1] Mat Desa, M.S.Z., Hassan, A., Arsad, A., and Mohamad, N.N.B., 2014, Mechanical properties of poly(lactic acid)/multiwalled carbon nanotubes nanocomposites, *Mater. Res. Innovations*, 18 (Suppl. 6), 14–17.

[2] Bijarimi, M., Ahmad, S., and Alam, A.K.M.M., 2017, Toughening effect of liquid natural rubber on the morphology and thermo-mechanical properties of the poly(lactic acid) ternary blend, *Polym. Bull.*, 74 (8), 3301–3317.

[3] Wu, N., Zhang, H., and Fu, G., 2017, Super-tough poly(lactide) thermoplastic vulcanizates based on modified natural rubber, *ACS Sustainable Chem. Eng.*, 5 (1), 78–84.

[4] Bijarimi, M., Ahmad, S., and Rasid, R., 2013, Mechanical, thermal and morphological properties of poly(lactic acid)/natural rubber nanocomposites, *J. Reinf. Plast. Compos.*, 32 (21), 1656–1667.

[5] Garcia, A., Berthelot, T., Viel, P., Mesnage, A., Jégou, P., Nekelson, F., Roussel, S, and Palacin, S., 2010, ABS polymer electroless plating through a one-step poly(acrylic acid) covalent grafting, *ACS Appl. Mater. Interfaces*, 2 (4), 1177–1183.

[6] Olivera, S., Muralidhara, HB., Venkatesh, K., Gopalakrishna, K., and Vivek, C.S., 2016, Plating on acrylonitrile–butadiene–styrene (ABS) plastic: A review, *J. Mater. Sci.*, 51 (8), 3657–3674.

[7] Hamad, K., Kaseem, M., and Deri, F., 2012, Poly(lactic acid)/low density polyethylene polymer blends: Preparation and characterization, *Asia-Pac. J. Chem. Eng.*, 7, S310–S316.

[8] Haniff, M., Bijarimi, M., Zaidi, M.S., and Sahrim, A., 2018, Preparation and characterization of poly(lactic acid) (PLA)/polyoxymethylene (POM) blends, *Mater. Sci. Forum*, 917, 3–6.

[9] Alam, A.K.M.M., Beg, M.D.H., Yunus, R.M., Bijarimi, M., Mina, M.F., Maria, K.H., and Mieno, T., 2018, Modification of structure and properties of well-dispersed dendrimer coated multi-walled carbon nanotube reinforced polyester nanocomposites, *Polym. Test.*, 68, 116–125.

[10] Mat Desa, M.S.Z., Hassan, A., Arsad, A., and Mohamad, N.N.B., 2016, Influence of rubber content on mechanical, thermal, and morphological behavior of natural rubber toughened poly(lactic acid)–multiwalled carbon nanotube nanocomposites, *J. Appl. Polym. Sci.*, 133 (48), 44344.

[11] Weng, Z., Wang, J., Senthil, T., and Wu, L., 2016, Mechanical and thermal properties of ABS/montmorillonite nanocomposites for fused deposition modeling 3D printing, *Mater. Des.*, 102, 276–283.

[12] Bouakaz, B.S., Habi, A., Grohens, Y., and Pillin, I.,

2017, Organomontmorillonite/graphene-PLA/PCL nanofilled blends: New strategy to enhance the functional properties of PLA/PCL blend, *Appl. Clay Sci.*, 139, 81–91.

[13] Young, R.J., Liu, M., Kinloch, I.A., Li, S., Zhao, X., Vallés, C., and Papageorgiou, D.G., 2018, The mechanics of reinforcement of polymers by graphene nanoplatelets, *Compos. Sci. Technol*, 154, 110–116.

[14] Li, Z., Chu, J., Yang, C., Hao, S., Bissett, M.A., Kinloch, I.A., and Young, R.J., 2018, Effect of functional groups on the agglomeration of graphene in nanocomposites, *Compos. Sci. Technol.*, 163, 116–122.

[15] Papageorgiou, D.G., Kinloch, I.A., and Young, R.J., 2017, Mechanical properties of graphene and graphene-based nanocomposites, *Prog. Mater. Sci.*, 90, 75–127.

[16] Hamid, F.A., Salleh, F.M., Mohamed, N.S., and Adnan, S.B.R.S., 2017, Effect of graphene content on the structure and conductivity of cellulose/graphene composite, *Sains Malays.*, 46 (7),1025–1031.

[17] Norhakim, N., Ahmad, S., Chia, C.H., and Huang, N.M., 2014, Mechanical and thermal properties of graphene oxide filled epoxy nanocomposites, *Sains Malays.*, 43 (4), 603–609.

[18] Abidin, H.E.Z., Hamzah, A.A., and Majlis, B.Y., 2017, Pencirian pertumbuhan lapisan nano grafin di atas elektrod antara digit superkapasitor MEMS, *Sains Malays.*, 46 (7), 1061–1067.

[19] Liang, J., Huang, Yi., Zhang, L., Wang, Y., Ma, Y., Guo, TG., and Chen, Y., 2009, Molecular-level dispersion of graphene into poly(vinyl alcohol) and effective reinforcement of their nanocomposites, *Adv. Funct. Mater.*, 19 (14), 2297–2302.

[20] Kuilla, T., Bhadra, S., Yao, D., Kim, N.H., Bose, S., and Lee, J.H., 2010, Recent advances in graphene based polymer composites, *Prog. Polym. Sci.*, 35 (11), 1350–1375.

[21] Bouakaz, B.S., Pillin, I., Habi, A., and Grohens, Y., 2015, Synergy between fillers in organo montmorillonite/graphene–PLA nanocomposites, *Appl. Clay Sci.*, 116-117, 69–77.

[22] Li, C., Li, Y., She, X., Vongsvivut, J., Li, J., She, F., Gao, W., and Kong, L., 2015, Reinforcement and deformation behaviors of polyvinyl alcohol/ graphene/montmorillonite clay composites, *Compos. Sci. Technol.*, 118, 1–8.

[23] Vadori, R., Misra, M., and Mohanty, A.K., 2016, Sustainable biobased blends from the reactive extrusion of polylactide and acrylonitrile butadiene styrene, *J. Appl. Polym. Sci.*, 133 (45), 43771.

Extraction of Omega-3 Fatty Acid from Jade Perch (*Scortum barcoo*) Using Enzymatic Hydrolysis Technique

Nur Izzati Iberahim*, Yee Chee Hann, Zainab Hamzah, and Khairunissa Syairah Ahmad Sohaimi

Department of Chemical Engineering Technology, Faculty of Engineering Technology, Universiti Malaysia Perlis (UniMAP), 02100 Sg Chuchuh, Padang Besar, Perlis, Malaysia

* ***Corresponding author:***

tel: +60-0176692384
email: izzatiiberahim@unimap.edu.my

Received: August 3, 2018
Accepted: December 14, 2018

DOI: 10.22146/ijc.40903

Abstract: *Extraction of omega-3 fatty acid from Jade Perch (*Scortum barcoo*) using enzymatic hydrolysis techniques are expected to be more economically possible techniques due to the uses of the enzyme with the characteristic of environmentally friendly, reusable and less energy required during large-scale production. Design of Experiments (DOE) was used to study the effect of process parameters such as the concentration of alcalase (0.5–1.5%), temperature (50–70 °C) and pH (6.5–8.5) towards the yield of oil. The findings showed 16.55% of oil yield was extracted from the jade perch under an optimum condition at 50 °C, 6.5 pH with 0.5% of enzyme concentration for 2 h incubation time. The fish oil was then undergone enzymatic concentration of omega-3 FA using lipase from* Candida rugosa. *The acid value and peroxide value of the fish oil was 71.422 mg KOH/g and 0.799 meq/kg, while the acid and peroxide value of the omega-3 concentrated oil was lower to 49.074 mg KOH/g and 0.399 meq/kg. The FTIR spectrum showed the presence of C–H stretch, =C–H stretch and C=O stretch bond justified the existence of lipids as it presents of alkanes, alkene, and carboxylic acids functional group. At the same time, GC-MS analysis showed the fish oil contains higher total PUFA content and omega-3 fatty acid content than omega-3 concentrated oil.*

Keywords: Scortum barcoo*; jade perch; lipase; omega-3 fatty acid; enzymatic hydrolysis*

■ INTRODUCTION

Recently, many efforts have been done by researchers in both academy and industry in the utilization of the fish waste as the raw material and transform it into a more valuable product such as biofuel, protein, and oil [1]. For most parts, the high concentration of omega-3 fatty acid in fish oil has many applications in the pharmaceutical and nutraceutical field. The omega-3 fatty acid is a class of essential fatty acids that can help in treatment and prevention of various diseases such as cardiovascular disease, rheumatoid arthritis, autoimmune diseases, Attention Deficit Hyperactivity Disorder (ADHD) and Alzheimer's disease [2]. Moreover, an omega-3 fatty acid also helps in promoting brain health during pregnancy and early life of a baby, reduce asthma in children, reduce fat in the liver as well as prevent colon, prostate and breast cancer.

Scortum barcoo is a species of fish under the family of Terapontidae which has a common name, jade perch. It is originate come from Lake Eyre Basin, Queensland, Australia, where it normally found in the river basins of Australia with the Lake Eyre Basin and Barcoo river [3]. Jade perch have the highest concentrations of omega-3 fish oils, which are 2483 mg/100 g of fish fillet than sawfish and Atlantic salmon [4]. Jade perch is believed to be an alternative source of omega-3 as it contents a high concentration of omega-3 fatty acid.

Extraction of omega-3 fatty acid from fish fillets using enzymatic hydrolysis techniques are expected to be more economically possible techniques due to the uses of the enzyme with the characteristic of reusable, environmentally friendly and less energy required during large-scale production. In other words, enzymatic hydrolysis improves the hydrolysis process by

utilizes enzymes that disrupt tissue resulting in the release of lipids would more environmentally friendly and safe method for the efficient release of oils [5]. Nowadays, it is important to utilize the fish waste which has been cause several environment effects in another country. Another extraction method, such as supercritical fluid extraction and heat extraction required high energy consumption, which will directly increase the cost of production and safety concern. In addition, solvent extraction utilizes a carcinogenic solvent, which will cause the environment and health concern as omega-3 fatty acids for human consumption. Moreover, there is a lack of research regarding the omega-3 fatty acid extraction from jade perch using enzymatic hydrolysis method. By considering this, the present investigation is focusing on extraction of omega-3 fatty acid from jade perch using enzymatic hydrolysis techniques that would later be optimized its recovery process for the improvement in term of quality of oil and its yield.

■ EXPERIMENTAL SECTION

Sample Collection and Preparation

Jade perch (*S. Barcoo*) which cultured by Institute of Agrotechnology Lestari (INSAT), Perlis was used as the sample in the experiment. The fillet of jade perch was chopped by using knife and chopper board without the addition of solvent or water to obtain a pure fish sample. Then, the fish fillet was weighed and put into the sealed plastic bag. The sample now is ready to conduct an experiment.

Procedure

Enzymatic hydrolysis of fish oil

About 50 g of fish sample was weighed in a 250 mL Erlenmeyer flask. In order to inactivate or denature the endogenous enzymes containing in the fish sample, the sample was heated at 95 °C for 5 min in the water bath. Next, 50 mL of distilled water was added into Erlenmeyer flask followed by pH adjustment to 6.5, 7.5 or 8.5 using 3 M NaOH. The flask was then transferred to preheated water bath shaker at temperature 50, 60 or 70 °C. The process of enzymatic hydrolysis was initiated when the alcalase concentration 0.5, 1.0 or 1.5% (w/w) of the fish sample was added into the Erlenmeyer flask. The hydrolysis process proceeded for 2 h at 120 rpm stirring speed in the water bath shaker. After the hydrolysis, the enzyme was inactivated or denatured by transferred the flask into the water bath for 5 min at 90 °C and then cooled into room temperature. In order to separate the oil with the solid sample, the mixture was transferred into a centrifuge tube and centrifuged at 3000 rpm for 20 min. Two layers of liquid consists of oil and emulsion layer formed on top were collected into another centrifuge tube. About 2 mL of NaCl solution with a concentration of 0.9% was added to extract impurities and centrifuged again for 10 min at 3000 rpm. The oil layer on top of the centrifuge tube was transferred into a test tube with the addition of anhydrous sodium sulfate to absorbs the water. The test tube was evenly stirred and allowed it to settle down. The oil was collected and keep at the pre-weighed universal bottle to determine the mass of oil extracted.

Preparation of fatty acid methyl ester (FAME)

Lipid extract with a volume of 100 µL was transferred into a cleaned 15 mL centrifuge tube which has been rinsed with chloroform and methanol 3 times respectively. Then, 3.0 mL of Hilditch reagent and 1.5 mL methylene chloride 0.01% v/w BHT was added subsequently into the vial. The preparation of Hilditch reagent was done by adding 1.5 mL of concentrated sulphuric acid (H_2SO_4) into the 100 mL of dry methanol. The preparation of 100 mL of dry methanol was done by transferring 100 mL methanol to a 100 mL volumetric flask, then anhydrous of sodium sulfate (Na_2SO_4) was added in sufficient amount to the methanol until the bottom of the flask was covered. The solution was mixed gently by inverting up and down for 10 min, then decanted. Next, the sample was capped and shake vigorously for 1 min. The tube was flushed with nitrogen, capped and sealed with Teflon® tape. Drying oven at 100 °C was used to incubate the sample for 1 h to make sure the transesterification reaction occurs. The tube was cooled to room temperature. 1.5 mL of hexane and 1 mL of distilled water was added into the tube followed by shake vigorously for 30 sec. The upper layer was pipetted to a new vial without disturbing the lower

layer. The step was repeated by adding 1.5 mL of hexane into the residue followed by shake vigorously for 30 sec, and the organic layer was collected. Evaporation of hexane was done with a gentle stream of nitrogen in a fume hood. 0.5 mL of hexane is added to re-suspend the fatty acid. Finally, the vial was capped with a nitrogen flush, followed by sealed with Teflon® tape.

Determination of acid value

About 0.5–2.5 g of oil sample was weighed using 250-mL glass Erlenmeyer flask. 2 mL of 1% of phenolphthalein indicator together with 125 mL of 1:1 toluene-isopropyl alcohol was poured into the 250-mL glass Erlenmeyer flask containing oil sample and mixed thoroughly in the 250 mL Erlenmeyer flask. 0.1 N KOH was used to titrate the sample until a permanent pink color appear. The acid value with a unit of mg KOH/g of sample was determined by the Eq. (1).

$$\text{Acid value}=\frac{(A-B)\times N\times 56.1}{W} \quad (1)$$

where A = Volume of KOH used in the titrating the sample (mL); B = Volume of KOH used in the titrating the blank (mL); N = normality of standard alkali; W = Mass of oil sample (g); and 56.1 = molecular weight of KOH in grams.

Determination of peroxide value

About 2.5 g of oil sample was weighted at the beginning and added into 250 mL Erlenmeyer flask. Next, 50 mL 3:2 acetic acid-chloroform was added into the flask and the flask was stirred until the oil sample dissolved into the solution. One milliliter of saturated potassium iodide (KI) solution was added and stand in room temperature for 1 min with occasional swirling. Then, 100 mL of distilled water was added into the flask. Titration was carried out until the light-yellow color appeared using 0.01 N sodium thiosulfate. Approximately 1 mL of starch indicator solution was added and continue titration until the colorless solution formed with constant agitation. On the other hand, the blank sample was prepared without the addition of the oil sample. The peroxide value (milliequivalents peroxide/1000 g sample) was determined by the Eq. (2).

$$\text{Peroxide value}=\frac{(S-B)\times N\times 1000}{W} \quad (2)$$

where B = Volume of sodium thiosulfate used for titration of blank (mL); S = Volume of sodium thiosulfate used for titration of sample (mL); N = normality of sodium thiosulfate solution; 1000 = per 1000 g of sample; W = Mass of sample (g).

Determination of lipid yield

The lipid yield was determined by the following formula:

$$\text{Lipid yield}(\%)=\frac{\text{Mass of total lipid content}}{\text{Mass of fish sample}}\times 100\% \quad (3)$$

FTIR spectroscopy analysis

The mid-infrared spectral (4000–700 cm^{-1}) data were collected by using an FTIR portable spectrometer (Perkin Elmer) equipped with a temperature-controlled, 5-bounce ZnSe crystal ATR. The sample which has been sealed with parafilm was cooled to room temperature prior to data collection. The data were recorded in duplicate. First, oil with a volume of 80 µL was deposited using micropipette on ATR sensor and kept at 65 °C, and the spectra were performed over a range of 4000–700 cm^{-1} at 4 cm^{-1} resolution. The spectra were collected in terms of absorbance using Perkin Elmer Spectrum Version 10.5.2.

Optimization of antimicrobial activity

Fatty acids were categorized into several classes based on the carbon atom by utilizing the Agilent 7890A Gas Chromatography (GC) system equipped with mass spectrometer system (MS) of an Agilent 5975C inert MSD with triple-axis detector which is shown in Table 1 as the protocol.

Optimization of extraction oil yield

The Design-Expert® is used to study the optimization of oil yield in the extraction of fish oil using enzymatic hydrolysis method using an alcalase enzyme. By using Response Surface Methodology (RSM) coupled with Central Composite Rotatable Design (CCRD), different enzyme concentration, incubate temperature, and pH is set as a parameter. The selected range of the parameter used is stated in Table 2.

Table 1. Protocol for fatty acid analysis using GC-MS

Instrumental Parts	Particulars
Gas Chromatography system	7890A, Agilent Technologies
Detector	Mass spectrometer system Agilent 5975C inert MSD
Column	BP20 (wax) polar capillary column 30 m in length, 0.25 mm of internal diameter and 0.25 μm film thicknesses
Carrier gas	Helium
Carrier gas flow rate	1 mL/min
Oven	Initially 55 °C for 3 min
	Ramping to 250 °C at a rate of 6 °C /min for 5 min
Injector Temperature	200 °C
Detector Temperature	230–230 °C (Ion generation)
	150–200 °C (Ion acceleration)

Table 2. The ranges of the studied parameter

Parameters	Range	
	Minimum	Maximum
Concentration of enzyme (%)	0.5	1.5
Temperature (°C)	50	70
pH	6.5	8.5

■ RESULTS AND DISCUSSION

Statistical Analysis for the Optimization Study

CCRD with duplication of factorial point and three central points was used to analyze the relationship between three different parameters (concentration of enzyme, temperature, and pH) towards the percentage of oil yield. The design model consists of a total of 22 runs of an experiment which is used to develop the regression model. Table 3 shows the complete design matrix and its response to parameters in CCRD. The highest percentage of oil yield is 16.86% at running 1 (0.50% enzyme concentration, 50 °C, pH 6.5); meanwhile, the lowest percentage of oil yield obtained is 12.24% at run 22 (1.00% enzyme concentration, 60 °C, pH 7.5).

The result of the Analysis of Variance (ANOVA) for response surface quadratic model on percentage oil yield was showed in Table 4. From Table 4, model F-value of 12.19 suggested that the model was significant due to the P-values of the model were less than 0.05, and thus, they were significant. In addition, the "Prob > F" of variable B were less than 0.05 means that the model terms were significant. In another word, factor B, which is temperature have a significant effect on the model with the highest F-value of 56.91. Therefore, the temperature is one of the significant factors that affect the enzyme activities towards hydrolysis process. Moreover, the mean of the model was 14.61, while the standard deviation was 0.68. The R^2 value indicates the correlation coefficient between the actual and predicted value was obtained, which is 0.8823. Therefore, the actual value was almost achieved the predicted value when the R^2 value is near to 1. The "lack of fit F-value" of 3.68 suggested that the lack of fit is not significant relative to the pure error. There was only a 5.09% chance that a model F-value could occur due to noise. Non-significant lack of fit is good and acceptable. The final model equations of actual factors were expressed as the following equation:

In term of actual factors:

$$\begin{aligned}\text{Oil yield}(\%) = {} & +26.17812 - 23.90937 * \text{Conc. of enzyme} \\ & +0.42347 * \text{Temp.} - 2.62208 * \text{pH} + 0.059375 * \text{Conc. of} \\ & \text{enzyme} * \text{Temp.} + 0.14875 * \text{Conc. of enzyme} * \text{pH} + \\ & 0.041063 * \text{Temp.} * \text{pH} + 9.79375 * \text{Conc. of enzyme}^2 \\ & -7.65313\text{E} - 003 * \text{Temp.}^2\end{aligned} \quad (4)$$

Temperature (B) which has a highest F value affect the percentage of oil yield obtained significantly, while the concentration of enzyme and pH showed an insignificant effect in ascending order toward the hydrolysis process at a 95% confidence level ($p < 0.05$). By compare run #10 and #14 as well as run #4 and #11 (or other comparable runs) respectively, an increase in temperature or pH caused a decrease in the percentage of lipid yield. High temperature and alkaline condition change the specific structure of the enzyme, disrupts the

Table 3. Complete design matrix and its response of parameters in CCRD

Run	Concentration of Enzyme (%)	Temperature (°C)	pH	Percentage of Oil Yield (%)	
				Actual	Predicted
1	0.50	50.00	6.50	16.86	16.98
2	0.50	50.00	6.50	16.83	16.98
3	1.50	50.00	6.50	17.16	16.6
4	1.50	50.00	6.50	16.80	16.6
5	0.50	70.00	6.50	12.94	13.02
6	0.50	70.00	6.50	13.86	13.02
7	1.50	70.00	6.50	13.67	13.82
8	1.50	70.00	6.50	13.69	13.82
9	0.50	50.00	8.50	16.12	15.99
10	0.50	50.00	8.50	16.14	15.99
11	1.50	50.00	8.50	15.08	15.90
12	1.50	50.00	8.50	15.96	15.90
13	0.50	70.00	8.50	13.47	13.67
14	0.50	70.00	8.50	13.10	13.67
15	1.50	70.00	8.50	15.23	14.77
16	1.50	70.00	8.50	14.58	14.77
17	1.00	40.00	7.50	12.90	12.90
18	1.00	60.00	5.50	13.56	13.43
19	1.00	60.00	9.50	14.51	13.39
20	1.00	60.00	7.50	14.01	13.41
21	1.00	60.00	7.50	12.73	13.41
22	1.00	60.00	7.50	12.24	13.41

Table 4. ANOVA for response surface quadratic model on percentage oil yield

Source	Sum of Square	DF	Mean Square	F Value	Prob > F	Remark
Model	44.6	8	5.58	12.19	< 0.0001[a]	significant
A	0.51	1	0.51	1.11	0.3114[b]	not significant
B	26.04	1	26.04	56.91	< 0.0001[a]	significant
C	0.0022	1	0.0022	0.0048	0.9457[b]	not significant
AB	1.41	1	1.14	3.08	0.1027[b]	not significant
AC	0.089	1	0.089	0.19	0.6473[b]	not significant
BC	2.70	1	2.70	5.90	0.0304[a]	significant
A^2	23.68	1	23.68	61.77	< 0.0001[a]	significant
B^2	6.46	1	6.46	14.13	0.0024[a]	significant
Residual	5.95	13	0.46			
Lack of fit	3.12	3	1.04	3.68	0.0509	not significant

R^2 = 0.8823; adjusted R^2 = 0.8099; standard deviation = 0.68; mean = 14.61

[a] Significant at 95% confident interval. [b] Not significant at 95% confident interval.

Notes: A: Concentration of enzyme; B: Temperature; C: pH

three-dimensional shape of functional alcalase as enzyme caused denaturation and inhibits the enzyme activity [7-8]. By comparing run #1 and #3 (or other comparable runs) in which an increase of the concentration of enzyme caused an increase in the percentage of lipid yield. Unfortunately, a 3-fold increase in the

concentration of enzyme contributes to a small increment in lipid yield [9]. Therefore, 0.5% w/w of enzyme load consider as an optimum point because increase the enzyme concentration does not significantly increase in lipid yield. Moreover, low enzyme concentration used to reduce the cost associated with the enzyme during production scale.

Optimal Design

Validation was carried out in order to validate the predicted responses designed by the software and figure out the optimal conditions by varying the parameters (concentration of enzyme, temperature, and pH) to produce the highest percentage oil yield. The optimal conditions obtained at 0.5% w/w concentration of alcalase enzyme, the temperature of 50 °C and pH of 6.5 with a desirability value of 0.964 and 16.98% predicted value which is within the range of parameters selected on hydrolysis of jade perch fish using alcalase. The validation was carried out by conduct triplicate experiments with the optimum variables. The average percentage of oil yield obtained is 16.545%, which is relatively lower than the predicted value. The percentage error has been calculated, which is 2.57%. Based on the experimental results obtained, the optimum response condition designed by RSMCCRD is valid and suitable for the enzyme-assisted extraction of oil because the percentage error is less than 10%.

Fourier Transform Infrared (FTIR) Spectroscopy Analysis

The fish oil samples before and after treated with lipase from *Candida rugosa* were tested with FTIR spectroscopy to determine the type of bonding and functional group presence in the sample based on FTIR spectra detected. The FTIR spectra were measured within the range of 4000–700 cm^{-1} wavelength. Fig. 1 shows the comparison of FTIR spectra between fish oil and omega-3 concentrated oil. The spectra of the sample showed the presence of similar functional group and compounds in both samples such as alkanes, alkenes, carboxylic acids, ester, ether, aromatics, amide, etc. The FTIR spectra showed the absorption peaks at 3100–3000 cm^{-1} is attributed to the C–H stretch from aromatics group and =C–H stretch from alkene group. These absorption band observed at 3007 cm^{-1} (fish oil) and 3006 cm^{-1} (omega-3 concentrated oil) indicated the presences of unsaturated fatty acid. The finding proved by the previous study which proportion of mono and polyunsaturated acyl groups present at peaks approximately 3008 cm^{-1} due to carbon double bond [10].

In addition, absent of peaks at approximately 3290 cm^{-1}, which is a strong O–H stretching modes of water represents both samples are free from the moisture [11]. The absorption peaks at 3000–2850 cm^{-1} shows the

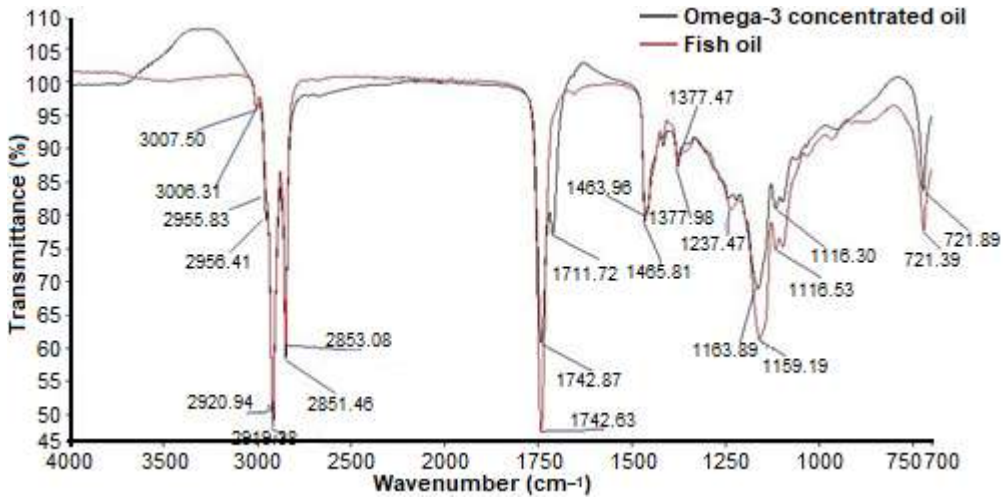

Fig 1. Comparison of FTIR spectrum between fish oil and omega-3 concentrated oil

presence of alkane group due to the C–H stretch while absorption peaks in the range of 3300–2500 cm^{-1} indicated the presence of carboxylic acids due to O-H stretch bond. Based on the result, the absorption band in oil sample before and after lipase treated observed at 2956, 2921, 2852 and 2956, 2919, 2851 cm^{-1} respectively shows the presence of alkane in the sample. Besides, absorption peaks at 1760–1665 and 1760–1690 cm^{-1} represented the presence of C=O stretch bond from carbonyls, carboxylic acids, ester, and saturated aliphatic group respectively. Those bonds detected justified the existence of lipids in the sample. In the previous study, it was reported that the absorption peaks were asymmetrical C–H stretch from methyl ($–CH_3$) group of lipids at ~2970 cm^{-1}, asymmetrical C–H stretch from methylene ($–CH_2$) group of lipids at ~2920 cm^{-1} and symmetrical C–H stretch from methylene ($–CH_2$) group of lipids at ~2850 cm^{-1} which have the same result obtained in the experiment [11].

Moreover, the finding also comes to an agreement that major bands can be observed resulting from lipids near 2930 cm^{-1} while from protein at near 1640 and 1550 cm^{-1} and carbohydrate near 1030 cm^{-1} [12]. Therefore, the sample is free from protein and carbohydrate molecule due to the absence of peaks in that region. Although the fish oil sample spectra having similarity especially in wavelength 3100–1600cm^{-1}, it shows differences in term of the amount of the specific type of bonding which reflected by the % transmittance due to the difference in nature and composition of fish oils [2].

Determination of acid value. The acid value used to determine the presence of FFAs and other non-lipid acid compounds in the oil [13-14]. Based on the result obtained, both oil sample before and after lipase activity having a high acid value which is 71.42 mg/KOH g and 49.07 mg/KOH g, respectively, as compared to the recommended value (≤ 5 mg/KOH g). This could be due to the high temperature, and acid/base condition increase the degree of unsaturation, caused the physicochemical changes of fish oil during incubation. Therefore, prolonged high temperature or exposed to acids or bases caused oil rancidity, which conversion of triacylglycerides occur, resulting in the formation of fatty acid and glycerol, which increase the acid value [15].

Determination of peroxide value. Peroxide value is the measurement of hydroperoxides and used to determine the primary oxidation of oil [13]. Based on the result obtained both oil sample before and after lipase activity having a low peroxide value which is 0.799 meq/kg and 0.399 meq/kg, respectively, as compared to the recommended value (≤ 5 meq/kg). The previous finding stated that low pH range decrease the lipid oxidation rate resulting in low peroxide value obtained. In addition, increase temperature caused the increase in peroxide value due to high temperature accelerated the lipid oxidation [7]. The finding was justified in which low peroxide value was obtained due to low pH (6.5–7) and low temperature (35–50 °C) condition during incubation.

Gas Chromatography-Mass Spectroscopy (GC-MS) Analysis

GC-MS analysis is used to analyze the fatty acid composition in the fish oil and also omega-3 concentrated oil [16]. About 20 fatty acids have been identified in crude jade perch fish oil using the GC analysis. Table 5 shows the summarized fatty acid composition of crude fish oil and omega-3 concentrated oil. Three main fatty acid composition such as saturated FA, monounsaturated FA, and polyunsaturated FA were obtained from crude oil which extracts from jade perch using enzymatic hydrolysis technique. Saturated FA is a fatty acid that saturated with hydrogen which forms a straight hydrocarbon chain. Monounsaturated FA consists of one carbon-carbon double bond in a different position which also known as monoenes. Polyunsaturated FA consists of two or more carbon-carbon double bond. omega-3 is the type of polyunsaturated FA in which the first double bond found between the third and fourth carbon atom while omega-6 also type of polyunsaturated FA where the first double bond found between the sixth and seventh carbon atom [17]. Based on Table 5, the highest concentration of fatty acids in both fish oil and omega-3 concentrated oil was elaidic acid (18:1 n-9) followed by palmitic acid (16:0). The predominant fatty acid content in both samples is monounsaturated fatty acids (MUFA)

Table 5. Comparison of the fatty acid composition of fish oil and Omega-3 concentrated oil

Fatty Acids	Composition (%)	
	Fish Oil	Omega-3 Concentrated Oil
Saturated Fatty Acids		
Dodecanoic acid (12:0)	0.5192	0.3795
Myristic acid (14:0)	2.601	2.422
Palmitic acid (16:0)	29.41	31.56
Arachidic acid / Eicosanoic acid (20:0)	0.1744	0.1271
Subtotal	32.70	34.49
Monounsaturated Fatty Acids		
Palmitoleic acid (16:1n-7)	4.139	4.167
Elaidic acid (18:1n-9)	37.75	37.98
Subtotal	41.89	42.15
Polyunsaturated Fatty Acids		
Omega-3 Fatty Acid		
α-linolenic acid, ALA(C18:3n−3)	0.7612	0.7025
Eicosapentaenoic acid, EPA(C20:5n−3)	-	0.173
Heneicosapentaenoic acid, HPA(21:5n-3)	0.2596	-
Docosahexaenoic acid, DHA(C22:6n−3)	0.8851	0.6619
Subtotal	1.906	1.537
Omega-6 Fatty Acids		
linoleic acid (18:2n-6)	11.58	10.86
γ-linolenic acid (18:3n-6)	1.104	1.240
Eicosadienoic acid (20:2n-6)	0.2315	0.5127
Dihomo-γ-linolenic acid (20:3n-6)	0.6817	0.5454
Subtotal	13.60	13.15
Omega-9 Fatty Acids		
Isolinoleic acid (18:2n-9,12)	1.345	1.440
Subtotal (PUFA)	16.85	16.13
Others compound	8.565	7.229
Total	100	100

followed saturated fatty acids. The percentage of total MUFA in the oil sample was in the range of 41.89 to 42.15%, which mainly consists of elaidic acid and palmitoleic acid.

Omega-3 concentrated oil contains higher elaidic acid (37.98%) than in the fish oil, which contains only 37.75%. Meanwhile, the highest fatty acids among saturated fatty acids group were palmitic acids, which contain 29.41% in a fish oil sample and 31.56% in omega-3 concentrated oil. However, the PUFA, which consists of omega-3, omega-6, and omega-9, were identified in the study. By referring to Table 5, the total PUFA content sample in fish oil is 16.85%, which is higher than in the omega-3 concentrated oil (16.13%). The result shows total omega-3 in fish oil was 1.906%, which consists of ALA, HPA, and DHA with the percentage of 0.7612, 0.2596, and 0.8851% respectively, while the percentage of omega-3 decreased to 1.5374% in omega-3 concentrated oil. The omega-3 presence in omega-3 concentrated oil consists of ALA, EPA, and DHA with the percentage of 0.7025, 0.173, and 0.6619% respectively. The decrease in omega-3 concentration may be due to the stirring effect during incubation. The finding proved by previous research in which low

stirring resulting in low omega-3 fatty acid content as enzyme are not oil soluble. Low stirring inhibits the formation of the enzyme-substrate complex and directly affect the rate of reaction [7]. In addition, auto-oxidation more flavor to occur in the presence of high quantities of n-3 PUFAs due to the high number of double bonds in the structure of PUFAs, which leads to successive degradation.

■ CONCLUSION

As a conclusion, extraction of fish oil has been successfully done using alcalase enzymatic hydrolysis technique. The parameters chosen are concentrations of enzyme, temperature, and pH, which play a major role in regulating the enzymatic hydrolysis process. The hydrolysis process optimum at 50 °C with pH 6.5 and 0.5% w/w enzyme concentration. The oil yield obtained from optimum condition was 16.55%. This model is applicable in industrial or research reference as the percentage error less than 10%. In FTIR analysis, the function groups alkanes, alkenes, carbonyl, and carboxylic acids are detected in both fish oil and omega-3 concentrated oil. Furthermore, the acid value for both fish oil and omega-3 enriched oil was excess the acceptable limits (< 5 mg KOH/g) which is 71.42 mg KOH/g and 49.07 mg KOH/g respectively. However, the peroxide value of fish oil and omega-3 enriched oil was 0.799 meq/kg and 0.399 meq/kg, respectively, which is within the allowed range (≤ 5 meq/kg). In qualitative and quantitative analysis, 1.906% of ALA, HPA, and DHA in the fish oil sample was analyzed using GC-MS. Lastly, ALA, EPA, and DHA were present in the omega-3 concentrated oil sample with a total percentage of 1.54%. The lipase concentrated process gives a negative effect toward the omega-3 content due to auto-oxidation. Therefore, jade perch was believed to be an alternative way for the source of omega-3 due to the presence of omega-3 fatty acid in fish fillet which has been successfully extracted using enzymatic hydrolysis technique in the experiment.

■ ACKNOWLEDGMENTS

The author would like to acknowledge support from the Short Term Grant under a grant number of 9001-00509, Universiti Malaysia Perlis (UniMAP).

■ REFERENCES

[1] Arvanitoyannis, I.S., Tserkezou, P., 2013, "Fish Waste Management" in *Seafood Processing: Technology, Quality, and Safety*, Eds., Boziaris, I.S., John Wiley & Sons, Ltd., 263–309.

[2] Zhang, J., 2009, Analysis and Characterization of Consumer Products by FTIR, Chemometric and Two Dimensional ATR-FTIR Correlation Spectroscopy, *Dissertation*, New Brunswick, Rutgers University, The State University of New Jersey.

[3] Ihwan, M.Z., Syahnon, M., Fakhrul, I.M., Marina, H., and Ambak, M.A., 2016, New report on Trichodiniasis (Protozoa: Ciliophora: Peritrichida) in jade perch; *Scortum barcoo* from Peninsular Malaysia, *J. Fish. Aquat. Sci.*, 11 (6), 437–443.

[4] Gapinski, F., 2010, Jade Perch–The Perfect *Aquaponics* Fish!, http://www.ecofilms.com.au/jade-perch-the-perfect-aquaponics-fish/, accessed on 1 March 2017.

[5] Vang, B., 2015, Recovery and properties of oil from the copepod *Calanus finmarchicus*, *Dissertation*, The Arctic University of Norway.

[6] Bhandari, K., Chaurasia, S.P., and Dalai, A.K., 2013, Hydrolysis of tuna fish oil using *Candida rugosa lipase* for producing fatty acids containing DHA, *IJANS*, 2 (3), 1–12.

[7] Mohanarangan, A.B., 2012, Extraction of Omega-3 Fatty Acids from Atlantic Herring (*Clupea harengus*), *Thesis*, Dalhousie University, Halifax, Nova Scotia.

[8] Sun, H., Chen, Z., Wen, P., Lei, H., Shi, J., Huang, M., and Wang, J., 2012, Optimization of enzymatic hydrolysis conditions for preparation of gingko peptides from ginkgo nuts, *Int. J. Food Eng.*, 8 (1), 1–15.

[9] Ramakrishnan, V.V., Ghaly, A.E., Brooks, M.S., and Budge, S.M., 2013, Extraction of proteins from mackerel fish processing waste using alcalase enzyme, *J. Bioprocess Biotechniq.*, 3 (2), 1000130.

[10] Ogunbusola, E.M., Fagbemi, T.N., and Osundahunsi, O.F., 2017, Fatty acid

characterisation, sterol composition and spectroscopic analysis of selected Cucurbitaceae seed oils, *Int. Food Res. J.*, 24 (2), 696–702.

[11] Vongsvivut, J., Heraud, P., Zhang, W., Kralovec, J.A., Mcnaughton, D., and Barrow, C.J., 2012, Quantitative determination of fatty acid compositions in micro-encapsulated fish-oil supplements using Fourier transform infrared (FTIR) spectroscopy, *Food Chem.*, 135 (2), 603–609.

[12] Hamzah, Z., Jeyaraman, S., Ibrahim, N.H., Hashim, O., Lee, B.B., and Hussin, K., 2013, A rapid technique to determine purity of edible bird nest, *Adv. Environ. Biol.*, 7 (12), 3758–3765.

[13] Deepika, D., 2014, The potential of fish processing wastes for biodiesel production, *Final Report*, Marine Institute of Memorial University of Newfoundland, Canada.

[14] Rubio-Rodríguez, N., Beltrán, S., Jaime, I., de Diego, S.M., Sanz, M.T., and Carballido, J.R., 2010, Production of omega-3 polyunsaturated fatty acid concentrates: A review, *Innovative Food Sci. Emerg. Technol.*, 11 (1), 1–12.

[15] Su Pak, C., Bragadottir, M., 2005, *Stability and quality of fish oil during typical domestic application*, The United Nations University, Fisheries Training Programme, Iceland.

[16] Iberahim, N.I., Hamzah. Z., Yin, Y.J, Sohaimi, K.S.A., 2018, Extraction and characterization of omega-3 fatty acid from catfish using enzymatic hydrolysis technique*, MATEC Web Conf.*, 187, 01005.

[17] Rustan, A.C., and Drevon, C.A., 2005, "Fatty Acids: Structure and Properties" in *Encyclopedia of Life Sciences,* John Wiley & Sons, Ltd., 1–7.

Effect of Steam Treatment on the Characteristics of Oil Palm Empty Fruit Bunch and Its Biocomposite

Abdul Muttalib Bin Bujang and Noor Ida Amalina Binti Ahamad Nordin*

Faculty of Chemical and Natural Resources Engineering, Universiti Malaysia Pahang, Lebuhraya Tun Razak 26300, Gambang, Pahang, Malaysia

** Corresponding author:*

tel: +60162022940
email: idamalina@ump.edu.my

Received: August 3, 2018
Accepted: December 12, 2018

DOI: 10.22146/ijc.40906

Abstract: *Oil palm empty fruit bunch (EFB) has a big potential in biocomposite production. The porous surface of EFB is advantageous for physical interlocking with polymer in composite fabrication. The objective of this study is to determine the properties of biocomposite prepared from steam-treated EFB with polypropylene (PP). The EFB was treated using steam at 120 °C for 30 min (Steam-30) and 60 min (Steam-60) in an autoclave. The biocomposite was prepared from EFB and PP at different fiber contents (10 and 30 wt.%). The Steam-30 EFB partially removed silica bodies and other impurities without damaging the surface of the EFB. The thermal stability improved from 276 to 283 °C. The Steam-30/PP biocomposite had the highest tensile strength at 10 and 30 wt.% EFB contents with the increments of 23.9 and 23.8%, respectively, compared to that of the untreated EFB/PP biocomposite. The Steam-30/PP biocomposite containing 30 wt.% of EFB had a low water absorption of 5.6% compared to that of the untreated EFB/PP biocomposite at 7.2%. In conclusion, steam treatment improved the characteristics of EFB and increased the compatibility between the fiber and polymer.*

Keywords: *empty fruit bunch (EFB); polypropylene (PP); biocomposite; tensile strength; water absorption*

■ INTRODUCTION

The production of conventional plastics is associated with carbon dioxide emission and depends on crude oil resources as the raw material. In addition, the disposal of petroleum-based plastic products is linked to environmental pollution such as polluting the rivers, lakes, and oceans [1]. The negative impacts of microplastic substances in the soil is also an emerging issue [2-3].

Therefore, biocomposites are considered to be more environmentally friendly as their products used less petroleum-based polymer and produce less toxic side products [4-5]. In palm oil mills, biomass fiber such as empty fruit bunch (EFB) is used for power generation (as a fuel for the boiler) and fertilizer in the plantation [6-7]. However, biomass fiber is not utilized efficiently due to the large amount generated on a daily basis. Therefore, there is a need to propose an alternative usage of the biomass fiber; thus it will add value to the biomass and at the same time will help in managing this biomass in the mill.

Since biomass fiber has high fiber content, it has the potential to be as reinforcement in the composite. However, to utilize EFB as a reinforcing material, there is a need to improve the characteristics of the fiber [8-9]. The incompatibility between the hydrophobic polymer and the hydrophilic fiber is the main drawback in the production of biocomposite. Steam treatment is one alternative that can be used as fiber treatment, and the treatment requires no chemical [10].

The aim of this research is to determine the properties of biocomposite prepared by steam-treated EFB and polypropylene (PP). The EFB underwent steam treatment at 120 °C for 30 and 60 min that modified the fiber surface. The preparation of biocomposite involves the use of PP at different fiber contents (10 and 30 wt.%). The characterization of the untreated and treated EFB was analyzed for its morphology and thermal analysis.

As for biocomposite, tensile test, scanning electron microscopy (SEM) and water absorption analysis was conducted. Water absorption analysis able to demonstrate the toleration of biocomposite in water.

■ EXPERIMENTAL SECTION

Materials

The materials used were PP, EFB, and sodium hydroxide (NaOH). The EFB was collected from Lepar Hilir Palm Oil Mill in Gambang, Pahang. PP was bought from Commercial Plastic Industries Sdn. Bhd., Selangor, Malaysia. NaOH was supplied by Merck (Darmstadt, Germany) and used as received.

Procedure

Fiber treatment

The fresh EFB collected was washed and dried to remove dirt and any impurities. Steam treatment was conducted using an autoclave at 120 °C and 21 psi for 30 min (Steam-30) and 60 min (Steam-60). For a comparison with the chemical treatment, the EFB was treated with 5 wt.% of NaOH (alkali) for 3 h at room temperature. The untreated and treated EFB were ground and sieved to isolate ground fiber with a size of 180–355 μm.

Preparation of EFB/PP biocomposites

In the production of EFB/PP biocomposite, the materials were blended in a twin screw extruder machine (Model: Prism Eurolab 16) with fiber contents of 10 and 30 wt.%. The extruder was operated with inlet and die temperatures of 200 and 160 °C, respectively at 50 rpm rotor speed. The blended biocomposites were pressed using hot and cold press machine (Model: Lotus Scientific-2205) with a pressure of 10 KPa to produce thin film EFB biocomposites with a size of 10 × 10 cm and 1 mm thick. The hot press machine was operated at 180 °C with molding and cooling times of 10 min each.

Thermal gravimetric analysis

The thermal gravimetric analysis (TGA) for the EFB fiber and EFB/PP biocomposite were done using Hitachi STA7200 thermal analysis. The analysis was conducted in a nitrogen atmosphere with a gas flow rate of 50 mL/min by heating from 30 to 600 °C at a heating rate of 10 °C/min. About 1–6 mg of samples were placed in an aluminum pan [11].

Morphological analysis

Hitachi TM3030 Plus tabletop microscope was used for SEM analysis. The samples were mounted on the aluminum specimen stubs using double-sided adhesive carbon tabs [11]. The SEM analysis was also done on the fractured biocomposite from tensile tests to observe the physical adhesion of EFB with the PP matrix.

Tensile strength properties

The tensile test was conducted at a crosshead speed of 10 mm/min using an AG-1 Shimadzu universal testing machine according to ASTM D638 and fitted with a 1000 N load cell [12]. The average value from five specimens was taken as the tensile strength of the EFB/PP biocomposite.

Water adsorption analysis

The weight of the samples was measured before and after the treatment. The samples were carefully cut in the size of 3 × 2 cm to avoid any cracks. The specimens were dried at 60 °C in an oven until a constant weight was reached. The initial weight of the dried samples was recorded. The samples were immersed in distilled water for 12 days at room temperature, and the weight increment was recorded [13].

■ RESULTS AND DISCUSSION

Thermal Stability Analysis of EFB

The thermal degradation of EFB analyzed by TGA is shown in Table 1 by indicating the weight loss of the sample at 5, 20, and 50% weight loss. Also included is the percentage of residual of EFB at 550 °C. Fig. 1 shows the weight loss of the EFB sample, and three regions are denoting the weight loss: (i) < 100 °C, (ii) 150–220 °C, and (iii) 240–350 °C. The weight loss at less than 100 °C was due to moisture content. The second region of weight loss may be due to the hemicellulose component. It was reported that hemicellulose is enriched with carbon sugars chain and branched structures, which are susceptible to decomposition at low temperature (200–260 °C) [14]. The third region of weight loss is contributed to cellulose degradation. The residual mass

Table 1. Thermal stability analysis for EFB

EFB sample	Temperature for 5% weight loss (°C)	Temperature for 20% weight loss (°C)	Temperature for 50% weight loss (°C)	Residue at 550 °C (%)
Untreated	54.22	276.53	326.29	24.33
Steam-30	66.37	283.26	328.27	25.13
Steam-60	55.09	279.93	327.34	24.70
Alkali	69.13	293.66	336.93	27.11

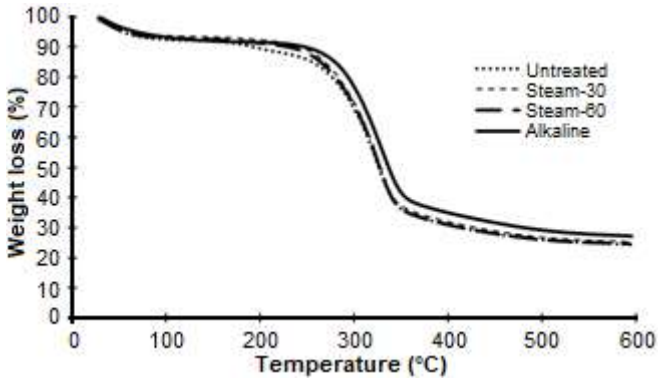

Fig 1. TG analysis for untreated and treated EFB

left at 550 °C mainly containing lignin [13].

In overall, the thermal degradation of treated EFB was increased compared to untreated EFB. The thermal degradation of the untreated EFB was recorded at a lower temperature compared to the treated EFB due to the presence of thermally unstable components such as hemicelluloses and low molecular lignin [15].

From Fig. 1, it can be observed that the weight loss in the temperature range of 150–220 °C contributes to hemicellulose content in the untreated EFB. While the partial removal of hemicelluloses after steam and alkali treatment increased the thermal degradation of the fiber [14]. Residue for treated samples was higher compared to the untreated fiber show that the treated fiber had a higher percentage of lignin. Lignin contains non-polar hydrocarbon and benzene rings making it less hydrophilic. Thus, the increased residue shows the treated fiber had better hydrophobicity compared to untreated fiber.

Morphological Analysis of EFB

Fig. 2 shows the images of EFB at 300×, 500×, and 1000× magnifications. The untreated EFB surfaces were covered with silica bodies. However, the silica bodies are not clearly observed due to wax and other impurities that covered the surface of the fiber. Silica bodies in nature act as a shield against fungal attack and give support to the plant structure [13]. Fig. 2(b) shows the structure of Steam-30 where it can be observed that the silica bodies were partially removed making the strand to have a rough surface. The removal of silica on fiber surface is good for fiber-matrix adhesion because it provides the physical interlocking between the fiber and polymer [11].

Fig. 2(c) shows a rough surface of Steam-60 compared to Steam-30 due to the longer retention time exposed to the high pressure of steam. More silica bodies were removed from the surfaces, and the fiber surfaces were cracked and damaged. The open structure of the fiber due to crack will benefit the adhesion between fiber and polymer, where the polymer can penetrate the

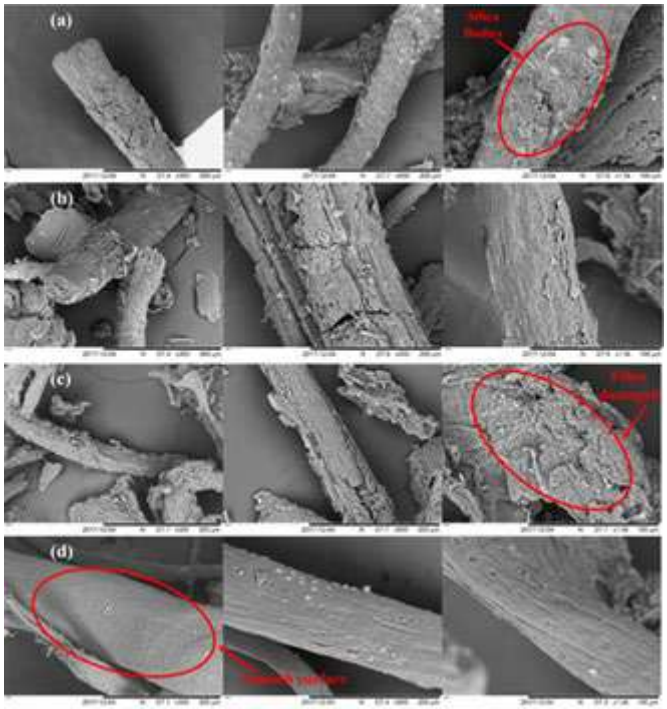

Fig 2. Morphology analyses of EFB, (a) Untreated, (b) Steam-30, (c) Steam-60, and (d) Alkali

structure of the fiber; thus adhesion is improved. Fig. 2(d) shows that the structure of Alkali treated EFB changed. According to Izani et al. [11], NaOH treatment removes the wax and cuticle by the interaction with sodium and makes the surfaces of EFB smoother [16].

Tensile Properties of EFB/PP Biocomposites

Table 2 shows the data for the tensile strength of EFB/PP biocomposites from different treatments and percentages of EFB loading. The tensile strength decreased as the percentage of EFB loading was increased. Steam-30 biocomposite had the highest tensile strengths for both 10 and 30 wt.% of EFB loadings followed by Alkali, untreated, and Steam-60 biocomposite.

It was reported that the tensile strength for pure PP was around 30–40 MPa [17]. Biocomposite prepared from 10 wt.% of EFB loading was able to improve the tensile strength of PP in the range of 43–60%. Meanwhile, 30 wt.% of EFB loading improved the tensile strength for 30–44%.

Thermal Stability Analysis of EFB/PP Biocomposites

Table 3 shows the thermal stability of the EFB/PP biocomposite. In overall, the thermal stability of biocomposites prepared from treated EFB had improved compared to untreated EFB biocomposite. Fig. 3 presents the weight loss of the untreated EFB and treated EFB/PP biocomposites at 30 wt.% of EFB loading.

The first stage of thermal degradation of EFB/PP biocomposite started at a temperature above 270 °C due to the fiber content in the polymer matrix. The second stage started to degrade at a temperature of 410 °C was due to the PP.

Morphological Analysis of EFB/PP Biocomposites

Fig. 4 shows the SEM images of the fractured sample from a tensile test of the EFB/PP biocomposites at 30 wt.% fiber loading.

Fig. 4(a) shows that the fiber was pulled out indicating a poor adhesion between the fibers and

Table 2. Tensile strengths of EFB/PP biocomposites

EFB/PP biocomposite	Tensile strength (MPa)	
	10 wt.% of EFB loading	30 wt.% of EFB loading
Untreated	72.22	51.70
Steam-30	89.45	64.00
Steam-60	62.21	50.91
Alkali	76.53	54.24

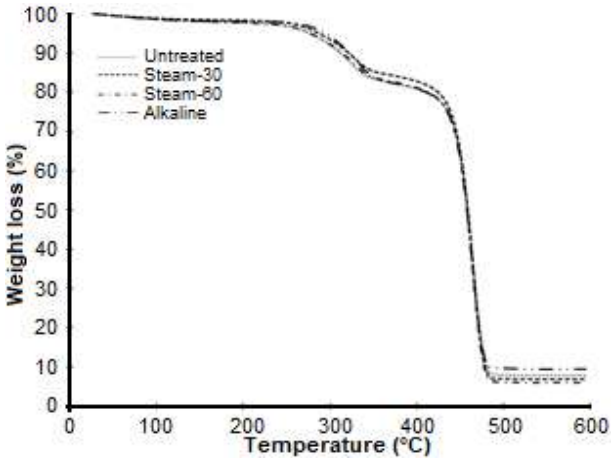

Fig 3. TG analysis of EFB/PP biocomposites

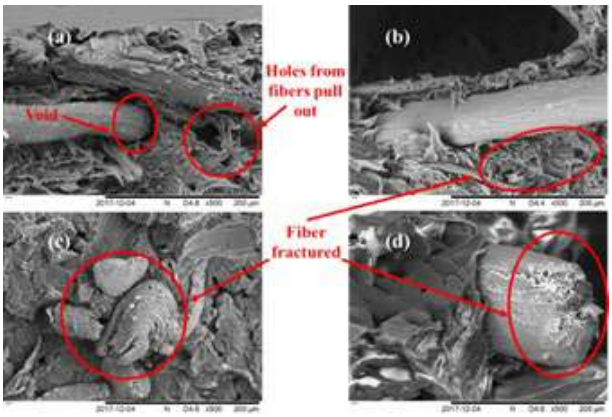

Fig 4. Morphology analysis of EFB/PP biocomposite: (a) Untreated, (b) Steam-30, (c) Steam-60, and (d) Alkali

Table 3. Thermal stability analysis of EFB/PP biocomposite with 30 wt.% fiber loading

EFB/PP biocomposites	Temperature for 5% weight loss (°C)	Temperature for 20% weight loss (°C)	Temperature for 50% weight loss (°C)	Residue at 550 °C (%)
Untreated	277.58	411.77	459.70	7.70
Steam-30	287.67	425.02	459.03	6.74
Steam-60	277.77	413.38	458.14	5.87
Alkali	295.29	410.95	458.22	9.38

matrix [18]. However, the treated EFB biocomposites have a better adhesion between fiber and PP matrix where fiber breakage can be observed. The fibers were well wetted by the PP matrix, and fiber breakages occurred due to strong adhesion.

According to Kabir et al. [19], better mechanical properties of composites can be achieved after modifying the surface of the natural fiber. The images were in agreement with results obtained from the tensile test.

Water Absorption Analysis of EFB/PP Biocomposite

Table 4 shows the maximum water absorption for the untreated and Steam-30 biocomposite was 7.16 and 5.59%, respectively.

Nadzri et al. [20] reported that the untreated fiber exhibited the highest water absorption that attributed the existed of void or gap between fiber and PP. The presence of a void in biocomposite structure makes it absorbs more water. Water absorption analysis for EFB/PP biocomposite was illustrated in Fig. 5.

Both biocomposite samples absorbed water after immersed in water until reaching the saturation point. The untreated EFB/PP biocomposite absorb 22% more water than Steam-30 biocomposite. Steam-30 biocomposite had low water absorption due to the removal of hemicellulose which makes the fiber less hydrophilic. Water will be absorbed by the hydroxyl groups contained in the hemicellulose which tends to make a hydrogen bond with water molecules that will increase the absorption of water [12]. Eliminating hydrophilic hydroxyl groups from the fiber structure through fiber treatments able to lower the water absorption of fiber [19]. In this study, steam treatment for 30 min was able to partially remove hemicellulose content in the EFB that directly decreased the water absorption of its EFB/PP biocomposite.

Table 4. Water absorption of untreated and Steam-30 biocomposite

EFB/PP biocomposite sample	Maximum water absorption (%)
Untreated	7.16
Steam-30	5.59

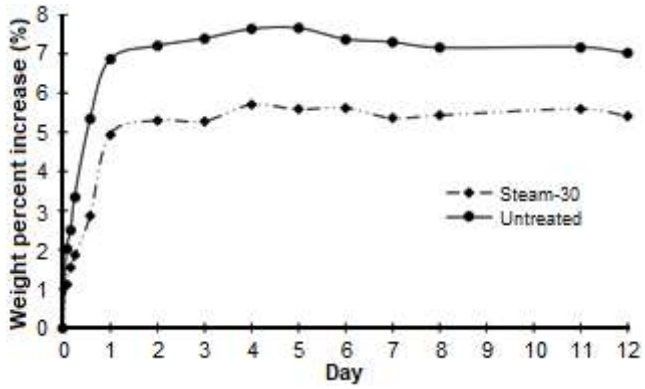

Fig 5. Water absorption of untreated and Steam-30 biocomposite with 30 wt.% EFB loading

■ CONCLUSION

The thermal stability, morphological, water absorption, and mechanical properties of the EFB/PP biocomposites were studied in this research. The tensile properties of the EFB/PP biocomposites improved after steam treatment for 30 min. However, the tensile strength decreased gradually with respect to the increased EFB loading. Meanwhile, the retention time of the steam treatment is very important to avoid the surface of the EFB fiber from damage and cracks where it will reduce the mechanical properties of the biocomposite. The steam treatment for 30 min showed the best performance in terms of thermal stability, morphological, mechanical properties, and water absorption. The thermal stability of Steam-30 increased from 276 to 283 °C. The treated fiber had a rough surface, low silica bodies, and presence of crater (due to the removal of silica) which will benefit for polymer adhesion. The tensile strength of Steam 30 with 30 wt.% of fiber content increased almost double compared to that of the pure PP composites. It also had low water absorption which was 22% lower than the untreated EFB biocomposite. In conclusion, steam treatment was able to treat the EFB fiber for better adhesion of the natural fiber EFB with the PP polymer matrix.

■ ACKNOWLEDGMENTS

The authors acknowledge Universiti Malaysia Pahang for financial support through grant number RDU1703177.

■ REFERENCES

[1] Akindoyo, J.O., Beg, M.D., Ghazali, S., Islam, M.R., and Mamun, A.A., 2015, Preparation and characterization of poly(lactic acid)-based composites reinforced with poly dimethyl siloxane/ultrasound-treated oil palm empty fruit bunch, *Polym. Plast. Technol. Eng.,* 54 (13), 1321–1333.

[2] Scherer, C., Emberger-Klein, A., and Menrad, K., 2017, Biogenic product alternatives for children: Consumer preferences for a set of sand toys made of bio-based plastic, *Sustainable Prod. Consumption*, 10, 1–14.

[3] Palamae, S., Dechatiwongse, P., Choorit, W., Chisti, Y., and Prasertsan, P., 2017, Cellulose and hemicellulose recovery from oil palm empty fruit bunch (EFB) fibers and production of sugars from the fibers, *Carbohydr. Polym.*, 155, 491–497.

[4] Brockhaus, S., Petersen, M., and Kersten, W., 2016, A crossroads for bioplastics: exploring product developers' challenges to move beyond petroleum-based plastics, *J. Cleaner Prod.*, 127, 84–95.

[5] Sanjay, M., Arpitha, G., Naik, L., Gopalakrishna, K., and Yogesha, B., 2016, Applications of natural fibers and its composites: An overview, *Nat. Resour.*, 7, 108–114.

[6] Shamsudin, S., Shah, U.K.M., Zainudin, H., Abd-Aziz, S., Kamal, S.M.M., Shirai, Y., and Hassan, M.A., 2012, Effect of steam pretreatment on oil palm empty fruit bunch for the production of sugars, *Biomass Bioenergy*, 36, 280–288.

[7] Awalludin, M.F., Sulaiman, O., Hashim, R., and Nadhari, W.N.A.W., 2015, An overview of the oil palm industry in Malaysia and its waste utilization through thermochemical conversion, specifically via liquefaction, *Renewable Sustainable Energy Rev.*, 50, 1469–1484.

[8] Dhandapani, S., Nayak, S., and Mohanty, S., 2015, Surface modification of oil palm fruit bunch and fibre reinforcement effect on bio-based polyester matrix composites: Dynamic, morphology, thermal and mechanical properties, *J. Elastomers Plast.*, 48 (5), 456–479.

[9] Hosseinaei, O., Wang, S., Enayati, A.A., and Rials, T.G., 2012, Effects of hemicellulose extraction on properties of wood flour and wood-plastic composites, *Composites Part A*, 43 (4), 686–694.

[10] Nordin, N.I.A.A., Ariffin, H., Andou, Y., Hassan, M.A., Shirai, Y., Nishida, H., Yunus, W.M.Z.W., Karuppuchamy, S., and Ibrahim, N.A., 2013, Modification of oil palm mesocarp fiber characteristics using superheated steam treatment, *Molecules*, 18 (8), 9132–9146.

[11] Izani, M.A.N., Paridah, M.T., Anwar, U.M.K., Nor, M.Y.M., and H'Ng, P.S., 2013, Effects of fiber treatment on morphology, tensile and thermogravimetric analysis of oil palm empty fruit bunches fibers, *Composites Part B*, 45 (1), 1251–1257.

[12] Beg, M.D.H., Akindoyo, J.O., Ghazali, S., and Mamun, A.A., 2015, Impact modified oil palm empty fruit bunch fiber/poly (lactic) acid composite, *Int. J. Chem. Nucl. Mater. Metall. Eng.*, 9 (1), 165–170.

[13] Abdullah, M.A., Nazir, M.S., Raza, M.R., Wahjoedi, B.A., and Yussof, A.W., 2016, Autoclave and ultra-sonication treatments of oil palm empty fruit bunch fibers for cellulose extraction and its polypropylene composite properties, *J. Cleaner Prod.*, 126, 686–697.

[14] Harun, N.A.F., Baharuddin, A.S., Zainudin, M.H.M., Bahrin, E.K., Naim, M.N., and Zakaria, R., 2013, Cellulase production from treated oil palm empty fruit bunch degradation by locally isolated *Thermobifida fusca*, *BioResources*, 8 (1), 676–687.

[15] Shinoj, S., Visvanathan, R., Panigrahi, S., and Kochubabu, M., 2011, Oil palm fiber (OPF) and its composites: A review, *Ind. Crops Prod.*, 33 (1), 7–22.

[16] Zailuddin, N.L.I., and Husseinsyah, S., 2016, Tensile properties and morphology of oil palm empty fruit bunch regenerated cellulose biocomposite films, *Procedia Chem.,* 19, 366–372.

[17] Rayung, M., Ibrahim, N., Zainuddin, N., Saad, W., Razak, N., and Chieng, B.W., 2014, The effect of

fiber bleaching treatment on the properties of poly(lactic acid)/oil palm empty fruit bunch fiber composites, *Int. J. Mol. Sci.*, 15 (8), 14728–14742.

[18] Jacob, M., Thomas, S., and Varughese, K.T., 2004, Mechanical properties of sisal/oil palm hybrid fiber reinforced natural rubber composites, *Compos. Sci. Technol.*, 64 (7-8), 955–965.

[19] Kabir, M.M., Wang, H., Lau, K.T., and Cardona, F., 2012, Chemical treatments on plant-based natural fibre reinforced polymer composites: An overview, *Composites Part B*, 43 (7), 2883–2892.

[20] Nadzri, N.I.M., Jamaludin, S.B., and Noor, M.M., 2012, Development and properties of coconut fiber reinforced composite cement with the addition of fly ash, *J. Sustainable Cem.-Based Mater.*, 1 (4), 186–191.

Physicochemical Characterization and Controlled Release Formulation on Intercalated 2-Methyl-4-chlorophenoxy Acetic Acid-Graphite Oxide (MCPA-GO) Nanocomposite

Norilyani Izzati Hasanuddin[1], Nur Nadia Dzulkifli[1], Siti Halimah Sarijo[2], and Sheikh Ahmad Izaddin Sheikh Mohd Ghazali[1,*]

[1]*Faculty of Applied Sciences, Universiti Teknologi MARA, Campus Kuala Pilah, 72000, Kuala Pilah, Negeri Sembilan, Malaysia*

[2]*Faculty of Applied Sciences, Universiti Teknologi MARA Shah Alam, 40450, Shah Alam, Selangor, Malaysia*

* ***Corresponding author:***

email:
sheikhahmadizaddin@ns.uitm.edu.my

Received: August 3, 2018
Accepted: December 11, 2018

DOI: 10.22146/ijc.40921

Abstract: *In this present work, herbicide named 2-methyl-4-chlorophenoxy acetic acid (MCPA) was intercalated into the graphite oxide through ion-exchange method to produce an MCPA-GO nanocomposite as an herbicide delivery system. The formation of MCPA-GO nanocomposite was confirmed by using PXRD, Fourier Transform Infrared Spectroscopy (FTIR), Thermal Gravimetric Analysis (TGA), UV-Visible Spectroscopy and Accelerated Surface Area Surface (ASAP). As for PXRD pattern, there was increasing in the basal spacing of the nanocomposite from the graphite oxide which by 9.3 to 9.7 Å indicated that MCPA has successfully inserted into the interlayers of the graphite oxide. Meanwhile, the FTIR spectrum showed the appearance of a new peak in MCPA-GO nanocomposite at 1308 cm^{-1} represents the functional group of carboxylate (COO^-). This peak is very necessary for the confirmation of the anionic form of MCPA inserted into the interlayers of graphite oxide. The controlled release property was also done for further investigation by using various aqueous media to determine the percentage release of MCPA from the nanocomposite. The percentage of herbicide release in Na_3PO_3 solution was higher than in Na_2CO_3 and NaCl solution proved that the release properties exhibit the potential application of graphite oxide as effective nanocarrier of herbicides. MCPA-GO nanocomposite suggested being most promising herbicide since it can lower the toxicity of precursor MCPA, high biocompatibility, and more efficient in herbicide delivery system.*

Keywords: *2-methyl-4-chlorophenoxy acetic acid; graphite oxide; herbicide; nanocomposite*

■ INTRODUCTION

Agricultural growth has been a strong pathway to define the economy of agro-based countries. In Malaysia alone, 12% of National Gross Domestic Product are emanated from the agricultural industry itself that providing about 16% of employment of current population. Correspondingly, the agricultural economists and chemists tend to focus on how to robust the agricultural growth as well as productivity and give a little attention to the side effect of agrochemical usage. As a result, pesticides, herbicides, and plant growth regulator have been widely used in modern agriculture. According to the Environmental Protection Agency (EPA) in the United States, 2-methyl-4-chlorophenoxy acetic acid (MCPA) is an example of herbicide that was sold approximately 4.6 million pounds each year for agricultural and residential usage. MCPA is a specific systemic chemical herbicide that applied to kill or inhibit the growth of specific plants such as noxious weed plant in cereals, wheat, rice, corn, peas, potatoes and grasslands [1]. However, the environmental problems arise once the residue of herbicide being swept away by rain that leads to soil pollution, strong water pollutant and they difficult to degrade and can rapidly move

around [2-3]. Besides, human health may also be affected by drinking water and direct exposure. Touloupakis et al. [4] mentioned in their journal that direct exposure of MCPA can worsen the health from asthma and skin rashes to chronic disorders.

The persistent of this slightly hazardous agrochemical, if accumulated in the environment, will increase the risks to human health. Many studies on the adsorption of pesticides by clay minerals for their removal from water and its immobilization in soils can be found in the open literature; however, studies on the increase the efficiency of the agrochemicals and reducing their leaching into the environment are very limited. A few attempts were made to intercalate the herbicide with a clay mineral, layered double hydroxide (LDH) and many other ways. However, there is no study reported yet by using graphite oxide as a nanocarrier. Contrarily, the percentage loading of drug/herbicides of the graphite oxide could reach up to 200% [11] which is considerably higher compared with other drugs/herbicides delivery systems or nanocomposite that usually have a loading percentage lower than 100%. It has been suggested that intercalation of herbicide with graphite oxide would be one of the feasible solutions.

Graphite oxide has been explored enormously as an exciting topic by the researchers in various fields such as electronic [5], catalysis, biosensors [6] and biomedical application [7]. In the current area of biomedical, the intercalation of the graphite oxide (GO) had received tremendous attention solely to emerge as new and competitive drugs delivery systems with the potential of targeting nanocarrier or host. It is because they are facilitating the good targeting, high loading and control release of drugs/herbicides. By exploring the area drugs delivery system, Barahuie et al. [8] have reported the graphite oxide as a nanocarrier for the active anticancer agent of chlorogenic acid while Dorniani et al. [9], makes their research on gallic acid as a cancer therapy by using the graphite oxide too. Besides that, Yu et al. [10] did some modification in their work to make the graphite oxide being able to be as a nanocarrier loaded with anticancer herbal drug berberine by combined the graphite oxide with PEG.

To the best of our knowledge, there is no literature reported yet in the field of herbicides delivery system by using graphite oxide as a nanocarrier. Therefore, in this present work, MCPA was intercalated into the graphite oxide to produce a better and even the safer improvise herbicide that may minimize the environmental problems and yet, still provide the maximum outcomes to the desirable plants. In addition, the residue or excess herbicide can be lessened by controlled-release (CR) formulations that make the herbicide exist in the interlayer region of graphite oxide and allows the herbicide to be released dependent to the desired concentration over the time. Moreover, it is green chemistry that would also consider environmental safety. This herbicide is environmentally friendly since it can naturally reduce in the environment through the action of ubiquitous Shewanella bacteria or decomposes to humic acids [11-12].

■ EXPERIMENTAL SECTION

Materials

Graphite powder and MCPA were purchased from Sigma Aldrich and were used without further purification. Sulphuric acid (98%), potassium permanganate, hydrochloric acid (35%), hydrogen peroxide and ethanol (98%), were obtained from R & M Chemical. All the solutions were prepared by using deionized water.

Procedure

Synthesis of graphite to graphite oxide

Graphite oxide was prepared by using the improved Hummer's Method. One gram of graphite powder and 23 mL of concentrated sulphuric acid were mixed in a beaker under mechanical stirring (150 rpm). The ice bath was placed under the beaker. Then, 3.0 g of potassium permanganate ($KMnO_4$) was added slowly into the beaker to keep the temperature of the suspension lower than 20 °C. Next, the reaction system was transferred to a 40 °C of oil bath for 30 min. In the beaker, 50 mL of deionized water was poured and the solution was stirred for 15 min at 95 °C. After that, 150 mL of deionized water was added and followed by a dropwise addition of 5 mL of 30% hydrogen peroxide.

During this step, the color of the solution was turned from dark brown to yellow color. The mixture was filtered and washed them with the hydrochloric acid aqueous solution to remove metal ions. Lastly, the precipitate was dried at 60 °C in the vacuum oven for 48 h.

Synthesis of MCPA-GO nanocomposite

The MCPA-GO nanocomposite was done by using ion-exchanged method [1]. This method was run under the room temperature. First, about 0.35 g of the prepared graphite oxide was reacted with 25 mL aqueous solution of MCPA in the 100 mL volumetric flask. As the mixture of graphite oxide and MCPA was mixed together, the mixture was stirred for 5 h on the hotplate before aging for 18 h at 70 °C in an oil bath shaker. Then, the slurry solution was taken for centrifuged at 180 rpm in 5 min and washed several times with deionized water. The product obtained was dried in an oven at a temperature of 70 °C for 72 h. The sample then is kept in a sample bottle for further characterization by using PXRD, FTIR and CHNS analysis.

Controlled release study of MCPA-GO nanocomposite

The release of MCPA from MCPA-GO nanocomposite was prepared with different aqueous media which were sodium phosphate (Na_3PO_4), sodium carbonate (Na_2CO_3) and sodium chloride (NaCl). Three milligrams of MCPA-GO nanocomposite was placed in the quartz cuvette on top of aqueous media. The percentage release of MCPA from MCPA-GO nanocomposite was measured by using a UV-Vis instrument with a wavelength of 237 nm.

■ RESULTS AND DISCUSSION

PXRD Analysis

Fig. 1 shows the XRD patterns for the graphite, graphite oxide and MCPA-GO nanocomposite. The basal spacing of these samples was calculated by using Bragg's Law as shown in Eq. (1).

$$n\lambda = 2d\sin\theta \quad (1)$$

As for graphite, the strong and sharp diffraction peak located in (003) orientation was observed at 2θ = 26.5° corresponding to the basal spacing of 3.4 Å. The PXRD pattern revealed that graphite has high crystallinity

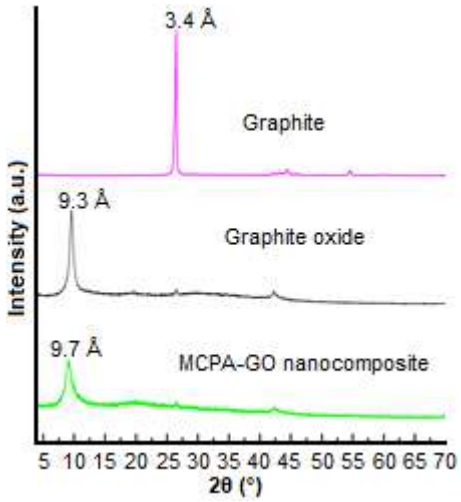

Fig 1. XRD pattern for graphite, GO and MCPA-GO nanocomposite

due to highly organized delocalized π hexagonal rings structure with 120° angle between each carbon atom in the plane of the layers [13]. Other than that, GO showed an intense and very strong peak at 2θ = 9.54° with diffraction orientation of (002). The increment of basal spacing around 9.3 Å of GO signifies the functionalization of the graphite was successful with the formation of oxygen-functional groups such as hydroxyl group, epoxide, and carboxyl group as well as water molecules at the edge and basal planes of sheets after the harsh chemical oxidation process [14-15].

The peak was shifted downwards to 2θ = 9.10° and became wider with a basal spacing of 9.7 Å after the intercalation process took place. The expansion of the interlayers of the nanocomposite with only single peak present has confirmed the inclusion of herbicide anion, MCPA during intercalation process. This extent of expansion may be due to several factors such as the anionic size of herbicide, charge, orientation, and interaction between graphite oxide and herbicide [1]. Theoretically, the intercalation of MCPA with graphite oxide involved non-covalent dynamic bonding interactions such as hydrogen bonding, π–π stacking, and electrostatic forces bounding to each other due to the presence of oxygen groups as the reactive sites [16]. The nanocomposite was analyzed with other complimentary analysis for further confirmation.

FTIR Spectra

Fig. 2 shows the FTIR-ATR spectra for GO, MCPA and MCPA-GO nanocomposite. In the GO spectrum, O-H stretching vibrations peak was found at 3362 cm^{-1} that corresponds to the carboxyl and hydroxyl groups and residual water in interlayers of GO. These functional groups enable GO to have better dispersibility in water [16]. Besides that, C=C bonds were detected at 1626 cm^{-1} indicating the main structure of graphite remained and unoxidized. A peak at 1730 cm^{-1} was referred to the stretching vibration of the C=O bond demonstrating the presence of carboxylic acid. Other vital peaks at 1221 and 1050 cm^{-1} were represented the functional group of epoxy (C-O) and alkoxy group (C-O), respectively. These oxygenated functional groups indeed confirmed the graphite had oxidized into GO which consistent with the literature [16-17].

For MCPA, peak at 2910 cm^{-1} represented the hydroxyl group (O-H) from the vibration of the COOH [18], and another peak at 2878 cm^{-1} signify the substituent of the methyl group. Next, the functional group of C=O stretching was detected at the sharp peak of 1707 cm^{-1}.

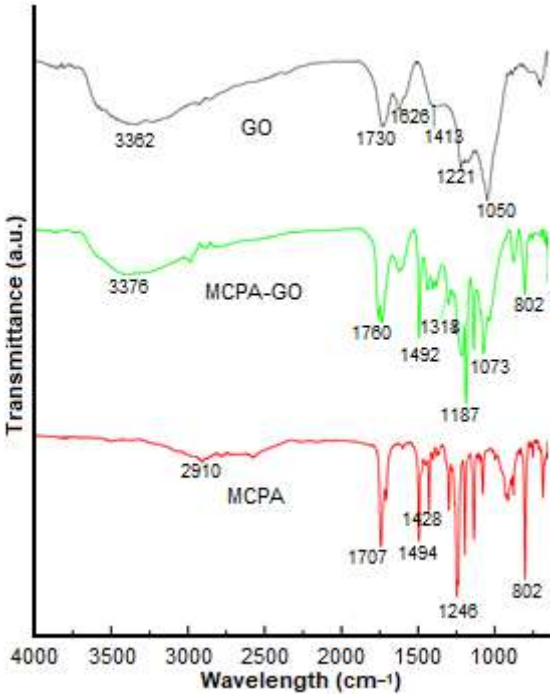

Fig 2. FTIR-ATR spectra for GO, MCPA and MCPA-GO nanocomposite

The peaks at 1494 and 1428 cm^{-1} were corresponding to the C=C, and a strong peak at 1298 cm^{-1} assemble the symmetric and asymmetric stretching mode of C-O-C vibration. A sharp peak at 802 cm^{-1} has been observed that belongs to the peak of C–Cl stretching.

The FTIR spectrum of MCPA-GO nanocomposite have exhibited the peaks resembles MCPA and graphite oxide spectra. The characteristic peaks of 1760 cm^{-1} with high intensity attributed to the stretching vibration of carbonyl groups of carboxylic group present. An observation of a new peak at 1308 cm^{-1} primarily due to the C=O vibration of the carboxylate anion as the result of intercalation. Furthermore, an obvious broad absorption peak at 3377 cm^{-1} was assigned to the O-H stretching vibration due to water molecules present in the nanocomposite.

UV-Vis Spectrum

Fig. 3 shows the UV-Visible spectrums for GO, MCPA and MCPA-GO nanocomposite. The spectra were analyzed by using range between 200 nm until 400 nm. The vital transitions for GO were ($n \rightarrow \sigma^*$) and ($\pi \rightarrow \pi^*$). The absorption was observed at 245 nm due to the aromatic C=C bond for transition ($n \rightarrow \sigma^*$) [19]. Furthermore, the absorption peak at 300 nm was stood for C=O bond transition ($\pi \rightarrow \pi^*$). For transition ($n \rightarrow \sigma^*$) in MCPA, the wavelength at 230 nm was recorded in

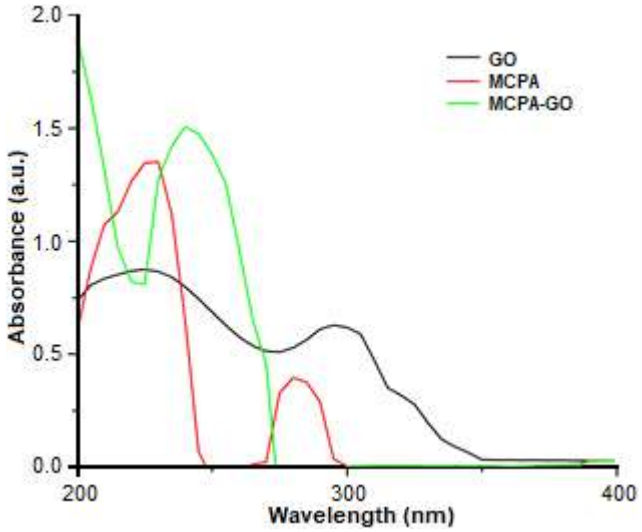

Fig 3. UV-Visible spectrums for GO, MCPA and MCPA-GO nanocomposite

which contributed to a carbonyl group where the excitation of the electron occurred in an unshared pair on oxygen to antibonding σ orbital. At 280 nm, ($\pi \rightarrow \pi^*$) transition presence due to the existence of carboxyl group. In contrast for MCPA-GO nanocomposite, ($n \rightarrow \sigma^*$) and ($\pi \rightarrow \pi^*$) transitions were shifted to lower wavelength with higher absorbance after intercalation between MCPA and GO occurred. This shifting was known as hypsochromic shift primarily due to withdrawing of oxygen electron from carbonyl carbon. But, ($n \rightarrow \pi^*$) was absent in this spectra may due to weak transition due to Laporte Forbidden and high probably the transition was overlapped with ($n \rightarrow \sigma^*$).

Thermal Analysis

TGA/DTG graphs of GO, MCPA, and MCPA-GO nanocomposite were displayed in Fig. 4. This is another complimentary techniques used for the confirmation of MCPA nanocomposite. Based on Fig. 4(a), GO showed two major stages of thermal decomposition in the region of 125–150 °C and 210–243 °C. The first stage occurred at the maximum temperature of 141 °C with a weight loss of 14% that associated with the removal of water molecules between the interlayers of GO. It was followed by the second stage with a sharp peak at 226 °C. This decomposition mainly due to the loss of unstable oxygenated functional groups with 24% weight loss. Next, Fig. 4(b) exhibited the decomposition of MCPA that corresponding to an intense peak at 217 °C. The weight loss occurred was 98.6% that primarily due to the decomposition and combustion organic matter of MCPA.

As expected, two stages of weight loss were observed through the TGA/DTG analysis of MCPA-GO nanocomposite in Fig. 4(c). Firstly, a rough 7% of weight loss occurred at a temperature of 123 °C which owing to the elimination of water molecules present. The second major stage was detected at 486 °C with the weight loss

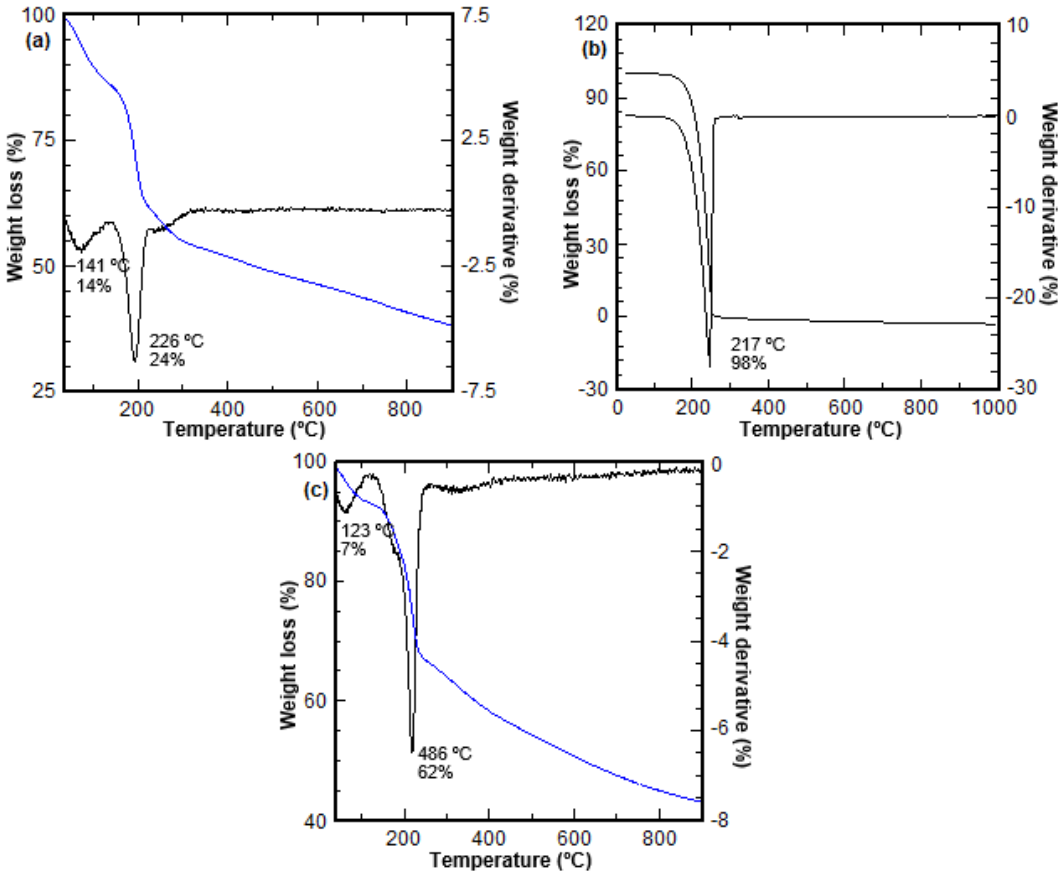

Fig 4. TGA/DTG thermogram of (a) GO, (b) MCPA and (c) MCPA-GO nanocomposite

of 32%. This stage was attributed to the decomposition of oxygenated functional groups and organic anion, MCPA that present in the MCPA-GO nanocomposite. From the results above, MCPA-GO nanocomposite indeed has higher thermal stability than pristine GO and MCPA.

Surface Properties

The surface area of GO and MCPA-GO nanocomposite were investigated to verify the successful intercalation process. The intercalation took place with the increased surface area of nanocomposite which was 8.4887 m^2/g whereas the surface area of GO was only 3.5274 m^2/g. The enlargement d-spacing due to the intercalation of a bigger anion, i.e., MCPA, in nanocomposite and will generate more pores in the crystallites. Thus, the surface area of nanocomposite increase significantly. Through the adsorption-desorption isotherms in Fig. 5, GO was identified to have microporous-type of material while MCPA-GO nanocomposite had an open loop in its graph. The BJH desorption pore size distribution for GO and MCPA-GO nanocomposite was observed in Fig. 6. From the results obtained, MCPA-GO nanocomposite had higher pore size distribution centered at 1938 Å than GO. This is related to the involvement of different size of the anion, interstitial pores between the crystallite and accumulation process during the formation of the nanocomposite.

Controlled Release Studies

The release profile for the controlled release study of MCPA in various aqueous solution was displayed in Fig. 7. The release of MCPA anion from MCPA-GO nanocomposite was recognized due to the π-π stacking interaction and hydrophobic bonding between MCPA and graphite oxide [20-21]. Besides, charge-density of the anion of aqueous media solution will also contribute to this phenomenon. Based on Fig. 7, the amount release of MCPA was found to be higher in Na_3PO_3 > Na_2CO_3 > NaCl depending on the availability of an anion in the aqueous solutions.

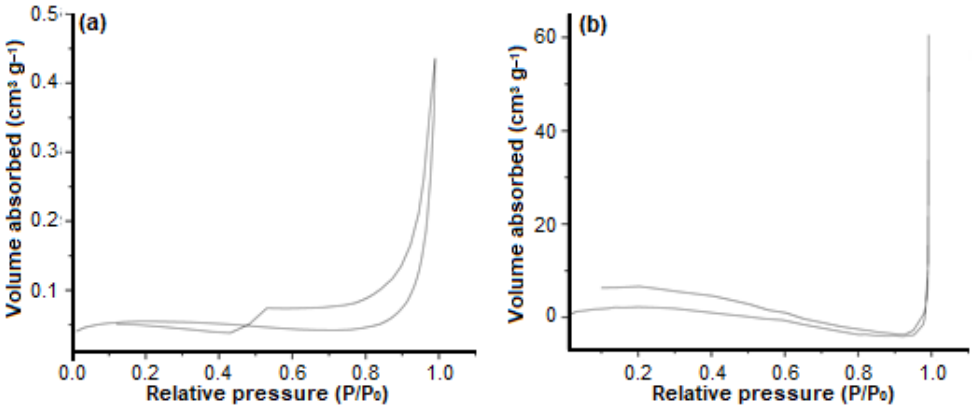

Fig 5. Adsorption-desorption isotherms of (a) GO and (b) MCPA-GO nanocomposite

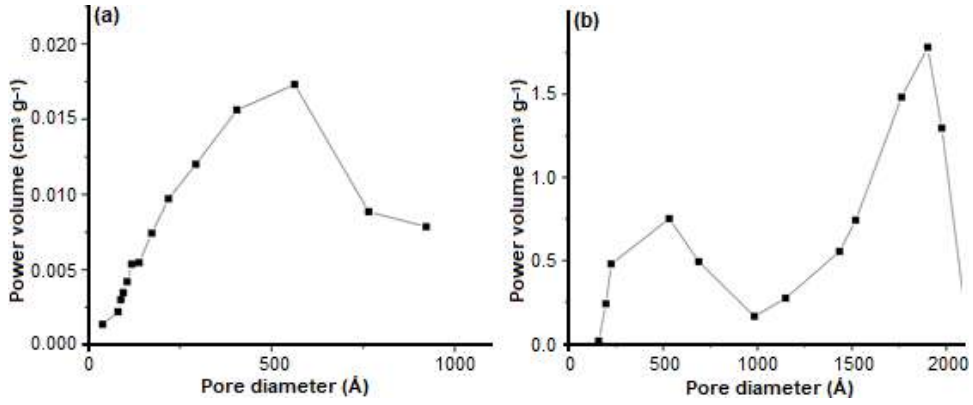

Fig 6. BJH pore size distribution of (a) GO and (b) MCPA-GO nanocomposite

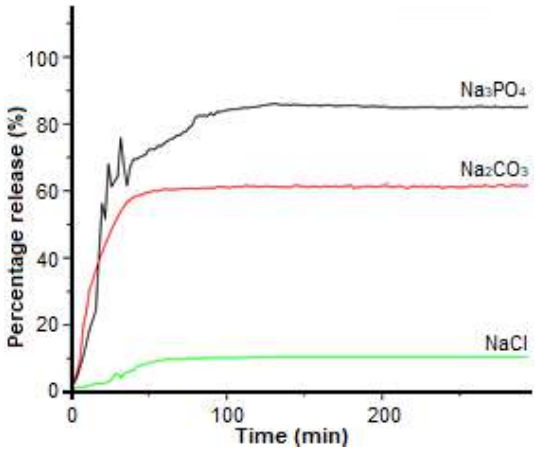

Fig 7. The controlled release of MCPA in Na_3PO_4, Na_2CO_3 and NaCl solution

The percentage release of MCPA was found to be 85, 61, and 10% in Na_3PO_3 solution, Na_2CO_3 solution and NaCl solution at the time of 116, 60, and 128 min, respectively. It is because PO_3^{3-} has a higher charge density than CO_3^{2-} and Cl^- causes more phosphite ion to be ion-exchanged with MCPA [1]. Phosphite ion that has high affinity towards graphite oxide interlayers enable the phosphite ion from aqueous media to exchange with the intercalated herbicide anion [22]. As a result, phosphite ion is incorporated into the interlayer of graphite oxide and at the same time, the MCPA will be released into the aqueous solutions.

Additionally, the burst effect that presence in the graph of the Na_3PO_3 solution may occur due to the surface characteristics of a graphite oxide material, the herbicide interactions and porous structure of the material [9]. The characteristics of the mechanism of the ion-exchange method would not lead the percentage of MCPA anion released from MCPA-GO nanocomposite at equilibrium reach 100%. This is because even though the anion was removed continuously but the loaded anions cannot be exchanged completely at equilibrium. These results show that the MCPA-GO nanocomposite has good potential to be used as an herbicide delivery system with sustainable controlled release properties.

■ CONCLUSION

We had successfully developed herbicide delivery system by using graphite oxide as a nanocarrier for MCPA with sustainable controlled release property. The successful formation of the nanocomposite was characterized by using PXRD, FTIR, TGA, UV-Visible Spectroscopy and ASAP. The FTIR spectrum of this nanocomposite was showed the resemblance of spectrum MCPA and graphite oxide while the appearance of only one strong peak with the wider basal spacing of 9.7 Å in XRD pattern proved that MCPA was successfully intercalated into the graphite oxide. In addition, the controlled release studies were done to figure out the percentage release of the MCPA in various aqueous media. As a result, GO revealed a sustainable of controlled release properties that made GO as a most promising nanocarrier. MCPA-GO nanocomposite has demonstrated the better properties of MCPA by lowering its toxicity, hence increasing the efficiency of its herbicide delivery system.

■ ACKNOWLEDGMENTS

This research was funded by the Ministry of Higher Education (MOHE) under the FRGS grant no. 600IRMI/FRGS5/3(66/216). The authors also would like to thank the Department of Academic Affairs of Universiti Teknologi Mara (UiTM) Negeri Sembilan Branch Kuala Pilah Campus for providing the fund and the facilities to carry out this study.

■ REFERENCES

[1] Sarijo, S.H., Ghazali, S.A.I.S.M., and Hussein, M.Z., 2015, Synthesis of dual herbicides-intercalated hydrotalcite-like nanohybrid compound with simultaneously controlled release property, *J. Porous Mater.*, 22 (2), 473–480.

[2] Al-Zaben, M.I., and Mekhamer, W.K., 2017, Removal of 4-chloro-2-methyl phenoxy acetic acid pesticide using coffee wastes from aqueous solution, *Arabian J. Chem.*, 10 (Suppl. 2), S1523–S1529.

[3] Touloupakis, E., Margelou, A., and Ghanotakis, D.F., 2011, Intercalation of the herbicide atrazine in layered double hydroxides for controlled-release applications, *Pest Manage. Sci.*, 67 (7), 837–841.

[4] Nejati, K., Davari, S., Rezvani, Z., and Dadashzadeh, M., 2015, Adsorption of 4-chloro-2-methylphenoxy

acetic acid (MCPA) from aqueous solution onto Cu-Fe-NO_3 layered double hydroxide nanoparticles, *J. Chin. Chem. Soc.*, 62 (4), 371–379.

[5] Jeong, H.K., Lee, Y.P., Jin, M.H., Kim, E.S., Bae, J.J., and Lee, Y.H., 2009, Thermal stability of graphite oxide, *Chem. Phys. Lett.*, 470 (4-6), 255–258.

[6] Kumar, A., and Lee, C.H, 2013, "Synthesis and Biomedical Applications of Graphene: Present and Future Trends", in *Advances in Graphene Science*, Eds., Aliofkhazraei, M., IntechOpen, 55–75.

[7] Wang, Y., Li, Z., Wang, J., Li, J., and Lin, Y., 2011, Graphene and graphene oxide: Biofunctionalization and applications in biotechnology, *Trends Biotechnol.,* 29 (5), 205–212.

[8] Barahuie, F., Hussein, M.Z., Fakurazi, S., and Zainal, Z., 2014, Development of drug delivery systems based on layered hydroxides for nanomedicine, *Int. J. Mol. Sci*., 15 (5), 7750–7786.

[9] Dorniani, D., Saifullah, B., Barahuie, F., Arulselvan, P., Hussein, M.Z.B., Fakurazi, S., and Twyman, L.J., 2016, Graphene oxide-gallic acid nanodelivery system for cancer therapy, *Nanoscale Res. Lett.*, 11, 491.

[10] Yu, D., Ruan, P., Meng, Z., and Zhou, J., 2015, The Structure-dependent electric release and enhanced oxidation of drug in graphene oxide-based nanocarrier loaded with anticancer herbal drug berberine, *J. Pharm. Sci.*, 104 (8), 2489–2500.

[11] Zhang, L., Xia, J., Zhao, Q., Liu, L., and Zhang, Z., 2010, Functional graphene oxide as a nanocarrier for controlled loading and targeted delivery of mixed anticancer drugs, *Small*, 6 (4), 537–544.

[12] Ceriotti, G., Romanchuk, A.Y., Slesarev, A.S., and Kalmykov, S.N., 2015, Rapid method for the purification of graphene oxide, *RSC Adv.*, 5 (62), 50365–50371.

[13] Chowdhury, D.R., Singh, C., and Paul, A., 2014, Role of graphite precursor and sodium nitrate in graphite oxide synthesis, *RSC Adv.*, 4 (29), 15138–15145.

[14] Dreyer, D.R., Park, S., Bielawski, C.W., and Ruoff, R.S., 2010, The chemistry of graphene oxide, *Chem. Soc. Rev*., 39 (1), 228–240.

[15] Song, J., Wang, X., and Chang, C.T., 2014, Preparation and characterization of graphene oxide, *J. Nanomater.*, 2014, 276143.

[16] Bardajee, G.R., Hooshyar, Z., Farsi, M., Mobini, A., and Sang, G, 2017, Synthesis of a novel thermo/pH sensitive nanogel based on salep modified graphene oxide for drug release, *Mater. Sci. Eng., C*, 72, 558–565.

[17] Chen, J., Li, Y., Huang, L., Li, C., and Shi, G., 2014, High-yield preparation of graphene oxide from small graphite flakes via an improved Hummers method with a simple purification process, *Carbon*, 81, 826–834.

[18] Marcano, D.C., Kosynkin, D.V., Berlin, J.M., Sinitskii, A., Sun, Z., Slesarev, A., Alemany, L.B., Lu, W., and Tour, J.M., 2010, Improved synthesis of graphene oxide, *ACS Nano*, 4 (8), 4806–4814.

[19] Salleh, N.M., Mohsin, S.M.N., Sarijo, S.H., and Ghazali, S.A.I.S.M., 2017, Synthesis and physico-chemical properties of zinc layered hydroxide-4-chloro-2-methylphenoxy acetic acid (ZMCPA) nanocomposite, *IOP Conf. Ser. Mater. Sci. Eng.*, 204, 012012.

[20] Han, W., Niu, W.Y., Sun, B., Shi, G.C., and Cui, X.Q., 2016, Biofabrication of polyphenols stabilized reduced graphene oxide and its anti-tuberculosis activity, *J. Photochem. Photobiol., B*, 165, 305–309.

[21] Liu, H., Li, T., Liu, Y., Qin, G., Wang, X., and Chen, T., 2016, Glucose-reduced graphene oxide with excellent biocompatibility and photothermal efficiency as well as drug loading, *Nanoscale Res. Lett.*, 11 (1), 211.

[22] Lv, Y., Tao, L., Bligh, S.W.A., Yang, H., Pan, Q., and Zhu, L., 2016, Targeted delivery and controlled release of doxorubicin into cancer cells using a multifunctional graphene oxide, *Mater. Sci. Eng., C*, 59, 652–660.

[23] Sarijo, S.H., Hussein, M.Z., Yahaya, A.H.J., and Zainal, Z., 2010, Effect of incoming and outgoing exchangeable anions on the release kinetics of phenoxy herbicides nanohybrids, *J. Hazard. Mater*., 182 (1-3), 563–569.

α-Glucosidase Inhibitory and A Leptospermone Derivative from *Rhodomyrtus tomentosa*

Ferlinahayati[1,*], Daniel Alfarado[1], Eliza[1], and Budi Untari[2]

[1]*Department of Chemistry, Faculty of Mathematics and Natural Sciences, University of Sriwijaya, Jl. Raya Palembang Prabumulih Km 32, Ogan Ilir 30622, South Sumatera, Indonesia*

[2]*Department of Pharmacy, Faculty of Mathematics and Natural Sciences, University of Sriwijaya, Jl. Raya Palembang Prabumulih Km 32, Ogan Ilir 30622, South Sumatera, Indonesia*

* ***Corresponding author:***

tel: +62-81394741890
email: etihayati74@yahoo.com

Received: November 16, 2018
Accepted: April 23, 2019

DOI: 10.22146/ijc.40990

Abstract: *One of the treatments for diabetes mellitus disease is to control blood sugar level using an inhibitor of α-glucosidase enzyme. The methanol extracts of the fruit, stem, and leaves of* Rhodomyrtus tomentosa *were found significant in inhibiting α-glucosidase with an IC_{50} value of 20.57, 20.36 and 43.99 μg/mL respectively. The ethyl acetate and* n-*butanol fractions from the methanol extract of* R. tomentosa *fruit exhibited the potent inhibition (IC_{50} 13.49 and 19.29 μg/mL) compare to acarbose and* n-*hexane fraction (IC_{50} 383.68 and 1175.16 μg/mL). A leptospermone derivative, rhodomyrtosone D, was isolated from the ethyl acetate fraction of* R. tomentosa *fruit. The structure of rhodomyrtosone D was identified based on spectroscopic analysis, as well as comparing with literature data. The α-glucosidase inhibition of rhodomyrtosone D (IC_{50} 110.45 μg/mL) was 3.5 fold more potent than acarbose. Thus,* R. tomentosa *plant could be potential as a natural resource of α-glucosidase inhibitor.*

Keywords: *α-glucosidase;* Rhodomyrtus tomentosa*; antidiabetic; rhodomyrtosone D; ethyl acetate fraction*

■ INTRODUCTION

Diabetes mellitus (DM) is a group of metabolic disorder, in which there are high blood sugar levels (hyperglycemia) over a prolonged period [1]. It will happen if the pancreas does not produce enough insulin that is able to convert sugar into energy, or the body's cells do not respond well to the insulin produced. Some serious complication of hyperglycemia such as cardiovascular disease, damage to the eyes, atherosclerosis, and chronic kidney disease (nephropathy) can also occur [2-3]. The control of blood sugar level by inhibition of carbohydrate-hydrolyzing enzymes in the digestive organ is believed to be important in hyperglycemia treatment [1]. The α-glucosidase, an enzyme in the small intestine, is responsible for the degradation of carbohydrate. The α-glucosidase inhibitor will interfere with the digestion of carbohydrate and thereby reduce the postprandial glucose level and insulin responses in a diabetic patient [2,4]. Acarbose, miglitol, and voglibose have been found as an α-glucosidase inhibitor and currently clinically used to control blood glucose of diabetic patients [5-6]. However, they have caused severe gastrointestinal side effects. Nowadays, natural resources have received tremendous attention as a therapeutic agent in the inhibition of α-glucosidase and have shown very promising biological activity.

Karamunting is locally named (Sumatera island) for *Rhodomyrtus tomentosa* and belonging to the Myrtaceae family. This plant is an evergreen shrub which is native to Southern Asia and Southeast Asia and is widely distributed in Indonesia. *R. tomentosa* is widely used as traditional medicines to treat a variety of disease caused by bacteria such as diarrhea, dysentery, and urinary tract infections [7-8]. In addition, its ripe fruits are used to boost the immune system [9]. Biologically, ethanolic extract of *R. tomentosa* fruits possesses potent antioxidant activities on DPPH radical scavenging

activity, reducing power as well as inhibition of lipid peroxidation activity [10] Furthermore, some extract of this plants were reported to have antibacterial and anti-hepatitis properties [11]. Chemically, various secondary metabolites have been reported, such as polyketide, flavonoids, anthocyanins, stilbenoids, and triterpenoids [9-13]. Rhodomyrtone, a phloroglucinol polyketide from *R. tomentosa* have displayed significant antibacterial activities against Gram-positive bacteria and suggested as a new candidate as a natural antibacterial drug [12,14].

Meanwhile, tomentosone A, hexacyclic phloroglucinol was reported as antimalarial against chloroquine-resistant and sensitive strains of *Plasmodium falciparum*. Resveratrol and piceatannol, a stilbenoid compound has been characterized by this plant [9]. A stilbenoid compound from *Syagrus romanzoffiana* was reported as a potential hypoglycemic agent. However, there is no literature on the α-glucosidase inhibitory of *R. tomentosa* and its bioactive chemical compound. In a search for potential α-glucosidase inhibitor from natural resources, the ability of *R. tomentosa* plant to inhibit the activity of the α-glucosidase enzyme as well as to isolate the bioactive compound have been investigated. One active compound, rhodomyrtosone D (**1**) was isolated, and its α-glucosidase inhibition was determined. The following describes the outcomes of these efforts.

■ EXPERIMENTAL SECTION

Materials

Rhodomyrtus tomentosa (fruits, leaves, and stem) were collected from Inderalaya, Ogan Ilir, South Sumatera. The plant was identified at Herbarium Anda, Department of Biology, University of Andalas. The solvents used, methanol, *n*-hexane, and ethyl acetate, were the technical grade that was distilled, while *n*-butanol and dimethylsulfoxide (DMSO) were pro analysis grade (p.a.) from Merck. The α-glucosidase (from *Saccharomyces cerevisiae*) and *p*-nitro-phenyl-α-D-glucopyranoside were purchased from Sigma-Aldrich. Bovine serum albumin (BSA) was purchased from Merck. Silica gel 60G (Merck) was used for vacuum liquid chromatography, and silica gel 60 PF_{254} (Merck) was used for radial chromatography. TLC analysis was performed on Kieselgel 60 GF_{254}, 0.25 mm aluminum plate (Merck) and visualized with cerium sulfate.

Instrumentation

Incubator Biosan PST-60HL was used for the sample incubation process. The absorbance of *p*-nitrophenol was measured by a Tecan Infinite F50 Microplate reader. The UV spectrum was recorded with Shimadzu UV-1240 spectrophotometer. IR spectrum was determined using KBr pellets on a Perkin Elmer FTIR Spectrum One spectrophotometer. ^{1}H-NMR (500 MHz) and ^{13}C-NMR (125 MHz) spectra were recorded with Agilent DD2 spectrometer, using residual and deuterated solvent peaks as reference standards.

Procedure

Extraction of sample for assay

As much as 100 g of each the dried powdered sample (fruits, leaves, and stem) of *R. tomentosa* were extracted by maceration method using methanol (400 mL) as the solvent at the room temperature. The maceration process was carried out three times (@ 24 h). The methanol solvents were evaporated in under reduce pressure to give crude extracts of methanol of fruit, leaves, and stem (4.6, 4.2 and 3.9 g respectively). The crude of methanol extract of fruit was partitioned successively with *n*-hexane, ethyl acetate, and *n*-butanol and produce of each fraction after the solvent was evaporated.

In-vitro *α-glucosidase inhibition assay*

The α-glucosidase assay has been performed using the spectrophotometric method as previously described [2,15] with slight modification. As much as 10 µL of the sample at various concentrations was added with 55 µL of 50 mM phosphate buffer (pH 6.8) and 10 µL of 10 mM *p*-nitrophenyl-α-D-glucopyranoside as the substrate. After preincubated for 5 min at 37 °C, 25 µL of 0.1 U/mL α-glucosidase (in the phosphate buffer pH 6.8 containing 0.1 mg/mL bovine serum albumin) was added. The mixture was then incubated for 30 min at 37 °C. After that, the stopped solution (100 µL of 200 mM Na_2CO_3) was added to the mixture. The absorbance of the *p*-nitrophenol released due to hydrolysis of the

substrate by the α-glucosidase was measured by a microplate reader at 405 nm. The blank solution was prepared by replaced sample solution by DMSO. Acarbose (Glucobay®) is used as a positive control. The percentage inhibition of α-glucosidase was calculated using the following equation:

$$\text{Inhibition } (\%) = \left[1 - \left(A_{\text{sample}} / A_{\text{blank}}\right)\right] \times 100\%$$

The IC_{50} was calculated by linear regression equation analysis between concentration and percentage inhibition.

Extraction and Isolation of R. tomentosa *fruits*

The dried fruits (2 kg) was extracted with methanol (3 × 7 L, 24 h each) by maceration method. The methanol extract was concentrated under reduced pressure to give 1.1 L syrup, which was suspended in distilled water. This suspension was partitioned successively with *n*-hexane, ethyl acetate, and *n*-butanol to afford *n*-hexane, ethyl acetate, and *n*-butanol fractions. The ethyl acetate fraction (15 g) was fractionated by vacuum liquid chromatography on silica gel 60 G, eluting with *n*-hexane-ethyl acetate system with increment ethyl acetate gradually (9:1, 8:2, 7:3, 6:4, 4:6, 2:8, 1:9, and 0:10, each 150 mL) to give 8 fractions (A-H). Fraction C (374 mg) was further separated using radial chromatography over silica gel 60 PF_{254} (1 mm), eluted with *n*-hexane-ethyl acetate gradually (85:15, 80:20, 75:25, 70:30, 60:40, 50:50) to yield a leptospermone derivative 1 (8.9 mg).

■ RESULTS AND DISCUSSION

The α-Glucosidase Inhibition of Extracts and Fractions

The extraction of three parts of *R. tomentosa*, namely, fruit, stem, and leaves produced methanol extract of 4.6, 3.9, and 4.2 g, respectively. All of these extracts were tested for the α-glucosidase inhibitory using *p*-nitrophenyl-α-D-glucopyranoside as the substrate and acarbose as the reference or positive control. The concentration of a substance that is required for 50% inhibition of α-glucosidase enzyme represented as IC_{50}. The methanol extract from the stem and fruit have a similar ability to inhibit α-glucosidase activity with the IC_{50} value were 20.36 and 20.57 μg/mL, respectively. Both of these extracts demonstrated two times more potent than the leaves methanol extract with the IC_{50} value was 43.99 μg/mL (Fig. 1). Base on the IC_{50} value, all three methanol extracts possessed high potency in inhibiting α-glucosidase compare to the reference drug, acarbose with the IC_{50} 383.68 μg/mL (Table 1).

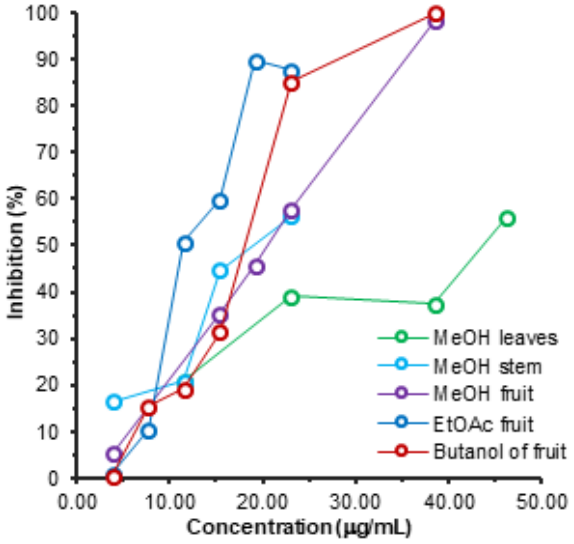

Fig 1. Effect of extracts and fractions on the inhibition of α-glucosidase

Table 1. Inhibitory effect of the extract, fraction and compound on α-glucosidase activity

Extract/compound	Inhibitor concentration (IC_{50}, μg/mL)
MeOH extract of the leaves	43.99
MeOH extract of the stem	20.36
MeOH extract of the fruit	20.57
n-hexane fraction of the fruit	1175.16
Ethyl acetate fraction of the fruit	13.49
n-butanol fraction of the fruit	19.29
Compound **1**	110.45
Acarbose*	383.68

*positive control

Previously, it has been reported that *R. tomentosa* fruit contains stilbenoid compound, such as resveratrol, and piceatannol [9]. These stilbenoids showed the more potent inhibition of α-glucosidase activity with IC_{50} 91 and 60 μg/mL respectively than acarbose with IC_{50} 247 μg/mL [5]. In addition, other phenolic compounds such as flavonoid isolated from *Morus alba* and anthocyanins isolated from noble muscadine grapes have been reported as a potential α-glucosidase inhibitory [16-17]. Meanwhile, the triterpenoid saponins from *Gypsophila oldhamiana* and highly oxygenated triterpenoid from *Fagara tessmannii* and *Luculia pinceana* also showed significant α-glucosidase inhibitory comparing to acarbose [1,18].

Based on its inhibition of α-glucosidase, the methanol extract of fruits was partitioned into *n*-hexane, ethyl acetate, and *n*-butanol. Ethyl acetate fraction had the highest α-glucosidase inhibitory with the IC_{50} of 13.49 μg/mL than an n-butanol fraction with the IC_{50} of 19.29 μg/mL due to its phenolic or stilbenoid content, meanwhile, the *n*-hexane fraction was not as potent as α-glucosidase inhibitory with the IC_{50} of 1175.16 μg/mL (Table 1 and Fig. 1). Compounds typically found in *n*-hexane fractions of *R. tomentosa* are nonpolar terpenoid like meroterpenoid and steroid [20]. These type of compound are usually inactive as an inhibitor of α-glucosidase. Meanwhile, oxygenated triterpenoid such as ursolic acid which found from a polar fraction of the leaves of *R. tomentosa* was reported as an inhibitor α-glucosidase [1,21].

Isolation and Structural Elucidation

The sequential partition to the methanol crude extract of *R. tomentosa* fruits (87 g) yielded *n*-hexane, ethyl acetate and *n*-butanol fraction of 1.54, 17.81 and 0.44 g, respectively. Ethyl acetate fraction with the highest α-glucosidase inhibition was chromatographed over silica gel with some chromatographic technique to afford compound **1**.

Compound **1** was isolated as a white powder with m.p. 120–121 °C. The UV spectrum in methanol showed the maximum absorption at 242 nm, which indicated the presence of α,β carbonyl unsaturated. The IR spectrum displayed absorption for the isolated carbonyl group at 1715 cm^{-1} as well as conjugated carbonyl group at 1678 and 1663 cm^{-1}, which consisted of the UV spectrum. In addition, there is absorption for C-H aliphatic group in 2976 and 2941 cm^{-1}. The ^{13}C-NMR (125 MHz, $CDCl_3$) was showed the presence of 14 signal. The two signals confirmed the existence of the isolated and conjugated carbonyl at δ_C 212.2 ppm and δ_C 192.2 ppm respectively. In addition, ^{13}C-NMR displayed the presence of five other quarternary carbon signal (δ_C 175.5 (oxy-carbon), 128.3, 113.2, 56.6, and 45.3 ppm), two signal for methine carbon (δ_C 46.6 and 34.5 ppm), and five signal for methyl carbon (δ_C 25.9, 24.5, 24.0, 22.4 and 15.6 ppm). The intensity of quarternary carbon signal at 128.3 ppm with the six other quarternary carbon (included the carbonyl) which has a ratio of 1:2, indicating that the six quarternary carbon is equivalent to twelve carbon. Furthermore, the five methyl carbon signals have an intensity ratio of 2:1 with a carbon methine signal at δ_C 34.5 ppm, consequently each of these methyl signals is identical for 2 methyl carbon (there are a total of 10 methyls). Based on this, compound **1** has 25 carbon atoms. The ^{1}H-NMR (500MHz, $CDCl_3$) spectrum exhibited the presence of a singlet signal of methine proton at δ_H 4.67 ppm. The spectrum also indicated the presence of an isopropyl unit with the appearance of a doublet signal at δ_H 1.00 ppm (6H, *d*, J = 6.9 Hz, 2xCH_3) which is adjacent to the methine proton at δ_H 2.35 ppm (1H, *sept*, J = 6.9 Hz). This constant coupling value indicates that both signals are correlated to each other as vicinal aliphatic protons.

In addition, there are three singlet signals at δH 1.41 (12H), 1.32 (6H), and 1.25 ppm (6H) which indicate the presence of 8 methyl groups. The HMBC correlation revealed a correlation of both methyl on a geminal dimethyl group (δ_H 1.25 and 1.32 ppm) to the isolated and conjugated carbonyl group (δ_C 212.2 and 192.2 ppm) as well as correlation of both methyl on another geminal dimethyl group to the isolated carbonyl (δ_C 212.2 ppm) and oxy-carbon (δ_C 175.5 ppm). These explained that both of geminal dimethyl is α position in β-triketone unit. Based on the previous NMR data, there are two symmetrical units of β-triketone. Furthermore,

Table 2. NMR data of compound **1** in $CDCl_3$ and rhodomyrtosone D

No	Compound 1			Rhodomyrtosone D [17]	
	δC	δ_H (ΣH, *mult*, J_{Hz})	HMBC (H→C)	δ_C	δ_H (*mult*, J_{Hz})
1 (1')	192.2	-	-	192.4	-
2(2')	56.6	-	-	56.4	-
3(3')	212.2	-	-	212.1	-
4(4')	45.3	-	-	45.2	-
5(5')	175.5	-	-	175.7	-
6(6')	113.2	-	-	113.0	-
7(7')	25.8	1.25 (6H, *s*)	C-3(3'), C-1(1'), C-2(2'), C-8(8')	25.7	1.27 (*s*)
8(8')	22.4	1.32 (6H, *s*)	C-3(3'), C- 1 (1'), C-2(2'), C-7(7')	22.3	1.34 (*s*)
9(9')	24.0	1.41 (6H, *s*)	C-3(3'), C-5(5'), C-4(4'), C-9(9'), C-10(10')	23.9	1.44 (*s*)
10(10')	24.5	1.41 (6H, *s*)	C-3(3'), C-5(5'), C-4(4'), C-9(9'), C-10(10')	24.4	1.44 (*s*)
1''	46.6	4.67 (1H, *s*)	C-5(5'), C-2'', C-6(6'), C-3''	46.5	4.69 (*s*)
2''	128.3	-	-	128.2	-
3''	34.5	2.35 (1H, *sept*, 6.9)	C-2'', C-1'', C-4'', C-5''	34.4	2.37 (*sept*, 6.9)
4'', 5''	15.6	1.00 (6H, *d*, 6.9)	C-2'', C-3'', C-4', C-5''	15.5	1.02 (*d*, 6.9)

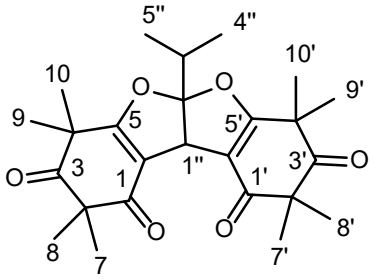

Fig 2. Structure of compound **1** (rhodomyrtosone D)

the correlation between of proton δ_H 4.67 ppm to isopropyl unit (δ_C 34.5 ppm) and oxy-carbon (δ_C 175.5 and 128.3 ppm) indicating that the isopropyl group was an adjacent bis-furan ring and the bis-furan ring was integrated with the β-triketone unit. According to this spectroscopic evidence (Table 2) and comparing to those of reported literature [17], the structure of compound **1** was established as rhodomyrtosone D (Fig. 2). This compound has been previously reported from *R. tomentosa* leaves [17].

The isolated compound **1** (rhodomyrtosone D) was examined for α-glucosidase inhibitory activity with concentration range about 30.77 to 0.24 μg/mL. The percentage of α-glucosidase inhibition from rhodomyrtosone D at the maximum test concentration of 30.77 μg/mL was 17.7%, while the inhibition of acarbose at the same concentration was 8.54%. Using the extrapolation method to linear regression, the IC_{50} of rhodomyrtosone D in inhibiting α-glucosidase was 110.45 μg/mL. This IC_{50} is lower compared to acarbose. Based on these values, rhodomyrtosone D has the ability to inhibit α-glucosidase enzyme stronger than acarbose.

■ CONCLUSION

The leaves, stem, and fruit of *R. tomentosa* plant were potential as a source of a natural antidiabetic, especially from the ethyl acetate fraction of the fruit. A bioactive compound, rhodomyrtosone D, was isolated from the fruit of *R. tomentosa* and showed higher α-glucosidase inhibition 3.5 fold than acarbose.

■ ACKNOWLEDGMENTS

The author would like thanks to Dr. Nurainas, M.Si., from Herbarium Anda, Andalas University for identification of plant specimen. We are grateful to the Ministry of Research, Technology, and Higher Education for research grants through PD-UPT scheme (No: 093/SP2H/LT/DPRM/IV/2018).

■ REFERENCES

[1] Yin, Z., Zhang, W., Feng, F., Zhang, Y., and Kang, W., 2014, α-Glucosidase inhibitors isolated from medicinal plants, *Food Sci. Hum. Wellness*, 3 (3-4), 136–174.

[2] Choudhary, M.I., Adhikari, A., Rasheed, S., Marasini, B.P., Hussain, N., Kaleem, W.A., and Rahman, A., 2011, Cyclopeptyde alkaloid of *Ziziphus oxyphylla* Edgw as novel inhibitors of α-glucosidase enzyme and protein glycation, *Phytochem. Lett.*, 4 (4), 404–406.

[3] Ortiz-Andrade, R.R., Jimenez, S.G., Castillo-España, P., Ramírez-Ávila, G., Villalobos-Molina, R., and Estrada-Soto, E., 2007, α-Glucosidase inhibitory activity of the methanolic extract from *Tournefortia hartwegiana*: An anti-hyperglycemic agent, *J. Ethnopharmacol.*, 109 (1), 48–53.

[4] Lam, S.H., Cheng, J.M., Kang, C.J., Chen, C.H., and Lee, S.S., 2008, α-Glucosidase inhibitors from the seed of *Syagrus romanzoffiana*, *Phytochemistry*, 69 (5), 1173–1178.

[5] Zhang, A.J., Rimando, A.M., Mizuno, C.S., and Mathews, S.T., 2017, α-Glucosidase inhibitory effect of resveratrol and piceatannol, *J. Nutr. Biochem.*, 47, 86–93.

[6] Kim, J.S., Yang, J., and Kim, M.J., 2011, Alpha glucosidase inhibitory effect, anti-microbial activity and UPLC analysis of *Rhus verniciflua* under various extract conditions, *J. Med. Plants Res.*, 5 (5), 778–783.

[7] Lavanya, G., Voravuthikunchai, S.P., and Towatana, N.H., 2012, Acetone extract from *Rhodomyrtus tomentosa*: A potent natural antioxidant, *Evid. Based Complement. Alternat. Med.*, 2012, 535479.

[8] Limsuwan, S., Kayser, O., and Voravuthikunchai, S.P., 2012, Antibacterial activity of *Rhodomyrtus tomentosa* (Aiton) Hassk. leaf extract against clinical isolates of *Streptococcus pyogenes*, *Evid. Based Complement. Alternat. Med.*, 2012, 697183.

[9] Lai, T.N.H., Herent, M.F., Quetin-Leclercq, J., Nguyen, T.B.T., Rogez, H., Larondelle, Y., and André, C.M., 2013, Piceatannol, a potent bioactive stilbene, as major phenolic component in *Rhodomyrtus tomentosa*, *Food Chem.*, 138 (2-3), 1421–1430.

[10] Wu, P., Ma, G., Li, N., Deng, Q., Yin, Y., and Huang, R., 2015, Investigation of *in vitro* and *in vivo* antioxidant activities of flavonoids rich extract from the berries of *Rhodomyrtus tomentosa* (Ait.) Hassk., *Food Chem.*, 173, 194–202.

[11] Hiranrat, A., Mahabusakaram, W., Carrol, A.R., Duffy, S., and Avery, V.M., 2012, Tomentosones A and B, hexacyclic phloroglucinol derivatives from the Thai shrub *Rhodomyrtus tomentosa*, *J. Org. Chem.*, 77 (1), 680–683.

[12] Limsuwan, S., Trip, E.N., Kouwen, T.R.H.M., Piersma, S., Hiranrat, A., Mahabusakaram, W., Voravuthikunchai, S.P., van Dijl, J.M., and Kayse, O., 2009, Rhodomyrtone, a new candidate as natural antibacterial drug from *Rhodomyrtus tomentosa*, *Phytomedicine*, 16 (6-7), 645–651.

[13] Liu, H.X., Zhang, W.M., Xu, Z.F., Chen, Y.C., Tan, H.B., and Qiu, S.X., 2016, Isolation, synthesis and biological activity of tomentosenol A from the leaves of *Rhodomyrtus tomentosa*, *RSC Adv.*, 6 (31), 25882–25886.

[14] Shou, Q., Smith, J.E., Mon, H., Brkljača, Z., Smith, A.S., Smith, D.M., Griesser, H.J., and Wohlmuth, H., 2014, Rhodomyrtals A-D, four unusual phloroglucinol-sesquiterpene adducts from *Rhodomyrtus psidioides*, *RSC Adv.*, 4 (26), 13514–13517.

[15] Anisah, L.N., Syafii, W., Pari, G., and Sari, R.K., 2018, Antidiabetic activities and identification of chemical compound from Samama (*Anthocephalus macrophyllus* (Roxb) Havil), *Indones. J. Chem.*, 18 (1), 66–74.

[16] Yang, Z., Wang, Y., Wang, Y., and Zhang, Y., 2012, Bioassay-guided screening and isolation of α-glucosidase and tyrosinase inhibitors from leaves of *Morus alba*, *Food Chem.*, 131 (2), 617–625.

[17] You, Q., Chen, F., Wang, X., Luo, P.G., and Jiang, Y., 2011, Inhibitory effect of muscadine anthocyanins on α-glucosidase and pancreatic lipase activities, *J. Agric. Food Chem.*, 59 (17), 9506–9511.

[18] Luo, J.G., Ma, L., and Kong, L.Y., 2008, New triterpenoid saponins with strong α-glucosidase inhibitory activity from the roots of *Gypsophila oldhamiana*, *Bioorg. Med. Chem.*, 16 (6), 2912–2920.

[19] Hiranrat, A., and Mahabusakaram, W., 2008, New acylphloroglucinols from the leaves of

Rhodomyrtus tomentosa, *Tetrahedron*, 64 (49), 11193–11197.

[20] Liu, J., Song, J.G., Su, J.C., Huang, X.J., Ye, W.C., and Wang, Y., 2018, Tomentodione E, a new sec-pentyl syncarpic acid-based meroterpenoid from the leaves of *Rhodomyrtus tomentosa*, *J. Asian Nat. Prod. Res.*, 20 (1), 67–74.

[21] Hui, W.H., and Li, M.M., 1976, Two new triterpenoids from *Rhodomyrtus tomentosa*, *Phytochemistry*, 15 (11), 1741–1743.

ZNO-Ag/PS and ZnO/PS Films for Photocatalytic Degradation of Methylene Blue

Hassan Khuder Naji[1], Amjed Mirza Oda[1,*], Wesam Abdulaljeleel[2], Hussein Abdilkadhim[2], and Rawaa Hefdhi[2]

[1]*Science Department, College of Basic Education, University of Babylon, Babylon 51002, Iraq*

[2]*Department of Chemistry, College of Sciences, University of Babylon, Babylon 51002, Iraq*

* ***Corresponding author:***

tel: +964-7812475243
email: almajid1981@yahoo.com

Received: November 27, 2018
Accepted: March 27, 2019

DOI: 10.22146/ijc.41347

Abstract: *Two films of ZnO-Ag/polystyrene (ZnO-Ag/PS) and ZnO/polystyrene (ZnO/PS) have been prepared and the photodegradation ability of stabilized catalysts was evaluated for methylene blue (MB) degradation. The efficiency of ZnO improved against recombination of electron-hole pair by modification of catalyst surface with Ag photodeposition to be more resistant towards photocorrosion. ZnO-Ag catalyst was characterized by SEM and EDS analysis to show high roughness of this catalyst and Ag deposited on the surface was 2% (molar ratio). ZnO-Ag/PS and ZnO/PS composites were made as films and were then analyzed by FTIR spectra that showed the interaction of ZnO and ZnO-Ag with polystyrene appeared in the range of 400–620 cm^{-1}, XRD pattern indicated the presence of Ag nanoparticles on the surface of ZnO and ZnO/PS film has maximum absorbance at 376 nm in UV-VIS spectra. This value shifted to 380 nm because of the photodeposition. The photocatalytic reaction was depicted using MB in the UV-irradiation action of stacked films in MB solution. The result showed that both ZnO-Ag/PS and ZnO/PS films gave efficiency to remove MB by 97% and 70%, respectively. The reusability test of the films showed that ZnO-Ag/PS was more resistant than ZnO/PS. The presence of Ag also increased the efficiency in photodegradation and resistance against photocorrosion.*

Keywords: *photocatalysis; photodeposition; ZnO-Ag; methylene blue*

■ INTRODUCTION

Photocatalysis techniques are new eco-friendly methods for environmental treatments to decontamination dyes in the wastewater. Metal oxide semiconductors as heterogeneous photocatalyst are an important material that utilized by many applications in industry and many technological processes like environmental and biomedical applications [1-2]. One of the serious problems in wastewater is contamination with an organic and inorganic dye that discharged to aquatic habit, which will add high risk to living organisms leading to pollution crises. Dyes are powerful coloring agent in the textile and leather industry.

On the other hand, these dyes are non-biodegradable when expelled to the ecosystem and resisted degradation so that it will cause health problems according to carcinogenic nature. Also, their presence made problem in an aquatic system like low illumination reaching the bottom and low oxygen demand [3-4]. Dyes can be removed using photocatalysis reaction in the presence of titanium dioxide (TiO_2) and zinc oxide (ZnO), and these catalysts can harvest light energy for photodegradation and significantly enhance the rate of degradation [5].

Semiconductor catalyst such as ZnO, when illuminated with photons forms in the valence band (VB) a positive hole (h^+) and the conduction band (CB) an electron (e^-). The positive hole oxidized by hydroxyl ions to produce hydroxyl radicals ($OH^•$) and causing degradation of organic contaminants directly or indirectly. In the conduction band, the electron is consumed by adsorbed oxygen and forms oxygen superoxide. These species enhance the rate of

degradation by destroying the chemical structure through several steps of oxidation, reaching mineralization the dyes converting into CO_2 and H_2O [6-7].

TiO_2 is most widely used in photocatalysis to decontamination of dyes, but ZnO also has similar activity to be useful like TiO_2 where its band gap energy is 3.2 eV. ZnO has a relatively lower cost of production and ease in the separation of electrons and holes charges. Thus ZnO can be used as an alternative catalyst instead of TiO_2 [8-10]. However, the capability of ZnO in photodegradation opposite its poor chemical stability under photocatalytic reaction [11] as it undergoes corrosion by self-oxidation under UV irradiation, leading to the loss of the photocatalytic activity. Thus, it needs to improve the photostability by incorporation into various composites like TiO_2 or by deposition of noble metals like Ag on the surface [5,12].

Efficient photocatalytic degradation of organic pollutants was reported by depositing TiO_2 ultrathin layer on Ag-ZnO nanorods, where the addition of Ag work as a sink for electron collector and prevent charges recombination. The TiO_2 layer increases the stability of photocatalyst against photo-corrosion under UV irradiation [12]. Several studies have designated that the photocatalytic rate increases with catalyst loading with metal, but at high concentrations of metal load will lose its efficiency, because of light scattering and screening effects happened [13]. Also, photodegradation is more efficient in case of increasing the lifetime of electron-hole separation and retarding recombination. According to this method, incorporation of species that accept electrons at conduction band of the photocatalyst, like transition metal ions or oxides increases the activity in degradation comparing to bare semiconductors. The consuming of a photo-excited hole by photooxidation species are expected could reduce the recombination process and make it highly efficient [5,12,14]. Usually, defect in photocatalyst by doping makes shifting in band gap to less value; therefore, the addition of dopants decrease the band gap causing surface modification by the new site and lifetime charges carriers' recombination is retarded and increase the photocatalyst ability in the photodegradation process [15-16].

In many previous reports, the photocatalytic reaction usually constructed according to the common protocol, where the photocatalyst is used as a powder and added to the dye solution with stirring to get a slurry, then illuminated with proper source of light to initiate the photocatalytic reaction. This protocol is limited to be used in industrial treatment units, because the recovery of catalyst and takes more times for continuing the treatment units work or expelled the catalyst to the environment, leading another problem. In our previous study, the photocatalyst is stabilized on a surface like cotton fiber by impregnation of in ZnO and ZnO-Ag and used for photodegradation of safranin O dye [17-18]. In addition, silver incorporation in TiO_2 and a polystyrene matrix was made to remove dye from wastewater as a floating photocatalyst [19]. Zinc oxide nanoparticles were also fixed on glass plates as a photocatalyst to remove Acid Red 88 dye in aqueous solution [20]. This strategic way reported that mixing the photocatalyst with polymer matrix gives a new technique in water purification with characteristic features like good photocatalytic activity, low cost in consuming of the catalyst and no need to recover the catalyst after water treatment [21].

Thus in this study, the action of ZnO doped Ag and comparison of photodegradation of methylene blue solution were demonstrated, where MB is likely used as an example to evaluate the photodegradation efficiency [22]. In the presence of ZnO/PS and ZnO-Ag/PS, both of them are stabilized in the polystyrene matrix controlling the photocatalyst to be not expelled to the environment. Some analysis like UV Vis, FTIR, XRD, SEM, EDS spectroscopy was used. The photodegradation of dye solution against time and the reusability of the films were also monitored and studied.

■ EXPERIMENTAL SECTION

Materials

Zinc oxide (ZnO) and methylene blue dye was supplied by Fluka Co., silver nitrate from BDH, polystyrene from local markets, acetone and chloroform by GCC, and were used without further purification.

Instrumentation

UV VIS spectra were recorded for polystyrene, ZnO/PS and ZnO-Ag/PS films in the range 200-800 nm using UV VIS spectrophotometer LF 4030, Scienco (Korea) by cutting pieces of the films (2 × 1) cm and inserted in the UV VIS holder to record the spectra and blank holder was air. FTIR analysis is done directly for the films and tested using Affinity IR instrument (Shimadzu, Japan) recorded in the range 400–4000 cm^{-1}, where the films located directly in the FTIR holder to record the spectra. XRD diffraction of ZnO and ZnO-Ag are characterized by XRD apparatus (DX-2700 SSC, USA) using the films in the range 20–60° of the diffraction angle (2theta). ZnO-Ag was analyzed by Scanning Electron Microscope Inspect 550, Netherland. EDS of ZnO-Ag was tested using energy dispersion X-ray (EDX), Bruker Nano GmbH, Germany, where the powder is suspended in absolute ethanol, and the suspension dropped on a piece of aluminium for SEM and EDS analysis.

Procedure

Preparation of composite of ZnO–Ag by photodeposition

ZnO powder about 5 g was weighed and suspended in 100 mL of a mixture of distilled water/Acetone (50:50) with stirring for 1 h. Silver nitrate was then added to the suspension, where the ratio of Ag was 2.5% molar ratio related to ZnO weight. The suspension was radiated using ultraviolet lamps (Phillips, 70 W) for 4 h, where this time all silver ion completely deposited on ZnO surface. $AgNO_3$ was added to the filtrate of ZnO suspension to ensure no AgCl precipitate is formed. Finally, the white suspension turned into grey color and continuing until the maximum of the solvent is evaporating. ZnO-Ag composite was then filtrated and washed with distilled water several times and dried at 80 °C for 12 h. This sample is prepared for analysis like SEM and EDS.

Preparation of ZnO–Ag/PS and ZnO/PS film

Polystyrene (0.95 g) was dissolved in 20 mL of chloroform using magnetic stirrer for 3 h in reflux apparatus and followed by the addition of 0.05 g of ZnO or ZnO-Ag with continuous stirring for 30 min to get a thick dispersed solution. After a slurry was formed, it was then poured in Petri dishes and left to evaporate in room temperature for 24 h to get casted films of ZnO/PS and ZnO-Ag/PS. The film without catalysts, which is polystyrene only, was used as a control film. These films are directly characterized by XRD, FTIR, and UV VIS spectroscopy.

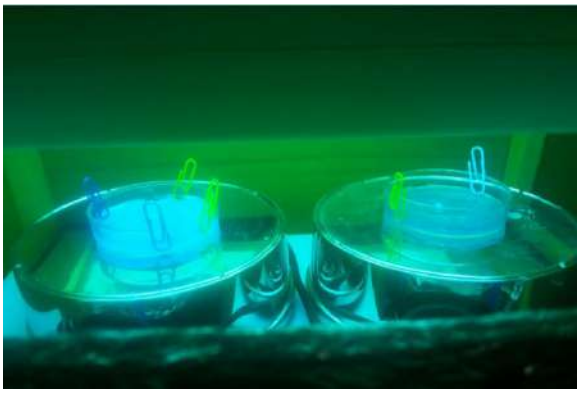

Fig 1. Photocatalytic degradation reaction installation (Petri dishes contain ZnO/PS film on the left and ZnO-Ag/PS film on the right were immersed in 10 ppm of methylene blue solution)

Photocatalytic degradation reaction

Photocatalytic degradation ability of ZnO-Ag and ZnO films was evaluated by the degradation of methylene blue under 70 watt UV lamp. In the degradation procedure, the film of ZnO–Ag/PS, ZnO/PS, or PS were stacked in 5 cm diameter Petri dish reaching the base of the dish with metal buckle, keeping the film against floating and most of the solution will be above the film as shown in Fig. 1. Then 10 mL of methylene blue solution (10 ppm) was added with ensuring most of the solution is above the film; it was then stirred for 15 min in the dark until the adsorption/desorption equilibrium was reached. This is enough time for adsorption according to the amount of catalyst in the PS matrix, that is only 5% w/w. The UV lamp was applied about 10 cm above the Petri dish, and the maximum absorbance of methylene blue was measured at 665 nm using UV–vis spectrophotometer scan between 200–800 nm wavelengths recorded every 15 min.

■ RESULTS AND DISCUSSION

ZnO-Ag/PS, ZnO/PS, and PS films were characterized by FTIR analysis and appeared in Fig. 2. The common main peaks are the same with no shifting, except after catalyst mixing leads to strong absorption at 400–550 cm^{-1}. Absorption bands at 3100 cm^{-1} belong to aromatic C-H stretching. The values of 2920 cm^{-1} and 2850 cm^{-1} absorption are assigned to CH_2 group for the asymmetric and symmetric stretching vibrations respectively. Aromatic C=C stretching peaks appeared at 1600 and 1500 cm^{-1}. The C-H deformation vibration band of benzene ring hydrogen appeared at 950 cm^{-1}. Also, the mono-substituted ring showed absorption peaks at 759 and 654, while the main peak of ZnO in the ZnO/PS composite was observed at the range 400–550 cm^{-1}. When compared to this value with recent works of literature, it is similar to this work [23-24].

UV-Vis spectrum of PS, ZnO/PS, and ZnO-Ag/PS are shown in Fig. 3, the PS does not show any appreciable absorption, and there is only a broad and less intense absorption band in the Vis region, while its absorption is 200–250 nm. For the composite films, it can be seen that there is UV absorption in all the samples, in the range of 240–390 nm, where the presence of zinc oxide enhances the UV absorption capacity of PS film. The ZnO content enhances the UV shielding properties of the polymer. When the number of dopant atoms increased, the gap of a semiconductor is lowered. Ag acts as a dopant that work as photo-sensitizer, which induce the separation of electron-hole pairs and prevent their recombination. Thus, the dopant works as a bridge to transfer charges between the localized stats [25]. Moreover, slight redshifts from 376 to 380 nm for the absorption peaks are observed in ZnO-Ag/PS film as a result of Ag doping. Such redshifts of the edge of absorption peaks of ZnO have also been reported [26].

XRD analysis was performed to analyze the degree of crystallinity and nature of ZnO and ZnO-Ag composites, with CuKα radiation (40 Kv, 30 mA). The diffraction of X-ray showed spectra of ZnO/PS and

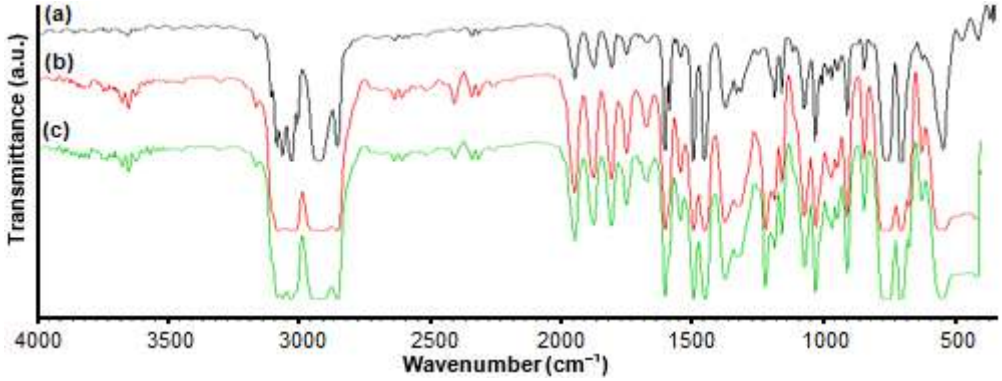

Fig 2. The FTIR spectra of (a) polystyrene films, (b) ZnO/PS films, and (c) ZnO–Ag/PS films

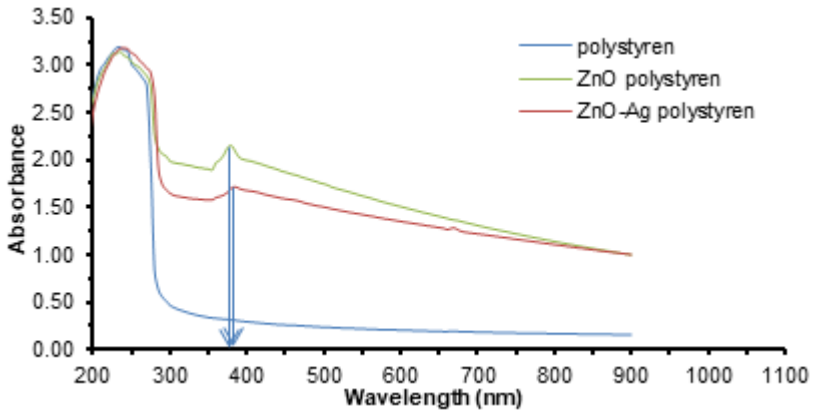

Fig 3. UV VIS spectra of PS, ZnO/PS, and ZnO-Ag/PS

ZnO-Ag/PS composites. Characteristic peaks appeared in the range of 2θ values of 20–60°, where the presence of several peaks indicating that the crystallinity of the composite is high, as shown in Fig. 4.

According to Fig. 4, ZnO-Ag peaks indicating the presence of silver and ZnO phases and no other structure is formed after doping. This means ZnO and Ag metal are the only phases that are found after photodeposition with successive reduction of Ag ion on to ZnO surface. XRD data for all studied samples are observed that the essential peaks occur at Miller indexes (100), (002), (101), (102), and (110), where the diffraction peaks are 31.80, 34.41, 36.21, 47.52, and 56.53. The main peaks of ZnO are similar to the ZnO phase liked wurtzite (hexagonal) structure, according to JCPDS card no. 36-1451. The new peak at 38.05° in ZnO-Ag/ PS spectra does not belong to ZnO, but it is an indication of the presence of a silver particle in the (111) crystal plane that rapped on ZnO surface. As the amount of Ag is low, the x-ray will not be sensitive to all diffracted peaks like 44.38 angle, thus (200) crystal planes of silver would not appear in the spectra [27].

ZnO-Ag composite was analyzed by SEM instrument to show the morphology of this photocatalyst and showed highly roughness, and the particles are distributed as dimensional form, which gives a good feature in surface area. Fig. 5(a) shows the SEM image of ZnO-Ag composite, and Fig. 5(b) is the EDS analysis of ZnO-Ag, and according to this test, the composite contained Zn, O, and Ag only. The presence of Ag peak indicates the successful modification of ZnO by Ag using photodeposition method. EDS analysis showed the atomic percentage that the amount of silver deposit on ZnO was 2%, while the percentage of Ag in the solution to prepare ZnO-Ag was 2.5% and this is a good result, where the error was low.

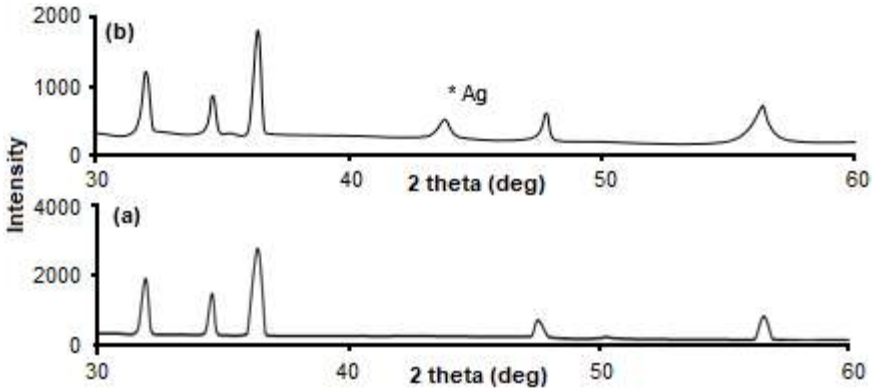

Fig 4. XRD of (a) ZnO/PS and (b) ZnO-Ag/PS

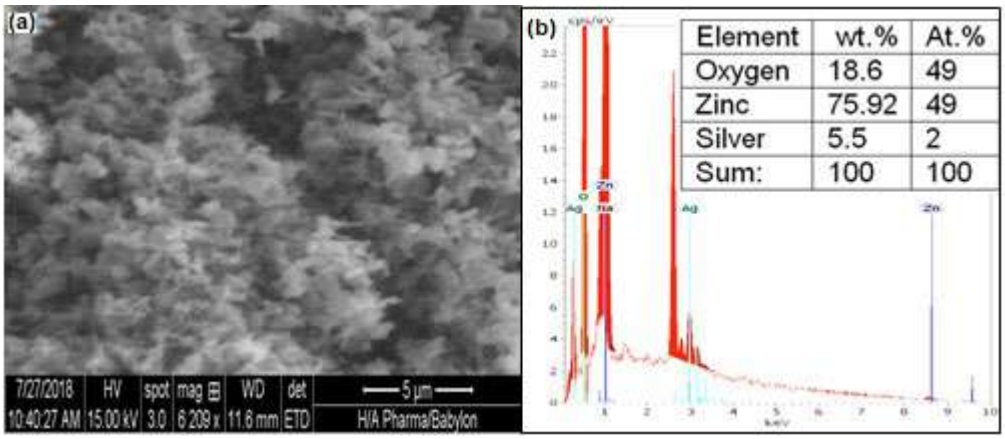

Fig 5. (a) SEM image and (b) EDS analysis of ZnO-Ag (the inserted table is weight and atomic elements percentage of ZnO-Ag)

Photocatalytic degradation activity of ZnO/PS and ZnO-Ag/PS were studied by degrading of MB dye under UV-irradiation in comparison to PS film. MB dye has maximum absorption at 665 nm, and the absorption is monitored to evaluate the photodegradation of MB, where in case of PS film there is a slight change in MB absorption, and this indicates the PS film has poor photocatalytic degradation.

In the case of ZnO-Ag/PS and ZnO/PS films, MB absorption is decreased with time due to the vanishing color by photocatalytic reaction, and this decreasing is continuing until the color of MB is disappeared. Fig. 6 shows the UV VIS spectra of MB solution with a concentration of 10 ppm in the presence of UV irradiation with proceeding time. In Fig. 6(a), the photodegradation of MB is very low as there is no photocatalyst, where PS film without catalyst, and the MB absorption was slightly changed related to initial concentration. Fig. 6(b) represents the effect of MB photodegradation by ZnO/PS film, and it can be seen that the absorption of MB is changing in time proceeding. This also revealed that MB degraded by the action of ZnO/PS film is a good method to eliminate the dyes from industrial textile effluent. The degradation of MB solution using ZnO-Ag/PS catalyst is shown in Fig. 6(c); MB was more degradable in the same conditions in comparison with ZnO-Ag/PS and PS films. According to this result, the degradation activity will be more efficient as much as exposing to UV irradiation. Finally, the color tends to be colorless of MB as the full destruction of chemical structure.

PS as a polymer has low degradation activity and this regards to wide bandgap; therefore, it did not show any degradation of MB solution. ZnO-Ag/PS was more effective in MB removal than ZnO/PS film, and this attributed to the Ag doping. This modification changed the surface nature and made new active sites, increasing the surface area. Also, the photocatalytic activity of ZnO-Ag/PS was enhanced due to metallic Ag deposition on the surface of ZnO, and this metal works as electrons

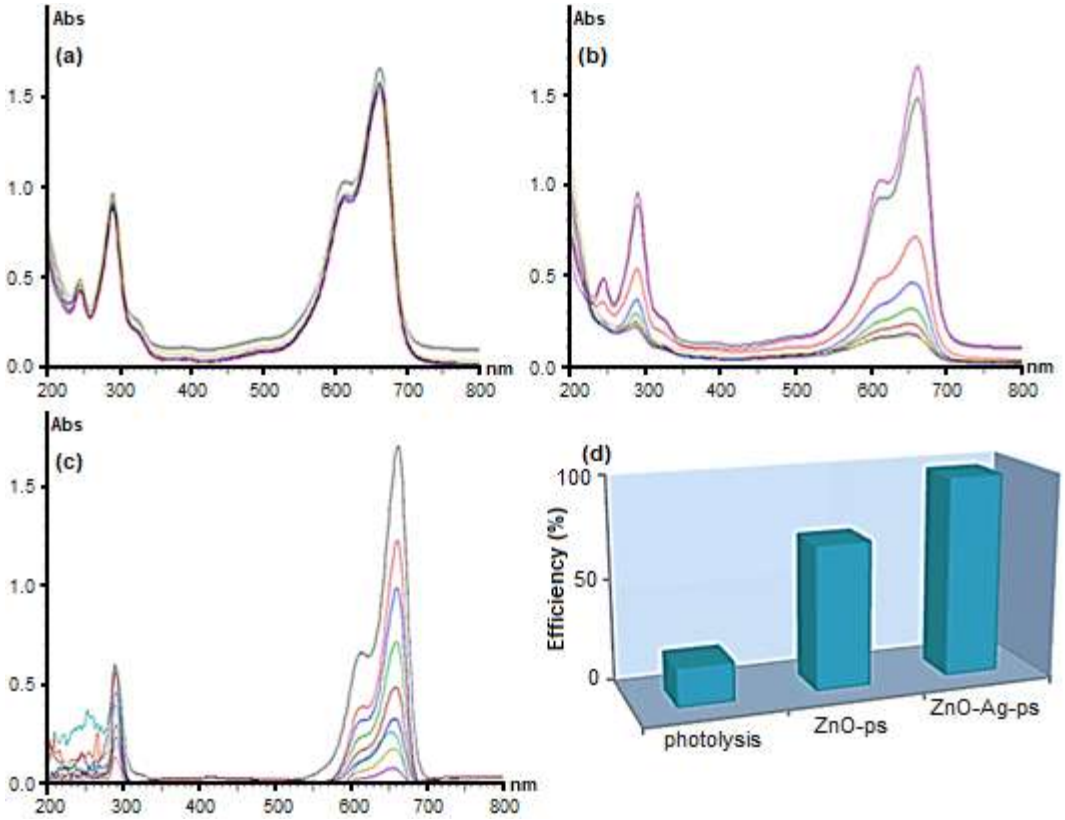

Fig 6. Photodegradation of MB by (a) PS film, (b) ZnO/PS film, (c) ZnO-Ag/PS film, and (d) efficiency of photodegradation of the three films

collectors. Silver nanoparticles that trapped on ZnO surface modify the surface with new geometrical active sites. This modification leads to change the electronic properties and increase the separation time of the electron-hole pair to give more time for electron trapping. Electrons trapped tend to move to an oxidized agent like the adsorbed molecular oxygen, and this prevents the recombination of electron-hole pairs. Thus the degradation efficiency was increased [28-29].

In addition, the ZnO-Ag/PS ability in MB degradation result from the electron-hole could have more than one pathway for the formation of electron-hole with more time and forbidding recombination as the three different interfaces of ZnO-Ag composite. The comparison of the photodegradation efficiency of the three films is shown in Fig. 6(d), where high efficiency of ZnO-Ag/ ps film in the same conditions is reached up to 97% for 120 min after reaction, while ZnO/ps was 70% and PS film alone was 19% and this result is similar as reported [30].

The photocatalytic reaction of films against MB removal kinetics was studied, and it found that this kind of reaction follows pseudo-first-order kinetics. The most mechanism that fallow this reaction is a Langmuir-Hinshelwood mechanism. This mechanism can explain the degradation activity of heterogeneous photocatalyst. Depending on the concentration of MB dye, when the concentration of MB dye is low, the rate expression can be written as $d[C]/dt = k[C]$. k is the apparent constant of first-order rate calculated by the linear regression of the equation the $k = \ln(C_{MBo}/C_{MB})/t$, where C_{oMB} and C_{MB} are the concentrations of MB dyes at the irradiation time 0 and t min, respectively. Plots of $\ln(C/C_o)$ against the time of irradiation gives a straight line, as shown in Fig. 7, and the slope of the linear fitted line represents the value of k. The calculated k values were equal to 0.0284, 0.0253, and 0.0007 min^{-1} for ZnO-Ag/PS, ZnO/PS, and PS films, respectively. It is obvious that ZnO-Ag/PS has a high degradation rate of MB dye under UV irradiation. According to these results, ZnO-Ag/PS can be used as treatment techniques to eliminate pollution by dyes through effluent wastewater [31-33].

The efficiency of MB photodegradation is clearly obvious in the presence of the photocatalyst ZnO/PS and ZnO-Ag/PS and PS. However, the amount of catalysts in the matrix in polystyrene film is low. ZnO/PS and ZnO-Ag/PS were highly active to diminish the color of MB, where ZnO-Ag/PS was very efficient as a result of a combination of Ag on ZnO surface. Fig. 8 shows the efficiency of photodegradation by UV light only, and the

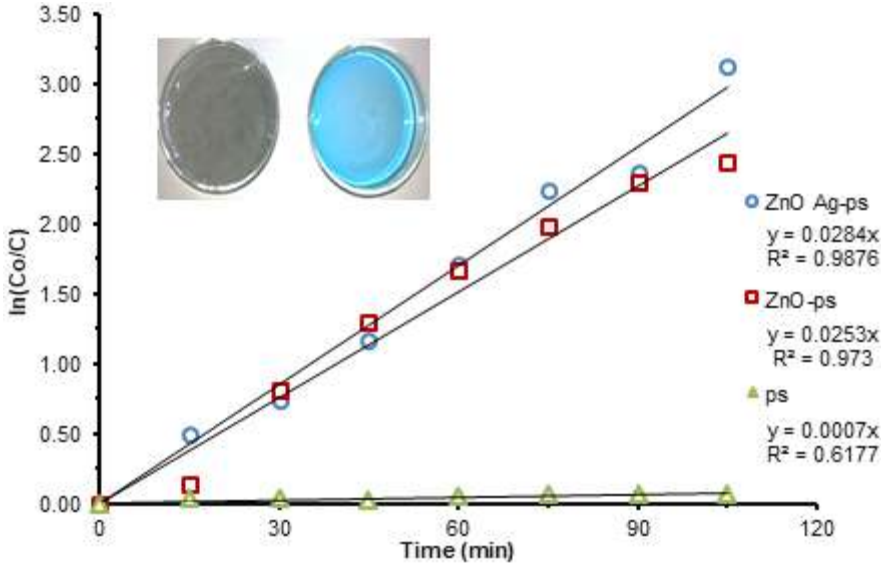

Fig 7. The first order plot of MB photodegradation (a) PS film, (b) ZnO/Ag film, (c) ZnO-Ag/PS film. The insight picture is Petri dishes of MB solution without catalyst on the right and with ZnO-Ag/PS film on the left at the end of the reaction

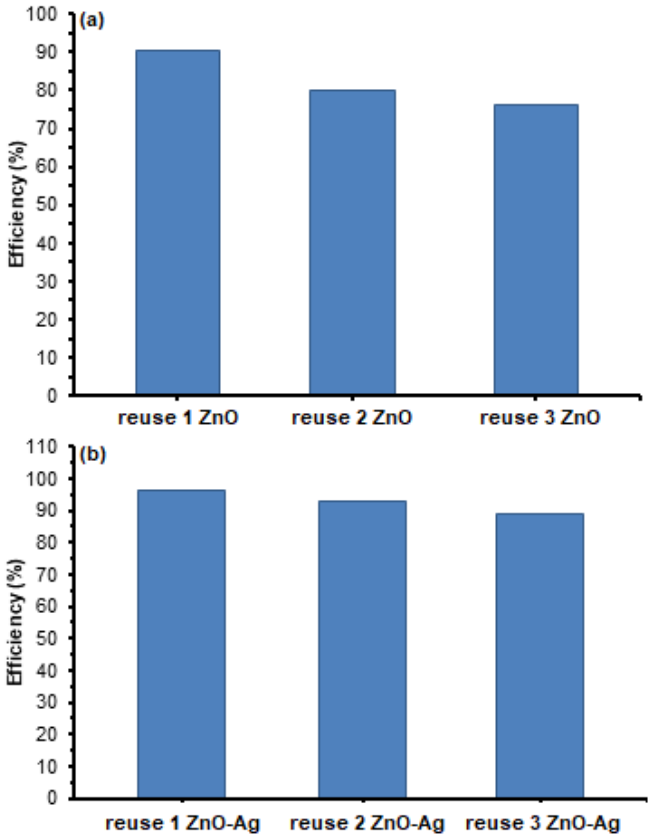

Fig 8. Photodegradation efficiency after reusing the (a) ZnO/PS and (b) ZnO-Ag/PS films

catalyst of ZnO/PS and ZnO-Ag/PS efficiency, which was 20, 80, and 96%, respectively. Another aspect of this study was testing the photodegradation activity after several runs, reusing the film again to ensure that the films can be used several times and measuring their efficiency in the degradation of MB. This experiment was accomplished by decanting the solution of MB after decolorization and replaced by a new solution of MB and illuminated by UV light, and the absorbance was measured so that the efficiency is calculated. Fig. 8 shows the efficiency of ZnO/PS and ZnO-Ag/PS films after were used in the first photodegradation and reused three times. ZnO/PS and ZnO-Ag/PA films have good reusability of photodegradation efficiency. The reusability of the catalysts is a benefit for cost-effectiveness to reduce the consumption of catalyst films each photodegradation process as reported [34-35].

■ CONCLUSION

ZnO and ZnO-Ag stabilized in polystyrene matrix give high efficiency in photocatalytic degradation of MB and had good reusability. Photodepositon of Ag on ZnO surface made a surface modification, according to the analysis of XRD, SEM, and EDS, making the MB degradation using ZnO-Ag/PS film was higher than using ZnO/PS film. In the same period of MB degradation, ZnO-Ag/PS efficiency was 97%, while it was 70% for ZnO/PS film. ZnO-Ag/PS film can be reused three times with the efficiency reached 89% compared to ZnO/PS film, which was 76%.

■ REFERENCES

[1] Sangpour, P., Hashemi, F., and Moshfegh, A.Z., 2010, Photoenhanced degradation of methylene blue on cosputtered M:TiO_2 (M = Au, Ag, Cu) nanocomposite systems: A comparative study, *J. Phys. Chem. C*, 114 (33), 13955–13961.

[2] Li, D., Zhang, Y., Wu, W., and Pan, C., 2014, Preparation of a ZnO/TiO_2 vertical-nanoneedle-on-film heterojunction and its photocatalytic properties, *RSC Adv.*, 4 (35), 18186–18192.

[3] Teh, C.M., and Mohamed, A.R., 2011, Roles of titanium dioxide and ion-doped titanium dioxide on photocatalytic degradation of organic pollutants (phenolic compounds and dyes) in aqueous solutions: A review, *J. Alloys Compd.*, 509 (5), 1648–1660.

[4] Josephine, G.S., and Sivasamy, A., 2014, Nanocrystalline ZnO doped on lanthanide oxide Dy_2O_3: A novel and UV light active photocatalyst for environmental remediation, *Environ. Sci. Technol. Lett.*, 1 (2), 172–178.

[5] Zhao, H., Deng, W., and Li, Y., 2018, Atomic layer deposited TiO_2 ultrathin layer on Ag_ZnO nanorods for stable and efficient photocatalytic degradation of RhB, *Adv. Compos. Hybrid Mater.*, 1 (2), 404–413.

[6] Ahmed, S., Rasul, M.G., Martens, W.N., Brown, R., and Hashib, M.A., 2010, Heterogeneous

photocatalytic degradation of phenols in wastewater: A review on current status and developments, *Desalination*, 261 (1-2), 3–18.

[7] Zheng, Y., Chen, C., Zhan, Y., Lin, X., Zheng, Q., Wei, K., and Zhu, J., 2008, Photocatalytic activity of Ag/ZnO heterostructure nanocatalyst: Correlation between structure and property, *J. Phys. Chem. C*, 112 (29), 10773–10777.

[8] Sapkota, A., Anceno, A.J., Baruah, S., Shipin, O.V., and Dutta, J., 2011, Zinc oxide nanorod mediated visible light photoinactivation of model microbes in water, *Nanotechnololy*, 22 (21), 215703.

[9] Khodja, A.A., Sehili, T., Pilichowski, J.F., and Boule, P., 2001, Photocatalytic degradation of 2-phenylphenol on TiO_2 and ZnO in aqueous suspensions, *J. Photochem. Photobiol., A*, 141 (2-3), 231–239.

[10] Chakrabarti, S., Chaudhuri, B., Bhattacharjee, S., Das, P., and Dutta, B.K., 2008, Degradation mechanism and kinetic model for photocatalytic oxidation of PVC–ZnO composite film in presence of a sensitizing dye and UV radiation, *J. Hazard. Mater.*, 154 (1-3), 230–236.

[11] Sridharan, K., Jang, E., Park, Y.M., and Park, T.J., 2015, Superior photostability and photocatalytic activity of ZnO nanoparticles coated with ultrathin TiO_2 layers through atomic-layer deposition, *Chem. Eur. J.*, 21 (52), 19136–19141.

[12] Fan, Y., Han, D., Song, Z., Sun, Z., Dong, X., and Niu, L., 2017, Regulations of silver halide nanostructure and composites on photocatalysis, *Adv. Compos. Hybrid Mater.*, 1 (2), 269–299.

[13] Pareek, V.K., and Adesina, A.A., 2004, Light intensity distribution in a photocatalytic reactor using finite volume, *AlChE J.*, 50 (6), 1273–1288.

[14] Pouretedal, H.R., Norozi, A., Keshavarz, M.H., and Semnani, A., 2009, Nanoparticles of zinc sulfide doped with manganese, nickel and copper as nanophotocatalyst in the degradation of organic dyes, *J. Hazard. Mater.*, 162 (2-3), 674–681.

[15] Rauf, M.A., Meetani, M.A., Khaleel, A., and Ahmed, A., 2010, Photocatalytic degradation of methylene blue using a mixed catalyst and product analysis by LC/MS, *Chem. Eng. J.*, 157 (2-3), 373–378.

[16] Oda, A.M., Ferhod, A.S., and Lafta, A.J., 2014, Modification of the photocatalytic activity of zinc oxide by doping silver, *IJSR*, 3 (11), 2133–2139.

[17] Oda, A.M., Ali, H.H., Lafta, A.J., Esmael, H.A., Jameel, A.A., Mohammed, A.M., and Mubarak, I.J., 2015, Study self-cleaning of Congo red from cotton fabric loaded by ZnO-Ag, *Int. J. Chem.*, 7 (2), 39–48.

[18] Oda, A.M., Khuder, H., Hashim, R., Rasheed, A., Hasan, A.A., Hazim, H., and Raheem, Z., 2016, Photocatalytic degradation of safranin O by ZnO-Ag loaded on cotton fabric, *Res. J. Pharm. Biol. Chem. Sci.*, 7 (5), 2915–2924.

[19] Singh, S., Singh, P.K., and Mahalingam, H., 2014, Novel floating Ag^+-doped TiO_2/polystyrene photocatalysts for the treatment of dye wastewater, *Ind. Eng. Chem. Res.*, 53 (42), 16332–16340.

[20] Zandsalimi, Y., Teymouri, P., Soltani, R.D.C., Rezaee, R., Abdullahi, N., and Safari, M., 2015, Photocatalytic removal of Acid Red 88 dye using zinc oxide nanoparticles fixed on glass plates, *J. Adv. Environ. Health Res.*, 3 (2), 102–110.

[21] Di Mauro, A., Cantarella, M., Nicotra, G., Pellegrino, G., Gulino, A., Brundo, M.V. Privitera, V., and Impellizzeri, G., 2017, Novel synthesis of ZnO/PMMA nanocomposites for photocatalytic applications, *Sci. Rep.*, 7, 40895.

[22] Kunarti, E.S., Kartini, I., Syoufian, A., and Widyandari, K.M., 2018, Synthesis and photoactivity of Fe_3O_4/TiO_2-Co as a magnetically separable visible light responsive photocatalyst, *Indones. J. Chem.*, 18 (3), 403–410.

[23] Chae, D.W., and Kim, B.C., 2005, Characterization on polystyrene/zinc oxide nanocomposites prepared from solution mixing, *Polym. Adv. Technol.*, 16 (11-12), 846–850.

[24] Kaniappan, K., and Latha, S., 2011, Certain investigations on the formulation and characterization of polystyrene/poly(methyl methacrylate) blends, *Int. J. ChemTech Res.*, 3 (2), 708–717.

[25] Sangawar, V.S., and Golchha, M.C., 2013, Evolution of the optical properties of polystyrene thin films filled with zinc oxide nanoparticles, *Int. J. Sci. Eng. Res.*, 4 (6), 2700–2705.

[26] Zhou, X.D., Xiao, X.H., Xu, J.X., Cai, G.X., Ren, F., and Jiang, C.Z., 2011, Mechanism of the enhancement and quenching of ZnO photoluminescence by ZnO-Ag coupling, *Europhys. Lett.*, 93 (5), 57009.

[27] Aazam E.S., 2014, Visible light photocatalytic degradation of thiophene using Ag–TiO_2/multi-walled carbon nanotubes nanocomposite, *Ceram. Int.*, 40 (5), 6705–6711.

[28] Ren, C., Yang, B., Wu, M., Xu, J., Fu, Z., lv, Y., Guo, T., Zhao, Y., and Zhu, C., 2010, Synthesis of Ag/ZnO nanorods array with enhanced photocatalytic performance, *J. Hazard. Mater.*, 182 (1-3), 123–129.

[29] Subash, B., Krishnakumar, B., Swaminathan, M., and Shanthi, M., 2013, Highly efficient, solar active, and reusable photocatalyst: Zr-loaded Ag–ZnO for reactive red 120 dye degradation with synergistic effect and dye-sensitized mechanism, *Langmuir*, 29 (3), 939–949.

[30] Fageria, P., Gangopadhyay, S., and Pande, S., 2014, Synthesis of ZnO/Au and ZnO/Ag nanoparticles and their photocatalytic application using UV and visible light, *RSC Adv.*, 4 (48), 24962–24972.

[31] Saravanan, R., Khan, M.M., Gupta, V.K., Mosquera, E., Gracia, F., Narayanan, V., and Stephen, A., 2015, ZnO/Ag/Mn_2O_3 nanocomposite for visible light-induced industrial textile effluent degradation, uric acid and ascorbic acid sensing and antimicrobial activity, *RSC Adv.*, 5 (44), 34645–34651.

[32] Byrappa, K., Subramani, A.K., Ananda, S., Rai, K.M.L., Dinesh, R., and Yoshimura, M., 2006, Photocatalytic degradation of rhodamine B dye using hydrothermally synthesized ZnO, *Bull. Mater. Sci.*, 29 (5), 433–438.

[33] Patchaiyappan, A., Saran, S., and Devipriya, S.P., 2016, Recovery and reuse of TiO_2 photocatalyst from aqueous suspension using plant based coagulant-A green approach, *Korean J. Chem. Eng.*, 33 (7), 2107–2113.

[34] Krishnakumar, B., Subash, B., and Swaminathan, M., 2012, AgBr–ZnO–An efficient nano-photocatalyst for the mineralization of acid black 1 with UV light, *Sep. Purif. Technol.*, 85, 35–44.

[35] Saravanan, R., Khan, M.M., Gupta, V.K., Mosquera, E., Gracia, F., Narayanan, V., and Stephen, A., 2015, ZnO/Ag/CdO nanocomposite for visible light-induced photocatalytic degradation of industrial textile effluents, *J. Colloid Interface Sci.*, 452, 126–133.

The Properties of Thermosensitive Zwitterionic Sulfobetaine NIPAM-*co*-DMAAPS Polymer and the Hydrogels: The Effects of Monomer Concentration on the Transition Temperature and Its Correlation with the Adsorption Behavior

Eva Oktavia Ningrum[1,*], Agus Purwanto[2], Galuh Chynintya Rosita[3], and Asep Bagus[3]

[1]*Department of Industrial Chemical Engineering, Faculty of Vocational Studies, Institut Teknologi Sepuluh Nopember, Kampus ITS Sukolilo, Surabaya, 60111, Indonesia*

[2]*Department of Chemical Engineering, Faculty of Engineering, Universitas Sebelas Maret, Jl. Ir. Sutami 36 A, Surakarta, Central Java 57126, Indonesia*

[3]*Department of Chemical Engineering, Faculty of Industrial Technology, Institut Teknologi Sepuluh Nopember, Kampus ITS Sukolilo, Surabaya 60111, Indonesia*

Corresponding author:

tel: +62-81335233410
email: eva-oktavia@chem-eng.its.ac.id

Received: December 1, 2018
Accepted: February 11, 2019

DOI: 10.22146/ijc.41499

Abstract: *The properties of N-isopropylacrylamide copolymerized with N,N-dimethyl (acrylamidopropyl)ammonium propane sulfonate [poly(NIPAM-co-DMAAPS)] prepared with various monomer ratios such as transition temperature, molecular structure, viscosity were systematically investigated in water and $Zn(NO_3)_2$ solution. Poly(NIPAM-co-DMAAPS) in water and $Zn(NO_3)_2$ solution exhibited a phase transition with a lower critical solution temperature (LCST). The higher ratio of NIPAM monomer in poly(NIPAM-co-DMAAPS), the lower the LCST of the polymer. Furthermore, the transition temperature of poly(NIPAM-co-DMAAPS) with a lower NIPAM concentration were not confirmed both in water nor $Zn(NO_3)_2$ solution. The more increase the NIPAM concentration used in the preparation, the more increase the polymer viscosity. Moreover, the more increase the adsorption amount of ions onto the gel, the more increase the polymer transmittance as well.*

Keywords: *transition temperature; thermosensitive; adsorption*

■ INTRODUCTION

As the impact of highly industrial activities, the amount of heavy metals increases every year. Heavy metals can cause various adverse health effects because of their accumulation in the human body. It is not only dangerous for the human body but also the environment. Heavy metals are able to form a complex chain when it enters the organism body. One of the areas in Indonesia, which is affected by heavy metals is Jakarta Bay. The accumulation of heavy metals in Jakarta Bay has increased significantly from the 1970s. It is reported in 2017 that the heavy metal ions contamination which hits Jakarta Bay has spread far into Seribu Islands. Maintaining the sediment in the coastal area is the most vital action to be performed since it can affect the existence of various aquatic and benthic organisms. Additionally, it can provide them habitats and food supply. A phenomenon that becomes a serious environmental issue, and it should be immediately mitigated is the accumulation of heavy metals in the bottom sediment of Jakarta bay [1-2].

The issue of heavy metals separation becomes the concern of many parties. Conventional methods commonly used in the recovery of heavy metals from liquid industrial waste are activated sludge process, chemical precipitation, flotation, ion exchange, membrane filtration, and electrodialysis [3-6]. The most frequently studied for heavy metal wastewater treatment are ion-exchange, adsorption, and membrane filtration, and the most effective and an economical method for heavy metal wastewater treatment with low concentration is adsorption by low-cost adsorbents and biosorbents since it has a function as an alternative

activated carbon (AC). Meanwhile, removing heavy metal ions with high efficiency can be done by using membrane filtration technology [7]. Activated sludge process is not effective because it results in sludge with high heavy metals concentration. The other methods are also not effective because of the high operation cost [8-10].

One of the novel technologies in heavy metals separation is by using adsorption with thermosensitive gel based on zwitterionic betaine as the adsorbent. This method is considered as the most effective to overcome the heavy metals contamination in the aquatic environment [11]. The advantage of zwitterionic betaine is having the ions selectivity as the consequence of the interaction among the ions and the positive and negative charges inside the chain [12]. Zwitterionic betaine is able to bond both anion and cation in liquid waste, simultaneously [13]. Zwitterionic betaine polymer is thermosensitive in aqueous solution, and also has Upper Critical Solution Temperature (UCST) or Lower Critical Solution Temperature (LCST) property or both of them. Besides, the zwitterionic gel is environmentally friendly and has a lower operational cost than the other methods.

Poly(*N*-isopropylacrylamide) [poly(NIPAM] is a thermosensitive polymer with Low Critical Solution Temperature (LCST) which is around 32 °C. NIPAM swells at low temperature and shrinks at high temperature because of its transition from hydrophilic to hydrophobic and has neutral charge [14]. *N,N*'-dimethyl (acrylamidopropyl)ammonium propane sulfonate (DMAAPS) is zwitterionic sulfobetaine polymer. The previous study reports that physical condition and transparency of poly(DMAAPS) strongly affected by the concentration and the temperature of the solution. In high monomer concentration, poly(DMAAPS) physically forms gels because of the interchain in zwitterionic group. Poly(DMAAPS) solution points out the thermoresponsive phase transition at UCST. That polymer completely dissolves in NaCl solution at room temperature as same as in water at a temperature above the UCST [15]. Takahashi [14] has studied the thermosensitive polymer property of NIPAM-*co*-DMAAPS in a salt solution. The LCST of poly(NIPAM-*co*-DMAAPS) increases along with the increase of DMAAPS concentration and decreases along with the increase of the salt solution concentration. In our previous study [13], the correlation between the ions adsorption and swelling ability of sulfobetaine gel was investigated. The polymer concentration was considered to explain this relationship, which was converted from the density of the gel divided by its swelling degree. When the polymer concentration is higher than 180 g/L, the number of Zn^{2+} adsorbed onto the gel remains constant with the increase of polymer concentration.

In contrast, when the polymer concentration gets lower, the number of Zn^{2+} adsorbed increases with the increase of polymer concentration. The effects of cross-linker concentration on adsorption and the swelling ability of DMAAPS gel were also investigated in this study. The higher the cross-linker concentration, the better the adsorption ability of DMAAPS gel.

None of the preceding studies focus on the correlation between transition behavior of poly(NIPAM-*co*-DMAAPS) towards ions adsorption ability of NIPAM-*co*-DMAAPS gel. Most of which have emphasized phase transition and property of polymer in heavy metal solution or adsorption behavior of the gel independently. UCST poly(DMAAPS) depend strongly on molecular weight, sulfobetaine monomer, or polymer concentration and also environmental conditions [13,16].

In the present study, the property of poly(NIPAM-*co*-DMAAPS) such as molecular structure, viscosity, transition temperature was investigated with the variation of monomer concentration and using $Zn(NO_3)_2$ solution as target solution. The effects of monomer concentration on the transition temperature and its correlation with the adsorption behavior of the hydrogel were also elucidated.

■ EXPERIMENTAL SECTION

Materials

The materials used in this research are N-isopropylacrylamide (NIPAM, ≥ 99.52%), 1,3-propane sultone, *N,N*-dimenthylaminopropylacrylamide (DMA PAA, ≥ 99.77%), *N,N*'-methylene-bisacrylamide (MBAA, 99%), *N,N,N',N*'-tetramethylethylenediamine (TEMED,

99%), ammonium peroxodisulfate (APS, ≥ 95%), acetonitrile and acetone. The first material was bought from KJ Chemicals Co., Ltd., Japan. The second material was bought from Tokyo Chemical Industry Co., Ltd. The third material was supplied by KJ. Chemicals Co., Ltd., Japan. MBAA, TEMED, and APS were bought from Sigma Aldrich Co. (USA). Acetonitrile was bought from Avantor Performance Materials, while the last material which acetone was bought from Smart Lab Indonesia. Some materials were purified before being used, while some others were used as they were received. The materials that were used after being purified are NIPAM through recrystallization process and DMAPAA through vacuum distillation. Meanwhile, the other materials were used without purification.

Synthesis of Poly[NIPAM-*co*-DMAAPS]

A copolymer consisting of zwitterionic betaine *N,N*-dimethyl(acrylamidopropyl)ammonium propane sulfonate (DMAAPS) and thermosensitive *N*-isopropylacrylamide (NIPAM) polymer and gel were characterized in order to elucidate the transition temperature and the adsorption amount of ions adsorbed onto the gel. The synthesis of NIPAM-*co*-DMAAPS is carried out in two steps; those are material purification and copolymer synthesis. The material purification step includes the purification of NIPAM and DMAPAA followed by the synthesis of DMAAPS monomer through a ring opening reaction of 1,3-propane sultone (PS) with *N,N'*-dimethylaminopropylacrylamide (DMAPAA). NIPAM and DMAAPS monomers were then copolymerized to form poly(NIPAM-*co*-DMAAPS).

Distillation of DMAPAA

DMAPAA has a characteristic which is easily polymerized with each other. Thus the storage was added by hydroquinone as an inhibitor in order to prevent any polymerization reaction. Therefore, before its use, DMAPAA must be separated first from hydroquinone through vacuum distillation. The distillation was carried out at a vacuum pressure of 2 cm Hg and a temperature of 160 °C.

The product obtained was clear yellowish, while the residue of hydroquinone was darker brownish yellow. From the visualization of the resulting product color, it can be concluded that the purification/ separation process of DMAPAA from the impurities was successfully performed.

Synthesis of DMAAPS

The monomer of *N,N*-dimethyl(acrylamidopropyl) ammonium propane sulfonate (DMAAPS) was synthesized through ring opening reaction of *N,N*-dimethylaminopropylacrylamide (DMAPAA) and 1,3-propane sultone (PS) proposed by Lee and Tsai [17] using the same method as in our previous study [18-20]. The following ring opening reaction occurs (Fig. 1).

DMAAPS is in the form of white crystal with a melting point of 105 °C and a yield of 92%. The formation of DMAAPS also involves the process of crystallization. The stirring is done to accelerate the formation of DMAAPS crystals. Acetone washing is done to remove the remaining acetonitrile and other impurities.

Recrystallization of NIPAM

The purification of NIPAM monomer is carried out by recrystallization from *n*-hexane. NIPAM (300 g) was dissolved in 510 mL benzene. The NIPAM-benzene solution was divided into six Erlenmeyer and added with hexane so that the total solution of NIPAM, benzene,

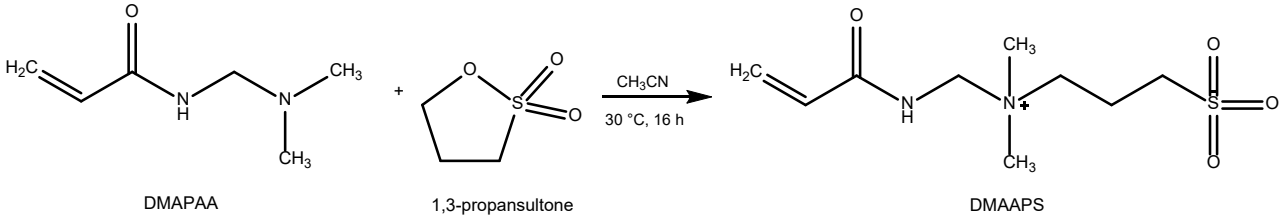

Fig 1. Synthesis route to *N,N*-dimethyl(acrylamidopropyl)ammonium propane sulfonate (DMAAPS) through ring opening reaction

and hexane was 1 L. The solution was then put it in the refrigerator for a day. The product obtained was separated by a vacuum filter, followed by dried into a vacuum oven for 2 h at a constant temperature of 50 °C. Finally, NIPAM was ready to be used for the synthesis of the copolymer.

Synthesis of copolymer

Free radical polymerization was used to synthesize the poly(NIPAM-*co*-DMAAPS). The accelerator of the synthesis was TEMED, while the initiator was APS. In addition, the concentration of both accelerator and initiator used in preparing NIPAM-*co*-DMAAPS were 10 and 2 mmol/L, respectively. NIPAM-*co*-DMAAPS were synthesized with NIPAM and DMAAPS molar ratio of 9:1, 8:2, and 7:3. The first solution was designated from NIPAM, which was dissolved in 50 mL of deionized water and put into a flask. The second solution was referred to as DMAAPS and TEMED, which were dissolved in aquadest of 50 mL put into another flask. The oxygen which was dissolved in the solution was then cleaned using nitrogen. A 20 mL of an aliquot from the APS of the dissolved purged oxygen was then added into a reactor containing the mixture of solution 1 and 2. The polymerization was conducted for 6 h at 10 °C under a nitrogen atmosphere. The reactions occur in the reactor were depicted in Fig. 2.

The release of radical persulfate ion from APS takes hydrogen atom from TEMED, so TEMED is activated and leaves molecule with a reactive unpaired electron was depicted in Fig. 3.

The activated TEMED attacks vinyl groups at NIPAM or DMAAPS to combine with it and activated in turn. As the chain of NIPAM or DMAAPS units grows, the active site shifts to the free end. The growing chain of NIPAM or DMAAPS joint together through their active site group.

Synthesis of NIPAM-co-DMAAPS gel

NIPAM-*co*-DMAAPS gels were synthesized in the same way as copolymer synthesis. However, in this synthesis, the cross-linker was 30 mmol/L of MBAA. The DMAAPS with active site shown in Fig. 4 are then incorporated by NIPAM or MBAA, which consist of two acrylamides. They were joint together through $-CONH_2$ groups lead to the formation of crosslinker between chains, as shown in Fig. 5.

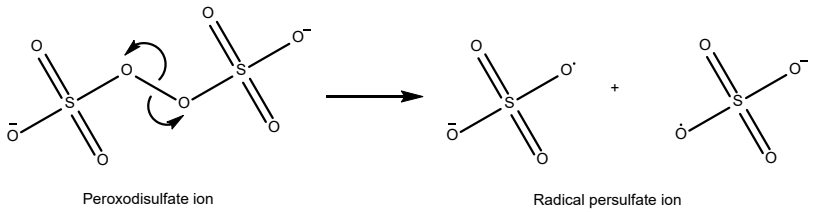

Fig 2. The release of radical persulfate ion from APS

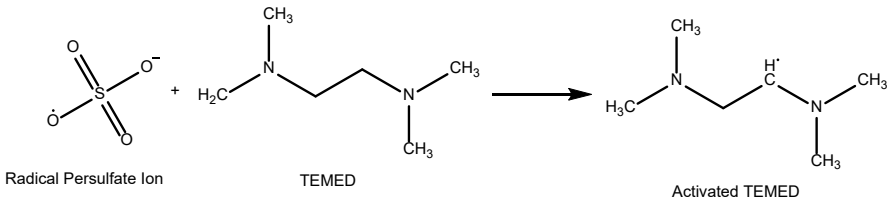

Fig 3. Activation of TEMED in the initiation stage of poly(NIPAM-*co*-DMAAPS) synthesis

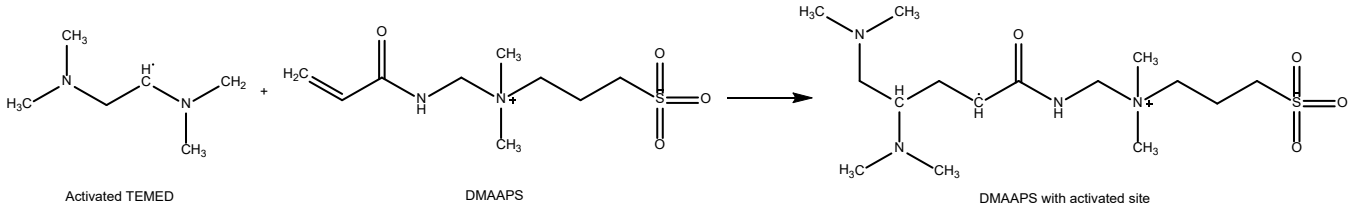

Fig 4. Propagation stage of DMAAPS chains

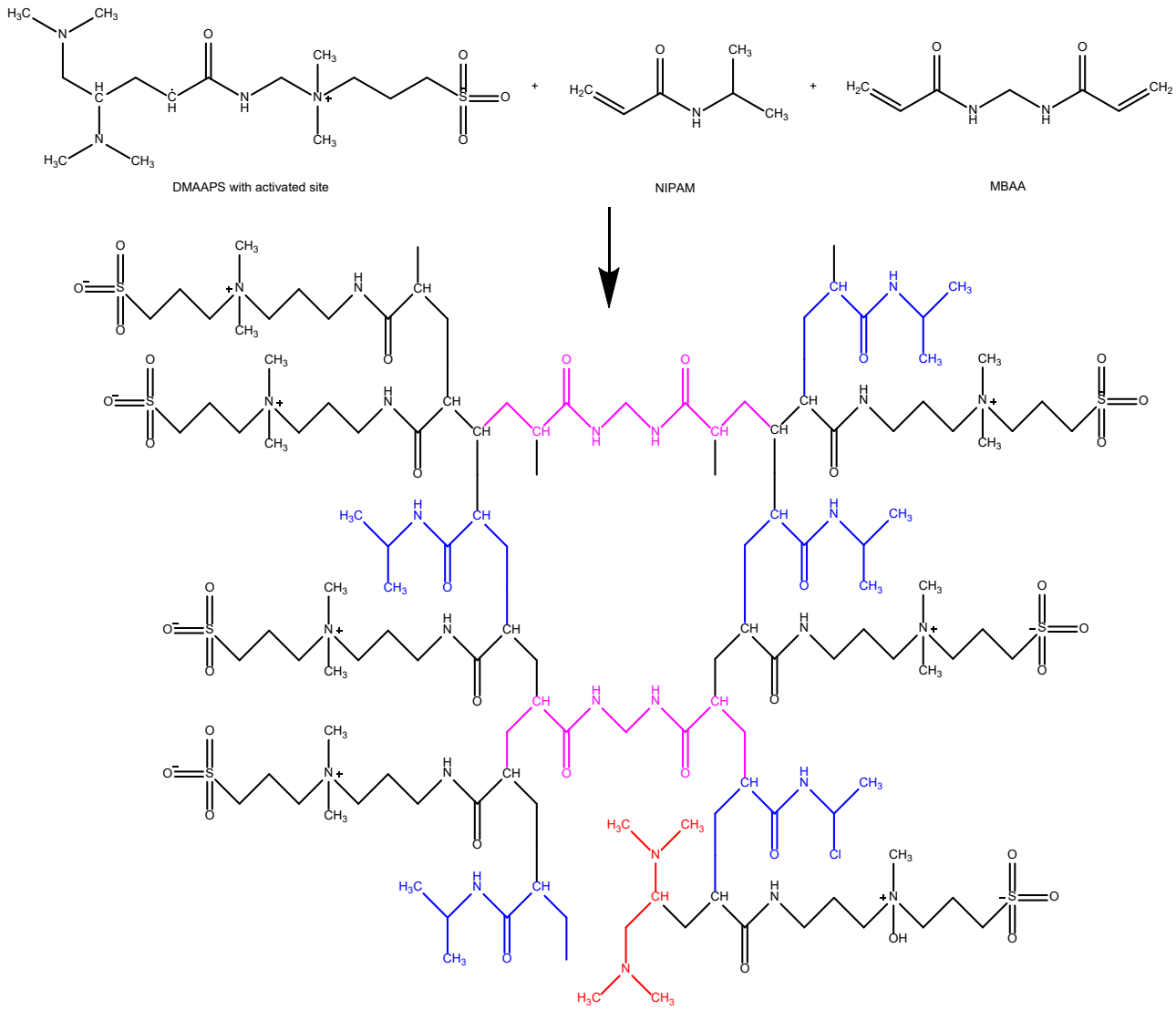

Fig 5. Chemical structure of *N,N*-dimethyl(acrylamidopropyl)ammonium propane sulfonate (DMAAPS), *N*-isopropylacrylamide (NIPAM), and NIPAM-*co*-DMAAPS gel (red: TEMED groups, black: DMAAPS groups, blue: NIPAM groups, magenta: MBAA groups)

Cylindrical tubes sized 30 mm in length, and 8 mm in diameter were placed inside the reactor for the preparation of the cylindrical gel. It was then cut into pieces of 8 mm in length and removed the unreacted monomers by being rinsed with distilled water. The gels were then dried on a Teflon sheet for 7 days. The Teflon sheet was spread on a Petri dish covered by a plastic film with small holes to make the drying goes slower since the gels tend to break apart if the drying is too fast. These cylindrical gels were used to measure the degree of swelling. The remaining gels were also cut into pieces, washed repeatedly for several days, dried in an oven, and grounded to make it into powder. The result was then filtered using a sieve with 90 mesh size. The final result would then be used for the adsorption experiments. The conditions employed in the synthesis of the NIPAM-*co*-DMAAPS gels are shown in Table 1.

Characterizations

Fourier Transform Infra-Red (FTIR) analysis

Fourier Transform Infra-Red (FTIR, Thermo Fisher Scientific Nicolet IS10, USA) was used to identify

Table 1. Synthesis condition of NIPAM-*co*-DMAAPS polymer and gel.

		Concentration (mmol/L)
Monomer	*N,N*-dimethyl(acrylamido-propyl)ammonium propane sulfonate (DMAAPS)	100, 200, 300
	N-isopropylacrylamide (NIPAM)	900, 800, 700
Cross-Linker	*N,N*'-Methylenebisacrylamide (MBAA)	
Accelerator	*N,N,N',N*'-tetramethyl-ethylenediamine (TEMED)	10
Initiator	Ammonium peroxodisulfate (APS)	2

Temperature: 10 °C, solvent: water, and reaction time: 6 h

the synthesized structure. FTIR analysis was carried out to determine the presence of monomer and copolymer constituent functional groups. This analysis used middle area infra-red radiation in wavenumber of 4000–500 cm^{-1}.

Nuclear Magnetic Resonance (NMR) spectroscopy analysis

NMR analysis was done to recognize the absolute structure of copolymer that has been synthesized. Agilent 500 MHz NMR spectrometer was used to record the ^1H NMR spectra. It was conducted using DD2 console system. In this test, a copolymer with monomer ratio NIPAM:DMAAPS of 8:2 was used. The test was done by dissolving 20 mg of the copolymer into 1 mL of D_2O (20 g/L D_2O) as the solvent.

Transition temperature

In order to investigate the transition temperature of poly(NIPAM-*co*-DMAAPS) in water and $Zn(NO_3)_2$ solution, the changes in the transmittance through the solutions with temperature were measured. An aqueous solution of poly(NIPAM-*co*-DMAAPS) becomes transparent, and the transmittance is almost 100% when it is at a temperature lower than the LCST since NIPAM has characteristics of hydrophilic and soluble in a solution. Meanwhile, if the solution is at a temperature above the LCST, it will become milky white, and the transmittance decreases since the poly(NIPAM-*co*-DMAAPS) is hydrophobic and insoluble in the solution. In this case, a spectrophotometer completed by a temperature control system was used to measure the transmittance at 600 nm. (JASCO Corp, V-630, Rev. 1.00). The concentration of poly(NIPAM-*co*-DMAAPS) in water and the heating rate were 1 wt.% and 1 °C/min, respectively.

Viscosity

In this stage, a Brookfield Digital Viscometer Model DV2T was used to obtain the viscosity of poly(NIPAM-*co*-DMAAPS) solution at various concentrations. The monomer ratio between NIPAM and DMAAPS were 9:1, 8:2, and 7:3 (10 g/L in water). In addition, the Brookfield Digital Viscometer used was also equipped by spindle No. 61 and 62, which have been found to be appropriately used for the viscosity measurement. The measurement was conducted at 27 °C, 10–20 rpm for 1–2 min. At least two readings mean were taken for each data point.

Adsorption test

In this study, the target solution used in the adsorption experiment was $Zn(NO_3)_2$. One gram of gel copolymer is added to the bottle glass containing 20 mL of an aqueous solution with a concentration of 10 mmol/L. The glass bottle was then placed in a water bath followed by stirring for 12 h at the desired temperature to achieve equilibrium adsorption. In order to calculate the concentration of cations and anions in the solution after the adsorption process, the gel was separated from the solution by centrifuge for 10 min. The gel was then filtered with a syringe filter. The following Eq. (1) was used to determine the amount of ions adsorbed onto the gel through the concentration of the ions. This measurement was done before and after the adsorption process.

$$Q = \frac{(C_0 - C)V}{m} \quad (1)$$

where Q is the number of cation (Zn^{2+}) or anion (NO_3^-) adsorbed, C_0 is the concentration of ions in the solution before the adsorption process, C is the concentration of ions in the solution after the adsorption process, V is the

solution volume, and m is the dry gel weight. Atomic Absorption Spectrophotometry analysis was conducted to measure the ions (Zn^{2+} or NO_3^-) concentration (AAS, Model 210 VGP) analysis.

■ RESULTS AND DISCUSSION

The Analysis of Fourier Transform Infra-Red Spectroscopy (FTIR)

FTIR analysis was conducted to determine the existence of functional groups composing NIPAM and DMAAPS monomers, as well as the NIPAM-*co*-DMAAPS copolymer. This analysis is used in the middle infrared radiation area from a wavelength of 4000–500 cm^{-1}.

Fig. 6 shows the result of FTIR analysis of NIPAM-*co*-DMAAPS copolymer with various monomer ratio NIPAM:DMAAPS of 9:1, 8:2 and 7:3 with a total concentration of 1000 mmol/L. In the spectra comparison of the three copolymers above, it can be seen that the three copolymers have a very similar spectral pattern. The C-N bond can be seen around a wavenumber of 1170 cm^{-1}. Meanwhile, S=O bond is shown around 1387 cm^{-1} wavenumber. However, there is a slight difference in 9:1 copolymer spectra, which is a peak of S=O and C-N groups in the range of 1000–1500 cm^{-1} that is lower than in copolymer 8:2 and 7:3. This is because the number of NIPAM is higher. Thus, the S=O and C-N groups from DMAAPS are less. In the three polymers, the N-H bond is shown at a wavenumber of 3280.17–3274.02 cm^{-1}. A wavenumber reaching points 1629.1–1627.82 cm^{-1} indicates the presence of C=O bond. The difference in the functional groups of each monomer and copolymer constituent is seen in the presence of vinyl groups of CH_2=CH- which determines the success of the copolymer reaction. Vinyl bond (CH_2=CH-) is located in the wavenumber range between 900 to 1000 cm^{-1}. At NIPAM, vinyl bond (CH_2=CH-) is seen at a wavenumber of 960.67 cm^{-1} (Fig. 6). At DMAAPS, the vinyl bond (CH_2=CH-) is also seen at a wavenumber of 980.55 cm^{-1} (Fig. 6). However, on the result of FTIR analysis from NIPAM-*co*-DMAAPS (Fig. 6), there is no peak which shows CH_2=CH- bond. This indicates the success of the copolymerization reaction between NIPAM and DMAAPS in forming the NIPAM-*co*-DMAAPS copolymer.

The Analysis of Nuclear Magnetic Resonance (NMR) Spectroscopy

The absolute structure of the poly(NIPAM-*co*-DMAAPS) can be further determined by analyzing it using NMR spectroscopy. The ^{1}H NMR (500 MHz)

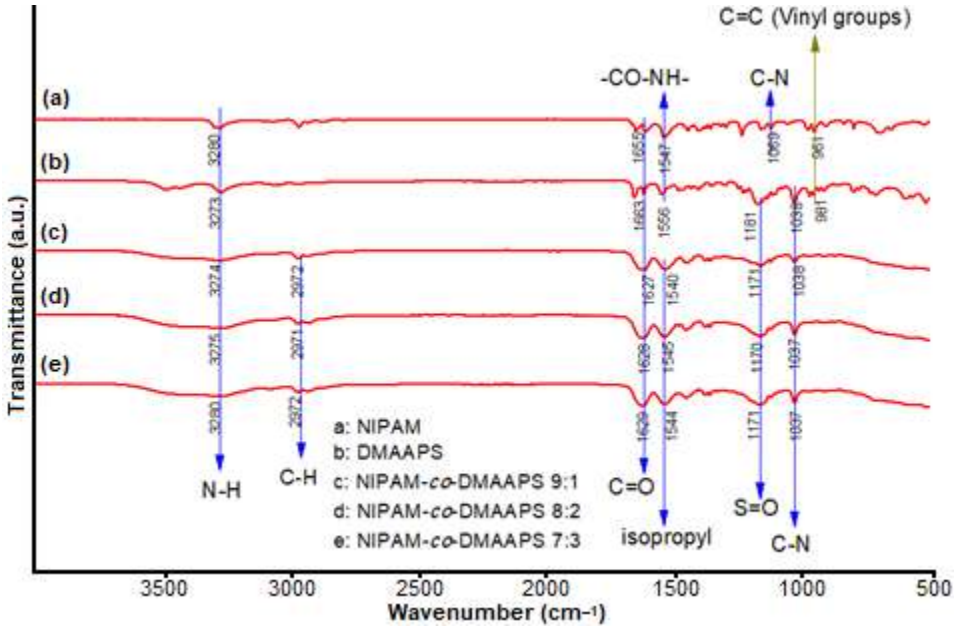

Fig 6. Infrared spectra of NIPAM, DMAAPS, and poly(NIPAM-*co*-DMAAPS) with various monomer ratios

spectra of the copolymer with monomer ratio NIPAM:DMAAPS of 8:2 is shown in Fig. 7. The highest peak in range 4.6–4.7 was relative to the signal of the solvent. The results were as follows: ^{1}H NMR [500 MHz, D_2O δ/ppm]: 0.91–1.13 (s, 6H, (CH_3-C-)), 1.25–1.68 (m, 3H, (-CH_2-CH-)), 1.8–2.05 (m, 2H, (-CH_2-CH_2-CH_2-)), 2.1–2.2 (t, 2H, (-CH_2-CH_2-CH_2-)), 2.5–2.7 (t, 2H, (-CH_2-CH_2-SO^{3-})), 2.92–3.08 (s, 6H, (CH_3-N^+-CH_3)), 3.22–3.3 (t, 2H, (-CH_2-CH_2-N^+-)), 3.34–3.46 (t, 2H, (-N^+-CH_2-CH_2-)), 3.5–3.56 (t, 2H, (-NH-CH_2-CH_2-)), 3.7–3.86 (s, 1H, CH)).

It is shown in Fig. 7 that a signal shown by a signal with code (a) and (j) is a resonance signal for proton that constructs a NIPAM, i.e. CH_3 and CH-N, while a signal shown by code (b), (c), (d), (e), (f), (g), and (h) was the proton signal that constructs DMAAPS i.e. CH_2-CH, CH_2-CH_2-CH_2, CH_2-CH_2-SO^{3-}, CH_3-N^+-CH_3, CH_2-CH_2-N, and NH-CH_2, which are constituent monomers of poly(NIPAM-*co*-DMAAPS). All the chemical shifts in Fig. 7 are in good agreement with the literature, which shows that NIPAM-co-DMAAPS is indeed the target copolymer [21].

Viscosity

Both the characteristic of the copolymer in solution and the association of the polymer charged group are affected by viscosity. The high value of viscosity owned by substances affects the substance to have a low mass transfer rate since the copolymer viscosity affects the density of the gel formed. The higher the viscosity of the copolymer, the denser the gel. The viscosity of poly(NIPAM-*co*-DMAAPS) with various monomer ratios and with a polymer concentration of 10 g/L was measured at 27 °C. The result is shown in Fig. 8 for comparison purpose, the viscosity of the polymer was measured at various speeds, i.e., 10 and 20 rpm and various time interval, i.e., 1 and 2 min. The results show that the viscosity of poly(NIPAM-*co*-DMAAPS) with various monomer ratios NIPAM:DMAAPS of 9:1, 8:2, and 7:3 tend to increase with the increase of NIPAM concentration and was observed in the range of 20–120 cP. However, it was also observed that no significant change in viscosity according to each monomer ratio being indicated at various speeds and time intervals.

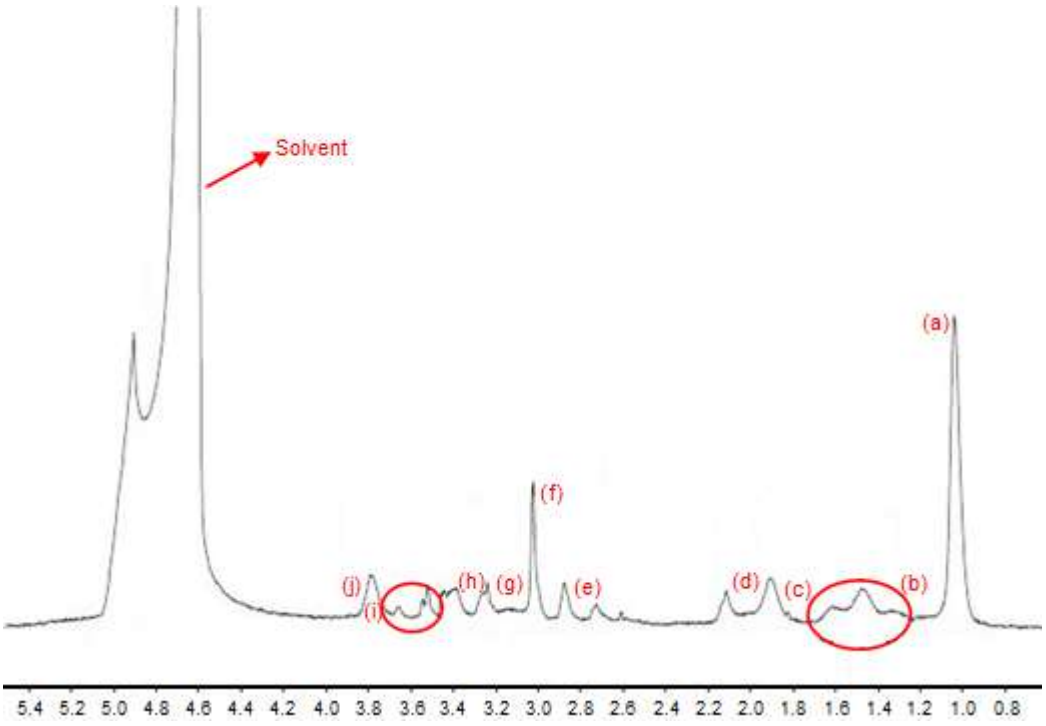

Fig 7. ^{1}H NMR spectrum of the poly(NIPAM-*co*-DMAAPS) with monomer ratio NIPAM:DMAAPS of 8:2

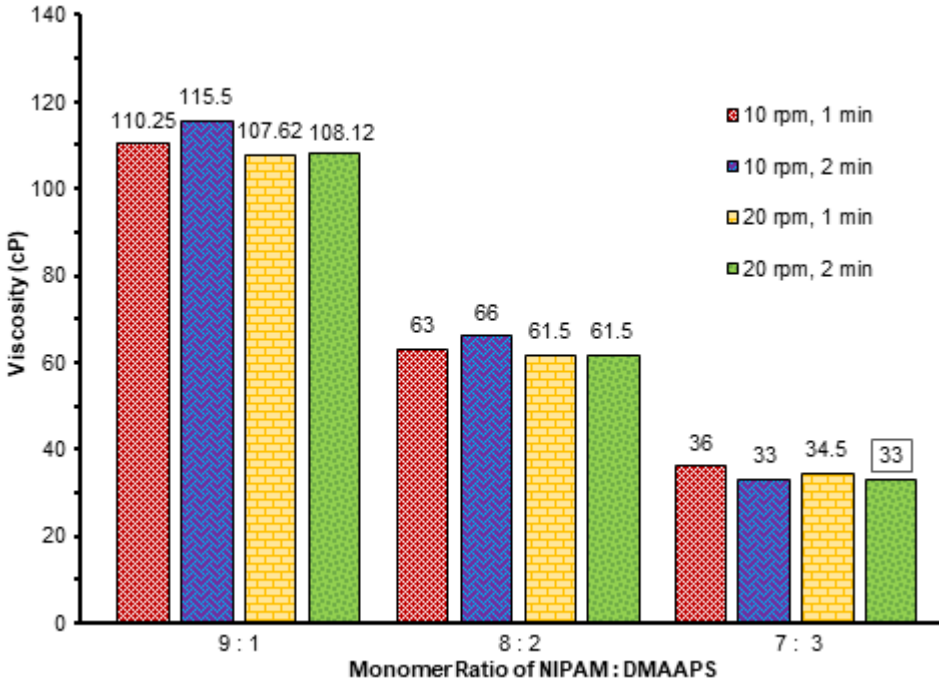

Fig 8. Viscosity of poly(NIPAM-*co*-DMAAPS) in water of 10 g/L at 27 °C at various monomer ratios

This result confirms that the poly(NIPAM-*co*-DMAAPS) with higher NIPAM concentration tends to break the intra-chain and intra-group association of charged groups from DMAAPS to form an inter-chain association. The higher the inter-chain association, the more entangled the polymer chain occurs, as a consequence of the increase of hydrophobicity and viscosity copolymer solution.

Transition Temperature

Fig. 9 shows LCST of poly(NIPAM-*co*-DMAAPS) solution carried out at 1 g/L polymer and a heating rate of 1 °C/min. The transition temperature is indicated by 50% of transmittance. The transmittance change as a function of temperature was measured at a wavelength of 600 nm using a UV/VIS spectrophotometer equipped with a thermostatic cell for polymer solution. The recording of transmittance changes was done during the heating process at a rate of 1 °C. The heating process was applied because transition can be easily observed on heating from a temperature below LCST when the polymer is completely dissolved.

LCST poly(NIPAM-*co*-DMAAPS) shown in Fig. 9 was strongly affected by monomer concentration and

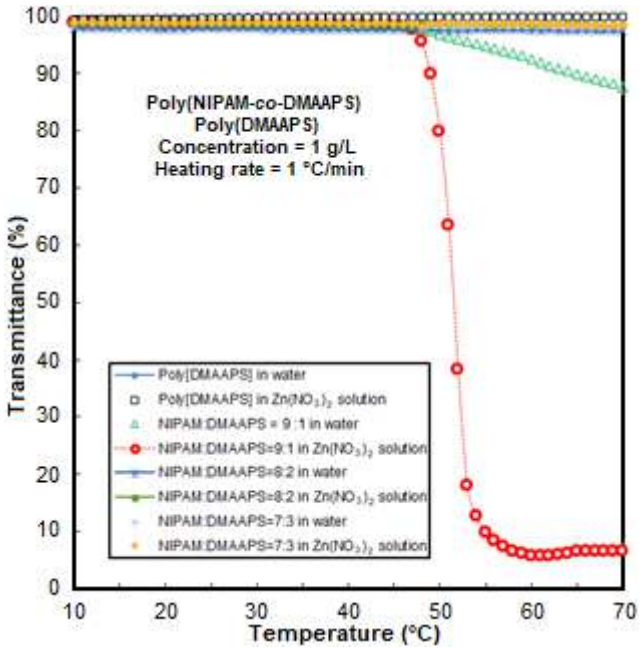

Fig 9. Transition temperature of poly(NIPAM-*co*-DMAAPS) with a polymer concentration of 1g/L at heating rate of 1 °C/min and various monomer ratios

solution. Initially, at a lower temperature, polymer with monomer ratio NIPAM:DMAAPS of 9:1 was completely dissolved in water as indicated by the transmittance value reaching almost 100%. Then, the transmittance

decreases gradually with the increase of temperature from 50–70 °C. However, the transmittance reduction is insignificant, and the transition phase change is not clear. This phenomenon is attributed to the fact that the charge groups interaction, i.e., intra-group, inter-chain, and intra-chain is quite strong, and there is no free ion in water which can bind to the zwitterion in the copolymer chain.

In contrast to a polymer with monomer ratio NIPAM:DMAAPS of 9:1 dissolved in $Zn(NO_3)_2$ solution, shows a transition temperature at 56.56 °C, this phase transition is in accordance with the initial hypothesis that the copolymer is dominated by NIPAM characteristic of LCST. However, this transition temperature in $Zn(NO_3)_2$ solution is lower than the transition temperature in water. The polymer solution becomes more hydrophobic in $Zn(NO_3)_2$ solution because the ions in the solution destroy the hydration layer around the NIPAM molecules in the poly(NIPAM-co-DMAAPS).

This phenomenon is different from poly(DMAAPS) and the copolymer with monomer ratio NIPAM: DMAAPS of 8:2 and 7:3 which does not experience a phase transition both in water and $Zn(NO_3)_2$ solution.

Correlation between Transition Temperature of the poly(NIPAM-*co*-DMAAPS) and Adsorption Behavior of the Gels

The correlation between transition temperature of the poly(NIPAM-*co*-DMAAPS) with monomer ratio NIPAM:DMAAPS of 9:1 and the amount of ions adsorbed onto the gel in $Zn(NO_3)_2$ solution is shown in Fig. 10. Fig. 10 shows that at a lower temperature of 10–30 °C, the number of ions adsorbed onto NIPAM-*co*-DMAAPS gel in $Zn(NO_3)_2$ solution was high, and the transmittance of the poly(NIPAM-*co*-DMAAPS) remained unchanged to nearly 100%. Meanwhile, the percentage of transmittance decreases significantly and clearly shows the transition temperature at 56.56 °C. The number of adsorbed ions begins to decrease at a temperature of 30 °C. Moreover, at higher temperature 50–70 °C the number of adsorbed ions onto NIPAM-*co*-DMAAPS gel in $Zn(NO_3)_2$ solution was the lowest, and the transmittance of the poly(NIPAM-*co*-DMAAPS) dropped to almost 0%.

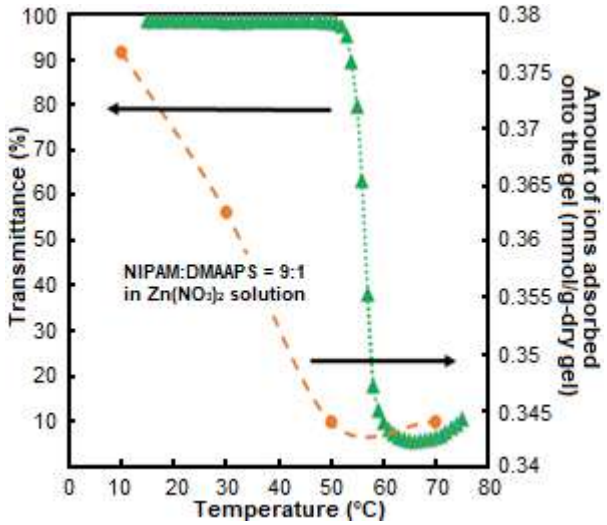

Fig 10. Correlation between transition temperature of the poly(NIPAM-*co*-DMAAPS) with monomer ratio NIPAM:DMAAPS of 9:1 and the amount of ions adsorbed onto the gel

This phenomenon implies that the higher transmittance is caused by more interaction of ions from solution with the charged groups (N^+ and SO_3-) of the gel that reduces the chain entanglement and association. In contrast, decreased transmittance shows less number of adsorbed ions because the polymers are more hydrophobic or immiscible in the solution. At that time, the polymer adsorbs a little ion.

■ CONCLUSION

The effect of various monomer ratios of NIPAM:DMAAPS in the preparation of poly(NIPAM-*co*-DMAAPS) on its properties such as transition temperature, molecular structure, and viscosity were systematically investigated in water and $Zn(NO_3)_2$ solution. The result of FTIR and NMR analysis indicates the success of the copolymerization reaction between NIPAM and DMAAPS in forming the NIPAM-*co*-DMAAPS copolymer. The higher ratio of NIPAM monomer in poly(NIPAM-*co*-DMAAPS), the lower the LCST of the polymer and the more increase the polymer viscosity. The correlation between transition temperature of the poly(NIPAM-*co*-DMAAPS) with monomer ratio NIPAM:DMAAPS of 9:1 and the amount of ions adsorbed onto the gel in $Zn(NO_3)_2$

solution was also investigated. As the adsorption amount of ions onto the gel increased, the polymer transmittance increased as well.

■ ACKNOWLEDGMENTS

This research was financially supported by the research grant of *Penelitian Pasca Doktor* 2018 (959/PKS/ITS/2018) for ten consecutive months from *Direktorat Jendral Penguatan Riset dan Pengembangan Kemenristekdikti*.

■ REFERENCES

[1] Kusuma, A.H., Prartono, T., Atmadipoera, A.S., and Arifin, T., 2016, Sebaran logam berat terlarut dan terendapkan di perairan teluk Jakarta, *Jurnal Teknologi Perikanan dan Kelautan*, 6 (1), 41–49.

[2] Cordova, M.R., Purbonegoro, T., Puspitasari, R., and Hindarti, D., 2016, Assessing contamination level of Jakarta bay nearshore sediments using green mussel (*Perna viridis*) larvae, *Mar. Res. Indonesia*, 41 (2), 67–76.

[3] Plattes, M., Bertrand, A., Schmitt, B., Sinner, J., Verstraeten, F., and Welfring, J., 2007, Removal of tungsten oxyanions from industrial wastewater by precipitation, coagulation and flocculation processes, *J. Hazard. Mater.*, 148 (3), 613–615.

[4] Papadopoulos, A., Fatta, D., Parperis, K., Mentzis, A., Haralambous, K.J., and Loizidou, M., 2004, Nickel uptake from a wastewater stream produced in a metal finishing industry by combination of ion-exchange and precipitation methods, *Sep. Purif. Technol.*, 39 (3), 181–188.

[5] Sadrzadeh, M., Mohammadi, T., Ivakpour, J., and Kasiri, N., 2009, Neural network modeling of Pb^{2+} removal from wastewater using electrodialysis, *Chem. Eng. Process.*, 48 (8), 1371–1381.

[6] Koseoglu, H., and Kitis, M., 2009, The recovery of silver from mining wastewaters using hybrid cyanidation and high-pressure membrane process, *Miner. Eng.*, 22 (5), 440–444.

[7] Fu, F., and Wang, Q., 2011, Removal of heavy metal ions from wastewaters: A review, *J. Environ. Manage.*, 92 (3), 407–418.

[8] Gunatilake, S.K., 2015, Methods of removing heavy metals from industrial wastewater, *J. Multidiscip. Eng. Sci. Stud.*, 1 (1), 12–18.

[9] Álvarez, E.A., Mochón, M.C., Sánchez, J.C.J., and Rodríguez, M.T., 2002, Heavy metal extractable forms in sludge from wastewater treatment plants, *Chemosphere*, 47 (7), 765–775.

[10] Barakat, M.A., 2011, New trends in removing heavy metals from industrial wastewater, *Arabian J. Chem.*, 4 (4), 361–377.

[11] Liu, J., Ma, Y., Xu, T., and Shao, G., 2010, Preparation of zwitterionic hybrid polymer and its application for the removal of heavy metal ions from water, *J. Hazard. Mater.*, 178 (1-3), 1021–1029.

[12] Neagu, V., Vasiliu, S., and Racovita, S., 2010, Adsorption studies of some inorganic and organic salts on new zwitterionic ion exchangers with carboxybetaine moieties, *Chem. Eng. J.*, 162 (3), 965–973.

[13] Ningrum, E.O., Murakami, Y., Ohfuka, Y., Gotoh, T., and Sakohara, S., 2014, Investigation of ion adsorption properties of sulfobetaine gel and relationship with its swelling behavior, *Polymer*, 55 (20), 5189–5197.

[14] Takahashi, A., Hamai, K., Okada, Y., and Sakohara, S., 2011, Thermosensitive properties of semi-IPN gel composed of amphiphilic gel and zwitterionic thermosensitive polymer in buffer solutions containing high concentration salt, *Polymer*, 52 (17), 3791–3799.

[15] Ning, J., Li, G., and Haraguchi, K., 2013, Synthesis of highly stretchable, mechanically tough, zwitterionic sulfobetaine nanocomposite gels with controlled thermosensitivities, *Macromolecules*, 46 (13), 5317–5328.

[16] Ning, J., Kubota, K., Li, G., and Haraguchi, K., 2013, Characteristics of zwitterionic sulfobetaine acrylamide polymer and the hydrogels prepared by free-radical polymerization and effects of physical and chemical crosslinks on the UCST, *React. Funct. Polym.*, 73 (7), 969–978.

[17] Lee, W.F., and Tsai, C.C., 1994, Synthesis and solubility of the poly (sulfobetaine)s and the

corresponding cationic polymers: 1. Synthesis and characterization of sulfobetaines and the corresponding cationic monomers by nuclear magnetic resonance spectra, *Polymer*, 35 (10), 2210–2217.

[18] Ningrum, E.O., Ohfuka, Y., Gotoh, T., and Sakohara, S., 2015, Effects of specific anions on the relationship between the ion-adsorption properties of sulfobetaine gel and its swelling behavior, *Polymer*, 59, 144–154.

[19] Ningrum, E.O., Purwanto, A., Mulyadi, E.O., Dewitasari, D.I., and Sumarno, S., 2017, Adsorption and desorption of Na^+ and NO_3^- ions on thermosensitive NIPAM-*co*-DMAAPS gel in aqueous solution, *Indones. J. Chem.*, 17 (3), 446–452.

[20] Ningrum, E.O., Purwanto, A., Ni'mah, H., Sumarno, Dewitasari, D.I., and Mulyadi, E.O., 2017, Ion adsorption and desorption behaviors of thermosensitive NIPAM-co-DMAAPS gel by temperature swing, *AIP Conf. Proc.*, 1840 (1), 090007.

[21] Ju, C., and Kang, H., 2017, Zwitterionic polymers showing upper critical solution temperature behavior as draw solutes for forward osmosis, *RSC Adv.,* 7 (89), 56426–56432.

Supplementary Data

This supplementary data is a part of paper entitled "*In Silico* Structural and Functional Annotation of Nine Essential Hypothetical Proteins from *Streptococcus pneumoniae*".

Table S1. 39 hypothetical proteins' locus tag with their respective NCBI-Protein ID

No.	Locus Tag [14]	NCBI-Protein ID Accession No.	No.	Locus Tag [14]	NCBI-Protein ID Accession No.
1	SPD_0008	ABJ54275.1	**21**	SPD_0880	ABJ54796.1
2	SPD_0403	ABJ55288.1	**22**	SPD_1136	ABJ55057.1
3	SPD_0408	ABJ54600.1	**23**	SPD_1197	ABJ54310.1
4	SPD_0965	ABJ54319.1	**24**	SPD_1198	ABJ54015.1
5	SPD_0990	ABJ53736.1	**25**	SPD_1288	ABJ54428.1
6	SPD_1392	ABJ54564.1	**26**	SPD_1333	ABJ53729.1
7	SPD_1405	ABJ54327.1	**27**	SPD_1346	ABJ53954.1
8	SPD_1435	ABJ53912.1	**28**	SPD_1391	ABJ55369.1
9	SPD_1522	ABJ53766.1	**29**	SPD_1416	ABJ54839.1
10	SPD_2029	ABJ53876.1	**30**	SPD_1417	ABJ54239.1
11	SPD_0131	ABJ53868.1	**31**	SPD_1549	ABJ55165.1
12	SPD_0339	ABJ54095.1	**32**	SPD_1560	ABJ55503.1
13	SPD_0350	ABJ55277.1	**33**	SPD_1672	ABJ55016.1
14	SPD_0394	ABJ54531.1	**34**	SPD_1706	ABJ54739.1
15	SPD_0402	ABJ54394.1	**35**	SPD_1743	ABJ54209.1
16	SPD_0476	ABJ55230.1	**36**	SPD_1803	ABJ53653.1
17	SPD_0478	ABJ54971.1	**37**	SPD_1898	ABJ55068.1
18	SPD_0675	ABJ53899.1	**38**	SPD_2043	ABJ54886.1
19	sufD	ABJ54405.1	**39**	SPD_2044	ABJ53789.1
20	SPD_0878	ABJ53627.1			

In Silico Structural and Functional Annotation of Nine Essential Hypothetical Proteins from *Streptococcus pneumoniae*

Khairiah Razali[1], Azzmer Azzar Abdul Hamid[1,2], Noor Hasniza Md Zin[1], Noraslinda Muhamad Bunnori[1,2], Hanani Ahmad Yusof[3], Kamarul Rahim Kamarudin[4], and Aisyah Mohamed Rehan[1,2,*]

[1]*Department of Biotechnology, Kulliyyah of Science, International Islamic University Malaysia, Jl. Sultan Ahmad Shah, 25200, Kuantan, Pahang, Malaysia*

[2]*Research Unit for Bioinformatics and Computational Biology (RUBIC), Kulliyyah of Science, International Islamic University Malaysia, Jl. Sultan Ahmad Shah, Kuantan, Pahang, 25200, Malaysia*

[3]*Department of Biomedical Sciences, Kulliyyah of Allied Health Sciences, International Islamic University Malaysia, Jl. Sultan Ahmad Shah, Kuantan, Pahang, 25200, Malaysia*

[4]*Department of Technology and Natural Resources, Faculty of Applied Sciences and Technology, Universiti Tun Hussein Onn Malaysia, Pagoh Campus, Pagoh Education Hub, Km 1, Jl. Panchor, Muar, Johor Darul Takzim, 84600, Malaysia*

* ***Corresponding author:***

tel: +6012-6848659
email: mraisyah@iium.edu.my

Received: December 13, 2018
Accepted: March 11, 2019

DOI: 10.22146/ijc.41817

Abstract: *The ability of* Streptococcus pneumoniae *to induce infections relies on its virulence factor machinery. A previous CRISPR interference (CRISPRi) study had identified 254 essential proteins that may be responsible for the pathogenicity of* S. pneumoniae *serotype 2 strain D39. However, 39 of them were functionally and structurally uncharacterized. Hence, by using in silico approach, this study aimed to annotate the function and structure of these un-annotated proteins. Initially, all 39 proteins went through primary screening for template availability and pathogenicity. From there, 11 of them were selected and underwent further physicochemical, functional, and structural categorization through an integrated bioinformatics approach by means of amino acid sequence- and structure- based analyses. The obtained data revealed that 9 targeted proteins showed a high possibility to be involved in either cell viability or cell pathogenicity mechanism of the bacterium, with SPD_1333 and SPD_1743 being the two most promising proteins to be further studied. Findings from this study can help in facilitating a better understanding of pathogenic ability of this microorganism and enhance drug development and target identification processes in the aim of improving pneumococcal disease control.*

Keywords: *hypothetical proteins;* S. pneumoniae *strain D39;* in silico *analysis of protein; bioinformatics tools*

■ INTRODUCTION

Streptococcus pneumoniae or pneumococcus is a Gram-positive bacterium under the family of Streptococcaceae. This facultative anaerobe is found mainly at the upper respiratory tract of human, specifically nose and throat. Despite being one of the normal floras inside a human, this organism is known to be the causative agent of infectious diseases such as pneumococcal pneumonia, meningitis, and otitis media. According to the World Health Organization (WHO), in 2015, 16% of the deaths of children under five years old are caused by pneumonia with developing countries being the most prominent to get this disease [1]. Susceptible individuals can develop an invasive pneumococcal infection that can be severe, and in the absence of appropriate antibiotics treatment, may lead to hospitalization, life-long disability, and death [1].

S. pneumoniae is transmitted through the respiratory

route, especially through inhalation of air-borne droplets generated by coughing and sneezing from infected individuals. The colonization of *S. pneumoniae* at host respiratory area can cause pneumonia while its excess to bloodstream enables it to colonize other parts of the body and cause diseases such as otitis media. Once the bacterium has succeeded in invading the bloodstream, it can travel to the blood-brain barrier hence attacking the brain and causing pneumococcal meningitis [2].

In order to cause diseases, pneumococci make use of its virulence factors machinery, which mostly involves its polysaccharide capsule, cell wall, and pneumolysin [3]. Over the past years, prevention and treatment of pneumococcal diseases are through vaccinations and antibiotics, respectively. Example of vaccines and antibiotics are pneumococcal conjugate vaccines (PCV) and amoxicillin, respectively. However, it is found that inappropriate antibiotic prescriptions in treating pneumococcal diseases have led to an increase in antibiotic- and multidrug- resistant pneumococci [4-5]. In addition, currently available vaccines are serotype-specific, and therefore, elicit serotype-specific immunity [6]. The developing countries displayed pneumococcal disease that is caused by a wider spectrum of serotypes as compared to developed countries [7]. Hence, the search for better vaccines and antibiotics with the aim of preventing or treating pneumococcal infections are essential. In order to do so, deep understanding on the virulence factors machinery of *S. pneumoniae* is very much needed.

Virulence factors play a large role in determining the capability among different strains of *S. pneumoniae* in causing diseases [8]. Understanding pneumococci virulence factors machinery demands full knowledge of its proteins and components involved. The most important factor in the virulence of this organism is its polysaccharide capsule [9]. Another study further demonstrates that variances in this capsule have raised the number of different pneumococcal strains and serotypes, thus leading to bacterial resistance [10]. Other virulence factors include the cell wall plus several proteins such as hyaluronate lyase, neuraminidase, and pneumolysin [11]. Presently, biotechnology and bioinformatics applications have enabled scientists to completely sequence the bacterial genome and assign structure and function to its proteins and enzymes [12]. Yet, due to the complexity and other constraints, one third of its proteins remain hypothetical with neither structural nor functional elucidations [13]. This problem has limited the potential of designing drugs capable of fighting pneumococci-related diseases.

Hence, this study aims to fill the gap between genome sequence information and virulent protein annotation by interpreting physicochemical characteristics, structures, and functions of selected hypothetical proteins from the previously identified essential proteins of *S. pneumoniae* strain D39 [14]. With suitable computational and bioinformatics tools as well as an available genome, proteome, and secretome databases, this study is expected to provide insights on the structure and role of hypothetical proteins in virulence factors machinery of *S. pneumoniae,* specifically for strain D39. Acquiring this information will later help researchers to continue with protein expression and purification studies on promising hypothetical protein targets for further analyses. In the longer term, this study will provide a promising platform for drug design and therapeutic studies of pneumonia-related diseases.

■ EXPERIMENTAL SECTION

Sequence Retrieval

The ID name and full sequence of each of the 39 hypothetical proteins were retrieved from UniProtKB (http://www. uniprot.org/) and the National Centre for Biotechnology Information (NCBI) website (https://www.ncbi.nlm.nih.gov/protein/). The corresponding NCBI-protein ID accession number for each of the 39 hypothetical proteins targets identified from [14] is listed in Table S1.

Virulence Prediction

MP3 server (http://metagenomics. iiserb.ac.in/mp3/) uses Support Vector Machines (SVM) or Hidden Markov Model (HMM) to calculate the algorithm and predict the pathogenesis of query protein [15]. All 39

hypothetical proteins were analyzed by this server for their virulence properties.

Template Availability

Next, the hypothetical proteins were streamed through NCBI BLASTP and PSI- BLAST servers against Protein Data Bank (PDB) proteins database for the search of homology. Hypothetical proteins having the template aligned at above 50% and similarity of 30 to 70% were of concern. It has been widely accepted that two proteins are considered homologous if their sequence similarity is beyond 30% [16]. At the end of the selection process, 11 out of 39 hypothetical proteins of *S. pneumoniae* strain D39 were selected to be the subjects of study.

Physicochemical Characteristics

Several physical and chemical parameters (molecular weight, isoelectric point, extinction coefficient, aliphatic index, instability index, and GRAVY) were analyzed using ExPASy ProtParam tool (https://web.expasy.org/protparam/) [17]. These parameters are important in knowing the state of the query protein, especially for means of experimental handling such as for protein isolation and purification.

Conserved Family and Domain

Pfam (https://pfam.xfam.org/) [18] and NCBI CD-Search servers [19] were used to predict possible domain or family of a query protein. Domain and family are able to give insight into the possible role or interaction that may be associated with the query protein by looking at the function and structure of proteins they are similar with.

Subcellular Localization, Trans-Membrane Helices, and Secretome Analyses

PSORT and PSORTb servers (http://www.psort.org/psortb/index.html) [20] were used to predict the subcellular localization of the query protein. Similarly, HMMTOP [21], as well as SignalP [22] and SecretomeP [23] servers, were used to determine the presence of trans-membrane helices and signal peptides, respectively. This information is important in categorizing whether a protein is a membrane protein, secretory protein, or cytoplasmic protein.

Protein-Protein Interaction

STRING website (https://string-db.org/) is an online server that contains protein databases of thousands of organisms and is useful in analyzing protein-protein interactions. STRING currently holds the databases of around 24 million proteins from 5090 organisms [24]. By using STRING, the interactions between the query protein and other surrounding proteins were accessed. This enables the identification of functional and regulatory interactions among proteins.

Secondary Structure Prediction

The initial structural annotation of the query protein was determined by predicting its secondary structure. The prediction allows the information on how many possible helices, strands, and loops are present in shaping the query protein. This step was done using PSIPRED server (bioinf.cs.ucl.ac.uk/psipred/) [25].

Tertiary Structure Prediction

In predicting the tertiary structure, three different servers, namely I-TASSER (https://zhanglab.ccmb.med.umich.edu/I-TASSER/) [26], (PS)2 (ps2.life.nctu.edu.tw/) [27] and ExPASy SWISS-MODEL (https://swissmodel.expasy.org/) [28] were used for each query protein.

All three predicted structures were then validated using Ramachandran plot assessment, Verify3D [29], and QMEAN4 score [30]. From the validation, the best-predicted structure was selected for structural refinement and further analyses.

Structural Refinement

The selected three-dimensional structure was converted from .pdb format to .gro to be subjected to structural refinement by Groningen Machine for Chemical Simulations (GROMACS) software (using force field gromos96 53a6) for improvement [31]. This process includes energy minimization, equilibration, and production stage. Prior to simulation, the box was solvated with water, and the protein system was neutralized. Equilibration and production took 100 ps and 10000 ps of simulation time, respectively.

The refined structure was again validated using the

three aforementioned servers and a graph of root mean square deviation (RMSD) against production time was retrieved. The visualization of the final structure was viewed using PyMOL software (The PyMOL Molecular Graphics System, Version 2.0 Schrödinger, LLC).

Active Site and Ligand Prediction

The refined tertiary model was sent to metaPocket 2.0 (projects.biotec.tu-dresden.de/metapocket/) for active site prediction [32]. This server allows the prediction of the top three possible ligand binding sites of the query protein. In addition, the refined structure was also sent to COACH server (https://zhanglab.ccmb.med.umich.edu/COACH/) for the prediction of possible ligand that may bind to the active sites of the query protein [33].

■ RESULTS AND DISCUSSION

Physicochemical Characteristics

The physicochemical characteristics analysis revealed that the isoelectric point (pI) value for all selected hypothetical proteins from this study fell between the ranges of 4.59 to 9.40. Next, the highest extinction coefficient (EC) belongs to SPD_1346 (38740 M^{-1} cm^{-1}) while the lowest is 2980 M^{-1} cm^{-1}, which belongs to SPD_0878. Moreover, in term of the instability index (II), 6 out of 11 proteins (SPD_0965, SPD_0402, SPD_1333, SPD_1392, SPD_1743 and SPD_0339) were predicted to be stable inside a test tube. Unstable proteins may require additional steps such as denaturation prior to isolation and purification. Other details on the parameters of each protein, such as the molecular weight, aliphatic index, and GRAVY value, are given in Table 1.

Protein Domains and Families

The initial step in understanding the functional property of a protein is to determine its domain and family. From this study, out of eleven selected hypothetical proteins, nine of them were classified into a specific domain(s) and family(s), while no record or identification was found on SPD_0965 and SPD_1898 (listed in Table 2). This may be due to their short amino acid length (52 and 59 residues, respectively). A study shows that mini-proteins (those with residues of not more than 100 amino acids) are difficult to be analyzed experimentally and computationally due to their small sizes and short gene lengths [34].

Subcellular Localization and Secretome Analyses

Determination of protein subcellular location is significant, especially for target identification [35]. Furthermore, location prediction can give an idea on the role of a query protein and whether it is categorized as a cytoplasmic, membrane, or secretory protein. Plus, it is also important to locate the presence of trans-membrane helices and signal peptide because the positive prediction of these two can further validate a protein's function in secretory or extracellular interactions [36].

Analyses done to all subjects of this study revealed

Table 1. Physicochemical characteristics by ExPASy ProtParam. EC: Extinction Coefficient; AI: Aliphatic Index; II: Instability Index; GRAVY; grand average of hydropathy

Gene ID	MW (Da)	pI	EC (M^{-1} cm^{-1})	AI	II	GRAVY
SPD_0965	5961.67	8.19	5500	65.77	15.95	-0.956
SPD_0131	9288.36	4.59	8940	82.34	66.60	-0.812
SPD_0402	12868.69	4.90	5960	107.02	13.89	0.134
SPD_1333	37756.89	5.08	33030	81.01	32.35	-0.434
SPD_1288	8258.25	9.40	8480	160.68	42.66	1.442
SPD_1898	7229.30	8.82	8480	80.85	50.00	-0.949
SPD_1392	30129.38	7.92	26930	121.66	31.99	0.362
SPD_1743	16401.74	4.73	15930	108.84	34.76	-0.190
SPD_0339	12575.29	4.74	4470	90.37	36.24	-0.456
SPD_0878	18970.57	4.88	2980	89.69	53.18	-0.852
SPD_1346	60797.40	5.07	38740	81.78	50.96	-0.528

Table 2. Conserved family(s) and domain(s) by Pfam and NCBI CD-Search

Gene ID	Pfam and NCBI CD-Search	Description
SPD_0965	-	-
SPD_0131	DUF1447 family	Protein of unknown function
SPD_0402	Asp23 superfamily, YloU family	Alkaline shock protein , cell envelope-related function
SPD_1333	Lactonase family	Lactonase, 7-bladed beta-propeller, carbohydrate transport and metabolism
SPD_1288	DUF4059 family	Protein of unknown function
SPD_1898	-	-
SPD_1392	DisA_N family	Diadenylate cyclase (c-di-AMP synthetase), DisA bacterial checkpoint controller nucleotide-binding
SPD_1743	P-loop NTPase superfamily, TsaE domain	Threonylcarbamoyl adenosine biosynthesis protein TsaE
SPD_0339	DivIVA family	Cell division protein
SPD_0878	HTH_24 domain, DUF536 family	Winged helix-turn-helix DNA binding, Protein of unknown function
SPD_1346	YceG-like family	Cell division protein YceG

five proteins to be at a cytoplasmic location, another five at the cell membrane and one indecisive. In term of the presence of trans-membrane helices, three proteins were predicted to have one transmembrane helix (SPD_0402, SPD_1346 and SPD_1898), one protein with two transmembrane helices (SPD_1288) and another one protein with three trans-membrane helices (SPD_1392) while the remaining six have no trans-membrane helix. None of the proteins were predicted to own a signal peptide, and five out of eleven proteins (SPD_0402, SPD_1333, SPD_1346, SPD_1288 and SPD_1392) were said to be responsible in secretory pathway mechanism (listed in Table 3).

Protein-Protein Interaction

The involvement of a protein in virulence factor machinery is pretty much influenced by its interactions with other proteins. Some proteins work in synergy in order to perform vital cellular functions [24]. Hence, knowing the relationship between a hypothetical protein and other proteins can give insights into its possible function or role. In accordance with this, the analysis of protein-protein interaction by STRING gave information on the types of relation (neighborhood, co-occurrence, text-mining, and experimental) between the query protein and others.

Table 3. Subcellular, trans-membrane helices, signal peptide, and secretome analyses

Gene ID	Subcellular localization		Trans-membrane helices	Signal peptide	Secretome analysis
	PSORT	PSORTb	HMMTOP	SignalP	SecretomeP (score)
SPD_0965	Bacterial cytoplasm	Extracellular	-	No	No (0.400)
SPD_0131	Bacterial cytoplasm	Cytoplasmic	-	No	No (0.100)
SPD_0402	Bacterial membrane	Cytoplasmic membrane	One (18-37)	No	Possibly (0.654)
SPD_1333	Bacterial cytoplasm	Cytoplasmic	-	No	Possibly (0.775)
SPD_1288	Bacterial membrane	Cytoplasmic membrane	Two (12-30, 51-72)	No	Possibly (0.950)
SPD_1898	Bacterial membrane	Unknown	One (4-20)	No	No (0.078)
SPD_1392	Bacterial membrane	Cytoplasmic membrane	Three (6-25, 34-54, 59-78)	No	Possibly (0.847)
SPD_1743	Bacterial cytoplasm	Cytoplasmic	-	No	No (0.057)
SPD_0339	Bacterial cytoplasm	Cytoplasmic	-	No	No (0.050)
SPD_0878	Bacterial cytoplasm	Cytoplasmic	-	No	No (0.089)
SPD_1346	Bacterial membrane	Unknown	One (188-206)	No	Possibly (0.927)

Table 4 shows the top three proteins of the highest interaction with the query protein. The score given for each interaction was in the range of 0 to 1, with 1 being the strongest interaction. From the analysis, it was revealed that most of the proteins involve directly with the virulence machinery of *S. pnuemoniae*.

Secondary and Tertiary Structure Prediction and Refinement

Another pivotal aspect to consider when annotating protein functional properties is its two- and three-dimensional structure. This prediction revealed possible shape or folding (helices, strands, and loops) of a query protein from its amino acid sequence. The knowledge on protein structure enables further identification on important protein characteristics such as active sites and binding ligands. Structural refinement, on the other hand, is crucial in improving the predicted structure to minimize the energy, thus obtaining more native protein folding [37].

In this study, all structures were successfully predicted and refined except for two proteins (SPD_1346 and SPD_0878) due to large atomistic structure. Based on the graph of root mean square deviation (RMSD) against

Table 4. Protein-protein interactions by STRING

Gene ID	Interacting protein	Protein function
SPD_0965	Obg protein,	Modulates vital processes,
	CpoA protein	Saccharides biosynthesis
SPD_0131	Ribonuclease J,	Hydrolyses β-lactam antibiotics,
	MecA protein,	Involves in bacterial pathogenesis,
	DivIB protein	Cell wall synthesis
SPD_0402	SPD_0403,	Catalyzes glycerol metabolic processes,
	SPD_1388	Key regulator for virulence of Gram-positive bacteria
SPD_1333	Zwf protein,	Carbohydrate degradation process,
	Gnd protein,	Carbohydrate degradation process,
	SPD_1330	ATP-binding cassette transporter
SPD_1288	TrxB protein,	Catalyzes the reduction of thioredoxin,
	SPD_1290,	ABC transporter,
	SPD_1293	Involves in aminoglycoside antibiotics resistance mechanism
SPD_1898	SPD_1899,	Purine nucleotide biosynthesis,
	SPD_1897,	Purine nucleotide biosynthesis,
	SPD_1895	Protein biosynthesis
SPD_1392	GlmM protein,	Catalyzes peptidoglycan biosynthesis,
	SPD_2032,	Involves in c-di-AMP homeostasis,
	SPD_1393	Catalyzes disulfide bonds formation
SPD_1743	TsaD protein,	Involves in tRNA processing machinery,
	NnrD protein,	Involves in bacterial stress adaptation,
	Recombinase A	Responses to β-lactam antibiotics
SPD_0339	EzrA protein,	Essential for growth, cell division, and cell size homeostasis,
	RecU protein,	Involves in DNA damage repair mechanism,
	Pbp2 protein	Involves in methicillin resistance mechanism
SPD_0878	MtnN protein,	Involves in virulence machinery of Gram negative bacteria,
	SPD_0875,	Controls cell homeostasis,
	GlmU protein	Cell membrane synthesis
SPD_1346	GreA protein,	Regulates RNA polymerase activity,
	MurC protein	Involves in peptidoglycan biosynthesis

time during the production stage, six out of nine refined structures had reached the plateau stage. However, the remaining three (SPD_0402, SPD_1288, and SPD_1392) still had an increasing RMSD, suggesting longer production time is needed (Table 5).

Structural Validation

Structural validation was done to verify the quality of predicted models. After the refinement process, final structures were again subjected to structural validation through Ramachandran plot assessment (to visualize the distribution of torsion angles in a protein structure), QMEAN4 (to describe the likelihood that a predicted model is of comparable quality to experimental structure) and Verify3D (to verify the propensity of protein's sequence with its predicted three- dimensional structure). In QMEAN4, the closer the score to 0 indicates better model quality. In Verify 3D, a score of above 80% indicates a high tendency of the sequence to take shape like its predicted structure.

Generally, based on Ramachandran plot assessment, 80% of residues of all structures fell in the favored region except for the two unrefined structures, SPD_0878 (79.0%) and SPD_1346 (63.9%). Similarly, QMEAN4 score obtained by all proteins showed value ranges between -0.09 to -5.61, with two outliers, again from SPD_0878 (-8.18) and SPD_1346 (-13.54). Lastly, when subjected to Verify 3D, only four out of eleven proteins (SPD_0965, SPD_0402, SPD_1333, and SPD_1743) had a score of above 80%. The summary of all assessments is shown in Table 5.

Active Sites and Ligand Prediction

It is essential to know the active sites and possible binding ligand of a query protein. Based on the predicted ligand, further interpretation on the functional property of the protein can be made more precisely. The type of ligand that binds to a particular protein determines its function in a cellular mechanism or pathway. Plus, it is also important for drug designing purpose [38].

Throughout the eleven subjects of study, the active sites and possible ligand of all proteins were able to be identified except for SPD_1346 (Table 6). This exception is due to the low validity of the unrefined model of SPD_1346 tertiary structure.

In terms of ligand binding prediction (Table 6), four proteins (SPD_1333, SPD_1392, SPD_0339, and SPD_0878) showed possibility in the involvement of the cell pathogenicity mechanism and five proteins (SPD_0965, SPD_0131, SPD_0402, SPD_1288 and SPD_1743) showed possible involvement in cell viability mechanism of *S. pneumoniae* strain D39. The remaining two proteins (SPD_1898 and SPD_1346) were inconclusive due to poor results of the binding ligand prediction. This limitation may need further *in silico* studies such as molecular docking to confirm their protein-ligand interactions.

Table 5. Summary of structural validation of final modeled structures

Gene ID	Ramachandran plot assessment			QMEAN4 score	Verify3D (%)	RMSD graph
	Favored region (%)	Allowed region (%)	Outlier region (%)			
SPD_0965	83.7	10.2	6.1	-3.97	100.00	Plateau
SPD_0131	86.5	8.1	5.4	-3.09	57.14	Plateau
SPD_0402	89.0	6.8	4.2	-2.15	100.00	Increasing
SPD_1333	87.4	9.0	3.6	-3.20	100.00	Plateau
SPD_1288	93.0	7.0	0.0	-3.49	8.11	Increasing
SPD_1898	87.5	8.9	3.6	-3.57	71.19	Plateau
SPD_1392	82.1	10.8	7.1	-5.61	75.28	Increasing
SPD_1743	89.6	9.0	1.4	-0.95	100.00	Plateau
SPD_0339	96.6	3.4	0.0	-0.09	2.44	Plateau
SPD_0878	79.5	11.2	9.3	-8.18	22.09	-
SPD_1346	63.9	23.7	12.4	-13.54	16.88	-

Table 6. Predicted function for each protein based on their binding ligand

Gene ID	Binding ligand			Predicted function
	Cell viability	Cell pathogenicity	Unknown	
SPD_0965	Glucose			Glucose metabolism
SPD_0131	ATP molecule			Energy production
SPD_0402	2,4-Dichlorophenol			Phenol metabolism
SPD_1333		Dilysine-containing molecule		Inhibits eukaryotic motifs
SPD_1288	Glycine			Survival and growth
SPD_1898			Null	-
SPD_1392		Cordycepin triphosphate (COTP)		Inhibits RNA chain elongation
SPD_1743	ADP molecule			ATPase activity
SPD_0339		Activator protein -1 (AP-1)		Stress adaptation
SPD_0878		Phosphatidylcholine (PC)		Stress adaptation
SPD_1346			Null	-

Potential Drug Design Candidates

The screening process of 39 essential hypothetical proteins revealed that 11 of them are suitable to be target proteins. In general, sequence- and structure- based analyses showed that the targeted proteins are diverse in terms of their physicochemical characteristics, structures, and functions. Overall, two proteins (SPD_1333 and SPD_1743) showed convenience in their assessments hence making them the best potential drug design candidates out of all 11 proteins.

For SPD_1333, the protein family prediction revealed that this protein contains a sequence of lactonase family member along with residues 4-335. The sequence encodes for 6-phosphogluconolactonase, an enzyme that hydrolyzes 6-phosphogluconolactone to 6-phosphogluconate in carbohydrate metabolism via pentose phosphate [39]. This pathway is important in synthesizing nucleotides and nucleic acids vital to cells. Hence, this suggests the role of SPD_1333 in maintaining cell mechanisms and viability.

Next, the secondary structure prediction of SPD_1333 by PSIPRED server showed that the protein contains 28 possible strands interconnected by loops with very good confidence. Besides, the tertiary model structured by I-TASSER server found that SPD_1333 is structurally closed to 3HFQ_A protein (99.1% alignment, 48.2% similarity). Based on Fig. 1(a), the structure reveals the formation made by these 28 strands, thus making up a seven-bladed beta propeller structure (name as described by Pfam server).

Lastly, COACH server predicted a dilysine-containing peptide molecule (xKxKxx) binding at pocket 2 of the query protein (Fig. 1(b)). This finding strengthens the suggestion on the possibility of SPD_1333 to be a membrane protein because dilysine motif plays a role in conferring the localization of this kind of protein [40]. Many types of motifs, including the dilysine motif, are known to mimic eukaryotic motifs, thus enabling pathogenic bacteria to disturb host's cellular functions [41]. From this, it is suggested that the ability of SPD_1333 to bind with dilysine motif-containing molecule may give benefit to this protein in accomplishing its virulence mission inside the host.

SPD_1743, on the other hand, contains TsaE domain, which is a domain that falls under P-loop NTPase superfamily and significant in synthesizing threonylcarbomyl adenosine biosynthesis protein. This protein is indirectly responsible in the N6-threonylcarbamoyladenosine (t(6)A) pathway. A study found that t6A involves in decoding accuracy of mRNA codons during protein synthesis [42]. Evidently, a defect in t(6)A pathway can lead to increased frame shift events, wrong start codon selections and occurrence of pleiotropic phenotypes [43]. Hence this shows that TsaE domain is important in maintaining cell viability.

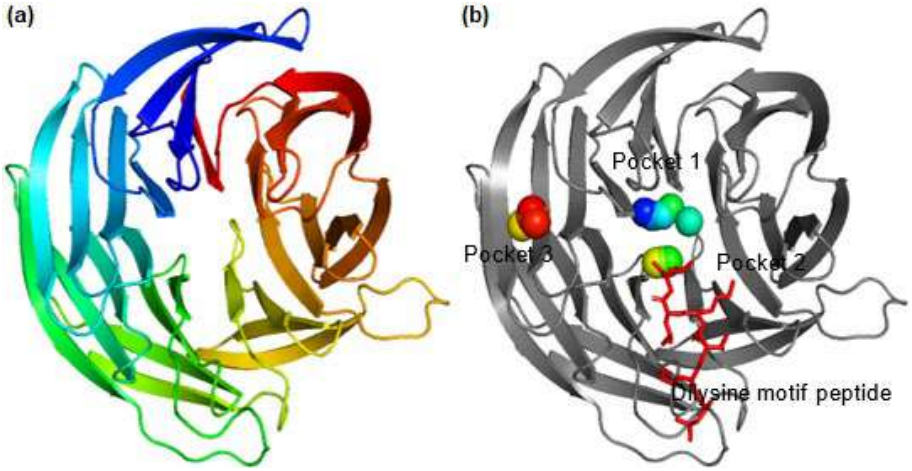

Fig 1. (a) Refined three-dimensional structure of SPD_1333 with twenty-eight strands; (b) Ligand binding site prediction by metaPocket server. Pocket 1, 2, and 3 represents the top three predicted sites. Ligand molecule containing dilysine peptide motif is represented in sticks

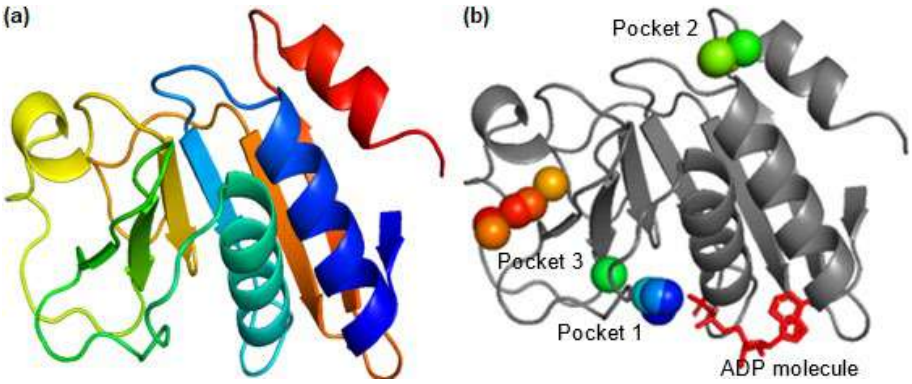

Fig 2. (a) Refined three-dimensional structure of SPD_1743 with four helices and seven strands; (b) Ligand binding site prediction by metaPocket server. Pocket 1, 2, and 3 (spheres) represents the top three predicted sites. Adenosine diphosphate (ADP) molecule is presented in sticks

In term of the secondary structure prediction, PSIPRED predicted SPD_1473 to have four helices and seven strands altogether. Similarly, tertiary structure prediction and refinement by I-TASSER and GROMACS using a functionally unknown 1HTW_A as a template (98.6% aligned, 27.6% identity) showed the same number of helices and strands (Fig. 2(a)).

Finally, ligand prediction by COACH predicted an adenosine diphosphate (ADP) molecule to bind at pocket 1 of the protein (Fig. 2(b)). The binding property is structurally similar to a protein of unknown function isolated from *Haemophilus influenza* (1HTW_A). Adenosine diphosphate, or alternatively known as adenosine pyrophosphate, is a hydrolyzed form of adenosine triphosphate (ATP), an organic molecule that involves in vital cellular processes such as cell respiration [44]. As evidently proven by a study done to 1HTW_A protein [45], the binding probability of SPD_1743 with the hydrolyzed ATP molecule may suggest its function in ATPase activity. Targeting SPD_1743 may alter its function in maintaining cell respiration hence provoking the viability of *S. pneumoniae* strain D39.

■ CONCLUSION

The analyses done on all eleven proteins revealed that seven of the proteins are classified under protein domain or family that involves in either pathogenicity or viability of *S. pneumoniae*. Furthermore, based on the

binding ligand assessment, five out of eleven proteins were strongly predicted to be involved in the pathogenesis and four in the survival mechanism of *S. pneumoniae* strain D39. Finally, the sequence- and structure- based assessments also showed that SPD_1333 (predicted to involve in cell pathogenicity mechanism) and SPD_1743 (predicted to involve in cell viability mechanism) are the best candidates to be further studied.

By using *in silico* sequence- and structure- based approaches, this study had successfully filled the information gap of previously un-annotated essential proteins in *S. pneumoniae* strain D39 by predicting probable physicochemical, functional and structural properties of selected hypothetical proteins.

■ ACKNOWLEDGMENTS

We would like to thank all staff at the Kulliyyah of Science, International Islamic University Malaysia, for their assistance. This study is funded by the IIUM RIGS research grant (RIGS16-312-0476) and FRGS research grant from the Malaysian Ministry of Education (FRGS/1/2016/SKK11/UIAM/02/1).

■ REFERENCES

[1] World Health Organization, *Pneumococcal Disease*, https://www.who.int/biologicals/vaccines/pneumococcal/en/, accessed on February 19, 2019.

[2] Weiser, J.N., Ferreira, D.M., and Paton, J.C., 2018, *Streptococcus pneumoniae*: Transmission, colonization and invasion, *Nat. Rev. Microbiol.*, 16 (6), 355–367.

[3] Henriques-Normark, B., and Tuomanen, E.I., 2013, The pneumococcus: Epidemiology, microbiology, and pathogenesis, *Cold Spring Harb. Perspect. Med.*, 3 (7), a010215.

[4] Song, J.H., 2013, Advances in pneumococcal antibiotic resistance, *Expert Rev. Respir. Med.*, 7 (5), 491–498.

[5] Cherazard, R., Epstein, M., Doan, T.L., Salim, T., Bharti, S., and Smith, M.A., 2017, Antimicrobial resistant *Streptococcus pneumoniae*, *Am. J. Ther.*, 24 (3), e361–e369.

[6] Lipsitch, M., and Siber, G.R., 2016, How can vaccines contribute to solving the antimicrobial resistance problem?, *MBio*, 7 (3), 00428-16.

[7] Rodgers, G.L., and Klugman, K.P., 2016, Surveillance of the impact of pneumococcal conjugate vaccines in developing countries, *Hum. Vaccin. Immunother.*, 12 (2), 417–420.

[8] Mitchell, A.M., and Mitchell, T.J., 2010, *Streptococcus pneumoniae*: Virulence factors and variation, *Clin. Microbiol. Infect.*, 16 (5), 411–418.

[9] Hyams, C., Camberlein, E., Cohen, J.M., Bax, K., and Brown, J.S., 2010, The *Streptococcus pneumoniae* capsule inhibits complement activity and neutrophil phagocytosis by multiple mechanisms, *Infect. Immun.*, 78 (2), 704–715.

[10] Mostowy, R., Croucher, N.J., Hanage, W.P., Harris, S.R., Bentley, S., and Fraser, C., 2014, Heterogeneity in the frequency and characteristics of homologous recombination in pneumococcal evolution, *PLoS Genet.*, 10 (5), 1004300.

[11] Jedrzejas, M.J., 2001, Pneumococcal virulence factors: Structure and function, *Microbiol. Mol. Biol. Rev.*, 65 (2), 187–207.

[12] Dahlström, K.M., 2015, From Protein Structure to Function with Bioinformatics, *Dissertation*, Faculty of Science and Engineering, Åbo Akademi University, Turku, Finland.

[13] Wuchty, S., Rajagopala, S.V., Blazie, S.M., Parrish, J.R., Khuri, S., Finley, R.L., and Uetz, P., 2017, The protein interactome of *Streptococcus pneumoniae* and bacterial meta-interactomes improve function predictions, *mSystems*, 2 (3), 00019-17.

[14] Liu, X., Kjos, M., Sorg, R.A., Veening, J., van Kessel, S.P., Zhang, J., Knoops, K., Slager, J., Domenech, A., and Gallay, C., 2017, High-throughput CRISPRi phenotyping identifies new essential genes in Streptococcus pneumoniae, *Mol. Syst. Biol.*, 13 (5), 931.

[15] Gupta, A., Kapil, R., Dhakan, D.B., and Sharma, V.K., 2014, MP3: A software tool for the prediction of pathogenic proteins in genomic and metagenomic data, *PLoS One*, 9 (4), e93907.

[16] Pearson, W.R., 2013, An introduction to sequence similarity ("homology") searching, *Curr. Protoc.*

Bioinf., 42 (1), 3.1.1–3.1.8.

[17] Bairoch, A., Gattiker, A., Wilkins, M.R., Gasteiger, E., Duvaud, S., Appel, R.D., and Hoogland, C., 2009, "Protein Identification and Analysis Tools on the ExPASy Server", in *The Proteomics Protocols Handbook*, Eds. Walker, J.M., Humana Press, 571–607.

[18] El-Gebali, S., Mistry, J., Bateman, A., Eddy, S.R., Luciani, A., Potter, S.C., Qureshi, M., Richardson, L.J., Salazar, G.A., Smart, A., Sonnhammer, E.L.L., Hirsh, L., Paladin, L., Piovesan, D., Tosatto, S.C.E., and Finn, R.D., 2019, The Pfam protein families database in 2019, *Nucleic Acids Res.*, 47 (D1), D427–D432.

[19] Marchler-Bauer, A., Bo, Y., Han, L., He, J., Lanczycki, C.J., Lu, S., Chitsaz, F., Derbyshire, M.K., Geer, R.C., Gonzales, N.R., Gwadz, M., Hurwitz, D.I., Lu, F., Marchler, G.H., Song, J.S., Thanki, N., Wang, Z., Yamashita, R.A., Zhang, D., Zheng, C., Geer, L.Y., and Bryant, S.H., 2017, CDD/SPARCLE: Functional classification of proteins via subfamily domain architectures, *Nucleic Acids Res.*, 45 (D1), D200–D203.

[20] Yu, N.Y., Wagner, J.R., Laird, M.R., Melli, G., Rey, S., Lo, R., Dao, P., Sahinalp, S.C., Ester, M., Foster, L.J., and Brinkman, F.S.L., 2010, PSORTb 3.0: Improved protein subcellular localization prediction with refined localization subcategories and predictive capabilities for all prokaryotes, *Bioinformatics*, 26 (13), 1608–1615.

[21] Tusnády, G.E., and Simon, I., 2001, The HMMTOP transmembrane topology prediction server, *Bioinformatics*, 17 (9), 849–850.

[22] Armenteros, J.J.A., Tsirigos, K.D., Sønderby, C.K., Petersen, T.N., Winther, O., Brunak, S., von Heijne, G., and Nielsen, H., 2019, SignalP 5.0 improves signal peptide predictions using deep neural networks, *Nat. Biotechnol.*, 37, 420–423.

[23] Bendtsen, J.D., Jensen, L.J., Blom, N., von Heijne, G., and Brunak, S., 2004, Feature-based prediction of non-classical and leaderless protein secretion, *Protein Eng. Des. Sel.*, 17 (4), 349–356.

[24] Szklarczyk, D., Gable, A.L., Lyon, D., Junge, A., Wyder, S., Huerta-Cepas, J., Simonovic, M., Doncheva, N.T., Morris, J.H., Bork, P., Jensen, L.J., and von Mering, C., 2019, STRING v11: Protein–protein association networks with increased coverage, supporting functional discovery in genome-wide experimental datasets, *Nucleic Acids Res.*, 47 (D1), D607–D613.

[25] Buchan, D.W.A., Minneci, F., Nugent, T.C.O., Bryson, K., and Jones, D.T., 2013, Scalable web services for the PSIPRED Protein Analysis Workbench, *Nucleic Acids Res.*, 41 (W1), W349–W357.

[26] Zhang, Y., 2008, I-TASSER server for protein 3D structure prediction, *BMC Bioinf.*, 9 (1), 40.

[27] Chen, C.C., Hwang, J.K., and Yang, J.M., 2006, $(PS)^2$: Protein structure prediction server, *Nucleic Acids Res.*, 34 (Web Server), W152–W157.

[28] Waterhouse, A., Bertoni, M., Bienert, S., Studer, G., Tauriello, G., Gumienny, R., Heer, F.T., de Beer, T.A.P., Rempfer, C., Bordoli, L., Lepore, R., and Schwede, T., 2018, SWISS-MODEL: Homology modelling of protein structures and complexes, *Nucleic Acids Res.*, 46 (W1), W296–W303.

[29] Eisenberg, D., Lüthy, R., and Bowie, J.U., 1997, VERIFY3D: Assessment of protein models with three-dimensional profiles, *Methods Enzymol.*, 277, 396–404.

[30] Benkert, P., Biasini, M., and Schwede, T., 2011, Toward the estimation of the absolute quality of individual protein structure models, *Bioinformatics*, 27 (3), 343–350.

[31] Abraham, M.J., Murtola, T., Schulz, R., Páll, S., Smith, J.C., Hess, B., and Lindahl, E., 2015, GROMACS: High performance molecular simulations through multi-level parallelism from laptops to supercomputers, *SoftwareX*, 1-2, 19–25.

[32] Huang, B., 2009, MetaPocket: A meta approach to improve protein ligand binding site prediction, *OMICS*, 13 (4), 325–330.

[33] Yang, J., Roy, A., and Zhang, Y., 2013, Protein–ligand binding site recognition using complementary binding-specific substructure comparison and sequence profile alignment,

Bioinformatics, 29 (20), 2588–2595.

[34] Wang, F., Xiao, J., Pan, L., Yang, M., Zhang, G., Jin, S., and Yu, J., 2008, A systematic survey of mini-proteins in bacteria and archaea, *PLoS One*, 3 (12), e4027.

[35] Wan, S., Duan, Y., and Zou, Q., 2017, HPSLPred: An ensemble multi-label classifier for human protein subcellular location prediction with imbalanced source, *Proteomics*, 17 (17-18), 1700262.

[36] Davis, M.J., Hanson, K.A., Clark, F., Fink, J.L., Zhang, F., Kasukawa, T., Kai, C., Kawai, J., Carninci, P., Hayashizaki, Y., and Teasdale, R.D., 2006, Differential use of signal peptides and membrane domains is a common occurrence in the protein output of transcriptional units, *PLoS Genet.*, 2 (4), e46.

[37] Rydzewski, J., Jakubowski, R., and Nowak, W., 2015, Communication: Entropic measure to prevent energy over-minimization in molecular dynamics simulations, *J. Chem. Phys.*, 143 (17), 171103.

[38] Chen, J., Almo, S.C., and Wu, Y., 2017, General principles of binding between cell surface receptors and multi-specific ligands: A computational study, *PLOS Comput. Biol.*, 13 (10), e1005805.

[39] Miclet, E., Stoven, V., Michels, P.A.M., Opperdoes, F.R., Lallemand, J.Y., and Duffieux, F., 2001, NMR spectroscopic analysis of the first two steps of the pentose-phosphate pathway elucidates the role of 6-phosphogluconolactonase, *J. Biol. Chem.*, 276 (37), 34840–34846.

[40] Andersson, H., Kappeler, F., and Hauri, H.P., 1999, Protein targeting to endoplasmic reticulum by dilysine signals involves direct retention in addition to retrieval, *J. Biol. Chem.*, 274 (21), 15080–15084.

[41] Ruhanen, H., Hurley, D., Ghosh, A., O'Brien, K.T., Johnston, C.R., and Shields, D.C., 2014, Potential of known and short prokaryotic protein motifs as a basis for novel peptide-based antibacterial therapeutics: a computational survey, *Front. Microbiol.*, 5, 4.

[42] Luthra, A., Swinehart, W., Bayooz, S., Phan, P., Stec, B., Iwata-Reuyl, D., and Swairjo, M.A., 2018, Structure and mechanism of a bacterial t6A biosynthesis system, *Nucleic Acids Res.*, 46 (3), 1395–1411.

[43] Miyauchi, K., Kimura, S., and Suzuki, T., 2013, A cyclic form of N6-threonylcarbamoyladenosine as a widely distributed tRNA hypermodification, *Nat. Chem. Biol.*, 9 (2), 105–111.

[44] Bugreev, D.V., and Mazin, A.V., 2004, Ca^{2+} activates human homologous recombination protein Rad51 by modulating its ATPase activity, *Proc. Natl. Acad. Sci. U.S.A.*, 101 (27), 9988–9993.

[45] Teplyakov, A., Obmolova, G., Tordova, M., Thanki, N., Bonander, N., Eisenstein, E., Howard, A.J., and Gilliland, G.L., 2002, Crystal structure of the YjeE protein from *Haemophilus influenzae*: A putative ATPase involved in cell wall synthesis, *Proteins Struct. Funct. Genet.*, 48 (2), 220–226.

Validation of Mineral (Fe, Zn, and Cu) Analysis Methods in Carbohydrate, Protein and Fat-Rich Samples Using Microwave Digestion Method

Didah Nur Faridah[1,*], Imas Solihat[1,2], and Nancy Dewi Yuliana[1]

[1]*Department of Food Science and Technology, Faculty of Agricultural Technology, Bogor Agricultural University, Jl. Tanjung, Kampus IPB Dramaga, Bogor 16680, Indonesia*

[2]*AKA Bogor Polytechnic, Jl. Pangeran Sogiri No. 283, Tanah Baru, Bogor 16154, West Java, Indonesia*

* ***Corresponding author:***

email: didah_nf@apps.ipb.ac.id

Received: December 31, 2018
Accepted: May 23, 2019

DOI: 10.22146/ijc.42297

Abstract: *Destruction process using both dry and wet conditions serves as a significant step in mineral quantification. Wet destruction using microwave-assisted digestion refers to the standard method of AOAC (2012); in this work, we modified the destruction procedures provided in the microwave digestion manual book, including temperature, reagent volume (HNO_3 and H_2O_2), and length of destruction. The experiment works aimed (1) to validate the procedures in destruction process using microwave digestion; (2) to quantify Fe, Zn and Cu in various food matrices (canned peas, canned fish, full cream powdered milk) using a validated method. The method was evaluated according to linearity, accuracy, precision, absolute and relative LOD, LOQ, and intra-reproducibility. Measurement of Fe, Zn and Cu were considered to have a satisfying accuracy at a range of 80–115%, with a good precision value (% RSD < 2/3 CV Horwitz), while regression curves $R^2 > 0.995$. The results showed that data collected from the modified method was not significantly different compared to those from the AOAC method. The currently developed method also fulfilled the acceptability requirements for laboratory analysis.*

Keywords: *minerals; F-AAS; method validation; microwave digestion*

■ INTRODUCTION

The constituents of food, including water, carbohydrates, proteins, vitamins, fats, and minerals, may affect the properties of the food. Specifically, essential minerals (Fe, Zn, and Cu) [1-5] are closely related to some disadvantageous effects on food such as rancidity, changes in color, taste, and aroma. Flame-AAS is commonly used for measuring mineral levels [6-10], in which the destruction process is considered as one of the most important steps [11], often carried out in dry and wet conditions [12-14]. Dry destruction accounts for the loss of some mineral components in the furnace, while it is also a time-consuming process [15-16]. Meanwhile, open system wet destruction contributes to contamination towards the environment, and certain minerals can be lost due to evaporation. On the other hand, wet destruction with the closed system using microwave-assisted digestion has some advantages, such as being rapid, easy, and produce accurate assessment [17-19], while also using less reagent.

In our experiment, the destruction method using microwave-assisted digestion is found to be more efficient in regards to the processing time, amount of solvent, and temperature, and regarded as a more renewable technique in comparison with the method prescribed by AOAC 2012. Based on the SOP for microwave digestion, destruction procedures may vary depending on the types of food matrices. In contrast, the procedure method of AOAC 2012 is applied for all types of sample, regardless of food matrices. The results of the analysis between the AOAC method and the modified method were not significantly different, resulting in a positive analysis gap.

The method for mineral destruction in this study which was derived from the manual of a microwave digestion device is different from the standard AOAC method 999.10 (2012) [20]. The differences included

reagent volume, temperature, and length of destruction. Different food matrices should require a specific treatment during the destruction process. For this reason, the food samples were selected according to the food matrix triangle (AOAC 2012), resulting in three main groups of food, i.e. protein-rich food (canned fish), fat-rich food (full cream milk powder) and carbohydrate-rich food (canned peas). The selection of canned food samples aimed to reduce factors that can cause instability in the method validation. The modified method was acceptable as long as it met the requirements after compared with the standard method [21].

The objective of this study was (1) to validate the quantification method of Fe, Zn and Cu using F-AAS with microwave digestion, and (2) to obtain data on the mineral content of Fe, Zn and Cu on several different food matrices using the validated method.

■ EXPERIMENTAL SECTION

Materials

The chemicals used were analytical grade, including aquademineral, HNO_3 (p) (Merck KgaA), H_2O_2 30% (Merck KgaA), standard Zn solution of 1000 ppm (CertiPUR Merck KgaA, no 1.19806), standard Fe solution of 1000 ppm (CertiPUR merge KgaA, no.1. 19781), standard Cu solution of 1000 ppm (CertiPUR merge KgaA, no.1.1986).

The food samples (canned peas, full cream powdered milk, and canned fish) were collected from similar brands, expired dates, and production batches. The powdered milk was stored in airtight packaging at room temperature (quartering sampling method), while canned peas and canned fish were stored in the freezer (homogenization sampling method) (FDA 2014) [22]. Homogenized samples were placed in 10 polyethylene bags, and their ash content was analyzed in duplicate [23]. The homogeneity of these samples was checked using different test criteria (F test) with the provision of $F_{count} < F_{table}$. Ash content test was achieved using the standard method of AOAC 900.02A.

Instrumentation

The instruments used were Close Microwave Digestion type SINEO MDS-6G, Flame-AAS type Shimadzu AA 2000 and hollow cathode lamp of Fe, Zn, and Cu. The F-AAS setting is presented in Table 1.

Procedure

Sample digestion procedure

Sample (0.5 g dry basis was added with HNO_3 (p) and H_2O_2 30%. The standard method setting of destruction and modification is presented in Table 2. After completion of digestion, the sample was homogenized in demineralized water in a 25 mL flask.

Table 1. Setting of Flame-AAS

Mineral	Wavelength (nm)	Fuel	Burner height (mm)	Fuel flow (L/min)	Lamp current (mA)	Slit bandwidth (nm)	Sensitivity Cu 2 ppm
Fe	248.3	Air-C_2H_2	9.0	2.2	4.0	0.2	0.0352
Zn	213.9	Air-C_2H_2	7.0	2.0	5.0	0.7	
Cu	324.8	Air-C_2H_2	7.0	1.8	8.0	0.7	

Table 2. The setting of microwave digestion

Sample	Standard method	Modified method
Full cream milk powder		130 °C/10 min/300 W
		150 °C/5 min/600 W
		180 °C/5 min/500 W
	30 °C/3 min/300 W	200 °C/10 min/300 W
Canned peas	150 °C/5 min/600 W	130 °C /10 min/300 W
	180 °C/22 min/500 W	150 °C/5 min/600 W
	200 °C/15 min/300 W	180 °C/15 min/500 W
Canned fish		130 °C/10 min/300 W
		150 °C/5 min/600 W
		180 °C/15 min/500 W

Control solution (comprising of nitric acid and hydrogen peroxide) was made according to the same procedure as the sample.

Validation of analysis methods

The developed method was evaluated for its acceptability according to the following indicators, i.e., linearity, relative and absolute LOD, LOQ, precision, accuracy, and intra-lab reproducibility.

Precision test. This test is done by measuring the concentration of samples as much as 7 times replication for the measurement of 3 types of minerals (Fe, Cu, and Zn).

Intra-lab reproducibility. Intra-lab reproducibility is determined by measuring the concentration of samples in the same laboratory, by the same operator at different times. Each test was performed with three replications. Furthermore, the RSD value of the analysis is compared with the RSD Horwitz value. Intra-lab reproducibility is satisfactory if it has an RSD value smaller than the RSD Horwitz value. Test results at two different weeks were tested using the t-test.

Accuracy. The test is performed using a sample spiked with a standard solution. The experimental concentration of spiking is the percentage of the sample concentration that is 80% (low concentration), 100% (medium), and 120% (high). Spiking is done at the beginning of the preparation before the microwave digestion. Accuracy is determined by calculating percent recovery.

Linearity. Instrument linearity was performed by measuring the absorbance of standard mineral solutions (Fe, Zn, and Cu) at various concentrations. The linearity test of Fe and Cu minerals used concentration 0–0.5 mg/L while Zn mineral concentration was 0–1.0 mg/L. Absorbance of each standard solution was measured and repetition was performed three times.

Limit of Detection (LOD) and Limit of Quantitation (LOQ). The values of LDI (Limit detection of instrument) and LOQ can be obtained from linearity analysis data by determining the standard value of calibration error (sy/x). Theoretical LDI is obtained from the formula [3 (sy/x)]/b. Confirmation was conducted by 7× repeated measurement of the solution according to the theoretical LDI concentration for 3 types of minerals (Fe, Zn and Cu), The theoretical LOQ is derived from [10 (sy/x)]/b. Confirmation of LOQ values was performed by making a solution with a concentration of the theoretical LOQ value and measured with seven replicates for each mineral (Fe, Zn, and Cu). The LDM (Limit detection of method) value is determined by measuring seven replications of the mineral concentration in the sample prepared according to the theoretical LDI values.

Data analysis

Data were expressed as mean, followed with deviation standard and relative standard deviation (RSD). Furthermore, statistical analysis was used to determine the p-value (independent t-test) in intra-lab reproducibility. Results obtained from the modified method were compared to the standard method.

■ RESULTS AND DISCUSSION

Preparation of Sample

Prior to destruction (by microwave digestion), the sample size needs to be reduced, allowing to produce a larger surface area and enhance the reaction rate. Samples containing organic solvents, such as wine, must be evaporated up to a fifth of the initial volume since the solvent can induce an explosion.

The selection of food matrix is based on major components such as carbohydrate, protein, and fat, arranged into the food matrix triangle (Fig. 1). The proximate analysis was in accordance with the placements on literature studies (USDA 2006) [24], exhibited in Table 3.

Furthermore, the water content in all samples (Table 4) was in the range of SNI and USDA standard. Moisture level in canned fish was found to be higher compared to literature USDA 15089, which might be ascribed to the difference in the type of sample. The determination of water content was conducted using a vacuum oven method. Vacuum oven drying was conducted at low temperature and pressure, in order to retain volatile components present in the samples tested [25].

The homogeneity test is performed by measuring ash content, enabling to ensure that the sample tested to contain a comparable amount of mineral and does not

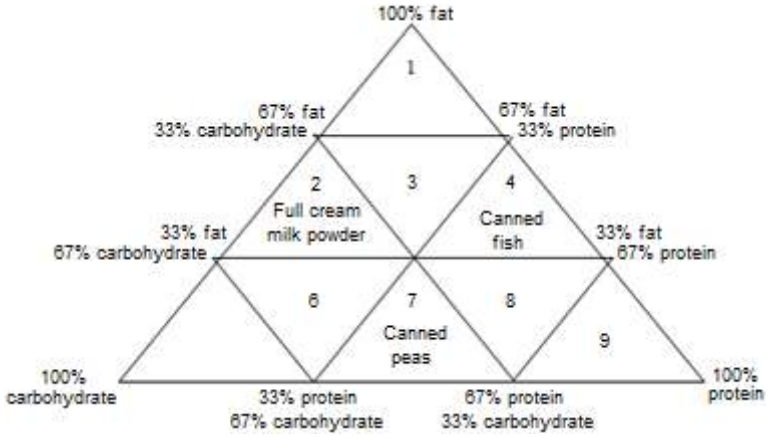

Fig 1. Food triangle

Table 3. Proximate composition based reference

Sample	Content (g/100g)					
	Water	Protein	Fat	Carbohydrate	Fiber	Total sugar
Canned peas	85.13	3.01	0.48	10.60	3.3	3.20
Canned fish	66.86	20.86	10.45	0.54	0.1	0.43
Full cream powdered milk	2.47	26.32	26.71	38.42	0	38.42

Source: USDA 2016

Table 4. Water content

Sample	Water content (%)	
	Analysis result	Reference
Full cream powdered milk	4.26	max 5 (SNI 2970-2015)
Canned peas	80.16	85.13 (USDA 11306)
Canned fish	76.54	66.86 (USDA 15089)

Table 5. Sample homogeneity test

Subject	Ash content (%)					
	Full cream milk powder		Canned peas		Canned fish	
	1 (ai)	(bi)	1 (ai)	2 (bi)	1 (ai)	2 (bi)
average	6.11	5.99	1.25	1.23	1.98	1.99
MSB	0.01		0.001		0.001	
MSW	0.01		0.001		0.001	
F_{count}	0.96		0.87		1.38	

Term of acceptance: $F_{count} < F_{table}$ (3.02)

contain disturbing matrix (Table 5). Ash content can be used as an illustration of the minerals contained in the sample [26]. The results demonstrated that the F value was 3.02, being lower than F table 5%, indicating the acceptable homogeneity.

Validation of the Methods

Precision

Table 6 presents the satisfying precision for the determination of Fe, Zn, and Cu in all samples, which was indicated by % RSD < 2/3 CV Horwitz. This result displays that all random errors can be controlled. The random errors include instability of instrument performance, changes in temperature, the difference in techniques, and analysts.

LOD and LOQ

The indicators for detection limit are absolute LOD (instrument LOD) and relative LOD (method LOD). Absolute LOD represents the smallest concentration of

Table 6. Precision test results

Sample repeat	Mineral concentration (mg/kg)								
	Full cream powdered milk			Canned peas			Canned fish		
	Cu	Zn	Fe	Cu	Zn	Fe	Cu	Zn	Fe
average	0.87	24.34	24.72	1.35	7.01	2.82	0.95	9.42	23.33
SD	0.05	0.50	0.53	0.02	0.06	0.06	0.05	0.07	0.18
RSD (%)	6.79	2.07	2.14	1.63	1.63	0.89	4.89	0.76	0.77
2/3CV Horwitz	10.77	6.60	6.58	10.19	10.20	7.96	10.75	7.61	6.64

Term of acceptance: %RSD<2/3 CV Horwitz

analyte that can still be detected by the instrument, while relative LOD is the smallest concentration of an analyte in the sample that can still be detected and the results are presented in Table 7. Limit detection testing was carried out by using a calibration curve with the formula 3[syx/b]. LOQ value constitutes the lowest limit of the calibration curve.

The results for relative LOD can be seen in Table 8. The absolute LOD values for the three minerals examined were smaller than those reported by a previous study [12], reaching 0.07 mg/mL for Cu, 0.07 mg/mL for Fe, and 0.11 mg/mL for Zn. It means the methods have good sensitivity. The relative LOD is essential in dealing with constraints due to different signals/responses for each food matrix.

Linearity

The regression equation for Fe, Cu, and Zn was presented as follows: y = 0.084x-0.0002 with R^2 = 0.9970;

Table 7. Absolute LOD and LOQ

Mineral		Absolute LOD (mg/L)	LOQ (mg/L)
Cu	average	0.01	0.1
	SD	0.0021	0.0032
	RSD (%)	16.60	3.28
	2/3CV Horwitz	5.14	15.18
Zn	average	0.02	0.2
	SD	0.0012	0.0047
	RSD (%)	17.52	2.38
	2/3CV Horwitz	22.70	13.64
Fe	average	0.05	0.1
	SD	0.0236	0.0081
	RSD (%)	52.10	7.61
	2/3CV Horwitz	17.00	22.40

Table 8. Relative LOD

Mineral		Relative LOD (mg/L)		
		Full cream powdered milk	Canned peas	Canned fish
Cu	average	0.03	0.07	0.01
	SD	0.0026	0.1578	0.0306
	RSD (%)	8.77	212.18	307.43
	2/3CV Horwitz	18.12	15.77	21.35
Zn	average	0.1	0.04	0.06
	SD	0.0853	0.0180	0.0042
	RSD (%)	70.67	44.12	6.78
	2/3CV Horwitz	14.66	17.26	16.23
Fe	average	0.06	0.09	0.06
	SD	0.0140	0.0173	0.0210
	RSD (%)	23.65	18.88	35.31
	2/3CV Horwitz	16.32	15.29	16.31

$y = 0.1335x-0.0004$ with $R^2 = 0.9969$; $y = 0.4125x + 0.0086$ with $R^2 = 0.9977$, respectively. As exhibited in Table 9, the experimental result showed satisfying linearity, in which the higher concentration of tested mineral corresponded to the rise of absorbance.

The intercept for Fe, Zn, and CU reached -0.0002, 0.0086 and -0.0004, respectively, suggesting the occurrence of systematic errors in F-AAS instrument. Furthermore, the R^2 value was >0.990, which is in accordance with the acceptance limit, as depicted in Fig. 2.

Intra-lab reproducibility

Table 10 presents the intra-lab reproducibility, showing p-value > α 5% for all minerals in canned fish, canned peas and full cream powdered milk, suggesting that the value did not significantly differ [27].

Accuracy

Accuracy represents the method efficiency based on recovery from standard solutions added to the sample (spiking). The results showed that the accuracy of Fe, Zn, and Cu levels varied from 80 to 100%, which is still in the range of acceptability limit of AOAC (75–120%). This indicates that the procedure in the modified method is acceptable for all minerals. Result of the recovery test can see in Table 11.

Mineral Analysis

To optimize the results, some conditions during the destruction phase in microwave digestion need to be controlled, including the amount of nitric acid and hydrogen peroxide, temperature, sample weight, pre-digestion, and destruction length. The optimization can be achieved using various techniques, such as the factorial design of Plackett-Burman. However, this step was excluded, considering that all procedures in this work are based on the standard of microwave digestion instrument for each food matrix. The efficiency of the destruction process using microwave digestion is influenced by the volume of acid substances (HNO_3 and H_2O_2), time, and temperature [28].

Power setting in both methods (standard and modified) was adopted from the manual book, while

Table 9. Linearity test results

Mineral	Concentration (ppm)	Average (abs)
Fe	0.1	0.0092
	0.2	0.0152
	0.3	0.0245
	0.4	0.0332
	0.5	0.0425
Zn	0.2	0.0954
	0.4	0.1817
	0.6	0.2730
	0.8	0.3421
	1.0	0.4237
Cu	0.1	0.0121
	0.2	0.0257
	0.3	0.0422
	0.4	0.0516
	0.5	0.0665

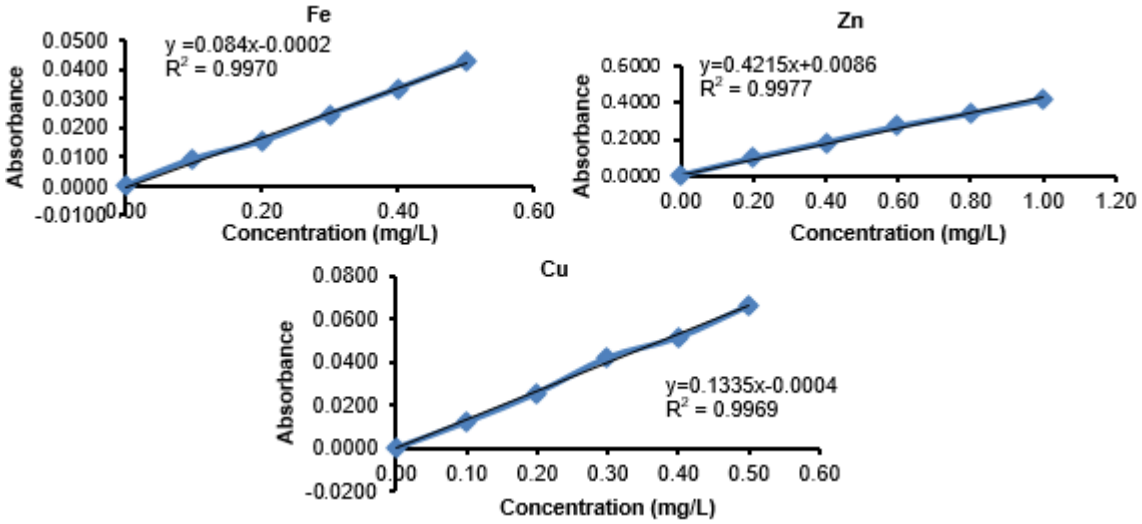

Fig 2. Linear regression curve for quantification of Fe, Zn, and Cu

Table 10. Intra-lab reproducibility

Repeat	Content (mg/kg)					
	Cu		Zn		Fe	
	1	2	1	2	1	2
Full cream milk powder						
average	0.94	0.87	24.34	24.48	24.72	25.01
SD	0.06	0.05	0.50	0.73	0.53	1.18
% RSD	6.78	5.78	2.07	2.99	2.14	4.70
2/3 CV Horwitz	16.15	16.33	9.89	9.88	9.87	9.86
p-value	0.110		0.712		0.545	
Canned peas						
average	1.36	1.34	7.01	6.88	2.82	2.80
SD	0.02	0.02	0.06	0.12	0.09	0.10
% RSD	1.51	1.52	0.89	1.73	3.45	3.59
2/3 CV Horwitz	15.28	15.31	11.94	11.97	13.69	13.70
p-value	0.120		0.089		0.668	
Canned fish						
average	0.95	0.95	9.42	9.48	23.33	23.24
SD	0.05	0.009	0.07	0.07	0.18	0.10
% RSD	4.89	1.02	0.76	0.77	0.77	0.43
2/3 CV Horwitz	16.12	16.12	11.41	11.40	9.96	9.96
p-value	0.821		0.210		0.355	

Term of acceptance: p-value > α 95%

Table 11. Results of the recovery test

Spiking minerals	Recovery (%)								
	Full cream powdered milk powder			Canned peas			Canned fish		
	80%	100%	120%	80%	100%	120%	80%	100%	120%
Fe	94.52	85.19	85.23	92.16	89.78	82.05	92.28	85.53	84.14
Zn	101.21	91.23	100.76	91.66	81.79	86.93	90.45	97.28	99.43
Cu	84.15	94.64	83.18	87.48	85.46	82.05	92.68	82.11	89.52

Term of acceptance: 80–115%

destruction temperature was carried out according to the standard of AOAC (2012). The sample weight (0.5 g, dry weight) was also based on the arrangement of AOAC. Destruction process allows changing the form of inorganic constituents to organic constituents, in which it involves the conversion of organic elements such as C, H, O, N, S and P into CO_2, H_2O, NO_2, while inorganic elements still exist in their original form. Open destruction using microwave digestion promotes several advantages, including faster time operation, fewer reagents used, higher accuracy, thereby reducing contamination in samples and loss of volatile elements.

During the microwave-assisted process, molecules are exposed to non-ionic electromagnetic radiation, which induces rotational dipole moments without changing their molecular structure [29]. The effect of the wave in microwave appears magnetically [30] and dielectrically [31]. Dielectric material comprised of molecules obtaining a dipole moment or a neutral charge (having a balanced positive and negative charge). Additionally, the dielectric wave in the microwave is due to the capability of storing electric charges at different potentials. Water is an electrical molecule, possessing hydrogen atoms (positively charged) and oxygen atoms (negatively charged). The exposure of the electrical field to dielectric materials led to changes in the direction of

the current because of repulsion and attraction within positive charges or negative charges; thus, the wave occurs magnetically. More heat was produced in samples containing more water than in those with less water. The frequency in the microwave ranged from 300 to 300.000 MHz with a wavelength of 1 mm–1 m.

Samples in microwave-assisted destruction are mixed with strong acids in a closed vessel. In that system, pressure (1.1–2.2 Mpa) and temperature (30–190 °C) increased due to microwave radiation, allowing to convert the solid form into a liquid. High pressure and temperature (around 200 °C) [32] on the vessel is able to raise the boiling point of nitric acid. Thus, it strengthens oxidation and accelerates the reaction. HNO_3 and H_2O_2 are used as oxidizing agents because they are capable to oxidize minerals into their salt form. Nitric acid at high temperature is decomposed into water-soluble oxides such as NO and NO_2. The use of mixed acids is better than a single acid for the mineral destruction process; the destruction process is incomplete if nitric acid is the only used compound, resulting in a cloudy solution [33]. The addition of H_2O_2 leads to intensifying the presence of O_2 in the vessel [34]. The oxidizing mixture consisting of HNO_3 and H_2O_2 produces a greater % recovery than a mixture of HNO_3 and HCl, and a mixture of HNO_3 and H_2SO_4 [35].

The gradient or multilevel heating system aims to intensify the reaction between NO and O_2 to form NO_2 [36]. The NO_2 is reabsorbed in acidic solution, and it regenerates HNO_3 [37]. The reaction process in the vessel is described in Fig. 3 [38].

The longer heating process in the microwave would lead to a higher temperature in the vessel, responsible for attenuation of the condensation process and eventually increase the mineral level in the solution. A complete destruction process is marked by the formation of a clear solution, which indicates the reformation of an organic compound. Sample solutions are then ready to be analyzed using F-AAS. F-AAS is recommended for use in measuring minerals because of its good sensitivity with a detection limit of more or less 1 ppm and also its low operational cost.

Soluble dietary fiber is a carbohydrate-based polymer widely found in nuts, fruits, and vegetables [39]. The dominant fiber contents in peas are stachyose (19.83 mg/g) and verbascose (16.10 mg/g) [40]. In addition, canned peas contain simple sugars, including glucose, fructose, sucrose, and galactose; hence, the destruction process starts from 130 °C to 180 °C. Addition of nitric acid (6 mL) is in accordance with a previous work of Bakkali et al. on vegetable samples, yielding the highest accuracy volume [6].

Full cream powdered milk is rich in fat. The covalent bond between fatty acids is difficult to break down, while fat has a low relative potential of oxidation, which means that there is a need to perform destruction at temperature up to 200 °C with a greater amount of oxidizing acid (10 mL). Lactose (D-galactose and D-glucose) constitutes a major simple sugar in milk [41]. Therefore, the initial temperature of digestion begins at 130 °C. Such destruction process was previously carried out by Belete et al. [42] in cow milk samples, using the destruction temperature of 165–190 °C following a 10 min pre-destruction phase.

Canned fish represents a food sample with high protein content. The main protein content in fish, i.e., actin and myosin, is susceptible to denaturation when exposed to microwaves (Fig. 4) [43]. Although these myofibrillar proteins start to denature at about 85 °C, a higher temperature was needed to induce denaturation when they exist in canned fish, reaching up to 130 °C. Protein molecules contain peptide bonds with a large molecular weight; thus, the amount of oxidizing acid needed is 7 mL.

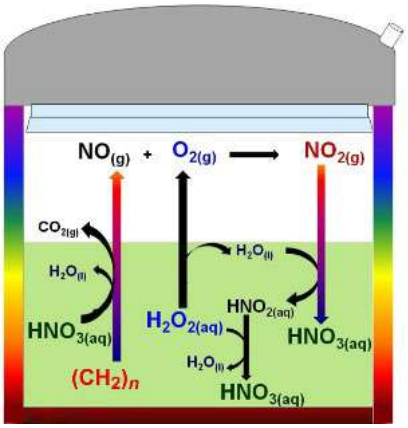

Fig 3. The reaction process in the microwave digestion vessel

The presence of minerals can affect the quality of food. Copper (Cu) and iron (Fe) play a role in oxidation-reduction reactions because the oxidation potential can cause unwanted changes in processed foods related to fat oxidation which promotes a decrease in the nutritional value of food [44]. In the process of oxidation of fat/oil, Fe and Cu are able to accelerate the process of initiation, propagation, and termination (acting as a catalyst). In addition, the valence of Fe dictates the color pigment of myoglobin and hemoglobin in fresh meat; ferric (+3 valence state) accounts for brown color, while ferrous (+2 valence state) accounts for red color. The reaction of Fe with sulfur in canned food also induces the formation of iron sulfide (FeS) complex, which is a black solid.

Enzymatic browning is also linked to the presence of Cu. This mineral serves as a cofactor of the enzyme polyphenol oxidase (PPO), as a catalyst for non-enzymatic browning reactions and oxidation of ascorbic acid. Zn can stabilize the color of canned green beans. ZnO can be used as a coating agent on canned foods capable of preventing the formation of FeS during the heating process. The levels of Fe, Zn, and Cu obtained through the standard and modified methods can be seen in Table 12.

Statistically, we found that data obtained from both protocols did not differ significantly, as evidenced by p-value > α = 5% for all samples examined.

In terms of time and cost, the modified method seemed to be more preferable than the standard method. The hydrogen peroxide was less needed in the currently developed method (1 mL for each sample) than the standard method (2 mL for each sample). It is noteworthy that hydrogen peroxide is three times more expensive than nitric acid. Additionally, the modified method required a shorter time of the process (30 min) than the standard method (45 min).

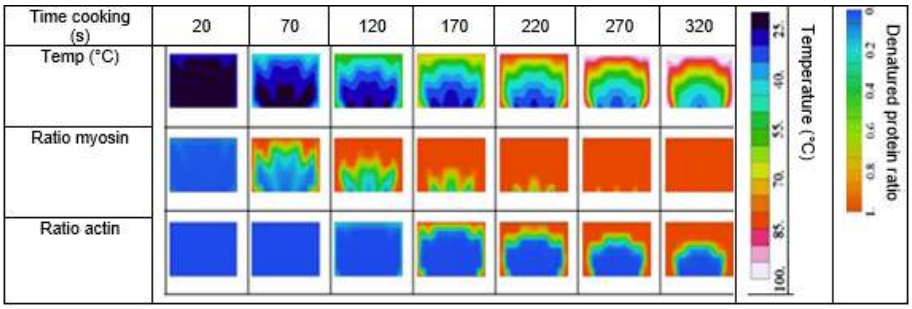

Fig 4. The process of actin and myosin denaturation [42]

Table 12. The result of analysis mineral with standard and modification method

Samples	Standard method (mg/kg)			Modified method (mg/kg)		
	Fe	Zn	Cu	Fe	Zn	Cu
Full cream powdered milk	24.99	24.62	0.85	24.60	24.54	0.84
SD	0.80	0.13	0.01	0.20	0.19	0.02
% RSD	3.21	0.51	1.69	0.81	0.76	2.95
2/3 CV Horwitz	6.57	6.59	10.92	6.59	6.59	10.95
p-value	0.575	0.714	0.561			
Canned peas	2.88	7.11	1.31	2.87	7.02	1.36
SD	0.06	0.03	0.02	0.04	0.04	0.01
% RSD	2.11	0.44	1.35	1.24	0.57	0.99
2/3 CV Horwitz	9.10	7.94	10.23	9.10	7.95	10.18
p-value	0.827	0.222	0.09			
Canned fish	23.44	9.78	1.04	23.44	9.47	0.99
SD	0.23	0.24	0.03	0.23	0.05	0.03
% RSD	0.98	2.43	2.50	0.98	0.49	2.70
2/3 CV Horwitz	6.63	7.57	10.60	6.63	7.60	10.67
p-value	0.245	0.211	0.262			

Table 13. Solvent alternative test

Parameters	Mineral content (mg/kg)					
	Cu		Zn		Fe	
	Demineralized water	HNO_3 0.05M	Demineralized water	HNO_3 0.05M	Demineralized water	HNO_3 0.05M
average (mg/kg)	0.94	1.25	24.34	25.88	24.72	28.86
SD	0.06	0.08	0.50	1.34	0.53	0.43
% RSD	6.78	6.10	2.07	5.18	2.14	1.50
CV Horwitz	16.15	15.48	9.89	9.80	9.87	9.646
p-value	0.000		0.028		0.000	

The suitability of solvent alternative was also observed, in which this experiment was only tested for full cream powdered milk. Toughness test was carried out to evaluate the effects of the solvents on analytical results. In this case, 0.05M HNO_3 was used instead of demineralized water; thus the sample condition was similar to the standard solution. Furthermore, the addition of acid to the solution can contribute towards igniting and preventing precipitation and absorption on the glass wall. The solubility of mineral seemed to possess a positive relation to the length of exposure to nitric acid [45]. The results showed that the type of solvent significantly altered the test results ($p < 0.05$) (Table 13). This suggests that replacement with 0.05 M HNO_3 was unacceptable.

The F-AAS performance test aims to ensure that the instrument is feasibly used in the analysis process to produce valid data. The number of atoms distributed in the flame is different, so it is necessary to determine the different burner height for each mineral.

■ CONCLUSION

Modification methods in the process of destruction for analysis of Fe, Zn, and Cu in various food matrices (canned peas, full cream powdered milk, and canned fish) were not significantly different from AOAC (2012) and has fulfilled the acceptability requirements for use in laboratory analysis. Mineral analysis result obtained by the modified method in the process of destruction for Fe, Zn and Cu minerals for canned peas: 2.87; 7.02;1.36 mg/kg, full cream powdered milk 24.60; 24.54; 0.86 mg/kg, canned fish: 23.44; 9.47; 0.99 mg/kg.

■ ACKNOWLEDGMENTS

Authors would like to thank AKA Bogor Polytechnic for financial support and research facilities of this work.

■ REFERENCES

[1] Lazarte, C., Carlsson, N.G., Almgren, A., Sandberg, A.S., and Granfeldt, Y., 2015, Phytate, zinc, iron, and calcium content of common Bolivian food and implications for mineral bioavailability, *J. Food Compos. Anal.*, 39, 111–119.

[2] Gómez-Nieto, B., Gismera, M.J., Sevilla, M.T., and Procopio, J.R., 2017, Determination of essential elements in beverages, herbal infusions and dietary supplements using a new straightforward sequential approach based on flame absorption spectrometry, *Food Chem.*, 219, 69–75.

[3] Zhu, F., Fan, W., Wang, X., Qu, L., and Yao, S., 2011, Health risk assessment of eight heavy metals in nine varieties of edible vegetable oils consumed in China, *Food Chem. Toxicol.*, 49 (12), 3081–3085.

[4] Tuzen, M., 2009, Toxic and essential trace elemental contents in fish species from the Black Sea, Turkey, *Food Chem. Toxicol.*, 47 (8), 1785–1790.

[5] Antoine, J.M.R., Fung, L.A.H., Grant, C.N., Dennis, H.T., and Lalor, G.C., 2012, Dietary intake of minerals and trace elements in rice on the Jamaican market, *J. Food Compos. Anal.*, 26 (1-2), 111–121.

[6] Bakkali, K., Martos, N.R., Souhail, B., and Ballesteros, E., 2009, Characterization of trace metals in vegetables by graphite furnace atomic absorption spectrometry after closed vessel microwave digestion, *Food Chem.*, 116 (2), 590–594.

[7] Helaluddin, A.B.M., Khalid, R.S., Alaama, M., and Abbas, S.A., 2016, Main analytical techniques used for elemental analysis in various matrices, *Trop. J. Pharm. Res.*, 15 (2), 427–434.

[8] Sharma, B., and Tyagi, S., 2013, Simplification of metal ion analysis in fresh water samples by atomic absorption spectroscopy for laboratory students, *J. Lab. Chem. Educ.*, 1 (3), 54–58.

[9] Lajunen, L.H., and Perämäki, P., 2004, *Spectrochemical analysis by atomic absorption and emission*, 2nd Ed., The Royal Society of Chemistry, Cambridge, UK, 6–8.

[10] Bader, N.R., and Zimmermann, B., 2012, Sample preparation for atomic spectroscopic analysis: An overview, *Adv. Appl. Sci. Res.*, 3 (3), 1733–1737.

[11] Korn, M.G.A., Morte, E.S., dos Santos, D.C.M.B., Castro, J.T., Barbosa, J.T.P., Teixeira, A.P., Fernandez, A.P., Welz, B., dos Santos, W.P.C., dos Santos, E.B.G.N., Korn, M., 2008, Sample preparation for the determination of metals in food samples using electroanalytical methods–A review, *Appl. Spectrosc. Rev.*, 43 (2), 67–92.

[12] Silvestre, M.D., Lagarda, M.J., Farré, R., Martínez-Costa, C., and Brines, J., 2000, Copper, iron and zinc determination in human milk using FAAS with microwave digestion, *Food Chem.*, 68 (1), 95–99.

[13] Bragg, S.A., and Xue, Z.L., 2011, Optimization of dry ashing of whole blood samples for trace metal analysis, *Am. J. Anal. Chem.*, 2, 979–983.

[14] Idera, F., Omotola, O., Adedayo, A., and Paul, U.J., 2015, Comparison of acid mixtures using conventional wet digestion methods for determination of heavy metals in fish tissues, *JSRR*, 8 (7), 1–9.

[15] Sneddon, J., Hardaway, C., Bobbadi, K.K., and Reddy, A.K., 2006, Sample preparation of solid samples for metal determination by atomic spectroscopy-An overview and selected recent applications, *Appl. Spectrosc. Rev.*, 41 (1), 1–14.

[16] Elmastas, M., Can, M., Uzun, S., and Aboulenein, H.Y., 2005, Determination of copper zinc, cadmium, and nickel in cows', goats', ewes', and human milk samples using flame atomic absorption spectrometry (FAAS) microwave digestion, *Anal. Lett.*, 38 (1), 157–165.

[17] Altundag, H., and Tuzen, M., 2011, Comparison of dry, wet, and microwave digestion method for the multi-element determination in some dried fruit samples by ICP-OES, *Food Chem. Toxicol.*, 49 (11), 2800–2807.

[18] Santos, J., Oliva-Teles, M.T., Delerue-Matos, C., and Oliveira, M.B.P.P., 2014, Multi-elemental analysis of ready-to-eat "baby leaf" vegetables using microwave digestion and high-resolution continuum source atomic absorption spectrometry, *Food Chem.*, 151, 311–316.

[19] Ranasinghe, P., Weerasinghe, S., and Kaumal, M.N., 2016, Determination of heavy metals in tilapia using various digestion methods, *IJSRIT*, 3 (6), 39–48.

[20] Association of Official Analytical Chemists (AOAC), 2012, *Official methods of analysis agricultural chemicals*, 10th Ed., Washington DC., (15), 237–242.

[21] National Association of Testing Authorities (NATA), 2004, *Guidelines for the validation and verification of quantitative and qualitative test methods*, Australia.

[22] Food and Drug Administration (FDA), 2014, *Elemental analysis manual for food and related product: Digestion and separation*, Rockville Maryland, USA, 2–3.

[23] Fiamegos, Y., Vahcic, M., Emteborg, H., Snell, J., Raber, G., Cordeiro, F., Robouch, P., and de la Calle, B., 2016, Determination of toxic trace element in canned vegetables. The importance of sample preparation, *TrAC, Trends Anal. Chem.*, 85, 57–66.

[24] United States Department of Agriculture (USDA), 2006, *Canned Peas, Canned Fish, Full Cream Powdered Milk*, USDA Publisher, United State.

[25] De Melo, I.L.P., and de Almeida-Muradian, L.B., 2011, Comparison of methodologies for moisture determination on dried bee pollen samples, *Ciênc. Tecnol. Aliment.*, 31 (1), 194–197.

[26] Mbatchou, V.C., and Dawda, S., 2013, The nutritional composition of four rice varieties grown and used in different food preparations in Kassena-Nankana district, Ghana, *Int. J. Res. Chem. Environ.*, 3 (1), 308–315.

[27] Solihat, I., Faridah, D.N., and Yuliana, N.D., 2018, Validation method of Flame-AAS with microwave

digestion for mineral analysis in carbohydrate-rich samples, *Molekul*, 13 (2), 133–140.

[28] Momen, A.A., Zachariadis, G.A., Anthemidis, A.N., and Stratis, J.A., 2007, Use of fractional design for optimization of digestion procedures followed by multi-element determination of essential and non-essential elements in nuts using ICP-OES technique, *Talanta*, 71 (1), 443–451.

[29] Belay, K., and Tadesse, A., 2014, Comparison of digestion methods for determination of Pb (II), Cr (VI) and Cd (II) contents in some Ethiopia spices using atomic absorption spectroscopy, *IJASR,* 2 (3), 42–53.

[30] Volkovskaya, I.I., Semenov, V.E., and Rybakov, K.I., 2017, Effective magnetic permeability of compacted metal powders at microwave frequencies, *EPJ Web Conf.*, 149–02008.

[31] Rybakov, K.I., and Semenov, V.E., 2017, Effective microwave dielectric properties of ensembles of spherical metal particles. *IEEE Trans. Microwave Theory Tech.*, 65 (5), 1479–1487.

[32] Ghanthimathi, S., Abdullah, A., Salmijah, S., Ujang, T., and Izzah, A.N., 2012, Comparison of microwave-assisted acid digestion methods for ICP-MS determination of total arsenic in fish tissue, *Sains Malays.*, 41 (12), 1557–1564.

[33] Yang, L., Yan, Q., Cao, Y., and Zhang, H., 2012, Determination of mineral elements of some coarse grains by microwave digestion with inductively coupled plasma atomic emission spectrometry, *E-J. Chem.*, 9 (1), 93–98.

[34] Nóbrega, J.A., Pirola, C., Fialho, L.L., Rota, G., de Campos Jordão, C.E.K.M.A., and Pollo, F., 2012, Microwave-assisted digestion of organic samples: How simple can it become?, *Talanta*, 98, 272–276.

[35] Demirel, S., Tuzen, M., Saracoglu, S., and Soylak, M., 2008, Evaluation of various digestion procedures for trace element contents of some food materials, *J. Hazard. Mater.*, 152 (3), 1020–1026.

[36] Barbosa, J.TP., Santos, C.M.M., Peralva, V.N., Flores, E.M.M., Korn, M., Nóbrega, J.A., and Korn, M.G.A., 2015, Microwave-assisted diluted acid digestion for trace element analysis of edible soybean products, *Food Chem.*, 175, 212–217.

[37] Ghriss, O., Amor, H.B., Jeday, M.R., and Thomas, D., 2019, Nitrogen oxides absorption into an aqueous nitric acid solution containing hydrogen peroxide tested using a cables-bundle contactor, *Atmos. Pollut. Res.*, 10 (1), 180–186.

[38] Bizzi, C.A., Nóbrega, J.A., and Barin, J.S., 2014, "Diluted Acids in Microwave-Assisted Wet Digestion" in *Microwave-Assisted Sample Preparation for Trace Element Determination*, 1st Ed., Eds. de Moraes Flores, E.M., Elsevier, 179–204.

[39] Chen, Y., Ye, R., Yin, L., and Zhang, N., 2014, Novel blasting extrusion processing improves the physicochemical properties of soluble dietary fiber from soybean residue and in vivo evaluation, *J. Food Eng.*, 120, 1–8.

[40] Brummer, Y., Kaviani, M., and Tosh, S.M., 2015, Structural and functional characteristic of dietary fibre in beans, lentils, peas and chickpeas, *Food Res. Int.*, 67, 117–125.

[41] Mourad, G., Bettache, G., and Samir, M., 2014, Composition and nutritional value of raw milk, *Issues Biol. Sci. Pharm. Res.,* 2 (10), 115–122.

[42] Belete, T., Hussen, A., and Rao, V.M., 2014, Determination of concentration of selected heavy metals in cow's milk: Borena zone, Ethiopia, *J. Health Sci.*, 4 (5), 105–112.

[43] Liu, S., Yu, X., Fukuoka, M., and Sakai, N., 2014, Modeling of fish boiling under microwave irradiation, *Int. J. Food Eng.*, 140, 9–18.

[44] Damodaran, S., Parkin, K.L., and Fennema, O.R., 2007, *Fennema's Food Chemistry*, 4th Ed., CRC Press, Boca Raton, Florida, US.

[45] Mohammed, E., Mohammed, T., and Mohammed, A., 2017, Optimization of an acid digestion procedure for the determination of Hg. As. Sb. Pb and Cd in fish muscle tissue, *MethodsX*, 4, 513–523.

Statistical Modelling of Oil Removal from Surfactant/Polymer Flooding Produced Water by Using Flotation Column

Ku Esyra Hani* **and Mohammed Abdalla Ayoub**

Department of Petroleum Engineering, Faculty of Geosciences and Petroleum Engineering, Universiti Teknologi Petronas, Bandar Seri Iskandar, Tronoh, Perak 31750, Malaysia

** **Corresponding author:***

tel: +60189480311
email: ku_g03452@utp.edu.my

Received: September 3, 2018
Accepted: January 26, 2019

DOI: 10.22146/ijc.42820

Abstract: *The objective of this study was to investigate the effect of polymer (GLP-100) and surfactant (MFOMAX) towards the efficiency of oil removal in a flotation column by using the Response Surface Methodology (RSM). Various concentrations of surfactant (250, 372 and 500 ppm) and polymer (450, 670, and 900 ppm) produced water were prepared. Dulang crude oil was used in the experiments. Flotation operating parameters such as gas flow rate (1–3 L/min) and duration of flotation (2–10 min) were also investigated. The efficiency of oil removal was calculated based on the difference between the initial concentration of oil and the final concentration of oil after the flotation process. From the ANOVA analysis, it was found that the gas flow rate, surfactant concentration, and polymer concentration contributed significantly to the efficiency of oil removal. Extra experiments were conducted to verify the developed equation at a randomly selected point using 450 ppm of polymer concentration, 250 ppm of surfactant concentration, 3 L/min gas flowrate and duration of 10 min. From these extra experiments, a low standard deviation of 1.96 was discovered. From this value, it indicates that the equation can be used to predict the efficiency of oil removal in the presence of surfactant and polymer (SP) by using a laboratory flotation column.*

Keywords: *enhanced oil recovery; produced water treatment; flotation process; statistical model*

■ INTRODUCTION

Management of produced water from Enhanced Oil Recovery (EOR) is one of the problems associated with the oil recovery since it produced large volumes of saline water, which should be managed as the by-product. The produced water contains several contaminants such as mineral ions, dispersed oil, grease, organics, heavy metals and other different contaminants [1] such as surfactant, polymer or the mixture of both surfactant and polymer (SP) resulting from the EOR injection. Good management of the produced water is important since it plays a major role in the environmental concern for reuse or discharge. Therefore, the produced water treatment is economically reasonable and technically feasible. The objectives of the produced water treatment are to remove the oil, desalination, removal of soluble organics, naturally radioactive materials, dissolve gases, suspended particles and sand, disinfection and softening [1]. These polluting components must be minimized to allow the level and threshold of oil in the produced water is limited by legislation during the discharging [2]. In Malaysia, the limit of monthly oil discharged is below 40 ppm [3].

The technologies used for the produced water treatment depends on whether the installation is based on onshore or offshore. The most commonly used techniques for separation of the oily wastewater include gravity separation [4], membrane filtration separation [5], flotation [6-8] and hydrocyclone [9-11]. For offshore installation, the footprint is generally a critical factor compared to the onshore installation because of the space limitation. Low energy, simple and high footprint technologies must be employed to remove the contaminants to maintain water quality target and for cost reduction purpose. Such a treatment process can be

improved by implementing the flotation process. A flotation process uses gas injection to create gas bubbles that help to increase the oil removal by attaching themselves to the oil droplets and bring the oil droplets to the surface for removal.

However, the efficiency of the flotation process in the produced water treatment system has degraded during the implementation of SP flooding in EOR due to the stable emulsions that are formed in the production fluids [4] caused by the SP chemicals. The function of SP in EOR is to increase oil recovery. In the past research, studies on the effect of the SP concentration to the viscosity, IFT and oil droplets size distribution that includes the coalescence and breakup of the oil droplets have been widely carried out. Some of them found that in the presence of a large amount of polymer, the viscosity of the produced water tend to increase which made the oil droplets rise very slowly to the surface. As a result, this makes the separation between the oil and water become inefficient [12]. However, several types of research found the presence of polymer in a lower concentration has triggered the separation of the oil and water by making the oil droplets bigger in size which decreases the time for oil droplets to rise to the surface [13]. Surfactant, on the other hand, has lower interfacial tension (IFT) between the oil and water which prevents the oil droplets from coalescing and decreases the separation efficiency between the oil and water.

Although the effect of SP to the oil-water separation have been investigated in the water treatment industry [13-19], little attention has been given to its effect by specifically using the flotation process. The oil and water separation in the flotation unit with the presence of gas bubbles is a complex process which is not well understood. This knowledge gap further increases the difficulty to optimize the flotation system. Moreover, the currently available flotation models failed to improve the efficiency of oil removal in the presence of SP [20-22] since it was tested in the conditions without SP chemicals.

Therefore, the main objective of this study was to investigate the performance of the flotation process in the removal of oil droplets from the SP containing produced water. The effect of SP, as well as other flotation operating parameters such as the gas flow rate and the duration of the flotation to the efficiency of oil removal, have been analyzed. Based on the experimental results, a statistical model was developed to predict the efficiency of oil removal by using the flotation process in the presence of SP chemicals.

■ EXPERIMENTAL SECTION

Materials

The type of surfactant, polymer and crude oil used in the study were MFOMAX, GLP-100, and Dulang crude oil respectively. These chemicals were supplied by PETRONAS Research Sdn Bhd. Brine was prepared by adding the different type of salts at a different concentration as shown in Table (1). All of these salts were purchased from R&M Chemicals, India.

In this research, the Dulang crude oil has a low water content of 0.01%, a low waxy point of 25.9 °C with the density 0.7987 g/cm^3 and viscosity of 3.1 cP at 60 °C. The viscosity was measured by using rheometer Anton Paar Model MCR302 and the oil droplets size distribution was measured by using particle size analyzer, DT-1202 from the Dispersion Technology.

Procedure

Synthetic produced water preparation

The synthetic SP produced water was prepared by mixing the brine, Dulang crude oil and various SP concentration based on the previous research. Synthetic SP produced water emulsion was prepared by mixing the MFOMAX (250–500 ppm) [4,23], GLP-100 (450–900 ppm) [23-24], Dulang crude oil with initial concentration of 1000 ppm [18,25] and brine at 14000 ppm (Table 1)

Table 1. Brine compositions

Salts	g/L
$CaCl_2.(H_2O)_2$	0.7251
$MgCl_2.(H_2O)_6$	0.7726
NaCl	10.0267
$FeCl_3$	0.0009
$SrCl_2.(H2O)_6$	0.0295
KCl	0.3129
$NaHCO_3$	3.6065
Na_2SO_4	0.7840

under the shear rate of 13000 rpm at 10 min [23,26] by using the Ultra Turrax mixer model T18. The range of the chemicals was selected based on the actual conditions used in Dulang Oilfield.

Experimental set-up and procedure

The as-prepared synthetic SP produced water was then fed into the flotation column. The schematic diagram of the process is shown in Fig. 1. The diameter of the flotation column is 5 cm and a length of 100 cm.

Nitrogen gas was injected through a 40–100 μm pores sparger plate at the bottom of the flotation column for the total time of 10 min. The pores size and duration of the flotation process was estimated from the work according to the work by Eftekhardadkhah et al. [2]. Samples at the water outlet were collected for every 2, 6 and 10 min and the oil concentration in the effluents was measured by a TD-500D device (UV-fluorescence technique). The efficiency of oil removal of the flotation column can be calculated by using Eq. (1).

$$\varepsilon = 1 - \frac{C_{effluent}}{C_{inlet}} \times 100\% \quad (1)$$

where $C_{effluent}$ is the oil concentration in the effluent and C_{inlet} is the oil concentration in the inlet.

Statistical model

The statistical analysis was performed by using Design Expert 9.0. A total of 45 runs were conducted based on the response surface methodology study by using randomized quadratic design to observe the experimental parameters. Based on the data obtained using this experimental design, a quartic equation was generated to establish the correlation between the independent variables and dependent variables. The independent variables in this study are the gas flow rate (L/min) (X_1), duration (min) (X_2), the concentration of MFOMAX (ppm) (X_3) and concentration of GLP-100 (ppm) (X_4). The predicted response of flotation efficiency (%) was designated as Y. The actual and coded values were summarized in Table 2.

■ RESULTS AND DISCUSSION

ANOVA Statistical Analysis

The quartic model equation represents the flotation efficiency (%) in the presence of SP (Y) which was expressed as the functions of concentration of polymer (ppm) (X_1), concentration of surfactant (ppm) (X_2), gas flow rate (L/min) (X_3) and duration of flotation (min) (X_4) for coded factors as shown in Eq. (2).

$$\begin{aligned} Y = {} & 26.32 + 11X_1 + 6.75X_2 - 5.99X_3 + 5.10X_4 - 0.00056X_1X_2 \\ & + 9.68X_1X_3 - 1.60X_1X_4 - 3.44X_2X_3 - 28.53X_2X_4 \\ & - 6.35X_3X_4 + 2.60X_1^2 - 36.64X_2^2 + 0.068X_1X_2X_3 \\ & - 8.33X_1X_2X_4 + 4.72X_1X_3X_4 + 2.31X_2X_3X_4 \\ & - 3.96X_1^2X_2 + 6.98X_1^2X_3 + 0.49X_1^2X_4 - 5.16X_1X_2^2 \\ & - 5.62X_2^2X_3 - 5.53X_2^2X_4 + 3.08X_2^3 + 6.11X_1^2X_2X_4 \\ & - 9.47X_1X_2^2X_3 + 17.01X_2^3X_4 + 30.30X_2^4 \end{aligned} \quad (2)$$

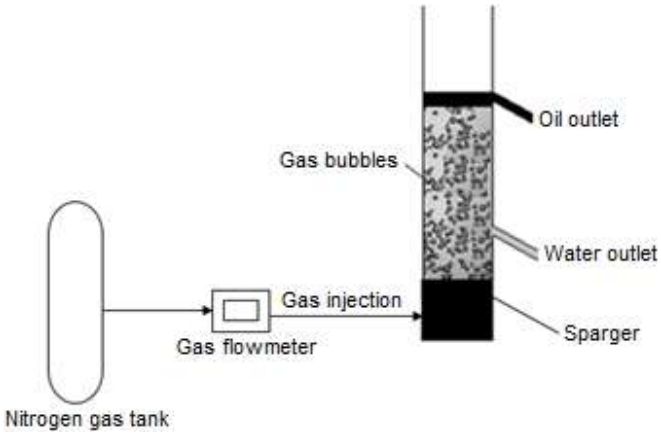

Fig 1. Schematic diagram of the flotation process

Table 2. Actual and coded experimental values

Parameter	Symbol	Parameter Level		
		Low -1	Center 0	High +1
		Actual value		
Gas flowrate (L/min)	X_1	1	3	5
Duration (min)	X_2	2	6	10
MFOMAX concentration (ppm)	X_3	250	372	500
GLP-100 concentration (ppm)	X_4	450	670	900

Table 3. The significance of the parameter

Source	F	p-value	
	Value	Prob > F	
Model	10.51	< 0.0001	Significant
X_1-Gas flowrate	21.00	0.0003	Significant
X_2-Durations	1.07	0.3157	
X_3-Surfactant concentration	10.17	0.0054	Significant
X_4-Polymer concentration	7.36	0.0148	Significant
X_1X_2	0.00	0.9974	
X_1X_3	16.25	0.0009	Significant
X_1X_4	1.31	0.2682	
X_2X_3	6.51	0.0207	Significant
X_2X_4	19.11	0.0004	Significant
X_3X_4	38.20	< 0.0001	Significant
X_1^2	1.17	0.2950	
X_2^2	4.09	0.0591	
$X_1X_2X_3$	0.00	0.9688	
$X_1X_2X_4$	23.51	0.0002	Significant
$X_1X_3X_4$	11.40	0.0036	Significant
$X_2X_3X_4$	2.94	0.1048	
$X_1^2X_2$	1.77	0.2007	
$X_1^2X_3$	10.91	0.0042	Significant
$X_1^2X_4$	0.054	0.8196	
$X_1X_2^2$	3.05	0.0985	
$X_2^2X_3$	6.06	0.0248	Significant
$X_2^2X_4$	5.87	0.0269	Significant
X_2^3	0.18	0.6759	
$X_1^2X_2X_4$	4.23	0.0555	
$X_1X_2^2X_3$	10.30	0.0051	Significant
$X_2^3X_4$	5.52	0.0312	Significant
X_2^4	3.07	0.0979	

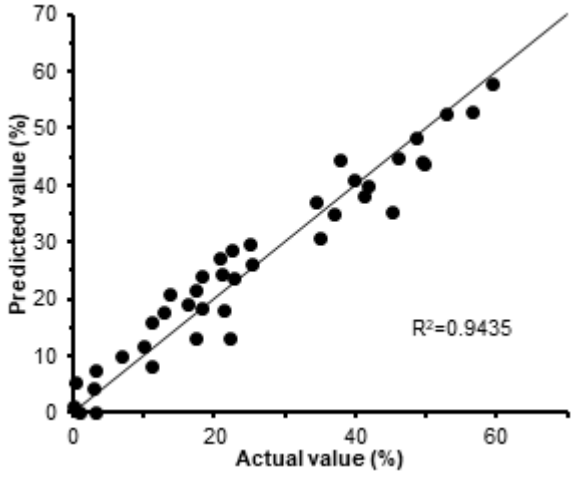

Fig 2. Actual and predicted data

Table 3 shows the significance of the parameters to the efficiency of oil removal in the flotation process. By referring to Table 3, the parameters that are significant in this model are the gas flow rate (L/min), MFOMAX concentration (ppm) and GLP-100 concentration (ppm) with the P-values of 0.0003, 0.0054 and 0.0148 respectively. Then, the actual and predicted values were plotted in a graph as shown in Fig. 2. The coefficient of R^2 was found to be 0.9435. The high value of R^2 is closer to 1 which indicates that the predicted model values were correlated well with the experimental values. This good correlation strongly illustrated that the quartic equation is a good representation of the experimental system. Extra experiments were conducted to validate the equation.

Validation of the Equation

Three experiments were performed to validate Eq. (2). A random condition with the gas flow rate of 3 L/min, polymer concentration of 450 ppm, the surfactant concentration of 250 ppm and duration of 10 min with the efficiency of 52.78% was selected for the validation. The results are shown in Table 4.

From the table, the mean value for the actual efficiency was 51.1% while the predicted efficiency value for the condition was 52.78%. The STD was as low as 1.96 indicating that this model can be used to predict the efficiency of the oil removal in the presence of SP at a lab condition.

Contour Plots

Contour plots for the effect of increasing surfactant concentration and gas flow rate at low polymer concentration (450 ppm) for 10 min as shown in Fig. 3.

Table 4. Actual and prediction efficiency for the validation experiments

	Actual Efficiency (%)	Prediction Efficiency (%)	Error
Point 1	49.3	52.78	-3.48
Point 2	53.2	52.78	0.42
Point 3	50.9	52.78	-1.88
Mean Efficiency	51.133	STD	1.960

The results for 2 and 6 min of flotation duration ware not shown since the factor was not significant to the oil and water separation as indicated in Table 3. In Fig. 3, the increase of surfactant concentration at 1 L/min had an insignificant effect on the efficiency of oil removal. However, when the gas flow rate increased to 3 and 5 L/min at 250 ppm surfactant concentration, the efficiency of the oil removal increased to 52.82% for 3 L/min and 59.4% for 5 L/min. This is because the increment of gas flow rate tends to increase the potential for attachment of the gas bubbles to the oil droplets. However, at 3 L/min and 5 L/min, increasing the surfactant concentration decreased the efficiency of the oil removal from 52.82 to 34.94% (at 3 L/min) and 59.4 to 39.67% (5 L/min) respectively. In the previous research, an increment in surfactant concentration alone (with the absence of polymer) tend to decrease the efficiency of the oil removal because of the decreasing in the IFT [12]. This result was contradicting at 1 L/min of gas flow rate as the presence of the polymer has balanced out the effect of the efficiency of oil removal by making the oil droplets flocculate [13,27]. This flocculation maintained the rate of oil removal in the presence of the surfactant. The same findings [12] were observed at 3 L/min and 5 L/min whereby increment of surfactant concentration tend to decrease the efficiency of the oil removal.

Further investigation was done to study the effect of polymer concentration on the flocculation of the oil droplets. Fig. 4 shows the effect of GLP-100 concentration on the oil droplets size. From the figure, the size range of the oil droplets gradually increased as the polymer concentration increased from 200 to 900 ppm. The size of oil droplets in the absence of polymer shown the smallest compared to the size in the presence of the polymer. Polymer promotes the coalescence of the oil droplets. This trend was inlined with other researchers [12,27].

Contour plots for the effect of surfactant and gas flowrate at high polymer concentration (900 ppm) at 10 min flotation duration were shown in Fig. 5. At a higher concentration of polymer (900 ppm), the increase in surfactant concentration at 1 L/min decreased the efficiency of the oil removal from 49.51% at 250 ppm of surfactant to 6.89% at 500 ppm of surfactant concentration.

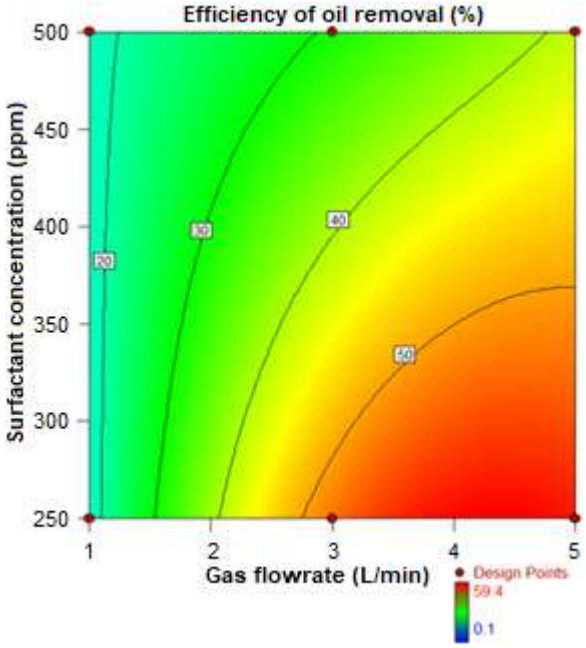

Fig 3. Contour plots for the increasing surfactant concentration and gas flow rate at low polymer concentration (450 ppm) at 10 min

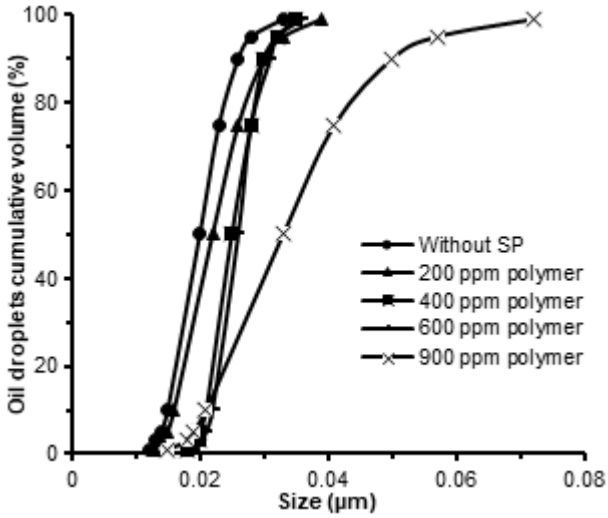

Fig 4. The effect of GLP-100 on the oil droplets size distribution

At 3 L/min, the efficiency dropped from 34.36% at 250 ppm surfactant concentration to 3% at 500 ppm surfactant concentration. Similar findings were observed at 5 L/min. The efficiency of oil removal decreased from 25.21 to 9.96% at 250 to 500 ppm. Comparing Fig. 3 and 5, the decreased in the efficiency was more significant in higher polymer concentration (900 ppm) (Fig. 3)

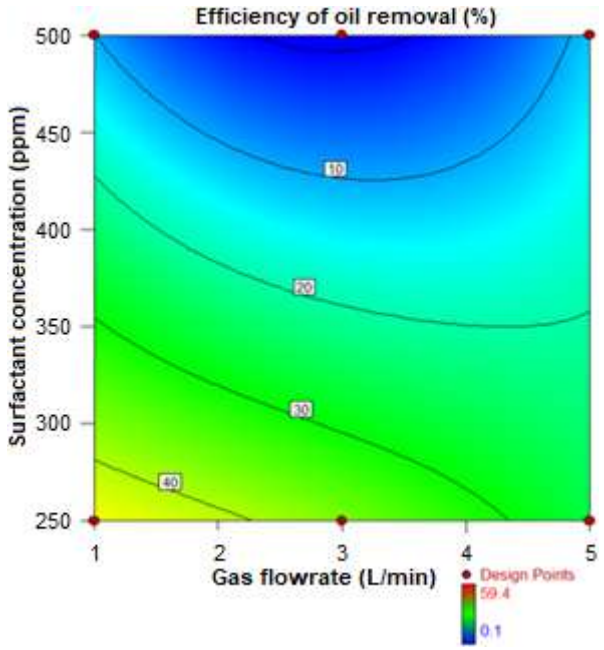

Fig 5. Contour plots for the effect of surfactant and gas flow rate at a high polymer concentration (900 ppm) at 10 min flotation duration

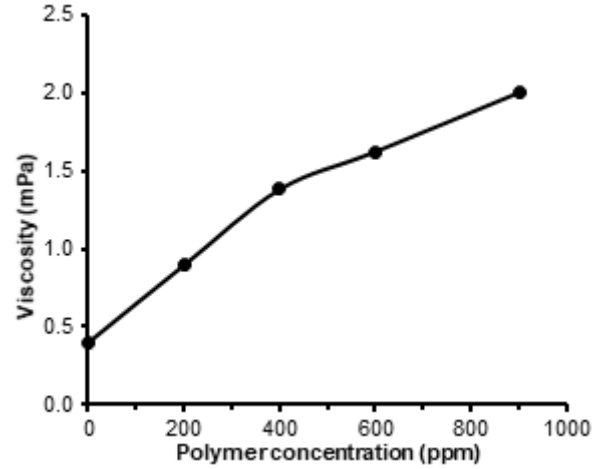

Fig 6. The effect of polymer concentration on the viscosity of the emulsion

compared to 450 ppm polymer concentration (Fig. 5). This is due to the increase in the emulsion viscosity caused by the increase in polymer concentration [13]. To validate this statement, the viscosity of the emulsion was tested with the increasing of polymer concentration as shown in Fig. 6. By referring to the figure, the increase of the polymer concentration tends to increase the viscosity of the emulsion. Therefore, instead of making the oil droplets flocculate, the high polymer concentration increased the viscosity of the emulsion and restricted the movement of the oil droplets to the surface. The effect of viscosity at 900 ppm overcome the flocculation effect at 450 ppm [13].

■ CONCLUSION

A statistical model was developed to describe the efficiency of oil removal in the presence of SP (MFOMAX and GLP-100). It was found that the gas flow rate, surfactant concentration, and polymer concentration affect the efficiency of the oil removal significantly while the duration of the flotation was not significant in the flotation process. Experiments were carried out to access the developed quartic equation and the comparison of the predicted value matched the experimental value with STD 1.96. Low STD indicated that this equation can be used to predict the efficiency of oil removal at a lab scale condition. This study can provide a guideline for the flotation process optimization in SP containing produced water.

■ ACKNOWLEDGMENTS

This study was supported by the Centre of Enhanced Oil recovery (CORERO), University Teknologi PETRONAS, in collaboration with PETRONAS Research Sdn. Bhd. We would like to thank PETRONAS for providing the grant No 0153CB-006 (2015-2018) for this project.

■ REFERENCES

[1] Fakharian, H., Ganji, H., and Naderifar, A., 2017, Saline produced water treatment using gas hydrates, *J. Environ. Chem. Eng.*, 5 (5), 4269–4273.

[2] Eftekhardadkhah, M., Aanesen, S.V., Rabe, K., and Øye, G., 2015, Oil removal from produced water during laboratory- and pilot-scale gas flotation: The influence of interfacial adsorption and induction times, *Energy Fuels*, 29 (11), 7734–7740.

[3] Yassin, A.A.M., 1988, Legislation on oil pollution prevention and control during petroleum production, *Jurnal Teknologi*, 11, 1–6.

[4] Al-Kayiem, H.H., and Khan, J.A., 2017, Evaluation of alkali/surfactant/polymer flooding on separation

and stabilization of water/oil emulsion by statistical modelling, *Energy Fuels*, 31 (9), 9290–9301.

[5] Zsirai, T., Al-Jaml, A.K., Qiblawey, H., Al-Marri, M., Ahmed, A., Bach, S., Watson, S., and Judd, S., 2016, Ceramic membrane filtration of produced water: Impact of membrane module, *Sep. Purif. Technol.*, 165, 214–221.

[6] da Silva, S.S., Chiavone-Filho, O., de Barros Neto, E.L., and Foletto, E.L., 2015, Oil removal from produced water by conjugation of flotation and photo-Fenton processes, *J. Environ. Manage.*, 147, 257–263.

[7] Hayatdavoudi, A., 2006, Removing oil and grease from produced water using micro bubble flotation technique, *The 8th International Conference on Health, Safety and Environment in Oil and Gas Exploration and Production*, Society of Petroleum Engineers, 2-4 April 2006, Abu Dhabi, UAE.

[8] Casaday, A.L., 1993, Advances in flotation unit design for produced water treatment, *SPE Production Operations Symposium*, Society of Petroleum Engineers, 21-23 March 1993, Oklahoma City, Oklahoma, USA.

[9] Santander, M., Rodrigues, R.T., and Rubio, J., 2011, Modified jet flotation in oil (petroleum) emulsion/water separations, *Colloids Surf., A*, 375 (1-3), 237–244.

[10] Pratarn, W., Kanawut, S., and Thanit, S., 2013, Experimental investigation of de-oiling hydrocyclone, *Key Eng. Mater.*, 545, 230–235.

[11] Bram, M.V., Hassan, A.A., Hansen, D.S., Durdevic, P., Pedersen, S., and Yang, Z., 2015, Experimental modeling of a deoiling hydrocyclone system, *The 20th International Conference on Methods and Model in Automation Robotics MMAR 2015*, 1080–1085.

[12] Deng, S., Bai, R., Chen, J.P., Yu, G., Jiang, Z., and Zhou, F., 2002, Effects of alkaline/surfactant/polymer on stability of oil droplets in produced water from ASP flooding, *Colloids Surf., A*, 211 (2-3), 275–284.

[13] Wang, B., Wu, T., Li, Y., Sun, D., Yang, M., Gao, Y., Lu, F., and Li, X., 2011, The effects of oil displacement agents on the stability of water produced from ASP (alkaline/surfactant/polymer) flooding, *Colloids Surf., A*, 379 (1-3), 121–126.

[14] Shutang, G., and Qiang, G., 2010, Recent progress and evaluation of ASP flooding for EOR in Daqing oil field, *SPE EOR Conference at Oil & Gas West Asia*, Society of Petroleum Engineers, 11-13 April 2010, Muscat, Oman.

[15] Deng, S., Yu, G., Jiang, Z., Zhang, R., and Ting, Y.P., 2005, Destabilization of oil droplets in produced water from ASP flooding, *Colloids Surf., A*, 252 (2-3), 113–119.

[16] Zhang, R., Liang, C., Wu, D., and Deng, S., 2006, Characterization and demulsification of produced liquid from weak base ASP flooding, *Colloids Surf., A*, 290 (1-3), 164–171.

[17] Zhang, F., Wang, F., Ouyang, J., and Zhang, H., 2011, The development and application of a demulsifier used for ASP flooding–produced liquid from the Xing 2 area of the Daqing oilfield, *Pet. Sci. Technol.*, 29 (1), 69–78.

[18] Qi, W.K., Yu, Z.C., Liu, Y.Y., and Li, Y.Y., 2013, Removal of emulsion oil from oilfield ASP wastewater by internal circulation flotation and kinetic models, *Chem. Eng. Sci.*, 91, 122–129.

[19] Li, C., and Chen, Z., 2015, "ASP Flooding Produced Fluid Characteristic and Treatment Process" in *Advances in Energy Science and Equipment Engineering*, Eds. Zhou, S., Patty, A., and Chen, S., Vol. 1, Taylor & Francis, London, UK, 147–150.

[20] Ksenofontov, B.S., and Ivanov, M.V., 2013, A novel multistage kinetic modeling of flotation for wastewater treatment, *Water Sci. Technol.*, 68 (4), 807–812.

[21] Maruyama, H., Seki, H., and Satoh, Y., 2012, Removal kinetic model of oil droplet from o/w emulsion by adding methylated milk casein in flotation, *Water Res.*, 46 (9), 3094–3100.

[22] Gharai, M., and Venugopal, R., 2015, Modeling of flotation process–An overview of different approaches, *Miner. Process. Extr. Metall. Rev.*, 37 (2), 120–133.

[23] Argillier, J.F., Henaut, I., Noik, C., Viera, R., Leon, F.R., and Aanesen, B., 2014, Influence of chemical

EOR on topside produced water management, *SPE Improved Oil Recovery Symposium*, Society of Petroleum Engineers, 12-16 April 2014, Tulsa, Oklahoma, USA.

[24] Richerand, F., and Peymani, Y., 2015, Improving flotation methods to treat EOR polymer rich produced water, *SPE Produced Water Handling & Management Symposium*, Society of Petroleum Engineers, 20–21 May 2015, Galveston, Texas, USA.

[25] Xu, H.X., Liu, J.T., Gao, L.H., Wang, Y.T., Deng, X.W., and Li, X.B., 2014, Study of oil removal kinetics using cyclone-static microbubble flotation column, *Sep. Sci. Technol.*, 49 (8), 1170–1177.

[26] Rambeau, O., Jacob, M., Rondon, M., Jouenne, S., and Cordelier, P., 2014, A tool to tackle the challenges of the treatment of the back produced viscosified water, *International Petroleum Technology Conference*, 19-22 January 2014, Doha, Qatar.

[27] Deng, S., Bai, R., Chen, J.P., Jiang, Z., Yu, G., Zhou, F., and Chen, Z., 2002, Produced water from polymer flooding process in crude oil extraction: Characterization and treatment by a novel crossflow oil-water separator, *Sep. Purif. Technol.*, 29 (3), 207–216.

Methylene Blue Adsorption onto Cockle Shells-Treated Banana Pith: Optimization, Isotherm, Kinetic, and Thermodynamic Studies

Rosalyza Hasan[1], Wong Jie Ying[1], Chong Chi Cheng[1], Nur Farhana Jaafar[2], Rohayu Jusoh[1], Aishah Abdul Jalil[3,4], and Herma Dina Setiabudi[1,5,*]

[1]*Faculty of Chemical and Natural Resources Engineering, Universiti Malaysia Pahang, Lebuhraya Tun Razak 26300, Gambang, Pahang, Malaysia*

[2]*School of Chemical Sciences, Universiti Sains Malaysia, 11800, Penang, Malaysia*

[3]*School of Chemical and Energy Engineering, Faculty of Engineering, Universiti Teknologi Malaysia, 81310 UTM Johor Bahru, Johor, Malaysia*

[4]*Centre of Hydrogen Energy, Institute of Future Energy, Universiti Teknologi Malaysia, 81310 UTM Johor Bahru, Johor, Malaysia*

[5]*Centre of Excellence for Advanced Research in Fluid Flow (CARIFF), Universiti Malaysia Pahang, Lebuhraya Tun Razak 26300, Gambang, Pahang, Malaysia*

** **Corresponding author:***

tel: +609-5492836
email: herma@ump.edu.my

Received: August 3, 2018
Accepted: January 28, 2019

DOI: 10.22146/ijc.42822

Abstract: *Two low-cost wastes, banana pith (BP) and cockle shells (CS) were explored towards methylene blue (MB) removal. The performance of cockle shells-treated banana pith (CS-BP) in MB removal was compared with untreated BP and commercially $Ca(OH)_2$-treated BP ($Ca(OH)_2$-BP). The adsorption efficacy was following the order of BP < CS-BP < $Ca(OH)_2$-BP, indicating the positive role of alkaline treatment towards MB removal and great potential of CS as a low-cost activation material. The optimization of MB removal onto CS-BP was executed by response surface methodology (RSM) with three independent variables (adsorbent dosage (X_1), initial pH (X_2) and initial MB concentration (X_3)), and the optimal condition was achieved at X_1 = 1.17 g/L, X_2 = pH 7 and X_3 = 214 mg/L, with 87.32% of predicted MB removal. The experimental data well-fitted the pseudo-second-order kinetic (R^2 > 0.99) and the Langmuir isotherm (R^2 = 0.999) models, demonstrating the chemisorption and naturally homogeneous process. Thermodynamics study discovered that the MB removal by CS-BP is endothermic, feasible, spontaneous and randomness growth at a solid-solute interface. It is affirmed that CS could be employed as a low-cost activation material and CS-BP as a low-cost adsorbent.*

Keywords: *cockleshells; banana pith; methylene blue; low-cost adsorbent; alkaline treatment*

■ INTRODUCTION

Numerous industries are using dyes in coloring their final product and consequently caused severe problems in the form of colored wastewaters that require pre-treatment before being disposed to the environment [1]. Majority of the commercial dyes used is poisonous to aquatic life owing to the existence of chlorides and metals. As a result, the treatment of dye-containing effluent is a crucial task and the scientific interest in decolorization of dye effluents has been increasing in the last few decades. The removal of dyes has been studied using several techniques including biological, physical and chemical methods, however, the biological method has not been very successful, owing to the essential non-biodegradable nature of most of the dyes [2]. In addition, the high difficulty to treat dye-containing effluent can be

claimed on the aerobic digestion resistant, recalcitrant organic molecules present and stability towards photo degradation, biodegradation and oxidizing agents [3].

Adsorption method appeared as the best technique among various dye removal techniques due to its good performance in the removal of different types of coloring materials [2,4-5]. Regarding the adsorbent material, activated carbon has been commercially used for adsorption process owing to its excellent adsorption ability [6-7]. Regrettably, its relatively high cost limits its widespread usage in wastewater treatment. For the sake of reducing the cost of treatment, alternative adsorbents, particularly from agricultural wastes, have been investigated and reported, on account of the arose disposal problem as well as the no economic value of agricultural wastes [2].

Banana pith (BP) is one of the agricultural wastes which is available abundantly all the year round, yet being disposed of without being utilized properly and effectively. Therefore, the attempt to utilize BP as an economical adsorbent not only can minimize environmental pollution but can also increase its economic value. However, the challenge arose when the untreated agricultural waste adsorbents possess drawbacks as reported in the literature, for instance, low performance in adsorption process [8].

Therein, researchers have studied the agricultural wastes activation, and alkaline treatment can be considered as one of the broadly adopted methods. It has been reported that alkaline treatment substantially influences the morphology of the adsorbent by producing a porous surface of adsorbent which is favorable for adsorption process [9]. However, in order to reduce the cost, it is desirable to study the utilization of wastes as alternative low-cost materials to substitute the commercial chemical materials for alkaline treatment. Cockle shells (CS) is an abundant and non-edible waste that is widely found in many coastal areas. Owing to the high composition of calcium carbonate ($CaCO_3$) in CS, CS has great potential as an economical activation material for alkaline treatment of BP.

In this study, we attempt to use BP as a low-cost adsorbent and its adsorption competency was improved by employing the cockle shell (CS) as the low-cost activation material. Adsorption conditions of Methylene Blue (MB) removal onto cockle shells-treated banana pith (CS-BP) was optimized using Response Surface Methodology (RSM), while the physicochemical properties of fresh and spent adsorbent were analyzed using several characterization analyzers.

■ EXPERIMENTAL SECTION

Materials

The banana piths (BPs) were collected from the banana farm, Pahang, Malaysia. The commercial calcium hydroxide ($Ca(OH)_2$) was purchased from Merck and used in the alkaline treatment of the adsorbent.

Instrumentation

Instruments used in this study included oven, furnace (Memmert UFB-500, Germany), stirring hotplate with digital display (Corning PC-420D), XRF (Bruker S8 TIGER ECO), FTIR (Nicolet iS5, Thermo Scientific), SEM (LYRA3 XM, Tescan) and BET (Quantachrome Autosorb-1 analyzer).

Procedure

Preparation of adsorbent

The BPs were cut into pieces in 1–2 cm length and soaked in water for adhering impurities elimination. The samples were oven-dried (80 °C, 12 h) before grounded and sieved (300–500 μm). Meanwhile, the cockle shells (CS, collected from the beach, Pahang, Malaysia) were cleaned with water, dried (80 °C, 12 h), grounded to the specific size (355–600 μm), and finally followed with calcination process (850 °C, 3 h). During the calcination process, calcium carbonate ($CaCO_3$) consist of CS changed to calcium oxide (CaO) via the decomposition process ($CaCO_3 \rightarrow CaO + CO_2$).

The BP pre-treatment with commercial $Ca(OH)_2$ was performed in accordance with the method described in the literature [2]. In brief, $Ca(OH)_2$ powder (8.6 g) was dissolved into deionized water (1 L), followed by the addition of powdered BP (10 g). The mixture was agitated (room temperature, 4 h), filtered and oven-dried (80 °C, 12 h) to produce $Ca(OH)_2$-BP. An identical technique was executed for preparing the CS-BP by using CS as

alkaline material. The CaO consist of calcined CS converted into $Ca(OH)_2$ once it contacts with H_2O.

Characterization of adsorbent

XRF was used to analyze the chemical composition of CS sample, meanwhile, the Fourier-transform infrared spectrometer (FTIR), surface area analyzer and scanning electron microscopy (SEM) were used to analyze the physicochemical properties of fresh adsorbents (BP, CS-BP) and spent adsorbent (MB-CS-BP). In brief, FTIR analysis was used for the study of adsorbents' chemical properties and functional groups involved in the adsorption process, while the morphological characteristics and surface features were studied using SEM. The textural properties (BET surface area (S_{BET}) and pore volume (V_p)) of adsorbents were quantified using BET analyzer at -196 °C.

Adsorption experiments

A total number of 16 adsorption experiments with 2 replicates at the center point were executed by alternating the process parameters corresponding to the experimental design generated by RSM for adsorption study. Prior to the adsorption experiments, the stock solution was prepared by dissolution of the finite quantity of measured MB ($C_{16}H_{18}N_3SCl$, C.I.52015, 99%, Merck) in deionized water, before being adjusted to desired concentrations (50–500 mg/L) and pH (pH 2–10). Adsorption experiments started with the addition of the requisite dosage of CS-BP (0.25–2.5 g/L) into MB solution (200 mL) under constant stirring (ambient temperature, 2 h). The samples were taken out at proper time intervals, followed by centrifugation (20 min). UV/Vis spectrophotometer (LAMBDA 850, PerkinElmer) was used to identify the remaining MB concentration with maximum wavelength (λ_{max}) of 664 nm. The experiments were conducted triplicates for accuracy. The amount of MB adsorbed at equilibrium, q_t (mg/g) and percentage of MB removal were calculated using Eq. (1) and (2), respectively.

$$q_t = \left(\frac{C_0 - C_t}{W}\right) \times V \quad (1)$$

$$\text{Removal (\%)} = \left(\frac{C_0 - C_t}{C_0}\right) \times 100 \quad (2)$$

where C_0 and C_t are the liquid phase concentration of the MB at time zero and at any time t (mg/L), W is the adsorbent mass (g) and V is the volume of the MB solution (L).

Experiment design and optimization

The process parameters influencing the adsorption process were analyzed using face-centered central design (FCCCD) method generated from RSM (Statsoft Statistica 8.0 software). Three independent variables (adsorbent dosage, initial pH, and initial concentration) were selected, and their relationship with response (MB removal) was appraised by the equation model. The significant of the equation model was assessed using analysis of variance (ANOVA, 5% level of significance) in accordance with the method described in the literature [10].

Adsorption kinetics

Pseudo-first-order and pseudo-second-order models were executed to govern the mechanism of the MB adsorption onto CS-BP. The linearized forms of the models are expressed as following equations [11]:

Pseudo-first-order:

$$\log(q_e - q_t) = \log q_e - \frac{k_1}{2.303} t \quad (3)$$

Pseudo-second-order:

$$\frac{t}{q_t} = \frac{1}{k_2 q_e^2} + \frac{1}{q_e} t \quad (4)$$

where q_e and q_t are the amounts of dye adsorbed at equilibrium (mg/g) and at any time t (mg/g), and k_1 and k_2 are the adsorptions constant of pseudo-first-order and pseudo-second-order model.

Adsorption isotherm

Langmuir [12], Freundlich [13], Temkin [14], and Dubinin-Radushkevich [15] models were executed to analyze the type of MB distribution, as well as the interaction between CS-BP surface and MB molecules. The linearized forms of the models are expressed as following equations:

Langmuir:

$$\frac{C_e}{q_e} = \frac{1}{q_m K_L} + \frac{C_e}{q_m} \quad (5)$$

Freundlich:

$$\log q_e = \log K_f + \frac{1}{n}\log C_e \quad (6)$$

Temkin:

$$q_e = B\ln A + B\ln C_e \quad (7)$$

Dubinin-Radushkevich:

$$\ln q_e = \ln q_m - K_{DR}\varepsilon^2 \quad (8)$$

where C_e and q_e are the MB concentration (mg/L) and MB adsorption capacity (mg/g) at equilibrium, while q_m is the maximum adsorption capacity (mg/g). K_L and K_f are the equilibrium constant for Langmuir (L/mg) and Freundlich ((mg/g)(L/mg)$^{1/n}$). n is an empirical constant for the Freundlich equation. For Eq. (8), A is the Temkin equilibrium binding constant (L/g), while B is the Temkin constant. For equation (9), K_{DR} is the Dubinin-Radushkevich constant (mol^2/kJ^2) and ε is the Polanyi potential (J/mol). ε can be determined from ε = RT ln (1+1/C_e), where R is the ideal gas constant (8.314 J/mol·K) and T is absolute temperature (K). The fundamental characteristic of the Langmuir isotherm can be analyzed using the dimensionless constant separation factor, R_L (R_L = 1/(1+K_LC_0)) [16]. The value of R_L parameter can be either R_L = 0, 0 < R_L < 1, R_L = 1, or R_L > 1, indicating to irreversible, favorable, linear, or unfavorable, respectively [16].

Adsorption thermodynamic

The Gibbs free energy (ΔG°), enthalpy (ΔH°) and entropy (ΔS°) were evaluated to investigate the thermodynamic nature of MB adsorption over CS-BP and the equations used as follows [2]:

$$\Delta G° = -RT\ln K_D \quad (9)$$

$$\ln K_D = \frac{\Delta H°}{RT} + \frac{\Delta S°}{R} \quad (10)$$

where R is the ideal gas constant (8.314 J/mol·K), T is the absolute temperature (K) and K_D is the Langmuir isotherm constant (L/mg).

■ RESULTS AND DISCUSSION

Effect of Alkaline Treatment

Fig. 1 depicts the influence of banana pith (BP) pre-treatment on the methylene blue (MB) removal, in which the error bars representing the standard errors by the mean of three replicates of the experiments carried out in this study. The performance of untreated BP on the adsorption of MB was compared with treated BP ($Ca(OH)_2$-BP and CS-BP). The $Ca(OH)_2$-BP (80.6%) and CS-BP (74.1%) show higher adsorption uptake as compared to the untreated BP (66.5%), indicating the positive role of alkaline treatment towards MB removal and great potential of CS as a low-cost activation material. The positive role of alkaline treatment might be due to an increase in the electronegativity and the surface areas of adsorbents after the alkaline treatment. The great potential of CS as an activation material in accordance with XRF analysis in which the calcined CS contains 98.2% of CaO, which can be considered as a promising economical replacement over commercial $Ca(OH)_2$. The positive role of adsorbent activation towards dye removal was also reported in the literature [17]. Jain and Gogate [9] found that the activation of *Prunus dulcis* leaves by NaOH increased the adsorption capacity of *Prunus dulcis* leaves towards Acid Blue 113 removal from 10.87 to 25.51 mg/g due to the presence of surface porous after NaOH activation which is favorable for adsorption process.

Characterization of Untreated BP and Treated-BP

The details on the functional groups involved during the pre-treatment process and the binding mechanism

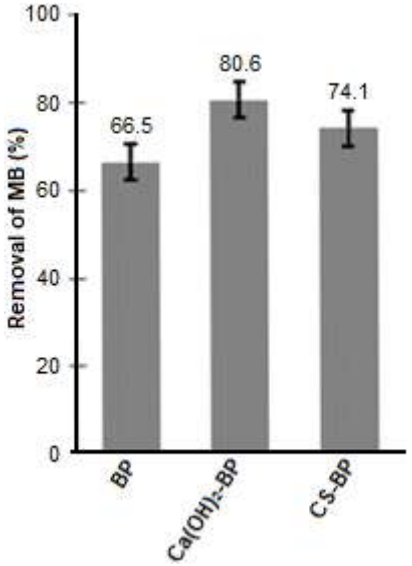

Fig 1. Influence of the alkaline treatment on the MB removal (m = 0.5 g/L, pH 6, C_0 = 100 mg/L, T = 30 °C, contact time = 120 min)

between treated BP and MB molecules were determined using FTIR analysis as shown in Fig. 2. Several major absorbance bands at 3283, 2917, 1591, 1316, 1031, 460 and 438 cm^{-1} were observed for BP. In accordance with the literature, the broad absorption peak at 3283 cm^{-1} corresponded to the O-H stretching in cellulose, while the peak observed at 2917 cm^{-1} assigned to the C–H asymmetric stretching of CH_2 groups [10,18]. The peaks at 1591 and 1316 cm^{-1} attributed to the C=C and C=O stretching, while 1031, 460 and 438 cm^{-1} attributed to the C-H deformation. New bands were discerned at 1386, 871 and 711 cm^{-1} after the BP treatment with CS indicating the presence of inorganic carbonate, demonstrating the success of alkaline treatment process. After the MB adsorption onto CS-BP, the intensities of the bands were slightly decreased and the existence of organic sulfur was observed at the band of 1419 cm^{-1} [18]. The decreased in the intensity at 871 and 711 cm^{-1} bands and the presence of a new band at 1419 cm^{-1} provide strong evidence of the interactions between dye molecules with the inorganic carbonate of CS-BP in accordance with the literature [19].

The topology of BP, CS-BP, and MB-CS-BP was identify using SEM analysis and the result is shown in Fig. 3. Before the treatment with CS, the crushed particles with clustered arrangement can be seen on the surface of BP (Fig. 3(a)). Rough BP surface was observed after the CS pre-treatment (Fig. 3(b)) which signifies the high possibility of MB to be adsorbed. The smooth surface of CS-BP-MB (Fig. 3(c)) confirming the coverage of CS-BP surface with MB molecules via the adsorption process.

The textural properties (S_{BET} and V_p) of BP, CS-BP and MB-CS-BP were S_{BET} = 12.31, 16.06 and 11.51 m^2/g, respectively, and V_p = 0.019, 0.023 and 0.011 cm^3/g, respectively. The findings revealed that the activation of BP using CS increase the number of pores and thus increase the S_{BET} and V_p. This advantage increases the possibility of MB molecules to be trapped onto the surface and pores of CS-BP, which was evidenced by the decrease of S_{BET} and V_p for MB-CS-BP. The changes in the surface features of adsorbent by alkaline activation were also reported by Jain and Gogate (2017) for NaOH treated *Prunus dulcis* leaves [9]. They stated that the increment in S_{BET} and V_p of the adsorbent which is favorable for adsorption process indeed resulted from the pores evolved upon NaOH activation.

Statistical Analysis of MB Removal by CS-BP

The influences of the independent variables on the response had been investigated by the batch study of 16 experiments using RSM and the results were presented in Table 1.

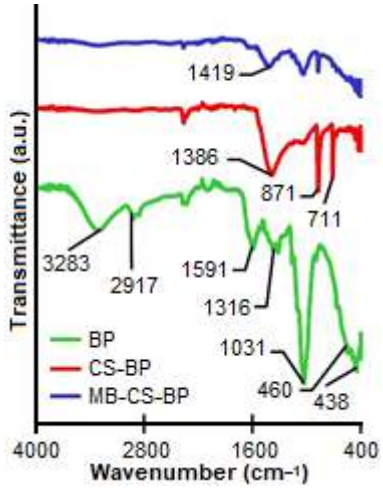

Fig 2. FTIR spectra of BP, CS-BP, and MB-CS-BP

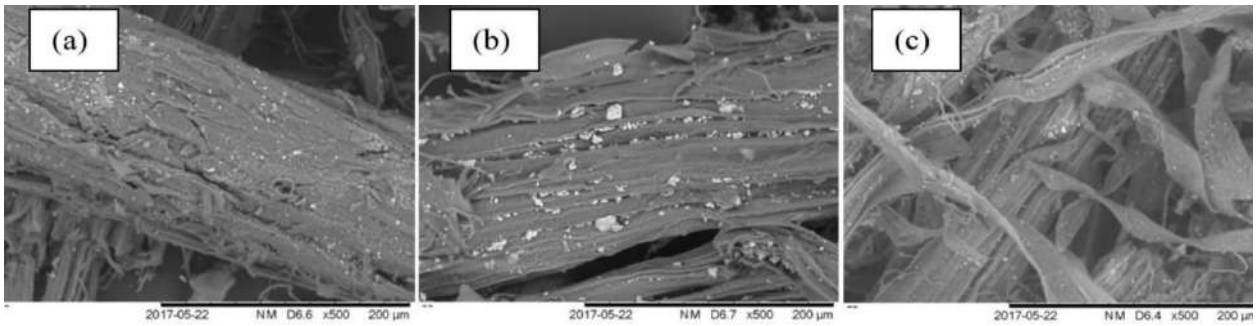

Fig 3. SEM images of (a) BP, (b) CS-BP, (c) MB-CS-BP

The quadratic model for MB removal by CS-BP is presented in Eq. (11):

$$Y = 65.9826 + 6.6710X_1 + 4.3866X_2 + 0.0253X_3 - 1.5075X_1^2 - 0.2736X_2^2 - 0.00004X_3^2 - 0.4139X_1X_2 - 0.0017X_1X_3 - 0.0011X_2X_3 \quad (11)$$

The validity of the statistical model was analyzed by plotting the graph of predicted values versus the experimental values (not shown). The linear coefficient of the graph is 0.9786 implying the reasonable of predicted values in conformity with the experimental values. The statistical significance of the model was accessed using ANOVA and the result was tabulated in Table 2. The result discovered the significance of the model as expressed by the larger F-value (30.671) in comparison with the tabulated F-value (4.10).

Fig. 4 shows the Pareto chart of MB removal onto CS-BP. The critical parameter for the regression model represents the smaller magnitude of the p-value and larger magnitude of the t-value. As shown in Fig. 4, all linear, quadratic and interaction terms are statistically significant ($p < 0.05$) excluding linear term of adsorbent

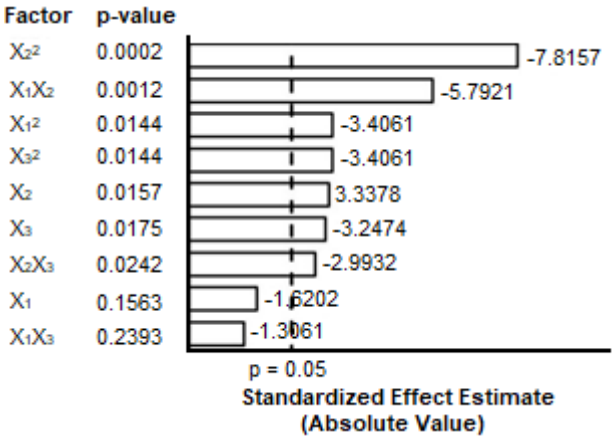

Fig 4. Pareto chart of MB removal by CS-BP

Table 1. The design of experiments and experimental response for MB removal by CS-BP

Run	Independent variables						Response
	Adsorbent dosage, X_1 (g/L)		Initial pH, X_2		Initial Concentration, X_3 (mg/L)		MB removal, Y (%)
	Coded	Uncoded	Coded	Uncoded	Coded	Uncoded	
1	-1	0.25	-1	2	-1	50	75.89
2	-1	0.25	-1	2	1	500	76.50
3	-1	0.25	1	10	-1	50	83.10
4	-1	0.25	1	10	1	500	81.00
5	1	2.50	-1	2	-1	50	79.47
6	1	2.50	-1	2	1	500	79.54
7	1	2.50	1	10	-1	50	80.37
8	1	2.50	1	10	1	500	75.45
9	-1	0.25	0	6	0	275	86.50
10	1	2.50	0	6	0	275	83.50
11	0	1.375	-1	2	0	275	81.99
12	0	1.375	1	10	0	275	83.07
13	0	1.375	0	6	-1	50	86.50
14	0	1.375	0	6	1	500	83.50
15 (C)	0	1.375	0	6	0	275	87.28
16 (C)	0	1.375	0	6	0	275	87.50

Table 2. ANOVA results for MB removal by CS-BP

Sources	Sum of Square (SS)	Degree of Freedom (df)	Mean Square (MS)	F-value
Regression (SSR)	227.10	9	25.233	30.671
Residual	4.9362	6	0.8227	
Total (SST)	232.03	15		

dosage (X_1) and an interaction term of adsorbent dosage and initial concentration (X_1X_3). The quadratic term of initial pH (X_2^2) was the utmost crucial variables for the adsorption of MB onto CS-BP.

Meanwhile, the least crucial factor on the MB adsorption was indicated by the X_1X_3. The crucial of the initial pH probably due to the properties of MB, which exists in the form of positively charged ions in aqueous solution. Thus, the changes in the charge of the initial MB solution will influence the adsorption performance.

Fig. 5 displays the 3D plots showing the influences of independent variables towards the removal of MB. As displayed in Fig. 5(a), the percentage of MB removal inclined parallel with the increment in adsorbent dosage and initial pH. At the adsorbent dosage of 0.8–1.5 g/L and an initial pH of 5.5–7.5, the maximum dye removal of > 86% was accomplished before slightly decreased at higher values. As the adsorbent dosage was increased, the quantity of the binding sites accessible for adsorption was increased as well due to the rise in the adsorbent's dosage.

Meanwhile, the enhancement of the MB removal at higher pH can be claimed on the electrostatically adsorbed of the positively charged of MB cations onto the negatively charged surface of CS-BP [20]. The influence of pH on the adsorption performance can be depicted on the basis of zero-point change (pH_{zpc}) of the CS-BP, which was confirmed at ~pH 7.45. The influence of pH on the removal percentage in agreement with the report declared for the MB removal onto cashew nutshell [21] and breadnut peel [22], in which the MB withdrawal percentage increased with increment in initial pH.

Fig. 5(b) displays the 3D plot for the influences of adsorbent dosage (X_1) and the initial concentration (X_3) on the MB removal percentage. The percentage of MB removal increase with the increase of the adsorbent dosage. In contrast, the MB removal was declined with the increment of the MB initial concentration. The reduced in the percentage of MB removal at higher concentration probably be due to the inadequate quantity of active adsorbent sites to accommodate the high concentration of dye ions [23]. The highest dye removal (> 86%) was accomplished at 0.9–1.6 g/L adsorbent dosage and 150-300 mg/L initial concentration.

The influences of initial pH (X_2) and initial concentration (X_3) on the MB removal are illustrated in Fig. 5(c). The plot shows that increasing pH and reducing initial MB concentration will subsequently increase the percentage of MB removal. This result related to the changes in the charge of the adsorbent surface and the ratio of dyes to the available surface site [24]. It was discovered that > 86% of MB withdrawal was acquired in the range of 5.5–7.5 initial pH and 150–300 mg/L initial concentration. An identical trend was claimed for the MB adsorption onto chitosan/zeolite composite [25], in which the MB withdrawal percentage increased with the growth of initial pH but a decline in the initial dye concentration.

The optimization study revealed that the optimal MB removal onto CS-BP was at 1.17 g/L adsorbent dosage, initial pH of 7 and 214 mg/L initial concentration with predicted percentage MB removal of 87.32%. An additional experiment was carried out at the optimal condition as validation purpose and the result showed 80.07% of MB removal was achieved.

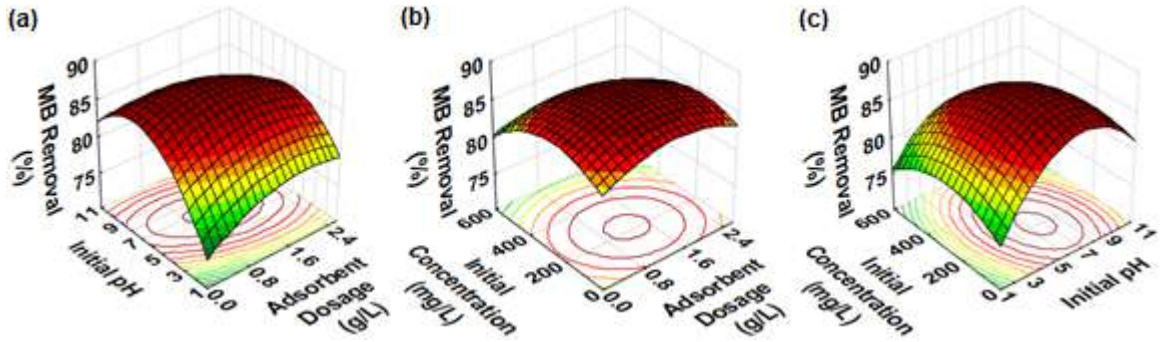

Fig 5. Response surface plots showing influences of (a) adsorbent dosage – initial pH interaction, (b) adsorbent dosage – initial concentration interaction, and (c) initial pH – initial concentration interaction, towards MB removal by CS-BP

Table 3. Kinetic parameters for adsorption of MB by CS-BP

Kinetic Model	Parameters	50 mg/L	100 mg/L	200 mg/L	300 mg/L	500 mg/L
Experimental	$q_{e,exp}$ (mg/g)	42.18	57.54	76.16	80.65	83.76
Pseudo-first order	q_e (mg/g)	2.575	4.462	4.467	4.558	4.788
	k_1 (min^{-1})	0.136	0.026	0.022	0.020	0.022
	R^2	0.962	0.966	0.971	0.981	0.932
Pseudo-second order	q_e (mg/g)	42.017	59.172	76.923	81.301	84.033
	k_2 (min^{-1})	0.008	0.003	0.003	0.002	0.002
	R^2	0.997	0.993	0.995	0.994	0.992

Adsorption Kinetic

The kinetic study was carried out at m_{CS-BP} = 1.17 g/L, pH 7, T = 30 °C and C_0 = 50–500 mg/L. As tabulated in Table 3, pseudo-second-order model was shown as the best model with higher R^2 (> 0.992) and closer q_e values to experimental data ($q_{e,exp}$) in comparison with the pseudo-first-order model. The findings depicted that the MB adsorption by CS-BP was controlled by the chemisorption process and the number of the available active sites directly affect the rate of reaction. The comparable adsorption kinetic finding was reported for MB adsorption by oil palm ash zeolite/chitosan [26], weeds [27] and *Ficus carica* bast [18].

Adsorption Isotherm

The isotherm study was executed at m_{CS-BP} = 1.17 g/L, pH 7, T = 30 °C and C_0 = 50–500 mg/L. As tabulated in Table 4, the Langmuir isotherm model was shown as the best model with the highest R^2 (0.999) amongst the four isotherms employed. The good fitting with the Langmuir isotherm model depicted that the MB adsorption onto CS-BP is monolayer adsorption and takes place on a surface that is homogeneous in nature [28]. Corresponding to Table 4, the K_L value was 0.102 which expresses that the MB molecules are favorably adsorbed on CS-BP with maximum adsorption capacity, q_m of 85.47 mg/g. An indistinguishable tendency was proclaimed for MB adsorption onto biomass fly ash geopolymer monoliths [29]. The value of q_m was compared to several untreated and modified biosorbents were tabulated in Table 5. As observed, CS-BP has superior adsorption volume than the others, denoting the

Table 4. Isotherm parameters for MB removal onto CS-BP

Isotherm Model	Parameters	Value
Langmuir	R^2	0.999
	q_m (mg/g)	85.47
	K_L (L/mg)	0.102
	R_L	0.089
Freundlich	R^2	0.959
	n	8.953
	K_f (mg/g)(L/mg)$^{1/n}$	5.124
Temkin	R^2	0.930
	B (J/mol)	15.44
	A (L/g)	15.65
Dubinin-Radushkevich	R^2	0.974
	q_m (mg/g)	6.756
	K_{ad} (10^4)	1

Table 5. Comparison of maximum adsorption capacity of MB onto various untreated and modified low-cost adsorbents

Adsorbent	Adsorption capacity (mg/g)	Ref
Cockle shells-treated banana pith	85.47	This study
Banana empty fruit bunch AC-H_3PO_4	76.13	[30]
Banana empty fruit bunch AC-KOH	71.06	[30]
Salix babylonica (Weeping willow) leaves	60.97	[31]
Banana leaves AC	48.01	[32]
Haloxylon recurvum stems	22.93	[33]
Brazil nut shells	7.81	[34]

Table 6. Thermodynamic parameter for MB removal onto CS-BP

ΔH°	ΔS°	ΔG° (kJ/mol)		
(kJ/mol)	(J/mol·K)	30 °C	35 °C	40 °C
13.7455	57.0041	-3.5281	-3.8087	-4.0983

capability of CS-BP as an alternate low-cost adsorbent for MB removal.

Thermodynamic Study

The thermodynamic study was investigated at optimal condition (m_{CS-BP} = 1.17 g/L, pH 7, C_0 = 214 mg/L, and time of contact = 120 min) within 30–40 °C temperature range and the findings are listed in Table 6. The positive values of ΔH° (+ 13.7455 kJ/mol) and ΔS° (+ 57.0041 J/mol) indicated the endothermic process and randomness increment at a solid-solute interface with certain structural alternations in adsorbent and adsorbate [35]. The decreasing ΔG° values with increasing temperature indicates that the removal of MB onto CS-BP is feasible, spontaneous and increase in the degree of spontaneity at a higher temperature.

■ CONCLUSION

A new low-cost adsorbent (cockle shells-treated banana pith (CS-BP)) was successfully developed owing to its effectiveness in MB removal. Besides providing additional advantageous over industrial wastewater treatment, the solid wastes disposal of CS and BP can also be minimized. Investigation of MB removal by RSM under three independent parameters (adsorbent dosage (X_1), initial pH (X_2) and initial dye concentration (X_3)) was executed. Optimum condition (X_1 = 1.17 g/L, X_2 = pH 7, X_3 = 214 mg/L) yielded predicted MB removal of 87.32% (according to RSM). Based on the Pareto chart, the most paramount factor for MB removal by CS-BP was the X_2^2. The experimental data was well-fitted with pseudo-second-order kinetic and Langmuir isotherm models, demonstrated a chemisorption process with monolayer and homogeneous process. Thermodynamic investigations revealed that the MB adsorption onto CS-BP is an endothermic, randomness growth at the solid-solute interface, feasible, spontaneous and increase in the degree of spontaneity at a higher temperature.

The higher surface area, the presence of new bands which implies the existence of inorganic carbonate and rough surface of CS-BP as shown by BET, FTIR and SEM results, demonstrating the success of the alkaline treatment process. These combinations are the main contributors to the good MB adsorption by CS-BP.

■ ACKNOWLEDGMENTS

This study was financially supported by Universiti Malaysia Pahang, Malaysia via Research University Grant (RDU170331).

■ REFERENCES

[1] Hasan, R., Razifuddin, N.A.M., Jusoh, N.W.C., Jusoh, R., and Setiabudi, H.D., 2018, *Artocarpus integer* peel as a highly effective low-cost adsorbent for methylene blue removal: Kinetics, isotherm, thermodynamic and pelletized studies, *Malays. J. Fundam. Appl. Sci.*, 14 (1), 25–31.

[2] Hasan, R., Chong, C.C., Setiabudi, H.D., Jusoh, R., and Jalil, A.A., 2019, Process optimization of methylene blue adsorption onto eggshell-treated palm oil fuel ash, *Environ. Technol. Innovation*, 13, 62–73.

[3] Liu, Q., Yang, B., Zhang, L., and Huang, R., 2015, Adsorption of an anionic azo dye by cross-linked chitosan/bentonite composite, *Int. J. Biol. Macromol.*, 72, 1129–1135.

[4] Vezentsev, A., Thuy, D.M., Goldovskaya-Peristaya, L.F., and Glukhareva, N.A., 2018, Adsorption of methylene blue on the composite sorbent based on bentonite-like clay and hydroxyapatite, *Indones. J. Chem.*, 18 (4), 733–741.

[5] Abdullah, R.H., Oda, A.M., Omran, A.R., Mottaleb, A.S., and Mubarakah, T.M., 2018, Study of adsorption characteristics a low-cost sawdust for the removal of direct blue 85 dye from aqueous solutions, *Indones. J. Chem.*, 18 (4), 724–732.

[6] Osasona, I., Aiyedatiwa, K., Johnson, J.A., and Faboya, O.L., 2018, Activated carbon from spent brewery barley husks for cadmium ion adsorption from aqueous solution, *Indones. J. Chem.*, 18 (1), 145–152.

[7] Taba, P., 2009, Nitrogen, water and benzene adsorption in mesoporous carbon (CMK-1) and commercial activated carbon (NORIT SX22), *Indones. J. Chem.*, 9 (3) 386–390.

[8] Fadzil, F., Ibrahim, S., and Hanafiah, M.A.K.M., 2016, Adsorption of lead(II) onto organic acid modified rubber leaf powder: Batch and column studies, *Process Saf. Environ. Prot.*, 100, 1–8.

[9] Jain, S.N., and Gogate, P.R., 2017, Acid blue 113 removal from aqueous solution using novel biosorbent based on NaOH treated and surfactant-modified fallen leaves of *Prunus dulcis*, *J. Environ. Chem. Eng.*, 5 (4), 3384–3394.

[10] Setiabudi, H.D., Jusoh, R., Suhaimi, S.F.R.M., and Masrur, S.F., 2016, Adsorption of methylene blue onto oil palm (*Elaeis guineensis*) leaves: Process optimization, isotherm, kinetics, and thermodynamic studies, *J. Taiwan Inst. Chem. Eng.*, 63, 363–370.

[11] Chen, L., Li, Y., Du, Q., Wang, Z., Xia, Y., Yedinak, E., Lou, J., and Ci, L., 2017, High-performance agar/graphene oxide composite aerogel for methylene blue removal, *Carbohydr. Polym.*, 155, 345–353.

[12] Langmuir, I., 1918, The adsorption of gases on plane surfaces of glass, mica and platinum, *J. Am. Chem. Soc.*, 40 (9), 1361–1403.

[13] Freundlich, H., 1906, Over adsorption in solution, *J. Phys. Chem. A*, 57, 385–470.

[14] Tempkin, M.I., and Pyzhev, V., 1940, Kinetics of ammonia synthesis on promoted iron catalyst, A*cta Physicochim. U.R.S.S.*, 12, 327–356.

[15] Dubinin, M.M., 1906, The potential theory of adsorption of gases and vapors for adsorbents with an energetically non-uniform surface, *Chem. Rev.*, 60 (2), 235–241.

[16] Hasan, R., Bukhari, S.N., Jusoh, R., Mutamin, N.S.A., and Setiabudi, H.D., 2018, Adsorption of Pb(II) onto KCC-1 from aqueous solution: Isotherm and kinetic study, *Mater. Today: Proc.*, 5 (10), 21574–21583.

[17] Spagnoli, A.A., Giannakoudakis, D.A., and Bashkova, S., 2017, Adsorption of methylene blue on cashew nut shell based carbons activated with zinc chloride: The role of surface and structural parameters, *J. Mol. Liq.*, 229, 465–471.

[18] Pathania, D., Sharma, S., and Singh, P., 2017, Removal of methylene blue by adsorption onto activated carbon developed from *Ficus carica* bast, *Arabian J. Chem.*, 10 (Suppl. 1), S1445–S1451.

[19] Liang, S., Guo, X., Feng, N., and Tian, Q., 2010, Isotherms, kinetics and thermodynamic studies of adsorption of Cu^{2+} from aqueous solutions by Mg^{2+}/K^{+} type orange peel adsorbents, *J. Hazard. Mater.*, 174 (1-3), 756–762.

[20] Hameed, B.H., Mahmoud, D.K., and Ahmad, A.L., 2008, Equilibrium modeling and kinetic studies on the adsorption of basic dye by a low-cost adsorbent: Coconut (*Cocos nucifera*) bunch waste, *J. Hazard. Mater.*, 158 (1), 65–72.

[21] Subramaniam, R., and Ponnusamy, S.K., 2015, Novel adsorbent from agricultural waste (cashew nut shell) for methylene blue dye removal: Optimization by response surface methodology, *Water Resour. Ind.*, 11, 64–70.

[22] Lim, L.B.L., Priyantha, N., Tennakoon, D.T.B., Chieng, H.I., Dahri, M.K., and Suklueng, M., 2017, Breadnut peel as a highly effective low-cost biosorbent for methylene blue: Equilibrium, thermodynamic and kinetic studies, *Arabian J. Chem.*, 10 (Suppl. 2), S3216–S3228.

[23] Islam, M.A., Ahmed, M.J., Khanday, W.A., Asif, M., and Hameed, B.H., 2017, Mesoporous activated carbon prepared from NaOH activation of rattan (*Lacosperma secundiflorum*) hydrochar for methylene blue removal, *Ecotoxicol. Environ. Saf.*, 138, 279–285.

[24] Saeed, M., Nadeem, R., and Yousaf, M., 2015, Removal of industrial pollutant (reactive orange 122 dye) using environment-friendly sorbent *Trapa bispinosa*'s peel and fruit, *Int. J. Environ. Sci. Technol.*, 12 (4), 1223–1234.

[25] Dehghani, M.H., Dehghan, A., Alidadi, H., Dolatabadi, M., Mehrabpour, M., and Converti, A., 2017, Removal of methylene blue dye from aqueous solutions by a new chitosan/zeolite composite from shrimp waste: Kinetic and equilibrium study, *Korean J. Chem. Eng.*, 34 (6), 1699–1707.

[26] Khanday, W.A., Asif, M., and Hameed, B.H., 2017, Cross-linked beads of activated oil palm ash zeolite/chitosan composite as a bio-adsorbent for the removal of methylene blue and acid blue 29 dyes, *Int. J. Biol. Macromol.*, 95, 895–902.

[27] Güzel, F., Sayğılı, H., Sayğılı, G.A., Koyuncu, F., and Yılmaz, C., 2017, Optimal oxidation with nitric acid of biochar derived from pyrolysis of weeds and its application in removal of hazardous dye methylene blue from aqueous solution, *J. Cleaner Prod.*, 144, 260–265.

[28] Karim, A.H., Jalil, A.A., Triwahyono, S., Kamarudin, N.H.N., and Ripin, A., 2014, Influence of multi-walled carbon nanotubes on textural and adsorption characteristics of in situ synthesized mesostructured silica, *J. Colloid Interface Sci.*, 421, 93–102.

[29] Novais, R.M., Ascensão, G., Tobaldi, D.M., Seabra, M.P., and Labrincha, J.A., 2018, Biomass fly ash geopolymer monoliths for effective methylene blue removal from wastewaters, *J. Cleaner Prod.*, 171, 783–794.

[30] Sugumaran, P., Susan, V.P., Ravichandran, P., and Seshadri, S., 2012, Production and characterization of activated carbon from banana empty fruit bunch and *Delonix regia* fruit pod, *J. Sustainable Energy Environ.*, 3, 125–132.

[31] Khodabandehloo, A., Rahbar-Kelishami, A., and Shayesteh, H, 2017, Methylene blue removal using *Salix babylonica* (weeping willow) leaves powder as a low-cost biosorbent in batch mode: Kinetic, equilibrium, and thermodynamic studies, *J. Mol. Liq.*, 244, 540–548.

[32] Martín-González, M.A., Susial, P., Pérez-Peña, J., and Doña-Rodríguez, J.M., 2013, Preparation of activated carbons from banana leaves by chemical activation with phosphoric acid: Adsorption of methylene blue, *Rev. Mex. Ing. Quím.*, 12 (3), 595–608.

[33] Hassan, W., Farooq, U., Ahmad, M., Athar, M., and Khan, M.A., 2017, Potential biosorbent, *Haloxylon recurvum* plant stems, for the removal of methylene blue dye, *Arabian J. Chem.*, 10 (Suppl. 2), S1512–S1522.

[34] de Oliveira Brito, S.M., Andrade, H.M.C., Soares, L.F., and de Azevedo, R.P., 2010, Brazil nut shells as a new biosorbent to remove methylene blue and indigo carmine from aqueous solutions, *J. Hazard. Mater.*, 174 (1-3), 84–92.

[35] Salleh, N.F.M., Jalil, A.A., Triwahyono, S., Ripin, A., Sidik, S.M., Fatah, N.A.A., Salamun, N., Jaafar, N.F., and Hassim, M.H., 2017, New direct consecutive formation of spinel phase in (Fe,Co,Ni)Al_2O_4 composites for enhanced Pd(II) ions removal, *J. Alloys Compd.*, 727, 744–756.

The Oriented Attachment Model Applied on Crystal Growth of Hydrothermal Derived Magnetite Nanoparticles

Ahmad Fadli[1,*], Amun Amri[1], Iwantono[2], Arisman Adnan[3], Sunarno[1], Sukoco[1], and Mayangsari[1]

[1]*Department of Chemical Engineering, Faculty of Engineering, Universitas Riau, Kampus Binawidya, Jl. HR. Soebrantas Km. 12.5, Simpang Baru, Panam Pekanbaru, Riau 28293, Indonesia*

[2]*Department of Physics, Faculty of Mathematics and Natural Sciences, Universitas Riau, Kampus Binawidya, Jl. HR. Soebrantas Km. 12.5, Simpang Baru, Panam Pekanbaru, Riau 28293, Indonesia*

[3]*Department of Mathematics, Faculty of Mathematics and Natural Sciences, Universitas Riau, Kampus Binawidya, Jl. HR. Soebrantas Km. 12.5, Simpang Baru, Panam Pekanbaru, Riau 28293, Indonesia*

* ***Corresponding author:***

tel: +62-761-588156
email: fadliunri@yahoo.com

Received: January 22, 2019
Accepted: May 9, 2019

DOI: 10.22146/ijc.42917

Abstract: *Magnetite (Fe_3O_4) nanoparticles are very promising to be applied as a drug delivery system (DDS) for cancer chemotherapy. In this research, the crystal growth of hydrothermal derived magnetite particles was studied by oriented attachment (OA) model. The OA model was used to investigate the mechanism and the statistical kinetic of crystal growth. The crystal diameter change as a function of time with different concentration was measured using XRD. Firstly, 0.3248 g $FeCl_3$ and 1.1764 g of sodium citrate, as well as 0.3604 g urea were dissolved into 40 mL of distilled water in a reactor. Subsequently, the reactor temperature was maintained at 210 °C and the reaction time of 3.5–12 h in an air oven. The morphology of obtained particles was characterized using TEM, whereas VSM was used to determine the magnetic hysteresis curve. The XRD pattern showed that magnetite was obtained at temperature 210 °C and 3.5 h reaction time, as well as its intensity, increased with reaction time. The crystal size of Fe_3O_4 was 9.44 nm at 3.5 h and was appropriate with the oriented attachment model. The magnetite nanoparticles with shaped core-shell had a size less than 50 nm and were suitable for biomedical application, especially as drug delivery.*

Keywords: *magnetite; oriented attachment; crystal growth; hydrothermal; nanoparticles*

■ INTRODUCTION

Nanomagnetite particles have been widely used in electronics, industry, biomedicine, and agriculture. In the electronics field, nanomagnetite has been applied as magnetic storage media, ferrofluids, sensors, supercapacitors, and data memory, whereas application of nanomagnetite in industries such as ceramics, catalyst, and energy storage. In the medical field, nanomagnetite has been used as magnetite resonance imaging (MRI) contrast media and drug delivery system (DDS) for cancer chemotherapy [1]. Cancer is one of the leading causes of death worldwide. Compared to conventional methods such as oral and injection, DDS has the ability to treat specific targets in the body, reduce drug doses, reduce drug concentration on non-target site and reduce the side effects caused by drug toxicity on non-target cells or tissues [2]. Nanomagnetite which can be applied as DDS has been carried out in many nanomagnetite synthesis studies, but there is no modeling that explains the tailoring process of nanomagnetite particles. Modeling is used to determine the evolution and factors that influence the growth of nanomagnetite crystals to obtain uniform size and morphology [3].

Two models can explain the growth of nanomagnetite particles, Ostwald Ripening (OR) and Oriented Attachments (OA). The OR model is a classic model that explains the growth of increasing nanomagnetite crystals through diffusion. This model has not been able to explain the limits of the enlargement

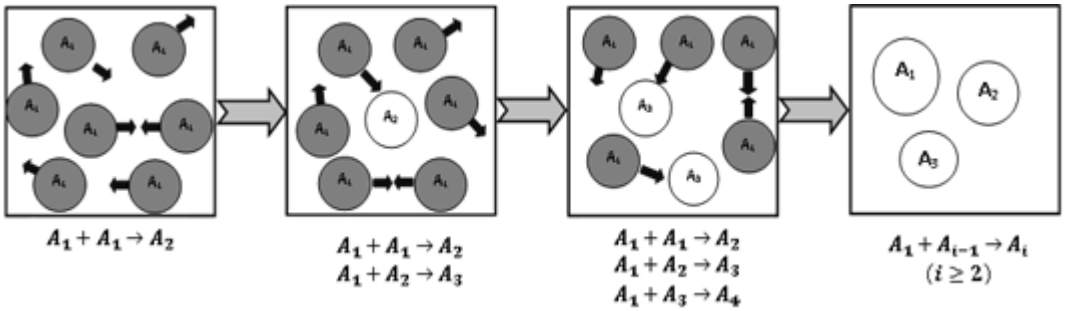

Fig 1. Schematic illustration of nanomagnetite crystal growth by Oriented Attachment (OA) model

of the nanomagnetite crystal particles. The OA model will explain more about the particle union, the factors that influence and the particle size limits so that the crystal diameter size of the nanomagnetite particles is uniform [4]. Model OA describes crystal growth based on the joining of crystalline particles. The primary particle meets the other primary particles to form secondary particles. Secondary particles meet with primary particles forming tertiary particles and so on. Illustration of nanomagnetite crystal growth scheme with the OA model can be described as Fig. 1. Primary particles A1 meet with the other primary particles A_1 (A_1+A_1) grow into secondary particles (A_2), then the union between the primary particles and multiple particles occurs (A_1+A_2), (A_1+A_3) and so on. The hypothesis stated by Zang et al. [5], the meeting between Ai and A_j for $A_i \geq 2$ and $A_j \geq 2$ is limited by assuming that the particle mass is uniform, if $A_j \geq 2$ then the particle mass is too large, immobility and opportunities for small interactions and reaction growth of nanomagnetite crystal are irreversible reactions. The kinetic model of OA is described by the following reactions:

$$A_1 + A_1 \xrightarrow{k_1} A_2 \quad (1)$$

where A_1 is the primary nanomagnetite particles, A_2 is the product of two united nanomagnetite particles and k_1 is the kinetic constant of the reaction between two particles. Primary nanomagnetite particles that combine with other primary particle products and so on (multiple particles) can be illustrated by the following reactions:

$$A_1 + A_{i-1} \xrightarrow{k_{i-1}} A_i \quad (2)$$

where A_i is a particle containing i primary and k_i is the reaction rate constant.

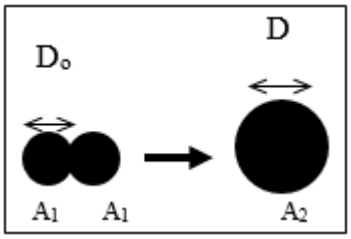

Fig 2. Illustration of growth of a nanomagnetite crystal in the OA model

It is assumed the particle with an average diameter of D_0 and the particle volume units N_0 at t = 0. After the particles have grown at a time period, t, the number of particles is N(t), and the number of particles that have grown is $N_2(t)$, and the average particle size is D_2. Assumed that the particles are spherical, the balance equation at t time is:

$$\frac{4}{3}\pi\left(\frac{D_0}{2}\right)^3 N_0\rho = \frac{4}{3}\pi\left(\frac{D_0}{2}\right)^3 N_{(t)}\rho + \frac{4}{3}\pi\left(\frac{D_2}{2}\right)^3 N_{2(t)}\rho \quad (3)$$

where ρ is the nanomagnetite particle density. This equation can be changed to:

$$\frac{1}{6}\pi(D_0)^3 N_0\rho = \frac{1}{6}\pi(D_0)^3 N_{(t)}\rho + \frac{1}{6}\pi(D_2)^3 N_{2(t)}\rho \quad (4)$$

where $V_2 = 2V_0$, then:

$$D_2 = \sqrt[3]{2D_0} \quad (5)$$

According to Huang et al. [6], because the amount of particle growth is the number of particles per unit volume at (t) then:

$$N_{2(t)} = \frac{N_0 - N_{(t)}}{2} \quad (6)$$

The kinetics integration of nanomagnetite particle growth can be explained in the equation:

$$N_{(t)} = \frac{N_0}{kt + 1} \quad (7)$$

Huang et al. [6], used the Scherer method with XRD, the diameter of each particle is declared with the equation:

$$D = N(t).D_0 + N_2(t).D_2 \quad (8)$$

If Eq. (5), (6) and ((7) is combined with the Eq. (8), then obtained:

$$D = \frac{D_0\left(\sqrt[3]{2kt}+1\right)}{(kt+1)} \quad (9)$$

The nanomagnetic synthesis was successfully carried out by Cheng et al. [4] used $FeCl_3$, citrate, urea, and polyacrylamide (PAM) by the hydrothermal method at temperature 200 °C. The nanomagnetite particles obtained are hollow and core shell. These particles have nanoparticle size and morphology that affect accessibility and residence time in blood circulation, superparamagnetic, high solubility in water and ideal for application as DDS [7].

In this study, the application of the OA model on the growth of nanomagnetite synthesis crystal in the hydrothermal method is carried out. Therefore, the nanomagnetite from the synthesis will be maximal and uniform that can be applied to the DDS.

■ EXPERIMENTAL SECTION

Materials

The materials used were $FeCl_3{\cdot}6H_2O$ (Nacalai Tesque), urea (Merck), ($C_6H_5O_7Na_3{\cdot}2H_2O$) (Merck), polyethylene glycol (PEG) 1000 (99%), aquabidest and ethanol (Merck).

Instrumentation

The crystallinity, composition, and size of nanoparticles were determined by XRD analysis, with Cu radiation lamps (λ 1.54 Å, 40 kV and 30 mA). The Debye-Scherrer method was used to calculate the particle size by using Eq. (10).

$$D = \frac{K\lambda}{B\cos\theta} \quad (10)$$

Morphology, topography, composition, and crystallographic information of samples were analyzed using Transmission Electron Microscope (TEM). Nanoparticle magnetism was analyzed by Vibrating Sample Magnetometer (VSM) VSM 1.2H Oxford type.

Procedure

Nanomagnetite synthesis using a hydrothermal method

Nanomagnetite synthesis used the hydrothermal method that has been carried out by Cheng et al. [4] with modification. 0.3248 g $FeCl_3{\cdot}6H_2O$, 1.1764 g sodium citrate, and 0.3604 g urea were dissolved in 40 mL distilled water, the 0.1 g of PEG was added while stirring until it dissolved completely, then it put in a Teflon reactor. The reactor was put into the oven and set at 210 °C. The reaction time used in this study was 3.5, 5, 7, 9, and 12 h. The black precipitate that was formed then carried out with the help of an external magnetic field so that the process could be carried out quickly and more effectively. Washing the sediment with an aqueous solution, repeat it several time to obtain pure Fe_3O_4 sample. The sample was then dried in an oven for 12 h at 60 °C. The dried precipitate was then weighed and determined by the yield percentage by comparing the weight of precipitate to the theoretical Fe_3O_4 weight obtained from the stoichiometric equation.

Nanomagnetite crystal growth model

From the experimental data obtained, the diameter of nanomagnetite crystal plotted with the synthesis time to obtain curve graphs. The curve obtained from the experiment was matched with the model curve of oriented attachment (OA).

■ RESULTS AND DISCUSSION

Nanomagnetite Synthesis

Nanomagnetite synthesis by the hydrothermal method was carried out by mixing a precursor with a reducer and water in an autoclave at high temperature for 3.5–12 h. Nanomagnetite is formed by the reaction between the molecules of Fe(II) hydroxide with 2 molecules of Fe(III) hydroxide [8], with the following reactions:

$$Fe(OH)_{2(s)} + 2Fe(OH)_{3(s)} \rightarrow Fe_3O_{4(s)} + 4H_2O_{aq}$$

Stoichiometrically, nanomagnetite crystals were formed from Fe^{3+} and Fe^{2+} with a 2:1 ratio [9]. Citrate addition acts not only as a reducing agent but also plays an important role in the formation of crystal morphology

and aggregation prevention.

PEG functions as a capping agent and as a substance that can form and control the pore size and structure. PEG can dissolve in water, methanol, benzene, and dichloromethane, besides PEG also has a low toxic content. PEG has an –OH group on the surface of the nanoparticles making the nanoparticles hydrophilic and negatively charged, it makes the nanoparticles have a longer residence time in the bloodstream (high bioavailability) because they correspond to the nature of plasma proteins which are also hydrophilic and negatively charged. Phagocytosis will occur in non-polar (hydrophobic) particles and positively charged [10].

The nanomagnetite formed was characterized by black precipitate that can interact with magnetic fields. At temperature 210 °C, the concentration 0.05 M, 3.5 h of synthesis the precipitate began to form. Precipitate dispersed in water can interact and were attracted to the magnet. Products of nanomagnetite synthesis at reaction times of 3.5, 5, 7, 9 and 12 h have a blackish brown in the form of fine powder that can interact with external magnets. Visually the synthesized product at a reaction time of 3.5, 5, 7, 9, and 12 h would see a change of color from brownish yellow and will be darker.

Nanomagnetite Properties

Based on the diffractogram form of XRD analysis, it was identified that precipitate at 210 °C and a reaction time of 3.5 h had formed nanomagnetite, and the intensity would increase with increasing synthesis time. In Fig. 3, it can be seen that the diffractogram pattern for each synthesis has the same pattern as the ICSD standard diffractogram No. 01-076-7168 and the highest intensity at 2θ of 35.54, 57.0564, and 62.66°. It also can be seen that nanoparticles consist of the pure compound, without the presence of other iron oxide compounds or the reactants used in the synthesis process. This indicates that the hydrothermal method carried out in this experiment has good performance and selectivity in synthesizing one type of nanoparticles.

Mass produced (yield) the products will increase with increasing the synthesis time, at 3.5, 5, 7 and 9 h of synthesis time the yield was 39.18, 71.84, 78.37, 98.6% and then decreased slightly after 12 h of synthesis, which was only 97.96%.

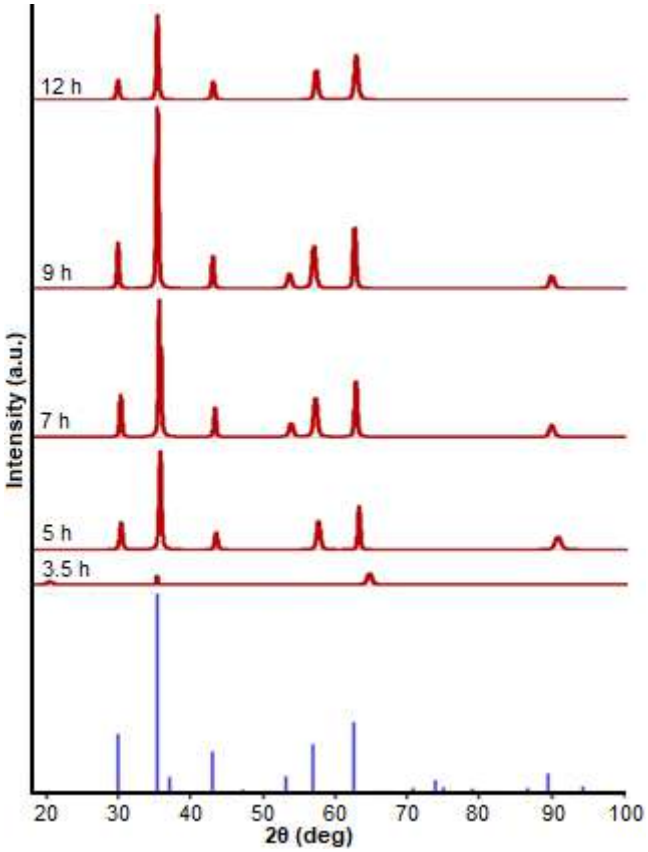

Fig 3. XRD diffractogram of nanomagnetite at 3.5, 5, 7, 9 and 12 h, temperature of 210 °C and concentration of 0.05 M

Table 1. Nanomagnetite crystal diameter at different synthesis time

Synthesis time (h)	Nanomagnetite crystal diameter (nm)
3.5	9.44
5	12.82
7	16.71
9	20.31
12	27.50

Using the Scherrer's equation, the crystal diameter of obtained magnetite at 3.5, 5, 7, 9, and 12 h were 9.44, 12.82, 16.71, 20.71, and 27.50 nm respectively.

To find out the magnetic properties, characterization was carried out using the vibrating sample magnetometer (VSM) method at 300 K with the application of an external magnetic field in the range of

-1 T to 1 T. Fig. 4 shows a hysteresis curve of nanomagnetite synthesized at 210 °C for 12 h with characteristic curves in the form of a symmetrical return sequence and a narrow curve. Based on the hysteresis loop curve, the saturation magnetic (Ms), coercivity field (Hc) and remnant magnetization (Mr) can be determined. The saturation magnetization value, also known as saturated magnetization, shows the ability of nanomagnetite particles to maintain the alignment of their magnetic domains when there are external magnets. The coercivity field is the amount of field needed to make the magnetization zero. The higher the coercivity field value, the stronger the magnetic properties of the material was. Meanwhile, the remnant magnetic shows the magnitude of the remaining magnetic field.

Narrow hysteresis loop shows small energy loss and ease of magnetization. This makes magnetite synthesis not only good to be applied as drug delivery but also very promising as recording media, data storage, and supercapacitor media. Nanomagnetite particles were soft magnetic; it can be seen from the hysteresis curve that has a symmetrical return sequence when there was a magnetic field. Soft magnetite needs very small energy for magnetization process. The superparamagnetic properties of magnetite are due to the electron transfer between Fe^{3+} and Fe^{2+} in octahedral lattice [11] and the presence of an unbalanced antiparallel spin pair on the crystal lattice [12]. Size is also an important factor that determines the paramagnetic properties. Nanomagnetite particles with a diameter of less than 30 nm and paramagnetic properties are obtained [4,12].

The diameter of nanomagnetite particles is related to their magnetic properties. At room temperature, a particle with a size of 5 nm is superparamagnetite without interaction between particles, 19 nm is ferrimagnetite and 11 nm iron oxide nanoparticles are superparamagnetite with several interactions between particles [13]. The saturation magnetization (Ms) is perpendicular to the degree of crystallinity of the nanoparticles. The increase of particle crystallinity also increases the saturation magnetization [14]. Due to the high crystallinity, nanomagnetite structure is almost close to the crystal structure of bulk material [15]. At synthesis time of 12 h with 0.05 M concentration, the Ms of nanomagnetite was 81 (Emu/g). The decrease in crystal diameter increased the susceptibility to the magnet because of the formation of a single electron spin domain [16-17]. The value of nanomagnetite saturation magnetization is smaller than the bulk material due to incomplete coordination between atoms on the surface and the presence of superexchange (SE) interactions between Fe ions connected by O^{2-} ions which cause the spin disorder on the particle surface [18].

Morphology characterization of nanoparticles was analyzed using JEM-1400 with TEM image. Based on

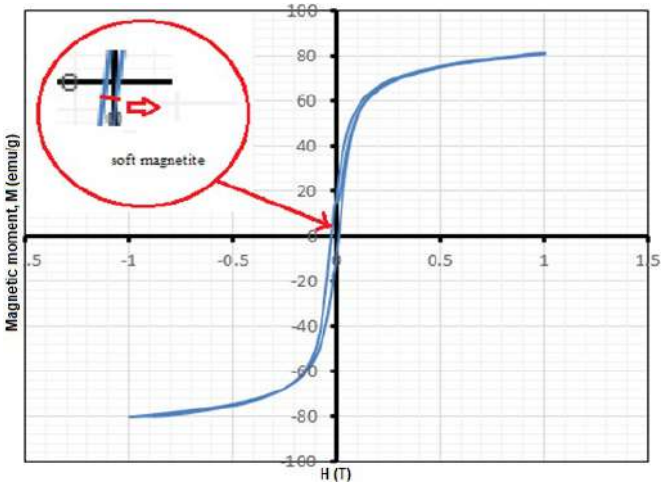

Fig 4. Magnetite loop hysteresis curve at the synthesis of 12 h 210 °C concentration of 0.05 M

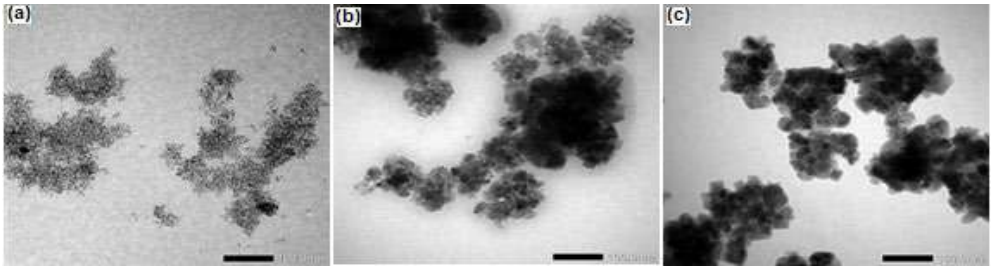

Fig 5. TEM images of synthesized samples at the time of (a) 3.5 h, (b) 5 h, and (c) 12 h

TEM images at 80,000 times magnification, the crystal morphology of nanomagnetite can be seen. Nanoparticles with 3.5 h of synthesis time were seen in TEM images as black and dark crystal.

At synthesis time of 3.5 h, it was generally seen that the particles formed were nano-sized with uniform size distribution and no agglomeration. Nanoparticles were spherical-form with a diameter of about 20 nm. Whereas the nanomagnetite synthesized with 7 h of synthesis time, the shape was close to the core-shell shape with a dark core and brighter part of the shell with a diameter less than 50 nm. At the synthesis time of 12 h, a perfect formation of nanomagnetite was formed with dense core-shell and diameter about 100 nm. This core-shell structure consists of small particles with a size of about 20 nm, which were agglomerated with high crystallinity in the core and amorphous in the shell.

Nanomagnetite Crystal Growth by Oriented Attachment (OA) Model

Based on experimental data obtained from XRD, the k value obtained from the concentration of 0.05 M with various reaction times is shown in Fig. 6. From the value of k, the diameter of the model was determined by substituting D_0 and t parameters, so the diameter of the model for certain time was obtained. Nanomagnetite crystal diameter from the calculation of the 0.05 M reactant concentration has a k value of –2.18. From the value of k, the diameter of nanomagnetite crystal could be calculated used the OA model.

The diameter of the model is still close to the experimental results with a small percent error, as seen in Fig. 7. At a temperature of 210 °C, the diameter of the model (D) for 3.5, 5, 7, 9, and 12 h of the reaction was 9.44, 11.69, 16.05, 20.41, and 26.72 nm, respectively whereas the experimental results of the particle diameter were 9.44, 12.82, 16.71, 20.31, and 27.50 nm.

The crystal diameter of the experimental and calculation results in the increase of reaction time will approach the model point where the elevation point will decrease from the reaction time of 5, 7, 9, and 12 h. The diameter of the model calculation approximates the experimental results with small percent errors. At 5 h of reaction time and 0.05 M concentration, the percentage error obtained was 9.6%. The increasing of reaction time, the growth of magnetite crystals will be more perfect with increasing reaction time and modeling of Oriented Attachment (OA).

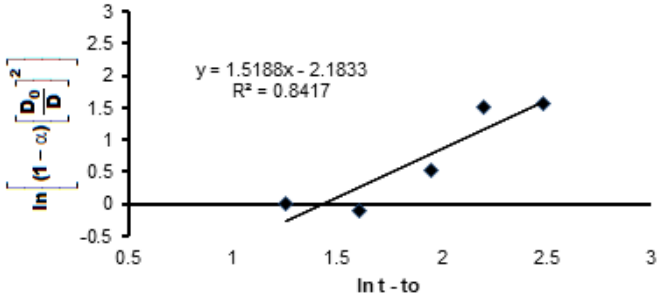

Fig 6. Graph value of k at 0.05 M 210 °C

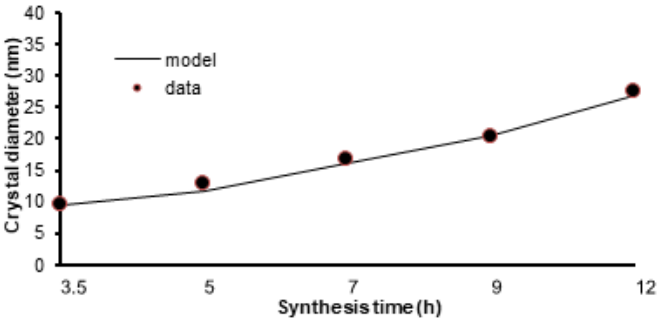

Fig 7. Diameter of magnetite crystal particle from experiment and modeling result

■ CONCLUSION

Nanomagnetite can be synthesized using a hydrothermal method with a synthesis time of 3.5, 5, 7, 9, and 12 h at 210 °C. The reaction time affects the growth of magnetite crystal. The crystal diameter magnetite increases from 9.44 to 27.50 nm with increasing synthesis time from 3.5 to 12 h. The morphology of nanomagnetite is core-shell shape without agglomeration with size particles approximately 100 nm. The saturation magnetization (Ms) of nanomagnetite at 12 h synthesis time is 81 (Emu/g) with superparamagnetic properties, showing that the obtained nanomagnetite is suitable for drug delivery system (DDS) application. Model of Oriented Attachment (OA) is appropriate for crystal growth of the magnetite with k value of –2.18.

■ ACKNOWLEDGMENTS

The authors are grateful for the financial support from Ministry of Research, Technology and Higher Education of Indonesia for the financing of this research with Contract Number 086/SP2H/LT/DRPM/2018.

■ REFERENCES

[1] Hung, L.H., and Lee, A.P., 2007, Microfluidic devices for the synthesis of nanoparticles and biomaterials, *J. Med. Biol. Eng.*, 27 (1), 1–6.

[2] Arruebo, M., Fernández-Pacheco, R., Ibarra, M.R., and Santamaría, J., 2007, Magnetics nanoparticles for drug delivery, *Nano Today*, 2 (3), 22–32.

[3] Chomoucka, J., Drbohlavova, J., Huska, D., Adam, V., Kizek, R., and Hubalek, J., 2010, Magnetic nanoparticles and targeted drug delivering, *Pharmacol. Res.*, 62 (2), 144–149.

[4] Cheng, W., Tang, K., Qi, Y., Sheng, J., and Liu, Z., 2010, One-step synthesis of superparamagnetic monodisperse porous Fe_3O_4 hollow, *J. Mater. Chem.*, 20 (9), 1799–1805.

[5] Zhang, J., Huang, F., and Lin, Z., 2010, Progress of nanocrystalline growth kinetics based on oriented attachment, *Nanoscale*, 2 (1), 18–34.

[6] Huang, F., Zhang, H., and Banfield, F.J., 2003, Two-stage crystal-growth kinetics observed during hydrothermal coarsening of nanocrystalline ZnS, *Nano Lett.*, 3 (3), 373–378.

[7] Bae, Y.H., and Park, K., 2011, Targeted drug delivery to tumors, myths, reality and possibility, *J. Phys. D: Appl. Phys.*, 153 (3), 198–205.

[8] Tartaj, P., Morales, M.P., Veintemillas-Verdaguer, S., González-Carreño, T., and Serna, C.J., 2003, The preparation of magnetic nanoparticles for applications in biomedicine, *J. Phys. D: Appl. Phys.*, 36 (13), 182–197.

[9] Mohapatra, M., and Anand, S., 2010, Synthesis and applications of nano-structured iron oxides/hydroxides – A review, *J. Eng. Sci. Technol.*, 2 (8), 127–146.

[10] Cao, X., Zhang, B., Zhao, F., and Feng L., 2012, Synthesis and properties of MPEG-coated superparamagnetic magnetite nanoparticles, *J. Nanomater.*, 2012, 607296.

[11] Zhang, H., and Banfield, J.F., 1999, New kinetic model for the nanocrystalline anatase-to-rutile transformation revealing rate dependence on number of particles, *Am. Mineral.*, 84 (4), 528–535.

[12] Hwang, N.M., Jung, J.S., and Lee, D.K., 2012, "Thermodynamics and kinetics in the synthesis of monodisperse nanoparticles" in *Thermodynamics-Fundamentals and Its Application in Science*, Eds. Morales-Rodriguez, M., InTech, 371–388.

[13] Hyeon, T., Lee, S., Park, J., Chung, Y., and Na, H.B., 2001, Synthesis of highly crystalline and monodisperse maghemite nanocrystallites without a size-selection process, *J. Am. Chem. Soc.*, 123 (51), 12798–12801.

[14] Lu, A., Salabas, E.L., and Schuth, F., 2007, Magnetic nanoparticles: Synthesis, protection, functionalization, and application, *Angew. Chem. Int. Ed.*, 46 (8), 222–244.

[15] Chen, B.A., Mao, P., Cheng, J., Gao, F., Xia, G.H., Xu, W.L., Shen, H.L., Ding, J.H., Gao, C., Sun, Q., Chen, W.J., Chen, N.N., Liu, L.J., Li, X.M., and Wang, X.M., 2010, Reversal of multidrug resistance by magnetic Fe_3O_4 nanoparticle copolymerizating daunorubicin and MDR1 shRNA expression vector in leukemia cells, *Int. J. Nanomed.*, 5, 437–444.

[16] Gustafson, H.H., Holt-Casper, D., Grainger, D.W., and Ghandehari, H., 2015, Nanoparticle uptake: The phagocyte problem, *Nano Today*, 10 (4), 487–510.

[17] Sabyrov, K., Burrows, N.D., and Penn, R.L., 2013, Size-dependent anatase to rutile phase transformation and particle growth, *Chem. Mater.*, 25 (8), 1408–1415.

[18] Coulter, J.A., Jain, S., Butterworth, K.T., Taggart, L.E., Dickson, G.R., McMahon, S.J., Hyland, W.B., Muir, M.F., Trainor, C., Hounsell, A.R., O'Sullivan, J.M., Schettino, G., Currell, F.J., Hirst, D.G., and Prise, K.M., 2012, Cell type-dependent uptake, localization, and cytotoxicity of 1.9 nm gold nanoparticles, *Int. J. Nanomed.*, 7, 2673–2685.

Further Analysis of *Burkholderia pseudomallei* MF2 and Identification of Putative Dehalogenase Gene by PCR

Mohamed Faraj Edbeib[1,2,*], Roswanira Abdul Wahab[3], Fahrul Huyop[3,4,], Hasan Murat Aksoy[2], and Yilmaz Kaya[5,6]**

[1]*Department of Animal Production, Faculty of Agriculture, Baniwalid University, Libya*

[2]*Department of Plant Pathology, Faculty of Agriculture, Ondokuz Mayis University, 55100 Samsun, Turkey*

[3]*Department of Chemistry, Faculty of Science, Universiti Teknologi Malaysia, 81310 UTM Johor Bahru, Malaysia*

[4]*Department of Biosciences, Faculty of Science, Universiti Teknologi Malaysia, 81310 UTM Johor Bahru, Malaysia*

[5]*Department of Agricultural Biotechnology, Faculty of Agriculture, Ondokuz Mayis University, 55100 Samsun, Turkey*

[6]*Department of Biology, Faculty of Science, Kyrgyz-Turkish Manas University, Kyrgyzstan*

** **Corresponding author:***

tel: +607-55334148
email: faemohamed2@live.utm.my; fahrul@utm.my***

Received: February 2, 2019
Accepted: August 1, 2019

DOI: 10.22146/ijc.43262

Abstract: *Halogenated organic compounds are extensively and widely used as pesticides, herbicides, and antibiotics that contribute to the pollution. This research was aimed to further analyze and characterize a bacterium that has the ability to utilize 2,2-dichloropropionic acid (2,2-DCP) as a model to study dehalogenase enzyme production. Microscopic observation, biochemical tests and PCR technique were carried out in order to characterize the isolated bacterium. Strain MF2 showed its ability to grow on 10 mM 2,2-DCP liquid minimal medium with doubling time of 13 h with maximum chloride ion released of 19.8 µmolCl^-/mL. The 16S rDNA analysis suggested that strain MF2 belongs to the genus* Burkholderia. *This was supported by the microscopic observation and biochemical tests. Dehalogenase gene was observed when using only primers $dehI_{for1}$ and $dehI_{rev2}$ derived from group I deh PCR primer sequences, whereas no amplification using dhlB-314-forward and dhlB-637-reverse (group II dehalogenase) and haloacetate dehalogenase (H2-1157-forward and H2-1662-reverse) PCR primer sequences. The results suggested that, possibly, dehalogenase from MF2 was related to group I deh. In conclusion, strain MF2 showed the ability to utilize 2,2-DCP as sole source of carbon and energy. Further analysis revealed the MF2 strain consisted of dehalogenase gene that could be used for degradation of man-made halogenated compounds present in the environment. Using existing dehalogenase PCR primers, it was possible to amplify the dehalogenase genes sequence.*

Keywords: Burkholderia pseudomallei*; 2,2-dichloropropionate; biodegradation; dehalogenase gene; 16S rDNA gene*

■ INTRODUCTION

Environmental contamination from industrial chemicals, herbicide or pesticide from agricultural activities is an ongoing dilemma to the society. 2,2-dichloropropionate (abbreviation known as 2,2-DCP) or Dalapon® is a synthetic halogenated compound used in herbicides. The demand for herbicide in agriculture is increasing and its use is inevitable to improve crop yields in many developing countries. In some areas like in the Pineapple Plantation, Pekan Nenas Johor, Malaysia, it is believed that herbicide use will solve all weed problems. Xenobiotic compounds, mostly man-made chemicals when present in high concentrations in the environment can be very hazardous to the ecosystem and some resistant to degradation [1]. Among these xenobiotics, halogenated compounds are considered very toxic and

may cause enormous problems to human health and the environment. However, the answer to such predicament perhaps lie in the very ground we stand on. It is believed that microorganisms are capable of degrading xenobiotics [2-3].

Soil microorganisms such as *Rhizobium* sp., *Methylobacterium* sp. HJ1 and *Arthrobacter* sp. have been reported to be capable of utilizing such compounds as their sole carbon source for growth while liberating the organically bound chlorine as chloride ions at the same time [4-6]. The molecular structure of the 2,2-DCP consists of three carbons with the molecular formula $CH_3CCl_2CO_2H$ (Fig. 1). The first carbon is a carboxylic functional group (-COOH) and followed by two chloride substituents at C-2 of α carbon position. From chemistry point of view, the α-chlorination is particularly important within the halogenated propionic series because it results in herbicidal activity. Acids chlorinated in other positions do not possess phytotoxic properties unless they are also α-chlorinated. Similarly, increasing chain length reduces the herbicidal activity of the α-chloroacids, for instance 2,2-dichlorohexanoic acid being completely inactive. It has been reported that substitution of other halogens for chloride generally decreases herbicidal activity of these acids [7].

Biodegradation using microorganisms is one of the main and natural processes that help remove xenobiotic chemicals such as chloroaliphatic compounds from the environment [8-9]. Also, microorganisms can benefit from the use of the contaminant as an electron donor and carbon source to support growth. Hydrolytic dehalogenases represent the key position in the degradation of haloaliphatic compounds. These enzymes catalyze the cleavage of carbon-halogen bonds by nucleophilic substitution, replacing the halogen ion by a hydroxyl group derived from water [10]. Dehalogenase enzymes metabolize chlorinated substituents and the halogens are enzymatically removed to form non-halogenated compounds. In cases where biodegradation of halogenated compounds are lacking, it is often due to the inability of microorganisms to effectively metabolize such compounds with chemical structures to which these microbes have yet to be exposed during the course of evolution. In other words, recalcitrance

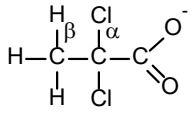

Fig 1. Basic structure of 2,2-DCP

of certain halogenated compounds generally is the result of a lack of efficient metabolic pathways. Nevertheless, there are reports of many microorganisms that have the ability to metabolize xenobiotic organohalogens [8]. This led to the idea that such microorganisms must have evolved their catabolic pathways during the past few decades and is thus suited to study the natural assembly of catabolic routes.

According to Slater et al. [11], dehalogenases can be classified based on substrate specificities. On the other hand, Hill et al. [12] classified dehalogenases based on genetic approach by investigating the diversity and molecular ecology of the dehalogenase genes. Using phylogenetic classification, dehalogenase is divided into group I and group II. These two families are evolutionarily unrelated and together represent almost all of α-halocarboxylic acid (αHA) *deh* genes as described. Group I is a non-stereospecific dehalogenase which act on C2-halogenated short chain aliphatic acids including D-isomer and L-isomer. For example, group I dehalogenases are able to act on D-2-chloropropionic acid (D-2-CP), L-2-chloropropionic acid (L-2-CP), D,L-2-chloropropionic acid (D,L-2-CP) and 2,2-DCP. Meanwhile, dehalogenases of group II is stereospecific that acts only on L-2-CP but not D-2-CP and 2,2-DCP [12]. Other kinds of dehalogenases, termed haloacetate dehalogenase (EC 3.8.1.3) that acts specifically on halogenated acetates to yield glycolate, are also in group II [13]. To understand how these dehalogenases function, *in silico* studies on enzyme-substrate binding need to be carried out provided that full dehalogenase sequence can be obtained in gene isolation by PCR [14-15].

Previous investigations have described that the molecular approach could be used to uncover genus/species and gene of interest like dehalogenase genes of the newly isolated microorganisms [16]. Therefore, the current study is focused on characterizing a bacterium isolated from mud soil from pineapple

plantation that can degrade 2,2-DCP and amplification of the putative dehalogenase gene using dehalogenase degenerate primers. In the current investigation, strain MF2 was further characterized and its putative dehalogenase classification was then determined.

■ EXPERIMENTAL SECTION

Isolation

The minimal growth media for growing bacteria was prepared as described by Hamid et al. [17]. Mud soil taken from a Pineapple agricultural area in Johor (10 g) was added into 250 mL conical flask containing 100 mL of minimal media with 10 mM of 2,2-DCP as the sole carbon and energy source. The bacterial culture was incubated in an incubator shaker for 3–7 days at 30 °C. For solid medium, Oxoid bacteriological agar No.1 (1.5% w/v) was added prior to sterilization. Bacterial culture was streaked onto the agar plate containing the same ingredients as the liquid minimal media. One pure colony was obtained after several subcultures by streaking on solid minimal media. The bacterial strain was characterized *via* morphological/biochemical tests as described in Bergey's Manual of Systematic Bacteriology [18].

Determination of Bacterial Growth

The extent of growth was determined by measuring the absorbance at A_{680nm} and the release of chloride ions was measured at A_{460nm} [19]. Measurement of the free halide released during the dehalogenation reaction was carried out by an adaptation of the method of Bergmann and Sanik [20]. The chloride ion released was defined 1 mM chloride is equivalent to 1 μmol Cl^-/mL.

PCR Amplification of 16S rDNA Gene

The chromosomal DNA was extracted using Qiagen DNA extraction kit as described by the manufacturer. PCR amplification was carried out using universal primers to amplify the 16S rDNA gene as described by Fulton and Cooper [21].

Partial Biochemical Tests

Different types of biochemical tests were carried to ascertain the identity of the bacteria by carrying out spore staining, catalase test, urease test, oxidase test, lactose utilization test, indole test, gelatin hydrolysis, motility test and nitrate reduction test.

PCR Amplification for Putative Dehalogenase Gene

The source of the primers were obtained from group I deh PCR primer sequences $dehI_{for1}$ and $dehI_{rev2}$ [12], *Xanthobacter autotrophicus* (dhlB314 and dhlB 637) belonging to group II *deh* PCR primer sequences and *Moraxella* sp. for primers dehH2-1157 and dehH2-1662 of the haloacetate dehalogenase [22]. The PCR primers and PCR cycles are summarized in Table 1 and 2, respectively.

Table 1. Dehalogenase oligonucleotide primers

Organisms	Genes	Primer sequences	Reference
	Group I Various sources	**$dehI_{for1}$ (Forward):** 5'-ACGCTGCGCGTGCCATGGGT-3' **$dehI_{rev2}$ (Reverse):** 5'-CGCAATCACATGGAAGTCACT-3'	Hill et al. [12]
Xanthobacter autotrophicus	Group II dehalogenase	**dhlB-314 (Forward):** 5'-TCTGGCGGCAGAAGCAGCTGG-3' **dhlB-637 (Reverse):** 5'-CGCGCTTGGCATCGACGCTGATG-3'	van Der Ploeg et al. [22]
Moroxella sp.	Haloacetate dehalogenase H-2	**dehH2-1157 (Forward):** 5'-CGGCACCCTCTACGATGTGCATTCGG-3' **dehH2-1662 (Reverse):** 5'-CATCCCATGGATTCGACGATACAAAGA-3'	Kawasaki et al. [13]

Table 2. PCR cycles for amplification of putative dehalogenase gene

Segments	Cycles	Temperature (°C)	Duration
1	1	94	2 min 30 sec
2	35	94	30 sec
		55	30 sec
		72	4 min
3	1	72	10 min
4	1	4	∞

DNA Sequencing and Molecular Analysis

The PCR products were purified using Promega Wizard® SV Gel and PCR Cleanup system. After purification, all PCR products were sent for sequencing at SOYGEN BIOTECHNOLOGY, Istanbul (Turkey).

Scanning Electron Microscopy (SEM)

Colonies of bacterial strain MF2 grown on solid media supplemented with 2,2-DCP for 24 h were excised as small agar blocks of 0.5 cm^3. The colonies were pre-fixed with 25% glutaraldehyde in 100 mM phosphate buffer (pH 7.2) for 2 h and then post fixed with 1% osmium tetroxide in the same buffer. The fixed cells were dehydrated in a series of increasing ethanol concentrations (30–95%) for 15 min and then in 100% ethanol for 20 min. The cells were substituted with absolute isoamyl acetate for 15 min and air-dried. The cells were coated with gold by using a gold sputter coater and examined with a Hitachi S.2500C (Hitachi Co., Japan) scanning electron microscopy.

■ RESULTS AND DISCUSSION

Analysis of Growth on 2,2-DCP Minimal Medium and Chloride Ion Released

The bacteria were screened on solid media containing 10 mM 2,2-DCP as a carbon source. After 7 days incubation, a pure colony was observed on 10 mM 2,2-DCP solid minimal medium. This colony was then grown in 10 mM 2,2-DCP liquid minimal medium. The bacterium showed the ability to utilize 2,2-DCP as sole source of carbon under aerobic conditions with doubling time of approximately 13 h (Fig. 2). Analysis of the chloride ions released was also determined with the maximum chloride released estimated at 19.8 µmol Cl^-/mL.

16S rDNA Gene Sequence Analysis

The 16S rDNA PCR product showed that approximately 1500 bp DNA band was amplified. All the 1544 bp 16S rDNA gene sequences were analyzed using BLASTn option (http:www.ncbi.nlm.nih.gov/BLAST/). The sequence matched with maximum identity of 99% to the bacterium *Burkholderia pseudomallei* (data not shown). Therefore, the current organism was designated as *Burkholderia pseudomallei* strain MF2.

Characterization based on biochemical properties and scanning electron microscopy (SEM) (Fig. 3) revealed the basic cellular morphology of the bacteria on

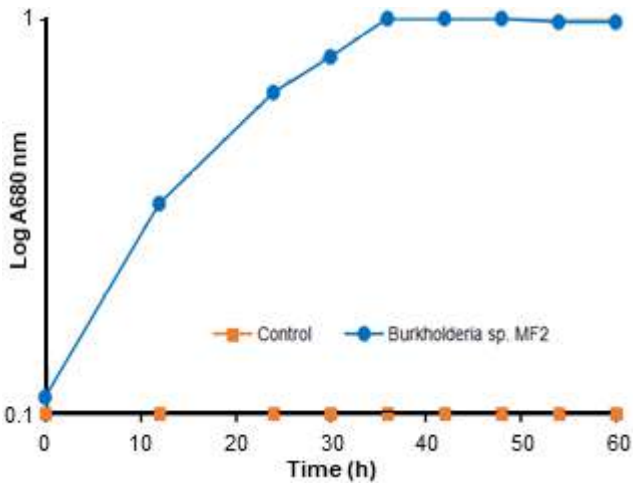

Fig 2. Maximum growth curve of *Burkholderia* sp. MF2 on 10 mM 2,2-DCP minimal medium. Control (*E. coli*) showing no growth in 10 mM 2,2-DCP minimal medium

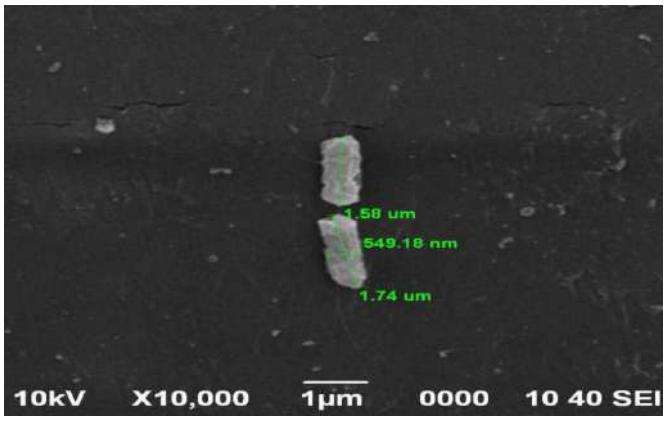

Fig 3. Electron microscopy analysis of strain MF2 appear as short rods with approximate length of 1.6–1.7 µm; width 0.55 µm (549 nm)

Table 3. Morphological and biochemical characterization of strain MF2

Properties	Details
Cell shape	rod
Size	length of 1.6~1.7 μm; width 0.55 μm
Colony morphology	Smooth, mucoid and somewhat elevated
Gram staining	Gram Negative
Spore staining	-
Oxygen requirement	Aerobic
Catalase	+
Oxidase	+
Urease	+
Gelatin hydrolysis	+
Citrate	+
Lactose utilization	-
Motility test	+
Nitrate reduction	-
Identity	*Burkholderia* sp.

+: positive, - : negative

solid minimal medium after 5 days incubation period at 30 °C. The bacteria were rod-shaped with colonies showing smooth, mucoid and somewhat elevated edges. Gram staining confirmed that strain MF2 was rod-shaped, Gram negative bacteria. Details of the physiological and biochemical properties of strain MF2 are depicted in Table 3.

Amplification of Putative Dehalogenase Gene

The PCR reaction was carried out as previously described and the PCR product was observed using gel electrophoresis. The result showed a single band of approximately 396 bp was amplified using primers related to group I dehalogenase. On the other hand, no amplification of DNA band was detected for the group II dehalogenase and haloacetate dehalogenase H-2.

Sequencing and Analysis of Putative Dehalogenase Gene

The partial sequence of putative dehalogenase was successfully sequenced and analyzed showing 360 bp DNA sequence (Fig. 4). The DNA Open Reading Frame (ORF) is a graphical analysis tool that can be used to find possible functional structural genes. The ORF Finder encodes for 120 amino acids only. The deduced sequence was short without start and stop codon. In order to check the identity of the current amino acids, multiple sequence analysis was carried out among both

```
1    GCGATCGCGATCTTGGACGCGTTGAGGAGGATCCCGACAGCTTGCAAACATTTTGTATGG 60
1    AlaIleAlaIleLeuAspAlaLeuArgArgIleProThrAlaCysLysHisPheValTrp 20

61   GTTTTAACTGATCCAAAACTCCTTGCTGTCTCACTGAATTGGATTCAACCCGTCCTCAAG 120
21   ValLeuThrAspProLysLeuLeuAlaValSerLeuAsnTrpIleGlnProValLeuLys 40

121  AGCGATCTTTTTCTTGACTACGCCACCGGGCTCGTGCTTAAGTCTGACGGGGAAGATGAA 180
41   SerAspLeuPheLeuAspTyrAlaThrGlyLeuValLeuLysSerAspGlyGluAspGlu 60

181  ACCAGGAAAGTTTCGTCTCGCTTCAGATTTGCAGATGGTTTGACGCTGCTGGCACTCTGT 240
61   ThrArgLysValSerSerArgPheArgPheAlaAspGlyLeuThrLeuLeuAlaLeuCys 80

241  CTGGAACCAATCATTCGACCTGCTTCTTCTGCCGGAAGAATCCCTTGGGTTGCTTTATAC 300
81   LeuGluProIleIleArgProAlaSerSerAlaGlyArgIleProTrpValAlaLeuTyr 100

301  CCATTCGACGAAGTACCATCGGTGTTACGGGAGCTCCGAGGCCGGGGGCTCAAGCTAGCA 360
101  IleLeuSerAsnGlySerProHisSerIleAsnAlaValValSerAsnAlaGlyLeuArg 120
```

Fig 4. Partial sequence of nucleotide and deduced amino acid of putative dehalogenase from strain MF2

groups I and II dehalogenases. The results showed there were no sequence identities with the known dehalogenases either group I or II, suggesting current isolate might be of a different kind of dehalogenase group. However, further analysis is needed to re-confirm this.

Burkholderia sp. can be found in the natural environment, such as soils, rhizospheres, water and from infected humans by melioidosis [23-26]. Very few halogenated aliphatic acids supported growth of the organisms. According to Watanabe et al. [27], there are differences between the bacteria isolated in the laboratory by enrichment and the bacteria performing the biodegradation *in situ*. The bacteria involved in biodegradation tend to be neglected more often when investigating pure culture isolates, since they are not always enriched in the process [28].

Burkholderia pseudomallei strain MF2 that was isolated from mud soil could grow on 2,2-DCP as sole source of carbon and energy. To allow growth on 2,2-DCP, there are some basic criteria to be fulfilled. First, the organism must either possess or synthesize dehalogenase which is capable of removing the substituent halogen(s) from halogenated compounds. Next, the dehalogenation product should be non-toxic and easily converted to an intermediate via the organism's central metabolic pathway. The halogenated compound should be able to enter cells either passively or by active transport in order to reach the site of dehalogenase activity. Last but not least, the halogenated compound should be non-toxic to the organism at normal intracellular concentrations [11].

This study sequenced the 1.5-kb 16S rDNA gene. The results of the sequence was analyzed by sequence comparisons to the sequence in the NCBI database. The phylogenetic analysis of 16S rDNA nucleotide sequence suggests the identity of the current isolate. Morphological and biochemical tests showed that MF2 is a rod-shaped Gram-negative bacteria. Based on the Bergey's manual of determinative bacteriology [18], the biochemical test supported the 16S rDNA indicating that strain MF2 belongs to the genus *Burkholderia* sp.

Cells doubling time of MF2 was calculated to be 13 h in 10 mM 2,2-DCP with concomitant release of chloride ions in the growth medium. The growth was relatively slower than that of *Serratia* sp [29], and more or less similar to the growth of *Rhizobium* sp. [30]. MF2 utilized 2,2-DCP as sole carbon source and it was believed to have eliminated the chlorine atom from the halogenated compound and produced pyruvate as a main product similar to what has been reported earlier by Slater et al. [11]. The maximum chloride ion released was 19.8 μmol Cl^-/mL, with almost all carbon source consumed after 42 h growth. It can be said that the MF2 strain exhibit a rather slow rate of 2,2-DCP utilization which could be attributed to a poor uptake system and/or low expression of the dehalogenase enzyme [31-35].

PCR amplification was used to detect partial dehalogenase genes. Group I *deh* genes, are specific towards both D and L forms of the substrate while group II *deh* genes are only active on the L form. Successful amplification of the putative dehalogenase gene was obtained using primers from group I suggesting the dehalogenase from MF2 might fall in the same category. In contrast, Bagherbaigi et al. [36] reported that strain S1 grew well on α/β–haloalkanoic acids (α/β-HA) and only group II primers [22] from *Xanthobacter autotrophicus* - dhlB314 and dhlB637 showed amplification. This observation was possibly due to L-2-haloacid dehalogenases being more common than group I dehalogenases. On the other hand, two possible reasons why using group I primers could not amplify the S1 gene: (1) the primers might not be universal for some bacteria, and (2) only a single dehalogenase gene may be present that acts on both αHA and βHA.

Rhizobium sp. RC1 was reported to contain more than one dehalogenase [34-35]. DehE or D,L-haloacid dehalogenase from *Rhizobium*sp. RC1 is unique because it can act on chiral carbons of both enantiomers. It is curious why *Rhizobium* sp. RC1 has more than one dehalogenases, when DehE alone can act on all of the substrates that DehD and DehL can also act on. Our current findings suggested that only a single dehalogenase may be present based on an *in silico* study by docking simulation [16,37-39]. Based on these findings, it can be inferred that some key catalytic residues of DehE is similar to that of dehalogenase of S1 that can grow on 3CP. However, more work involving

gene cloning and protein analysis are required for further characterization.

■ CONCLUSION

In conclusion, a molecular approach can be used to screen new genes of interest provided that the specific universal primers has no limitation. This study is the first study to investigate the presence of a putative dehalogenase gene in *Burkholderia pseudomallei* strain MF2 isolated from mud soil, associated with growth on 2,2-DCP or αHA. Using molecular tools, primers belonging to group I or II dehalogenases are possibly able to probe dehalogenase gene(s) present in the newly isolated microorganisms in the soil community.

■ ACKNOWLEDGMENTS

Yilmaz Kaya and Fahrul Huyop would like to thank, The Scientific Technological Research Council of Turkey (TUBITAK), Program 2221 - Fellowships for Visiting Scientists and Scientists on Sabbatical Leave and Grant number 1059B211800242 for partly sponsoring this research. MFE and HMA thanks the Scientific Technological Research Council of Turkey (TUBITAK), Program 2216 – Research Fellowship Program for International Researchers Grant number 1059B211800242 for partly supporting this research. YK would like to thank Ondokuz Mayis University for joint financial support of the project (PYO.ZRT.1911.15.001).

■ REFERENCES

[1] Rieger, P.G., Meier, H.M., Gerle, M., Vogt, U., Groth, T., and Knackmuss, H.J., 2002, Xenobiotics in the environment: Present and future strategies to obviate the problem of biological persistence, *J. Biotechnol.*, 94 (1), 101–123.

[2] van Pée, K.H., and Unversucht, S., 2003, Biological dehalogenation and halogenation reactions, *Chemosphere*, 52 (2), 299–312.

[3] Karpouzas, D.G., and Singh, B.K., 2006, Microbial degradation of organophosphorus xenobiotics: Metabolic pathways and molecular basis, *Adv. Microb. Physiol.*, 51, 119–225.

[4] Huyop, F., Yusn, T.Y., Ismail, M., Wahab, R.A., and Cooper, R.A., 2004, Overexpression and characterisation of non-stereospecific haloacid dehalogenase E (DehE) of *Rhizobium* sp, *Asia Pac. J. Mol. Biol. Biotechnol.*, 12 (1-2), 15–20.

[5] Huyop, F., Jing, N.H., and Cooper, R.A., 2008, Overexpression, purification and analysis of dehalogenase D of *Rhizobium* sp, *Can. J. Pure Appl. Sci.*, 2 (2), 389–392.

[6] Edbeib, M.F., Wahab, R.A., and Huyop, F., 2016, Characterization of an α-haloalkanoic acid–degrading *Pseudomonas aeruginosa* MX1 isolated from contaminated seawater, *Biorem. J.*, 20 (2), 89–97.

[7] Leasure, J.K., 1964, Metabolism of herbicides, halogenated aliphatic acids, *J. Agric. Food Chem.*, 12 (1), 40–43.

[8] Sinha, S., Chattopadhyay, P., Pan, I., Chatterjee, S., Chanda, P., Bandyopadhyay, D., Das, K., and Sen, S.K., 2009, Microbial transformation of xenobiotics for environmental bioremediation, *Afr. J. Biotechnol.*, 8 (22), 6016–6027.

[9] Edbeib, M.F., Wahab, R.A., Kaya, Y., and Huyop, F., 2017, In silico characterization of a novel dehalogenase (DehHX) from the halophile *Pseudomonas halophila* HX isolated from Tuz Gölü Lake, Turkey: Insights into a hypersaline-adapted dehalogenase, *Ann. Microbiol.*, 67 (5), 371–382.

[10] Schwarze, R., Brokamp, A., and Schmidt, R.J.F., 1997, Isolation and characterization of dehalogenases from 2,2-dichloropropionate-degrading soil bacteria, *Curr. Microbiol.*, 34 (2), 103–109.

[11] Slater, J.H., Bull, A.T., and Hardman, D.J., 1996, Microbial dehalogenation of halogenated alkanoic acids, alcohols and alkanes, *Adv. Microb. Physiol.*, 38, 133–176.

[12] Hill, K.E., Marchesi, J.R., and Weightman, A.J., 1999, Investigation of two evolutionarily unrelated halocarboxylic acid dehalogenase gene families, *J. Bacteriol.*, 181 (8), 2535–2547.

[13] Kawasaki, H., Tsuda, K., Matsushita, I., and Tonomura, K., 1992, Lack of homology between two haloacetate dehalogenase genes encoded on a plasmid from *Moraxella* sp. strain B, *J. Gen. Microbiol.*, 138 (7), 1317–1323.

[14] Adamu, A., Wahab, R.A., Shamsir, M.S., Aliyu, F., and Huyop, F., 2017, Deciphering the catalytic amino acid residues of l-2-haloacid dehalogenase (DehL) from *Rhizobium* sp. RC1: An *in silico* analysis, *Comput. Biol. Chem.*, 70, 125–132.

[15] Adamu, A., Shamsir, M.S., Wahab, R.A., Parvizpour, S., and Huyop, F., 2017, Multi-template homology-based structural model of L-2-haloacid dehalogenase (DehL) from *Rhizobium* sp. RC1, *J. Biomol. Struct. Dyn.*, 35 (15), 3285–3296.

[16] Nemati, M., Abdulghader, H.F., Gicana, R.G., Lamis, R.J.S., Ibrahim, N., Hamid, A.A.A., and Huyop, F.Z., 2013, Identification of putative Cof-like hydrolase associated with dehalogenase in *Enterobacter cloacae* MN1 isolated from the contaminated sea-side area of the Philippines, *Malays. J. Microbiol.*, 9 (3), 253–259.

[17] Hamid, A.A.A., Hamdan, S., Ariffin, S.H., and Huyop, F., 2010, Molecular prediction of dehalogenase producing microorganism using 16S rDNA analysis of 2,2-dichloropropionate (Dalapon) degrading bacterium isolated from volcanic soil, *J. Biol. Sci.*, 10 (3), 190–199.

[18] Bergey, D.H., and Holt, J.G., 1994, *Bergey's Manual of Determinative Bacteriology*, 9th Ed., Williams and Wilkins, Baltimore.

[19] Alomar, D., Hamid, A.A.A., Khosrowabadi, E., Gicana, R.G., Lamis, R.J., Huyop, F., and Tengku Abdul Hamid, T.H., 2014, Molecular characterization of monochloroacetate-degrading *Arthrobacter* sp. strain D2 isolated from Universiti Teknologi Malaysia agricultural area, *Biorem. J.*, 18 (1), 12–19.

[20] Bergmann, J., and Sanik, J.J., 1957, Determination of trace amounts of chlorine in naphtha, *Anal. Chem.*, 29 (2), 241–243.

[21] Fulton, C.K., and Cooper, R.A., 2005, Catabolism of sulfamate by *Mycobacterium* sp. CF1, *Environ. Microbiol.*, 7 (3), 378–381.

[22] van der Ploeg, J., van Hall, G., and Janssen, D.B., 1991, Characterization of the haloacid dehalogenase from *Xanthobacter autotrophicus* GJ10 and sequencing of the dhlB gene, *J. Bacteriol.*, 173 (24), 7925–7933.

[23] Fortin, N., Fulthorpe, R.R., Allen, D.G., and Greer, C.W., 1998, Molecular analysis of bacterial isolates and total community DNA from kraft pulp mill effluent treatment systems, *Can. J. Microbiol.*, 44 (6), 537–546.

[24] Dance, D.A.B., Limmathurotsakul, D., and Currie, B.J., 2017, *Burkholderia pseudomallei*: Challenges for the clinical microbiology laboratory–A response from the front line, *J. Clin. Microbiol.*, 55 (3), 980–982.

[25] Vial, L., Chapalain, A., Groleau, M.C., and Déziel, E., 2011, The various lifestyles of the *Burkholderia cepacia* complex species: A tribute to adaptation, *Environ. Microbiol.*, 13 (1), 1–12.

[26] Coenye, T., and Andamme, P., 2003, Diversity and significance of *Burkholderia* species occupying diverse ecological niches, *Environ. Microbiol.*, 5 (9), 719–729.

[27] Watanabe, K., Teramoto, M., Futamata, H., and Harayama, S., 1998, Molecular detection, isolation, and physiological characterization of functionally dominant phenol-degrading bacteria in activated sludge, *Appl. Environ. Microbiol.*, 64 (11), 4396–4402.

[28] Watanabe, K., and Baker, P.W., 2000, Environmentally relevant microorganisms, *J. Biosci. Bioeng.*, 89 (1), 1–11.

[29] Abel, E., Ibrahim, N., and Huyop, F., 2012, Identification of *Serratia marcescens* SE1 and determination of its herbicide 2,2-dichloropropionate (2,2-DCP) degradation potential, *Malays. J. Microbiol.*, 8 (4), 259–264.

[30] Allison, N., Skinner, A.J., and Cooper, R.A., 1983, The dehalogenases of a 2,2-dichloropropionate-degrading bacterium, *J. Gen. Microbiol.*, 129 (5), 1283–1293.

[31] Abel, E., Ibrahim, N., and Huyop, F., 2012, Identification of *Serratia marcescens* SE1 and determination of its herbicide 2,2-dichloropropionate (2,2-DCP) degradation potential, *Malays. J. Microbiol.*, 8 (4), 259–264.

[32] Abel, E., Pakingking Jr., R.V., Pagador, G., Wint, M.T., and Huyop, F., 2012, Characteristics of

dehalogenase from bacteria isolated from the gut of pond-reared rohu (*Labeo rohita*) Juveniles in Myanmar, *Adv. Biosci. Biotechnol.*, 3, 353–361.

[33] Jing, N.H., Wahab, R.A., Hamdan, S., and Huyop, F., 2010, Cloning and DNA sequence analysis of the alhoalkanoic permease uptake gene from *Rhizobium* sp. RC 1, *Biotechnology*, 9 (3), 319–325.

[34] Su, X., and Tsang, J.S.H., 2013, Existence of a robust haloacid transport system in a *Burkholderia* species bacterium, *Biochim. Biophys. Acta, Biomembr.*, 1828 (2), 187–192.

[35] Musa, M.A., Wahab, R.A., and Huyop, F., 2018, Homology modelling and *in silico* substrate-binding analysis of a *Rhizobium* sp. RC1 haloalkanoic acid permease, *Biotechnol. Biotechnol. Equip.*, 32 (2), 339–349.

[36] Bagherbaigi, S., Gicana, R.G., Lamis, R.J., Nemati, M., and Huyop, F., 2013, Characterisation of *Arthrobacter* sp. S1 that can degrade α and β-haloalkanoic acids isolated from contaminated soil, *Ann. Microbiol.*, 63 (4), 1363–1369.

[37] Cairns, S.S., Cornish, A., and Cooper, R.A., 1996, Cloning, sequencing and expression in *Escherichia coli* of two *Rhizobium* sp. genes encoding haloalkanoate dehalogenases of opposite stereospecificity, *Eur. J. Biochem.*, 235 (3), 744–749.

[38] Hamid, A.A.A., Wong, E.L., Joyce-Tan, K.H., Shamsir, M.S., Tengku Abdul Hamid, T.H., and Huyop, F., 2013, Molecular modelling and functional studies of the non-stereospecific α-haloalkanoic acid dehalogenase (DehE) from *Rhizobium* sp. RC1 and its association with 3-chloropropionic acid (β-chlorinated aliphatic acid), *Biotechnol. Biotechnol. Equip.*, 27 (2), 3725–3736.

[39] Batumalaie, K., Edbeib, M.F., Mahat, N.A., Huyop, F., and Wahab, R.A., 2018, In silico and empirical approaches toward understanding the structural adaptation of the alkaline-stable lipase KV1 from *Acinetobacter haemolyticus*, *J. Biomol. Struct. Dyn.*, 36 (12), 3077–3093.

The Study of Phosphate Release from Artificial Sediment into Water Body Using Diffusive Gradient in Thin Film (DGT) Device in Oxic Condition

Ardina Purnama Tirta[1,*], Asep Saefumillah[2], Foliatini[1], and Herawati[1]

[1]*Department of Analytical Chemistry, Polytechnic AKA Bogor,*
Jl. Pangeran Sogiri No. 283, Tanah Baru, Bogor 16154, West Java, Indonesia

[2]*Department of Chemistry, Faculty of Mathematics and Natural Sciences, Universitas Indonesia, Depok Campus,*
Depok 16424, Indonesia

* ***Corresponding author:***

tel: +62-8176565490
email: ana.ardina@gmail.com

Received: February 8, 2019
Accepted: July 29, 2019

DOI: 10.22146/ijc.43482

Abstract: *The phenomenon of phosphate release in sediments into water bodies under oxic environment has been investigated using the Diffusive Gradient in Thin Film (DGT) technique. This research consists of several stages: polymer synthesis and DGT probe assembly, sediment sampling, DGT deployment in oxic conditions, and phosphate analysis from DGT adsorption results. Acrylamide polymer was successfully synthesized with a composition of 15% acrylamide; N-N'-methylenebisacrylamide 0.1% and ferrihydrite as binding gels. DGT probes were assembled by placing a 16 x 3.2 cm polyacrylamide gel, binding gels and filter membranes on the DGT probes. The sediment sample was taken from the Bogor Botanical Gardens at the coordinates 6°36'00.6" S; 106°47'51.0" E. The DGT probe was placed in sediment samples for 1, 3 and 7 days in oxic conditions. After the prescribed time, the binding gel was removed and cut every 1 cm depth, then eluted using 0.25 M H_2SO_4 and the phosphate concentration was measured using spectrophotometry method. The results showed that the phosphate concentration tends to be higher with the increasing incubation time and depth. Maximum C_{DGT} phosphate released on day 1, day 3 and day 7 were 1.00 µg/L at a depth of 14 cm, 6.61 µg/L at a depth of 14 cm, and 20.92 µg/L at a depth of 11 cm, respectively. This ensures that the phosphate in water bodies comes from biogeochemical processes that occur in sediments and is successfully measured through DGT techniques.*

Keywords: *DGT; oxic; phosphate release; sediment*

■ INTRODUCTION

Eutrophication is one of the problems of the aquatic environment caused by the emergence of excessive nutrients export from catchment soils into the water ecosystem, due to urbanization [1]. Eutrophication can cause a very rapid growth process of plants compared to their normal growth, known as blooming.

The blooming of aquatic plants such as algae can cause problems in aquatic ecosystems such as the down turn of dissolved oxygen concentration that can affect aquatic living organisms like fish and other species, causing them to not grow properly, leading to dwindling of its population. The loss of fish and other animals in the water ecosystem chain may even harm the entire ecological system [2-3]. On the other hand, there are types of algae known as cyanobacteria (blue-green algae). These algae can act as an indicator of pollution [4], in which they contain toxins that can adversely affect the health of humans and other living organisms [5-6]. Eutrophication occurs as a result of the raise of nutrients quantity in the water.

In most lakes, phosphorus is a limiting factor [7-8] in the process of algae photosynthesis because its availability is relatively insufficient compared to the number of aquatic organisms that need it. Eutrophication in inland and coastal waters is caused by increased application of nitrogen (N) and phosphorus (P) fertilizers [9].

Although phosphate concentration in a water body is reduced, eutrophication can still occur due to the accumulation of large quantities of land-sourced pollutants from various sources through water flow and sediment deposition, through physical, chemical and biochemical processes [10-11]. It is clearly seen that sediment plays an important role in the availability of phosphates in the water because they act as phosphate sources and reservoirs. Therefore, the examination of phosphate distribution in sediment and how it interacts with the water body must be included in the monitoring of phosphate contamination in the water.

Organic phosphate can undergo species change into inorganic phosphate through mineralization. Organic phosphate mineralization in sediment occurs in anoxic conditions [12]. The process of phosphate mineralization in sediment causes phosphate migration from sediment to the water body. Phosphate migration from sediment is influenced by the reduction and oxidation reaction of metal iron (Fe) ions [13].

Accurate phosphorous measurement is difficult to do because during the long sample storage, phosphorus species can change due to dynamic interactions of phosphorus species in the natural system. Therefore, in situ techniques for measuring phosphorous needs to developed. Diffusive Gradient in Thin Film (DGT) technique has been developed for in situ measurements of vanadate, arsenate, antimonate, and molybdate in water [14], methyl mercury in rice plants [15], reactive phosphorus species in natural water, sediment and soil [16] and others. The principle of phosphate measurement using the DGT technique is based on the diffusion of phosphate species through the polyacrylamide gel layer and then bound by the ferrihydrite layer embedded in the next gel layer [17]. Phosphate mass bound by ferrihydrite in a given dispersion time is measured colorimetrically after going through acid elution treatment. The concentration of analyte species bound by DGT is considered to be the same as the concentration that might diffuse into aquatic biota.

DGT is a device consisting of membrane filter, diffusive gel, and adsorbent packed in a plastic device. The diffusive gel used is an acrylamide polymer in the form of a hydrogel. In the manufacture of acrylamide polymers, DGT Crosslinker is commonly used as a crosslinker. *N,N′*-methylenebisacrylamide can be used as a crosslinking agent in the manufacture of polyacrylamide gel [18-19].

In this study, the authors utilize the DGT technique with ferrihydrite as a binding gel and *N-N′*-methylenebisacrylamide as a crosslinking agent for measuring phosphate released from sediment to water body in oxic condition. Measurement of released phosphate from sediment was carried out at different depths, 1–15 cm.

■ EXPERIMENTAL SECTION

The research consisted of several stages: (1) polymer synthesis and DGT sediment probe assembly, (2) sediment sampling, (3) DGT deployment in oxic condition, and (4) phosphate analysis from DGT adsorption results.

Materials

The materials used were 40% Acrylamide from Sigma Aldrich, *N,N′*-methylenebisacrylamide from Sigma Aldrich, Ammonium persulfate from Sigma Aldrich, *N,N,N′N′*-Tetramethylethylenediamine (TEMED) 99% from Sigma Aldrich, cellulose nitrate membrane filter from Whatman, Aquademineralization, KH_2PO_4, Sodium hydroxide from Merck, Sodium Nitrate/$NaNO_3$ (Merck), H_2SO_4 (p), Ammonium molybdate from Merck), Potassium antimonyl tartrate from Merck, Ascorbic Acid from Merck, $Fe(NO_3)_3{\cdot}9H_2O$ from Merck, Acetonitrile from Merck.

Instrumentation

The tools used were the Peterson Grab, ice box, pH meter, and thermometer QIS F-390, Portable DO meter Martini MI 605, label sticker, gloves, glassware, furnace, UV-Vis spectrophotometer Shimadzu with accuracy for phosphate analysis about 99.63–100.18%, AAS Shimadzu 6300 with accuracy for Fe analysis about 99.63–100.18% and for Mn about 99.80–105.89%, FTIR Bruker, Millipore water purifier, Agilent pH meter, Thermo science shaker, Thermo science hot plate, analytic balance, Memmert oven, Thermo science stirring hot

plate, Iwaki glassware, DGT probe, ultrasonic, and centrifuge.

Procedure

The preparation of diffusive gel and ferrihydrite was conducted using the procedure reported by Zhang and Davison [16]. Available phosphate species was measured using a DGT technique with ferrihydrite as a diffusive gel. The gel solution was made with a composition of 15% acrylamide and 0.1% crosslinker. The crosslinker used in this study was *N,N*-methylenebisacrylamide (MBA). For binding gel, ferrihydrite was added into the gel solution. The thickness of the prepared gels was 0.23 cm.

Sediment samples were taken from the lake of the Bogor Botanical Garden, precisely in the Lake in front of Bogor Palace at the coordinates 6°36'00.6" S; 106°47'51.0" E. The sediment were collected and filtered used a 200 mesh size filter, then stored in a reservoir. DGT probe was deployed for 7 days in oxic condition with the bubbling of oxygen. For initial data, DGT probe was deployed for 2 h without bubbling of oxygen. At each retrieval time, the binding gel was removed from the probe and then cut every 1 cm. The binding gel eluted by 0.25 M H_2SO_4 solution and the concentration of phosphate was measured by spectrophotometer UV-Visible with blue molybdenum method. Phosphate concentration absorbed by ferrihydrite binding (C_{DGT}) was calculated using the following formula:

$$C = \frac{M \times \Delta_g}{D \times t \times A}$$

where, M is mass of phosphate accumulated in the resin gel layer, Δ_g is the thickness of the diffusive gel plus the thickness of the filter membrane (typically 0.123 cm), D is the diffusion coefficient of phosphate in the gel (1.63×10^{-6} cm^2/s), t is deployment time and A is exposure area (A = 44.8 cm^2).

■ RESULTS AND DISCUSSION

Polymer Synthesis and DGT Probe Assembly

DGT is a device consisting of a membrane filter, diffusive gel and binding gel, packed in a plastic device. In this study, the diffusive gel used was an acrylamide polymer in the form of a hydrogel, while the binding gel was a diffusive gel added by an adsorbent to bind with the analyte to be analyzed, and ferrihydrite was used as an adsorbent to bind with phosphate. The first step in the synthesis of the diffusive gel was the preparation of a gel solution consisting of acrylamide, crosslinker, and water.

The crosslinker used in this study was *N,N*-methylenebisacrylamide (MBA). After a homogeneous gel solution was formed, ammonium persulfate was added as an initiator which would trigger the occurrence of acrylamide free radical and TEMED as a catalyst. The binding gel was made in the same way as making a diffusive gel, but before adding the initiator and TEMED catalyst, ferrihydrite slurry was added first until the solution was homogeneous. The DGT probe assembly process was done as shown in Fig. 1.

This DGT device consists of a cellulose nitrate filter membrane with a pore size of 0.45 nm. The function of this membrane filter is to filter the analyte that will enter the DGT device. The phosphate species that passes the filter with a 0.45 nm pore size is a dissolved phosphate species. Dissolved phosphate is divided into organic phosphate (dissolved organic phosphate, DOP) and inorganic phosphate (dissolved inorganic phosphate, DIP) [20]. Both of these species are selected in the next DGT layer, the diffusive gel layer which is an analytic diffusion medium. Phosphate species which can diffuse into this diffusive gel is inorganic phosphate (dissolved inorganic phosphate, DIP), which consists of orthophosphate and polyphosphate. This inorganic phosphate species bound by ferrihydrite binding gel is an available form and needed by plants. Phosphate concentration measured through this DGT device can be utilized to measure phosphate bioavailability.

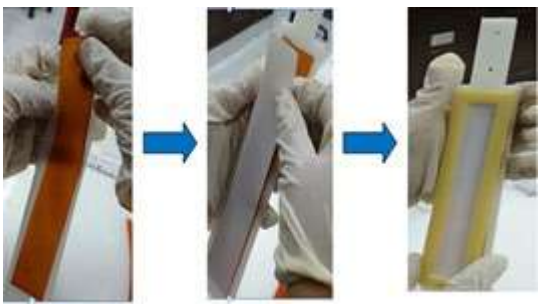

Fig 1. Sediment probe DGT assembly process

FTIR Characterization of Synthesized Polymer

FTIR characterization was carried out to confirm that acrylamide polymer was successfully synthesized. The results of the FTIR spectrum can be seen in Fig. 2. There were two peaks at wave number of 3337 and 3188 cm^{-1} for the samples of diffusive gel, while for ferrihydrite gel samples, there were also two peaks at wave numbers of 3338 and 3181 cm^{-1}. Meanwhile, typical uptake of primary amines ($–NH_2$) were at wave numbers of 3300–3600 cm^{-1} with moderate intensity form. The peak at the wave number of 1648 cm^{-1} for the diffusive gel sample and 1649 cm^{-1} for the ferrihydrite sample revealed the absorption of amide carbonyl (–CONH–), usually found at wave number of 1690–1650 cm^{-1} with strong intensity form. The peak at wave number of 1186 cm^{-1} for diffusive gel sample and 1187 cm^{-1} for ferrihydrite sample showed aliphatic amine uptake (C–N) usually found at wave number of 1250–1020 cm^{-1} with moderate intensity form. The functional group appearing was the main functional group of the acrylamide polymer, so it can be concluded that the acrylamide polymer has been successfully synthesized.

The functional group appearing in diffusive gel and binding gel were not significantly different, so it can be concluded that there is no change in polymer structure in the presence of ferrihydrite. The data also shows that the interaction between ferrihydrite and acrylamide polymer is physical interaction.

Sediment Sampling and In Situ Water Analysis

Sediment sampling was performed in the lake of the Bogor Botanical Garden, precisely in the lake in front of Bogor Palace at the coordinates 6°36'00.6" S; 106°47'51.0" E. Sediment samples were taken using a grab sampler at several adjacent points with a distance of not more than 5 meters. Measurement of some physico-chemical water parameters including temperature, pH and dissolved oxygen values was done simultaneously at the time of sediment collection and the results are shown in Table 1.

Lake water temperatures ranging from 28.0–30.0 °C are considered as good enough for the growth and life of organisms in the water. Temperature is one parameter to determine the quality of lake water. Water pH values ranging in the interval of 7.12–7.13 indicates that the pH

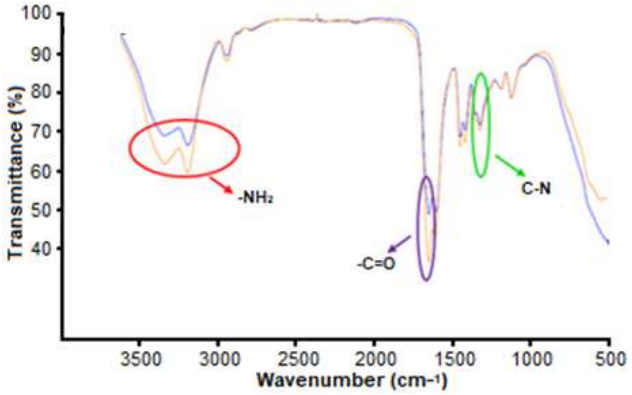

Fig 2. Spectrum FTIR ■ diffusive gel ■ ferrihydrite gel

Table 1. Measurement of temperature, pH and dissolved oxygen of the lake in front of Bogor Palace

No	Parameter	Result
1.	Temperature	28.0–30.0 °C
2.	pH	7.12–7.13
3.	Dissolved oxygen	7.43–7.61 mg/L

of the water is normal. Similar to temperature, the pH of water can also affect the process and balance of chemical reactions that occur in the water. At a low pH value, dissolved oxygen content will decrease, which can directly affect the life of aquatic biota. At high pH values, the solubility of metal compounds decreases, followed by the development of decomposition rate, which has an impact on the decline of dissolved oxygen value [21].

DO values can show biological changes by aerobic or anaerobic organisms, therefore DO measurements are very important in monitoring water quality. The optimum value for good water conditions is when DO values are 4–6 mg/L [22]. Dissolved oxygen values ranging from 7.43 to 7.61 mg/L are still considered good. The value of dissolved oxygen is one of the parameters that can be used as an indicator of pollution. Dissolved oxygen is needed by aquatic biota for the respiratory process and metabolism, and can induce energy production for its growth and breeding process.

Sediment Characterization

In this study, sediment samples were taken from the lake and filtered using a 200 mesh size filter, then stored in a reservoir. Before the DGT was deployed, sediment characterization was conducted. Sediment

characterization measurements were performed in 6 points with 3 different depths on the reservoir like the simulation shown in Fig. 3. The characteristics of sediment measured involved water content, Lost of Ignition, Organic C, total Mn, and total Fe content.

Sediment characterization was done to determine the initial conditions of the sediment before being treated. The results of the sediment characterization measurements are presented in Table 2.

From the data in Table 2, the level of Lost of Ignition (LOI) is 20.01 ± 0.82% (b/b). The LOI level was determined to see how much organic compounds are in the sediment. Fe and Mn levels were determined because both of these metals have an effect on the process of releasing phosphate from sediment to the body of water through the redox process of the two metals.

In the sediment characterization for phosphate measurements, total phosphate measurements were done, phosphate fraction from gradual extraction process was inorganic phosphate, and organic phosphate was calculated by substracting total phosphate with inorganic phosphate. The results of sediment characterization measurement are presented in Table 3.

Total phosphate determination was done with destruction process by using the persulfate method. The gradual extraction of the phosphate fraction was performed according to the method proposed by Hieltjes and Lijklema (extraction 'H & L'). Based on this stepwise extraction "H & L" method, the first fraction is extracted using NH_4Cl solution. At this stage, the easily released phosphorus compound is extracted. The types of chemical compounds in this fraction are not clearly known yet but are thought to be orthophosphate compounds found on the surface of the water. Afterwards, the second fraction is extracted using 0.1 M NaOH solution. At this stage, the phosphate compound bound by Fe (Fe(OOH) ≈ P) is released. The third fraction is extracted using a 0.5 M HCl solution to extract phosphorus bound by calcium carbonate ($CaCO_3$ ≈ P). The fourth fraction is inorganic phosphate residue. Organic phosphate levels are obtained from the difference in total P levels to the sum of the levels of each fraction [23].

Fig 3. Sediment sampling simulation for sediment characterization

Table 2. Characterization result of sediment of Bogor Botanical Garden Lake

Parameter Analysis	Result		
	Top	Middle	Bottom
Total Fe (%)	1.09 ± 0.24	1.14 ± 0.22	1.11 ± 0.34
Total Mn (mg/kg)	265.24 ± 16.15	287.12 ± 21.74	292.74 ± 33.64
Water content (%)	70.53 ± 1.00	68.86 ± 1.76	66.92 ± 1.20
LOI content (%)	20.28 ± 1.96	19.96 ± 1.10	20.01 ± 0.82
Organic C (%)	0.57 ± 0.26	0.58 ± 0.16	0.61 ± 0.16

Table 3. Determination of total P and P fraction level in sediment samples

Parameter	Conc. P (mg/kg)		
	Top	Middle	Bottom
Total P	363.04 ± 56.68	381.40 ± 25.20	370.42 ± 40.84
Fraction 1	2.27 ± 2.04	3.01 ± 1.70	1.55 ± 0.62
Fraction 2	15.52 ± 4.54	13.52 ± 2.34	13.56 ± 3.14
Fraction 3	0.52 ± 0.85	0.61 ± 0.54	0.62 ± 0.48
Residual P	1.98 ± 8.12	2.81 ± 8.70	4.34 ± 6.78
Organic P	342.76 ± 60.26	361.45 ± 27.09	350.36 ± 43.60

From the data in Table 3, it is shown that the largest phosphorus fraction in the sediments of Bogor Botanical Garden Lake was organic phosphorus and the second largest fraction was phosphorus bound by Fe.

DGT Deployment in Oxic Conditions

DGT deployment in artificial sediment samples was conducted by weighing 1200 g of sediment into a test tube with a tube diameter of 9 cm and a tube height of 28 cm. 200 mL of distilled water was added, then the DGT probe was placed until it touched the sediment. The spread of DGT in the sediment sample was performed in oxic condition by bubbling oxygen through an aerator flow. During the operation, dissolved oxygen values, temperature and pH of water on the surface of the sediment was monitored. After seven days of monitoring, we obtained some results. The temperature value range was 24.8–25.7 °C, dissolved oxygen content range was 5.91–7.91 and pH value range was 6.95–7.36. The deployment time was varied from day 1, 3 and 7.

Phosphate Analysis from DGT Adsorption Results

After the specific time of deployment, the DGT probe was removed from the system and then rinsed with double distilled water. The DGT device was removed and the rollout gel was cut every 1 cm in height, then the phosphate level was measured by spectrophotometry method after performing the acid elution process. The phosphate absorbed into the binding gel are thought to be the phosphate which escapes from the sediment to the pore water. Data of phosphate concentration absorbed by ferrihydrite binding (C_{DGT}) during the deployment time in oxic condition can be seen in Table 4.

The concentration of analyte species bound by DGT is considered as similar to the concentration of analytes that may diffuse into aquatic biota, so this DGT device can be used to measure bioavailability of several analytes in the aquatic environment [17,24]. In this study, phosphate measurement using DGT devices was carried out to determine the phosphate concentration which might diffuse into aquatic biota.

Based on the data in Table 4, there is a tendency for C_{DGT} to increase along with the increase in deployment time. The maximum phosphate C_{DGT} that was obtained when the device was released on day 1, day 3 and day 7 were 1.00 µg/L at a depth of 14 cm, 6.61 µg/L at depth of 14 cm, and 20.92 µg/L at a depth of 11 cm, respectively. The C_{DGT} phosphate profile absorbed by the DGT device at different depths during the deployment time is shown in Fig. 4. Based on the C_{DGT} profile in Fig. 4, there is a tendency that as the depth increases, phosphate C_{DGT} from the sediment decreases. This is because, as the level of sediment becomes deeper the oxygen concentration is

Table 4. Phosphate C_{DGT} absorbed by binding gel during deployment time in oxic condition

Depth (cm)	C_{DGT} PO_4 in oxic condition (µg/L)		
	Day 1	Day 3	Day 7
1	0.00 ± 0.00	1.34 ± 1.67	10.12 ± 4.39
2	0.00 ± 0.00	0.00 ± 0.00	20.47 ± 5.34
3	0.00 ± 0.00	3.12 ± 5.40	16.52 ± 5.54
4	0.00 ± 0.00	4.79 ± 6.27	12.83 ± 9.21
5	0.00 ± 0.00	0.00 ± 0.00	15.58 ± 5.03
6	0.00 ± 0.00	0.00 ± 0.00	16.01 ± 2.41
7	0.00 ± 0.00	0.00 ± 0.00	19.49 ± 2.24
8	0.00 ± 0.00	0.56 ± 0.96	17.52 ± 4.16
9	0.00 ± 0.00	5.01 ± 8.68	14.86 ± 4.02
10	0.00 ± 0.00	0.22 ± 0.39	18.62 ± 5.52
11	0.00 ± 0.00	6.03 ± 5.74	20.92 ± 5.71
12	0.00 ± 0.00	0.00 ± 0.00	17.40 ± 6.64
13	0.00 ± 0.00	0.00 ± 0.01	19.37 ± 3.15
14	1.00 ± 1.74	6.61 ± 11.45	16.86 ± 4.34
15	0.73 ± 1.27	0.42 ± 0.73	17.78 ± 3.88

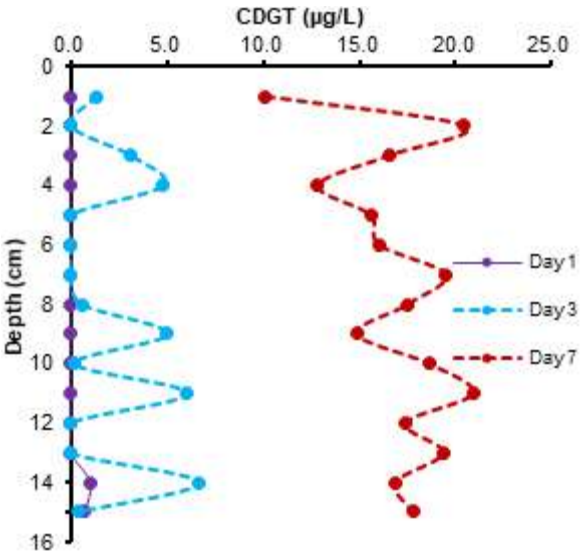

Fig 4. C_{DGT} Phosphate profile for 1 day, 3 days and 7 days

decreased so that the sediment is in anoxic condition. On the sediment interface layer with a water body, the oxygen level will be higher due to the diffusion process between water and free air. The surface layer exposed to sunlight allows photosynthesis to produce oxygen. With the increase of the depth, the dissolved oxygen level became smaller, caused by the decreasing sunlight intensity that penetrates to the water which leads to photosynthesis inhibition. In addition, the availability of oxygen used for respiratory by water organisms and the oxidation of organic and inorganic materials is limited.

When phosphate in the water body is excessive, it can be deposited back into the sediment through various ways including precipitation, adsorption, and microbial activity [1]. In anoxic condition, sediment will release phosphate bound by iron hydroxide which causes the increase of phosphate level in the water. Where as in oxic condition, the presence of iron(III) will bind with phosphate, resulting in phosphate deposition in the sediment [25]. This causes phosphate concentrations at the anoxic condition to be higher than in oxic condition. In addition, in anoxic condition, phosphorus bound by the organic phase is released from microbial activity during degradation of organic matter [26]. This ensures that the phosphate in pore water comes from biogeochemical processes that occur in sediments.

■ CONCLUSION

Acrylamide polymers have been successfully synthesized with the composition of 15% acrylamide; 0.1% *N,N*'-methylenebisacrylamide and ferrihydrite as a binding gel. The DGT probe assembly was carried out using 16 × 3.2 cm polyacrylamide gel sheets assembled on DGT probes with bindings facing upwards, followed by placing diffusive gel and filter membrane. The results of characterization of the lake sediment in Bogor Botanical Gardens at coordinates 6°36'00.6 "S; 106°47'51.0 "E showed that the largest phosphorus fraction in the sediments of the Bogor Botanical Garden Lake was organic phosphorus and the second largest fraction was the phosphorus bound by Fe. The result of DGT spread in sediments for 1, 3 and 7 days in oxic conditions with dissolved oxygen content about 5.91–7.91, revealed that the release of phosphate from the sediment to the water body was influenced by incubation time and depth. The released phosphate concentration tends to be higher with the increasing depth and incubation time. Maximum C_{DGT} phosphate released on day 1, day 3 and day 7 were 1.00 µg/L at a depth of 14 cm, 6.61 µg/L at a depth of 14 cm, and 20.92 µg/L at a depth of 11 cm, respectively. This ensures that the phosphate in pore water comes from biogeochemical processes that occur in sediments. In this work, we already showed the success of the use of DGT as a probe to examine the released phosphate from the sediment to the water body. And we believe that the examination of phosphate distribution in sediments and how it interacts with the water body must be included in the monitoring of phosphate contamination in the water.

■ ACKNOWLEDGMENTS

This work was supported by Polytechnic AKA Bogor.

■ REFERENCES

[1] Jenny, J.P., Normandeau, A., Francus, P., Taranu, Z.E., Gregory-Eaves, I., Lapointe, F., Jautzy, J., Ojala, A.E.K., Dorioz, J.M., Schimmelmann, A., and Zolitschka, B., 2016, Urban point sources of nutrients were the leading cause for the historical spread of hypoxia across European lakes, *Proc. Natl. Acad. Sci. U.S.A.*, 113 (45), 12655–12660.

[2] Granéli, E., and Hansen, P.J., 2006, "Allelopathy in harmful algae: A mechanism to compete for resources?" in *Ecology of Harmful Algae*, Vol. 189, Eds. Granéli, E., and Turner, J.T., Springer-Verlag Berlin Heidelberg, 189–201.

[3] Paerl, H.W., and Paul, W.J., 2012, Climate change: Links to the global expansion of harmful cyanobacterial, *Water Res.*, 46 (5), 1349–1363.

[4] Kozak, A., Celewicz-Gołdyn, S., and Kuczyńska-Kippen, N., 2019, Cyanobacteria in small water bodies: The effect of habitat and catchment area conditions, *Sci. Total Environ.*, 646, 1578–1587.

[5] Glibert, P.M., and Burkholder, J.M., 2011, Harmful algal blooms and eutrophication: "Strategies" for

nutrient uptake and growth outside the Redfield comfort zone, *Chin. J. Oceanol. Limnol.*, 29 (4), 724–738.

[6] Krajewska, M., Szymczak-Żyła, M., Kobos, J., Witak, M., and Kowaleska, G., 2019, Canthaxanthin in recent sediments as an indicator of heterocystous cyanobacteria in coastal waters, *Oceanologia*, 61 (1), 78–88.

[7] Haas, M., Baumann, F., Castella, D., Haghipour, N., Reusch, A., Strasser, M., Eglinton, T.I., and Dubois, N., 2019, Roman-driven cultural eutrophication of Lake Murten, Switzerland, *Earth Planet. Sci. Lett.*, 505, 110–117

[8] Burns, E.E., Comber, S., Blake. W., Goddard, R., and Couldrick, L., 2015, Determining riverine sediment storage mechanisms of biologically reactive phosphorus in situ using DGT, *Environ. Sci. Pollut. Res.*, 22 (13), 9816–9828.

[9] Huang, J., Xu, C., Ridoutt, B.G., Wang, X., and Ren, P., 2017, Nitrogen and phosphorus losses and eutrophication potential associated with fertilizer application to cropland in China, *J. Cleaner Prod.*, 159, 171–179.

[10] Guan, Y.F., Wang, J.Z., Ni, H.G., and Zeng, E.Y., 2009, Organochlorine pesticides and polychlorinated biphenyls in the riverine runoff of the Pearl River Delta, China: Assessment of mass loading, input source, and environmental fate, *Environ. Pollut.*, 157 (2), 618–624.

[11] Gopal, V., Shanmugasundaram, A., Nithya, B., Magesh, N.S., and Jayaprakash, M., 2018, Water quality of the Uppanar estuary, Southern India: Implications on the level of dissolved nutrients and trace elements, *Mar. Pollut. Bull.*, 130, 279–286.

[12] Rumhayati, B., 2010, Studi senyawa fosfat dalam sedimen dan air menggunakan teknik diffusive gradient in thin films (DGT), *JID*, 11 (2), 160–166.

[13] Baken, S., Verbeeck, M., Verheyen, D., Diels, J., and Smolders, E., 2015, Phosphorus losses from agricultural land to natural waters are reduced by immobilization in iron-rich sediments of drainage ditches, *Water Res.*, 71, 160–170.

[14] Zhang, S., Williams, P.N., Zhou, C.Y., Ma, L.Q., and Luo, J., 2017, Extending the functionality of the slurry ferrihydrite-DGT method: Performance evaluation for the measurement of vanadate, arsenate, antimonate, and molybdate in water, *Chemosphere*, 184, 812–819.

[15] Liu, J., Feng, X., Qiu, G., Anderson, C.W., and Yao, H., 2012, Prediction of methyl mercury uptake by rice plants (*Oryza sativa* L.) using the diffusive gradient in thin films technique, *Environ. Sci. Technol.*, 46 (20), 11013–11020.

[16] Zhang, C., Ding, S., Xu, D., Tang, Y., and Wong, M.H., 2014, Bioavailability assessment of phosphorus and metals in soils and sediments: A review of diffusive gradients in thin films (DGT), *Environ. Monit. Assess.*, 186 (11), 7367–7378.

[17] Davison, W., and Zhang, H., 2012, Progress in understanding the use of diffusive gradients in thin films (DGT) – back to basics, *Environ. Chem.*, 9, 1–13.

[18] Zhang, H., 2003, *DGT for Measurements in Waters, Soils and Sediments*, DGT Research Ltd., Lancaster, http://www.dgtresearch.com/WebProducts.aspx?CATID=TEC, accessed on 12 December 2019.

[19] Saefumillah, A., and Rahmaniarti, R., 2015, Pengembangan metode DGT (*diffusive gradients in thin film*) dengan binding gel Fe-Al-Oksida dan pengikat silang *N,N'-methylenebisacrylamide* untuk penyerapan fosfat dalam air, *Valensi*, 1 (1), 20–15.

[20] Zorn, M.E., Waples, J.T., Valenta, T., Kennedy, J.A., and Klump, J.V., 2018, In situ, high resolution time series of dissolved phosphate in Green Bay, Lake Michigan, *J. Great Lakes Res.*, 44 (5), 875–882.

[21] Jiang, L., Li, Y., Zhao, X., Tillotson, M.R., Wang, W., Zhang, S., Sarpong, L., Asmaa, Q., and Pan, B., 2018, Parameter uncertainty and sensitivity analysis of the water quality model in Lake Taihu, China, *Ecol. Model.*, 375, 1–12.

[22] Şener, S., Şener, E., and Davraz, A., 2017, Evaluation of water quality using water quality index (WQI) method and GIS in Aksu River (SW-Turkey), *Sci. Total Environ*, 584-585, 131–144.

[23] Pelcová, P., Dočekalová, H., and Kleckerová, A., 2015, Determination of mercury species by the diffusive gradient in thin film technique and liquid chromatography – atomic fluorescence spectrometry after microwave extraction, *Anal. Chim. Acta*, 866, 21–26.

[24] Ding, S., Wang, Y., Zhang, L., Xu, L., Gong, M., and Zhang, C., 2016, New holder configurations for use in the diffusive gradients in thin films (DGT) technique, *RSC Adv.*, 6 (91), 88143–88156.

[25] Ekholm, P., and Lehtoranta, J., 2012, Does control of soil erosion inhibit eutrophication?, *J. Environ. Manage.*, 93 (1), 140–146.

[26] Ni, Z., Wang, S., Zhang, B.T., Wang, Y., and Li, H., 2019, Response of sediment organic phosphorus composition to lake trophic status in China, *Sci. Total. Environ.*, 652, 495–504.

Preparation, Characterization and Study of the Photodecolorization of Mixed-Ligand Binuclear Co(II) Complex of Schiff Base by ZnO

Suhad Kareem Abass[1], Jassim Abbas Al-Hilfi[2], Sawsan Khudhair Abbas[1], and Luma Majeed Ahmed[1,*]

[1]*Department of Chemistry, College of Science, University of Kerbala, Kerbala 56001, Iraq*

[2]*Department of Chemistry, Collage of Science, University of Misan, Misan 62001, Iraq*

* ***Corresponding author:***

email: luma.ahmed@uokerbala.edu.iq

Received: March 15, 2019
Accepted: August 15, 2019

DOI: 10.22146/ijc.44192

Abstract: *In this work, a new mixed-ligand binuclear Co(II) complex of Schiff base was prepared. Moreover, the characterization of this prepared complex was performed by measurement of melting points, UV-Vis spectra, FT-IR spectra, and magnetic susceptibility measurements, and later compared with metal and ligand solutions. It has been discovered that the Schiff bases with Co(II) ion forms a binuclear complex with a stoichiometry of molar ratio 1:2 from "metal:ligand". The photodecolorization of this complex was done under UV light for ZnO's suspension solution. The results of this photodecolorization showed that the greatest efficiency was obtained with the use of ZnO dose of 300 mg/100 mL and at an initial pH of 7. The decolorization activation energy for this complex is a small value of 11.289 kJ mol^{-1}. Additionally, the thermodynamic study for this reaction is non-spontaneous, endothermic and less random.*

Keywords: *Schiff base; binuclear Co(II) complex; photodecolorization; ZnO; UV-A light*

■ INTRODUCTION

In reality, the metal complexes of Schiff bases play a crucial role in the development of coordination chemistry, which has generated an enormous number of publications, ranging from pure synthetic projects to physicochemical studies [1]. They are important chelating ligands with a variety of active applications [2-3]. These Schiff bases can be employed in catalytic, photochemical biological activities such as antiviral, anticancer and antifungal activities [4], electrochemical processes such as oxidation reactions [5] and agriculture applications [6]. As a result, they are also used as ligands to obtain metal complexes because they have high stability of the coordinating compounds and good solubility in common solvents [7]. The produced metal complexes of Schiff bases can serve as models in the understanding of biological systems [8-9]. The reaction medium affects the kinetics and mechanism of chemical transformations, which is considered one of the key problems of modern physical chemistry. In addition, the polarity of the medium as a solvent effect [10] and the temperature change [11] were extensively researched for organic compounds under photolysis. However, the photo reaction is helpful in the presence of light for the degradation of the color of organic molecules.

Direct photochemical transformation occurs closely when the energy of light attacks the bonds within an organic compound [12] that absorbs the light and leads to the treatment of effluent water. This process indicates the occurrence of chemical change and leads to the formation of carbon dioxide and treated water [13]. The purpose of this manuscript is to prepare a new mixed-ligand binuclear Co(II) complex of Schiff base and then investigate the characteristics of the components of these compounds by using UV-Vis. spectrometry, FT-IR spectrometry, magnetic measurements, and melting points. Moreover, the photodecolorization of this prepared complex is conducted under distinct circumstances such as ZnO dose, initial pH and the effect of temperature.

■ EXPERIMENTAL SECTION

Materials

All the used chemicals and solvents such as ethanol,

glacial acetic acid, DMSO, ethanol, DMF and other solvents were used in high purity. Benzedrine, salicylaldehyde, cobalt chloride hexa-hydrates [$CoCl_2{\cdot}6H_2O$], ethanol, DMF, DMSO, potassium hydroxide and *o*-phenylenediamine were supplied by BDH and Sigma-Aldrich companies. Commercial ZnO was purchased from Fluka Company in 99.5% purity.

Instrumentation

The melting point was measured by melting point apparatus (Stuart-England). FT-IR spectra were recorded in the range of 4000–400 cm^{-1} as KBr disc with a FT-IR-8000 S-Shimadzu spectrophotometer (Japan). Electronic spectra with methyl formamide (DMF) as a solvent in concentration 1×10^{-3} M at room temperature and the concentrations of binuclear Co(II) complex after irradiation were recorded by using a Shimadzu UV-240 UV-visible spectrophotometer (Japan). The magnetic measurements for samples were detected using auto Magnetic susceptibility balance-MSBMKI-USA.

Procedure

Synthesis of binuclear Co(II) complex

In a round bottom flask with a capacity of 100 mL, 0.5 g (0.00058 mmol) of 2,2-(([1,1'-biphyneyl]-4,4'-diylbis (azanylylidene)) bis (methanylylidene)) dipheno ligand (H_2L) was dissolved in potassium hydroxide-ethanol solution. This solution was mixed with 0.2 g (0.00116 mmol) of *o*-phenylenediamine, and 25 mL of Co(II) ethanol-solution containing 0.0137g (0.00116 mol) [$CoCl_2{\cdot}6H_2O$] to produce the mole ratio of H_2L:*o*-phenylene diamine:metal of 1:2:2. The mixture was refluxed with heating at 55 °C for 2–3 h. The final product (greenish brown) was filtered and washed using hot ethanol and lastly dried for 24 h. The melting point for this complex was recorded at 296 °C with the yield 75%, as shown in Scheme 1.

Method of photodecolorization

The photocatalytic decolorization reactions of the binuclear Co(II) complex with ZnO were made by using a homemade photoreactor shown in Fig. 1. This photo reactor consists of a wooden box. This wooden box contains a magnetic stirrer, a fan, a beaker for the reaction and a High pressure mercury lamp-250 Watts (Radium-Germany) as the radiation source, which has a light intensity equal to 1.458×10^{-7} Ens s^{-1} by using a chemical actinometric solution [14]. In this work, an

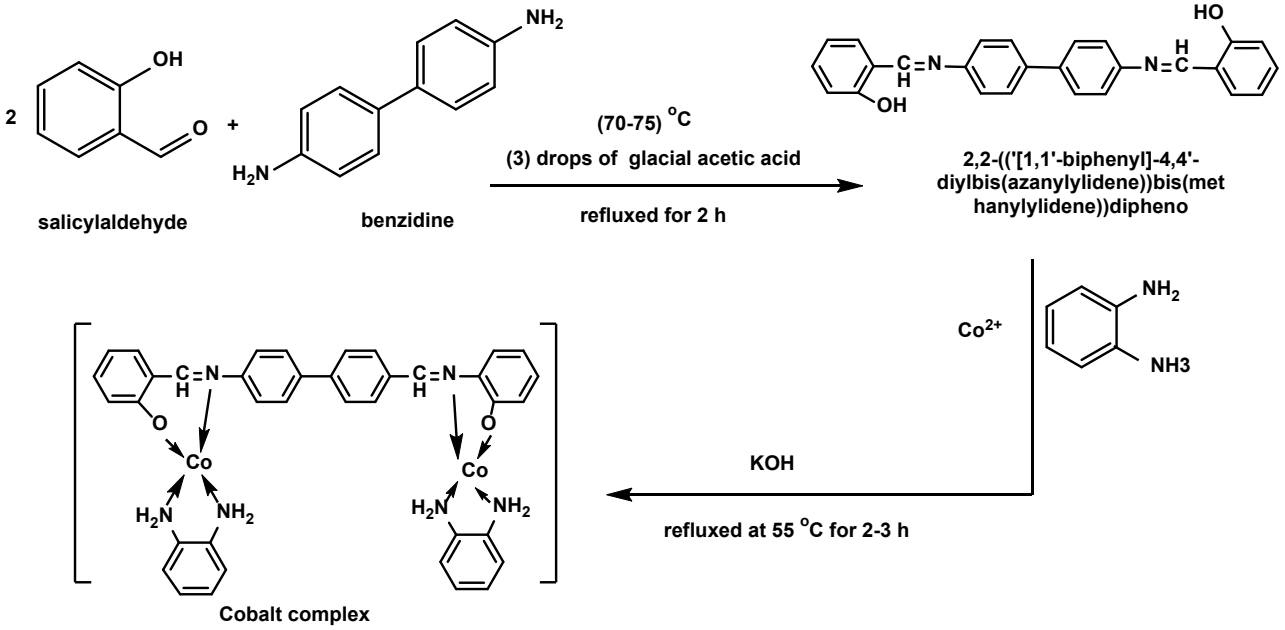

Scheme 1. Schematic diagram for the preparation of the ligand and cobalt complex

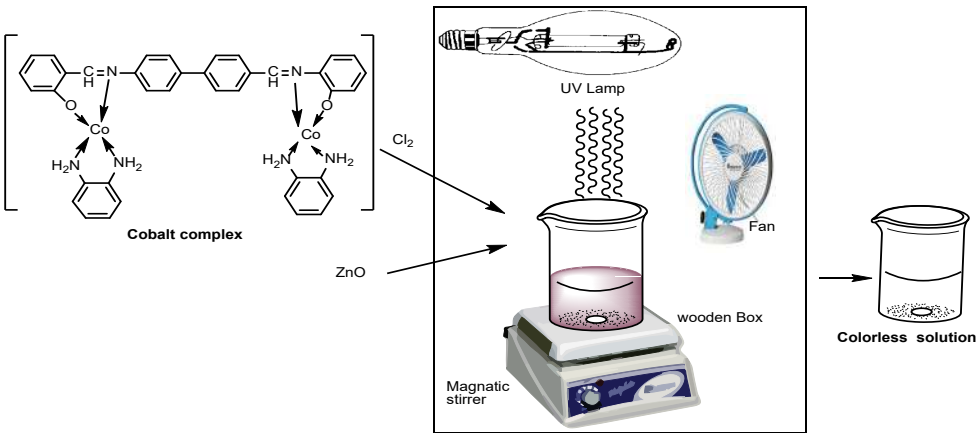

Fig 1. The photo reaction system for the decolorization of the binuclear Co(II) complex

appropriate amount of commercial ZnO was added to 50 mL of binuclear Co(II) complex solution with continuous mixing by a magnetic stirrer.

In the beginning, the dark reaction was carried out for 30 min, when UV-A light illuminated the generated suspension solution. At steady time periods, approximately 3 mL of the formed suspension solution was taken away and centrifuged twice to guarantee the removal of all the fine ZnO catalyst particles at 4000 rpm for 10 min. The absorbance of the residue complex in the solution was recorded by using a UV-Vis spectrophotometer (Shimadzu-UV-240) at 417 nm.

At the low concentration of the studied complex, the rate constant (k_{app}) was explained by Eq. (1), which is based on the Langmuir-Hinshelwood kinetic expression [15].

$$\ln\left(\frac{C_0}{C_t}\right) = k_{app}.t \quad (1)$$

where C_0 is an initial concentration of binuclear Co(II) complex without light (dark reaction) or 0 min of irradiation. C_t is the concentration of the same studied complex at the time of irradiation.

The photodecolorization efficiency (PDE) of binuclear Co(II) complex from aqueous solution is expressed by Eq. (2) [16].

$$PDE = \left(\frac{C_0 - C_t}{C_0}\right) \times 100 \quad (2)$$

■ RESULTS AND DISCUSSION

Physical Properties

Some physical features for H_2L and its complex are explained in Table 1, including the change in the color and the melting points. The color of the ligand is altered from bright yellow to greenish brown when it is reacting with cobalt ion. In addition, the elevated melting point of the complex compared with the melting point of the ligand indicates the high stability of the complex towards air and light.

FT-IR Spectra

The IR absorption spectrum of the Schiff base for the H_2L in Fig. 2 shows the absence of two absorption bands at 3412 and 3295 cm^{-1} which belongs to $-NH_2$ stretching of benzidine, and C=O absorption band at 1700 cm^{-1} of salicylaldehyde, and the appearance of C=N absorption band at 1618 cm^{-1}. The infrared spectrum of the H_2L ligand appeared as a broad band at (3465 cm^{-1}), which indicated the –OH group [17]. The ν (O–H) band is absent in the IR spectrum of the Co-complex confirmed by the absence of the O–H bending band for H_2L in the complex of the mixed ligand. Meanwhile, the appearance of the band in the range of 3330–3340 cm^{-1} indicated the presence of the $-NH_2$ group. The absorption band of the C=N group in H_2L appeared at 1618 cm^{-1} [18]. The band of the C=N group was shifted to

Table 1. Physical properties for the ligand H_2L and the binuclear Co(II) complex

Compounds	Color	Melting points (°C)	Yield
H_2L	Bright Yellow	209	90.01%
$[Co_2(OPD)_2L)]Cl_2$	Greenish Brown	296	75%

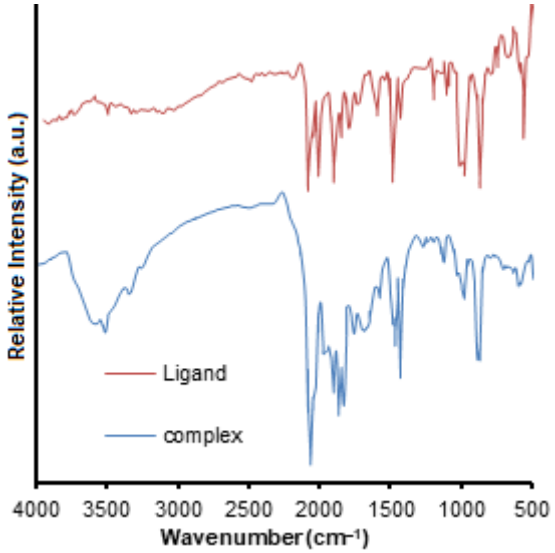

Fig 2. FT-IR spectra of H_2L and $[Co_2(OPD)_2(L)]Cl_2$ complex

lower frequencies because of the coordination with metal ions through the nitrogen atom shown in Fig. 2. The new bands that appeared in the regions, 468.72–542.02 cm^{-1}, may be due to the generation of M–O, and M–N bands [19].

UV–Vis Spectra

Two absorption peaks were displayed in the UV-Vis spectrum of the ligand H_2L as shown in Fig. 3. The first peak at 279 nm (35842 cm^{-1}) was assigned to π–π^* electronic transition of the benzene rings. The second peak at 370 nm (27027 cm^{-1}) was attributed to n–π^* electronic transition of the non-bonding electrons (i.e. free electron pair) that is found on the nitrogen in the Schiff base part of the ligand as the transition of the molecular orbital of C=N chromophore [20-21]. Meanwhile the UV-Vis spectrum of the binuclear Co(II) complex shown in Fig. 3 displayed three absorption peaks. The first peak at 272 nm (36764 cm^{-1}) was assigned to the ligand field, while the second peak at 363 nm (27548 cm^{-1}) refers to the charge transfer electronic transition. The third peak was attributed to d-d electronic transition tetrahedral geometry around the central ion Co(II) at 979 nm (10214 cm^{-1}), which mostly observes as a new weak and much broader peak [20].

Magnetic Susceptibility Measurements of Complexes

The magnetic moment of this complex was 5.089 B.M. This indicates that the generated complexes has tetrahedral form [20], as observed in Table 2.

Photodecolorization Reaction of $[Co_2(OPD)_2(L)]Cl_2$ Complex

Effect of ZnO dose on the decolorization of $[Co_2(OPD)_2(L)]Cl_2$ complex

The effect of ZnO doses in the range of 0.1–0.5 g/100 mL is depicted in Fig. 4 and 5. This study is essential to eschew the excess of the catalyst used, which reduces the efficiency of the photoreaction. The apparent rate constants for the decolorization of binuclear Co(II) complex were raised with increased dose of ZnO with a maximum value of 0.3 g/100 mL, due to the sufficient amount of active sites on the catalyst surface to raise the chance of radical formation [22-23]. On the other hand, the high amount of ZnO induced the decrease of the rate of this reaction due to the reduction of the penetration ability of light into this solution which acts as a screen [24-25]. In Fig. 5, the maximum PDE% was reached at 99.129% after 70 min.

Effect of the initial pH on the decolorization of $[Co_2(OPD)_2(L)]Cl_2$ complex

The study of the initial pH of the aqueous solution

Table 2. Magnetic susceptibility measurements of binuclear Co(II) complex

Complex	Xg $\times 10^{-6}$	XM $\times 10^{-6}$	XA $\times 10^{-6}$	μeff B.M
$[Co_2(OPD)_2(L)]Cl_2$	13.5	10731.15	11128.15	5.089

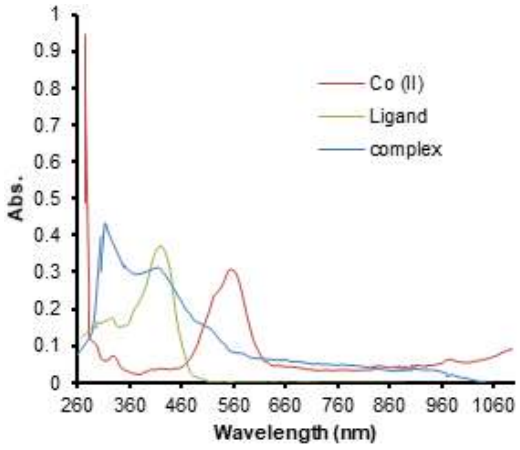

Fig 3. UV-Vis spectra for H_2L ligand, Metal (Co(II) and complex $[Co_2(OPD)_2(L)]Cl_2$

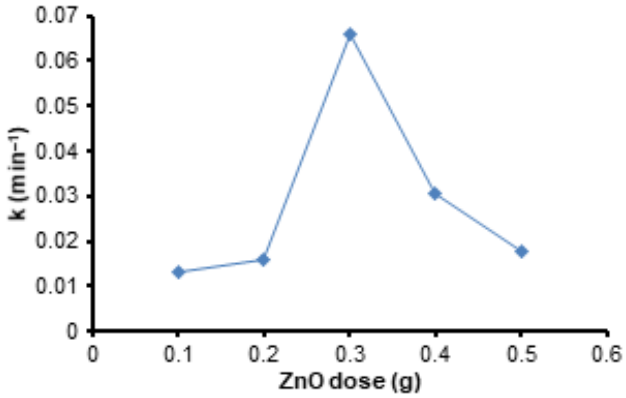

Fig 4. Effect of ZnO dosage on the apparent rate constant of reaction. At conditions: ZnO dosage 0.1–0.5 g/100 mL, binuclear Co(II) complex conc. 25 ppm, initial pH of solution 7.00 and T 311.15 K

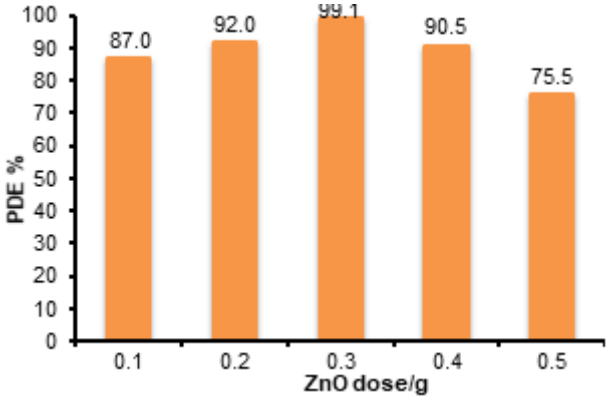

Fig 5. PDE % of binuclear Co(II) complex solution at different ZnO dosage. At conditions: ZnO dosage 0.1–0.5 g/100 mL, binuclear Co(II) complex conc. 25 ppm, initial pH of solution 7.00 and T 311.15 K

for this complex was monitored at a pH range of 3–11, as explained in Fig. 6 and 7. The pH is considered to be a vital factor in increasing the decolorization of this complex because it affects the nature of the complex, and also the nature and surface properties of ZnO, thus affecting the hydroxyl radical generated [26-27]. The maximum decolorization for the binuclear Co(II) complex occurred at pH 7 with maximum PDE% equal to 99.128% at 70 min. In fact, the results demonstrated that when the pH was more or less than pH 7, the rate of decolorization and the PDE% declined, based on the following two causes [27]: At elevated acidic medium, ZnO may have undergone photocorrosion and altered to Zn(II) ion [23,28].

$$ZnO + 2h^{+} \rightarrow Zn^{2+} + \frac{1}{2}O_2 \quad \text{(acidic pH)} \qquad (3)$$

or

$$ZnO + 2H^{+} \rightarrow Zn^{2+} + H_2O \quad \text{(acidic pH)} \qquad (4)$$

Inversely, in high basic pH, ZnO can be negatively charged and lead to the decrease in the photocatalytic activity [23,25].

$$Zn{-}OH + OH^{-} \rightarrow Zn{-}O^{-} + H_2O \quad \text{(basic pH)} \qquad (5)$$

or

$$ZnO + H_2O + 2OH^{-} \rightarrow \left[Zn(OH)_4\right]^{2-} \quad \text{(basic pH)} \qquad (6)$$

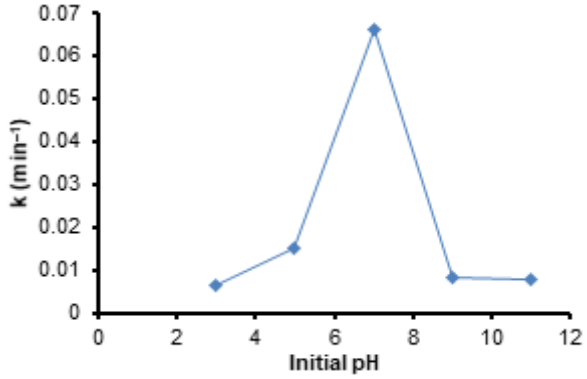

Fig 6. Effect of initial pH of binuclear Co(II) complex solution on the apparent rate constant of reaction. Conditions: ZnO dose 0.3 g/100 mL, binuclear Co(II) complex conc. 25 ppm, initial pH of solution 3–11 and T 311.15 K

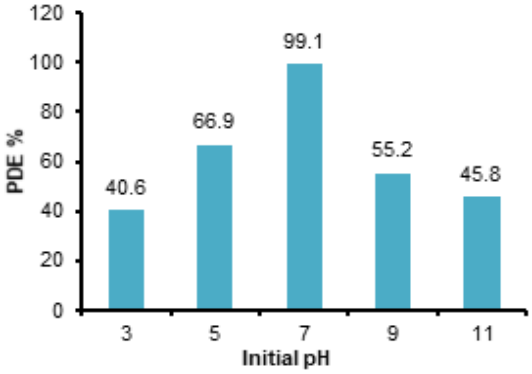

Fig 7. PDE % of binuclear Co(II) complex solution at different ZnO dosage. Conditions: ZnO dose 0.3 g/100 mL, binuclear Co(II) complex conc. 25 ppm, initial pH of solution 3–11 and T 311.15 K.

Effect of temperature on the decolorization of $[Co_2(OPD)_2(L)]Cl_2$ complex

At temperatures in the range of 288.15–303.15 K, the results in Fig. 8 and 9 show that the decolorization process for the binuclear Co(II) complex is elevated with raised temperature. The plotted Arrhenius equation (Eq. (7)) [29,23], and Eyring-Polanyi equation (Eq. (8)) [25,30] were demonstrated.

$$\ln k_{app} = \frac{-E_a}{RT} + \ln A \quad (7)$$

where E_a is activation energy, k is rate constant, R is gas constant, T is the temperature of reaction and A is a frequency constant.

$\Delta H^{\#}$ and $\Delta S^{\#}$ were calculated based on the Eyring-Polanyi equation [25,30-31]

$$\ln\left(\frac{k_{app.}}{T}\right) = \frac{-\Delta H^{\#}}{RT} + \left(\ln\left(\frac{k_B}{h}\right) + \frac{\Delta S^{\#}}{R}\right) \quad (8)$$

where k_B is a Boltzmann's constant, h is a Plank's constant, R is a gas constant and T is the temperature of the reaction.

The activation energy for the decolorization of the binuclear Co(II) complex is small and equals to 11.289 kJ/mol, which proves this photoreaction is fast speed [32-33] and the reaction is endothermic where the change in enthalpy equals to 8.832 kJ/mol as listed in Table 2. $\Delta G^{\#}$ of the photo reaction was calculated using the Gibbs equation (Eq. (9)) based on the fitting results of the Eyring-Polanyi equation [29-31].

$$\Delta G^{\#} = \Delta H^{\#} - T\Delta S^{\#} \quad (9)$$

All fitted factors of the thermodynamics functions and the activation energy are listed in Table 3.

The positive $\Delta H^{\#}$ (endothermic) and positive $\Delta G^{\#}_{303.15}$ (non-spontaneous) for the decolorization of the binuclear Co(II) complex demonstrated that the transition state between the complex molecules and intermediates (hydroxyl radicals) is a well solvated structure. The negative values of $\Delta S^{\#}$ for the decolorization of the binuclear Co(II) complex species formed is less random than the reactants. These results have similar behavior with other photo reactions observed by several researchers [25,31,34].

Mechanism of the Photodecolorization of $[Co_2(OPD)_2(L)]Cl_2$ Complex

The series of redox processes can take place via the presence of ZnO as a suspension in an aqueous solution of $[Co_2(OPD)_2(L)]Cl_2$ complex. The best species [16,35] which can decolorize the $[Co_2(OPD)_2(L)]Cl_2$ complex are HO and HOO under irradiation by UV-A light, as explained in Fig. 10.

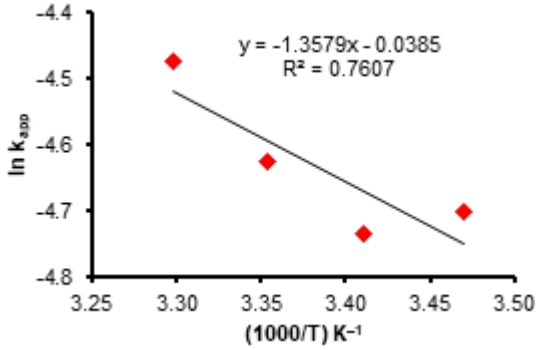

Fig 8. Arrhenius equation plotted at varying temperatures, at 288.15–303.15 K. Conditions: ZnO dose 0.3 g/100 mL, binuclear Co(II) complex conc. 25 ppm, initial pH of solution 7

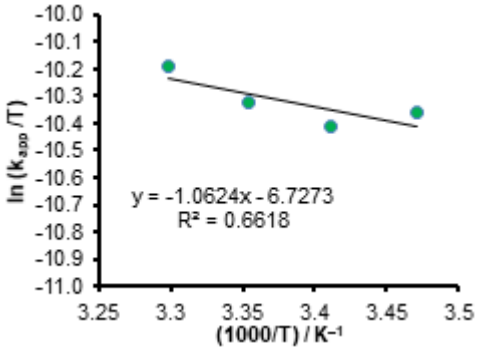

Fig 9. Eyring plot of (ln (k/T)) vs. 1/T. Conditions: ZnO dose 0.3 g/100 mL, binuclear Co(II) complex conc. 25 ppm, initial pH of solution 7

Table 3. The activation energy and thermodynamic parameters of the decolorization of the binuclear Co(II) complex under UV-A light

Type of lamp (UV-A)	E_a kJ mol^{-1}	$\Delta H^{\#}$ kJ mol^{-1}	$\Delta S^{\#}$ J mol^{-1} K^{-1}	$\Delta G^{\#}_{303.15}$ kJ mol^{-1}
250 Watt	11.289	8.832	-3.666	9.945

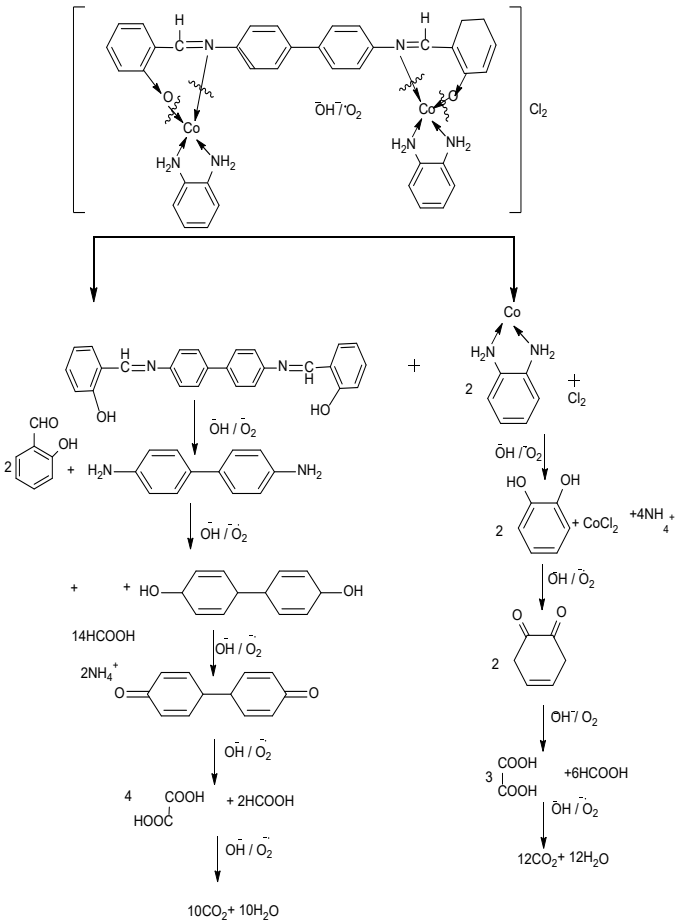

Fig10. Schematic diagram of the suggested mechanism of the photodecolorization of $[Co_2(OPD)_2L)]Cl_2$ complex with photocatalyst ZnO

■ CONCLUSION

The main conclusions are referred to the forming of $[Co_2(OPD)_2L)]Cl_2$ complex in the mole ratio of 1:2 "metal:ligand" stoichiometry and with greenish brown color. From FTIR analysis, new bands appeared in the regions, 469–542 cm^{-1} which may be due to the formation of M-O and M-N bands. The increased melting point is proven to be a binuclear Co(II) complex. In the UV-Visible spectrum, the appearance of the new weak and much broader peak at 979 nm were attributed to d-d electronic transition tetrahedral geometry around the Co(II) central ion. The optimum conditions for photodecolorization of the binuclear Co(II) complex were observed at 300 mg of ZnO/100 mL from binuclear Co(II) complex solution, initial pH of 7, with low activation energy, endothermic, less random and non-spontaneous reaction.

■ ACKNOWLEDGMENTS

Authors would like to acknowledge to those who have encouraged this research at the Physical and Inorganic Laboratories at the University of Kerbala, College of Science in the Department of Chemistry in Iraq.

■ REFERENCES

[1] AL-Hilfi, J.A., Abood, N., Fahad, T.A., and Turner, S., 2015, Synthesis and structural study of some new metal complexes of Schiff base from 2-thenoyltrifluoroacetone with alkyl amine and its thione derivative by NMR, IR and TGA analysis methods, *Der Chemica Sinica*, 6 (11), 37–41.

[2] Al-Shemari, R.K., and Shafiq, Z.A., A.S., 2015, Synthesis, characterization and biological activity for binuclear complexes Co(II), Cu(II), Ni(II), Mn(II) and Hg(II) with Schiff base ligand type N_2O_2, *Asian J. Pharm. Sci. Technol.*, 5 (3), 172–178.

[3] Samir, A.H, Hasan, H.A., Aziz, M.R., and Shaker, S.M., 2010, Synthesis of some metal complexes of azo type ligand and evaluation of their antibacterial activity, *J. Coll. Educ.*, 1, 305–318.

[4] Hamak, K.F., and Eissa, H.H., 2013, Synthesis, characterization, biological evaluation and anti corrosion activity of some heterocyclic compounds oxazepine derivatives from Schiff bases, *Org. Chem. Curr. Res.*, 2 (3), 121.

[5] Yang, Z., and Sun, P., 2006, Compare of three ways of synthesis of simple Schiff base, *Molbank*, 6, M514.

[6] Li, L., Li, Z., Wang, K., Zhao, S., Feng, J., Li, J., Yang, P., Liu, Y., Wang, L., Li, Y., Shang, H., and Wang, Q., 2014, Design, synthesis, and biological activities of aromatic gossypol Schiff base derivatives, *J. Agric. Food Chem.*, 62 (46), 11080–11088.

[7] Gupta, Y.K., Agarwal, S.C., Madnawat, S.P., and Ram, N., 2012, Synthesis, characterization, and antimicrobial studies of some transition metal complexes of Schiff bases, *Res. J. Chem. Sci.*, 2 (4), 68–71.

[8] Tajmir-Riahi, H.A., 1991, Coordination chemistry of vitamin C. Part II. Interaction of L-ascorbic acid with Zn(II), Cd(II), Hg(II) and Mn(II) ions in the solid state and in aqueous solution, *J. Inorg. Biochem.*, 42 (1), 47–55.

[9] Saravanakumar, D., Sengottuvelan, N., Priyadarshni, G., Kandaswamy, M., and Okawa, H., 2004, Synthesis of unsymmetrical 'end-off' phenoxo and oximinato di bridged copper(II) and nickel(II) complexes: Spectral, electrochemical and magnetic properties, *Polyhedron*, 23 (4), 665–672.

[10] Kumar, R., and Yusuf, M., 2009, Photolysis of some 2-butenyl/butynylbischromones: Effect of solvent polarity, *Org. Commun*., 2 (1), 17–19.

[11] Shareef, K.M., Naman, S.A.M.A., and Muhamad, S.G., 2010, Temperature and pH affecting the catalytic photodegradation of 2,4-D and MCPA pesticides in aqueous medium, *J. Koya Univ.*, 15, 152–159.

[12] Al-Momani, F., 2003, Combination of photo-oxidation processes with biological treatment, *Dissertation*, University of Barcelona, Spain.

[13] Gernjak, W., 2006, Solar photo-Fenton treatment of EU priority substances – Process parameters and control strategies, *Dissertation*, Universität für Bodenkultur Wien, Vienna.

[14] Mahammed, B.A., and Ahmed, L.M., 2017, Enhanced photocatalytic properties of pure and Cr-modified ZnS powders synthesized by precipitation method, *J. Geosci. Environ. Prot.*, 5 (10), 101–111.

[15] Eesa, M.T., Juda, A.M., and Ahmed, L.M., 2016, Kinetic and thermodynamic study of the photocatalytic decolourization of Light Green SF Yellowish (acid green 5) dye using commercial bulk titania and commercial nanotitania, *Int. J. Sci. Res.*, 5 (11), 1495–1500.

[16] Ahmed, L.M., Saaed, S.I., and Marhoon, A.A., 2018, Effect of oxidation agents on photo-decolorization of vitamin B12 in the presence of ZnO/UV-A system, *Indones. J. Chem.*, 18 (2), 272–278.

[17] Cozzi, P.G., 2004, Metal–salen Schiff base complexes in catalysis, *Chem. Soc. Rev*., 33 (7), 410–421.

[18] Krishnankutty, K., Ummathur, M.B., and Sayudevi, P., 2008, Metal complexes of Schiff bases derived from dicinnamoylmethane and aromatic amines, *J. Argent. Chem. Soc.*, 96 (1-2), 13–21.

[19] Singh, M.S., and Singh, P.K., 2000, A new class of organosilicon(IV) compound based upon tetradentate (N_2O_2) chelating ligand, *Main Group Met. Chem.*, 23 (3), 183–188.

[20] Gerloch, M., and Constable, E.G., 1994, *Transition metal chemistry: The valence shell in the d-block chemistry*, Wiley-VCH, Weinheim, Germany, 46–58.

[21] Aranha, P.E., dos Santos, M.P., Romera, S., and Dockal, E.R., 2007, Synthesis, characterization, and spectroscopic studies of tetradentate Schiff base chromium(III) complexes, *Polyhedron*, 26 (7), 1373–1382.

[22] Byrappa, K., Subramani, A.K., Ananda, S., Rai, K.M.L., Dinesh, R., and Yoshimura, M., 2006, Photocatalytic degradation of rhodamine B dye using hydrothermally synthesized ZnO, *Bull. Mater. Sci.*, 29 (5), 433–438.

[23] Fathal, E.S., and Ahmed, L.M., 2015, Optimization of photocatalytic decolourization of methyl green dye using commercial zinc oxide as a catalyst, *J. Kerbala Univ.*, 13 (1), 53–63.

[24] Munesh, Swati, and Meena, R.C., 2012, Photocatalytic decolorization of Acid Red 186 using alternative developed photocatalyst MBIR Dowex 11, *Res. J. Chem. Sci*., 2 (9), 56–62.

[25] Ahmed, L.M., Tawfeeq, F.T., Al-Ameer, M.H.A., Al-Hussein, K.A., and Athaab, A.R., 2016, Photo-degradation of Reactive Yellow 14 dye (a textile dye) employing ZnO as photocatalyst, *J. Geosci. Environ. Prot.*, 4, 34–44.

[26] Ahmed, L.M., Jassim, M.A., Mohammed, M.Q., and Hamza, D.T., 2018, Advanced oxidation processes for carmoisine (E122) dye in UVA/ZnO system: Influencing pH, temperature and oxidant agents on dye solution, *JGPT*, 10 (7), 248–254.

[27] Mohabansi, N.P., Patil, V.B., and Yenkie, N., 2011, A comparative study on photo degradation of methylene blue dye effluent by advanced oxidation

process by using TiO2/ZnO photo catalyst, *Rasayan J. Chem.*, 4 (4), 814–819.

[28] Nadi, H., Alizadeh, M., Ahmadabadi, M., Yari, A.R., and Hashemi, S., 2012, Removal of reactive dyes (green, orange, and yellow) from aqueous solutions by peanut shell powder as a natural adsorbent, *Arch. Hyg. Sci.*, 1 (2), 41–47.

[29] Hussein, Z.A., Abbas, S.K., and Ahmed, L.M., 2018, UV-A activated ZrO_2 via photodecolorization of methyl green dye, *IOP Conf. Ser.: Mater. Sci. Eng.*, 454, 012132.

[30] Ahmed, L.M., 2018, Photo-decolourization kinetics of acid red 87 dye in ZnO suspension under different types of UV-A light, *Asian J. Chem.*, 30 (9), 2134–2140.

[31] Fakhri, F.H., and Ahmed, L.M., 2019, Incorporation CdS with ZnS as nanocomposite and using in photo-decolorization of Congo red dye, *Indones. J. Chem.*, 19 (4), 936–943.

[32] Qadri, M., Nisar, S., and Fatima, N., 2015, Photokinetics of the oxidation of Coomassie brilliant blue by potassium dichromate in acidic medium, *Int. J. Adv. Res.*, 3 (2), 888–898.

[33] Kzar, K.O., Mohammed, Z.F., Saeed, S.I., Ahmed, L.M., Kareem, D.I., Hadyi, H., and Kadhim, A.J., 2019, Heterogeneous photo-decolourization of cobaltous phthalocyaninate dye (Reactive green dye) catalyzed by ZnO, *AIP Conf. Proc.*, 2144, 020004.

[34] Gajbhiye, S.B., 2012, Photocatalytic degradation study of methylene blue solutions and its application to dye industry effluent, *Int. J. Mod. Eng. Res.*, 2 (3), 1204–1208.

[35] Jasim, K.M., and Ahmed, L.M., 2019, TiO_2 nanoparticles sensitized by safranine O dye using UV-A light system, *IOP Conf. Ser.: Mater. Sci. Eng.*, 571, 012064.

Effect of Reaction Time and Stability Properties of Gold Nanoparticles Synthesized by *p*-Aminobenzoic Acid and *p*-Aminosalicylic Acid

Abdul Aji, Sri Juari Santosa, and Eko Sri Kunarti*

Department of Chemistry, Faculty of Mathematics and Natural Sciences, Universitas Gadjah Mada, Sekip Utara, Yogyakarta 55281, Indonesia

* ***Corresponding author:***

email: eko_kunarti@ugm.ac.id

Received: April 2, 2019
Accepted: August 14, 2019

DOI: 10.22146/ijc.44674

Abstract: *In this work, we determined the influence of reaction time in the synthesis of gold nanoparticles (AuNPs) by* p*-aminosalicylic acid and* p*-aminobenzoic acid as reducing agents. Besides working as a reducing agent, the* p*-aminobenzoic acid and* p*-aminosalicylic acid also simultaneously played a role as a capping agent/stabilizing agent. Gold ions were first mixed with the pH adjusted* p*-aminobenzoic acid and* p*-aminosalicylic acid. The mixture was then heated in boiling water at 86 °C. The formation of AuNPs was indicated by the appearance of red color and analyzed with UV/Vis spectrophotometry to evaluate their surface plasmon resonance (SPR) absorption in the wavelength range of 400–800 nm. The reducing ability of the reducing agents was affected by its structure. Gold nanoparticles that were synthesized with* p*-aminosalicylic acid were more stable, formed faster and had a smaller size than its counterpart that were synthesized with* p*-aminobenzoic acid. The stability test over a period of 5 months showed that the AuNPs were relatively stable.*

Keywords: *gold nanoparticles;* p*-aminosalicylic acid;* p*-aminobenzoic acid*

■ INTRODUCTION

Metal nanoparticles have become an incessant part of the current research in nanotechnology. They exhibit unusual physical and chemical properties which are quite different from their bulk counterparts [1]. When particles are reduced to their nano level, their physical and chemical properties (e.g., melting point, fluorescence, electrical conductivity, magnetic permeability, and chemical reactivity) can drastically change. The changes in these properties are highly influenced by their size, shape, and nature of the surrounding environment [2]. Application of nanomaterial follows its unique properties including high surface to volume ratio, high surface energy, and unique mechanical, thermal, electrical, magnetic and optical behaviors [3].

Gold nanoparticles are the most compatible nanomaterial for preparation of engineered nanoplatforms in smart sensing devices. Surface plasmon resonance property of gold nanoparticles makes them most suitable engineered nanomaterial for bioimaging, biomedical therapeutics, and biodiagnostic tools. Gold nanoparticles colloids have attracted increasing attention due to their unique properties in multi-disciplinary research fields [4].

A gold nanoparticle is generally synthesized through the reduction of the $HAuCl_4$ solution with $NaBH_4$ in high temperature [5]. However, the synthesized AuNPs tend to aggregate as soon as it is formed. The use of other reducing agents, such as citric acid, polyols, sugars, hydrazine, formaldehyde, hydrogen peroxide, and ascorbic acid still could not solve the aggregation problem of gold nanoparticles. To protect the particles from aggregation and reduce the collision possibility between particles of gold, in order to make AuNPs become stable, the researchers use stabilizers [6]. The most common capping agents used in previous studies were SDS [7], PVA [8], cysteamine [9], and surfactant [10]. The stabilizing agent was added after the reduction process to maintain the size of gold nanoparticles. The formation of AuNPs are indicated by the colloid formation with red or purple color and has strong adsorption of visible light at the wavelengths between 520–550 nm [11]. Nguyen et al. synthesized AuNPs by capping Au^{3+} ion using a CTAB

and then reducing with $NaBH_4$ [12]. $NaBH_4$ was also used as a reducing agent for gold nanoparticles. Wu et al. [13] added trisodium citrate as a stabilizing agent and used it for pesticides detection. However, the use of two different compounds was less effective.

Previous studies have been conducted by using the same chemicals as reducing agent and stabilizer. In 2004, Aslam et al. synthesized gold nanoparticles using oleylamine as both a reducing agent and stabilizing agent. The particle size of the gold nanoparticles that were synthesized with this method was 8–12 nm [14]. In 2016, Gusrizal et al. had synthesized AgNPs using *p*-hydroxy benzoic acid and *m*-hydroxybenzoic acid as both a reducing agent and capping agent [15]. The reduction process occurs by the presence of hydroxyl group (–OH) and the amino group that can reduce Au^{3+} to Au^0 and the presence of the carboxylic group (–COOH) that can facilitate electrostatic interactions with Au^{3+} ions in solution. This interaction can prevent the aggregation of Au^{3+} ions so it will not precipitate.

In previous work, we reported the optimalization condition of gold nanoparticles that were synthesized with the double function of *p*-aminobenzoic acid and *p*-aminosalicylic acid as reducing and capping agents in the formation of AuNPs. Several parameters, such as pH, the concentration of reducing agent and precursor concentration have been reported [16]. In this work, we studied the effect of reaction time in the synthesis of gold nanoparticles using *p*-aminobenzoic acid and *p*-aminosalicylic acid as a reducing agent and stabilizing agent. In addition, we reported the advanced study of the stability properties of gold nanoparticles that were formed. Effect of reaction time in the formation of gold nanoparticles was studied using UV-visible spectroscopy to monitor the appearance of surface plasmon resonance absorption. Stability properties of the gold nanoparticles were determined by UV-visible spectroscopy, transmission electron microscopy (TEM), zeta potential data and dynamic light scattering (DLS).

■ EXPERIMENTAL SECTION

Materials

The materials that were used in this research were gold(III) chloride acid solution ($HAuCl_4$ 100 ppm), *p*-aminobenzoic acid ($C_7H_7NO_2$, Merck), *p*-aminosalicylic acid ($C_7H_7NO_3$, Merck), and sodium hydroxide (NaOH, Merck). For the preparation of the mixture solution, double distilled water was used in all experiments.

Instrumentation

SPR spectra of gold nanoparticles were obtained by measurement using a UV-visible spectrophotometer (Shimadzu UV-1700 PharmaSpec instrument). Transmission electron microscope (JEOL JEM-1400) was used to determine the size and morphology of gold nanoparticles. Fourier transmission infrared spectrophotometer (Shimadzu FTIR Prestige-21) was used to identify functional groups present in the gold nanoparticles and to investigate the interaction of the AuNPs surface with the reducing agents. Zeta potential data was determined using Horiba SZ-100.

Procedure

Sample preparation

AuNPs were synthesized by reducing $HAuCl_4$ solution with *p*-aminobenzoic acid and *p*-aminosalicylic acid as reducing agents at pH 12 and 13, respectively, by adding a solution of NaOH. Ten mL of 20 mM reducing agents were put into a beaker glass and added with 10 mL of 100 ppm $HAuCl_4$ solution. The mixture was stirred vigorously and heated at temperature of 86 °C. The reaction time was varied from 0–100 min to obtain the optimum reaction time. Formation of gold nanoparticles was visually identified by observing the color change of the reaction from light yellow to pink or light red. All solutions were also monitored by UV/Vis Spectrophotometer at a wavelength of 300–800 nm. The presence of maximum absorption at the wavelength range of 520–550 nm showed that AuNPs are formed [16].

Characterization of gold nanoparticles

The UV-visible spectra of the samples were recorded in the wavelength range of 300–800 nm at room temperature. All UV-Visible measurements were performed using 1 cm optical path length quartz cuvette. To obtain the stability of gold nanoparticles, UV-visible measurements were performed periodically for a period of 5 months.

The solid sample for FTIR analysis was prepared using gold nanoparticles recovered from colloidal via centrifugation at 12000 rpm and then were dried at 60 °C in an oven. Approximately, a sample of 5 mg was mixed with KBr and condensed into pellet using a hydraulic press. This method was used for all FTIR spectra analysis.

The sample for TEM analysis was prepared by dropping the samples and depositing them in TEM carbon covered copper grids, and letting it evaporate at room temperature. The TEM image was recorded with a 120 kV acceleration voltage. The size of the particles was calculated using ImageJ software.

■ RESULTS AND DISCUSSION

Synthesis of Gold Nanoparticles

Several synthesis parameters of gold nanoparticles using *p*-aminobenzoic acid and *p*-aminosalicylic acids, such as pH condition, precursor concentration, and reducing agent concentration were reported in previous work [16]. Based on previous work, in this study, the formation of gold nanoparticles was performed by mixing $HAuCl_4$ solution with *p*-aminobenzoic acid and *p*-aminosalicylic acid as reducing agents at pH 12 and 13, respectively, by adding a solution of NaOH. When *p*-aminobenzoic acid and *p*-aminosalicylic acid reduced the gold ions, the color of the solution changed to pink or red color indicating the formation of gold nanoparticles. The change in color of the reaction medium indicated the formation of gold nanoparticles due to surface plasmon resonance phenomenon. To prove the formation of gold nanoparticles, the solutions were analyzed by UV-Vis spectrophotometer at the wavelength range of 300–800 nm. The formation of gold nanoparticles was indicated by the maximum absorbance which happened in the wavelength range of 520–550 nm [17]. The result in Fig. 1 showed that the gold nanoparticles were formed. The narrow SPR peak of the gold nanoparticles that were synthesized by *p*-aminosalicylic acid indicated that the size of the AuNPs were uniform. On the other hand, the broadening SPR peak of the gold nanoparticles that were synthesized by *p*-aminobenzoic acid indicated that the size of the AuNPs were non-uniform. The SPR peak showed only one plasmon band centered at about 520 nm, indicating that

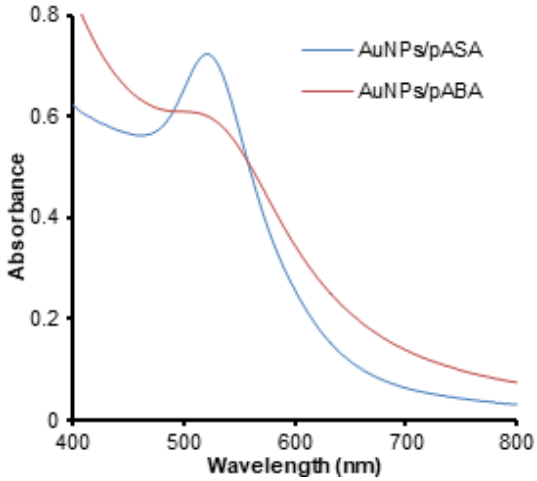

Fig 1. UV-visible spectra of gold nanoparticles made from 100 ppm $HAuCl_4$ and 20 mM reducing agent

the shape of the AuNPs were spherical with the size of 2–50 nm. Meanwhile, two SPR bands usually appear when the symmetry is reduced from spherical to cylindrical, i.e., in gold nanorods [18]. Fig. 1 showed that *p*-aminosalicylic acid as a reducing agent produced more gold nanoparticles than *p*-aminobenzoic acid on equal synthesis conditions. This data indicated that the structure of the reducing agents influenced the reducing ability.

Effect of Reaction Time on the Formation of Gold Nanoparticles

Another factor that is very important in the synthesis of gold nanoparticles using *p*-aminobenzoic acid and *p*-aminosalicylic acid is reaction time. Kumari et al. demonstrated in their study the evolution of the morphology of gold nanoparticles from nanospheres to triangular nanoprisms with an increase in time in *T. asperellum* [19]. The difference in reaction time using the same method could induce different sizes of gold nanoparticles that could be synthesized. The spherical nanoparticles can be produced in a relatively short reaction time. The reduction of Au^{3+} ions to Au^0 mediated by *p*-aminobenzoic acid and *p*-aminosalicylic acid at optimum conditions was examined spectroscopically at different reaction times and the stacked spectra are displayed in Fig. 2. All reactions showed the formation of gold nanoparticles. Although the intensity of peaks was different at different reaction times, all peaks were centered at 520–530 nm.

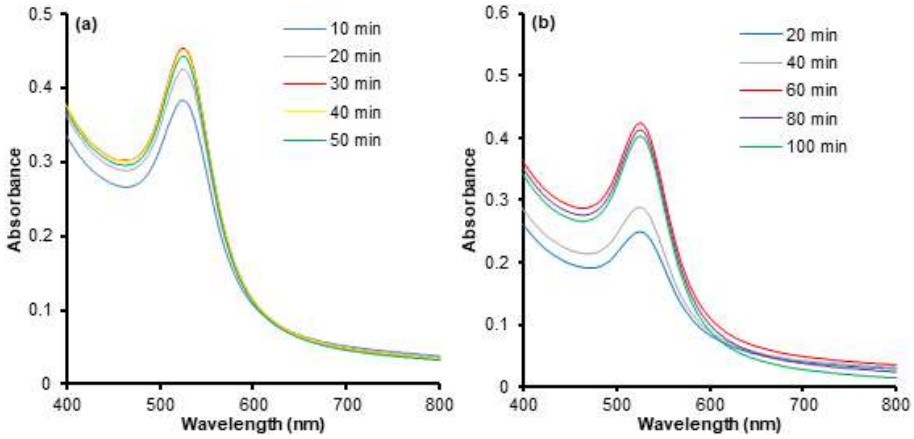

Fig 2. UV/Vis spectra of gold nanoparticles with various reaction times with (a) *p*-aminosalicylic acid at pH 12 and (b) *p*-aminobenzoic acid at pH 13

Fig. 2 shows that the formation of gold nanoparticles with *p*-aminosalicylic acid as the reducing agent was faster than with *p*-aminobenzoic acid. Using 20 mM *p*-amino salicylic acid and 100 ppm $HAuCl_4$ solution, the optimum reaction time was 30 min. Increase in absorbance during 10 min to 30 min of reaction time was attributed to the reduction of gold precursors and an increase in the population of AuNPs. The absorbance value became constant and slightly decreased after 30 min of reaction time due to the complete reduction of available gold ions. The synthesis was found to be completed within 30 min because no further rise in the intensity of the SPR band was detected. In addition, the optimum reaction time using 20 mM *p*-aminobenzoic acid and 100 ppm $HAuCl_4$ solution took 60 min. As the reaction continues, the intensity of this band increased together with a little blue shift attributed to the creation of small sized spherical nanoparticles. The synthesis was found to be completed within 60 min and no further rise in the intensity of the SPR band was detected.

After the reaction, the colloidal gold nanoparticles was stored for 7 days and its absorbance was re-measured. This is done to evaluate the influence of heating time on the stabilization performance of AuNPs that was synthesized by *p*-aminobenzoic acid and *p*-aminosalicylic acid. Based on the data in Fig. 3, it can be explained that the gold nanoparticles that were formed by *p*-amino salicylic acid at less than 30 min of heating time were not stable because its absorbance still increased after 7 days. This data showed that the formation of gold nanoparticles still continued when the reaction was stopped. The gold nanoparticles formed by *p*-aminosalicylic acid at 30 min

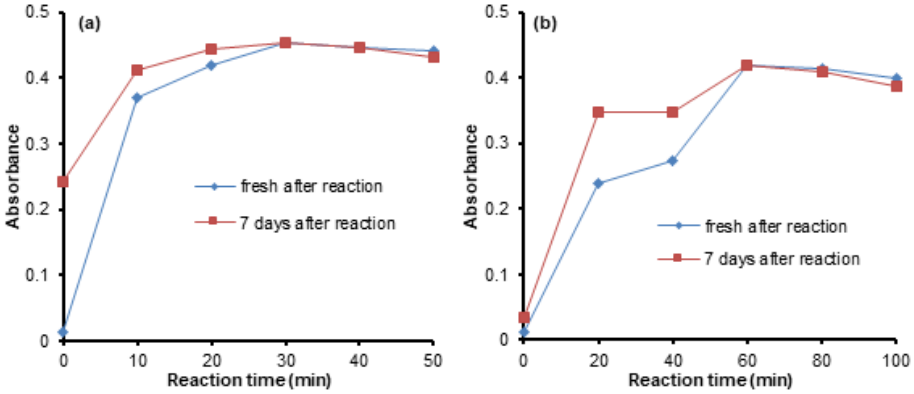

Fig 3. UV/Vis absorbance of fresh-synthesized and 7 days-stored of AuNPs with various reaction times with (a) *p*-aminosalicylic acid at pH 12 and (b) *p*-aminobenzoic acid at pH 13

reaction time was most stable, shown by the unchanged value of absorbance after 7 days. Meanwhile, the gold nanoparticles formed by *p*-aminosalicylic acid at more than 30 min reaction time was less stable because its absorbance slightly decreased after 7 days. The gold nanoparticles formed by *p*-aminobenzoic acid at 60 min reaction time was most stable shown by the unchanged value of absorbance after 7 days. After 7 days stored, the gold nanoparticles formed by *p*-aminobenzoic acid had the same pattern with the gold nanoparticles formed by *p*-aminosalicylic acid. The gold nanoparticles that were formed by *p*-aminobenzoic acid at less than 60 min reaction time was not stable because its absorbance still increased after 7 days. On the other hand, the gold nanoparticles formed by *p*-aminobenzoic acid at more than 60 min reaction time was less stable because its absorbance slightly decreased after 7 days. It is predicted that the longer the solution is heated, the molecules in the solution would still be active, even when the heating process has stopped. The active molecules will react further so the reduction process would still occur even when the heating has been stopped [20].

The best reducing and stabilizing performance of *p*-aminosalicylic was obtained at the reaction time of 30 min. This optimum reaction time was faster than using *p*-aminobenzoic acid as a reducing and stabilizing agent, which needed 60 min to reach the optimum reaction time. In *p*-aminosalicylic, the hydrogen atom at the hydroxyl group and the oxygen atom at the carboxyl group could produce intramolecular hydrogen bonding. Intramolecular hydrogen bonding in the *p*-aminosalicylic acid structure causes the reduction reaction to be more effective [21]. Therefore, the performance of *p*-aminosalicylic acid as a reducing agent and capping agent was better than *p*-aminobenzoic acid.

p-Aminobenzoic Acid and *p*-Aminosalicylic Acid as a Capping Agent

The stability test was performed to gold nanoparticles produced by the reaction of 100 ppm $HAuCl_4$ solution with 20 mM reducing agent to describe the role of *p*-aminobenzoic acid and *p*-aminosalicylic acid as a capping agent. The gold nanoparticles were stored in a capped bottle at room temperature condition for 5 months. After 5 months of observation, all gold nanoparticles that was resulted did not give significant decrease in absorbance value (Fig. 4), only 0.126 (15.47%) for *p*-aminosalicylic acid and 0.210 (29.13%) for *p*-aminobenzoic acid. This data described that all resulted gold nanoparticles were relatively stable until 5 months.

Other than the absorbance decrease, the stability of gold nanoparticles can also be studied from the maximum wavelength shift. The maximum wavelength shift happened after 5 months as far as 3 nm for *p*-aminosalicylic acid and 6.5 nm for *p*-aminobenzoic acid. The longer storage will decrease the gold nanoparticles stability because the particles are suspended by agglomeration (Fig. 5). However, after the shift, the maximum wavelength was still located around 520 nm. It means that the gold nanoparticles were relatively stable over a period of 5 months.

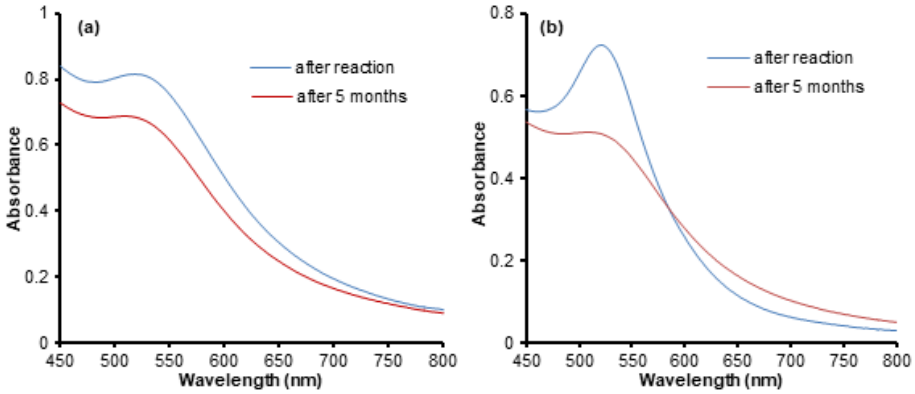

Fig 4. UV/Vis spectra of fresh and after 5 months stored of AuNPs at room temperature (a) AuNPs produced from *p*-aminosalicylic acid (b) AuNPs produced from *p*-aminobenzoic acid

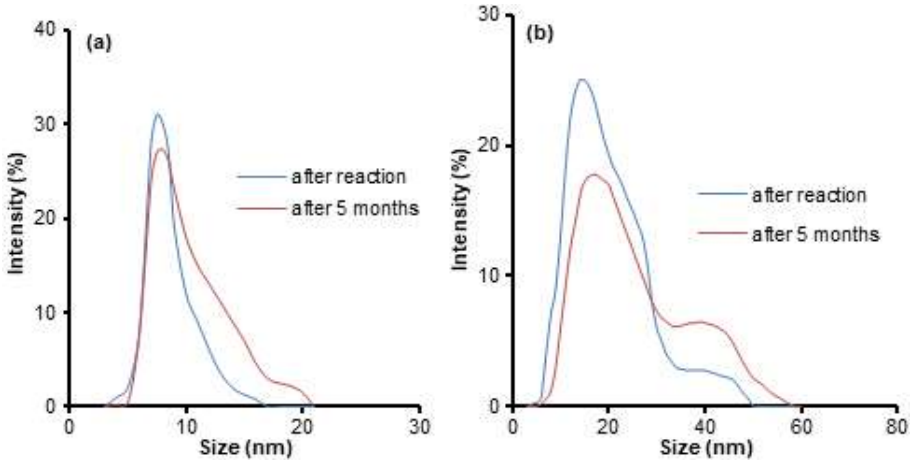

Fig 5. DLS spectra of fresh and after 5 months stored of AuNPs at room temperature (a) AuNPs produced from *p*-aminosalicylic acid (b) AuNPs produced from *p*-aminobenzoic acid

For comparison, the gold nanoparticles that were synthesized by *p*-aminosalicylic acid was more stable than the gold nanoparticles that resulted from *p*-aminobenzoic acid. This fact may indicate that the existence of the hydroxyl group in *p*-aminosalicylic acid can increase the stability of gold nanoparticles. In *p*-aminosalicylic, the hydrogen atom at the hydroxyl group and the oxygen atom at the carboxyl group could produce intramolecular hydrogen bonding. Intramolecular hydrogen bonding in the *p*-aminosalicylic acid structure can cause the reduction reaction to be more effective and increase the stability of the AuNPs.

The size and morphology of the resulted gold nanoparticles were observed using DLS data and TEM, shown in Fig. 6. The TEM results showed that both reducing agents gave the same shape but different size of gold nanoparticles. The *p*-aminosalicylic acid reducing agent (Fig. 5(a)) gave a round shape and smaller particle size than gold nanoparticles that were reduced by *p*-aminobenzoic acid. The *p*-aminobenzoic acid reducing agent (Fig. 6(b)) gave a round shape and less uniform size of gold nanoparticles. The aggregation did not happen with both *p*-aminobenzoic acid and *p*-aminosalicylic acid reducing agent, which showed that the reducing agents can also act as stabilizers.

The stability of the colloidal gold nanoparticles is often described by their zeta potential value [22]. The higher zeta potential value indicates the smaller size and higher stability of gold nanoparticles. In this work, gold nanoparticles that were synthesized by *p*-aminosalicylic acid had a higher zeta potential value than gold nanoparticles that were synthesized by *p*-aminobenzoic acid. The zeta potential value of the AuNPs that were synthesized by *p*-aminosalicylic acid and by *p*-aminobenzoic acid was -42.8 mV and -32.4 mV, respectively. Particles with zeta potentials of more than +30 mV and more negative than -30 mV are normally considered stable. The greater the zeta potential value causes higher repulsion between the particles, so aggregation could be prevented [23]. Therefore, the size of gold nanoparticles that were synthesized by *p*-aminosalicylic acid was smaller and more stable than the ones synthesized by *p*-aminobenzoic acid. The negative value in this data indicates the presence of negative charge at the surface of the gold nanoparticles [24]. This zeta potential value is in agreement with the size data from the TEM image and the stability data that was determined from the UV/Vis spectra of the gold nanoparticles.

The presence of *p*-aminosalicylic acid and *p*-aminobenzoic acid as a capping agent should be a result from the interaction of gold nanoparticles with the functional groups of the reducing agent. FTIR analysis was performed to characterize any chemical changes that occurred during the synthesis of gold nanoparticles with *p*-aminosalicylic acid and *p*-aminobenzoic acid as a

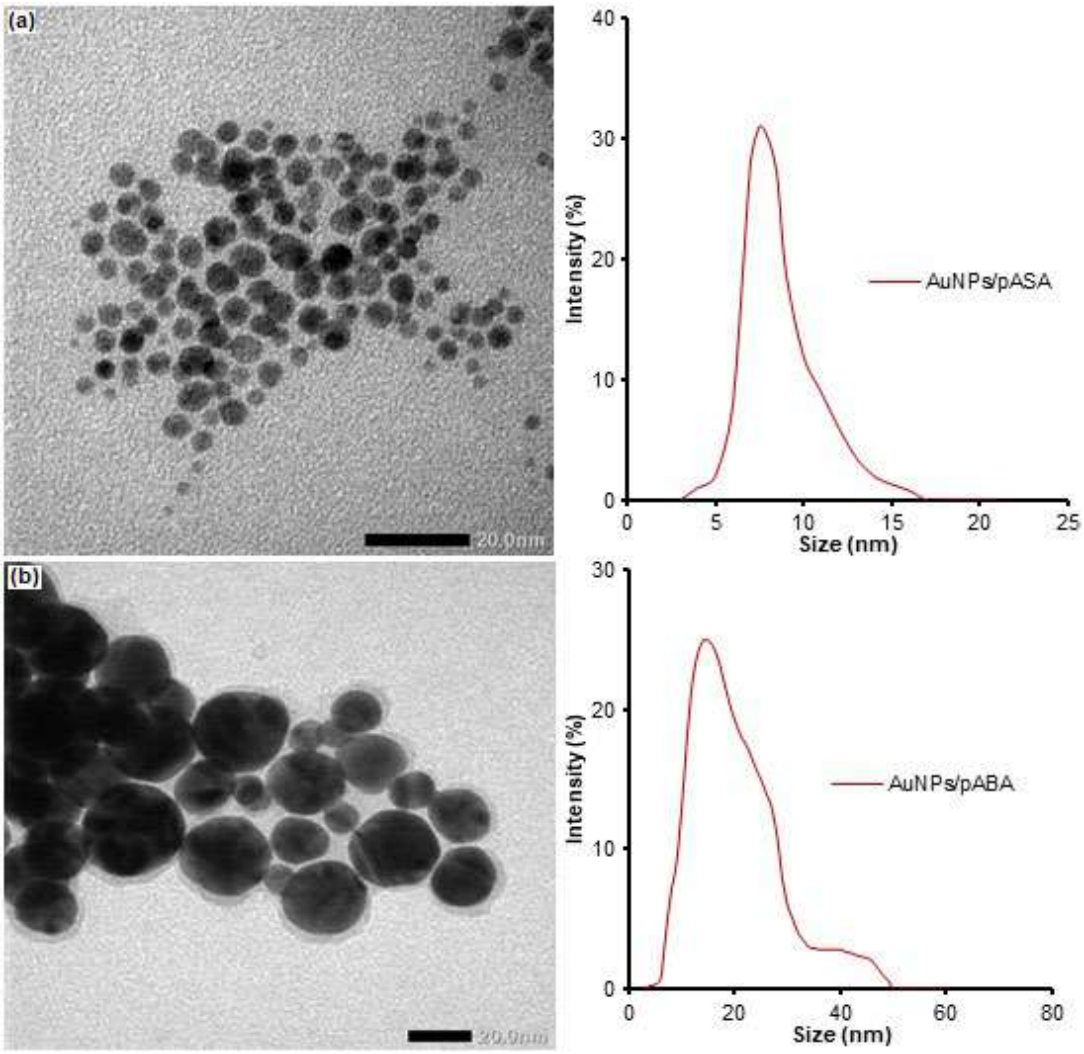

Fig 6. The TEM image and particle size distribution of gold nanoparticles synthesized by a reducing agent (a) *p*-aminosalicylic acid at pH 12 (b) *p*-aminobenzoic acid at pH 13

capping agent (Fig. 7). Because no additional capping agent was used in this experiment, it is clear that the reducing agents not only acted as a reducing agent but also as a capping agent.

FTIR spectra of p-aminobenzoic acid showed two strong absorption bands at 3476 and 3383 cm^{-1}, while *p*-aminosalicylic acid showed two strong absorption bands at 3490 and 3381 cm^{-1} which are due to the asymmetric and symmetric N–H stretching vibrations of the $–NH_2$ group. The band of valence vibrations of the C=O group in the carboxyl acid was observed at 1638 cm^{-1} for *p*-aminobenzoic acid and 1609 cm^{-1} for *p*-aminosalicylic acid. The absorption bands at 1604, 1575 and 1524 cm^{-1} correspond to the valence vibrations of C=C bonds in the benzene ring. The absorption band of the valence vibrations of the C–N bond in the amino group connected with the benzene ring was observed at 1314 cm^{-1} for *p*-aminobenzoic acid and 1317 cm^{-1} for *p*-aminosalicylic acid. It can be observed that the characteristic spectral bands of *p*-aminobenzoic acid and *p*-aminosalicylic were completely shifted or changed by the functionalization of the AuNPs. Additionally, the characteristic features of stretching modes of benzene were observed at 1597, 1512 and 1442 cm^{-1} and –COOH and $–NH_2$ stretching modes were observed at 1635 and 3425 cm^{-1}, respectively. The results indicate that *p*-aminobenzoic acid and *p*-aminosalicylic molecules were successfully assembled on the surfaces of the AuNPs.

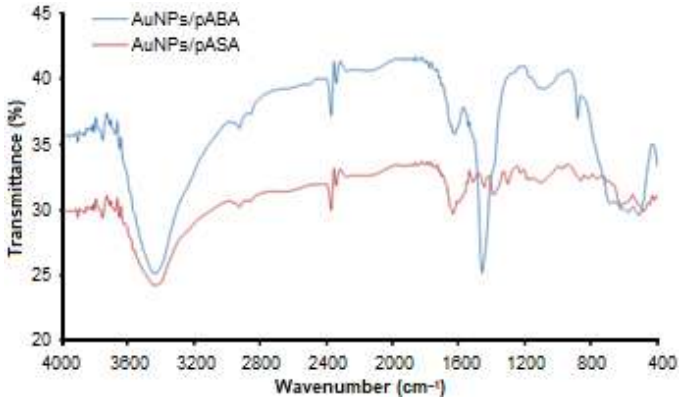

Fig 7. FTIR spectra of gold nanoparticle that synthesized by *p*-aminosalicylic acid at pH 12 (AuNPs/pASA) and *p*-aminobenzoic acid at pH 13 (AuNPs/pABA)

Furthermore, the spectral changes give clear evidence of amine groups interactions on the surfaces of the AuNPs, which was well agreed with the reported methods on the functionalization of metal NPs with two organic molecules including amino group containing ligand [25].

■ CONCLUSION

p-Aminosalicylic acid and *p*-aminobenzoic acid have been successfully used as reducing agents and also stabilizing agents in the synthesis process of gold nanoparticles. This reaction process was highly influenced by reaction time. AuNPs that were synthesized by *p*-aminosalicylic acid was produced faster than the AuNPs that were synthesized by *p*-aminobenzoic acid. The stability of the AuNPs that were synthesized by *p*-aminosalicylic acid was better than the AuNPs that were synthesized by *p*-aminobenzoic acid until 5 months of observation. In addition, the *p*-aminosalicylic acid reducing agent can produce smaller gold nanoparticles than the ones by *p*-aminobenzoic acid. Results from UV/vis spectra, TEM, Zeta potential and FTIR proved that *p*-aminosalicylic acid as a reducing agent and also a stabilizing agent had better performance than *p*-aminobenzoic acid.

■ ACKNOWLEDGMENTS

The authors give thanks to the Ministry of Research Technology and Higher Education of the Indonesian Republic which has partly supported this research activity by providing a scholarship of Master Education Program Leading to Doctoral Degree for Excellent Graduates (PMDSU).

■ REFERENCES

[1] Tyagi, H., Kushwaha, A., Kumar, A., and Aslam, M., 2011, pH Dependent synthesis of stabilized of gold nanoparticles using ascorbic acid, *Int. J. Nanosci.*, 10 (4-5), 857–860.

[2] Shah, M., Badwaik, V., Kherde, Y., Waghwani, H.K., Modi, T., Aguilar, Z.P., Rodgers, H., Hamilton, W., Marutharaj, T., Webb, C., Lawrenz, M.B., and Dakshinamurthy, R., 2014, Gold nanoparticles: Various methods of synthesis and antibacterial activity, *Front. Biosci.*, 19, 1320–1344.

[3] Chen, G., Roy, I., Yang, C., and Prasad, P.N., 2016, Nanochemistry and nanomedicine for nanoparticle-based diagnostics and therapy, *Chem. Rev.*, 116 (5), 2826–2885.

[4] Verma, N.H., Singh, P., and Chavan, R.M., 2014, Gold nanoparticle: Synthesis and characterization, *Vet. World*, 7, 72–77.

[5] Turkevich, J., Stevenson, P.C., and Hillier, J., 1951, A study of the nucleation and growth process in the synthesis of colloidal gold, *Discuss. Faraday Soc.*, 11, 55–75.

[6] Bin Ahmad, M., Lim, J.J., Shameli, K., Ibrahim, N.A., and Tay, M.Y., 2011, Synthesis of silver nanoparticles in chitosan, gelatin and chitosan/gelatin bionano composites by a chemical reducing agent and their characterization, *Molecules*, 16 (9), 7237–7248.

[7] Barman, G., Maiti, G., and Laha, J.K., 2013, Bio-fabrication of gold nanoparticles using aqueous extract of red tomato and its use as a colorimetric sensor, *Nanoscale Res. Lett.*, 8 (1), 181–190.

[8] Walekar, L.S., Pawar, S.P., Gore, A.H., Suryavanshi, V.D., Undare, S.S., Anbhule, P.V., Patil, S.R., and Kolekar, G.B., 2016, Surfactant stabilized AgNPs as a colorimetric probe for simple and selective detection of hypochlorite anion in aqueous solution: Environmental sample analysis, *Colloids Surf., A*, 491, 78–85.

[9] Choi, H., Kang, T., Um, K., and Lee, K., 2014, Reduction of silver ions in gold nanoparticle

suspension on detection of dihydroxybenzene isomers, *Colloids Surf.,* 459, 120–127.

[10] Zhao, P., Li, N., and Astruc, D., 2013, State of the arts in gold nanoparticle synthesis, *Coord. Chem. Rev.*, 257 (3-4), 638–665.

[11] Lu, Y.C., and Chou, K.S., 2008, A simple and effective route for the synthesis nano-silver colloidal dispersions, *J. Chin. Inst. Chem. Eng*., 39 (6), 673–678.

[12] Nguyen, T.H.D., Zhang, Z., Mustapha, A., Li, H., and Lin, M., 2014, Use of graphene and gold nanorods as substrates for the detection of pesticides by surface enhanced Raman spectroscopy, *J. Agric. Food Chem.*, 62 (43), 10445–10451.

[13] Wu, S., Lan, X., Zhao, W., Li, Y., Zhang, L., Wang, H., Han, M., and Tao, S., 2011, Controlled immobilization of acetylcholinesterase on improved hydrophobic gold nanoparticle/Prussian blue modified surface for ultra-trace organophosphate pesticide detection, *Biosens. Bioelectron.*, 27 (1), 82–87.

[14] Aslam, M., Fu, L., Su, M., Vijayamohanan, K., and Dravid, P.V., 2004, Novel one step synthesis of amine-stabilized aqueous colloidal gold nanoparticles, *J. Mater. Chem.*, 14 (12), 1795–1797.

[15] Gusrizal, G., Santosa, S.J., Kunarti, E.S., and Rusdiarso, B., 2016, Dual function of *p*-hydroxybenzoic acid as reducing agent and capping agent in rapid and simple formation of stable silver nanoparticles, *Int. J. ChemTech Res.*, 9 (9), 472–482.

[16] Aji, A., Kunarti, E.S., and Santosa, S.J., 2019, Synthesis of gold nanoparticles using *p*-aminobenzoic acid and *p*-aminosalicylic acid reducing agent, *Indones. J. Chem.*, 19 (1), 68–77.

[17] Nita, R., Trammell, S.A., Ellis, G.A., Moore, M.H., Soto, C.M., Leary, D.H., Fontana, J., Talebzadeh, S.F., and Knight, D.A., 2016, Kinetic analysis of the hydrolysis of methyl parathion using citrate-stabilized 10 nm gold nanoparticles, *Chemosphere*, 144, 1916–1919.

[18] Amendola, V., Pilot, R., Frasconi, M., Maragò, O.M., and Latì, M.A., 2017, Surface plasmon resonance in gold nanoparticles: A review, *J. Phys.: Condens. Matter*, 29 (20), 203002.

[19] Kumari, M., Mishra, A., Pandey, S., Singh, S.P., Chaudhry, V., Mudiam, M.K.R., Shukla, S., Kakkar, P., and Nautiyal, C.S., 2016, Pshyco-chemical condition optimization during biosynthesis lead to development of improved and catalytically efficient gold nanoparticles, *Sci. Rep.*, 6, 27575.

[20] Susanthy, D., Santosa, S.J., and Kunarti, E.S., 2018, The synthesis and stability study of silver nanoparticles prepared using *p*-aminobenzoic acid as reducing and stabilizing agent, *Indones. J. Chem.*, 18 (3), 421–427.

[21] Alvarez-Ros, M.C., Sánchez-Cortéz, S., and García-Ramos, J.V., 2000, Vibrational study of the salicylate interaction with metallic ion and surfaces, *Spectrochim. Acta, Part A*, 56 (12), 2471–2477.

[22] Litvin, V.A., and Minaev, B.F., 2014, The size controllable, one step synthesis and characterization of gold nanoparticles protected by synthetic humic substances, *Mater. Chem. Phys.*, 144 (1-2), 168–178.

[23] Nara, S., Tripathi, V., Singh, H., and Shrivastav, G., 2010, Colloidal gold probe based rapid immunochromatographic strip assay for cortisol, *Anal. Chim. Acta*, 682 (1-2), 66–71.

[24] Tabrizi, A., Ayhan, F., and Ayhan, H., 2009, Gold nanoparticle synthesis and characterization, *Hacettepe J. Biol. Chem*., 37 (3), 217–226.

[25] Buduru, P., and Reddy, S.R., 2016, Oxamic acid and *p*-aminobenzoic acid functionalized gold nanoparticles as a probe for colorimetric detection of Fe^{3+} ion, *Sens. Actuators, B*, 237, 935–943.

Fuel Production from LDPE-based Plastic Waste over Chromium Supported on Sulfated Zirconia

Latifah Hauli, Karna Wijaya*, and Akhmad Syoufian

Department of Chemistry, Faculty of Mathematics and Natural Sciences, Universitas Gadjah Mada, Sekip Utara, Yogyakarta 55281, Indonesia

* ***Corresponding author:***

email: karnawijaya@ugm.ac.id

Received: May 9, 2019
Accepted: August 16, 2019

DOI: 10.22146/ijc.45694

Abstract: *The preparation, characterization, and catalytic activity test of sulfated zirconia (SZ) modified with chromium for the hydrocracking of LDPE-based plastic waste have been investigated. SZ was prepared by wet impregnation method using zirconia nanopowder (ZrO_2) and H_2SO_4 solution. SZ was further modified with chromium (0.5, 1.0, and 1.5% wt.%) by refluxing in aqueous solution of $Cr(NO_3)_3{\cdot}9H_2O$, followed by calcination and reduction processes. The prepared catalysts were characterized by SEM-Mapping and TEM. Hydrocracking of LDPE-based plastic waste was conducted at various temperatures and various catalysts. In addition, the optimum catalyst was repeatedly used for the reaction to demonstrate the stability of the catalyst. Liquid products obtained by hydrocracking were characterized by GCMS. The results showed that the morphology of the prepared catalysts had different sizes and disordered shapes after the addition of sulfate and Cr. The effective temperature for hydrocracking was 250 °C. The highest selectivity to liquid product and gasoline fraction were 40.99 and 93.42 wt.%, respectively, and were obtained over Cr/SZ with 1.0 wt.% Cr. Hydrocracking of plastic waste over the used Cr/SZ catalyst with 1.0 wt.% Cr showed that the Cr/SZ catalyst was stable and reusable up to three repetitions.*

Keywords: *sulfated zirconia; chromium; catalyst; LDPE plastic; fuel*

■ INTRODUCTION

Hydrocracking is a method that can be used to overcome plastic waste-related problems [1]. It is well-known that plastic wastes require a very long time to be naturally degraded [2]. In addition, burning plastic wastes has a dangerous impact because it can produce compounds that are potentially carcinogenic [3]. Hydrocracking can be carried out by thermal and catalytic methods. Thermal hydrocracking requires very high temperatures while catalytic hydrocracking is carried out using a catalyst at a relatively lower temperature. Recently, the catalyst which is widely developed for hydrocracking process is in the form of a metal oxide such as zirconia (ZrO_2) [4-6].

ZrO_2 is a material that is often used as a catalyst in many studies. This material is very attractive due to its high thermal stability, low thermal conductivity, and its resistance to corrosion [7-10]. ZrO_2 can be modified with sulfuric acid to increase its acidity. This modified product is called sulfated zirconia (SZ). Some applications such as hydrocracking, isomerization, and esterification usually require catalysts that have high acidity and, in this term, SZ is widely reported to be used as a catalyst [11-14]. The high acidity of SZ is caused by the presence of Brønsted and Lewis acid sites [15]. Catalytic properties of SZ can be determined from the modification method, sulfate agent, temperature of thermal treatment, and ZrO_2 precursor [16]. The crystalline phase of SZ depends on the crystalline phase of the initial ZrO_2 precursor used. It is known that ZrO_2 has three crystalline phases namely monoclinic, tetragonal, and cubic phases. These phases are influenced by calcination temperature [17]. But in the SZ case, very high temperatures can remove the sulfate groups from the catalyst [18]. In morphology, the particle shape of SZ can be affected by some factors such as pH of solution, the applied precursor, and the calcination

temperature. The increase of calcination temperature can also increase the particle separation and decrease the size of the SZ particles. This factor tends to make SZ form particle agglomeration [9]. The presence of metal on SZ can promote particle agglomeration as reported by Aboul-Gheit et al. [25]. However, it depends on the treatment process and the precursor used in the catalyst preparation.

Modification of SZ with metals can increase its catalytic activity and reduce coke formation [19]. Having high acidity, however, can cause SZ to suffer from deactivation due to the coke formation at high temperatures [20]. This deactivation can be overcome by modifying SZ with metals. Promotion of SZ with platinum has been widely reported as a catalyst that exhibits better catalytic activity [21]. However, platinum is very expensive. Alternatively, researchers use other transition metals to be impregnated to SZ. Amin et al. reported that the presence of Ni on SZ can diminish coke formation and enhance the catalytic activity in hydrocracking of plastic waste [22]. In addition, this enhancement gives high liquid product in the hydrocracking reaction. Thus, we expected that transition metals other than Ni would also have a positive impact on the catalytic performance for hydrocracking reactions. In this research, Cr was doped to SZ as a promoter. Since there are only a few reports on the application of Cr/SZ for the hydrocracking of plastic waste, this research is expected to provide useful information about the catalyst activity and selectivity in the hydrocracking process.

■ EXPERIMENTAL SECTION

Materials

ZrO_2 nanopowder was purchased from Hongwu International Group Ltd. H_2SO_4 (98%) and $Cr(NO_3)_3{\cdot}9H_2O$ were purchased from Merck. Low-density polyethylene (LDPE) waste materials were collected from the final disposal site in Yogyakarta. H_2 gas was supplied by PT. Samator Gas Industri.

Procedure

Catalyst preparation and characterization

Sulfated zirconia was obtained by wet impregnation method from 10 g ZrO_2 nanopowder material and 150 mL of 0.8 M H_2SO_4 solution. The sample was stirred for 24 h, dried in an oven at 100 °C for 24 h, and calcined at 600 °C for 4 h, sequentially. The catalyst produced was labeled as SZ [23].

Chromium (0.5, 1.0, and 1.5 wt.%) was added by reflux technique to the calcined SZ support using aqueous solution of $Cr(NO_3)_3{\cdot}9H_2O$ at 90 °C for 4 h. The obtained samples were dried in the oven at 100 °C for 24 h, calcined at 600 °C for 4 h, and then reduced at 400 °C for 3 h in H_2 gas stream (10 mL/min) [24]. The obtained catalysts were labeled as Cr1/SZ, Cr2/SZ, and Cr3/SZ which correspond to SZ with 0.5, 1.0, and 1.5 wt.% Cr, respectively. Surface morphology of the catalysts was characterized by SEM-Mapping (JEOL, JSM-6510). The morphology of catalysts was also characterized by TEM (JEOL JEM-1400).

Hydrocracking experiment

Plastic pyrolysis was conducted at 300–400 °C for 4 h using a pyrolysis reactor (Fig. 1). The plastic was washed, dried, and cut into small pieces before being put into the reactor. The obtained liquid was hydrocracked by using a hydrocracking microreactor (Fig. 2). The catalyst sample was placed in the catalyst container while the pyrolysis product was in the feed container of the hydrocracking microreactor then the reaction was observed for 1 h with the feed/catalyst ratio of 100 in H_2 gas stream (10 mL/min). The catalytic activity and selectivity tests were done at various temperatures (250, 300, and 350 °C), using various catalysts (ZrO_2, SZ, Cr1/SZ, Cr2/SZ, and Cr3/SZ), and over the reuse of the optimum catalyst. The type of plastic was investigated by FTIR (Shimadzu Prestige-21). The obtained liquid from

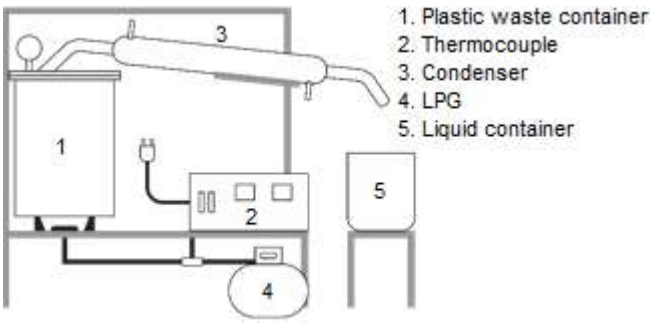

Fig 1. The schematic diagram of the plastic pyrolysis apparatus

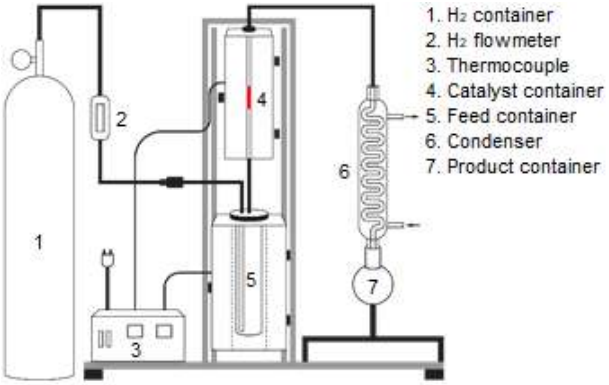

Fig 2. The schematic diagram of the hydrocracking microreactor

the hydrocracking process was characterized by GCMS (Shimadzu QP 2010S). The conversion yield was calculated by using the following equations:

$$\text{Liquid product (wt.\%)} = \frac{\text{weight of liquid product}}{\text{weight of feed}} \times 100\% \quad (1)$$

$$\text{Coke product (wt.\%)} = \frac{\text{weight gain of catalyst hydrocracking}}{\text{weight of feed}} \times 100\% \quad (2)$$

$$\text{Gas product (wt.\%)} = 100\% - \text{wt.\%}(\text{liquid} + \text{coke}) \quad (3)$$

■ RESULTS AND DISCUSSION

Catalyst Characterization

The SEM images of ZrO_2, SZ, Cr1/SZ, Cr2/SZ, and Cr3/SZ catalysts are presented in Fig. 3. SEM results

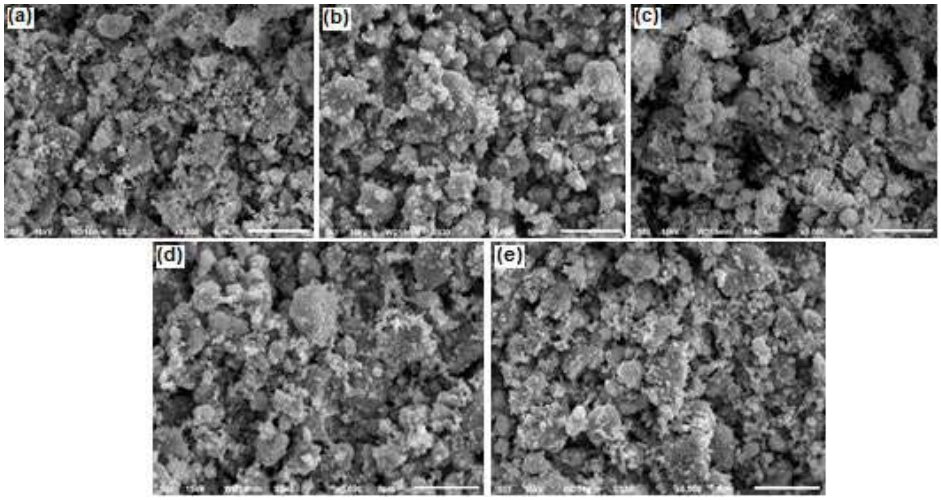

Fig 3. SEM images of (a) ZrO_2, (b) SZ, (c) Cr1/SZ, (d) Cr2/SZ, and (e) Cr3/SZ

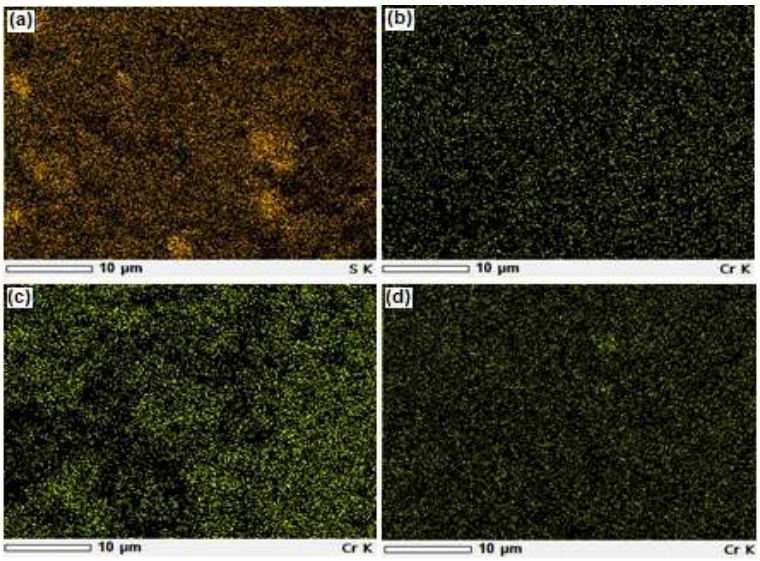

Fig 4. Mapping of (a) SZ, (b) Cr1/SZ, (c) Cr2/SZ, (d) Cr3/SZ

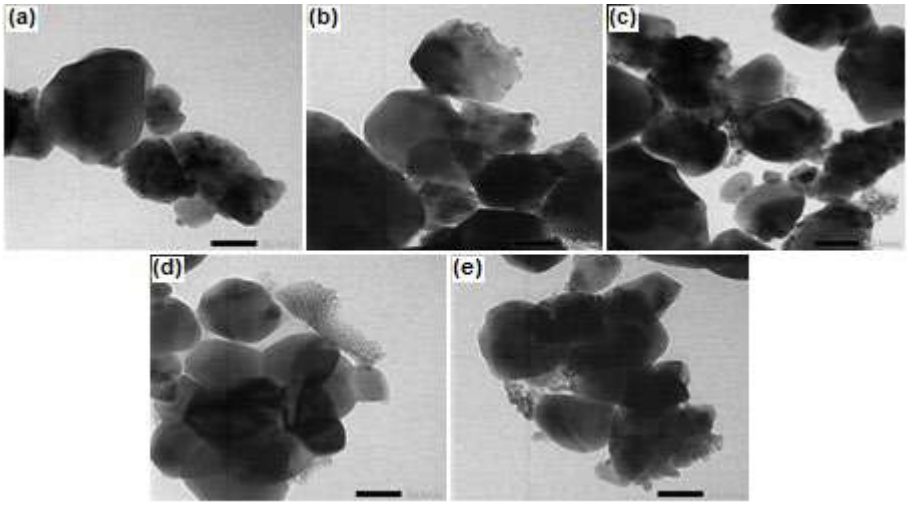

Fig 5. TEM images of (a) ZrO_2, (b) SZ, (c) Cr1/SZ, (d) Cr2/SZ, (e) Cr3/SZ

showed the particle agglomeration with different sizes and disordered shapes on the ZrO_2 surface after the addition of sulfate and Cr [20]. This agglomeration was possible due to sulfate and Cr dispersion on the ZrO_2 surface. The presence and distribution of sulfate and Cr could be detected by Mapping as shown in Fig. 4. Mapping results presented that sulfate on ZrO_2 and Cr on SZ could be distributed evenly on the surface. It indicated that sulfate and Cr were successfully impregnated on ZrO_2.

TEM images of ZrO_2, SZ, Cr1/SZ, Cr2/SZ, and Cr3/SZ catalysts are presented in Fig. 5. TEM results also showed the presence of particle agglomeration after the addition of sulfate and Cr which could be caused by heat treatment [10]. It also showed that there were no visible metallic Cr aggregates. The black areas might represent groups of the accumulated particles [25]. However, this observation also exhibited the morphology of the catalysts with different sizes and disordered shapes for each catalyst.

Catalyst Activity and Selectivity

Fig. 6 shows an IR spectrum of the plastic waste used in this study. IR spectrum was taken in the range of 4000–500 cm^{-1}. The results show that the absorption bands at 2924 and 2855 cm^{-1} were attributed to the stretching vibration of the C–H bond. The absorption band at 1458 cm^{-1} corresponds to the bending vibration of CH_2 [26]. The absorption band at 1373 cm^{-1} was assignable to the bending vibration of CH_3, exhibiting the characteristic of LDPE [27]. The absorption bands at around 730–717 cm^{-1} were attributed to the rocking vibration of CH_2. The result of this characterization strengthened the type of plastic used in this study.

The effect of temperature in the hydrocracking process over Cr2/SZ catalyst is shown in Table 1. It can be seen that the higher temperature used in the hydrocracking

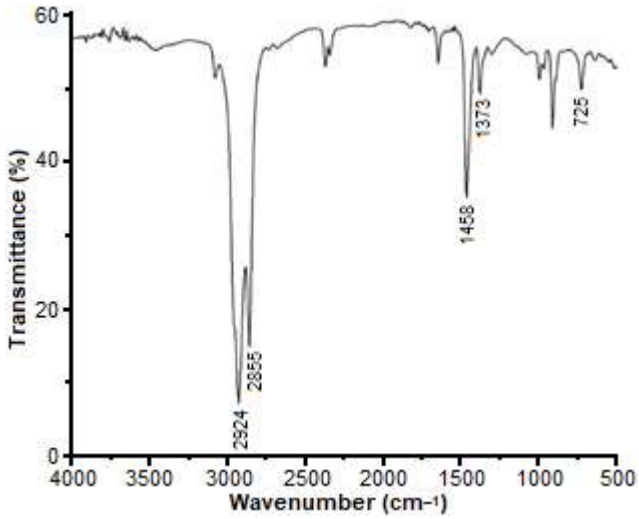

Fig 6. IR spectrum of LDPE-based plastic waste

Table 1. Products for hydrocracking of LDPE-based plastic waste over Cr2/SZ

Temperature (°C)	Yield (wt.%)		
	Liquid	Coke	Gas
250	40.99	0.01	59.00
300	30.13	0.55	69.32
350	11.43	0.93	87.65

process the fewer the liquid product. The higher temperature caused the higher formation of the coke and gas produced. This can be proven by seeing the yield of the coke and gas at the highest temperature level, which were 0.93 and 87.65%, respectively. It can be assumed that the coke that was produced covered the active sites of the catalyst thus it lowered the formation of the liquid product [31]. Based on the results, it was concluded that the effective temperature for the hydrocracking of LDPE was 250 °C. The selectivity in liquid products at various temperatures is presented in Fig. 7. It shows that the higher temperature used in the hydrocracking process could decrease the selectivity for gasoline fractions and instead increase that of diesel.

The hydrocracking of LDPE-based plastic waste was conducted in the presence of ZrO_2, SZ, Cr1/SZ, Cr2/SZ, and Cr3/SZ as catalyst. The yields of products for various catalysts are summarized in Table 2. It can be seen from the table that the presence of sulfate and Cr on ZrO_2 could increase the yields of the liquid products. The high yield of the liquid products can be brought by the catalyst acidity. The impregnation of sulfate on ZrO_2 and that of Cr on SZ can increase the acidity because of the contribution of Brønsted and Lewis acid sites. Variations in metal concentrations in the SZ catalyst also gave the difference in the liquid products in which the highest metal concentration could reduce the liquid product. As reported in a previous research [24], the acidity of catalysts is also decreased by the modification of excess metal to SZ. The acidity values of the catalysts was the smallest with the highest metal concentration. This factor certainly could influence the decreasing catalytic activity in the highest metal concentration. The highest liquid product was obtained by Cr2/SZ catalyst, being 40.99%. The table also shows the decrease of solid products by the presence of Cr on SZ. Modification of SZ with Cr has been proven to reduce coke formation, preventing the deactivation of the catalyst as discussed before. Catalytic hydrocracking proceeds through a carbonium ions mechanism [28]. Carbonium ions could be formed by the interaction of olefins with acidic sites. This stage was stated as the initiation stage. This stage could also occur for paraffin compounds that lost a hydride ion [29]. Sie reported a new

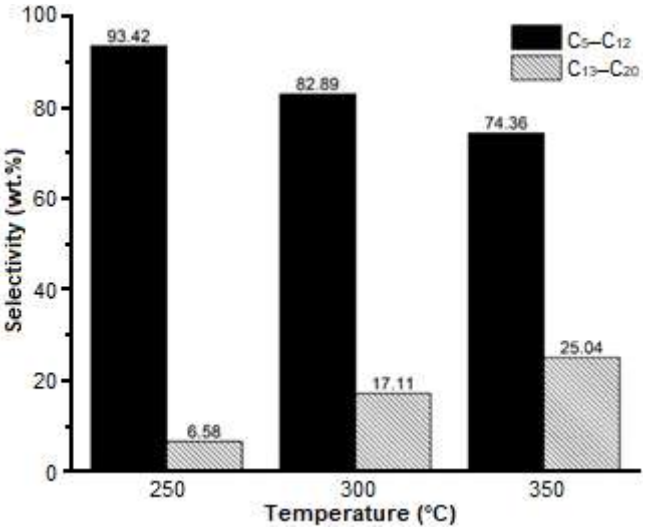

Fig 7. Selectivity in liquid products over Cr2/SZ at various temperatures

Table 2. Products for hydrocracking of LDPE-based plastic waste over various catalysts at 250 °C

Catalyst	Yield (wt.%)		
	Liquid	Coke	Gas
ZrO_2	17.39	0.36	82.25
SZ	28.72	0.34	70.94
Cr1/SZ	33.48	0.01	66.51
Cr2/SZ	40.99	0.01	59.00
Cr3/SZ	37.51	0.01	62.48

mechanism for paraffin cracking over acid catalysts [30]. Such activated paraffin hydrocarbons undergo rearrangement to produce protonated cyclopropane ions (with a more stable state than their linear form). The carbonium intermediates were protonated with hydrogen and broken down into short chains of branched hydrocarbons (gasoline fraction) and long chains of straight hydrocarbons (diesel fractions). Carbonium intermediate with an increasing number of carbon atoms would crack more easily.

The selectivity values in the liquid product for the hydrocracking of LDPE waste over all catalysts are shown in Fig. 8. All of the catalysts showed that the selectivity for the gasoline fraction was higher than that of diesel. However, the presence of sulfate and Cr on ZrO_2 could increase the selectivity towards the gasoline fraction (C_5-C_{12}) and decrease that of the diesel fraction (C_{13}-C_{20}), representing the desired result. The highest selectivity for

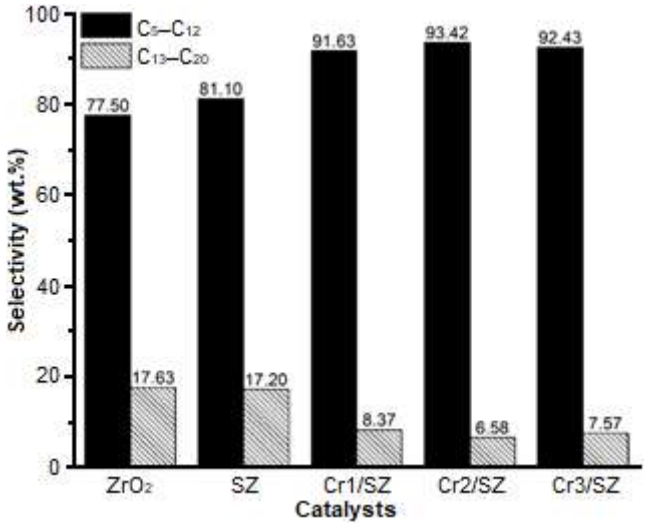

Fig 8. Selectivity in liquid products over various catalysts

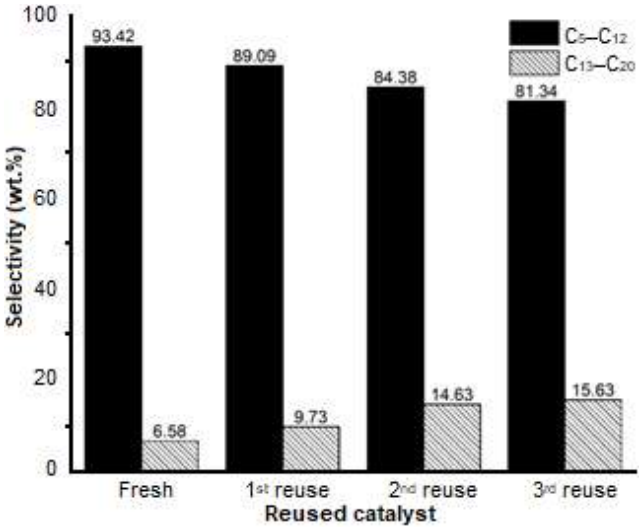

Fig 9. Selectivity in liquid products over reused Cr2/SZ

Table 3. Products of LDPE waste hydrocracking over reused Cr2/SZ

Catalyst	Yield (wt.%)		
	Liquid	Coke	Gas
Fresh	40.99	0.01	59.00
1st reuse	32.71	0.02	67.28
2nd reuse	32.54	0.11	67.35
3rd reuse	30.93	0.17	68.90

the gasoline fraction, which was 93.42%, was obtained over the Cr2/SZ catalyst.

The results of the repeated use of Cr2/SZ for the hydrocracking of LDPE are given in Table 3. The results show that the liquid products decreased gradually with the repeated use, but the Cr2/SZ catalyst was still active even after three repetitions. The yield of the solid products were also getting higher as a result of the reuse. The selectivity values are presented in Fig. 9. The used Cr2/SZ catalyst for hydrocracking was also able to decrease the selectivity to gasoline fraction and increase that of the diesel fraction, because of the formation of high yields of solid products due to the non optimal condition of the plastic cracking process.

■ CONCLUSION

The morphology of the prepared catalysts with the addition of sulfate and Cr showed the different sizes and disordered shapes of the catalysts. The effective temperature for hydrocracking was demonstrated to be 250 °C and the result also showed that the higher temperature in the hydrocracking process could decrease the selectivity for the gasoline fractions and instead increase that of diesel. The highest liquid product and gasoline fraction selectivity were obtained over Cr2/SZ, being 40.99 and 93.42 wt.%, respectively. Cr2/SZ catalyst was stable and reusable up to three repetitions.

■ ACKNOWLEDGMENTS

The authors thank the Ministry of Research and Higher Education of Indonesia which had financially supported this research under the Scholarship Program of PMDSU Batch II with contract number: 2028/UN1/DITLIT/DIT-LIT/LT/2018.

■ REFERENCES

[1] Sriningsih, W., Saerodji, M.G., Trisunaryanti, W., Armunanto, R., and Falah, I.I., 2014, Fuel production from LDPE plastic waste over natural zeolite supported Ni, Ni-Mo, Co and Co-Mo metals, *Procedia Environ. Sci.*, 20, 215–224.

[2] Sarker, M., Rashid, M.M., Rahman, M.S., and Molla, M., 2012, Environmentally harmful low density waste plastic conversion into kerosene grade fuel, *J. Environ. Prot.*, 3 (8), 700–708.

[3] Burange, A.S., Gawande, M.B., Lam, F.L.Y., Jayaram, R.V., and Luque, R., 2015,

Heterogeneously catalyzed strategies for the deconstruction of high density polyethylene: Plastic waste valorisation to fuels, *Green Chem.*, 17 (1), 146–156.

[4] Fatimah, I., Wijaya, K., and Setyawan, K.H., 2008, Synthesis ZrO_2-montmorillonite and application as catalyst in catalytic cracking of heavy fraction of crude oil, *Bull. Chem. React. Eng. Catal.*, 3 (1-3), 9–13.

[5] Zhao, J., Yue, Y., Hua, W., He, H., and Gao, Z., 2007, Catalytic activities and properties of sulfated zirconia supported on mesostructured γ-Al_2O_3, *Appl. Catal., A*, 336 (1-2), 133–139.

[6] Hasanudin, Said, M., Faizal, M., Dahlan, M.H., and Wijaya, K., 2012, Hydrocracking of oil residue from palm oil mill effluent to biofuel, *Sustainable Environ. Res.*, 22 (6), 395–400.

[7] Suseno, A., Wijaya, K., Trisunaryanti, W., and Shidiq, M., 2015, Synthesis and characterization of ZrO_2-pillared bentonites, *Asian J. Chem.*, 27 (7), 2619–2623.

[8] Yu, S., Jiang, P., Dong, Y., Zhang, P., Zhang, Y., and Zhang, W., 2012, Hydrothermal synthesis of nanosized sulfated zirconia as an efficient and reusable catalyst for esterification of acetic acid with *n*-butanol, *Bull. Korean Chem. Soc.*, 33 (2), 524–528.

[9] Heshmatpour, F., and Aghakhanpour, R.B., 2012, Synthesis and characterization of superfine pure tetragonal nanocrystalline sulfated zirconia powder by a non-alkoxide sol–gel route, *Adv. Powder Technol.*, 23 (1), 80–87.

[10] Said, A.E.A., El-Wahab, M.M.A., and El-Aal, M.A., 2014, Chemical the catalytic performance of sulfated zirconia in the dehydration of methanol to dimethyl ether, *J. Mol. Catal. A: Chem.*, 394, 40–47.

[11] Patel, A., Brahmkhatri, V., and Singh, N., 2013, Biodiesel production by esterification of free fatty acid over sulfated zirconia, *Renewable Energy*, 51, 227–233.

[12] Wang, P., Zhang, J., Wang, G., Li, C., and Yang, C., 2016, Nature of active sites and deactivation mechanism for *n*-butane isomerization over alumina-promoted sulfated zirconia, *J. Catal.*, 338, 124–134.

[13] Hauli, L., Wijaya, K., and Syoufian, A., 2019, Hydrocracking of LDPE plastic waste into liquid fuel over sulfated zirconia from a commercial zirconia nanopowder, *Orient. J. Chem.*, 35 (1), 128–133.

[14] Jiang, K., Tong, D., Tang, J., Song, R., and Hu, C., 2010, The Co-promotion effect of Mo and Nd on the activity and stability of sulfated zirconia-based solid acids in esterification, *Appl. Catal., A*, 389 (1-2), 46–51.

[15] Saravanan, K., Tyagi, B., Shukla, R.S., and Bajaj, H.C., 2016, Solvent free synthesis of methyl palmitate over sulfated zirconia solid acid catalyst, *Fuel*, 165, 298–305.

[16] Reddy, B.M., and Patil, M.K., 2009, Organic syntheses and transformations catalyzed by sulfated zirconia, *Chem. Rev.*, 109 (6), 2185–2208.

[17] Subbarao, E.C., Maiti, H.S., and Srivastava, K.K., 1974, Martensitic transformation in zirconia, *Phys. Status Solidi A*, 21 (1), 9–40.

[18] Utami, M., Wijaya, K., and Trisunaryanti, W., 2017, Effect of sulfuric acid treatment and calcination on commercial zirconia nanopowder, *Key Eng. Mater.*, 757, 131–137.

[19] Belskaya O.B., Danilova, I.G., Kazakov, M.O., Gulyaeva, T.I., Kibis, L.S., Boronin, A.I., Lavrenov, V.A., and Likholobov, V.A., 2010, Investigation of active metal species formation in Pd-promoted sulfated zirconia isomerization catalyst, *Appl. Catal., A*, 387 (1-2), 5–12.

[20] Yadav, G.D., and Nair, J.J., 1999, Sulfated zirconia and its modified versions as promising catalysts for industrial processes, *Microporous Mesoporous Mater.*, 33 (1-3), 1–48.

[21] Utami, M., Wijaya, K., and Trisunaryanti, W., 2018, Pt-promoted sulfated zirconia as catalyst for hydrocracking of LDPE plastic waste into liquid fuels, *Mater. Chem. Phys.*, 213, 548–555.

[22] Amin, A.K., Wijaya, K., and Trisunaryanti, W., 2018, The catalytic performance of ZrO_2-SO_4 and Ni/ZrO_2-SO_4 prepared from commercial ZrO_2 in hydrocracking of LDPE plastic waste into liquid fuels, *Orient. J. Chem.*, 34 (6), 3070–3078.

[23] Hauli, L., Wijaya, K., and Armunanto, R., 2018, Preparation and characterization of sulfated zirconia from a commercial zirconia nanopowder, *Orient. J. Chem.*, 34 (3), 1559–1564.

[24] Hauli, L., Wijaya, K., and Armunanto, R., 2019, Preparation of Cr metal supported on sulfated zirconia catalyst, *Mater. Sci. Forum*, 948, 221–227.

[25] Aboul-Gheit, A.K., Gad, F.K., Abdel-Aleem, G.F., and El-Desouki, D.S., 2014, Pt, Re and Pt–Re incorporation in sulfated zirconia as catalysts for n-pentane isomerization, *Egypt. J. Pet.*, 23 (3), 303–314.

[26] Asensio, R.C., Moya, M.S.A., de la Roja, J.M., and Gómez, M., 2009, Analytical characterization of polymers used in conservation and restoration by ATR-FTIR spectroscopy, *Anal. Bioanal. Chem.*, 395 (7), 2081–2096.

[27] Jung M.R., Horgen, F.D., Orski, S.V., Rodriguez, C.V., Beers, K.L., Balazs, G.H., Jones, T.T., Work, T.M., Brignac, K.C., Royer, S.J., Hyrenbach, K.D., Jensen, B.A., and Lynch, J.M., 2018, Validation of ATR FT-IR to identify polymers of plastic marine debris, including those ingested by marine organisms, *Mar. Pollut. Bull.*, 127, 704–716.

[28] Trisunaryanti, W., Armunanto, R., Hastuti, L.P., Ristiana, D.D., and Ginting, R.V., 2018, Hydrocracking of α-cellulose using Co, Ni, and Pd supported on mordenite catalysts, *Indones. J. Chem.*, 18 (1), 166–172.

[29] Buekens, A.G., and Huang, H., 1998, Catalytic plastics cracking for recovery of gasoline-range hydrocarbons from municipal plastic wastes, *Resour. Conserv. Recycl.*, 23 (3), 163–181.

[30] Sie, S.T., 1992, Acid-catalyzed cracking of paraffinic hydrocarbons. 1. Discussion of existing mechanisms and proposal of a new mechanism, *Ind. Eng. Chem. Res.*, 31 (8), 1881–1889.

[31] Pongsendana, M., Trisunaryanti, W., Artanti, F.W., Falah, I.I., and Sutarno, 2017, Hydrocracking of waste lubricant into gasoline fraction over CoMo catalyst supported on mesoporous carbon from bovine bone gelatin, *Korean J. Chem. Eng.*, 34 (10), 2591–2596.

Orange Peel Essential Oil Nanoemulsions Supported by Nanosilver for Antibacterial Application

Doan Van Dat[1,*], Nguyen Van Cuong[1], Pham Hoang Ai Le[1], Tran Thi Lan Anh[1], Pham Tan Viet[2], and Nguyen Thi Lan Huong[2]

[1]*Faculty of Chemical Engineering, Industrial University of Ho Chi Minh City, No. 12 Nguyen Van Bao, Ward 4, Go Vap District, Ho Chi Minh City 70000, Vietnam*

[2]*Institute of Biotechnology and Food Technology, Industrial University of Ho Chi Minh City, No. 12 Nguyen Van Bao, Ward 4, Go Vap District, Ho Chi Minh City 70000, Vietnam*

* ***Corresponding author:***

email: doanvandat@iuh.edu.vn

Received: May 22, 2019
Accepted: July 29, 2019

DOI: 10.22146/ijc.46042

Abstract: *This study is devoted to the synthesis of King Orange peel essential oil in water nanoemulsions combined with nanosilver by ultrasonic method supported by mechanical stirring for antibacterial application. The samples were characterized by Gas chromatography-mass spectrometry (GC-MS), Ultraviolet–visible (UV-Vis), Transmission electron microscopy (TEM), and Dynamic light scattering (DLS) methods. According to the above-experimental results, it was found that the emulsions based on orange essential oil (without nanosilver) and the ones combined with nanosilver have the average particle size from 66.2 nm and 42.9 nm, respectively. The obtained nanoemulsions were also tested to examine their antibacterial ability against* Escherichia coli *(*E. coli*) by the disc diffusion method. It has been also found that nanoemulsions based on orange essential oil supported by nanosilver have the superior antibacterial ability, compared with individual components of the materials.*

Keywords: *nanoemulsions; orange peel essential oil; nanosilver; antibacterial application*

■ INTRODUCTION

In recent years, nanoemulsions based on plant essential oils are paid great attention because of their unique properties such as small droplet size (about 20–500 nm), good stability, transparent appearance, and tunable rheology [1-4]. Therefore, they have been used widely in the cosmetic, pharmaceutical industries, food, and drug delivery, and antimicrobial applications [5-8].

Among high value plant essential oils, orange essential oil - scientific name of *Citrus sinensis* Osbeck, belonging to the family *Rutaceae*, has been one of the most widely used oils in the world, mainly extracted from cells in the orange peel, a few in the leaves and flowers. The main sweet aroma of the orange essential oil that can bring pleasant feeling, pleasant mood, and make people happy and cheerful is D-Limonene (90%) [9]. Orange essential oil is also a natural antibacterial agent, which can inhibit the growth and eradication of *E. coli*, a very dangerous bacteria that causes kidney disease and might lead to death. In addition, the orange essential oil can inhibit the spread and development of Salmonella bacteria because it contains strong antimicrobial components, especially terpenes. In 2017, Lou et al. detailly reported the antimicrobial resistance of essential oils from citrus trees and indicated that citrus essential oil could inhibit the growth of *S. aureus* and *E. coli* [10].

Orange essential oil reveals less dissolve property in water. To enhance its solubility and stability properties of the oil, emulsion technology is one of the essential processes widely used for this purpose [11]. In the past decade, there has been a number of studies on nanomaterials based on essential oil form that showed their high effectiveness in food and health-protecting products applications. Li et al., in 2018, combined the citrus orange essential oil with chitosan to form

microcapsules thanks to a variety of surfactants by gel ionic emulsion method to produce nanoemulsion particles larger than 289.3 nm [12]. Zhang et al., in 2016, reported the synthesis of nano clove essential oil and nano cinnamon essential oil with a particle size of 8.69 nm effective in antimicrobial resistance for *Escherichia coli, Bacillus subtilis, Salmonella Typhimurium* and *Staphylococcus aureus* [13]. Shahavi et al., in 2015, reported the optimal method of ultrasound for the synthesis of clove nano essential oil. This method gave the emulsion nanoparticles of size smaller than 50 nm, stably distributed in the water environment [14]. Mehmood et al., in 2017, reported the optimum method to synthesis olive nano essential oil that produced the essential oil nanoparticles with a particle size of 151.68 nm [15]. Amrutha et al., in 2017, reported the synthesis of nano essential oil from *Cuminum cynium* and *Pepper (Piper nirgrum).* These essential oils were used in ultrasound to inhibit the activity of *E. coli* and *S. enteria* [16].

However, researches have been focused mainly on the efficient production of essential oils, the biological and chemical properties of essential oils extracting from nature, as well as the conversion of essential oils to nanoemulsion form. Nanoemulsions, supported by metal nanoparticles, namely, nanosilver for antibacterial applications, have not been widely reported. Only one article was found, in which Najafi-Taher et al. in 2018 reported a combination method of silver nanoparticle-loaded tea tree oil nanoemulsion that showed a good antibacterial effect against *E. coli* and *S. aureus* [17]. Meanwhile, nanosilver is a material with a very large surface area, has the following unique characteristics such as disinfection, anti-fungus, deodorization, unharmful to human health at relatively high doses, ability to disperse stably in various solvents, high chemical stability, almost unchanged under the action of light and conventional oxidation-reduction agents [18].

Nanoemulsions are usually produced using high-energy emulsions, such as high-pressure homogenization, microfluidic diffusion, and high-intensity ultrasound [19]. Of these, the use of ultrasound to produce nanoemulsions becomes a recent trend [20]. Lower energy and surface stabilizer consumption, smaller particle size, higher dispersion, and higher stability of nanoemulsions are one of the main advantages of this technique over other methods [21]. To the best of our knowledge, nanosilver-loaded nanoemulsion based on King Orange essential oil from peel has not been reported yet. Therefore, the purpose of this work is devoted to synthesizing nanoemulsion based on essential oil from King Orange peel and combine it with silver nanoparticles by ultrasonic method for antimicrobial application.

■ EXPERIMENTAL SECTION

Materials

The chemicals used for the synthesis of nanoemulsion are silver nitrate ($AgNO_3$, 99.8%), trisodium citrate ($Na_3C_6H_5O_7{\cdot}2H_2O$, 99%), tween 80 ($C_{64}H_{124}O_{26}$, 99%), span 80 ($C_{24}H_{44}O_6$, 99%) of chemical reagent grade purchased from Shanghai Shenglong Chemical Co., China. Fresh orange peels were collected from King Orange (*Citrus reticulata* × *Citrus sinensis*) planted in southern Vietnam. Bidistilled water was used as a solvent for the preparation of all necessary solutions. The direct steam distillation method was used to extract the orange essential oil from orange peel.

Procedure

Synthesis of nanoemulsion based on orange essential oil

In this method, tween 80 and span 80 were selected as effective emulsifiers for the emulsion system; meanwhile, the dispersion process was conducted by the ultrasonic method supported by mechanical stirring according to the following procedure. A certain volume ratio of Tween 80 and Span 80 stabilizers (0:1; 0.25:0.75; 0.5:0.5; 0.75:0.25; 1:0) were firstly taken into beakers, then different volume of orange essential oil ranging from 0.5 to 3 mL was added. The mixture was preliminarily stirred; after that, an appropriate amount of distilled water was poured slowly with a rate of 5 mL/min into the mixture to get the total liquid volume of 50 mL. The mixture was then homogenized by a mechanical stirrer for 10 min at a speed of 2100 rpm and put under ultrasonic vibration in an ultrasonic

Homogenizer Q500 Sonicator (Qsonica, USA) with an amplitude of 25% for 10 min. The obtained emulsions were examined by the DLS method for particle size distribution on a Horiba SZ-100 analyzer (Horiba, Japan).

Synthesis of nanosilver suspension

In the past decades, there are many methods for the synthesis of nanosilver, in which chemical reduction is most commonly used. In this method, trisodium citrate was used as a reducing agent for the synthesis of silver nanoparticles because of low cost, simple synthesis, and easy to get silver nanoparticles with particle size in the range of 30–50 nm [22-23]. The synthesis procedure is as follows. 50 mL of 0.002 M $AgNO_3$ solution was prepared in a flask that was wrapped totally by aluminum paper to protect from light, and 40 mL of $Na_3C_6H_5O_7$ 0.005 M solution was also prepared in a 100 mL beaker. Both solutions were heated in a thermobath at the same time to get the temperature up to about 75–80 °C. The 0.005 M $Na_3C_6H_5O_7$ solution was then added slowly into 0.002 M $AgNO_3$ solution under stirring at 350 rpm. The mixture was then heated and kept at 85 °C until the mixture turned to light yellow, stop heating, and cool down the mixture to room temperature. After synthesis, the suspension was stored in the dark to avoid the decomposition of silver nanoparticles by light.

Method of combining nano essential oil with nanosilver 50 ppm suspension

Orange peel essential oil nanoemulsions supported by nanosilver was synthesized similarly to orange peel essential oil nanoemulsion, in which the solution of 100 ppm silver nanoparticles served as stock solution was diluted by distilled water and used as dispersion media instead of pure water for combining nano essential oil with nanosilver, so that the final concentration of silver nanoparticles was unchanged and reached 50 ppm.

Modern physico-chemical methods for studying composition, morphology and particle size of samples

Gas chromatography–mass spectrometry (GC-MS) method was employed on an Agilent 7890a Series (Agilent, USA) for the examination of orange essential oil composition with evaporation temperatures for essential oil prior to analysis at 320 and 600 °C. The particle size distribution and zeta potential were examined by dynamic light scattering (DLS) method using a Horiba SZ-100 nanoscale particle size analyzer (Horiba, Japan). The size of silver nanoparticles was determined by the transmission electron microscopy (TEM) method using a Jeol JEM-1400, Japan (Jeol, Japan). The Ultraviolet–visible (UV-Vis) spectra of silver nanoparticles were determined on a UV-2450 (Shimadzu, Japan).

Methods of antibacterial studies

The antibacterial ability of samples was examined by the disc diffusion method for determining the susceptibility of *Escherichia coli (E. coli*) to orange peel essential oil nano-emulsions supported by nanosilver. Test procedure: the mentioned above bacteria were placed in a petri dish containing Luria Bertani agar; then, the bacteria were spread out of the agar surface. Six millimeters sterile paper disc was placed on the surface of the agar and then impregnated by 10 µL of the test sample. A sample of antibiotics – ampicillin as positive evidence was also placed on the surface of the agar. The petri dish was covered by a sterile paper and kept at room temperature for 1–2 days. The rings surrounding antibacterial plates were observed for evaluating the antibacterial activity of the obtained samples. Orange essential oil, emulsion based on orange essential oil and silver nanoparticles suspension were used as blank samples for comparing their antibacterial activity with orange peel essential oil nanoemulsions supported by nanosilver. The antibacterial ability of all samples was tested at the Institute of Food and Biotechnology – Industrial University of Ho Chi Minh City, Vietnam.

■ RESULTS AND DISCUSSION

Chemical Composition Analysis of Orange Peel Essential Oil by GC-MS Method

The chemical composition of orange peel essential oil at two evaporation temperatures of 320 and 600 °C was presented in Table 1.

From Table 1, it can be obviously seen that the main components of the King Orange peel essential oil are terpenium compounds (61–95%), especially Limonene as major constituent of citrus fruits' essential oils [24]. Next is alcohol compounds (0.3–5%), while the

Table 1. The chemical composition of evaporated orange essential oil at 320 and 600 °C

Compounds	320 °C	600 °C
	Constituent content (%)	
α-Pinene	0.54	0.45
β-Myricene	0.24	-
(+)-Limonene	**75.79**	**61.64**
Limonene oxide	**8.88**	**17.00**
Cis-Carveol	4.17	4.54
Carvone	6.42	5.46
Cyclopentenone	0.32	-
1,4-Pentadiene	0.24	-
1,2-Cyclononadiene	0.61	-
1,9-Decadiyne	1.85	-
E-p-Mentha-2,8-dienol	0.94	-
Carhydrine	-	3.67
Hexadenol	-	0.34
Alloocimene	-	0.67
1,2-Pentadien	-	1.97
1,9-Decadiyne	-	0.41
Ocimene	-	0.41
Total	**100**	**99.98**

"-": not detected

compounds of sesquiterpenes group occupy a very small part in the obtained oil (1 to 2.5%). Espina et al., in 2013, described the good inactivation of *E. coli* by (+)-limonene (97% purum) in detail and showed its potential in food preservation, either acting alone or in combination with other techniques [24].

Analysis of Silver Nanoparticles Suspension

Silver nanoparticles suspension obtained by the given method gets a light-yellow color, the higher the silver nanoparticles concentration, the darker the color of the solution.

An interesting phenomenon of nano metal particles called surface plasmon resonance is that each metal in nanosize absorbs electromagnetic radiation at a certain wavelength. The characteristics of this absorption vary depending on the size, shape, and structure of the particles and can be determined by UV-Vis spectra. For silver nanoparticles, the characteristic absorption peaks in the wavelength range around 425 nm. UV-Vis spectrum of the 50-ppm silver concentration sample (Fig. 1) showed the peak absorption at 424.50 nm, indicated the presence of silver nanoparticles in suspension [25].

TEM image analysis showed that silver nanoparticles in the obtained suspension were spherical with an average size of 40–50 nm (Fig. 2(a)). The DLS results of the silver nanoparticles suspension also confirmed the average nanosilver size of 42 nm (Fig. 2(b)).

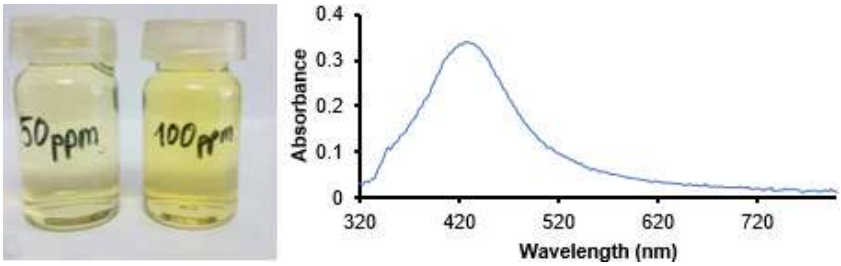

Fig 1. UV-Vis spectrum of 50 ppm nanosilver suspension

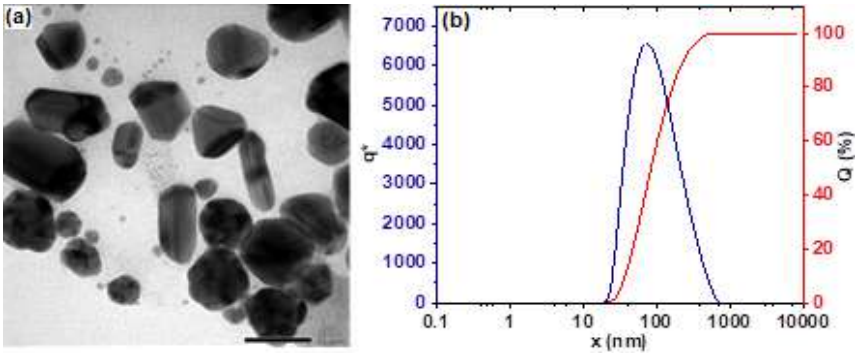

Fig 2. (a) TEM image of 50 ppm nanosilver suspension; (b) Size distribution of silver nanoparticles in 50 ppm silver nanoparticles suspension

The similar results about the average size with 36–39 nm of nanosilver, synthesized by using trisodium citrate dihydrate as reductant were also found in [26].

The Study of Emulsifier Selection

The suitable emulsifiers can be selected based on their amphiphilic character characterized by the hydrophilic–lipophilic balance (HLB), firstly described by Griffin in 1949. The optimal stability of each nanoemulsion required a precise HLB value that could be given by mixing some surfactants, according to Griffin formula [27]. In this work, different mixtures of Span 80 with HLB = 4.3 and Tween 80 with HLB = 15 were applied to find out the appropriate HLB value for stabilization of nanoemulsion based on King Orange essential oil as follows. Various volume ratios of Tween 80 and Span 80 (0:1; 0.25:0.75; 0.5:0.5; 0.75:0.25; 1:0) corresponded with HLB values of 4.24; 6.38; 9.63; 12.31; 15.00 were mixed with 1 mL of orange oil and distilled water to get 50 mL suspension according to the described above procedure. The particle size distribution of 5 obtained samples after synthesis named B6-B10 was determined by the DLS method and presented in Table 2. The stability of the obtained samples had also been observed for 20 days (Fig. 3).

It has been found that all the samples of emulsion based on orange essential oil are nano-sized (Table 3). However, after 20 days, the lower part of sample B6 and sample B7 are lighter than the upper part of the bottle, indicating that the two samples are less stable due to the oil is lighter than the water, leading to floating up. The remaining three samples get better stability and have not yet been separated after 20 days (Fig. 3(b)). The experiment results also indicated that Tween 80 with the HLB value of 15 is the best surface stabilizer for nanoemulsion based on orange essential oil production, as it retains the aroma of orange essential oil, high transparency, high stability and it gives the nanoemulsion with smallest particle size about 66 nm (Fig. 4). The obtained results are consistent with previous studies that emulsifiers with a small range of HLB values (4–6) generally stabilize water in oil nanoemulsions whereas higher HLB values above 8 would stabilize oil in water nanoemulsions [28-29].

Combination of Nanoemulsion Based on Essential Oil with Nanosilver 50 ppm Suspension

Orange essential oil with different volume from 0.5 to 3 mL was emulsified by Tween 80 (with a volume oil/emulsifier ratio of 2:3), 25 mL 100 ppm nanosilver suspension, and an appropriate volume of distilled water to get 50 mL nanoemulsion with unchanged silver

Fig 3. Nanoemulsions based on orange essential oil sample: (a) on first day, (b) after 20 days synthesis

Table 2. Particle size distribution of nanoemulsions based on orange essential oil with different ratio between tween 80 and span 80

Sample	Tween:Span [mL:mL)	Average size [nm]	Observation
B6	0:1	78.4	White opaque, heavy smell of Span
B7	0.25:0.75	94.7	White opaque, heavy smell of Span
B8	0.5:0.5	85.4	White and slightly in clear, light orange smell
B9	0.75:0.25	106.1	White opaque, light orange smell
B10	1:0	66.2	Transparent, orange aromatic smell

nanoparticles concentration of 50 ppm. The obtained samples were named by D1 to D6, respectively. 50 ppm nanosilver solution sample, which is named NB, plays the role of a blank sample for antibacterial test.

DLS results showed that the emulsion synthesis method of combination with nanosilver could be used to produce nanoemulsions with average particle size ranging from 42.9 to 135.5 nm. The diagram indicated proportion of particle size distribution in the sample, in which the wider diagram, the lower the uniformity is. Compared to other works [30], the obtained DLS diagrams have narrow widths (Fig. 5); therefore, all the

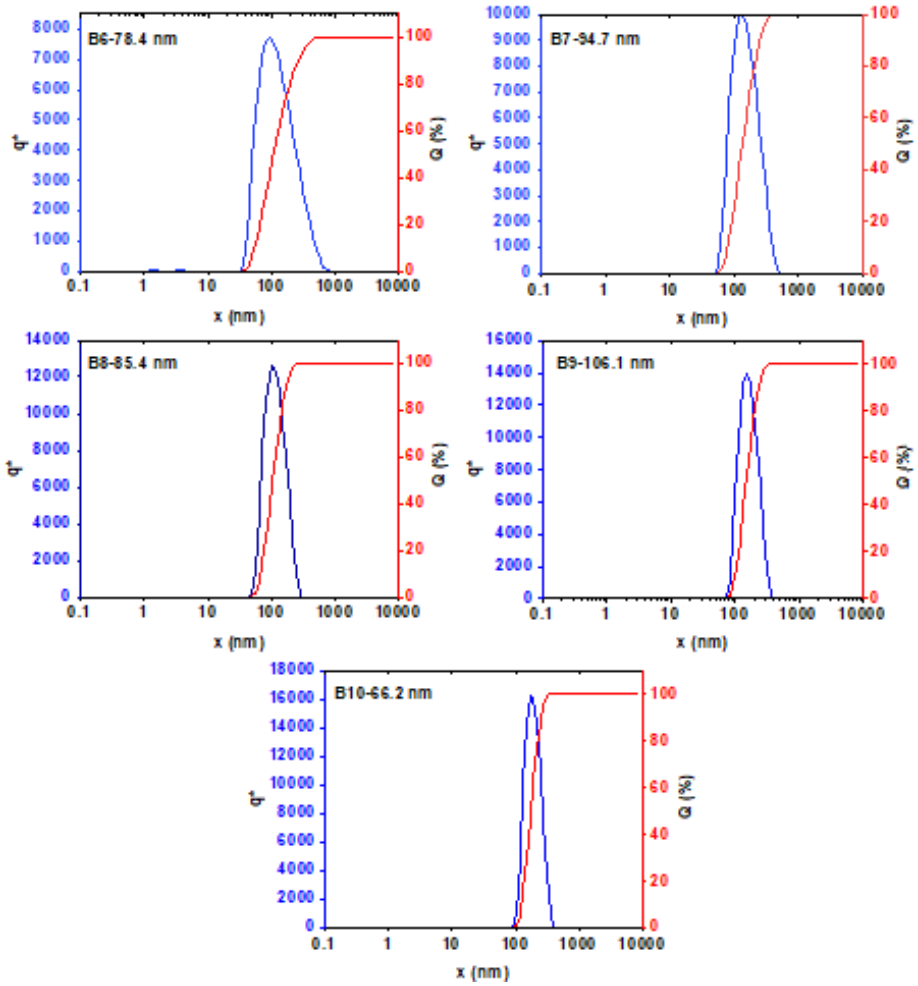

Fig 4. Particle size distribution of nanoemulsions based on orange essential oil only (without nanosilver)

Table 3. Particle size distribution of nanoemulsions based on orange essential oil combined with silver nanoparticles

Sample	Orange essential oil (mL)	Silver nanoparticles solution 100 ppm mL	H_2O (mL)	Particle size (nm)
D1	0.5	25	23.75	135.5
D2	1	25	22.50	69.3
D3	1.5	25	21.25	60.4
D4	2	25	20.00	58.3
D5	2.5	25	18.75	42.9
D6	3	25	17.50	115.8
NB	-	25	25.00	42.7

"-": the component was not added

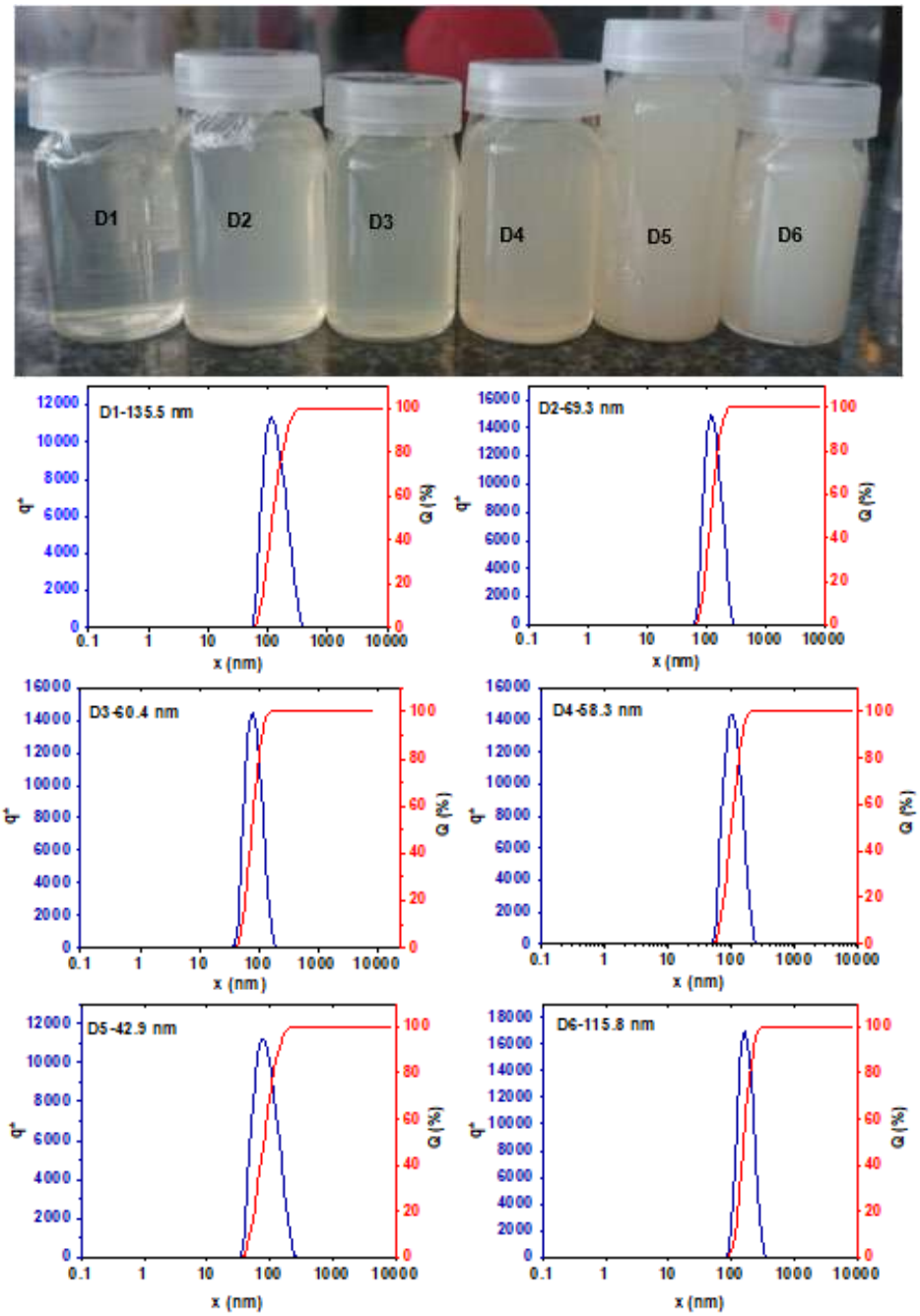

Fig 5. Nanoemulsions based on orange essential oil supported by silver nanoparticles with their particle size distribution

nanoemulsion samples have relatively high homogeneity, in which the D5 sample with 2.5 mL essential oil and 3.75 mL tween 80 as stabilizer has the smallest average particle size of 42.9 nm. It has been found that the size of nanoemulsion particles tends to decrease with the addition of nanosilver. It could be explained that in the case without nanosilver, surfactant and oil together form a complex film at the oil water interface and thus generate emulsion droplets with hydrophobic tails bunched up, hydrophilic heads pointing towards the water [31]. In addition of nanosilver, nanosilver might be played the role of a hydrophobic core of emulsion

droplet and attracted monolayer hydrophobic tails to form smaller nanoemulsion particles.

Antibacterial Test for Nanoemulsions Based on Orange Essential Oil Combining with Silver Nanoparticles

In the antibacterial test, 10 µL of each sample was put onto a paper plate placed on the surface of the LB medium that contained *E. coli* bacteria. B6 to B10 samples are nanoemulsions based on orange essential oil combined with nanosilver 100 ppm suspension. For comparison purposes, 50 ppm nanosilver suspension sample, named NB and the nanoemulsions samples with different volumes of orange essential oils (without nanosilver), named D1 to D6, respectively - were also tested (Fig. 6).

It was observed that all the nanoemulsion samples based on orange essential oils are able to against *E. coli* bacteria, regardless of very low oil content. As combining with nanosilver, the antibacterial ability of the samples significantly increased, in which D3 sample with the average size of 60.4 nm and 1.5 mL orange oil has the greatest antibacterial ability, better than its individual components, although it is not the smallest particle size sample. It has been found that antibacterial ability of nanoemulsions based on orange essential oil combining with silver nanoparticles depends on both particle size and the volume ratio between the oil and emulsifier. The addictive antibacterial mechanism of nanosilver-loaded nanoemulsion based on orange essential oil could be proposed as follows. Firstly, the essential oil layer with the main component consisted of limonene inactivated bacteria action by causing sub-lethal damages to the cytoplasmic or the outer membrane of bacteria [24]. Secondly, nanosilver acted with bacteria by linking disulfide (S-S) bridges in the enzyme structure of bacteria, disable this enzyme or break down bacterial cell membranes with oxidation reactions, resulting in bacteria destruction [32].

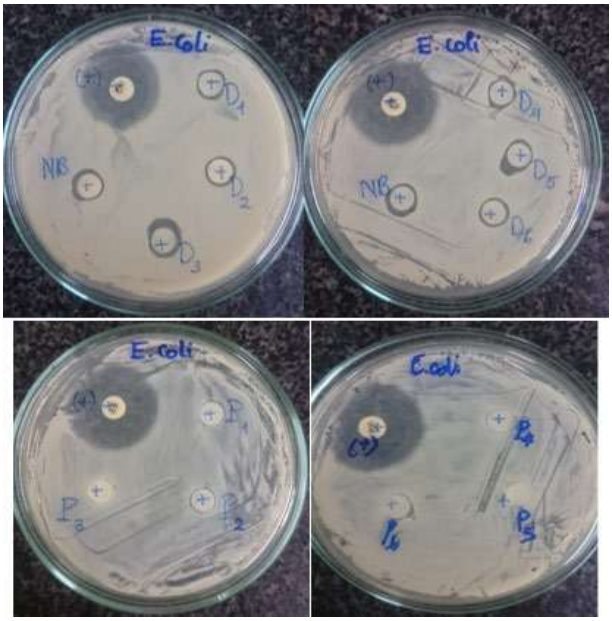

Fig 6. Antibacterial test against *E. coli*

■ CONCLUSION

Orange peel essential oil nanoemulsions combined with nanosilver was successfully synthesized by ultrasonic method supported by mechanical stirring, using tween 80 as an effective emulsifier. All the obtained samples are nanosized and revealed a good antibacterial capacity against *E. coli*. It has been also found that the antibacterial ability of nanoemulsions based on orange essential oil combining with silver nanoparticles depends not only on the particle size of individual components but also on the volume ratio between them.

■ ACKNOWLEDGMENTS

This work was supported by scientific research project number 184.HH05 funded by the Industrial University of Ho Chi Minh city under contract No. 39/HD-DHCN.

■ REFERENCES

[1] Hakemi-Vala, M., Rafati, H., Aliahmadi, A., and Ardalan, A., 2017, "Nanoemulsions: A Novel Antimicrobial Delivery System" in *Nano- and Microscale Drug Delivery Systems*, Eds. Grumezescu, A., Elsevier, London, 245–63.

[2] Ostróżka-Cieślik, A., and Sarecka-Hujar, B., 2017, "The Use of Nanotechnology in Modern Pharmacotherapy" in *Multifunctional Systems for Combined Delivery, Biosensing and Diagnostics,* Eds. Grumezescu, A., Elsevier, London, 139–158.

[3] Bernardi, D.S., Pereira, T.A., Maciel, N.R., Bortoloto, J., Viera, G.S., Oliveira, G.C., and Rocha-Filho, P.A., 2011, Formation and stability of oil-in-water nanoemulsions containing rice bran oil: in vitro and in vivo assessments, *J. Nanobiotechnol.*, 9, 44.

[4] Silva, J., Fernandes, A.R., and Baptista, P.V., 2014, *Application of Nanotechnology in Drug Delivery*, IntechOpen, London, 127–54.

[5] Amaral, D.M.F., and Bhargava, K., 2015, Essential oil nanoemulsions and food applications, *Adv. Food Technol. Nutr. Sci.*, 1 (4), 84–87.

[6] Prakash, A., Vadivel, V., Rubini, D., and Nithyanand, P., 2019, Antibacterial and antibiofilm activities of linalool nanoemulsions against S*almonella* Typhimurium, *Food Biosci.*, 28, 57–65.

[7] Silva, H.D., Poejo, J., Pinheiro, A.C., Donsì, F., Serra, A.T., Duarte, C.M.M., Ferrari, G., Cerqueira, M.A., and Vicente, A.A., 2018, Evaluating the behaviour of curcumin nanoemulsions and multilayer nanoemulsions during dynamic *in vitro* digestion, *J. Funct. Foods*, 48, 605–613.

[8] Gupta, A., Eral, H.B., Hatton, T.A., and Doyle, P.S., 2016, Nanoemulsions: Formation, properties and applications, *Soft Matter*, 12 (11), 2826–2841.

[9] Milind, P., and Dev, C., 2012, Orange: Range of benefits, *Int. Res. J. Pharm.*, 3 (7), 59–63.

[10] Lou, Z., Chen, J., Yu, F., Wang, H., Kou, X., Ma, C., and Zhu, S., 2017, The antioxidant, antibacterial, antibiofilm activity of essential oil from *Citrus medica L. var. sarcodactylis* and its nanoemulsion, *LWT Food Sci. Technol.*, 80, 371–377.

[11] Anwer, M.K., Jamil, S., Ibnouf, E.O., and Shakeel, F., 2014, Enhanced antibacterial effects of clove essential oil by nanoemulsion, *J. Oleo Sci.*, 63 (4), 347–354.

[12] Li, Y., Wu, C., Wu, T., Wang, L., Chen, S., Ding, T., and Hu, Y., 2018, Preparation and characterization of citrus essential oils loaded in chitosan microcapsules by using different emulsifiers, *J. Food Eng.*, 217, 108–114.

[13] Zhang, S., Zhang, M., Fang, Z., and Liu, Y., 2017, Preparation and characterization of blended cloves/cinnamon essential oil nanoemulsions, *LWT Food Sci. Technol.*, 75, 316–322.

[14] Shahavi, M.H., Hosseini, M., Jahanshahi, M., Meyer, R.L., and Darzi, G.N., 2016, Clove oil nanoemulsion as an effective antibacterial agent: Taguchi optimization method, *Desalin. Water Treat.*, 57 (39), 18379–18390.

[15] Mehmood, T., Ahmad, A., Ahmed, A., and Ahmed, Z., 2017, Optimization of olive oil based O/W nanoemulsions prepared through ultrasonic homogenization: A response surface methodology approach, *Food Chem.*, 229, 790–796.

[16] Amrutha, B., Sundar, K., and Shetty, P.H., 2017, Spice oil nanoemulsions: Potential natural inhibitors against pathogenic *E. coli* and *Salmonella* spp. from fresh fruits and vegetables, *LWT Food Sci. Technol.*, 79, 152–159.

[17] Najafi-Taher, R., Ghaemi, B., Kharrazi, S., Rasoulikoohi, S., and Amani, A., 2019, Promising antibacterial effects of silver nanoparticle-loaded tea tree oil nanoemulsion: A synergistic combination against resistance threat, *AAPS PharmSciTech*, 19 (3), 1133–1140.

[18] Deshmukh, S.P., Patil, S.M., Mullani, S.B., and Delekar, S.D., 2019, Silver nanoparticles as an effective disinfectant: A review, *Mater. Sci. Eng., C*, 97, 954–965.

[19] Rao, J., and McClements, D.J., 2011, Formation of flavor oil microemulsions, nanoemulsions and emulsions: Influence of composition and preparation method, *J. Agric. Food Chem.*, 59 (9), 5026–5035.

[20] Li, P.H., and Chiang, B.H., 2012, Process optimization and stability of D-limonene-in-water nanoemulsions prepared by ultrasonic emulsification using response surface methodology, *Ultrason. Sonochem.*, 19 (1), 192–197.

[21] Kentish, S., Wooster, T.J., Ashokkumar, M., Balachandran, S., Mawson, R., and Simons, L., 2008, The use of ultrasonics for nanoemulsion preparation, *Innovative Food Sci. Emerg. Technol.*, 9 (2), 170–175.

[22] El-Nour, K.M.M.A., Eftaiha, A., Al-Warthan, A., and Ammar, R.A.A., 2010, Synthesis and applications of silver nanoparticles, *Arabian J. Chem.*, 3 (3), 135–140.

[23] Chowdhury, S., Yusof, F., Faruck, M.O., and Sulaiman, N., 2016, Process optimization of silver nanoparticle synthesis using response surface methodology, *Procedia Eng.*, 148, 992–999.

[24] Espina, L., Gelaw, T.K., de Lamo-Castellví, S., Pagán, R., and García-Gonzalo, D., 2013, Mechanism of bacterial inactivation by (+)-limonene and its potential use in food preservation combined processes, *PLoS One,* 8 (2), e56769.

[25] Vo, T.T., Dang, C.H., Doan, V.D., Dang, V.S., and Nguyen, T.D., 2019, Biogenic synthesis of silver and gold nanoparticles from *Lactuca indica* leaf extract and their application in catalytic degradation of toxic compounds, *J. Inorg. Organomet. Polym. Mater.*, 1–12.

[26] Ghazali, S., Jaafar, M., and Azizan, A., 2014, Synthesis of silver nanoparticles by chemical reduction method: Effect of reducing agent and surfactant concentration, *IJAME*, 105, 1920–1927.

[27] McClements, D.J., 2017, *Nanoparticle- and Microparticle-based Delivery System: Encapsulation, Protection and Lease of Active Compounds*, 1st Ed., CRC Press, New York.

[28] Bos, M.A., and van Vliet, T., 2001, Interfacial rheological properties of adsorbed protein layers and surfactants: A review, *Adv. Colloid Interface Sci.*, 91 (3), 437–471.

[29] Pichot, R., Spyropoulos, F., and Norton, I.T., 2010, O/W emulsions stabilised by both low molecular weight surfactants and colloidal particles: The effect of surfactant type and concentration, *J. Colloid Interface Sci.*, 352 (1), 128–135.

[30] Costa, I.C., Rodrigues, R.F., Almeida, F.B., Favacho, H.A., Falcão, D.Q., Ferreira, A.M., Vilhena, J.C.E., Florentino, A.C., Carvalho, J.C.T., and Fernandes, C.P., 2014, Development of jojoba oil (*Simmondsia chinensis* (Link) C.K. Schneid.) based nanoemulsions, *Lat. Am. J. Pharm.*, 33 (3), 459–463.

[31] Kale, S.N., and Deore, S.L., 2017, Emulsion micro emulsion and nano emulsion: A review, *Sys. Rev. Pharm.*, 8 (1), 39–47.

[32] Hajipour, M.J., Fromm, K.M., Ashkarran, A.A., de Aberasturi, D.J., de Larramendi, I.R., Rojo, T., Serpooshan, V., Parak, W.J., and Mahmoudi, M., 2012, Antibacterial properties of nanoparticles, *Trends Biotechnol.*, 30 (10), 499–511.

DFT Study, POM Analyses and Molecular Docking of Novel Oxazaphosphinanes: Identification of Antifungal Pharmacophore Site

Khadidja Otmane Rachedi[1], Rania Bahadi[1], Mohamed Aissaoui[1], Taibi Ben Hadda[2,3], Billel Belhani[1], Abdeslem Bouzina[1], and Malika Berredjem[1,*]

[1]*Laboratory of Applied Organic Chemistry LCOA, Synthesis of Biomolecules and MolecularModeling Group, Badji-Mokhtar - Annaba University, Box 12, 23000 Annaba, Algeria*

[2]*Department of Pharmaceutical Chemistry, Faculty of Pharmacy, Umm Al-Qura University, Makkah Almukkarramah, Saudi Arabia*

[3]*Laboratoire de Chimie des Matériaux, FSO, Université Mohammed 1er, Oujda 60000, Morocco*

* ***Corresponding author:***

email:malika.berredjem@univ-annaba.org

Received: May 29, 2019
Accepted: July 21, 2019

DOI: 10.22146/ijc.46375

Abstract: *A computational Petra/Osiris/Molinspiration/DFT(POM/DFT) based model has been developed for the identification of physico-chemical parameters governing the bioactivity of series of oxazaphosphinanes derivatives **1a-1f** containing potential antifungal* O,N*-pharmacophore. A molecular docking study was performed in order to evaluate synthesized compounds, their possible antifungal properties, and their interactions in the binding site. Molecular docking studies revealed that the compounds **1a-1f** have the potential to become lead molecules in the drug discovery process. The six compounds **1a–1f** analyzed here were previously synthesized by our group.*

Keywords: *oxazaphosphinane; DFT; Petra/Osiris/Molinspiration (POM) analyses; molecular docking*

■ INTRODUCTION

The 6-membered P-heterocycles have attracted considerable attention from the scientific community because of their wide biological activities spectrum [1]. Examples cited in the literature include oxazaphosphinanes **1** with antiproliferative properties [2-3], azaphosphinane **2**, which has been shown to be effective as a biodegradable insecticide [4], and antitumoral [5-6] as alkylating agent drugs such as cyclophosphamide and ifosfamide **5**, **6**.

Research teams have described the synthesis of a series of oxazaphosphinane **3**, an analog of hydroxybupropion, which has been evaluated as an antidepressant agent [7]. In the past 20 years, significant effort has been devoted to the synthesis of a particular family of organophosphorus compounds: such as **4** [8] and (±)-2-aryl-3,3,5,5-tetramethyl-[1,4,2]-oxazaphosphinanes **7** [6].

Among methods used of quantum mechanics, density functional theory (DFT) methods that have been widely used in many studies because of the smaller computational resources needed to describe very large systems. Specially, they have been found to be efficient in the description of systems dominated by hydrogen bonding interactions [9].

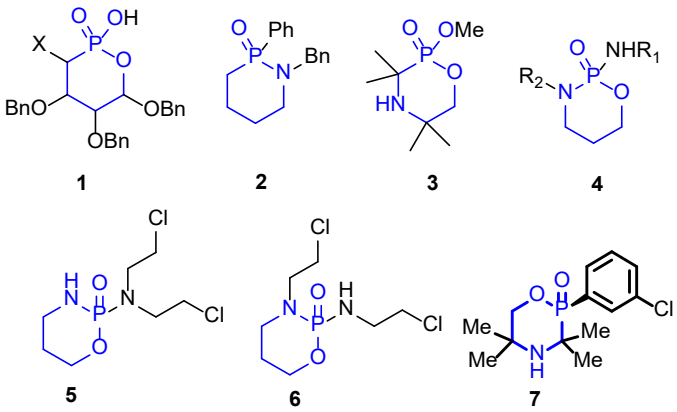

1 **2** **3** **4** **5** **6** **7**

Fig 1. Examples of important bioactive oxazaphosphinanes and their derivatives

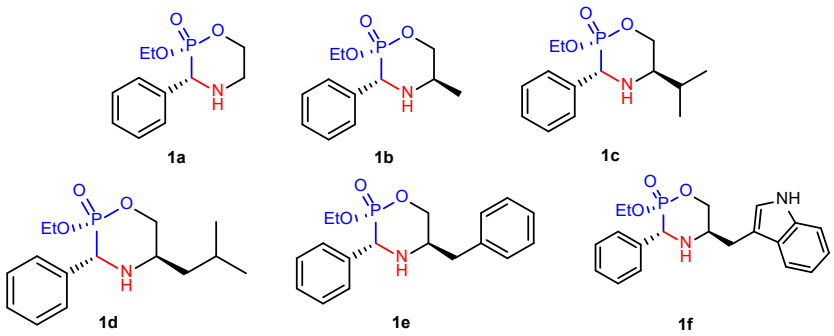

Fig 2. Chemical structure of studied compounds

Recently, DFT has been accepted by the quantum chemistry community as a cost-effective approach for the computation of molecular structure, vibration frequencies, and energies of chemical reactions. Many studies have shown that molecular modeling has had a profound effect on procedure modeling through a better understanding of the fundamental physical and chemical interactions, through forming the basis for predicting physico-chemical properties of molecules that are difficult to calculate using experimental procedures [10].

The most important orbitals in determining chemical reactivity are the highest occupied molecular orbital (HOMO) and the lowest unoccupied molecular orbital (LUMO). The energy difference between the HOMO and LUMO, means the band gap, can sometimes be useful to measure of the molecule excitability, the smaller energy, the more easily it will be excited [11-14]. In the past few years, there have been some theoretical studies of oxazaphosphinane using molecular modeling [15-16].

The aim of our work is the theoretical study of reactivity and to determine energies, dipole moments and vibrational study of six novel oxazaphosphinanes [17] (Fig. 2), using the density functional theory method (DFT). POM (Petra/Osiris/Molinspiration) analyses have been executed with the aim of evaluating the performance of physic-chemical properties of tested compounds. As a result, an antifungal *O,N*-pharmacophore site is identified**.** A docking study was carried out to achieve the interaction on the active site.

■ COMPUTATIONAL METHODS

The studied compounds were optimized with DFT by program package GAUSSIAN 09 using the B3LYP/6-31G(d) method. The B3LYP density functional method is one of the most commonly Hybrid functional used, which stands for Becke, 3 parameters, Lee-Yang-Parr [18]. We employed well established *in silico* tools POM Osiris, Petra, and Molinspiration, validated with about 7000 drug molecules available in databases [19].

The inaugural molecular docking program, DOCK, developed by Kuntz and co-workers, has a long history of new advances and accomplishments in the field of structure-based design. We briefly present methods for preparing the system and performing pose reproduction experiments in the program DOCK. First, the molecular surface of the receptor absent hydrogen atoms and the ligand was determined using the DMS [20] program, then, the DOCK accessory programs sphgen [21] and show box were used to generate spheres and box within the ligand binding site. The DOCK accessory program GRID [22] was used to precompute energy interactions between a dummy probe atom and all receptor atoms on a 0.3 A° resolution grid within the box. Finally, for pose reproduction experiments, the ligands were treated as flexible based on the FLX protocol (standard flexible docking) by Mukherjee et al. [23].

■ RESULTS AND DISCUSSION

DFT Studies

The molecular geometry of oxazaphosphinanes and the nature of their substituents are often correlated with their stability and their reactivity. In order to specify the relationship between the experimental results of the activities with the structure of the molecules and to evaluate this relationship, theoretical studies were carried out by molecular modeling. Thus, modeling

gives some important and necessary information on the structure and reactivity of oxazaphosphinane.

Geometry optimization

The optimization of different structures has been obtained by Gaussian 09 [24] using the B3LYP/6-31G(d) [25-26] method. The optimized geometries were used to calculate the level of energy HOMO, LUMO, and gap. The structures of the six compounds obtained after geometric optimizations in the DMSO solvent are shown in Fig. 3.

The values of hydrophobicity coefficient (log P) thus energetic levels of the (HOMO, LUMO), gap energies, total energy, dipolar moment (μ) and linear polarizability (α_{Tot}) calculated by DFT method using B3LYP/6-31G(d) in the gas phase and DMSO solvent are presented in Table 1.

The compound **1e** has the highest gap energy in both gas phase and DMSO; it is more stable and less active. In the gas phase, **1a** is the more active compound, while in the DMSO solvent, the more active compound is **1f**. The results in Table 1 show that the gap energy (ΔE gap) is inversely proportional to the dipolar moment.

Chemical reactivity

In order to understand the activities of titled compounds, the conceptual density functional theory (DFT) was employed to obtain the chemical reactivity

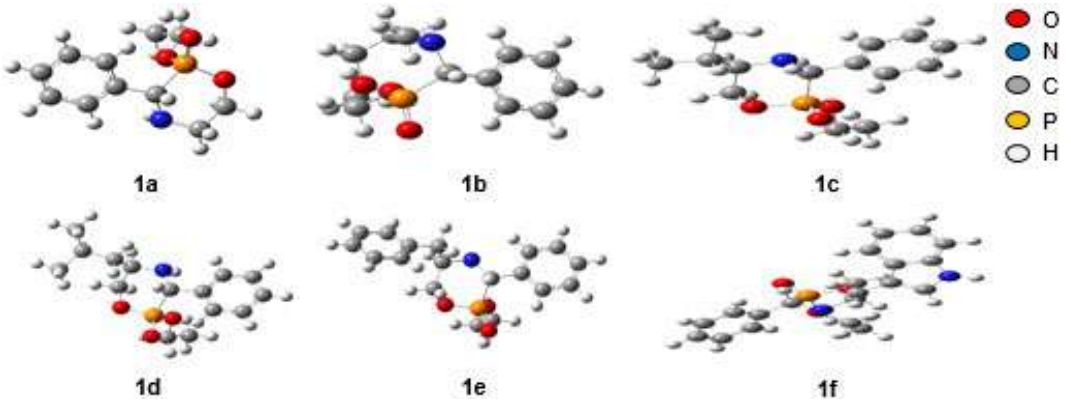

Fig 3. Optimized structures of titled compounds obtained at B3LYP/6-31G(d) level in DMSO

Table 1. The calculated parameters of compounds **1a-1f** obtained by the B3LYP/6-31G(d) method in the gas phase and DMSO solvent

Descriptors	**Gas phase**					
Molecule	**1a**	**1b**	**1c**	**1d**	**1e**	**1f**
Log p	1.87	2.29	3.16	3.84	3.97	3.28
α_{Tot} (Bohr^3)	141.33	151.78	173.78	185.18	211.95	239.34
μ (D)	4.0263	3.9571	3.9546	3.9755	2.7887	6.9136
E_{HOMO} (eV)	-6.41399	-6.42216	-6.40964	-6.40175	-6.54788	-6.23957
E_{LUMO} (eV)	-1.37717	-1.34179	-1.32792	-1.33227	-0.69688	-0.86342
ΔEgap (eV)	5.03683	5.08037	5.08173	5.06948	5.85099	5.37615
E (u.a)	-1050.634	-1089.9483	-1168.573	-1207.884	-1320.994	-1452.557
Descriptors	**DMSO**					
Molecule	**1a**	**1b**	**1c**	**1d**	**1e**	**1f**
α_{Tot} (Bohr^3)	182.41	196.09	224.11	237.84	272.91	313.01
μ (D)	5.8327	5.8691	5.7702	5.8942	4.5032	10.0717
E_{HOMO} (eV)	-6.64230	-6.64067	-6.64012	-6.64203	-6.59033	-6.27278
E_{LUMO} (eV)	-1.59704	-1.57799	-1.57173	-1.57363	-1.30506	-3.10917
ΔEgap (eV)	5.04526	5.06268	5.06839	5.06839	5.28527	3.16360
E (u.a)	-1050.648	-1089.962	-1168.587	-1207.898	-1321.008	-1452.577

descriptors, using the HOMO's and the LUMO's energy level (Fig. 4).

Electronegativity, noted χ, is a chemical property that describes the ability of an atom to attract a shared pair of electrons (or electron density) towards itself [27]. Chemical hardness [28], noted η, is a measure of the resistance to change the electron cloud density of the chemical system, its reciprocal softness, noted S. The electrophilicity index, noted ω, is used to measure the stabilization in energy when the system acquires an additional electronic charge from the environment [29]. These different values are illustrated in Table 2.

Table 2 shows the reactivities of the new molecules. According to this, the compound **1e** has the highest chemical hardness and is more stable. In addition, the most active compound is **1a** in the gas phase and **1f** in

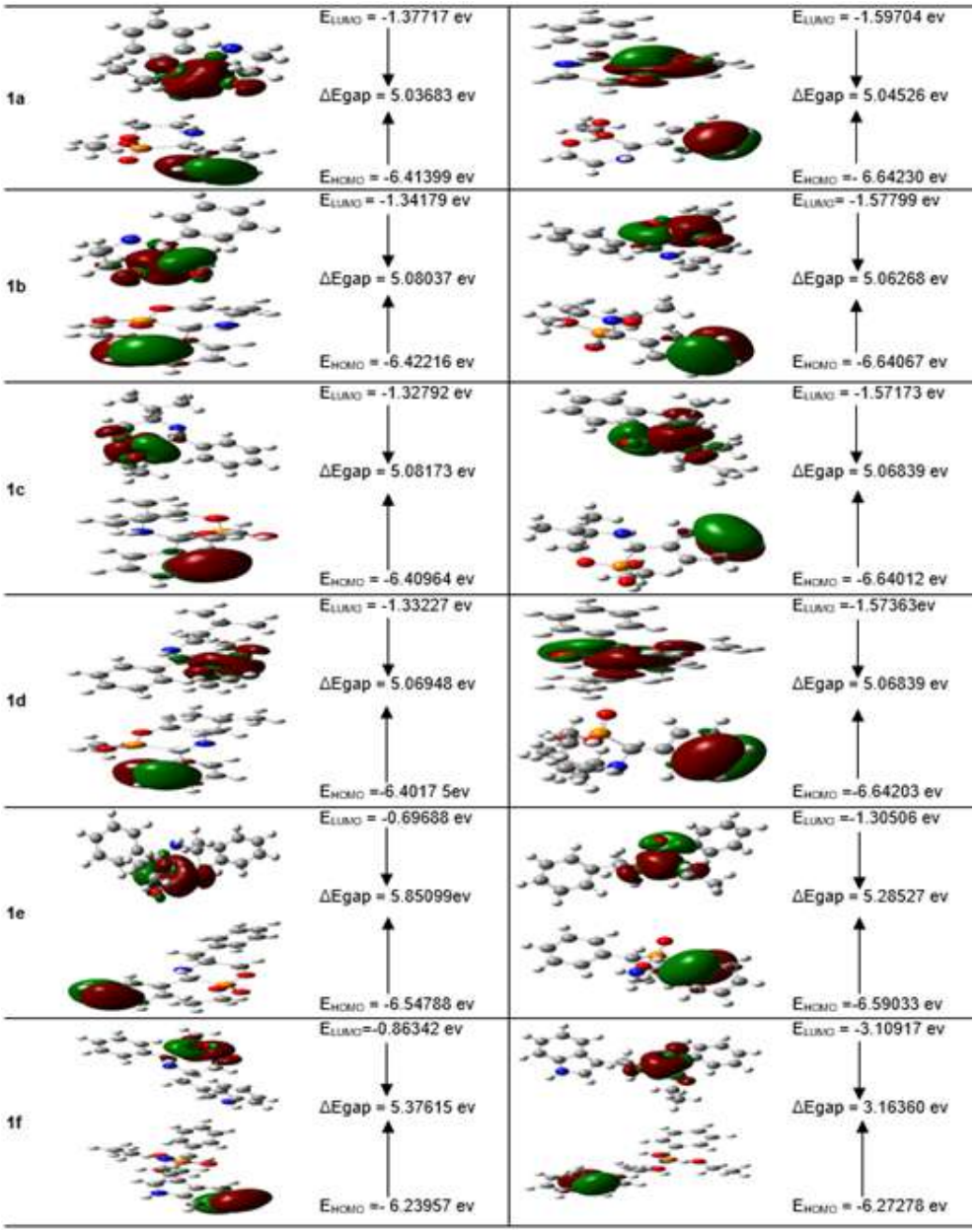

Fig 4. HOMO, LUMO orbitals and their energy gap (ΔEgap) for **1a-1f** obtained at the B3LYP/6-31G(d) level using a contour threshold of 0.02 a.u in the gas phase and DMSO solvent

Table 2. Calculated values of chemical hardness, electronegativity, Electronic chemical potential, and global values electrophilicity index for the compounds studied by B3LYP/6-31G(d)

	Gas phase					DMSO				
	η	s	μ	χ	ω	η	s	μ	χ	ω
1a	2.5198	0.3969	-3.8967	3.8967	3.0123	2.5226	0.3964	-4.1198	4.1198	3.3633
1b	2.5415	0.3935	-3.8831	3.8831	2.9660	2.5306	0.3952	-4.1089	4.1089	3.3361
1c	2.5415	0.3934	-3.8695	3.8695	2.9443	2.5334	0.3947	-4.1062	4.1062	3.3252
1d	2.5361	0.3943	-3.8667	3.8667	2.9497	2.5334	0.3947	-4.1089	4.1089	3.3307
1e	2.9252	0.3419	-3.6218	3.6218	2.2422	2.6422	0.3785	-3.9483	3.9484	2.9497
1f	2.6885	0.3720	-3.5511	3.5511	2.3456	1.5810	0.6325	-4.6912	4.6912	6.9552

DMSO. In the gas phase, the compound **1a** has the highest ω and μ values, so it is the most susceptible molecule to nucleophilic attack.

Molecular electrostatic potential surface

The electrostatic potential maps are the energy of interaction of a positive charge (an electrophile) with the nuclei and electrons of a molecule. Negative electrostatic potentials indicate probable initial sites for the electrophilic attack. Enough small value of the electron density gives overall molecular size and shape. The electrostatic potential can be mapped onto a particular value of the total electron density by using color to represent the value of the potential. The regions of the molecule with negative values of the electrostatic potential are indicated by red color, while color blue indicates positive values of the potential. The green color corresponds to an intermediate potential situated between the two extremes (red and dark blue). The yellow and light blue color split the difference between the medium color (green) and the extremes (red/dark blue).

Based on these considerations, oxygen would be related with the red region of the diagram, and nitrogen would be found with the blue region; the phosphorus, carbon, and hydrogen situated between these two extremes, phosphorus in the yellow region and the green region for carbon and hydrogen (Fig. 5).

The molecular electrostatic potential's representation of title compounds that the oxygen atom (red region) presents the electrophilic attack site with high electron density; furthermore, analysis of the NBO charge in DMSO shows that phosphonyl oxygen atoms have an average charge of -0.871 in all compounds except in **1e** -0.864 and

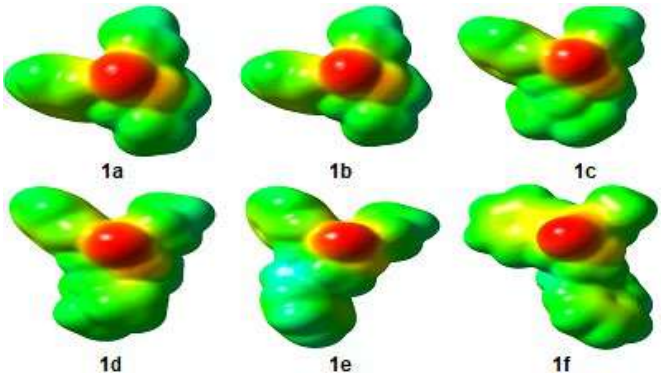

Fig 5. Molecular electrostatic potential MESP for titled compounds on total density (Isovalue = 0.0004 a.u)

-0.869 in **1f**, as well as nitrogen amide, carried a charge of -0.699 in **1a**, -0.704 in **1b**, -0.703 in **1c**, -0.702 in **1d**, -0.702 in **1e** and an average charge of -0.629 in **1f**. On the other hand, MESPs shows one major nucleophilic active centers at the proximity of hydrogens atoms related to nitrogen atom, with a NBO charge of 0.399 in **1a**, 0.401 in **1b**, 0.403 in **1c**, 0.401 in **1d**, 0.409 in **1e** and an average charge of 0.428 in **1f**, and another nucleophilic center in all compounds due to the presence of ethoxy group.

POM Analyses of Compounds (1a-1f)

For a molecule to be a potential drug, besides having a good biological activity, it must have good pharmacokinetic properties in human biological systems. To access the pharmacokinetic profile of the tested compounds, we employed Petra/Osiris/Molinspiration (POM) analyses. The results of theoretical toxicity risks of compounds **1a-1f**, which are calculated with the aid of the Petra/Osiris/Molinspiration (POM) program are shown in Table 3 [30-32]. Our findings reveal that all

synthesized compounds **1a-1f**, are not toxic and can be utilized as therapeutic agents.

Interestingly **1b** deserves pharmacomodulation (DS = 47%). The hydrophilicity character of each compound has been calculated. All of the compounds (**1a-1f**) have accepted cLog*P* values (cLog*P*<*3*). The geometrical conformation of pharmacophore site is taken into consideration (Fig. 6). This is because it is flexible for all compounds (**1a-1f**). The absorption, distribution, characteristics, and bioactivity were proved to be dependent on the geometrical parameter and the aqueous solubility of each compound.

On the other hand, drug-likeness (DL) of (**1a-1f**) is not in the comparable zone with the used standard drug. The compounds (**1a-1f**) showed a high capacity to excellent DS as compared with **Ifosfamide** (Table 3).

Topological polar surface area (TPSA), i.e., surface belonging to polar atoms and molecular weight, is the descriptors that correlate with passive molecular transport through membranes that allow prediction of the route of transport of drugs through the barrier membranes the intestine and blood-brain barrier (BBB). All tested compounds have no violation of Lipinski rules (NV = 0). Prediction results of compounds (**1a-1f)** with molecular properties (GPCRL, ICM and enzyme inhibitors) are recorded in Table 4.

Molecular Docking Study

From the previous results of the POM program, and with the aim of achieving the interaction on the active site, a docking study was carried out. Computer-based molecular docking can facilitate the early stages of drug discovery through systematic prescreening of ligands (i.e., small molecules) for shape and energetic compatibility with a receptor (i.e., protein) prior to experimental evaluation [33-35]. Recently, small chemical ligands have been reported to inhibit cytochrome P450 sterol 14α-demethylase in a wide spectrum of fungal species [36-38]. To understand the mechanism of action and antifungal activity of our synthesized analogues, molecular docking studies were employed using the crystal structure of human cytochrome P450 2E1 that was picked from the Protein Data Bank (CYP2E1; pdb code: 3e4e) (http://www.rcsb.org/pdb). The protein was processed, optimized, and minimized by using the protein preparation wizard of Schrodinger Suite by applying OPLS3 force field [39].

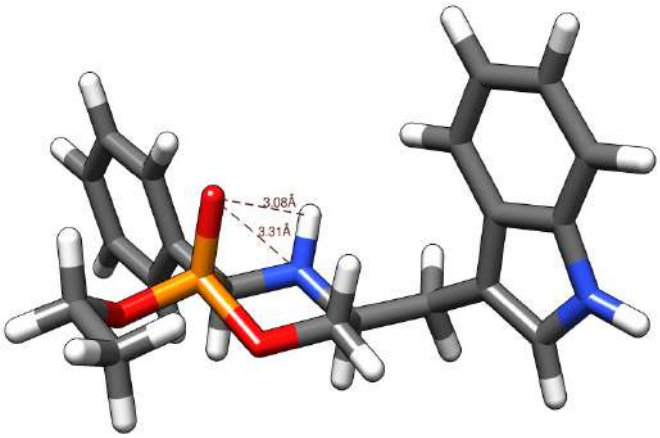

Fig 6. Identification antifungal *O, N*-pharmacophore site of compound **1f**

Table 3. Osiris calculations of toxicity risks of compounds (**1a-1f**)

Compounds	MW	Toxicity Risks[a]				Osiris calculations[b]			
		MUT	TUM	IRRI	REP	cLog*P*	cLog*S*	DL	DS
1a	241					1.01	-1.93	-30.92	0.47
1b	255					1.34	-2.31	-29.71	0.47
1c	283					2.01	-2.74	-31.38	0.45
1d	297					2.46	-3.01	-30.71	0.43
1e	331					2.78	-3.44	-30.32	0.41
1f	370					2.82	-3.98	-29.06	0.38
Ifosfamide(Holoxan®)	260					1.06	-1,89	-10,7	0.1

Highly toxic, Slightly toxic, Not toxic;

[a]MUT: Mutagenic, TUM: Tumorigenic, IRRIT: Irritant, RE: Reproductive effective. [b]Sol: Solubility, DL: Druglikness, DS: Drug-Score

Table 4. Molinspiration calculations of compounds (**1a-1f**)

Compounds	Molinspiration calculations [a]				Drug-likeness [b]					
	TPSA	NONH	NV	VOL	GPCRL	ICM	KI	NRL	PI	EI
1a	48	1	0	216	-0.62	0.39	-0.64	-0.90	0.04	0.26
1b	48	1	0	232	-0.52	0.25	-0.69	-0.86	0.06	0.27
1c	48	1	0	266	-0.34	0.18	0.50	-0.68	0.34	0.32
1d	48	1	0	282	-0.22	0.21	-0.44	-0.43	0.46	0.37
1e	48	1	0	304	-0.04	0.31	-0.19	-0.39	0.45	0.36
1f	63	1	0	333	0.15	0.37	0.04	-0.35	0.45	0.41
Ifosfamide(Holoxan®)	42	1	0	209	-0.71	-0.45	-0.65	-1.02	-0.29	0.55

[a]TPSA: Total molecular polar surface area; NONH: number of OH---N or O---NH interaction, NV: number of violation of five Lipinsky rules; VOL: volume. [b]GPCRL: GPCR ligand; ICM: Ion channel modulator; KI: Kinase inhibitor; NRL: Nuclear receptor ligand; PI: Protease inhibitor; EI: Enzyme inhibitor

In the docking study, the 6 compounds mentioned above were prepared using open babel [40] software and docked into the catalytic site of the human cytochrome P450 (Fig. 7). Docking studies revealed that oxazaphosphinanes derivatives prove interesting stability inside the cavity, with remarkable superimposition (Fig. 8). All compounds were ranked by the total energy of predicted pose in the binding site (Table 5). Otherwise, the 6 derivatives interact with active site residues mainly through hydrogen bonds, as well as hydrophobic interactions.

Compound **1f,** which has the least binding total energy (-41.319 kcal/mol) is most favorable, with the most interesting interaction inside the pocket. Fig. 10 shows that compound **1f** was docked to the pocket of human cytochrome P450. Compound **1f** formed 4 hydrogen bonds with the residues of Cys437 and Thr303, 2 hydrogen bonds as a donor with the nitrogen atom, and 2 others as an acceptor with the oxygen atom. Otherwise, 3 hydrophobics interactions occur with the residues of Phe430, Phe298, and Ile115, which makes it the most stable ligand.

Table 5. Ranking of the six oxazaphosphinanes derivatives after docking study

Compounds	Total energy (kcal/mol)	Docking score
1a	-22.892	-4.728
1b	-28.506	-4.457
1c	-32.58	-5.112
1d	-33.413	-4.271
1e	-38.496	-6.219
1f	-41.319	-9.949
Ref ligand (4PZ)	-37.21	7.123

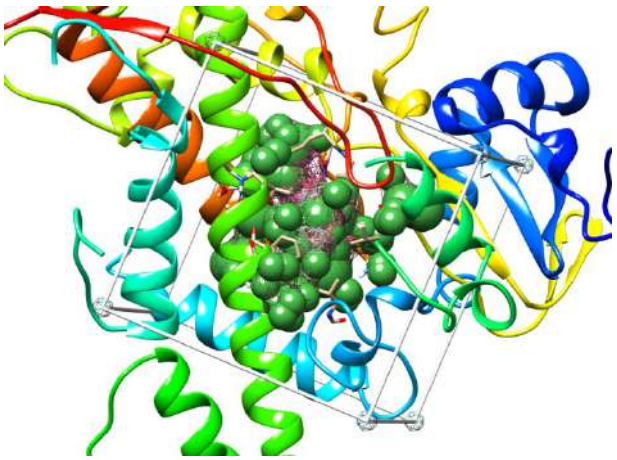

Fig 7. The active site of the human cytochrome P450 (Green spheres)

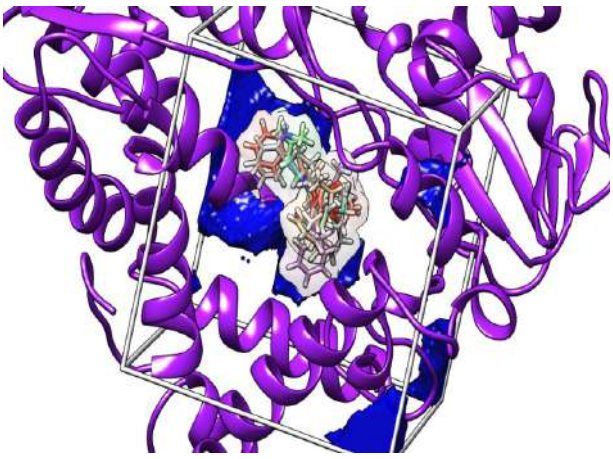

Fig 8. Super imposition of the six oxazaphosphinanes derivatives in the cavity after docking calculation

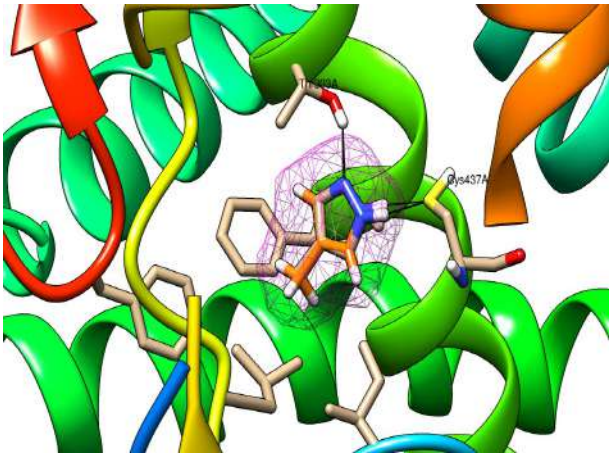

Fig 9. Conserved active site architecture after self-docking for the co-crystallized ligand (4PZ). Hydrogen bonding interactions are shown in black

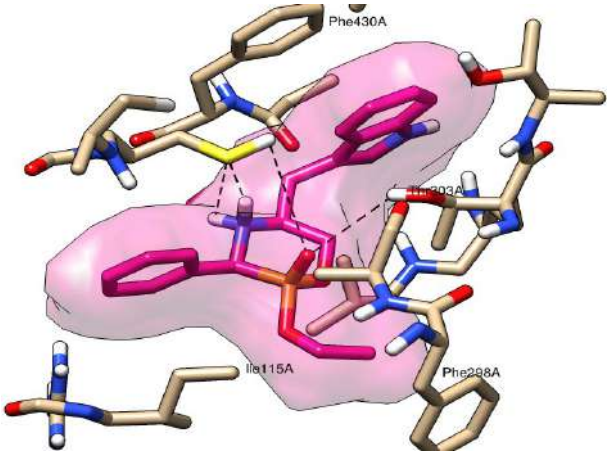

Fig 10. Binding model of compound **1f** in the binding pocket of human cytochrome P450. The amino acid residues and compound **1f** are shown as stick models, H-bonds are shown as black dashed lines

Prior to the docking analysis, a self-docking evaluation of the main cytochrome-inhibitor X-ray complexes has been carried out using the Dock v6.9 program [41]. The use of this program resulted to be the most reliable as it showed the lower average root-mean-square deviation (RMSD) (Fig. 9).

■ CONCLUSION

This work reports the computational analysis of a new series of oxazaphosphinane derivatives. The geometry of all synthesized compounds was optimized with DFT/B3LYP methods using 6-31G(d) basis to determine tasks that coordinate electron density with energy. Our findings reveal that all synthesized compounds, **1a-1f**, are not toxic and can be utilized as therapeutic agents. All oxazaphosphinane derivatives represent an important antifungal *O,N*-pharmacophore site, which needs a separated supplementary antifungal screening. The nature of the pharmacophore site assignment of the oxazaphosphinane compounds was based on their docking and Petra/Osiris/Molinspiration (POM) analyses.

■ ACKNOWLEDGMENTS

The General Directorate for Scientific Research and Technological Development (DG-RSDT), Algerian Ministry of Scientific Research, Applied Organic Laboratory (FNR 2000), financially supported this work.

■ REFERENCES

[1] Masao, C., Kunitomo, A., Yoshihito, T., Kunio, S., Hirofumi, M., Ayumi, T., and Masatoshi, K., 2005, *Phosphinane compounds with immunomodulating activity*, PAT: WO2005014603.

[2] Zhang, H., Tsukuhara, R., Tigyi, G., and Prestwich, G.D., 2006, Synthesis of cyclic phosphonate analogues of (lyso)phosphatidic acid using a ring-closing metathesis reaction, *J. Org. Chem.*, 71 (16), 6061–6066.

[3] Babouri, R., Rolland, M., Sainte-Catherine, O., Kabouche, Z., Lecouvey, M., Bakalara, N., Volle, J.N., Virieux, D., and Pirat, J.L., 2015, α-Halogenated oxaphosphinanes: Synthesis, unexpected reactions, and evaluation as inhibitors of cancer cell proliferation, *Eur. J. Med. Chem.*, 104, 33–41.

[4] Hewitt, D.G., and Newland, G.L., 1977, Organo phosphorus compounds. P-Arylated perhydro-1,2-azaphosphorines, *Aust. J. Chem.*, 30 (3), 579–587.

[5] Shipov, A.E., Genkina, G.K., Petrovskii, P.V., Goryunov, E.I., and Makarov, M.V., 2011, Novel biologically active 1,3,2-oxazaphosphinane derivatives, *Phosphorus Sulfur Silicon Relat. Elem.*, 186 (4), 945–951.

[6] Gilard, V., Martino, R., Malet-Martino, M., Niemeyer, U., and Pohl, J., 1999, Chemical stability

and fate of the cytostatic drug ifosfamide and its *N*-dichloroethylated metabolites in acidic aqueous solutions, *J. Med. Chem.*, 42 (14), 2542–2560.

[7] Volle, J.N., Kaloyanov, N., Saada, M.C., Virieux, D., and Pirat, J.L., 2007, Phosphinyl analogues of hydroxybupropion: (±)-2-aryl-3,3,5,5-tetramethyl-[1,4,2]-oxazaphosphinanes, *Tetrahedron Lett.*, 48 (27), 4695–4697.

[8] Silverman, R.B., 2004, *The Organic Chemistry of Drug Design and Drug Action*, 2nd Ed., Academic Press, Burlington, Massachusetts.

[9] Tarakeshwar, P, Kim, D, Lee, H.M., Suh, S.B., and Kim, K.S., 2004, "Theoretical approaches to the design of functional nanomaterials" in *Computational Materials Science*, Vol. 15, Eds. Leszczynski, J., Elsevier B.V., Amsterdam, Netherlands, 119–170.

[10] Lakshmanan, A., McBrien, A., Zhang, J., and Dhole, V., 2014, Transformation of process engineering – A software perspective, *Comput. Aided Chem. Eng.*, 34, 186–195.

[11] Fleming, I., 2010, *Molecular Orbitals and Organic Chemical Reactions–Reference Edition*, John Wiley & Sons, Chichester, United Kingdom.

[12] Boufas, W., Dupont, N., Berredjem, M., Berrezag, K., Becheker, I., Berredjem, H., and Aouf, N.E., 2014, Synthesis and antibacterial activity of sulfonamides. SAR and DFT studies, *J. Mol. Struct.*, 1074, 180–185.

[13] Cheloufi, H., Bechlem, K., Boufas, W., Barbey, C., Bouzina, A., Belhani, B., Dupont, N., Aouf, N.E., and Berredjem, M., 2017, Synthesis, X-ray crystallographic and DFT studies of two new *N*-acylsulfonamides, *J. Mater. Environ. Sci.*, 8 (3), 997–1003.

[14] Rachedi, K.O., Ouk, T.S., Bahadi, R., Bouzina, A., Djouad, S.E., Bechlem, K., Zerrouki, R., Ben Hadda, T., Almalki, F., and Berredjem, M., 2019, Synthesis, DFT and POM analyses of cytotoxicity activity of α-amidophosphonates derivatives: Identification of potential antiviral *O,O*-pharmacophore site, *J. Mol. Struct.*, 1197, 196–203.

[15] Schuster, I., Koch, A., Heydenreich, M., Kleinpeter, E., Lázár, L., and Fülöp, F., 2008, Synthesis and conformational analysis of phenyl-substituted 1,3,2-oxazaphosphino[4,3-*a*]- and 1,2,3-oxathiazino[4,3-*a*]isoquinolines, *J. Mol. Struct.*, 888 (1-3), 124–137.

[16] Cristau, H.J., Pirat, J.L., Virieux, D., Monbrun, J., Ciptadi, C., and Bekro, Y.A., 2005, Synthesis, reactivity and stereochemistry of new phosphorus heterocycles with 5- or 6-membered rings, *J. Organomet. Chem.*, 690 (10), 2472–2481.

[17] Belhani, B., Bouzina, A., Berredjem, M., and Aouf, N.E., 2015, One-pot synthesis of novel oxazaphosphinanes under ultrasound irradiation and solvent-free conditions, *Monatsh. Chem.*, 146 (11), 1871–1875.

[18] Lee, C., Yang, W., and Parr, R.G., 1988, Development of the Colle-Salvetti correlation-energy formula into a functional of the electron density, *Phys. Rev. B: Condens. Matter*, 37 (2), 785–789.

[19] *Organic Chemistry Portal*, 2012, http://www.organic-chemistry.org/prog/peo/, accessed on 15 January 2016.

[20] Lourenço, A.L.P.G., Vegi, P.F., Faria, J.V., Pinto, G.S.P., dos Santos, M.S., Sathler, P.C., Saito, M.S., Santana, M., Dutra, T.P.P., Rodrigues, C.R., Monteiro, R.Q., Bernardino, A.M.R., and Castro, H.C., 2019, Pyrazolyl-tetrazoles and imidazolyl-pyrazoles as potential anticoagulants and their integrated multiplex analysis virtual screening, *J. Braz. Chem. Soc.*, 30 (1), 33–47.

[21] DesJarlais, R.L., Sheridan, R.P., Seibel, G.L., Dixon, J.S., Kuntz, I.D., and Venkataraghavan, R., 1988, Using shape complementarity as an initial screen in designing ligands for a receptor binding site of known three-dimensional structure, *J. Med. Chem.*, 31 (4), 722–729.

[22] Kuntz, I.D., 1992, Structure-based strategies for drug design and discovery, *Science*, 257 (5073), 1078–1082.

[23] Mukherjee, S., Balius, T.E., and Rizzo, R.C., 2010, Docking validation resources: Protein family and ligand flexibility experiments, *J. Chem. Inf. Model.*, 50 (11), 1986–2000.

[24] Frisch, M.J., Trucks, G.W., Schlegel, H.B., Scuseria, G.E., Robb, M.A., Cheeseman, J.R., Scalmani, G.,

Barone, V., Petersson, G.A., Nakatsuji, H., Li, X., Caricato, M., Marenich, A., Bloino, J., Janesko, B.G., Gomperts, R., Mennucci, B., Hratchian, H.P., Ortiz, J.V., Izmaylov, A.F., Sonnenberg, J.L., Williams-Young, D., Ding, F., Lipparini, F., Egidi, F., Goings, J., Peng, B., Petrone, A., Henderson, T., Ranasinghe, D., Zakrzewski, V.G., Gao, J., Rega, N., Zheng, G., Liang, W., Hada, M., Ehara, M., Toyota, K., Fukuda, R., Hasegawa, J., Ishida, M., Nakajima, T., Honda, Y., Kitao, O., Nakai, H., Vreven, T., Throssell, K., Montgomery, J.A., Jr., Peralta, J.E., Ogliaro, F., Bearpark, M., Heyd, J.J., Brothers, E., Kudin, K.N., Staroverov, V.N., Keith, T., Kobayashi, R., Normand, J., Raghavachari, K., Rendell, A., Burant, J.C., Iyengar, S.S., Tomasi, J., Cossi, M., Millam, J.M., Klene, M., Adamo, C., Cammi, R., Ochterski, J.W., Martin, R.L., Morokuma, K., Farkas, O., Foresman, J.B., and Fox, D.J., 2016, *Gaussian 09, Revision A.02*, Gaussian 09 Inc., Wallingford CT.

[25] Becke. A.D., 1993, Density-functional thermo chemistry. III. The role of exact exchange, *J. Chem. Phys*., 98 (7), 5648–5652.

[26] Francl, M.M., Pietro, W.J., Hehre, W.J., Binkley, J.S., Gordon, M.S., DeFrees, D.J., and Pople, J.A., 1982, Self-consistent molecular orbital methods. XXIII. A polarization-type basis set for second-row elements, *J. Chem. Phys*., 77 (7), 3654–3665.

[27] Pauling, L., 1932, The nature of the chemical bond. IV. The energy of single bonds and the relative electronegativity of atoms, *J. Am. Chem. Soc.*, 54 (9), 3570–3582.

[28] Pearson, R.G., 2005, Chemical hardness and density functional theory, *J. Chem. Sci*., 117 (5), 369–377.

[29] Parr, R.G., Szentpály, L.V., and Liu, S., 1999, Electrophilicity index, *J. Am. Chem. Soc.*, 121 (9), 1922–1924.

[30] Mabkhot, Y.N., Alatibi, F., El-Sayed, N., Al-Showiman, S., Kheder, N.A., Wadood, A., Rauf, A., Bawazeer, S., and Ben Hadda, T.B., 2016, Antimicrobial activity of some novel armed thiophene derivatives and petra/osiris/molinspiration (POM) analyses, *Molecules*, 21 (2), 222–238.

[31] Mabkhot, Y.N., Arfan, M., Zgou, H., Genc, Z.K., Genc, M., Rauf, A., Bawazeer, S., and Hadda, T.B., 2016, How to improve antifungal bioactivity: POM and DFT study of some chiral amides derivatives of diacetyl-L-tartaric acid and amines, *Res. Chem. Intermed*., 42 (12), 8055–8068.

[32] Sajid, Z., Ahmad, M., Aslam, S., Ashfaq, U.A., Zahoor, A.F., Saddique, F.A., Parvez, M., Hameed, A., Sultan, S., Zgou, H., and Hadda, T.B., 2016, Novel armed pyrazolobenzothiazine derivatives: Synthesis, X-ray crystal structure and POM analyses of biological activity against drug resistant clinical isolate of *Staphylococcus aureus*, *Pharm. Chem. J*., 50 (3), 172–180.

[33] Ooms, F., 2000, Molecular modeling and computer aided drug design. Examples of their applications in medicinal chemistry, *Curr. Med. Chem*., 7 (2), 141–158.

[34] Shoichet, B.K., 2004, Virtual screening of chemical libraries, *Nature*, 432 (7019), 862–865.

[35] Jorgensen, W.L., 2004, The many roles of computation in drug discovery, *Science*, 303 (5665), 1813–1818.

[36] Aouad, M.R., Mayaba, M.M., Naqvi, A., Bardaweel, S.K., Al-Blewi, F.F., Messali, M., and Rezki, N., 2017, Design, synthesis, in silico and in vitro antimicrobial screenings of novel 1,2,4-triazoles carrying 1,2,3-triazole scaffold with lipophilic side chain tether, *Chem. Cent. J*., 11 (1), 117.

[37] Hashemi, S.M., Badali, H., Faramarzi, M.A., Samadi, N., Afsarian, M.H., Irannejad, H., and Emami, S., 2015, Novel triazole alcohol antifungals derived from fluconazole: Design, synthesis, and biological activity, *Mol. Diversity*, 19 (1), 15–27.

[38] Wu, J., Ni, T., Chai, X., Wang, T., Wang, H., Chen, J., Jin, Y., Zhang, D., Yu, S., and Jiang, Y., 2018, Molecular docking, design, synthesis and antifungal activity study of novel triazole derivatives, *Eur. J. Med. Chem.*, 143, 1840–1846.

[39] Sastry, G.M., Adzhigirey, M., Day, T., Annabhimoju, R., and Sherman, W., 2013, Protein and ligand preparation: Parameters, protocols, and influence on virtual screening enrichments, *J. Comput.-Aided Mol. Des.*, 27 (3), 221–234.

[40] O'Boyle, N.M., Banck, M., James, C.A., Morley, C., Vandermeersch, T., and Hutchison, G.R., 2011, Open Babel: An open chemical toolbox, *J. Cheminf.*, 3, 33.

[41] Kuntz, I.D., Blaney, J.M., Oatley, S.J., Langridge, R., and Ferrin, T.E., 1982, A geometric approach to macromolecule-ligand interactions, *J. Mol. Biol.*, 161 (2), 269–288.

Manganese(III) Complexes with Tetradentate Schiff Base Ligands: IR, UV/Vis, Electrochemistry and Fluorescence Properties

Naser Eltaher Eltayeb

Department of Chemistry, Rabigh College of Science and Arts, King Abdulaziz University, P.O. Box 344, Jeddah, Saudi Arabia

* ***Corresponding author:***

email: netaha@kau.edu.sa; nasertaha90@hotmail.com

Received: May 30, 2019
Accepted: July 30, 2019

DOI: 10.22146/ijc.46395

Abstract: *Three trivalent manganese complexes have been synthesized, isolated, and characterized, namely, [MnCl(OH$_2$)(Lx)].nH$_2$O (**I-III**). Lx is a tetradentate Shiff base ligand, where Lx = **LI**, 2,2'-{1,2-phenylenebis [nitrilomethylylidene]}bis(phenolate), **LII**, 2,2'-{1,2-phenylenebis[nitrilomethylylidene]}bis(5-methoxyphenolate), and **LIII**, 2,2'-{1,2-phenylenebis[nitrilomethylylidene]}bis(4-methoxyphenolate), n = 1, 1.5 and 0 for **I**, **II** and **III**, respectively. These complexes were characterized using IR, elemental analysis and UV-Vis spectroscopy. In addition, the fluorescence, photoluminescence (PL), electrochemistry and thermal stability of these complexes were studied.*

Keywords: *manganese; Schiff base; electrochemistry; photoluminescence*

■ INTRODUCTION

Schiff base ligands attracted the attention of researchers for many decades because of their unique properties and their ease of synthesis and tailoring [1-5]. The coordination of Schiff base ligands with transition metals results in complexes with better properties in term of solubility, biological and catalytic activity [1-7]. Thus, organic-metal chelate complexes, in particular, have attracted a lot of attention. Manganese-Schiff base complexes are actively used as catalysts due to their ability to epoxidize unfunctionalized alkenes with high stereoselectivity [8]. The structural characterization of the manganese-Schiff base complexes used to improve enantioselectivity has been reported [9-10]. The Mn-Schiff base compounds exhibit the subtle changes to its property due to the nature of the axial ligands. Therefore, solvents used for crystallization give a significant impact to the crystal structure of the complex [11-12]. Organic-metal complexes of salicylaldehyde Schiff base ligands are expected to show good luminescent properties because its hydroxyl group and a coordinating nitrogen atom and a delocalized π-system [13-14].

In this paper, three ligands formed from the reaction of salicylaldehyde and its alkoxy substituents with *o*-phenylenediamine namely **LI**, 2,2'-{1,2-phenylenebis[nitrilomethylylidene]}bis(phenolate), **LII**, 2,2'-{1,2-phenylenebis[nitrilomethylylidene]}bis(6-methoxyphenolate), **LIII**, 2,2'-{1,2-phenylenebis[nitrilomethylylidene]}bis(5-methoxyphenolate), and their respective complexes with Mn(III) ion as well as their electrochemical and photoluminescent properties are presented.

■ EXPERIMENTAL SECTION

Materials

All the chemicals and solvents used for the synthesis were reagent grade. Manganese chloride tetrahydrate, [MnCl$_2$·4H$_2$O] (Acros), Salicylaldehyde (Acros), *o*-phenylenediamine (Merck), Triethylamine (Merck), 4-methoxysalicylaldehyde (Acros), and 5-methoxysalicylaldehyde (Acros) were used as received.

Procedure

Physical measurements

Microanalyses (CHN) were performed on a Perkin-Elmer 2400II elemental analyzer. Electronic spectra were obtained using a JASCO V-500 spectrophotometer for UV/VIS in solution and Perkin-Elmer lambda 35 for solid state. FT-IR spectra were recorded on Perkin-Elmer 2000 FT-IR with samples were prepared as KBr pellets. Electrochemical experiments were carried out using an Epsilon potentiostat with three-electrode configuration consisting of a platinum working electrode, a Pt wire as

auxiliary electrode and Ag/AgCl as the reference electrode and 0.1 mol dm^{-3} tetrabutylammonium tetrafluoroborate as supporting electrolyte in DMF solution under dry nitrogen atmosphere with a scan rate of 0.1 V s^{-1}. Data were collected using Epsilon EC-V160 software supplied by Bioanalytical. Fluorescence spectra were obtained using JASCO spectrofluorometer FP-750. Photoluminescence (PL) spectra were executed at room temperature by using Jobin Yvon HR800UV system. Thermal investigations (TGA/DGA) were carried out on a Perkin Elmer thermogravimetric analyzer TGA7 under nitrogen environment on heating rate 10 °C min^{-1}.

Synthesis

General method: using our previous method [15-16], the complexes **I**-**III** were prepared by refluxing a mixture of the corresponding aldehyde (4 mmol) [**I**, salicylaldehyde; **II**, 4-methoxysalicylaldehyde and **III**, 5-methoxysalicylaldehyde], and *o*-phenylenediamine (2 mmol), in ethanol (20 mL) in a 50 mL round-bottom flask equipped with a magnetic stir bar and a water-cooled reflux condenser for 30 min. Then $MnCl_2{\cdot}4H_2O$ (2 mmol) in 10 of mL ethanol was added, followed by the addition of 0.5 mL triethylamine. The mixture was stirred for three hours at room temperature. The brown precipitate obtained by filtration was washed with ethanol about 5 mL, then washed by copious amount of diethyl ether, and dried at room temperature. The general scheme of chemical equations is illustrated in Fig. 1.

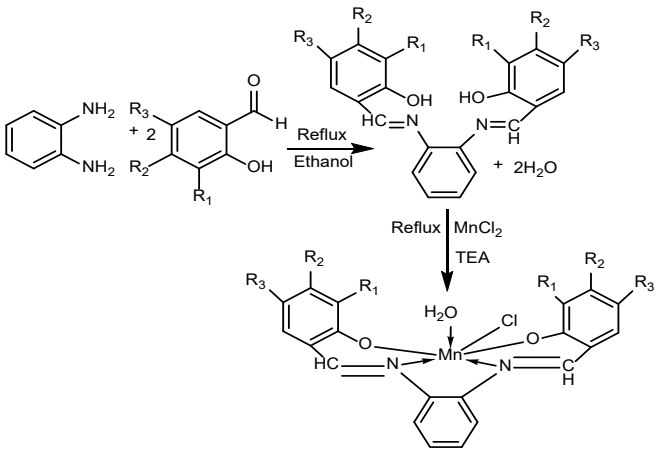

Fig 1. General scheme of synthesis of complexes **I**, **II** and **III**

Synthesis of aquachloro-2,2'-{1,2-phenylenebis[nitrilomethylylidene]}bis(phenolate)manganese(III)] H_2O, I. The complex was prepared by the general method, using salicylaldehyde, (yield: 0.519 g, 58.87%, m.p. > 300 °C). IR spectroscopy (KBr, cm^{-1}): ν(O-H) H_2O 3413, ν(C-H) aromatic 3016 , ν(C=N) 1604, ν(C=C) 1578, 1537, 1494. UV/Vis spectroscopy (in acetonitrile, λ_{max} nm, ε (dm^3 mol^{-1} cm^{-1})): 246 (41.9 × 10^3), 336 (27.6 × 10^3), 434 (10.2 × 10^3). UV/Vis spectroscopy (solid, λ_{max} nm): 214, 245, 327. Anal. Calc. For $C_{20}H_{16}ClMnN_2O_3{\cdot}H_2O$: C, 54.50; H, 4.12; N, 6.36, Mn, 12.46%. Found: C, 54.27; H, 3.65; N, 6.53; Mn, 12.94%.

Synthesis of aquachloro-2,2'-{1,2-phenylenebis [nitrilomethylylidene]}bis(5-methoxyphenolate) manganese(III)]·1.5H_2O, II. The complex was prepared by the general method, using 4-methoxysalicylaldehyde, (yield: 0.773 g, 75.81%, m.p. > 300 °C). IR spectroscopy (KBr, cm^{-1}): ν(O-H) H_2O 3411, ν(C-H) aromatic 3007, ν(C-H) CH_3 2938, 2837, ν(C=N) 1619, ν(C=C) 1598, 1573, 1522. UV/Vis spectroscopy (in acetonitrile, λ_{max} nm, ε (dm^3 mol^{-1} cm^{-1})): 254 (30.58 × 10^3), 347 (28.43 × 10^3), 436 (14.70 × 10^3). UV/Vis spectroscopy (solid, λ_{max} nm):238, 252, 318, 361, 401. Anal. Calc. For $C_{22}H_{20}ClMnN_2O_5{\cdot}1.5H_2O$: C, 51.83; H, 3.53; N, 5.49, Mn, 10.78%. Found: C, 52.04; H, 3.64; N, 5.46; Mn, 11.11%.

Synthesis of aquachloro-2,2'-{1,2-phenylenebis [nitrilomethylylidene]}bis(4-methoxyphenol)manganese(III)], III. The complex was prepared by the general method, using 5-methoxysalicylaldehyde (yield: 0.517 g, 53.54%, m.p. > 300 °C). IR spectroscopy (KBr, cm^{-1}): ν(O-H) H_2O 3475, 3412, ν(C-H) aromatic 3023, ν(C-H) CH_3 2939, 2833, ν(C=N) 1618, ν(C=C) 1601, 1580, 1534. UV/Vis spectroscopy (in acetonitrile, λ_{max} nm, ε (dm^3 mol^{-1} cm^{-1})): 249 (39.91 × 10^3), 299 (22.26 × 10^3), 335 (23.10 × 10^3), 460 (8.82 × 10^3). UV/Vis spectroscopy (solid, λ_{max} nm): 236, 253, 311, 359, 402, 480. Anal. Calc. For $C_{22}H_{20}ClMnN_2O_5$: C, 54.73; H, 4.18; N, 5.80, Mn, 11.38%. Found: C, 54.75; H, 3.63; N, 5.76; Mn, 10.91%.

■ RESULTS AND DISCUSSION

Infrared Spectrum

All the complexes show a broad band between 3424–3411 cm^{-1} in their infrared spectra, attributed to

O-H stretching of coordinate/lattice water. Aromatic C-H band appears between 3058–3007 cm^{-1}, C=N band appears between 1640–1604 cm^{-1} [17], and for all complexes, the C=N band was shifted to higher wavenumbers than in free ligands, except **I** which may be due to the alkoxy substituent effect. Aromatic C=C bands appear at their normal position between 1601–1494 cm^{-1}, as shown in Fig. 2.

Electronic Spectrum

The electronic spectra of Mn(III) complexes in acetonitrile have mostly similar features, consisting of an intense band at 204–250 nm (49019.6–40000.0 cm^{-1}), bands of moderate-intensity at ca. 300–360 nm (33333.3–27777.8 cm^{-1}) and one band or shoulder at 430–460 nm (23255.8–21739.1 cm^{-1}) (Fig. 2). The first two bands can be assigned as π to π^* azomethane intraligand transition, while the third one can be assigned to phenolate O (pπ) to Mn ($d\pi^*$) ligand to metal charge transfer [18]. No d-d bands observed due to the presence of strong tail of the charge transfer band at lower energy. Electronic spectra of all the Mn(III) complexes in solid state show similar spectra to those obtained in acetonitrile except that the shoulder appearing in the region of 525–644 nm (19047.62–15528.0 cm^{-1}), is either reduced or shifted to lower wavelength in acetonitrile (Fig. 3).

Electrochemical Properties

The electrochemical properties of **I**-**III** investigated by cyclic voltammetry (CV) in DMF solution, containing 0.1 M tetrabutylammonium tetrafluoroborate as supporting electrolyte, using an Ag/AgCl reference electrode under a dry nitrogen atmosphere with a scan

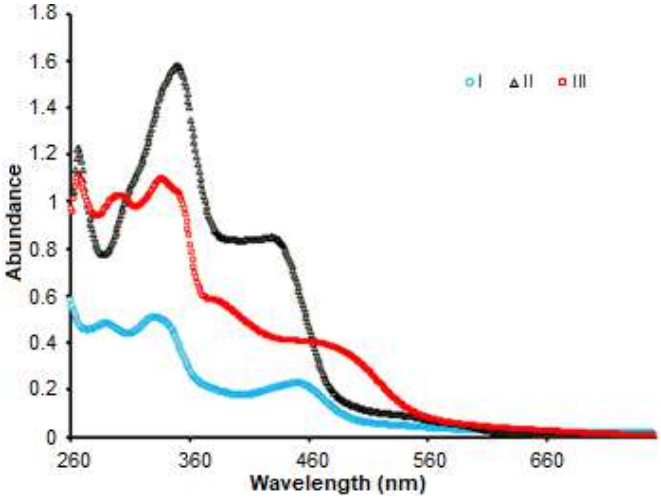

Fig 3. Electronic spectra of **I**, **II** and **III** (in acetonitrile, 1.0×10^{-6} M)

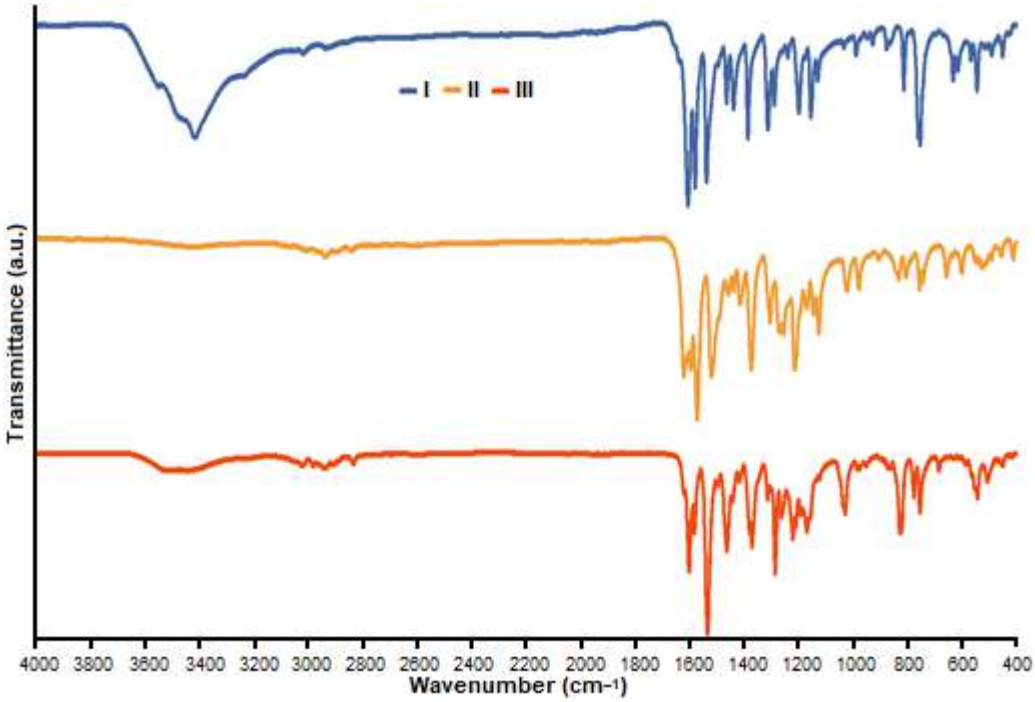

Fig 2. IR spectra of complexes **I**, **II** and **III**

rate of 0.1 V s^{-1}. Compounds **I-III** exhibit quasi-reversible reduction-oxidation wave, all the reduction peaks are observed at negative potentials (**I** -0.217, **II** -0.353 and **III** -0.325,), and all the oxidation peaks are observed at positive potential (**I** 0.061, **II** 0.096 and **III** 0.066) (Fig. 4 and Table 1). The quasi-reversible reduction-oxidation due to Mn^{3+}/Mn^{2+} couple has been observed for previously reported complexes with similar ligand environment [18-20].

Fluorescence Properties

The fluorescence and photoluminescence spectra of compounds **I-III**, and their ligands **LI-LIII** are characterized by broad bands, in the region between 400–600 nm, typical of the intramolecular charge-transfer bands [21]. The photophysical data of the present systems in DMF are listed in Table 2 and showed in Fig. 5. The general feature, the blue shift in the range (18–65 nm) is observed in the fluorescence spectra in DMF compared with the photoluminescence spectra in the solid state, attributable to the DMF dielectric constant [22]. The other feature observed is the blue shift in the range 13–20 nm in compounds **I**, and **II**, in the fluorescence spectra, compare with their ligands. This blue shift may

Table 1. The electrochemical properties of **I-III** were investigated by cyclic voltammetry in acetonitrile

Compound	E_{red} (V)	E_{ox} (V)	$E_{1/2}$ (V)	$\Delta E_{ox\text{-}red}$
I	-0.217	0.061	-0.078	0.278
II	-0.353	0.096	-0.128	0.449
III	-0.325	0.066	-0.129	0.391

Note: $E_{1/2}= (E_{ox}+ E_{red})/2$

$\Delta E_{ox\text{-}red}= E_{pa}-E_{pc}$, V, where Epa and Epc are anodic and cathodic peak potentials, respectively

Table 2. The fluorescence and photoluminescence (PL) of compounds **I-III** and their respective ligands **LI-LIII**

Compound	λ_{max} excitation	λ_{max} fluorescence	λ_{max} PL*
I	330	480	529
LI	396	500	534
II	330	472	537
LII	383	485	537
III	346	518	528
LIII	342	520	553

Note: * all photoluminescence was obtained by excitation at 325 nm

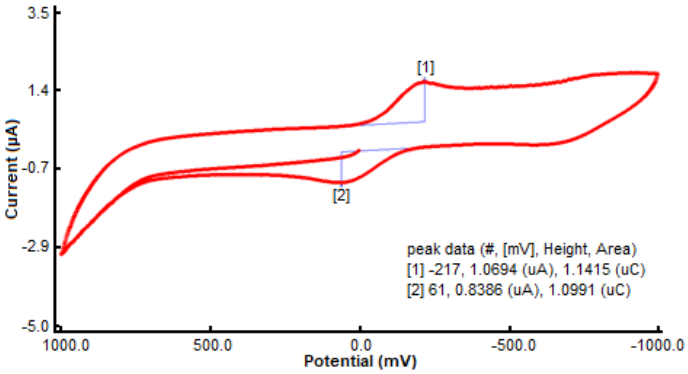

Fig 4. Cyclic voltammetry of compound **I**, in DMF with 0.1 mol dm^{-1} tetrabutylammonium tetrafluoroborate as supporting electrolyte (working electrode, platinum; reference electrode, Ag/AgCl; Scan rate 100 mV s^{-1})

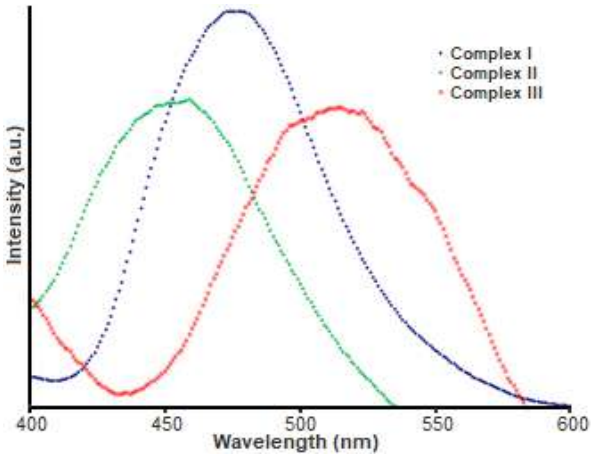

Fig 5. Fluorescence emission spectra of manganese complexes in solution

be due to the effect of the coordination of Mn(III) with the ligands. This shift was not observed in the rest of the complexes because of high emission intensity of their ligands and its broaden band.

Thermogravimetric Analysis

The thermogravimetric analyses (TGA) of compounds **I**-**III** were performed in the temperature range of 30–900 °C and under N_2 atmosphere. All the complexes exhibited remarkable thermal stability and had an onset temperature for decomposition at about 260 °C, after release of solvated and coordinated water. The results indicate that these complexes are thermally stable, and the details can be seen in Fig. 6.

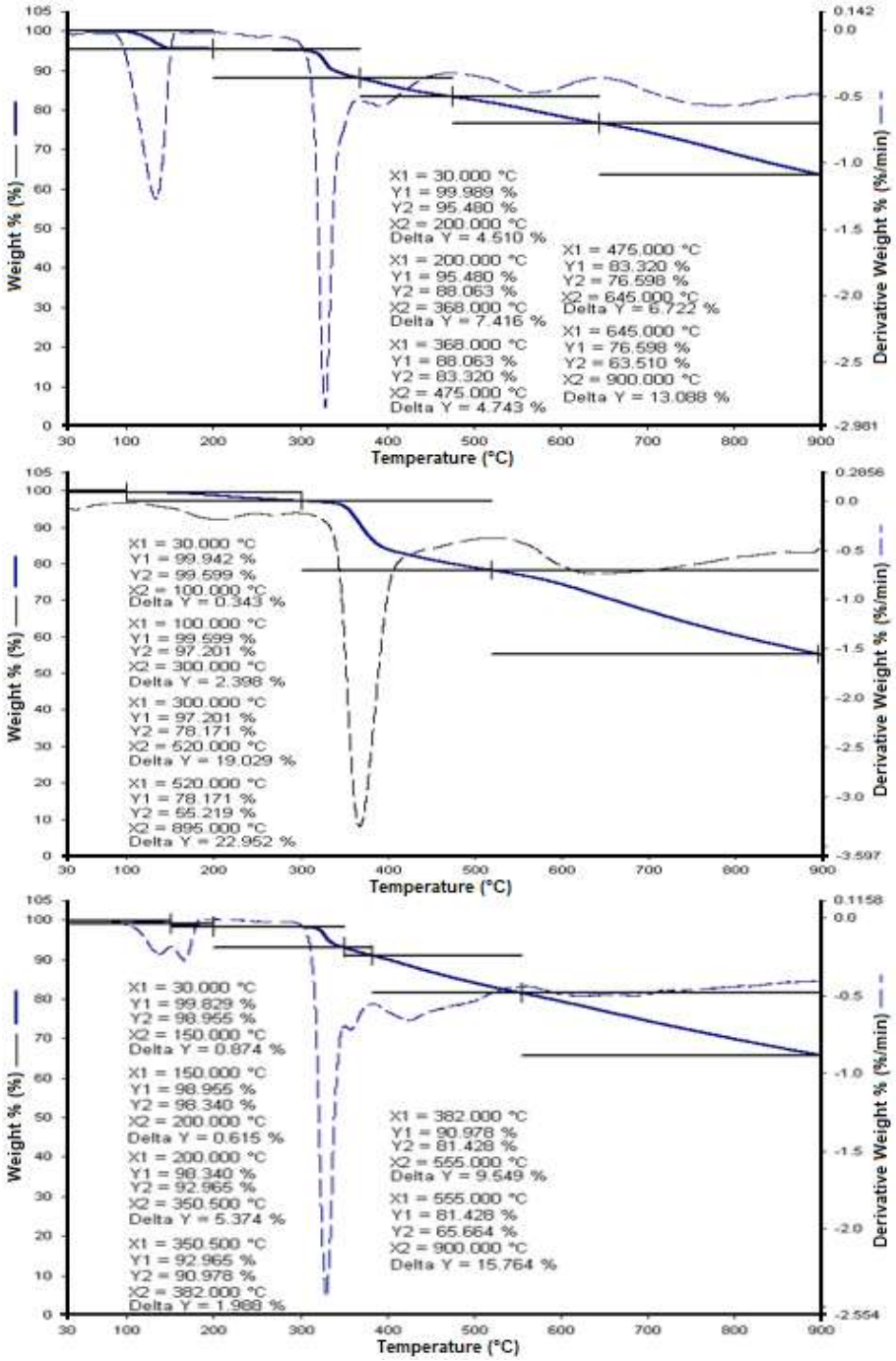

Fig 6. Thermogram of complexes **I**-**III** under nitrogen environment on heating rate 10 °C/min

■ CONCLUSION

In this paper, three tetradentate Schiff base ligands and their Mn(III) complexes, namely, **I, II** and **III**, were successfully prepared through the coordination of Mn(III) to NONO in the ligand center. These complexes have been isolated and characterized using infrared spectroscopy (IR), elemental analysis (CHN), atomic absorption spectroscopy (AAS), and UV-Vis spectroscopy. In addition, the fluorescence, photoluminescence (PL), electrochemistry and thermal stability of these complexes were studied. The results showed that these complexes display fluorescence emission, reversible redox properties, and good thermal stability. From these studies, it can be concluded that the substitution position of the methoxy group affects the properties of these complexes and can be used to tune the optical properties of these complexes.

■ REFERENCES

[1] Zhang, J., Xu, L., and Wong, W.Y., 2018, Energy materials based on metal Schiff base complexes, *Coord. Chem. Rev.*, 355, 180–198.

[2] Kaczmarek, M.T., Zabiszak, M., Nowak, M., and Jastrzab, R., 2018, Lanthanides: Schiff base complexes, applications in cancer diagnosis, therapy, and antibacterial activity, *Coord. Chem. Rev.*, 370, 42–54.

[3] Das, P., and Linert, W., 2018, Schiff base-derived homogeneous and heterogeneous palladium catalysts for the Suzuki–Miyaura reaction, *Coord. Chem. Rev.*, 311, 1–23.

[4] Rezaeivala, M., and Keypour, H., 2014, Schiff base and non-Schiff base macrocyclic ligands and complexes incorporating the pyridine moiety – The first 50 years, *Coord. Chem. Rev.*, 280, 203–253.

[5] Gupta, K.C., and Sutar, A.K., 2008, Catalytic activities of Schiff base transition metal complexes, *Coor. Chem. Rev.*, 252 (12-14), 1420–1450.

[6] Eltayeb, N.E., Teoh, S.G., Kusrini, E., Adnan, R., and Fun H.K., 2010, The manganese(III) complex with chelating Schiff base ligand: X-ray structure, spectroscopic and computational studies, *Spectrochim. Acta, Part A*, 75 (1), 453–457.

[7] Paul, L., Banerjee, B., Bhaumik, A., and Ali, M., 2017, Catecholase activity of a manganese Schiff base complex functionalized over SBA-15 in aqueous heterogeneous medium, *Microporous Mesoporous Mater.*, 249, 78–87.

[8] Lane, B.S., and Burgess, K., 2003, Metal-catalyzed epoxidations of alkenes with hydrogen peroxide, *Chem. Rev.*, 103 (7), 2457–2474.

[9] Linker, T., 1997, The Jacobsen–Katsuki epoxidation and its controversial mechanism, *Angew. Chem. Int. Ed.*, 36 (19), 2060–2062.

[10] Korendovych, I.V., and Rybak-Akimova, E.V., 2004, Chloro{2,2′-[(1*S*,2*S*)-1,2-diphenyl-1,2-ethanediylbis(nitrilomethylidyne)]diphenolato-κ^4*O*,*N*,*N*′,*O*′}(ethanol-κ*O*)manganese(III), *Acta Crystallogr., Sect. C: Cryst. Struct. Commun.*, 60 (2), m82–m84.

[11] Horwitz, C.P., Dailey, G.C., and Tham, F.S., 1995, Aquachloro[bis(5-chlorosalicylidene)ethylenediaminato]manganese(III), *Acta Crystallogr., Sect. C: Cryst. Struct. Commun.*, 51 (5), 815–817.

[12] Martínez, D., Motevalli M., and Watkinson, M., 2002, Aquachloro[*N*,*N*′-ethylenebis(salicylideneiminato)]manganese(III), *Acta Crystallogr., Sect. C: Cryst. Struct. Commun.*, 58 (4), m258–m260.

[13] Shen, Y.Z., Gu, H., Pan, Y., Dong, G., Wu, T., Jin, X.P., Huang, X.Y., and Hu, H., 2000, Synthesis and characterization of dialkylgallium (dialkylindium) complexes of *N*-salicylidene 2-aminopyridine and *N*-salicylidene 2-methoxyaniline: Crystal structure of dimethyl[*N*-salicylidene 2-aminopyridine] gallium, *J. Organomet. Chem.*, 605 (2), 234–238.

[14] Chen, T.R., 2005, Luminescence and electroluminescence of bis (2-(benzimidazol-2-yl) quinolinato) zinc. Exciplex formation and energy transfer in mixed film of bis (2-(benzimidazol-2-yl) quinolinato) zinc and *N*,*N*′-bis-(1-naphthyl)-*N*,*N*′-diphenyl-1,1′-biphenyl-4,4′-diamine, *J. Mol. Struct.*, 737 (1), 35–41.

[15] Eltayeb, N.E., Teoh, S.G., Chantrapromma, S., Fun, H.K., and Adnan, R., 2008, Chlorido{5,5′-dimethoxy-2,2′-[1,2-phenylenebis(nitrilomethylidyne)]diphenolato-κ^4*O*,*N*,*N*′,*O*′}manganese(III), *Acta Crystallogr.,*

Sect. E: Struct. Rep. Online, 64, m670–m671.

[16] Eltayeb, N.E., Teoh, S.G., Chantrapromma, S., Fun, H.K., and Ibrahim, K., 2007, Chlorido{4,4'-dimethoxy -2,2'-[1,2-phenylenebis(nitrilomethylidyne)]dipheno lato}methanolmanganese(III), *Acta Crystallogr., Sect. E: Struct. Rep. Online*, 63 (12), m3193–m3194.

[17] Silverstein, R.M., Bassler, G.C., and Morrill, T.C., 1991, *Spectrometric Identification of Organic Compounds*, 5th Ed., John Wiley & Sons, Inc., Chichester, England.

[18] Biswas, S., Mitra, K., Schwalbe, C.H., Lucas, C.R., Chattopadhyay, S.K., and Adhikary, B., 2005, Synthesis and characterization of some Mn(II) and Mn(III) complexes of *N*,*N*′-*o*-phenylenebis(salicyli deneimine)(LH_2) and *N*,*N*′-*o*-phenylenebis(5-bromo salicylideneimine)($L'H_2$). Crystal structures of [Mn(L)(H_2O)(ClO_4)], [Mn(L)(NCS)] and an infinite linear chain of [Mn(L)(OAc)], *Inorg. Chim. Acta*, 358 (8), 2473–2481.

[19] Panja, A., Shaikh, N., Ali, M., Vojtíšek, P., and Banerjee, P., 2003, Structural characterization of a new manganese(III)–salen complex [H_2salen=*N*,*N*′-bis(salicylidene)ethane-1,2-diamine] and study of its electron transfer kinetics with hydroquinone and catechol, *Polyhedron*, 22 (9), 1191–1198.

[20] Maneiro, M., Bermejo, M.R., Sousa, A., Fondo, M., González, A.M., Sousa-Pedrares, A., and McAuliffe, C.A., 2000, Synthesis and structural characterisation of new manganese(II) and (III) complexes. Study of their photolytic and catalase activity and X-ray crystal structure of [Mn(3-OMe, 5-Br-*salpn*)(EtOH) (H_2O)]ClO_4, *Polyhedron*, 19 (1), 47–54.

[21] Asher, S., and Sauer, K., 1976, Resonance Raman spectroscopy of Mn(III) etioporphyrin I at the $\pi\rightarrow\pi^*$ and charge transfer bands: The use of charge transfer bands to monitor the complexation state of metalloporphyrins, *J. Chem. Phys.*, 64 (10), 4115.

[22] Guilbault, G.G., 1973, *Practical Fluorescence: Theory, Methods, and Techniques*, Marcel Dekker, Inc., New York.

Mathematical Modeling of Reactive Extraction of Solute from Slab Solid Material

Indah Hartati[1,2], Hary Sulistyo[1], Wahyudi Budi Sediawan[1,*], Muhammad Mufti Azis[1], and Moh Fahrurrozi[1]

[1]*Department of Chemical Engineering, Faculty of Engineering, Universitas Gadjah Mada, Jl. Grafika No. 2, Yogyakarta 55281, Indonesia*

[2]*Department of Chemical Engineering, Faculty of Engineering, Universitas Wahid Hasyim, Jl. Menoreh Tengah X No. 22, Semarang 50236, Central Java, Indonesia*

* ***Corresponding author:***

email: wbsediawan@ugm.ac.id

Received: July 1, 2019
Accepted: August 30, 2019

DOI: 10.22146/ijc.47181

Abstract: *Reactive extraction is gaining higher attention due its wide application in various solute separation processes. Here, a mathematical model of reactive extraction in slab has been proposed. The model was developed by considering simultaneous processes of active compound intra particle diffusion, second order elemental reaction of solute-active compound, and intra-particle product diffusion. The obtained partial differential equations (PDEs) were solved using Finite Difference Approximation (FDA) method by using realistic parameters. Concentration profile as well as product yield were evaluated as a function of time. As a result, the model proposed here may serve as a basis design for reactive extraction unit. Sensitivity analyses was conducted to inspect the influence of slab thickness, diffusivity and reaction rate constant to the product yield. Eventually, model validation was conducted by comparing the simulation results with analytical solutions for special cases. Validation results showed that the model gave good agreement with the analytical solution.*

Keywords: *mathematical modeling; reactive extraction; separation; slab; simulation*

■ INTRODUCTION

In recent years, reactive extraction has been shown as an attractive and promising technique for separation of various valuable solutes and for synthesis of various products. Its attractiveness is due to the combination of physical and chemical processes which may enhance the extraction yield of valuable solutes and products [1]. The combination of two processes leads to a higher solute distribution coefficient, a higher extraction efficiency, and allowing transport processes intensification by increasing mass transfer and chemical reactions rates [1-2]. Reactive extraction is also prized for its simplicity, technical accessibility, novelty, moderate conditions and possibility of utilization of green, cheap and efficient chemicals [3-4].

Reactive extraction has been studied and applied in various systems, either in liquid-liquid system [4], solid-fluid system [5] and gas-liquid-liquid system [6]. In practical terms, reactive extraction is commercially applied in separation of metals [7-8], separation of intermediates [9-10], separation of organic acids [11-12], separation of vitamins [13], separation of lignin [14-16], synthesis of biodiesel [17] and preparation of green oxidants such as hydrogen peroxide [6].

There have been numerous extensive fundamental studies focused on process optimization, kinetics, equilibrium and modeling of liquid-liquid reactive extraction processes[18-20]. Meanwhile, Lu et al. [6] investigated the kinetics aspects of gas-liquid-liquid reactive extraction process for hydrogen peroxide production. Moreover, in the case of solid-liquid reactive extraction processes, available literature that mainly focus on the development of a mathematical model for solid liquid reactive extraction is still limited. Hence, the aim of this paper was to develop a mathematical model of solid liquid reactive extraction to extract valuable solute from a slab solid material.

■ MODELING METHOD

By using chemical engineering principles, a mathematical model could be developed to improve scientific understanding related to the reactive extraction system behavior and to support the design of reactive extraction system for commercial purposes.

Model Development

The mathematical model of reactive extraction of solute from a slab material was developed based on mass balance equations, rate process and equilibrium concepts. The model was constructed by applying the following mechanisms and assumptions:

(i) The solid-liquid extraction of solute from slab material consists of the following consecutive steps:
   (a) $A_{(bulk\ liquid)} \rightarrow A_{(surface)}$: the active compound (A) is transferred from the bulk of liquid to the solid surface
   (b) $A_{(surface)} \rightarrow A_{(interior)}$: the active compound in solid surface diffuses to the inner part of the solid particle
   (c) A + B → C: the active compound reacts with the targeted solute B producing a soluble product C
   (d) $C_{(interior)} \rightarrow C_{(surface)}$: the product C diffuses from the interior part to the solid surface
   (e) $C_{(surface)} \rightarrow C_{(bulk\ liquid)}$: the product C is transferred to the bulk of the liquid.

   The concentration profile of A, B and C can be schematically illustrated as shown in Fig. 1.

(ii) Step (a) and (e) are fast enough, so they do not control the overall rate of the process and the solute concentrations in the liquid in contact with the slab surface and the one in the bulk are equal.

(iii) Diffusion of the active compound (A) and of the soluble product (C) in the solid particle follows Fick's type equation: $N_A = -D_{eA}.\frac{\partial C_A}{\partial x}$ and $N_C = -D_{eC}.\frac{\partial C_C}{\partial x}$, respectively

(iv) The rate of chemical reaction can be approximated by an elemental kinetics: $-rA = -rB = rC = k_r.C_A.C_B$

(v) The unreacted solute, B, is immobile in the solid.

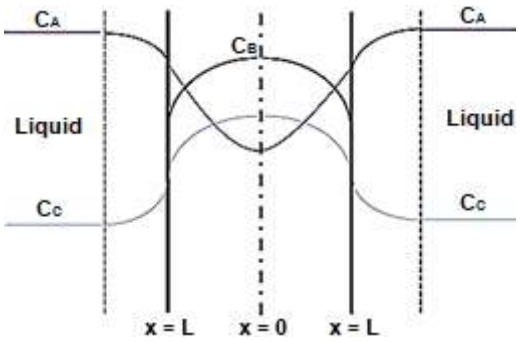

Fig 1. Schematic diagram of the concentration profile of the active compound (A), solute (B) and product (C)

The volume element in one dimensional simultaneous diffusion and chemical reaction simplified as shown in Fig. 2.

The unsteady state mole balance in axial direction of the active compound (A) in the solid volume element with the thickness of Δx and cross section area of S can be written as:

Rate of mass input – Rate of mass output = Rate of mass accumulation

$$\left(-D_{eA}\cdot S\cdot\left.\frac{\partial C_A}{\partial x}\right|_x\right)-\left(-D_{eA}\cdot S\cdot\left.\frac{\partial C_A}{\partial x}\right|_{x+\Delta x}\right)-S\cdot\Delta x\cdot k_r\cdot C_A C_B = S\cdot\Delta x\cdot\varepsilon\cdot\frac{\partial C_A}{\partial t} \quad (1)$$

In this case, the advection term is to be neglected because inside the particle, the liquid is practically stationary. After algebraic arrangement, it is obtained:

$$\lim_{\Delta x\to 0} D_{eA}\frac{\left.\frac{\partial C_A}{\partial x}\right|_{x+\Delta x}-\left.\frac{\partial C_A}{\partial x}\right|_x}{\Delta x}-k_r C_A C_B=\varepsilon\frac{\partial C_A}{\partial t} \quad (2)$$

If Δx is taken to be infinitely small, the following differential equation is formed:

$$\frac{\partial^2 C_A}{\partial x^2}-\frac{k_r\cdot C_A C_B}{D_{eA}}=\frac{\varepsilon}{D_{eA}}\frac{\partial C_A}{\partial t} \quad (3)$$

The mole balance of solute (B) in solid volume element was developed by assuming that the solute reacted

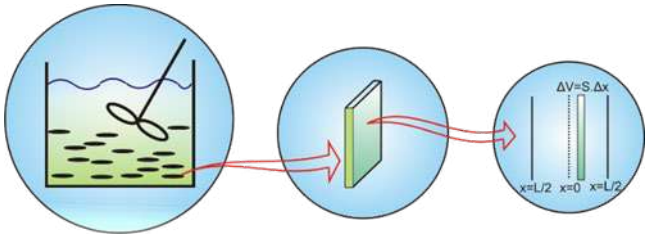

Fig 2. Schematic diagram of reactive extraction modeling in various scales

with the active compound (A) and produces a soluble product (C). In addition, the remaining solute is immobile thus the mass balance was arranged without considering the diffusion of B in the slab. Derivation of mass balance of B gives:

$$\frac{\partial C_B}{\partial t} = -\frac{k_r \cdot C_A C_B}{\varepsilon} \quad (4)$$

Construction of mole balance of product C was based on simultaneous internal diffusion and reaction in the solid. Similar to the mole balance of A, the mass balance for component C results in:

$$\frac{\partial^2 C_C}{\partial x^2} + \frac{k_r \cdot C_A C_B}{D_{eC}} = \frac{\varepsilon}{D_{eC}} \frac{\partial C_C}{\partial t} \quad (5)$$

The initial conditions for Eq. (3-5) are:

$$C_A(t=0,x)=0; C_B(t=0,x)=C_{B0}; C_C(t=0,x)=0 \quad (6)$$

The boundary conditions for Eq. (3-5), in which comprised of the boundary conditions at the outer surface of the slab (Eq. (7)) and the ones at the center of the slab (Eq. (8)) are:

$$C_A(t,x=\pm L/2)=C_{Af}; C_C(t,x=\pm L/2)=C_{Cf} \quad (7)$$

$$\frac{\partial C_A}{\partial x}(t,x=0)=0; \frac{\partial C_B}{\partial x}(t,x=0)=0; \frac{\partial C_c}{\partial x}(t,x=0)=0 \quad (8)$$

The mass balance of A in the liquid phase produces:

$$\frac{\partial C_{Af}}{\partial t} = -\frac{D_{eA}}{V_L} \cdot 2S \cdot Nb \cdot \left.\frac{\partial C_A}{\partial x}\right|_{L/2} \quad (9)$$

Similarly, it is obtained by the mass balance of component C that:

$$\frac{\partial C_{Cf}}{\partial t} = -\frac{D_{eC}}{V_L} \cdot 2S \cdot Nb \cdot \left.\frac{\partial C_C}{\partial x}\right|_{L/2} \quad (10)$$

Eq. (9-10) were solved based on the following initial conditions:

$$C_A(t=0)=C_{A0}; C_C(t=0)=0 \quad (11)$$

Simulation Method: Finite Difference Approximation and Method of Lines

The set of equations which represents the reactive extraction system was numerically solved using the FDA method. Due to the symmetrical system, Eq. (3-5) were solved only from x = 0 (at the center of the slab) to x = L/2 at the outer surface of the slab. For FDA computation, central finite difference approach was used to discretize the first and second order differential equation in axial direction. The results were displayed in a surface plot with color map showing the concentration in axial position and time.

Evaluation of the Conversion of B (X_B) and Yield of C

The concentration profile of B in the slab interior facilitates the evaluation of the conversion of B as a function of time. The overall conversion of B (X_B) was evaluated via integration of the total mass of B remaining in the solid. Similarly, the extraction yield of product C can also be computed as the ratio of the amount of C released into the liquid and the initial amount of B in the slab.

■ RESULTS AND DISCUSSION

Simulation Result of Base Case

One example of solid-liquid reactive extraction system is the separation of lignin from various biomass using sulfuric acid as the active compound. Hence, the proposed model was constructed and simulated by assuming that sulfuric acid acted as the active compound (A), lignin as the solute (B) and soluble lignin product as the reactive extraction product (C). In the case of lignin separation from lignocellulosic biomass, lignin is strongly bonded to the other two components that exist in the biomass, namely cellulose and hemicellulose, thus the unreacted lignin was assumed to be immobile.

The parameters for base case simulation of reactive extraction mathematical model are tabulated in Table 1, and the background for the parameters value set for the simulation are presented in this section. The dimension parameters of the slab material applied for the base case simulation were based on the dimension of the lignocellulose material, i.e. sugarcane bagasse, which is frequently utilized as raw material for the reactive

Table 1. Parameters for base case simulation of reactive extraction mathematical model

Parameter	Unit	Parameter	Unit
L = 0.4	cm	$D_{eC} = 1.10^{-4}$	cm^2/min
nx = 20	-	$D_{eA} = 2.10^{-4}$	cm^2/min
dx = L/(2.nx)	Cm	$k_r = 2.10^{-1}$	$cm^3/(mol.min)$
S = 4	cm^2	$C_{A0} = 0.1$	mol/cm^3
$V_L = 1.10^3$	cm^3	$C_{B0} = 0.2$	mol/cm^3
$N_b = 1.10^2$	-	$\varepsilon = 0.4$	-

extraction of lignin. Zhao et al. [21] stated that lignocellulose generally denotes to the secondary cell wall tissue of plants and that the shape of the sugarcane bagasse cell is simplified as a 3D cuboid with a slab shape cell wall. Sugarcane bagasse fiber length is reported to vary from 120 to 160 μm [22-23]. The thickness of the slab material in this simulation was set to 4 mm and the cross sectional area of the slab, perpendicular to the x-axis (cm^2), was 4 cm^2. The length of the slab was assumed to be equal to the width of the slab, hence the length of the slab was 2 cm. It is logical since the milling process usually produces bigger and longer dimensions of biomass compared to the fiber dimension. The aspect ratio (AR), which is defined as the dimensionless ratio between the length and the thickness of the particle [24], was 5. This is also a realistic assumption since according to particle classification based on its shape factors, particles are classified into several classes, in which one of the classes is rectangle fibrous which has AR higher than 3.3 [24]. The effective diffusivity of the active compound (D_{eA}) and the soluble product of reactive extraction (D_{eC}) used in the base case simulation were 2.10^{-4} cm^2/min and 1.10^{-4} cm^2/min, respectively. The effective diffusivity of the active compound value taken in this simulation was reasonable since it was smaller than the molecular diffusivity of the active compound in the liquid system commonly utilized in the reactive extraction [21]. In the case of lignin separation, sulphuric acid is one of the commercially active compounds commonly used in the reactive extraction of lignin. Since Pirogov et al. [25] mentioned that the effective diffusivity of sulphuric acid in aqueous solution is 2.04×10^{-2} cm^2/min and Zhao et al. [21] stated that the effective diffusivity of chemical compounds in solid systems are smaller than the one in the liquid system, then for this simulation, the effective diffusivity of the active compound D_{eA} which was set smaller than the effective diffusivity of sulphuric acid in aqueous system was realistic. Moreover, the effective diffusivity of the soluble product, D_{eC}, was set smaller than the effective diffusivity of the active compound. Li et al. [26] found that diffusivity of linear and globular molecules decrease with increasing molecular weight, in which the linear molecules decreasing rate is faster than the one of the globular molecules. In the case of the reactive extraction of lignin, the soluble product has high molecular weight and larger size than the active compound such as sulphuric acid. Lignin is reported to have molecular weight ranging from 2,330–21,500 g mol^{-1} depending on the biomass sources and the separation processes applied [27], while molecular weight of sulphuric acid is 98.08 g mol^{-1}. Furthermore, the reaction rate constant for the simulation of the reactive extraction of lignin using sulphuric acid as the active compound was set to 2×10^{-1} cm^3/(mol-min), six orders of magnitudes bigger than the reaction rate constant for lignin extraction reported by Zhao et al. in [21] which utilized acetic acid for the reactive extraction of lignin. It was reported that the reaction rate constant in the early stage of sugarcane bagasse lignin reactive extraction in acetic acid medium ranged from 2.64×10^{-6}–2.46×10^{-7} cm^3/(mol.min) for reactive extraction conducted at temperatures that ranged from 90 °C–100 °C and acetic acid concentration ranging from 70%–90% [21]. The high reaction rate constant applied in this work was logical since sulphuric acid is stronger than acetic acid.

The simulation results for the base case presented in Fig. 3 shows the color maps concentration of A, B, C as a function of the axial position (x-axis) and extraction time (y-axis). It should be noted that x = 0 and 0.2 denoted the center and the surface of the slab, respectively. Fig. 3(a) shows penetration of the active compound A from the exterior to the interior part of the slab along with extraction time. The presence of A in the slab caused reaction with solute B. As a result, the amount of B in the slab was depleted (Fig. 3(b)). In addition, the production of C can be seen clearly occurring simultaneously which showed 'hot spots' of concentration of C at the center of the slab within the interval of 50–150 min (Fig. 3(c)). With the increase of extraction time, product C would gradually release to the bulk liquid and cause the removal of compound C from the slab.

Evaluation of Conversion of B (X_B) and Yield C

Fig. 4 displays the results of X_B and Yield C as a function of time. As seen here, both X_B and Yield C increased with extraction time. However, the increase of X_B was faster than the Yield C. The slow increase of Yield C

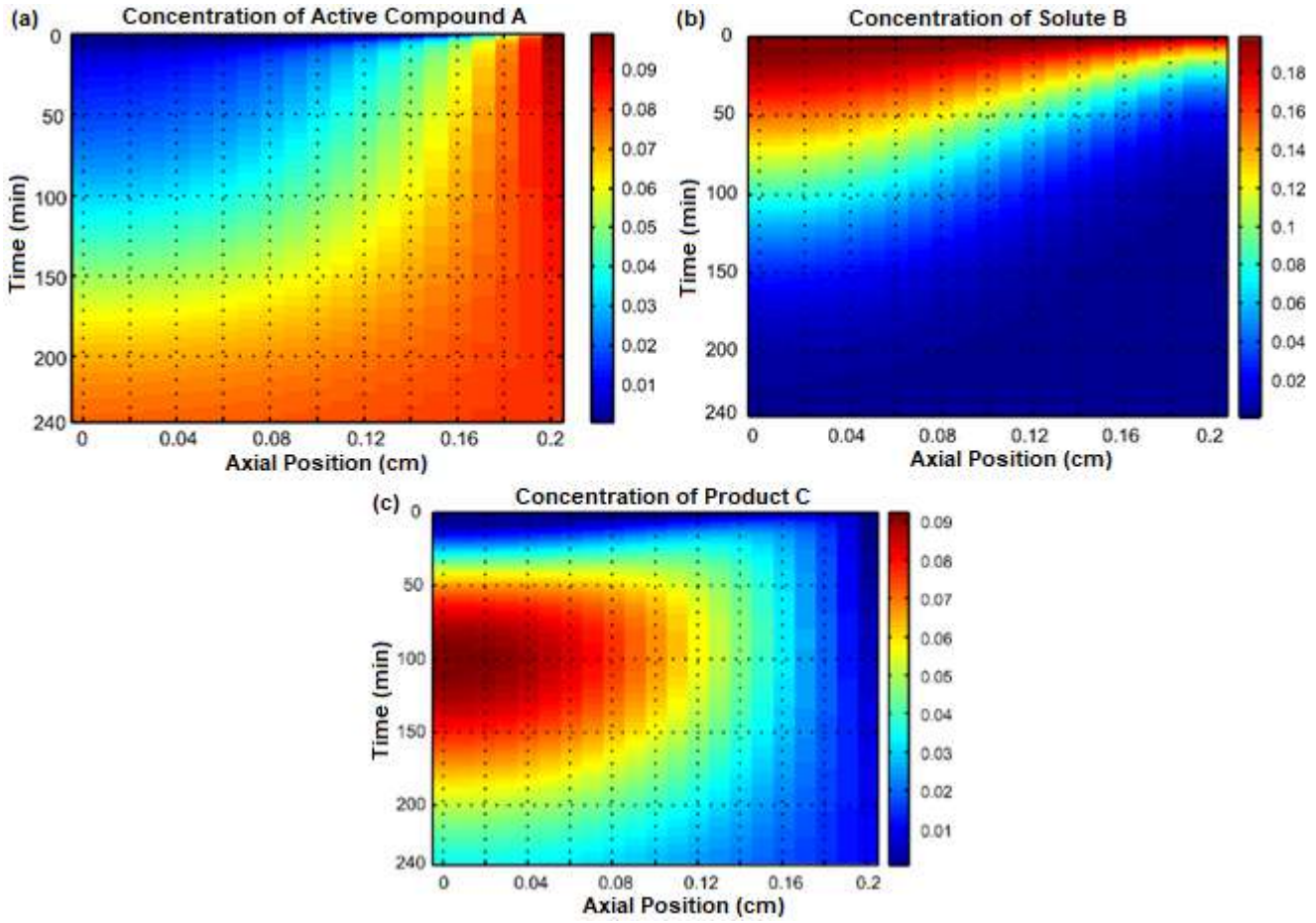

Fig 3. Concentration profile of A (a), B (b), C (c) in the slab interior as a function of time and position

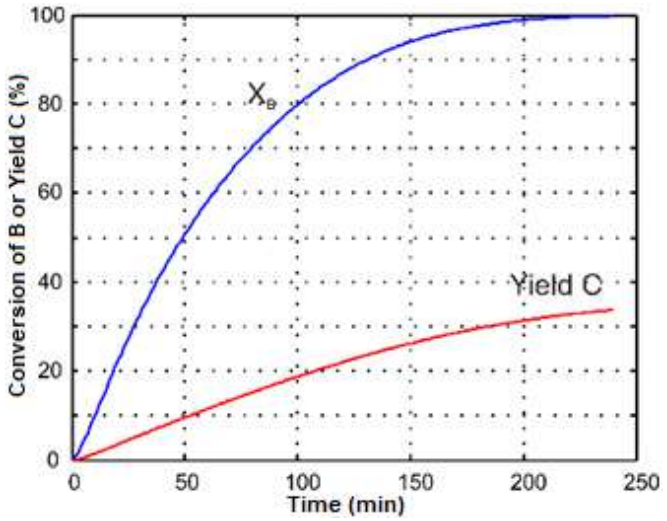

Fig 4. The evolution of X_B and Yield C as a function of extraction time

was conceivable due to internal mass transport resistance for product C in the slab. The effective diffusivity of the soluble product was smaller than the one of the active compound, hence some of the soluble products produced were entrapped in the pores of the slab particle and resulted in the slower rate of the increase of Yield C than the increase of X_B. Conversion of B as high as 99% was achieved at 207 min while the highest Yield of C was 33.7% at the end of 240 min.

Sensitivity Analyses

Sensitivity analyses, one of the essential aspect in good modeling practice, were performed to investigate how variations in the observable outcome of the mathematical model proposed can be attributed to variations in its input factors [28]. The sensitivity analysis was conducted to study the influence of slab thickness, effective diffusivity of A and the reaction rate constant to the yield of C in the liquid phase. The influence of each parameter was evaluated by systematically changing their

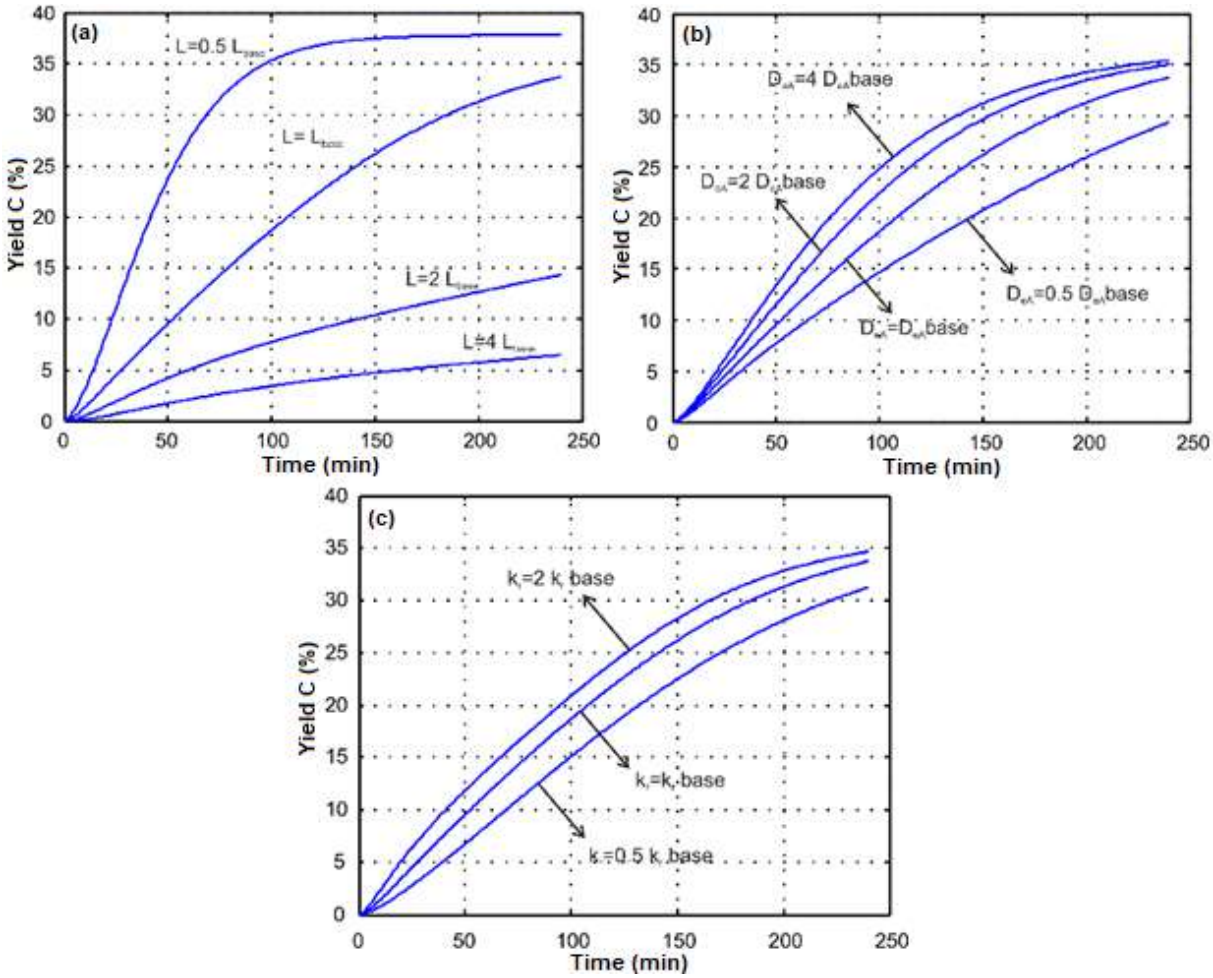

Fig 5. The influence of slab thickness (a), D_{eA} (b) and k_r (c) to the yield of C in the liquid phase

values using one of the local sensitivity analysis, One Factor at a Time (OFAT) method.

Fig. 5(a) shows the influence of slab thickness to the Yield C. As seen here, reducing the slab half from the base case would give an increase of Yield. On the contrary, a thicker slab would give lower yield. This is conceivable as the thicker the slab the higher the internal mass transfer resistance in the slab. The influence of D_{eA} was evaluated (Fig. 5(b)) to the yield of C. It appeared that higher D_{eA} gave higher Yield. However, increasing the D_{eA} from $2D_{eA}$ base to $4D_{eA}$ base gave marginal increase of the Yield. It could be inferred that when D_{eA} is high, the Thiele Module, a measure for the ratio of the reaction rate to the rate of diffusion, would be smaller [29]. Fogler [30] and Sulaiman et al. [17] mentioned that the small value of the Thiele Module indicates that the chemical reaction is rate-limiting, and as a result, the Yield of C would largely be controlled by the chemical reaction. Sensitivity of Yield to the reaction rate constant (k_r) is shown in Fig. 5(c). It is logical that increasing the k_r would give higher reaction rate and thus an increase of Yield C which was confirmed by the model.

Model Validation

The validation of the model was conducted by comparing the results of the proposed model to the analytical solution for special cases in which their analytical solutions are available.

Scenario 1: The case of very slow reaction and constant active compound concentration in the liquid

In the case of very slow reaction and constant active compound concentration in the liquid (by setting the volume of the liquid to be very large), the model proposed would exhibit similar phenomena as in the

pure absorption in a slab in which its analytical solution is widely available from literature. The differential equation of pure absorption is:

$$\frac{\partial^2 C_A}{\partial x^2} = \frac{\varepsilon}{D_{eA}} \frac{\partial C_A}{\partial t} \quad (12)$$

The initial condition and the boundary conditions of the problem are:

$$C_A = 0 \text{ for } t = 0 \text{ at all } x \quad (13)$$

$$C_A = C_{A0}, \text{at } x = L, \text{ all } t \quad (14a)$$

$$\frac{\partial C_A}{\partial x} = 0, \text{ at } x = 0, \text{ all } t \quad (14b)$$

$$C_A = C_{Af}, \text{at } t = \infty, \text{ all } x \quad (14c)$$

Solution method for Eq. (12) with the initial and boundary conditions of Eq.(13) and Eq. (14a-c) was found in a previous research [31], and the solution is as follows:

$$C_{A,anal} = C_{Af0}\left[1 - \frac{4}{\pi}\sum_{n=0}^{\infty}\frac{(-1)^n}{2n+1}\cos\left(\frac{(2n+1)\pi x}{2L}\right)\exp\left(-\frac{(2n+1)^2(\pi)^2 D_{eA} t}{4\varepsilon L^2}\right)\right] \quad (15)$$

For simulations of the pure absorption of A, we set a number of parameters as follows: half slab thickness of 0.4 cm, diffusivity of active compound in the solid particle (D_{eA}) of 2.10^{-4} cm^2/min, reaction rate constant of 1.10^{-6} cm^3/min-mol, time of extraction of 30 min by keeping other parameters the same as in the base case. The comparison of the numerical simulation using the reactive extraction model and the analytical solutions are presented in Fig. 6. It is clear that the model results are very close to the analytical solutions. This result shows that the model proposed for this special case is consistent.

Scenario 2: The case of very slow diffusivity or thick slab

For very thick slab or very slow diffusivity in the solid slab, which occurs at relatively short time, the penetration of the active compound will be limited to the vicinity of the slab surface. The analytical solution for this case is also available. The differential equation is similar to Eq. (12). Meanwhile the initial and boundary conditions are:

$$C_A = 0 \text{ for } t = 0 \text{ at } x \quad (16)$$

$$C_A = C_{Af} \text{ at } x = 0 \text{ all t; } C_A = 0 \text{ at } x = \infty \text{ all t} \quad (17)$$

in which x is the distance from the surface of the slab. The solution of Eq. (12) with boundary conditions of Eq. (16-17) is as follows [32]:

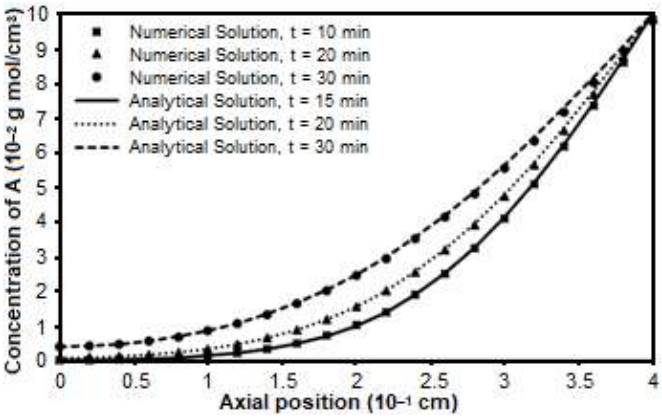

Fig 6. Comparison of analytical solutions and the ones from the model proposed for very slow reaction

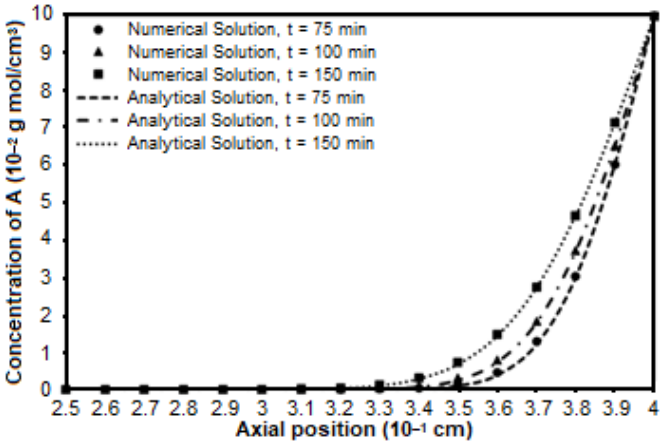

Fig 7. Comparison of analytical solutions and the ones from the model proposed for very slow diffusion and no reaction

$$C_{A,anal} = C_{Af0}\left[1 - \text{erf}\left(\frac{x\sqrt{\varepsilon}}{\sqrt{4D_{eA}t}}\right)\right] \quad (18)$$

Fig. 6 illustrates the comparison of the numerical simulation using the reactive extraction model and the analytical solutions for the simulations of short penetration of the active compound from the liquid to slab with half slab thickness of 0.4 cm, diffusivity of active compound in the solid particle (D_{eA}) of 1.10^{-6} cm^2/min, reaction rate constant of 1.10^{-6} cm^3/min/mol, time of extraction of 150 min, and the other model parameters were in accordance to the base case. The comparison of the results is presented in Fig. 7. It can be observed that the model results are very close to the analytical solutions. Hence, the consistency of the model is again confirmed.

■ CONCLUSION

Modeling of reactive extraction in a slab was presented in this study. Simultaneous PDEs were solved with the FDA method by using realistic parameters. The simulation results gave a concentration profile as well as product yield as a function of extraction time. It is expected that the model may give better understanding on the mechanism of reactive extraction and it may serve as a basis design for reactive extraction unit as well. Sensitivity analyses were conducted to inspect the influence of slab thickness, diffusivity and reaction rate constant to the product yield. Model validation was conducted by comparing numerical and analytical solutions for simple cases. The validation shows that the results of the proposed model are in good agreement with the analytical solutions for special cases.

■ ACKNOWLEDGMENTS

This work is supported by the Ministry of Research, Technology and Higher Education of Republic of Indonesia through PDUPT research grant of 2018, contract number of 118/UN1/DITLIT/DIT-LIT/LT/2018.

■ Nomenclature

C_A	concentration of active compound in the liquid in the pore of the solid (mol/cm^3)
C_{Af}	concentration of the active compound in the bulk of the liquid (mol/cm^3)
C_B	concentration of unreacted solute in the liquid in the pore of the solid (mol/cm^3)
C_C	concentration of reaction product in the liquid in the pore of the solid (mol/cm^3)
C_{Cf}	concentration of soluble product in the bulk of the liquid (mol/cm^3)
D_{eA}, D_{eC}	effective diffusivity of A and C, respectively (cm^2/min)
ε	slab porosity
k_r	reaction rate constant (cm^3/(mol-min))
L	slab thickness (cm)
N_b	the number of thin slabs
S	cross sectional of slab, perpendicular to x axis (cm^2)
V_L	volume of liquid (cm^3)

■ REFERENCES

[1] Sharma, S., Agarwal, G.K., and Dutta, N.N., 2019, LSER analysis of reactive extraction of Zn and Cu with bis (2-ethylhexyl) phosphate (HDEHP) in six different diluents, *Sep. Sci. Technol.*, 54 (7), 1167–1173.

[2] Zeng, Q., Qin, H., Cheng, H., Chen, L., and Qi, Z., 2019, Development of a reactive extraction process for isobutyl isobutyrate formation intensified by bifunctional ionic liquid, *Chem. Eng. Sci. X*, 1, 100001.

[3] Pradhan, S., Madankar, C.S., Mohanty, P., and Naik, S.N., 2012, Optimization of reactive extraction of castor seed to produce biodiesel using response surface methodology, *Fuel*, 97, 848–855.

[4] Santoso, I., Buchari, Amran, M.B., and Sulaeman, A., 2007, The effect of concentration of carrier, pH and time of extraction on separation's factor of penicillin G-phenyl acetate by reactive extraction, *Indones. J. Chem.*, 7 (2), 185–189.

[5] Tuntiwiwattanapun, N., and Tongcumpou, C., 2018, Sequential extraction and reactive extraction processing of spent coffee grounds: An alternative approach for pretreatment of biodiesel feedstocks and biodiesel production, *Ind. Crops Prod.*, 117, 359–365.

[6] Lu, S., Wang, L., Wang, Y., and Mi, Z., 2011, Kinetic model of gas-liquid-liquid reactive extraction for production of hydrogen peroxide, *Chem. Eng. Technol.*, 34 (5), 823–830.

[7] Chemarin, F., Moussa, M., Chadni, M., Pollet, B., Lieben, P., Allais, F., Trelea, I.C., and Athès, V., 2017, New insights in reactive extraction mechanisms of organic acids: An experimental approach for 3-hydroxypropionic acid extraction with tri-*n*-octylamine, *Sep. Purif. Technol.*, 179, 523–532.

[8] Lu, X., Zhang, D., He, S., Feng, J., Reda, A.T., Liu, C., Yang, Z., Shi, L., and Li, J., 2017, Reactive extraction of europium(III) and neodymium(III)

by carboxylic acid modified calixarene derivatives: Equilibrium, thermodynamics and kinetics, *Sep. Purif. Technol.*, 188, 250–259.

[9] Gorden, J., Zeiner, T., and Brandenbusch, C., 2015, Reactive extraction of *cis,cis*-muconic acid, *Fluid Phase Equilib.*, 393, 78–84.

[10] Waghmare, M.D., Wasewar, K.L., Sonawane, S.S., and Shende, D.Z., 2013, Reactive extraction of picolinic and nicotinic acid by natural non-toxic solvent, *Sep. Purif. Technol.*, 120, 296–303.

[11] Tang, K., Miao, J., Zhou, T., and Liu, Y., 2011, Equilibrium studies on liquid-liquid reactive extraction of phenylsuccinic acid enantiomers using hydrophilic β-CD derivatives extractants, *Chin. J. Chem. Eng.*, 19 (3), 397–403.

[12] Chemarin, F., Moussa, M., Allais, F., Athès, V., and Trelea, I.C., 2017, Mechanistic modeling and equilibrium prediction of the reactive extraction of organic acids with amines: A comparative study of two complexation-solvation models using 3-hydroxypropionic acid, *Sep. Purif. Technol.*, 189, 475–487.

[13] Blaga, A.C., and Malutan, T., 2012, Selective separation of vitamin C by reactive extraction, *J. Chem. Eng. Data*, 57 (2), 431–435.

[14] Salmi, T., Wärn, J., Mikkola, J.P., and Rönnholm, M., 2005, Modelling and simulation of porous, reactive particles in liquids: Delignification of wood, *Comput. Aided Chem. Eng.*, 20, 325–330.

[15] Bludworth, J., and Knopf, F.C., 1993, Reactive extraction of lignin from wood using supercritical ammonia-water mixtures, *J. Supercrit. Fluids*, 6 (4), 249–254.

[16] Constant, S., Basset, C., Dumas, C., Di Renzo, F., Robitzer, M., Barakat, A., and Quignard, F., 2015, Reactive organosolv lignin extraction from wheat straw: Influence of Lewis acid catalysts on structural and chemical properties of lignins, *Ind. Crops Prod.*, 65, 180–189.

[17] Sulaiman, S., Aziz, A.R.A., and Aroua, M.K., 2013, Reactive extraction of solid coconut waste to produce biodiesel, *J. Taiwan Inst. Chem. Eng.*, 44 (2), 233–238.

[18] Thakre, N., Datta, D., Prajapati, A.K., Chaudhari, P.K., and Pal, D., 2017, Reactive extraction of citric acid using different extractants: Equilibrium, kinetics and modeling, *Chem. Biochem. Eng. Q.*, 31 (4), 437–446.

[19] Eda, S., Borra, A., Parthasarathy, R., Bankupalli, S., Bhargava, S., and Thella, P.K., 2018, Recovery of levulinic acid by reactive extraction using tri-*n*-octylamine in methyl isobutyl ketone: Equilibrium and thermodynamic studies and optimization using Taguchi multivariate approach, *Sep. Purif. Technol.*, 197, 314–324.

[20] Bora, M.M., Ghosh, A.C., Dutta, N.N., and Mathur, R.K., 1997, Reactive extraction or 6-aminopenicillanic acid with aliquat-336: Equilibrium and kinetics, *Can. J. Chem. Eng.*, 75 (3), 520–526.

[21] Zhao, X., Wu, R., and Liu, D., 2018, Evaluation of the mass transfer effects on delignification kinetics of atmospheric acetic acid fractionation of sugarcane bagasse with a shrinking-layer model, *Bioresour. Technol.*, 261, 52–61.

[22] Hajiha, H., and Sain, M., 2015, "The use of sugarcane bagasse fibres as reinforcements in composites" in *Biofiber Reinforcements in Composite Materials*, Eds. Faruk, O., and Sain, M., Woodhead Publishing Company, Cambridge, 525–549.

[23] Hemmasi, A.H., Samariha, A., Tabei, A., Nemati, M., and Khakifirooz, A., 2011, Study of morphological and chemical composition of fibers from Iranian sugarcane bagasse, *Am. Eurasian J. Agric. Environ. Sci.*, 11 (4), 478–481.

[24] Gil, M., Teruel, E., and Arauzo, I., 2014, Analysis of standard sieving method for milled biomass through image processing. Effects of particle shape and size for poplar and corn stover, *Fuel*, 116, 328–340.

[25] Pirogov, B.Y., and Zelinskii, A.G., 2009, Mass transport and effective diffusion coefficient in the reduction of hydrogen ions from aqueous sulfuric acid solutions: Numerical modeling, *Russ. J. Electrochem.*, 45 (3), 336–344.

[26] Li, W., You, L., Schaffler, M.B., and Wang, L., 2009,

The dependency of solute diffusion on molecular weight and shape in intact bone, *Bone*, 45 (5), 1017–1023.

[27] Tolbert, A., Akinosho, H., Khunsupat, R., Naskar, A.K., and Ragauskas, A.J., 2014, Characterization and analysis of the molecular weight of lignin for biorefining studies, *Biofuels, Bioprod. Biorefin.*, 8 (6), 836–856.

[28] Pianosi, F., Beven, K., Freer, J., Hall, J.W., Rougier, J., Stephenson, D.B., and Wagener, T., 2016, Sensitivity analysis of environmental models: A systematic review with practical workflow, *Environ. Modell. Software*, 79, 214–232.

[29] Nan, H.S., Dias, M.M., Lopes, J.C.B., and Rodrigues, A.E., 1996, Diffusion, convection and reaction in catalyst particles: Analogy between slab and cylinder geometries, *Chem. Eng. J.*, 61 (2), 113–122.

[30] Fogler, H.S., 2016, *Elements of Chemical Reaction Engineering*, 5th Ed., Prentice Hall, New Jersey.

[31] Crank, J., 1975, *The Mathematics of Diffusion*, 2nd Ed., Clarendon Press, Oxford.

[32] Cussler, E.L., 2009, *Diffusion: Mass Transfer in Fluid Systems*, 3rd Ed., Cambridge University Press, Cambridge.

Supplementary Data

This supplementary data is a part of paper entitled "Chemical Literacy: Performance of First Year Chemistry Students on Chemical Kinetics".

APPENDIX. Example of Items and Their Contexts of MC-CLTI

READINGS MATERIAL FOR PROBLEMS NUMBER 1 - 8: BREAD DOUGH FERMENTATION

Bread dough is made from flour (starch), salt, yeast, butter, oil and water. To make it, all ingredients are mixed together and stirred to make it homogeneous. The dough is then put into a container and stored in a room at 25 °C for two hours. In this phase, yeast (fungi) converts some carbohydrates of flour (starch), such as glucose, into alcohol and carbon dioxide. This process is called alcoholic fermentation. The simplified of alcoholic fermentation reactions can be symbolized by the equation:

$$\mathbf{C_6H_{12}O_6}(s) \rightarrow \mathbf{2\ CO_2}(g) + \mathbf{2\ CH_3CH_2OH}(l)$$

Glucose carbon dioxide alcohol

25. Bread dough is made from flour, salt, yeast, butter, oil and water. Explain, what makes the volume of the mixture expand?

A. Fermentation produces gases whose particles volume are greater than the particles volume of solids and liquids
B. Fermentation produces ethanol so that the mass of the dough increases
C. Fermentation produces gas which causes a hollow dough
D. Fermentation causes the ingredients of the dough to be arranged so that the volume expands
E. Yeast binds substances in the air so that the size of the dough expands

5. Glucose ($C_6H_{12}O_6$) can be obtained from the hydrolysis of sugar sucrose ($C_{12}H_{22}O_{11}$) using a hydrochloric acid catalyst. In simple terms, the reaction equation can be written:

$$C_{12}H_{22}O_{11}(aq) + H_2O(l) \xrightarrow{HCl} 2\ C_6H_{12}O_6(aq)$$

Glucose water sugar

An experiment on the relationship between the initial concentration of the reactants and the initial rate of the reaction provides the following data:

Experiment Number	Initial Concentration (M)		Initial Rate ($M\ s^{-1}$)
	[HCl]	$[C_{12}H_{22}O_{11}]$	
1	0,010	0,010	0,024
2	0,010	0,015	0,036
3	0,020	0,010	0,048

According to the data, what is the law of the rate of sucrose sugar hydrolysis?

A. $r = k\ [C_{12}H_{22}O_{11}][HCl]$
B. $r = k\ [C_{12}H_{22}O_{11}]^2[HCl]$
C. $r = k\ [C_{12}H_{22}O_{11}][HCl]^2$
D. $r = k\ [C_{12}H_{22}O_{11}][H_2O]$

E. $r = k [HCl][H_2O]$

8. To find out the effect of HCl concentration on the rate of sugar hydrolysis, a group of students made the concentration of sugar $[C_{12}H_{22}O_{11}]$ as a control variable. Why do they make concentration $[C_{12}H_{22}O_{11}]$ as a control variable? Explain!

   A. The sugar concentration also influences the concentration of HCl added to the reaction mixture
   B. The sugar concentration also affects the reaction rate
   C. The sugar concentration does not affect the concentration of HCl added to the reaction mixture
   D. The sugar concentration does not affect the reaction rate
   E. The sugar concentration also affects the concentration of HCl added to the reaction mixture and reaction rate

READINGS MATERIAL FOR PROBLEMS NUMBER 9 – 15: CARBON DIOXIDE IN LIFE

Carbon dioxide (CO_2) is a colorless gas whose density is 53% higher than dry air. At low concentrations this gas is odorless, while at high concentrations smells sharp and sour. Carbon dioxide is widely used as an inert gas in fire engine, supercritical solvents in the manufacture of low caffeine coffee, chemical process raw materials, carbonated beverage making materials, and as a refrigerant. The main source of carbon dioxide is combustion, organism respiration, fermentation, and acidification of limestone. Limestone reacts with hydrochloric acid according to the equation:

$$\mathbf{CaCO_3}(s) + 2\ \mathbf{HCl}(aq) \rightarrow \mathbf{CaCl_2}(aq) + \mathbf{H_2O}(l) + \mathbf{CO_2}(g)$$

9. A group of students intends to conduct research on the effect of surface area on the rate of reaction $CaCO_3$ and HCl (see the equation of reaction in the reading material). If the research is carried out at a fixed pressure, which variable must be controlled?

   A. Mass of $CaCO_3$
   B. Volume of H_2O and CO_2
   C. Volume of CO_2
   D. Volume of H_2O
   E. Size of granules of $CaCO_3$

10. Note the equation of $CaCO_3$ and HCl reaction in the text above. You are asked to do research with the question, "How does the reactant surface area affect the reaction rate?"

    Which component do you choose as an independent variable?

    A. Concentration of HCl
    B. Particle size of $CaCO_3$ granules
    C. Volume of CO_2
    D. Concentration of $CaCl_2$
    E. Mass of $CaCO_3$

11. For reaction: $CaCO_3(s) + 2\ HCl(aq) \rightarrow CaCl_2(aq) + H_2O(l) + CO_2(g)$
What magnitude should be measured to answer the question, "How does the effect of the reactant surface area on the reaction rate?"

    A. Concentration of HCl
    B. Mass of $CaCO_3$
    C. Volume of CO_2
    D. Volume of H_2O and CO_2
    E. Time of reaction

12. The results of a research showed that the higher concentration of reactants was the higher rate of reaction. How is the claim explained?

    A. The higher concentration of reactants, the greater volume of reaction, the faster rate of reaction
    B. The higher concentration of reactants, the wider touch area of the reaction, the faster rate of reaction
    C. The higher concentration of reactants, the higher temperature of reaction, the higher frequency of collision, the faster rate of reaction
    D. The higher concentration of reactants, the greater particle size of HCl, the easier the particles collide, the faster rate of reaction
    E. The higher concentration of reactants, the greater frequency of collision, the higher rate of reaction

13. Based on the findings of an investigation "the higher temperature of reaction the higher rate of the reaction", a group of students explained:

    "The increase of reaction temperature increases the frequency of collisions of reactant particles so that the reaction rate also increases."

    Evaluate the explanation!

    A. True, the higher the temperature, the particles of reactants having similar properties are close to each other, the higher frequency of collision
    B. True, the higher temperature, the higher kinetic energy of the particle, the higher the effective collision frequency producing reaction
    C. True, the higher temperature, the higher activation energy of reaction, the higher frequency of collisions of reactant particles, the higher rate of reaction
    D. False, even though the reaction temperature is increased but if it does not reach the activation energy, the reaction rate will also not increase
    E. False, even though the reaction temperature is increased but if the collision frequency does not rise, the reaction rate will also not increase

15. Based on literature search, a student found a graph of carbon dioxide emissions into the atmosphere and changes in atmospheric temperature in the period 1860 s.d. 1990 as follows:

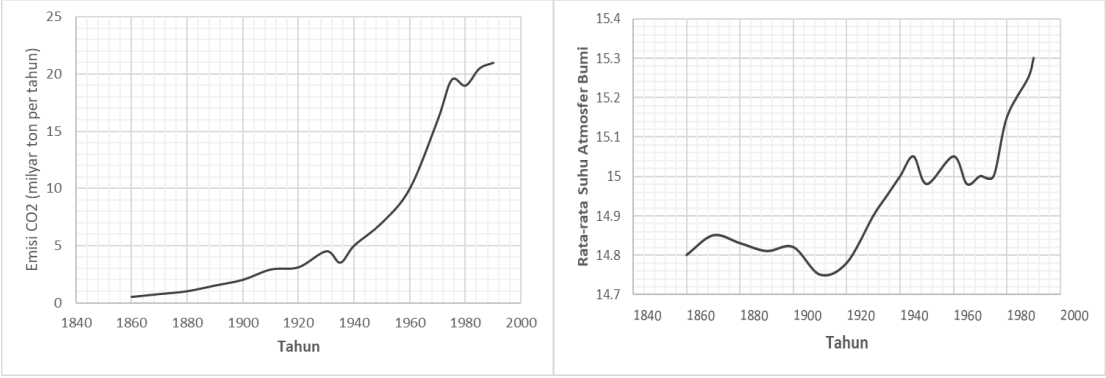

Based on the two graphs above a student confidently concluded that the increase in the average temperature of the Earth's atmosphere was caused by an increase in carbon dioxide gas emissions.

Is the conclusion in accordance with the available data? Explain!

A. It is appropriate, because the average carbon dioxide emissions into and the average temperature of atmosphere in 1990 are higher than in 1860B.
B. It is appropriate, because the average carbon dioxide emissions into and the average temperature of atmosphere are measured in the same timeframes
C. It is appropriate, because the both of data describe the atmospheric conditions, namely the mass of carbon dioxide gas emitted into the atmosphere and atmospheric temperature
D. It is not appropriate, the increase in carbon dioxide emissions into the atmosphere is not always followed by an increase in atmospheric temperature
E. It is not appropriate, because the related variables are not similar, carbon dioxide is a chemical in the form of gases while the atmosphere temperature reflects the kinetic energy of air

READING MATERIAL FOR PROBLEMS NUMBER 16 – 23: H_2O_2 AND ASEPTIC TECHNOLOGY

Through decades of observation and investigation, scientists finally found a food packaging technology involving no preservatives. The technology was known as aseptic technology. This technology can preserve food and drinks more than 6 months without damage. The principle of this technology is the manufacture of sterile packaged foods (free from destructive microbes), both the food, the packaging, and the packaging processes.

The packaging sterilization process involves a solution of 30% of hydrogen peroxide (H_2O_2) ~~30%~~. At 70 °C, H_2O_2 sterilizes material in six seconds. This compound kills microbes by oxidizing the materials composing of the microbial tissue.

Mammalian bodies also contain H_2O_2 as a byproduct of metabolism. This compound is toxic but easily decomposes according to the equation:

$$2\ H_2O_2(aq) \rightarrow 2\ H_2O(l) + O_2(g)$$

In the body this decomposition is catalyzed by the catalase enzyme, whereas in the laboratory is carried out by iodide (I^-) ion.

16. You are asked to find out the answer of the question:

"What is the effect of the reactant concentration on the rate of hydrogen peroxide decomposition carried out using iodide ions as catalyst?"

How do you make a design of the investigation?

A. Putting $[H_2O_2]$ and $[I^-]$ as independent variables
B. Placing $[H_2O_2]$ and $[I^-]$ as independent variables, and $[H_2O]$ and $[O_2]$ as dependent variables
C. Putting $[H_2O_2]$ and $[I^-]$ as independent variables and the rate of reaction as the dependent variable
D. Placing $[I^-]$ as a control variable
E. Placing $[I^-]$, temperature and pressure as control variables

17. What data are needed to answer the question "What is the effect of reactant concentration on rate of hydrogen peroxide decomposition catalyzed by iodide ions"?

A. Variation in concentration of $[H_2O_2]$ and $[I^-]$
B. Variation in concentration of $[H_2O]$ and volume of O_2
C. Variation in concentration of $[H_2O_2]$ and volume of O_2
D. Variation in concentration of $[H_2O_2]$ and time of reaction
E. Variation in concentration of $[H_2O]$ and time of reaction

18. If all control variables are controlled, what data do you need to answer the question:

"What is the effect of catalyst concentration of $[I^-]$ on the rate of hydrogen peroxide decomposition?"

A. Concentration of H_2O_2 and time of reaction
B. Concentration of H_2O_2 and the rate of reaction
C. Concentration of I^- and time of reaction
D. Concentration of I^- and the rate of reaction
E. Concentration of H_2O_2 and I^- and the rate of reaction

19. The results showed that the higher the concentration of the **I^-** catalyst the shorter the time of decomposition of H_2O_2.

What does the conclusion mean?

A. The higher concentration of catalyst, the higher rate of reaction, regardless of the concentration of reactants and the conditions of reaction
B. The higher the concentration of catalyst, the higher the rate of reaction, regardless of the concentration of reactants and the conditions of reaction
C. At a certain reactant concentration, the higher concentration of catalyst the higher rate of reaction
D. Under a certain reaction conditions, the higher concentration of catalyst the higher rate of reaction
E. At a certain concentration of reactants and the conditions of reaction, the higher concentration of catalyst the higher rate of reaction

20. The decomposition of hydrogen peroxide is estimated to occur in two stages following ~~to~~ the mechanism of:

Stage I (fast) : $H_2O_2 + I^- \rightarrow H_2O + IO^-$
Stage II (slow) : $H_2O_2 + IO^- \rightarrow H_2O + O_2 + I^-$

Based on the mechanism, what is the rate of the reaction law?

A. $r = k[H_2O_2]^2$
B. $r = k[H_2O_2][I^-]$
C. $r = k[H_2O_2][IO^-]$

D. $r = k[I^-][IO^-]$
E. $r = k[H_2O_2]^2[I^-][IO^-]$

21. According to the hydrogen peroxide decomposition mechanism (see problem number 20), which of the following species acts as an intermediate?

A. H_2O_2 D. I^-
B. H_2O E. IO^-
C. I^- and IO^-

22. A company promotes the benefits of hydrogen peroxide for food products as follows:

- sterilizes packaging
- cleans food products from sulfur dioxide and chlorine residues
- can be used as food bleaching
- can be used as microbial activating compounds in cheese making
- can be used as an oxidizer in drying of egg whites

Which of these scientific evidences below supports the claim that hydrogen peroxide is a useful compound?

A. decomposes at room temperature
B. available in the market
C. a strong reducing agent
D. decomposes into environmentally friendly water and oxygen
E. killing bacteria

23. Which of the following statements is a theory?

A. The higher temperature of reaction, the higher decomposition rate of hydrogen peroxide
B. Reactions only occur when the reacting particles collide with one another with sufficient energy and appropriate orientation
C. The higher the concentration of reactants, the lower the rate of reaction
D. Chemical reaction can be observed from the formation of gas, changes in color, formation of sediments and changes in temperature
E. Reactions of gases can be observed from changes in pressure

READING MATERIAL FOR PROBLEMS NUMBER 24 – 30: CATALYTIC CONVERTER CONTROLS EMISSION OF CAR EXHAUST POLLUTANT

Air pollution has become a global problem. About 92% of the world's population lives in areas with air pollution above the threshold determined by the WHO. Some air pollutants such as SO_2, NO_x, and CO come from burning fossil fuels that occur inside motor car engines. To reduce exhaust emissions of air pollutants, scientists construct a catalytic converter, a device that is installed between the engine and the exhaust of motor cars. This device contains a catalyst for catalytic reaction of the toxic exhaust gases to non-toxic compounds. In air, nitrogen oxide (NO, N_2O_5) reacts according to the equation:

$2\ NO(g) + O_2(g) \rightarrow 2\ NO_2(g)$; $2\ N_2O_5(g) \rightarrow 4\ NO_2(g) + O_2(g)$

Whereas carbon monoxide (CO) follows the equation:

$2\ CO(g) + O_2(g) \rightarrow 2\ CO_2(g)$

24. The following three submicroscopic representations represent the mixture of reaction between NO gas (black marbles) and O_2 gas (gray marbles).

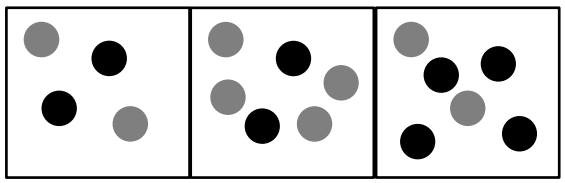

(A) **(B)** **(C)**

If the ratio of reaction rate of mixture (A):(B):(C) is 1:2:4, what is the total reaction order of NO_2 formation from NO and O_2?

A. 1
B. 3
C. 5
D. 2
E. 4

25. In accordance with the submicroscopic representation of NO and O_2 gases (see problem number 24), what factors influence the rate of that reaction?

A. Pressure
B. Catalyst
C. Kind of substances
D. Temperature
E. Surface area

26. Investigations about the effect of using the "Catalytic Converter" inside of motor car exhausts on CO gas emissions carried out in various engine speed provide the following data:

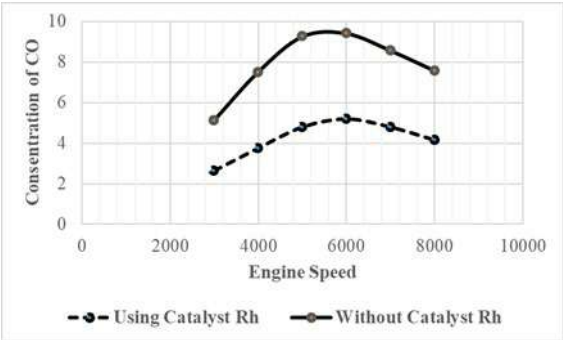

Which does of the following claims correspond to those data?

A. The higher the engine speed, the higher the CO concentration in the exhaust gas
B. The higher the engine speed, the lower the CO concentration in the exhaust gas
C. Catalytic converters are not effective in reducing CO concentrations in the flue gas
D. Catalytic converters reduce CO concentration in the flue gas
E. The catalytic converter does not affect the CO gas concentration in the exhaust gas

28. You are asked to answer the question: "Which is more effective in reducing pollutants contained in the exhaust gas of motor vehicles, platinum converter or rhodium converter?"

Which of the following research designs do you choose?

A. Take three different types of cars; the first type was installed with a platinum converter, the second type was installed with a rhodium converter, and the third type was not installed with a catalytic converter. Measurement of exhaust emissions is carried out at the same engine speed.
B. Take three different types of cars; the first type was installed with a platinum converter, the second type was installed with a rhodium converter, and the third type was not installed with a catalytic converter. The measurement of exhaust emissions is carried out at different engine speed.
C. Take the same three cars; The first is a platinum converter, the second is a rhodium converter, and the third is not installed with a catalytic converter. The measurement of exhaust emissions is carried out at the same engine speed.
D. Take the same three cars; The first is a platinum converter, the second is a rhodium converter, and the third is not installed with a catalytic converter. The measurement of exhaust emissions is carried out at different engine speed.
E. Take the same three cars; The first is a platinum converter, the second is a rhodium converter, and the third is not installed with a catalytic converter. The measurement of exhaust emissions is carried out for three different types of fuel.

29. N_2O_5 can be broken down according to the equation:

$$2\ N_2O_5(g) \rightarrow 4\ NO_2(g) + O_2(g)$$

A student found that the rate of N_2O_5 decomposition can be determined by two ways, i.e., the initial rate of reaction way and the concentration as a function of time way. Both of the ways can be used to determine the reaction order.

Based on this information, what do you think about the scientific method?

A. The scientific method actually does not exist. Always can be used to find knowledge
B. There is only one scientific method that can be used to find scientific knowledge
C. The scientific method is diverse, all the ways that can be used to find scientific knowledge are scientific methods
D. The same scientific knowledge can be obtained using different scientific methods
E. Determination of the order of N_2O_5 gas decomposition reaction can be done using two methods

30. Pay your attention to the equation of decomposition reaction of N_2O_5 gas as shown in number 29. If the initial concentration of N_2O_5 is 0.620 M, what is its concentration after 3 half-life periods?

A. 0,0825 M
B. 0,3100 M
C. 0,1030 M
D. 0,0775 M
E. 0,2070 M